nanomaterials

Advanced Materials and Technologies in Nanogenerators

Edited by
Zhen Wen, Hengyu Guo and Longfei Wang

Printed Edition of the Special Issue Published in *Nanomaterials*

www.mdpi.com/journal/nanomaterials

MDPI

Advanced Materials and Technologies in Nanogenerators

Advanced Materials and Technologies in Nanogenerators

Editors

Zhen Wen
Hengyu Guo
Longfei Wang

MDPI • Basel • Beijing • Wuhan • Barcelona • Belgrade • Manchester • Tokyo • Cluj • Tianjin

Editors

Zhen Wen
Institute of Functional Nano Soft Materials (FUNSOM)
Soochow University
Suzhou
China

Hengyu Guo
Department of Physics
Chongqing University
Chongqing
China

Longfei Wang
Beijing Institute of Nanoenergy and Nanosystems
Chinese Academy of Sciences
Beijing
China

Editorial Office
MDPI
St. Alban-Anlage 66
4052 Basel, Switzerland

This is a reprint of articles from the Special Issue published online in the open access journal *Nanomaterials* (ISSN 2079-4991) (available at: www.mdpi.com/journal/nanomaterials/special_issues/_nanogenerators).

For citation purposes, cite each article independently as indicated on the article page online and as indicated below:

LastName, A.A.; LastName, B.B.; LastName, C.C. Article Title. *Journal Name* **Year**, *Volume Number*, Page Range.

ISBN 978-3-0365-5902-5 (Hbk)
ISBN 978-3-0365-5901-8 (PDF)

Contents

About the Editors

Zhen Wen

Prof. Zhen Wen received his B.S. degree in Materials Science and Engineering from China University of Mining and Technology (CUMT) in 2011 and his Ph.D. degree in Materials Physics and Chemistry from Zhejiang University (ZJU) in 2016. During 2014–2016, he was supported by the program of China Scholarship Council (CSC) as a joint Ph.D. student at Georgia Institute of Technology (GT). Now, he is a full professor at Institute of Functional Nano & Soft Materials (FUNSOM), Soochow University. His main research interests focus on triboelectric nanogenerator-based energy harvesting and self-powered sensing systems.

Hengyu Guo

Prof. Hengyu Guo received his B.S. and Ph.D. degrees in Applied Physics from Chongqing University, China. Then, he worked as a postdoctoral fellow in Zhong Lin Wang's group, Georgia Institute of Technology, US. Now, he is a professor in the Department of Physics, Chongqing University, China. His current research interest is triboelectric nanogenerator-based energy and sensors.

Longfei Wang

Prof. Longfei Wang received his B.S. (2012) in Materials Science and Engineering from China University of Geosciences (Be) and his Ph.D. (2017) in Nanoscience and Technology from BeInstitute of Nanoenergy and Nanosystems, Chinese Academy of Sciences. Then, he worked as a postdoctoral fellow in Professor Zhong Lin Wang's group at Georgia Institute of Technology. Now, he is a professor of BeInstitute of Nanoenergy and Nanosystems. His current research focuses on piezotronics and flexoelectronics.

nanomaterials

MDPI

Editorial

Editorial for Special Issue: Advanced Materials and Technologies in Nanogenerators

Zhen Wen [1,*], Hengyu Guo [2] and Longfei Wang [3]

[1] Institute of Functional Nano and Soft Materials (FUNSOM), Soochow University, Suzhou 215123, China
[2] Department of Physics, Chongqing University, Chongqing 401331, China
[3] Beijing Institute of Nanoenergy and Nanosystems, Chinese Academy of Sciences, Beijing 101400, China
* Correspondence: wenzhen2011@suda.edu.cn

Citation: Wen, Z.; Guo, H.; Wang, L. Editorial for Special Issue: Advanced Materials and Technologies in Nanogenerators. *Nanomaterials* **2022**, *12*, 3606. https://doi.org/10.3390/nano12203606

Received: 10 October 2022
Accepted: 12 October 2022
Published: 14 October 2022

Nanogenerators, based on Maxwell's displacement current as the driving force, have inspired a new and developing field since their invention in 2006. In less than 20 years, nanogenerators have rapidly developed into a research hotspot in the field of energy harvesting and self-powered sensing. Based on new technologies and nanomaterials, nanogenerators can efficiently harvest and store energy from the environment for the sustainable operation of micro systems. This lays the foundation for the popularization of their broad applications in energy science, environmental protection, wearable electronics, self-powered sensors, medical science, robotics, and artificial intelligence. The Special Issue 'Advanced Materials and Technologies in Nanogenerators' selected 12 articles, including 9 original research articles and 3 reviews, to show the current applications and future evolution of nanogenerators.

Marcos Duque and Gonzalo Murillo [1] reported a triboelectric nanogenerator (TENG) that can harvest mechanical energy by manual tapping. In order to create a high-performance TENG, the authors improved the charge density by correctly selecting materials, designing new spacers, and charging high-voltage corona for charge injection. This kind of TENG can provide a sustainable power supply for miniature electronic sensors.

Yuan et al. [2] proposed a high-performance coniform Helmholtz resonator-based TENG for efficiently harvesting acoustic energy. The novel design in the CHR-TENG can improve its output performance and broaden its response band over harvesting acoustic energy. With the optimized design, the maximum acoustic sensitivity per unit area of the CHR-TENG can reach 1.68 V/Pa·m^2, while the power density per unit of sound pressure is 2.88 W/Pa·m^2, obtaining a 58.2% improvement over previously reported results. In addition, the CHR-TENG was demonstrated to charge a 1000 μF capacitor up to 3 V in 165 s, power a sensor for continuous temperature and humidity monitoring, and light up as many as 464 commercial LED bulbs for acoustic energy harvesting.

Shi et al. [3] described a system that activates O_2 via the direct modulation of its spin state by mechanical energy-induced triboelectric corona plasma, enabling a CO oxidation reaction under normal temperature and pressure. Under optimized reaction conditions, the activity was 7.2 μmol h^{-1}, and the energy consumption per mole CO was 4.2 MJ. The results of kinetic isotope effect, colorimetry, and density functional theory calculation studies demonstrated that electrons generated in the triboelectric plasma were directly injected into the antibonding orbital of O_2 to form highly reactive negative O_2^- ions, which effectively promoted the rate-limiting step of O_2 dissociation. The barrier of the reaction of O_2^- ions and molecular CO was 3.4 eV lower than that of O_2 and molecular CO. This work provides an effective strategy for using renewable and green mechanical energy to realize spin-forbidden reactions of small molecules.

Wan et al. [4] constructed a self-powered magnetic sensor based on a subtle triboelectric nanogenerator that consists of a magnetorheological elastomer (MRE). This magnetic sensor relies on triboelectrification and electrostatic induction to produce electrical signals in

response to the MRE's deformation induced by the variational magnetic field without using any external power sources. The fabricated magnetic sensor showed a fast response of 80 ms and a desirable sensitivity of 31.6 mV/mT in a magnetic field range of 35–60 mT as well as preliminary vectorability enabled by the multichannel layout. Their work provides a new route for monitoring dynamic magnetic fields and paves the way for self-powered electric–magnetic coupled applications.

Zhang et al. [5] proposed a triboelectric technology-based all-in-one self-powered HMI (Human–Machine Interaction) system. The hydrogel-based triboelectric nanogenerator harvests mechanical energy from the human body and provides power for the whole system. Gesture sensing signals are wirelessly transmitted to the intelligent car for remote telemetry and control. This technology expands the application potential of wearable devices integrated in self-powered HMI systems.

Ding et al. [6] reported a new triboelectric nanogenerator based on sodium chloride powder (S-TENG) to obtain mechanical energy. The polytetrafluoroethylene (PTFE) film and sodium chloride powder layer serve as the triboelectric pair. After testing and calculation, the internal resistance of S-TENG was 30 MΩ, and the output power of S-TENG could arrive at about 403.3 μW. Furthermore, the S-TENG can achieve an open-circuit voltage (Voc) of 198 V and a short-circuit current (Isc) of 6.66 μA, respectively. Moreover, owing to the moisture absorption of sodium chloride powder, the S-TENG device also has the function of a humidity sensor. This work proposed a functional TENG device, and it can promote the advancement of self-powered sensors based on the TENG devices.

Wang et al. [7] introduced a highly conductive organogel ion conductor that acts as a self-powered sensor. The addition of small-molecular-weight lithium salt resulted in a conductivity of up to 9.1×10^{-4} S·cm^{-1} and the organogel exhibited excellent temperature stability in the temperature range of −70 to 100 °C. This gel-based piezoelectric sensor provides a stable energy output under pressure and can withstand long-term durability tests.

Liu et al. [8] reported a framework for monitoring the evolutionary path of nanogenerator technology based on the Sentence-BERT and phrase-mining methods. The method combines both scientific and technological dimensions to analyze technological evolution in the field of nanogenerators through an improved theme-evolution modeling approach (SKT) with multi-source text vectorization.

Liu et al. [9] proposed a novel framework to monitor the evolutionary pathways of nanogenerator technology based on multi-source data and a knowledge graph. In the framework, the knowledge graph makes full use of text information, and the multi-source data fully considers the evolutionary pathways from different data perspectives. While analyzing the evolution pathways of some developed nanogenerator technologies, this research finds several emerging research directions for nanogenerators, such as novel energy sources and fiber structure of nanogenerators.

Li et al. [10] reviewed the recent research progress of rare earth metal-modified metal halide perovskite materials and their corresponding optoelectronic devices. First of all, Ln^{3+} ions made up the deficiency of utilization for solar spectrum by perovskite materials. In addition, Ln^{3+} ions were used as dopants to improve device performance. Finally, Ln^{3+} ions were also used in the fields of photodetectors and solar luminescent concentrators. It indicates the huge potential of rare-earth metals in improving the performances of the perovskite optoelectronic devices.

The review authored by Cao et al. [11] discussed the latest technical issues and prospects of TENG in fluid dynamics sensing. The authors introduced the advantages and key problems of TENG applied in fluid dynamics sensing, which has attracted more scholars' attention. This review analyzed the principles of the TENG and illustrated the feasibility and advantages of using the TENG as a fluid dynamics sensor for local fluid phenomena and environments. The authors summarized the recent works of the TENG as a fluid dynamics sensor and help guide the future direction of the TENG in fluid dynamics sensing.

Si et al. [12] summarized the working mode and basic theory of TENGs. Then, the authors reviewed the applications of TENGs in AR, VR, and other wearable electronic devices. In addition, this paper also summarized the design methods of TENGs as self-powered sensor modules in these devices. Finally, the authors analyzed and proposed future application areas.

In summary, this Special Issue discusses the wide applications, new materials, and evolution in the field of nanogenerators. I hope these articles will be beneficial for readers in future research and more new creations will be submitted to this journal.

Funding: This research received no external funding.

Acknowledgments: We are grateful to all the authors who contributed to this Special Issue. We also express our acknowledgments to the referees for reviewing the manuscripts. Special thanks go to the team at MDPI for their great support and assistance during the making of this special issue.

Conflicts of Interest: The authors declare no conflict of interest.

References

1. Duque, M.; Murillo, G. Tapping-Actuated Triboelectric Nanogenerator with Surface Charge Density Optimization for Human Motion Energy Harvesting. *Nanomaterials* **2022**, *12*, 3271. [CrossRef]
2. Yuan, H.; Yu, H.; Liu, X.; Zhao, H.; Zhang, Y.; Xi, Z.; Zhang, Q.; Liu, L.; Lin, Y.; Pan, X.; et al. A High-Performance Coniform Helmholtz Resonator-Based Triboelectric Nanogenerator for Acoustic Energy Harvesting. *Nanomaterials* **2021**, *11*, 3431. [CrossRef] [PubMed]
3. Shi, X.; Li, S.; Zhang, B.; Wang, J.; Xiang, X.; Zhu, Y.; Zhao, K.; Shang, W.; Gu, G.; Guo, J.; et al. The Regulation of O_2 Spin State and Direct Oxidation of CO at Room Temperature Using Triboelectric Plasma by Harvesting Mechanical Energy. *Nanomaterials* **2021**, *11*, 3408. [CrossRef] [PubMed]
4. Wan, D.; Ma, N.; Zhao, T.; Cui, X.; Wang, Z.; Zhang, H.; Zhuo, K. Magnetorheological Elastomer-Based Self-Powered Triboelectric Nanosensor for Monitoring Magnetic Field. *Nanomaterials* **2021**, *11*, 2815. [CrossRef] [PubMed]
5. Zhang, T.; Xie, L.; Li, J.; Huang, Z.; Lei, H.; Liu, Y.; Wen, Z.; Xie, Y.; Sun, X. All-in-One Self-Powered Human–Machine Interaction System for Wireless Remote Telemetry and Control of Intelligent Cars. *Nanomaterials* **2021**, *11*, 2711. [CrossRef] [PubMed]
6. Ding, Z.; Zou, M.; Yao, P.; Zhu, Z.; Fan, L. A Triboelectric Nanogenerator Based on Sodium Chloride Powder for Self-Powered Humidity Sensor. *Nanomaterials* **2021**, *11*, 2657. [CrossRef] [PubMed]
7. Wang, L.; Wang, Z.; Li, Y.; Luo, Y.; Lu, B.; Gao, Y.; Yu, W.; Gao, G.; Ding, S. An Ionically Conductive, Self-Powered and Stable Organogel for Pressure Sensing. *Nanomaterials* **2022**, *12*, 714. [CrossRef] [PubMed]
8. Liu, H.; Zhang, R.; Liu, Y.; He, C. Unveiling Evolutionary Path of Nanogenerator Technology: A Novel Method Based on Sentence-BERT. *Nanomaterials* **2022**, *12*, 2018. [CrossRef] [PubMed]
9. Liu, Y.; Wang, G.; Zhou, Y.; Liu, Y. Advanced Technology Evolution Pathways of Nanogenerators: A Novel Framework Based on Multi-Source Data and Knowledge Graph. *Nanomaterials* **2022**, *12*, 838. [CrossRef] [PubMed]
10. Li, B.; Tian, F.; Cui, X.; Xiang, B.; Zhao, H.; Zhang, H.; Wang, D.; Li, J.; Wang, X.; Fang, X.; et al. Review for Rare-Earth-Modified Perovskite Materials and Optoelectronic Applications. *Nanomaterials* **2022**, *12*, 1773. [CrossRef] [PubMed]
11. Cao, L.N.Y.; Xu, Z.; Wang, Z.L. Application of Triboelectric Nanogenerator in Fluid Dynamics Sensing: Past and Future. *Nanomaterials* **2022**, *12*, 3261. [CrossRef]
12. Si, J.; Duan, R.; Zhang, M.; Liu, X. Recent Progress Regarding Materials and Structures of Triboelectric Nanogenerators for AR and VR. *Nanomaterials* **2022**, *12*, 1385. [CrossRef] [PubMed]

nanomaterials

MDPI

Article

Tapping-Actuated Triboelectric Nanogenerator with Surface Charge Density Optimization for Human Motion Energy Harvesting

Marcos Duque and Gonzalo Murillo *

Department of Nano and Microsystems, Instituto de Microelectrónica de Barcelona (IMB-CNM, CSIC), 08193 Bellaterra, Spain
* Correspondence: gonzalo.murillo@csic.es

Abstract: In this article, triboelectric effect has been used to harvest mechanical energy from human motion and convert it into electrical energy. To do so, different ways of optimizing the energy generated have been studied through the correct selection of materials, the design of new spacers to improve the contact surface area, and charge injection by high-voltage corona charging to increase the charge density of dielectric materials. Finally, a triboelectric nanogenerator (TENG) has been manufactured, which is capable of collecting the mechanical energy of the force applied by hand tapping and using it to power miniaturized electronic sensors in a self-sufficient and sustainable way. This work shows the theoretical concept and simulations of the proposed TENG device, as well as the experimental work carried out.

Keywords: energy harvesting; triboelectricity; triboelectric nanogenerator; TENG; contact-separation mode; corona charging; IoT

Citation: Duque, M.; Murillo, G. Tapping-Actuated Triboelectric Nanogenerator with Surface Charge Density Optimization for Human Motion Energy Harvesting. *Nanomaterials* **2022**, *12*, 3271. https://doi.org/10.3390/nano12193271

Academic Editors: Zhen Wen, Hengyu Guo and Longfei Wang

Received: 29 July 2022
Accepted: 15 September 2022
Published: 20 September 2022

1. Introduction

The triboelectric effect, also called contact electrification, has been known for thousands of years and implies that when two different materials come into contact, charges will be transferred from one material to the other, depending on their respective electron affinity [1]. Due to its inherent characteristics, the triboelectric effect can cause extremely high voltages. Traditionally, it has been considered a negative effect, especially in the electronics industry, due to the damage that it can cause to integrated circuits. In 2012, triboelectric nanogenerators (TENGs) were invented to take advantage of this previously negative effect and use it for energy harvesting [2,3].

Due to the great advancement of technology and telecommunications, the interest in the Internet of things (IoT) is increasing rapidly [4]. This concept allows the interconnection of thousands of wireless sensors to capture environmental information and make decisions without human interaction. Nevertheless, these sensors must be powered, and this is a major drawback due to their dependence on batteries. An alternative to avoid the use of batteries is to harvest ambient energy and convert it into electricity.

A lot of attention has been dedicated to the use of TENGs for energy harvesting, as they have been shown to be an easy and low-cost way of converting mechanical energy into electricity. This mechanical energy is produced by many sources such as ambient vibrations [5–7], magnetic fields [8,9], human motion [10–17], wind [18–20], water [21], waves [22,23], vibration by moving vehicles [24,25] and time-limited and random vibrations [26–28]. This widely distributed and collected ambient mechanical energy can be used to supply low-power electronic sensors in a self-sufficient way and can be used for common IoT applications for predictive maintenance, system sensing, or the measurement of environmental parameters.

As shown in Figure 1, there are four basic working modes to operate a TENG [29]. Contact-separation mode uses polarization in the vertical direction, so the system energy is increased when the electrodes separate, which corresponds to the decrease in the capacitance in a parallel-plate capacitor. Lateral-sliding mode uses polarization in the lateral direction because of the relative slip between the two materials. The material friction creates the charge separation, as well as a capacitance change. Single-electrode mode harvests energy from a freely moving surface without opposite electrode. Free-standing mode is designed for power generation by electrostatic induction between a pair of electrodes, due to the presence of a sliding charge structure. In many cases, two or more modes can work together.

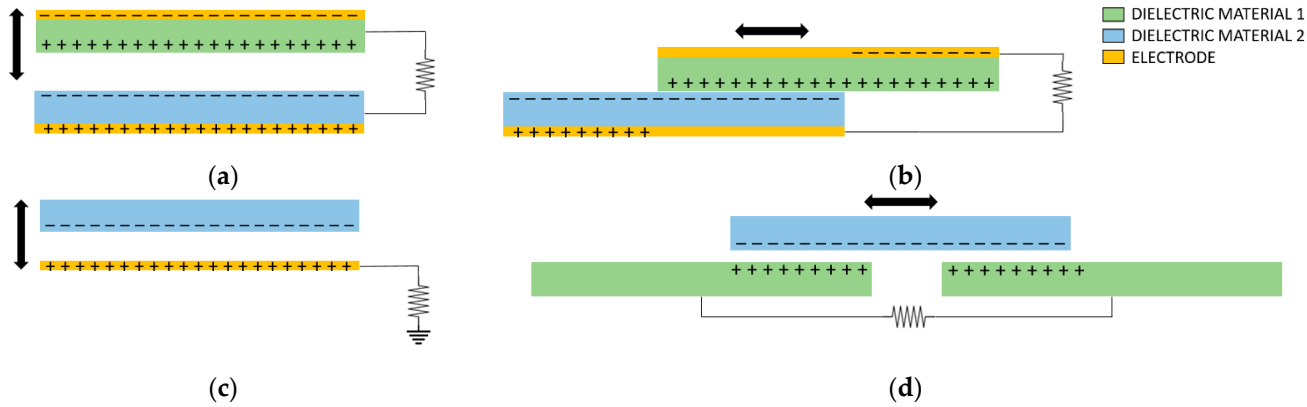

Figure 1. Four basic modes of work of a TENG: (**a**) vertical contact-separation mode; (**b**) lateral-sliding mode; (**c**) single-electrode mode; (**d**) free-standing mode.

Contact-separation mode is the one used in our work. This mode requires an external force for the triboelectric material and the electrode to come into contact, to later separate the contact surfaces. This subsequent separation is usually carried out by means of springs, a spacer, or the deformation of the material itself. The use of additional spacers, by means of gaskets [30,31], sponges [32,33], and springs [34,35] or the general deformation of the substrate such as an arched shape [36,37] or triangle prisms [38], increases the cost of the TENG due to greater manufacturing complexity. In addition, many spacers require a greater expansion of the deformation area.

Previous works have proposed a TENG with an etched pattern spacer [39]. This design etches different patterns into the substrate and folds them into small spacers that are evenly distributed on the contact surface. This system presents problems in the generation of energy, due to the fact that there is always a contact between the top electrode and the triboelectric material and, thus, a deficiency in the work area contact. Here, in this work, a system using an engraving pattern in the outer zone of the contact surface of the materials is presented.

Voltage and current outputs of TENGs are proportional to the triboelectric charge density on the contact surfaces. Therefore, a key approach to improve the TENG output performance is to increase the triboelectric charge density through the correct choice of utilized materials, e.g., [40–42]. That is, by choosing materials with a higher electron transfer capacity after contact electrification, a higher energy generation will be achieved. Surface modification enlarges the surface area, such as: nanoparticles self-assembly [35], pyramid patterns from photolithographic patterning [36], and surface dry-etched polymer nanowires [43,44]. Structure optimization maximizes the contact area, such as: cylindrical rotating TENG with multiple-layer integration [45] or an advanced PCB composite disk-structure TENG with narrow gratings [46] and the use of a specific power management circuit named Bennet's doubler to maximize energy efficiency [47]. However, further improvements in performance are needed to be able to supply low-power electronic sensors in a self-sufficient and sustainable way.

Due to the intrinsic properties of dielectric materials to almost permanently retain large amounts of charge (known as electret), the surface charge density of dielectric films can be increased several times by charge injection. Charge injection methods include ionized-air injection, plasma polarization, high-voltage corona charging, and electron beam bombardment [48,49]. High voltage corona charging is the simplest, cheapest, and most widely used process in industrial manufacturing.

In this work, research on the triboelectric materials with the highest intrinsic surface charge density and lowest cost is carried out. Furthermore, a study on the increase in charge injection of different triboelectric materials, by means of high-voltage corona charging, is performed. In addition, an adaptation of a triboelectric generator with engraved pattern spacers is proposed for the improvement of the contact area and its subsequent fabrication. In order to validate the measurements obtained after the injection of charge, a finite element modeling (FEM) has been carried out using COMSOL Multiphysics. Finally, an example of an application is shown, where the mechanical energy from hand tapping is collected and used to power a group of 30 light emitting diodes (LEDs).

2. Experimental Section

2.1. Study of Triboelectric Materials

The selection process of the materials to be studied is based on numerous works reporting triboelectric series [41,42]. For this case, materials with the highest intrinsic surface charge density have been chosen, also taking into account the material cost. These selected materials are polytetrafluoroethylene (PTFE), polyamide (Kapton), polyether ether ketone (PEEK), and biaxially oriented polyethylene terephthalate (BoPET, Mylar).

The open-circuit voltage V_{oc} of a *TENG* can be expressed as [50]:

$$V_{OC}(TENG) = \frac{\sigma\, x(t)}{\varepsilon_0}\,, \tag{1}$$

where σ is the surface triboelectric charge density between the electrification materials, ε_0 is the vacuum permittivity and is the separation distance.

For the characterization of these materials, we integrated different triboelectric materials in a test platform (10 cm × 10 cm) made of PMMA with four metal guides and four springs to retract both surfaces after touching. The triboelectric material and the copper layers are disposed of in between the PMMA structure faces. Different samples of the triboelectric material, 5 cm × 5 cm in size and 50 μm thick, have been used. As shown in Figure 2a, two copper electrodes and a single dielectric material are used (contact separation mode). Periodically, the top electrode separates after getting in contact with the dielectric surface to effect charge transfer. In order to carry out the electrical measurements, a characterization setup has been assembled (Figure 2b,c) consisting of a stepper motor (Zaber LSQ075B-T3-MC03 and X-MCB1-KX13B), a dynamometer (Mark M5i and MR03-20 sensor for a maximum force of 100 N), a sourcemeter (Keithley 2470), and a LabVIEW program that controls the entire electrical characterization setup.

For the characterization of the materials, the linear motor produces a vertical motion to make physical contact between the material and the top electrode. A force of 50 N, which is approximately the force generated by a human footstep, is applied. Figure 3 shows the different triboelectric materials and the average generated voltages. As observed, voltages ranging from −35 V to −57 V can be achieved with a single piece of material. All the measurements were performed with three samples of each type (n = 3). For all the tests, the measured ambient temperature and relative humidity were around 30 °C and 20%, respectively.

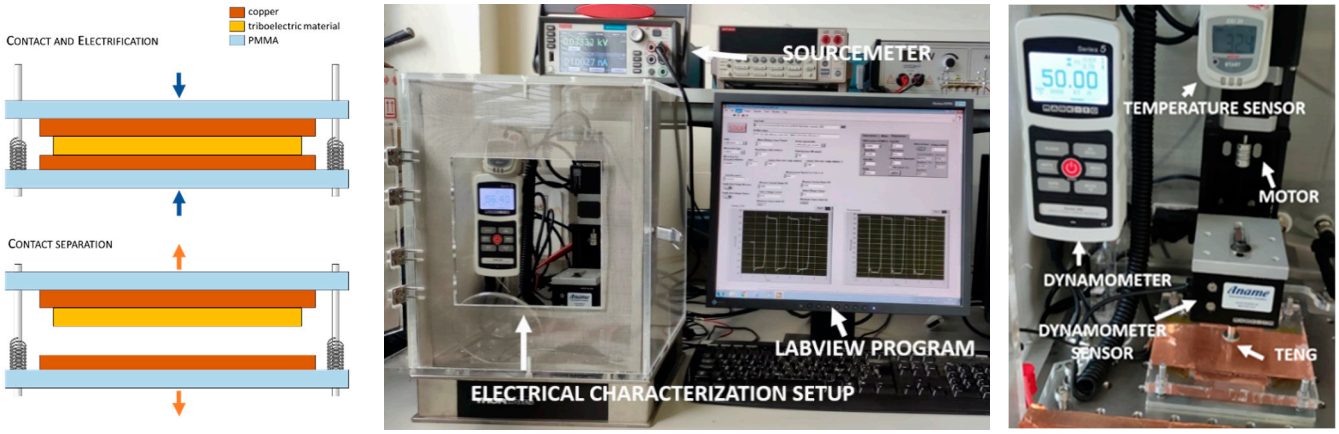

(**a**) (**b**) (**c**)

Figure 2. (**a**) Schematic of material and electrode used for the characterization of the materials; (**b**,**c**) ad hoc setup for electromechanical characterization of triboelectric devices.

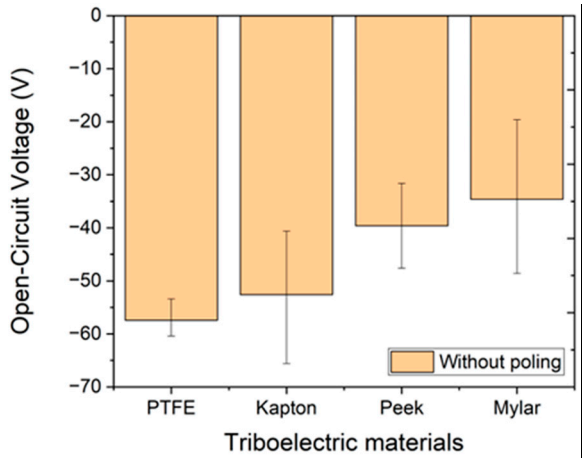

Figure 3. Comparison of voltages generated for the different material samples.

2.2. Surface Charging Process

To increase the surface charge density of dielectric films, as already mentioned above, charge injection is performed by high-voltage corona charging. To do so, as shown in Figure 4a, a PCB with multiple metal tips was designed and manufactured. Using a high-voltage source (Frederiksen 3670.60), a high voltage is applied to the multi-tip electrode. The current flows from the high-potential multi-tip electrode to the ground plane, through the air, by ionizing and creating a region of plasma around the needles. The ions eventually pass the charge to lower potential areas of the dielectric material. In order to clarify this process, Figure 4b shows the schematic of the injection process discussed above.

Firstly, to study the optimum voltage and time to be applied to the corona, PTFE has been chosen as the material, since it is the material that generates the highest output voltage for an applied force. A voltage sweep is performed from 1000 V to 6000 V, with a gradual increase of 1000 V. Figure 5a shows the open-circuit voltage that the material can generate with an electrode separation of 5 mm. The greater the voltage applied to the corona, the greater the increase in charge density of the material.

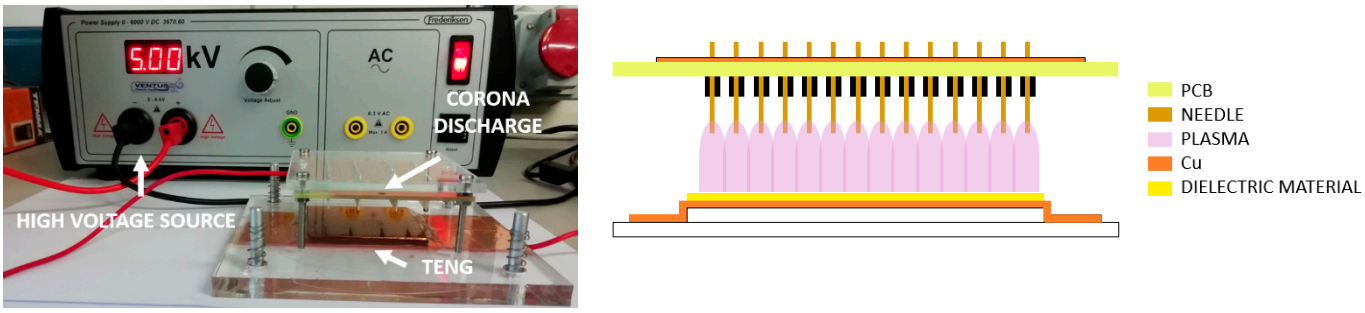

(**a**) (**b**)

Figure 4. (**a**) Charge injection setup using high voltage corona charging; (**b**) schematic of the process of charge injection by corona.

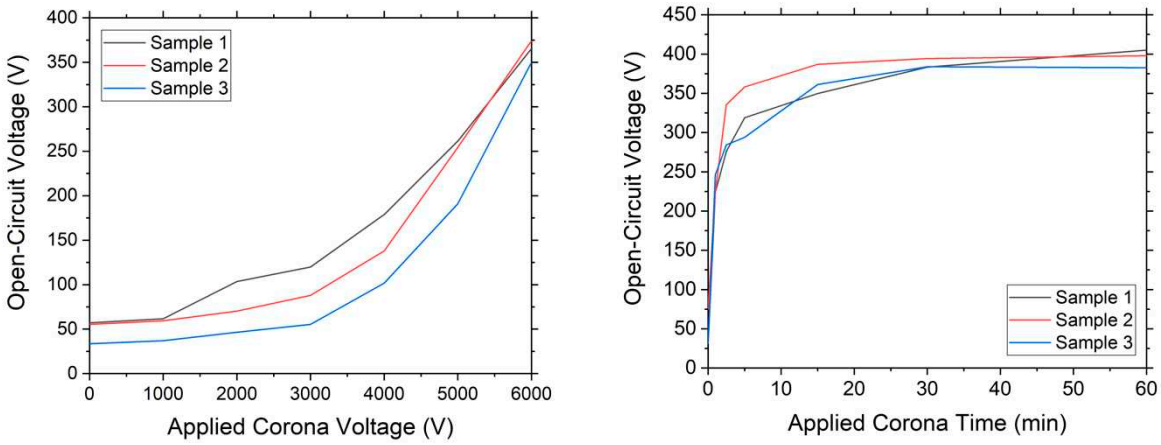

(**a**) (**b**)

Figure 5. (**a**) Graph of the generated open-circuit voltage as a function of the voltage applied to the corona discharge; (**b**) graph of the open-circuit voltage that can be generated by the material as a function of the injection time with a constant corona discharge voltage of 6000 V.

For a constant voltage of 6000 V applied to the corona discharge, we performed a study on how long it takes to achieve the maximum surface charge. As can be seen in Figure 5b, after 15 min of application time, the maximum voltage generated stabilizes, and, therefore, the maximum surface charge density that the material can support is reached.

Although the humidity and temperature were monitored during the charging process, it can be very sensitive to tiny changes in these parameters, air pressure, or surface cleanness. All the parameters and samples were identical; however, a variability can be observed from one to another. The best future solution to increase reproducibility is to have a specific chamber with a specific gas at controlled pressure and temperature.

Finally, the charge injection is carried out by applying a constant voltage of 6000 V and a period of 15 min. In the Figure 6a, it can be seen how the materials with the lowest intrinsic charge density, such as PEEK and Mylar, are now the ones with the highest surface charge density and, therefore, the ones that generate the highest maximum voltage.

Concerning the permanent effect of this polarization, the surface charge density is limited by the breakdown of the electric field in the air. This ion-injection method is an effective way to increase the output power by up to 25 times. This has been proven to be stable over 5 months and 400,000 continuous operation cycles [51]. In our case, as shown in Figure 6b, after 1500 cycles, the voltage drops 6%, and, after 2500 cycles, it drops 12%. Finally, after 2500 cycles, the voltage remains stable.

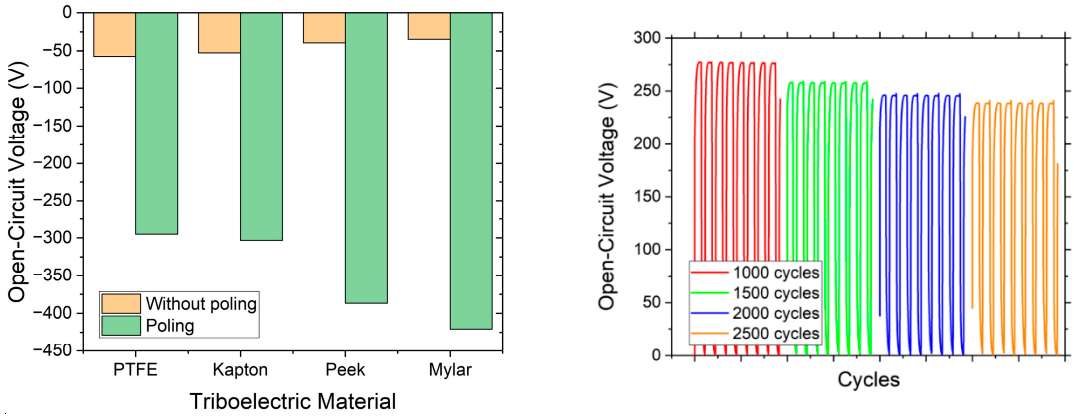

(**a**) (**b**)

Figure 6. (**a**) Comparison of voltages generated with the different samples of polarized materials for 15 min and a voltage of 6000 V; (**b**) measurements of eight contact cycles for each material to validate the permanent effect of polarization.

2.3. Finite Element Modeling

TENG devices have been simulated with COMSOL Multiphysics to compare the results of the electrical characterization with a theoretical model. The used module for this simulation is AC/DC Module (Electrostatics). The 2D model built in COMSOL consists of a box air (20 cm × 20 cm), the triboelectric material, and the copper electrodes, one is defined as ground and the other as floating potential. A specific surface charge density calculated by using Equation (1) has been assigned to the surface of the triboelectric material.

The model is created using a fine triangular mesh. The mesh contains more than 50,000 elements. Figure 7a shows the electric potential generated by the Mylar sample, with distance of 5 mm between the electrodes. Figure 7b,c show the output open-circuit voltage for different triboelectric materials without and with corona charging respectively. As seen, the simulated results are in agreement with the electrical measurements.

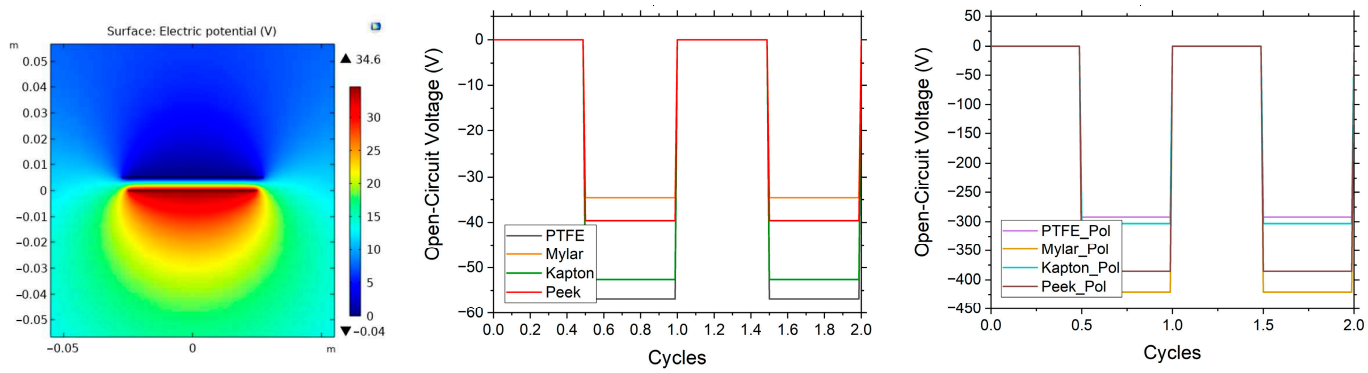

(**a**) (**b**) (**c**)

Figure 7. (**a**) Electric potential (in volts) generated by the Mylar sample with an electrode separation of 5 mm. (**b**,**c**) Open-circuit voltage for different triboelectric materials without and with corona charging, respectively.

2.4. Fabrication of the Prototype

Figure 8a,b show the schematic and operating scheme of the TENG device based on contact separation mode. The specific working process in divided into three steps. In the first step, the spacers are flattered by the impact force so that the copper electrode fully contacts the dielectric film. Here, copper is used as the tribometallic material and top electrode. Due to the significant difference in the electronic affinity of the two materials, net

positive charges are generated on the surface of the copper layer, and equal net negative charges are left on the surface of the dielectric film. Second, the spacers return to their original folded state due to their inherent elastic force, until the maximum vertical distance is reached. This conducts free electrons from the bottom copper electrode of the dielectric film to the top copper electrode through an external circuit to compensate for the potential difference between the two electrodes. Finally, the spacers are pressed again under another external mechanical impact, the top electrode and dielectric film are fully in contact again, and free electrons will flow from the top electrode through the external charge back to the bottom electrode. The previous three steps of the TENG formed a complete and repeatable cycle of electrical power generation.

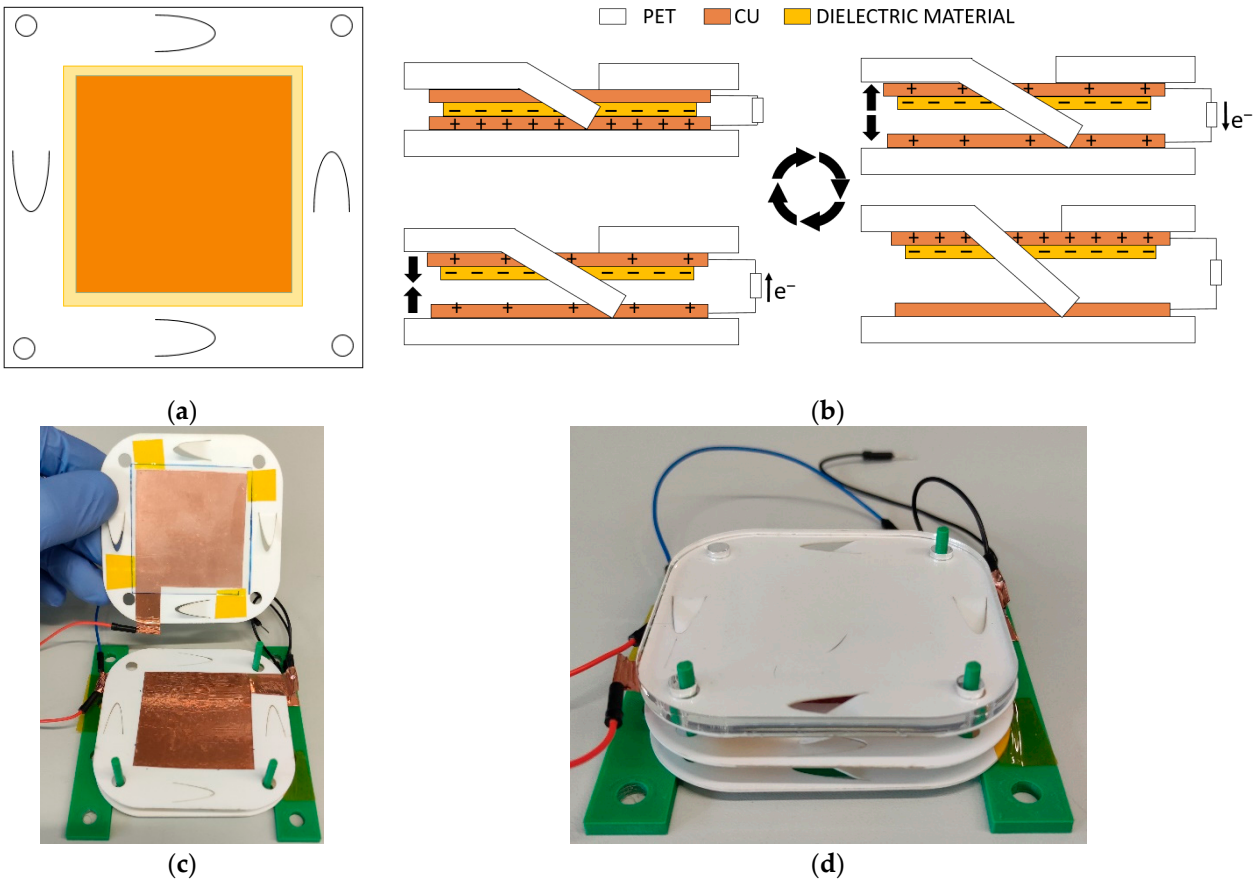

Figure 8. (**a**) Scheme of the TENG device; (**b**) scheme of operation of the TENG device; (**c**,**d**) image of the manufactured TENG device before and after assembling, respectively.

For the manufacturing of the TENG device, a 70 mm × 70 mm × 0.5 mm PET (polyethylene terephthalate) substrate has been used for the bottom part. On the PET substrate, a piece of adhesive copper of 45 mm × 45 mm × 0.05 mm is adhered. This electrode will be smaller than the dielectric material to avoid possible shortcuts between electrodes. Finally, a Mylar layer is adhered to the bottom copper electrode, 50 mm × 50 mm × 0.05 mm. For the top electrode, we use a PET sample of the same dimensions as the bottom one, but with the different spacers engraved by laser cutting at the ends of the structure. A 45 mm × 45 mm × 0.05 mm piece of adhesive copper is also attached as the top electrode.

To improve the energy generated by the TENG device, two of them have been manufactured in a stack (Figure 8c,d) and have been measured individually, connected in series and in parallel. For this stack manufacturing, the process is identical, but, in this case, the top PET substrate of the first TENG and the bottom one of the second are shared to minimize cost and volume.

2.5. Electrical Characterization

For the electrical characterization of this TENG device, as shown in Figure 8, two different measurements have been carried out. First, we measured the maximum voltage generated by contacting the device directly to the sourcemeter. Second, we connected the device to a diode bridge and a capacitor of 10 µF to rectify the signal and store the energy. Then, by means of a switch, the stored energy is connected to 30 LEDs. For these measurements, in order to show a real application, instead of applying 50 N of force with a stepper motor, the force was applied with the palm of the hand, obtaining an average of 8 N of force.

For the first measurement, each of the dielectrics was measured separately. As shown in Figure 9a, the maximum voltages are very similar, reaching a value of 170 V. By connecting the two materials in series, the voltage increases to 250 V. Ideally, the voltage should be doubled, but manually applying the force and not contacting each dielectric with its top electrode in phase do not reach this maximum voltage. An improvement of 50% improvement over a single individually connected device is obtained.

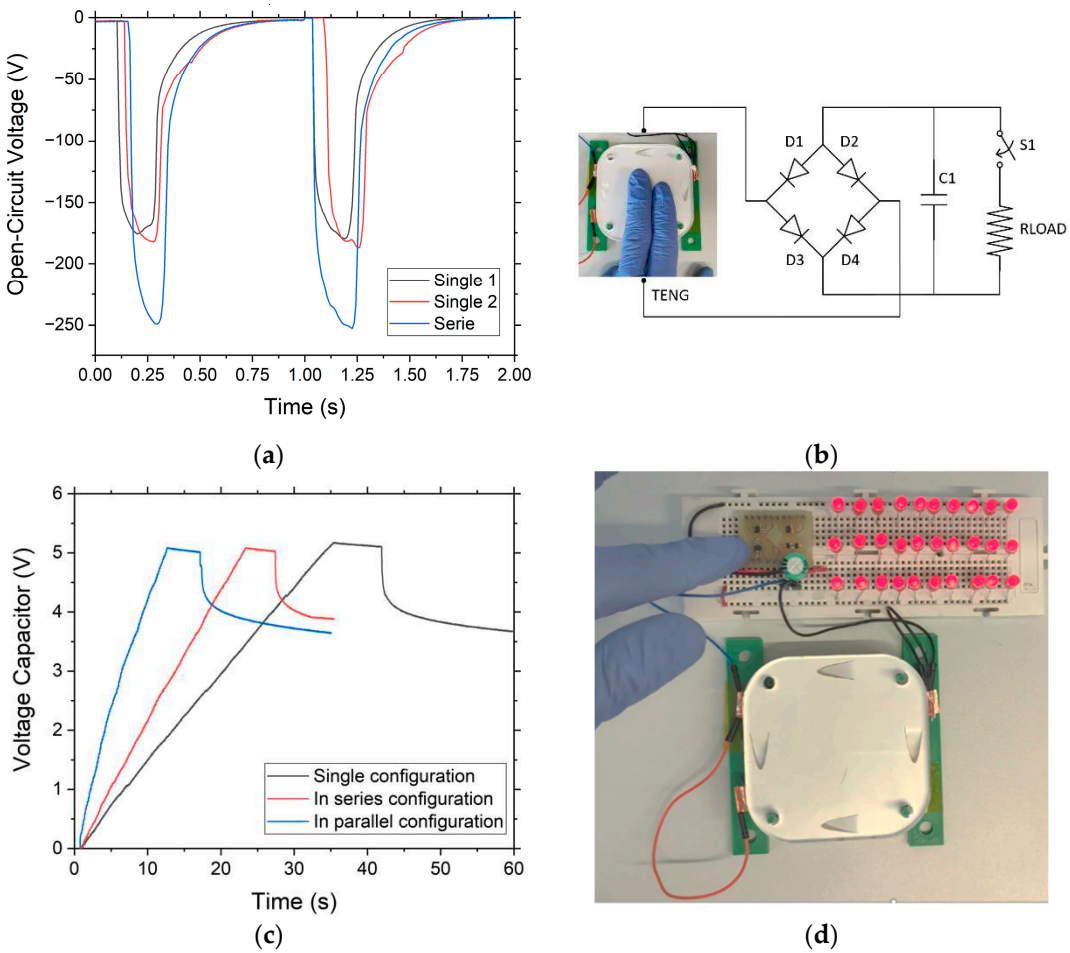

Figure 9. (**a**) Voltage generated by each device individually and connected in series; (**b**) circuit diagram and photograph of the TENG device powering the 30 LEDs; (**c**) process of charging and discharging the capacitor for a capacity of 10 µF; (**d**) TENG device used to light 30 LEDs up.

In the second characterization, as previously mentioned and shown in the schematic of Figure 9b, the device output is connected to a diode bridge, together with a capacitor of 10 µF, and is charged up to 5 V. Once the 5 V is reached, which corresponds to a stored capacitor energy of 125 µJ, there are a few seconds without charging, and then the LEDs are connected through the switch to illuminate them for 150 ms (Figure 9d). Figure 9c shows

the comparative graph of charge and discharge of the 10 μF capacitor when powering the 30 LEDs and applying force with the palm of the hand at an approximate frequency of 6 Hz. It can be observed that when using a single device, the charging process takes 35 s, while when connecting two devices in series, this time is reduced to 23 s. Decreasing the charging time of the capacitor by 35%. In the same way, if the two devices are connected in parallel, the charging time is reduced to 12 s. This decreases the time by 65%, compared to the single device. From these results, we can infer that a power of 10 μW can be generated by two devices connected in parallel.

3. Discussion and Conclusions

In this article, the fabrication of a TENG device has been carried out, which can collect the mechanical energy of the force applied by tapping with the palm of the hand. This energy could be used to power low-power electronic sensors in a self-sufficient way.

In order to manufacture the TENG devices, the most suitable materials (i.e., those with the highest surface charge transfer and most cost-effective) have been studied. In addition, the design of the spacers has been optimized to improve the contact surface and reduce the final costs of the device.

To increase the surface charge density, charge injection was carried out by means of high-voltage corona charging. The voltages to be applied and the optimal time for this charge injection were examined.

To validate the correct operation of the TENG device, electrical characterizations with different mounting configurations were carried out. By using a stack of only two devices connected in parallel, 30 LEDs were illuminated every 12 s, thanks to a power generation of 10 μW produced by hand tapping.

Supplementary Materials: The following supporting information can be downloaded at: https://www.mdpi.com/article/10.3390/nano12193271/s1. Video S1: Device lighting 30 LEDs.

Author Contributions: Conceptualization, M.D. and G.M.; methodology, M.D. and G.M.; investigation, M.D. and G.M.; writing—original draft preparation, M.D.; writing—review and editing, G.M.; supervision, G.M. All authors have read and agreed to the published version of the manuscript.

Funding: This research was funded by the La Caixa Foundation under the Junior Leader Retaining program (LCF/BQ/PR19/11700010), EUR2020-112082 under the Dynamization Actions "Europa Excelencia 2020" funded by the NextGenerationEU Instrument, and Ramon y Cajal Fellowship 2020 (RYC2020-030501-I).

Institutional Review Board Statement: Not applicable.

Informed Consent Statement: Not applicable.

Data Availability Statement: Data are contained within the article or Supplementary Material.

Acknowledgments: G.M. appreciates the financial support from the La Caixa Foundation under the Junior Leader Retaining Fellowship (LCF/BQ/PR19/11700010), project EUR2020-112082 under the Dynamization Actions "Europa Excelencia 2020" funded by the NextGenerationEU Instrument, and the Ramon y Cajal Fellowship 2020. This work has been carried out in collaboration with ENERGIOT DEVICES SL (www.energiot.com) and in the framework of the doctoral program in Electronic and Telecommunication Engineering of the Autonomous University of Barcelona.

Conflicts of Interest: The authors declare no conflict of interest.

References

1. Xu, C.; Zhang, B.; Wang, A.C.; Zou, H.; Liu, G.; Ding, W.; Wu, C.; Ma, M.; Feng, P.; Lin, Z.; et al. Contact-Electrification between Two Identical Materials: Curvature Effect. *ACS Nano* **2019**, *13*, 2034–2041. [CrossRef] [PubMed]
2. Zhang, H.; Zhang, X.; Han, M. (Eds.) *Flexible and Stretchable Triboelectric Nanogenerator Devices: Toward Self-Powered Systems*; Willey: Hoboken, NJ, USA, 2019; ISBN 9783527345724.
3. Liu, Z.; Li, H.; Shi, B.; Fan, Y.; Wang, Z.L.; Li, Z. Wearable and Implantable Triboelectric Nanogenerators. *Adv. Funct. Mater.* **2019**, *29*, 1808820. [CrossRef]

4. Rose, K.; Eldridge, S.; Chapin, L. The Internet of Things: An Overview Understanding the Issues and Challenges of a More Connected World. *Internet Soc.* **2015**, *80*, 1–50.
5. Chen, J.; Zhu, G.; Yang, W.; Jing, Q.; Bai, P.; Yang, Y.; Hou, T.-C.; Wang, Z.L. Harmonic-Resonator-Based Triboelectric Nanogenerator as a Sustainable Power Source and a Self-Powered Active Vibration Sensor. *Adv. Mater.* **2013**, *25*, 6094–6099. [CrossRef]
6. Zhang, H.; Yang, Y.; Su, Y.; Chen, J.; Adams, K.; Lee, S.; Hu, C.; Wang, Z.L. Triboelectric Nanogenerator for Harvesting Vibration Energy in Full Space and as Self-Powered Acceleration Sensor. *Adv. Funct. Mater.* **2013**, *24*, 1401–1407. [CrossRef]
7. Chen, J.; Wang, Z.L. Reviving Vibration Energy Harvesting and Self-Powered Sensing by a Triboelectric Nanogenerator. *Joule* **2017**, *1*, 480–521. [CrossRef]
8. Zhao, J.; Zhen, G.; Liu, G.; Bu, T.; Liu, W.; Fu, X.; Zhang, P.; Zhang, C.; Wang, Z.L. Remarkable merits of triboelectric nanogenerator than electromagnetic generator for harvesting small-amplitude mechanical energy. *Nano Energy* **2019**, *61*, 111–118. [CrossRef]
9. Liu, L.; Shi, Q.; Sun, Z.; Lee, C. Magnetic-interaction assisted hybridized triboelectric-electromagnetic nanogenerator for advanced human-machine interfaces. *Nano Energy* **2021**, *86*, 106154. [CrossRef]
10. Tian, Z.; He, J.; Chen, X.; Zhang, Z.; Wen, T.; Zhai, C.; Han, J.; Mu, J.; Hou, X.; Chou, X.; et al. Performance-boosted triboelectric textile for harvesting human motion energy. *Nano Energy* **2017**, *39*, 562–570. [CrossRef]
11. Wang, S.; Xie, Y.; Niu, S.; Lin, L.; Wang, Z.L. Freestanding Triboelectric-Layer-Based Nanogenerators for Harvesting Energy from a Moving Object or Human Motion in Contact and Non-contact Modes. *Adv. Mater.* **2014**, *26*, 2818–2824. [CrossRef]
12. Zhu, G.; Bai, P.; Chen, J.; Wang, Z.L. Power-generating shoe insole based on triboelectric nanogenerators for self-powered consumer electronics. *Nano Energy* **2013**, *2*, 688–692. [CrossRef]
13. Lee, D.W.; Jeong, D.G.; Kim, J.H.; Kim, H.S.; Murillo, G.; Lee, G.-H.; Song, H.-C.; Jung, J.H. Polarization-controlled PVDF-based hybrid nanogenerator for an effective vibrational energy harvesting from human foot. *Nano Energy* **2020**, *76*, 105066. [CrossRef]
14. He, M.; Du, W.; Feng, Y.; Li, S.; Wang, W.; Zhang, X.; Yu, A.; Wan, L.; Zhai, J. Flexible and stretchable triboelectric nanogenerator fabric for biomechanical energy harvesting and self-powered dual-mode human motion monitoring. *Nano Energy* **2021**, *86*, 106058. [CrossRef]
15. Yang, Y.; Chen, L.; He, J.; Hou, X.; Qiao, X.; Xiong, J.; Chou, X. Flexible and Extendable Honeycomb-Shaped Triboelectric Nanogenerator for Effective Human Motion Energy Harvesting and Biomechanical Sensing. *Adv. Mater. Technol.* **2021**, *7*, 2100702. [CrossRef]
16. Li, X.; Zhu, P.; Zhang, S.; Wang, X.; Luo, X.; Leng, Z.; Zhou, H.; Pan, Z.; Mao, Y. A Self-Supporting, Conductor-Exposing, Stretchable, Ultrathin, and Recyclable Kirigami-Structured Liquid Metal Paper for Multifunctional E-Skin. *ACS Nano* **2022**, *16*, 5909–5919. [CrossRef] [PubMed]
17. Luo, J.; Li, Y.; He, M.; Wang, Z.; Li, C.; Liu, D.; An, J.; Xie, W.; He, Y.; Xiao, W.; et al. Rehabilitation of Total Knee Arthroplasty by Integrating Conjoint Isometric Myodynamia and Real-Time Rotation Sensing System. *Adv. Sci.* **2022**, *9*, 2105219. [CrossRef]
18. Yang, Y.; Zhu, G.; Zhang, H.; Chen, J.; Zhong, X.; Lin, Z.-H.; Su, Y.; Bai, P.; Wen, X.; Wang, Z.L. Triboelectric Nanogenerator for Harvesting Wind Energy and as Self-Powered Wind Vector Sensor System. *ACS Nano* **2013**, *7*, 9461–9468. [CrossRef]
19. Xie, Y.; Wang, S.; Lin, L.; Jing, Q.; Lin, Z.-H.; Niu, S.; Wu, Z.; Wang, Z.L. Rotary Triboelectric Nanogenerator Based on a Hybridized Mechanism for Harvesting Wind Energy. *ACS Nano* **2013**, *7*, 7119–7125. [CrossRef]
20. Chen, B.; Yang, Y.; Wang, Z.L. Scavenging Wind Energy by Triboelectric Nanogenerators. *Adv. Energy Mater.* **2018**, 8. [CrossRef]
21. Kil Yun, B.; Kim, H.S.; Ko, Y.J.; Murillo, G.; Jung, J.H. Interdigital electrode based triboelectric nanogenerator for effective energy harvesting from water. *Nano Energy* **2017**, *36*, 233–240. [CrossRef]
22. Kim, H.S.; Kim, D.Y.; Kim, J.; Kim, J.H.; Kong, D.S.; Murillo, G.; Lee, G.; Park, J.Y.; Jung, J.H. Ferroelectric-Polymer-Enabled Contactless Electric Power Generation in Triboelectric Nanogenerators. *Adv. Funct. Mater.* **2019**, 29. [CrossRef]
23. Kim, D.Y.; Kim, H.S.; Kong, D.S.; Choi, M.; Kim, H.B.; Lee, J.-H.; Murillo, G.; Lee, M.; Kim, S.S.; Jung, J.H. Floating buoy-based triboelectric nanogenerator for an effective vibrational energy harvesting from irregular and random water waves in wild sea. *Nano Energy* **2018**, *45*, 247–254. [CrossRef]
24. Ju, S.-H.; Lin, H.-T.; Huang, J.-Y. Dominant frequencies of train-induced vibrations. *J. Sound Vib.* **2009**, *319*, 247–259. [CrossRef]
25. Cleante, V.G.; Brennan, M.J.; Gatti, G.; Thompson, D.J. Energy harvesting from the vibrations of a passing train: Effect of speed variability. *J. Phys. Conf. Ser.* **2016**, *744*, 12080. [CrossRef]
26. Yang, G.; Stark, B.H.; Hollis, S.J.; Burrow, S.G. Challenges for Energy Harvesting Systems Under Intermittent Excitation. *IEEE J. Emerg. Sel. Top. Circuits Syst.* **2014**, *4*, 364–374. [CrossRef]
27. Brennan, M.J.; Gatti, G. Harvesting Energy from Time-Limited Harmonic Vibrations: Mechanical Considerations. *J. Vib. Acoust.* **2017**, *139*, 51019. [CrossRef]
28. Hu, Y.; Wang, X.; Qin, Y.; Li, Z.; Wang, C.; Wu, H. A robust hybrid generator for harvesting vehicle suspension vibration energy from random road excitation. *Appl. Energy* **2022**, *309*, 118506. [CrossRef]
29. Wang, Z.L. On Maxwell's displacement current for energy and sensors: The origin of nanogenerators. *Mater. Today* **2017**, *20*, 74–82. [CrossRef]
30. Shen, X.; Han, W.; Jiang, Y.; Ding, Q.; Li, X.; Zhao, X.; Li, Z. Punching pores on cellulose fiber paper as the spacer of triboelectric nanogenerator for monitoring human motion. *Energy Rep.* **2020**, *6*, 2851–2860. [CrossRef]
31. Zhu, M.; Huang, Y.; Ng, W.S.; Liu, J.; Wang, Z.; Wang, Z.; Hu, H.; Zhi, C. 3D spacer fabric based multifunctional triboelectric nanogenerator with great feasibility for mechanized large-scale production. *Nano Energy* **2016**, *27*, 439–446. [CrossRef]

32. Hou, T.-C.; Yang, Y.; Zhang, H.; Chen, J.; Chen, L.-J.; Wang, Z.L. Triboelectric nanogenerator built inside shoe insole for harvesting walking energy. *Nano Energy* **2013**, *2*, 856–862. [CrossRef]
33. Lee, K.Y.; Chun, J.; Lee, J.-H.; Kim, K.N.; Kang, N.-R.; Kim, J.-Y.; Kim, M.H.; Shin, K.-S.; Gupta, M.K.; Baik, J.M.; et al. Hydrophobic Sponge Structure-Based Triboelectric Nanogenerator. *Adv. Mater.* **2014**, *26*, 5037–5042. [CrossRef] [PubMed]
34. Lee, Y.; Kim, W.; Bhatia, D.; Hwang, H.J.; Lee, S.; Choi, D. Cam-based sustainable triboelectric nanogenerators with a resolution-free 3D-printed system. *Nano Energy* **2017**, *38*, 326–334. [CrossRef]
35. Zhu, G.; Lin, Z.-H.; Jing, Q.; Bai, P.; Pan, C.; Yang, Y.; Zhou, Y.; Wang, Z.L. Toward Large-Scale Energy Harvesting by a Nanoparticle-Enhanced Triboelectric Nanogenerator. *Nano Lett.* **2013**, *13*, 847–853. [CrossRef] [PubMed]
36. Wang, S.; Lin, L.; Wang, Z.L. Nanoscale Triboelectric-Effect-Enabled Energy Conversion for Sustainably Powering Portable Electronics. *Nano Lett.* **2012**, *12*, 6339–6346. [CrossRef] [PubMed]
37. Fang, H.; Li, Q.; He, W.; Li, J.; Xue, Q.; Xu, C.; Zhang, L.; Ren, T.; Dong, G.; Chan, H.L.W.; et al. A high performance triboelectric nanogenerator for self-powered non-volatile ferroelectric transistor memory. *Nanoscale* **2015**, *7*, 17306–17311. [CrossRef]
38. Zhang, H.; Lu, Y.; Ghaffarinejad, A.; Basset, P. Progressive contact-separate triboelectric nanogenerator based on conductive polyurethane foam regulated with a Bennet doubler conditioning circuit. *Nano Energy* **2018**, *51*, 10–18. [CrossRef]
39. Zhong, W.; Xu, B.; Gao, Y. Engraved Pattern Spacer Triboelectric Nanogenerators for Mechanical Energy Harvesting. *Nano Energy* **2021**, *92*, 106782. [CrossRef]
40. Wei, X.Y.; Zhu, G.; Wang, Z.L. Surface-charge engineering for high-performance triboelectric nanogenerator based on identical electrification materials. *Nano Energy* **2014**, *10*, 83–89. [CrossRef]
41. Diaz, A.; Felix-Navarro, R. A semi-quantitative tribo-electric series for polymeric materials: The influence of chemical structure and properties. *J. Electrost.* **2004**, *62*, 277–290. [CrossRef]
42. Zou, H.; Zhang, Y.; Guo, L.; Wang, P.; He, X.; Dai, G.; Zheng, H.; Chen, C.; Wang, A.C.; Xu, C.; et al. Quantifying the triboelectric series. *Nat. Commun.* **2019**, *10*, 1–9. [CrossRef] [PubMed]
43. Zhu, G.; Pan, C.; Guo, W.; Chen, C.-Y.; Zhou, Y.; Yu, R.; Wang, Z.L. Triboelectric-Generator-Driven Pulse Electrodeposition for Micropatterning. *Nano Lett.* **2012**, *12*, 4960–4965. [CrossRef] [PubMed]
44. Wang, S.; Lin, L.; Xie, Y.; Jing, Q.; Niu, S.; Wang, Z.L. Sliding-Triboelectric Nanogenerators Based on In-Plane Charge-Separation Mechanism. *Nano Lett.* **2013**, *13*, 2226–2233. [CrossRef] [PubMed]
45. Tang, W.; Zhang, C.; Han, C.B.; Wang, Z.L. Enhancing Output Power of Cylindrical Triboelectric Nanogenerators by Segmentation Design and Multilayer Integration. *Adv. Funct. Mater.* **2014**, *24*, 6684–6690. [CrossRef]
46. Han, C.; Zhang, C.; Tang, W.; Li, X.; Wang, Z.L. High power triboelectric nanogenerator based on printed circuit board (PCB) technology. *Nano Res.* **2014**, *8*, 722–730. [CrossRef]
47. Ghaffarinejad, A.; Lu, Y.; Hinchet, R.; Galayko, D.; Hasani, J.Y.; Basset, P. Bennet's charge doubler boosting triboelectric kinetic energy harvesters. *J. Phys. Conf. Ser.* **2018**, *1052*, 12027. [CrossRef]
48. Wang, S.; Xie, Y.; Niu, S.; Lin, L.; Liu, C.; Zhou, Y.S.; Wang, Z.L. Maximum Surface Charge Density for Triboelectric Nanogenerators Achieved by Ionized-Air Injection: Methodology and Theoretical Understanding. *Adv. Mater.* **2014**, *26*, 6720–6728. [CrossRef]
49. Nie, J.; Chen, X.; Wang, Z.L. Electrically Responsive Materials and Devices Directly Driven by the High Voltage of Triboelectric Nanogenerators. *Adv. Funct. Mater.* **2018**, 29. [CrossRef]
50. Niu, S.; Wang, S.; Lin, L.; Liu, Y.; Zhou, Y.S.; Hu, Y.; Wang, Z.L. Theoretical study of contact-mode triboelectric nanogenerators as an effective power source. *Energy Environ. Sci.* **2013**, *6*, 3576–3583. [CrossRef]
51. Peng, H.; Sun, X.; Weng, W.; Fang, X. *Polymer Materials for Energy and Electronic Applications*; Fudan University: Shanghai, China, 2016; ISBN 9780128110928.

nanomaterials

MDPI

Article

A High-Performance Coniform Helmholtz Resonator-Based Triboelectric Nanogenerator for Acoustic Energy Harvesting

Haichao Yuan [1,†], Hongyong Yu [1,†], Xiangyu Liu [1], Hongfa Zhao [2], Yiping Zhang [1], Ziyue Xi [1], Qiqi Zhang [1], Ling Liu [1], Yejin Lin [1,*], Xinxiang Pan [1,3,*] and Minyi Xu [1,*]

[1] Dalian Key Lab of Marine Micro/Nano Energy and Self-Powered System, Marine Engineering College Dalian Maritime University, Dalian 116026, China; yuanhc@dlmu.edu.cn (H.Y.); yuhongyong2020@dlmu.edu.cn (H.Y.); simonlxy@dlmu.edu.cn (X.L.); zyp672216686@dlmu.edu.cn (Y.Z.); yyds@dlmu.edu.cn (Z.X.); qiqizhang@dlmu.edu.cn (Q.Z.); pinky@dlmu.edu.com (L.L.)
[2] Tsinghua-Berkeley Shenzhen Institute, Tsinghua Shenzhen International Graduate School, Tsinghua University, Shenzhen 518055, China; zhaohf21@mails.tsinghua.edu.cn
[3] School of Electronics and Information Technology, Guangdong Ocean University, Zhanjiang 524088, China
* Correspondence: linyj@dlmu.edu.cn (Y.L.); panxx@dlmu.edu.cn (X.P.); xuminyi@dlmu.edu.cn (M.X.)
† These authors contributed equally to this work.

Abstract: Harvesting acoustic energy in the environment and converting it into electricity can provide essential ideas for self-powering the widely distributed sensor devices in the age of the Internet of Things. In this study, we propose a low-cost, easily fabricated and high-performance coniform Helmholtz resonator-based Triboelectric Nanogenerator (CHR-TENG) with the purpose of acoustic energy harvesting. Output performances of the CHR-TENG with varied geometrical sizes were systematically investigated under different acoustic energy conditions. Remarkably, the CHR-TENG could achieve a 58.2% higher power density per unit of sound pressure of acoustic energy harvesting compared with the ever-reported best result. In addition, the reported CHR-TENG was demonstrated by charging a 1000 μF capacitor up to 3 V in 165 s, powering a sensor for continuous temperature and humidity monitoring and lighting up as many as five 0.5 W commercial LED bulbs for acoustic energy harvesting. With a collection features of high output performance, lightweight, wide frequency response band and environmental friendliness, the cleverly designed CHR-TENG represents a practicable acoustic energy harvesting approach for powering sensor devices in the age of the Internet of Things.

Keywords: coniform Helmholtz resonator; triboelectric nanogenerator; acoustic energy harvesting

Citation: Yuan, H.; Yu, H.; Liu, X.; Zhao, H.; Zhang, Y.; Xi, Z.; Zhang, Q.; Liu, L.; Lin, Y.; Pan, X.; et al. A High-Performance Coniform Helmholtz Resonator-Based Triboelectric Nanogenerator for Acoustic Energy Harvesting. *Nanomaterials* **2021**, *11*, 3431. https://doi.org/10.3390/nano11123431

Academic Editor: João Pedro Araujo

Received: 29 October 2021
Accepted: 15 December 2021
Published: 17 December 2021

1. Introduction

In the era of the Internet of Things (IoT), it is highly desired for the development of sensor devices that are environmentally friendly, independent and operation maintenance-free [1,2]. Since various forms of energy exist in the working environment of sensor facilities, such as solar energy, vibration energy, wind energy, sound energy, etc., energy harvesting from the environment provides a practical solution for the sustainable power supply for sensor equipment [3–7]. Among different energy forms in environment, as a green, abundant and sustainable energy source, acoustic energy is gaining the intrigue of energy harvesting researchers [8–11]. However, acoustic energy is mainly wasted due to its low energy density of sound waves and the lack of practical energy harvesting technologies [12]. If such a widely distributed energy were collected, converted into electricity and utilized in a managed manner, it would provide an essential solution for the self-powering of the IoT sensor nodes. Nevertheless, most previous studies focused on piezoelectricity or electromagnetic induction have inevitable disadvantages, such as low electrical output performance or complex structure design [13–17]. Hence, it is imperative to develop acoustic energy harvesting devices with high electrical output performance and reasonable practicability.

In 2012, Professor Wang Zhonglin reported a new approach to transforming environment low-frequency energy into electrical energy by utilizing a Triboelectric Nanogenerator (TENG) [18]. With its features of low cost, light weight, easy manufacture and high power density, TENG demonstrates great competitiveness in low-frequency energy collection and has been deemed to be the most prospective approach to achieve distributed energy harvesting (vibration energy [19–22], wind energy [23–26], wave energy [27–30], and acoustic energy [31–34]) and self-powered sensing [35–38]. Among the studies on acoustic energy harvesting by utilizing TENG, Yang et al. [39] first explored the TENG acoustic energy harvester based on organic film, amazingly, by utilizing a Helmholtz resonator, the device achieves a maximum output voltage of 60.5 V, a maximum output current of 15.1 μA and a maximum power density of 60.2 mW/m^2 output performance at the acoustic frequency of 240 Hz. Regarding innovation structure of the TENG acoustic energy harvester, Cui et al. [40] investigated a novel mesh TENG acoustic energy harvester that could operate in a wide frequency range (50~425 Hz). The mesh structure design enhances the electrical output performance of the apparatus, which can generate a current density of 45 mA/m^2 with a maximum open-circuit voltage of 90 V. More recently, Wang et al. [41] reported a new sound-driven TENG with an integrated embroidery hoop, which could generate 500 V, 124 μA electricity output. Although the device is simple in design and fabrication, it cannot achieve the convergence and reinforcement of acoustic energy. In terms of structural innovation for enhanced acoustic energy collection, the Helmholtz resonator is of great help to strengthen the energy harvesting effect. Particularly, our group has designed an improved Helmholtz resonator-based TENG for efficient acoustic energy harvesting [33] in which dual tubes were installed on the outside of the resonator. Through optimized design, the sound pressure sensitivity of TENG per area reaches 1.23 $V/Pa{\cdot}cm^2$, and the power density per unit acoustic pressure reaches 1.82 $W/Pa{\cdot}cm^2$, which achieves the best sound energy collection and power generation effect in the field. However, there is very little research on the internal structure optimization of Helmholtz resonator-based TENG for high-performance acoustic energy collection. It is still essential and necessary to further improve the performance of acoustic energy harvesting and widen the frequency range of collected sound for developing self-powered devices based on acoustic energy.

Herein, we developed a novel coniform Helmholtz resonator Triboelectric Nanogenerator (CHR-TENG) for efficient collection of acoustic energy in environment. The CHR-TENG is composed of a coniform Helmholtz resonance cavity, an aluminum film with uniformly distributed acoustic holes and a fluorinated ethylene propylene (FEP) film with conductive ink printed electrodes. To identify the characteristics of acoustic energy harvesting effect, output performances of the CHR-TENG with different geometrical sizes under different acoustic conditions were systematically investigated. Compared with the conventional acoustoelectric conversion devices, the CHR-TENG demonstrates better output performance due to its capture and reinforcement effects on sound energy.

2. Results and Discussion

2.1. Structure Design of the CHR-TENG

Figure 1 depicts the structure design of the CHR-TENG, which can be used in various acoustic generation sources for energy harvesting for self-powering wireless sensor nodes, such as transportation scenarios of vehicles, airplanes or ships, where there have frequent activities and monitoring are needed. Generally speaking, acoustic levels in the transportation scenarios are mainly in the form of low frequency and high sound pressure level. Detailed acoustic levels can be seen Table S1 in Supplementary Materials. Figure 1b displays the schematic of the acoustic energy harvesting system: specifically, the acoustic source produces acoustic wave energy in the vibration form; the acoustic energy collection device focuses the energy and then utilizes the acoustic–electric conversion technology to convert acoustic waves from vibration energy to electrical energy; the electricity output is rectified by the energy management module with optimal impedance matching, which is ultimately used to power sensors, electrical energy storage or small power supplies. The

detailed structure design of the CHR-TENG is illustrated in Figure 1c. The CHR-TENG consists of a front-end acoustic gathering structure (3D plastic printed, hereafter named as "reflector" for the sake of simplification), a coniform Helmholtz resonance cavity (3D plastic printed) and an electricity generation unit. The electricity generation unit comprises an aluminum membrane with uniformly distributed acoustic holes etched by laser (Figure 1c-i) and an FEP membrane with conductive ink-printed electrodes. A spacer cavity is designed and inserted between the FEP membrane and the aluminum membrane to realize a better contact separation effect. The conical Helmholtz resonance cavity is a kind of acoustic resonance system that amplifies the acoustic energy through the resonance cavity and enhances the output performance of the TENG by resonance effect. FEP film and aluminum are common materials for TENG energy harvesting devices. FEP material is highly electronegative in nature, resulting in a large amount of charge transfer when it separates from the aluminum electrode in contact. Surface treatment of FEP contributes to reinforce output performance of the TENG [42]. In this work, to improve the output performance of the CHR-TENG, FEP film was polished to increase its surface roughness with surface features scanned by electron microscopy (Figure 1c-ii). Figure 1d displays the physical images of the CHR-TENG.

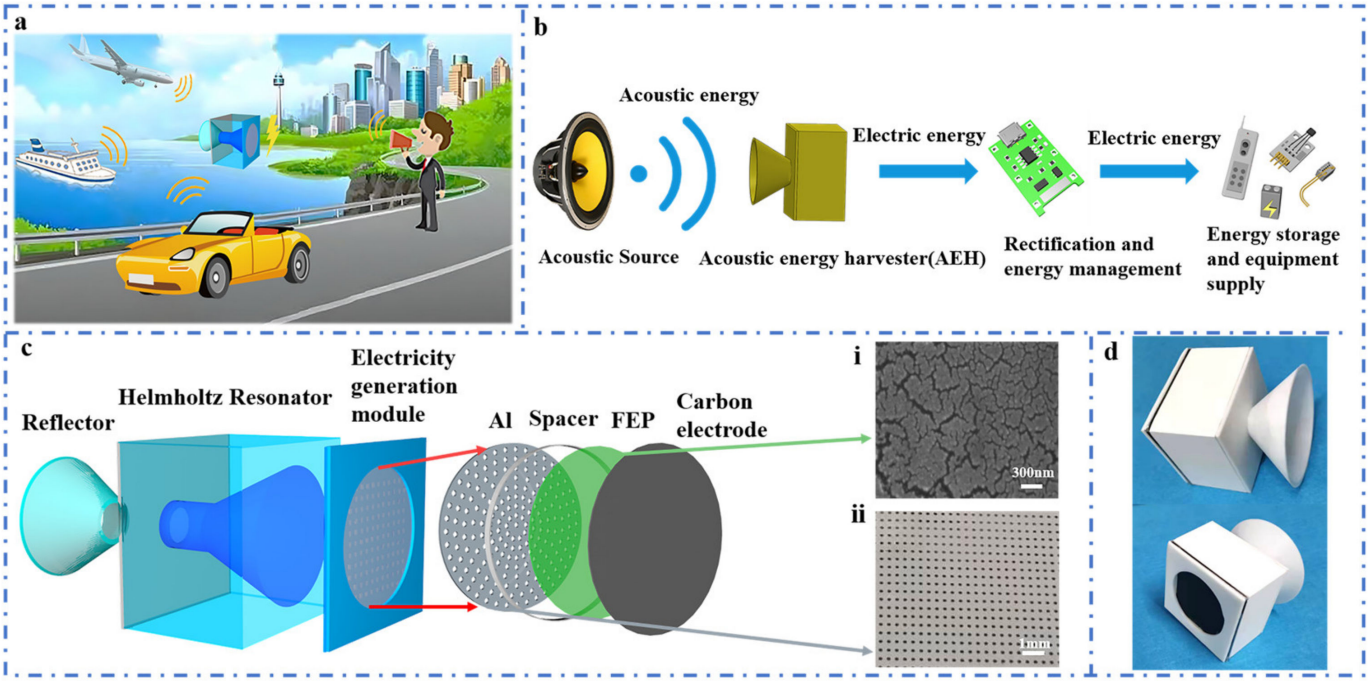

Figure 1. The structure design of the CHR-TENG. (**a**) Schematic diagram of various applications of the CHR-TENG in acoustic energy harvesting. (**b**) Schematic diagram of the acoustic energy harvesting and management system. (**c**) A schematic illustration of the CHR-TENG. (**d**) Physical images of the CHR-TENG.

2.2. Working Principle of the CHR-TENG

Figure 2 depicts the working principle of the CHR-TENG. Figure 2a illustrates the schematic diagram of the acoustic energy harvesting experimental process. The signal generator provides a stable and frequency adjustable sine wave electrical signal, and the power amplifier amplifies power of the electrical signal to drive the loudspeaker to generate acoustic waves. The acoustic frequency of the system can be adjusted by the signal generator, and the sound pressure level is controlled by the power amplifier. The FEP film in the CHR-TENG is driven by acoustic force to periodically separate from the aluminum electrode, generating a corresponding change in the electrical signal. The electrical output signals could be detected by an electrostatic high-resistance meter, received by a data acquisition card, and then plotted into a real-time change curve by LABVIEW

software on the computer. The sound level meter is placed next to the FEP membrane, with measurement accuracy and resolution of 1.5 dB and 0.1 dB, respectively. To ensure accuracy and consistency of the experiments, the same TENG unit was used in all electricity generation performance and comparison experiments conducted in this study to exclude the systematic bias of the experiments. Since the resonator geometric dimension of the CHR-TENG is far less than that of the incident acoustic wavelength, the coniform Helmholtz resonator could be simplified as a 1D lumped system [43]. As schematically illustrated in Figure 2b, the coniform Helmholtz resonator is simplified to a mass–spring–damper model. Once driven by outside acoustic waves, the air inside the coniform Helmholtz cavity will operate as an air spring, while the air in the neck area will oscillate like a mass, forcing the air spring to expand and contract back and forth. Viscous losses generated due to damping mainly come from the friction of oscillating air at the neck region and radiation losses at the neck end. Formulation of the resonance frequency of the coniform cavity can be expressed as:

$$F_r = \frac{C}{2\pi}\sqrt{\frac{3A_n}{4V_cH_n}} \tag{1}$$

where c is the speed of sound in air, A_n is the neck area, V_c represents the volume of the resonant cavity and H_n is the neck length. Figure 2c shows the distribution of sound pressure levels of the coniform Helmholtz resonator at the first resonant frequency. It can be seen from the simulation that the acoustic pressure is the highest at the bottom of the resonator cavity. A higher sound pressure in the cavity will result in a better resonance effect and, thus, a higher electrical output of the CHR-TENG. Therefore, the TENG electrical powering unit is placed at the bottom of the resonator cavity to ensure the best electrical output performance. Figure 2d presents a schematic depiction of the working mechanism of the CHR-TENG. The acoustic wave propagation causes the pressure between the FEP membrane and aluminum electrode to change periodically, generating repetitive vibrations of the FEP up and down. When the FEP membrane contacts the aluminum electrode, electron transfer is caused by electronegativity difference between the two materials, thus resulting in a negatively charged FEP surface and a positively charged aluminum electrode (Figure 2d-i). As the FEP film separates from the aluminum electrode caused by the acoustic pressure change, to equalize the local electric field, free electrons will flow from the conductive ink electrode to the aluminum electrode through external circuit, thus generating positive charges (Figure 2d-ii). Electron flow continues to the maximum distance between the two contact surfaces (Figure 2d-iii). After that the acoustic waves push the FEP film toward the aluminum electrode. During this stage, the voltage difference diminishes, and free electrons inside the aluminum electrode pass through an external circuit back to the conductive ink electrode (Figure 2d-iv). Ultimately, surfaces of the FEP film and the aluminum electrode come into contact again, and the charge distribution returns to the initial condition (Figure 2d-i). Hereto, the whole electricity generation cycle of the CHR-TENG completes, and the output of alternating current pulses under the action of acoustic waves is generated. To further investigate the acoustic field distribution of the conical Helmholtz resonator and the potential distribution change between electrodes of the CHR-TENG, COMSOL was employed to carry out finite element analysis, the simulation results of which are shown in Figure 2e,f, respectively. Simulation conditions are provided in the Supplementary Materials. The acoustic field distribution of the coniform resonator is illustrated in Figure 2e. The sound pressure level gradually increases from the opening to the end in the reflector structure, indicating a good sound convergence effect. To ensure the optimum output performance of the CHR-TENG, the TENG power generation unit is placed at the bottom of the coniform resonator, where the acoustic pressure level reaches the maximum. Figure 2f depicts the electrical potential distribution change between the FEP and the aluminum electrode.

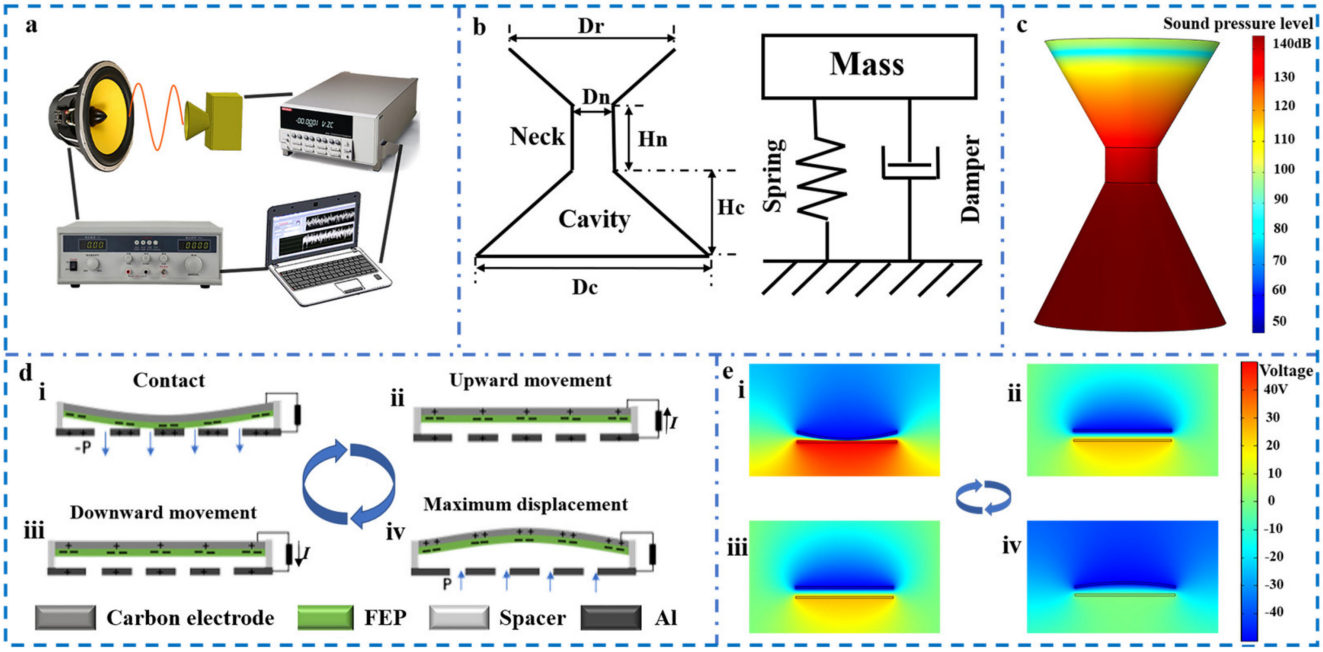

Figure 2. Working principle of the CHR-TENG. (**a**) Schematic diagram of acoustic energy collection experimental process. (**b**) The coniform Helmholtz resonator simplified by the mass–spring–damper system. (**c**) Distribution of sound pressure levels of the coniform Helmholtz resonator at the 1st resonant frequency. (**d**) The working mechanism of the CHR-TENG. (**e**) Periodic potential distribution change of the two electrodes simulated by COMSOL.

2.3. Performance of the CHR-TENG

The electrical output performance of the CHR-TENG is influenced by the acoustic characteristics. This work systematically investigated the effects of acoustic pressure levels as well as distances to acoustic sources on the output performance of the CHR-TENG. Figure 3a depicts a schematic diagram of acoustic wave propagation and capture. The influence of the distance between the CHR-TENG and the sound source on the output performance was first investigated. Figure 3b shows output curves of the peak open-circuit voltage of the CHR-TENG at different distances in specific acoustic frequency (acoustic frequency range 40 to 200 Hz), with acoustic pressure levels ranging from 64 to 96.4 dB. Experimental results show that the output performance of the CHR-TENG gradually decreases with the increase of distance from the acoustic source. When the distance from the acoustic source was 20 mm, the CHR-TENG generated the peak open-circuit voltage 115 V at 140 Hz. When the distance increased from 20 mm to 110 mm, the CHR-TENG produced the peak open-circuit voltage of 18 V at 59 Hz. The output performance trend of short-circuit current and transferred charge is also consistent with that of the open-circuit voltage, which is due to the fact that output performance of the CHR-TENG is influenced by the coupling of acoustic propagation and electricity generation. In practical applications, we can choose the solution of getting as close to the acoustic source as possible or designing the array harvesters to enhance the energy harvesting and improve the output performance. The CHR-TENG operates in the pattern of contact and separation, whose control equation can be specified as:

$$V_{oc} = \frac{\sigma \cdot x(t)}{\varepsilon_0} \tag{2}$$

where V_{oc} is open-circuit voltage, σ is charge density, x(t) is film displacement and ε_0 is dielectric constant. It can be seen from the formula that the electric output performance of the CHR-TENG is proportional to the film displacement when the material is selected constant. The effect of the sound pressure level and the distance from the acoustic source on the output performance of the CHR-TENG were investigated as the two elements that

will influence the film displacement. In addition, the electricity output of the CHR-TENG was measured with acoustic pressure levels ranging from 50 dB to 100 dB. As shown in Figure 3c, the output voltage increases as the acoustic pressure increases. This is mainly attributed to the fact that the increase in acoustic pressure results in increased radial displacement of the FEP film. As the acoustic pressure levels increased from 50 dB to 100 dB, the open-circuit voltage increased from 4 V to 270 V, the short-circuit current rose from 0.1 to 85 μA (Figure 3d) and the transfer charge increased from 3 to 84 nC (Figure 3e).

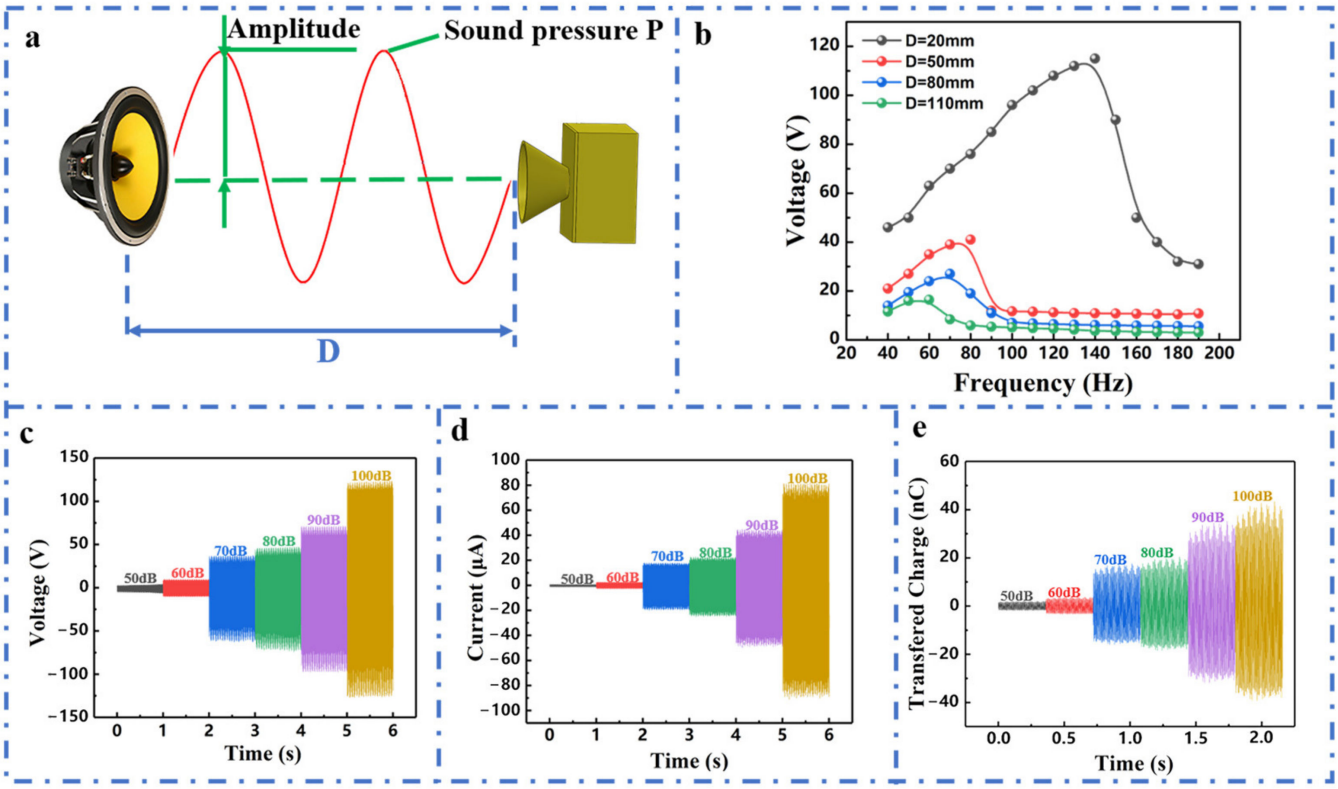

Figure 3. Electrical output performance of the CHR-TENG under different sound energy conditions. (**a**) Schematic diagram of acoustic wave propagation and capture. (**b**) Open-circuit voltage output of the CHR-TENG under the excitation of acoustic waves with different frequencies in distances ranging from 20 to 110 mm. (**c**) Open-circuit voltage, (**d**) short-circuit current and (**e**) transferred charge output of the CHR-TENG under acoustic excitation with pressure levels varying from 50 to 100 dB.

Among all the parameters in the resonance frequency formulation, V_c is one of the main influencing parameters on the resonance frequency of the resonator. The variation of the V_c will change the resonance frequency of the resonator and, thus, further influence the output performance of the CHR-TENG under the combined action of the electricity generation module. In order to explore the influence of V_c on the output performance of the CHR-TENG, we prefer to change the resonator thickness to change the resonator volume. To investigate the influence of the resonator's thickness on electrical output performance of the CHR-TENG, we studied the output of the CHR-TENG with resonator thicknesses of 30 mm, 40 mm and 50 mm, respectively. As shown in Figure 4a, generally, the maximum peak open-circuit voltage outputs of the three CHR-TENGs have little difference: the maximum peak open-circuit voltage of the CHR-TENG with the thickness of 30 mm is 112 V, and the difference between 40 mm and 50 mm is not much, within only 5 V. Furthermore, a comparison is conducted to explore the open-circuit voltage outputs of the CHR-TENGs with different thicknesses at the same acoustic conditions (acoustic frequency 40–250 Hz, sound pressure level 60.3–92 dB).

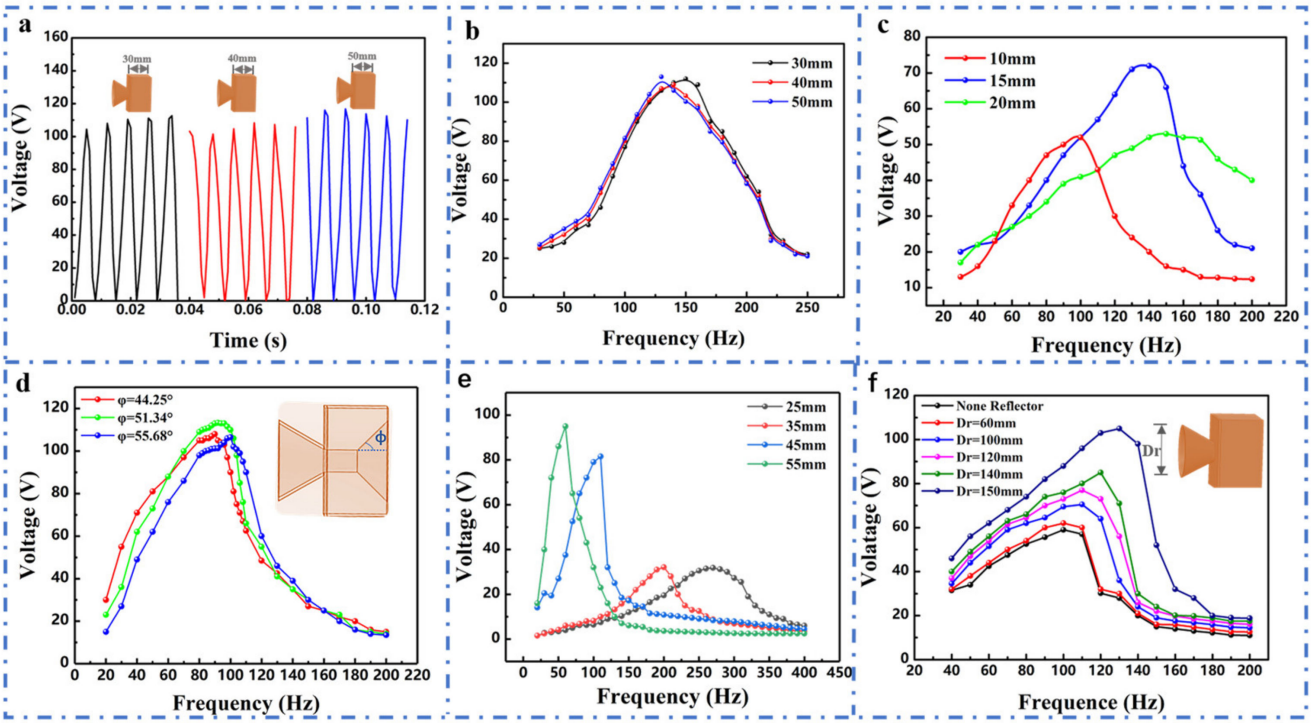

Figure 4. Electric output characterization of the CHR-TENG with varied geometrical sizes. (**a**) The maximum peak open-circuit voltage output of the CHR-TENG with different resonator thicknesses. (**b**) Open-circuit voltage output of the CHR-TENG with different resonator thicknesses. (**c**) Open-circuit voltage output of the CHR-TENG with different cross-sectional areas. (**d**) Open-circuit voltage output of the CHR-TENG with different coniform angles. (**e**) Open-circuit voltage output of the CHR-TENG with varied FEP film sizes. (**f**) Open-circuit voltage output of the CHR-TENG with different reflector sizes.

As illustrated in Figure 4b, the acoustic frequency of generating the peak open-circuit voltage (optimal response frequency) decreased from 140 Hz to 130 Hz when the resonator's thickness changed from 30 mm to 50 mm. This is due to the fact that the increase of the resonator thickness adds the resonator's volume V_c, and the resonator frequency will be lower with a bigger V_c. However, it can be seen in the present experimental conditions that the enhancement of the acoustic wave by the resonator cavity does not improve as V_c changes. To investigate the influence of the cross-sectional area of the connecting tube on the electric output performance, three CHR-TENGs with different cross-sectional areas were employed to measure the output power under the acoustic condition of frequency range 30 to 200 Hz and sound pressure level range 60.2 to 83.5 dB, as the results are shown in Figure 4c. As the cross-sectional area increases, the power output varies in different frequency ranges. The optimal response frequency increases with the cross-sectional area; meanwhile, the acoustic response band is also broadened. However, the output performance of the CHR-TENG does not get better with increased area. This result is because the acoustic energy entering the resonator cavity is less when the cross-sectional area is small. However, when the cross-sectional area is too large, a good mass–spring damping system cannot be formed, resulting in poor acoustic pressure level implication. Therefore, the cross-sectional area of the CHR-TENG can be designed and selected based on the acoustic frequency band of the actual application scenarios. As the coniform angle is an important parameter of the coniform cavity structure, a comparison was conducted by varying coniform angles of the resonator cavity of the CHR-TENG, in which the experiment was carried out under the acoustic environment of frequency 20–200 Hz and sound pressure level 61–90.4 dB. The peak open-circuit voltages of the CHR-TENG were measured with coniform angles of 44.25, 51.34 and 55.68, respectively. It was found that the open-circuit voltage of the CHR-TENG would be an increasing and then decreasing trend for each one

of the conical angles, as shown in Figure 4d. When the coniform angle was 44.25, the output voltage increased from 30 V to 108 V (the optimal output) as the frequency changed from 20 to 90 Hz, and then the output voltage gradually decreased to 15 V with the increasing sound frequency. The peak output voltage was 113.3 V for the CHR-TENG with a conical angle of 51.34, while the peak output voltage was 106.5 V for the CHR-TENG with a conical angle of 55.68. Obviously, the optimal response frequency of the CHR-TENG increases gradually with the increase of cone angle, but the increase is not large. The circular FEP film with fixed edges is driven by the air pressure difference generated by the acoustic source and vibrates reciprocally. The vibration of the circular FEP film is influenced by its size. We have investigated the influence of film size on the power output of the CHR-TENG.

As displayed in Figure 4e, the optimal response acoustic frequency changed from 270 Hz (FEP film diameter 25 mm) to 60 Hz (FEP film diameter 55 mm) with the increase of the FEP film size, while the optimal peak voltage for the optimal response acoustic frequency increased from 31.8 V to 96 V. More interestingly, the response bandwidth of the CHR-TENG with high output performance becomes narrower as the optimal response frequency decreases. The higher output results from the larger FEP film deformation, which can provide basic guidance for modulating the acoustic frequency response of the CHR-TENG. To enhance the acoustic energy collection, the front-end sound converging structure is installed on the CHR-TENG; hereafter, it is named as the reflector for the sake of simplification. The reflector on the CHR-TENG could effectively gather acoustic energy into the resonance cavity, thus contributing to improve its efficiency of acoustic–electric conversion. To systematically investigate the power output of the CHR-TENG for sufficient collecting acoustic energy into the resonance cavity, reflectors with diameters from 60 to 150 mm were employed to measure the output performance under the acoustic conditions of frequency from 40 to 200 Hz and sound pressure levels from 62.5 to 98.5 dB, as the results are shown in Figure 4f. Obviously, with the increase of reflector's diameter (D_r), the output peak open-circuit voltage of the CHR-TENG increases gradually. This is mainly ascribed to the fact that the increase in D_r results in a larger acoustic energy act on the CHR-TENG, thus, a better output performance. Meanwhile, the increase of the reflector's diameter is equivalent to the increase of S in Equation (1). The optimal response frequency of the CHR-TENG increases with the reflector diameter, which shows that experimental results are consistent with the theoretical results. Therefore, to enhance the efficiency of acoustic–electric conversion, a sufficiently large reflector should be installed as far as the environmental space allows.

2.4. Demonstration of the CHR-TENG

To the best of our knowledge, the maximum power density per unit area structure in the published articles is the dual-tube Helmholtz resonated TENG (HR-TENG) proposed by our group [33]. Figure 5a shows the peak open-circuit voltage of the two acoustic energy harvesting TENGs under the excitation of the same acoustic waves. The open-circuit voltage of the CHR-TENG can achieve approximately 110 V at the optimal electrical performance output frequency of 140 Hz, which is 83.3% higher than the maximum open-circuit voltage of the dual-tube HR-TENG. In terms of the electrical output performance at various acoustic frequencies, electric output of the dual-tube HR-TENG under a frequency of 30 Hz to 50 Hz raised relatively slowly (from 12 V to 14 V); the output voltage increased from 14 V to 60 V when the frequency changed from 50 Hz to 100 Hz. After that, with the increase of the sound frequency, the peak voltage of the HR-TENG declined rapidly. When the frequency rose to 150 Hz, the open-circuit voltage output dropped to about 14 V; then, with the increase in frequency, the output voltage remained unchanged, which indicates that the response frequency of the dual-tube HR-TENG is between 50 and 150 Hz. As for the output performance of the CHR-TENG, the peak open-circuit voltage increased from 20 V to 110 V under the sound frequency of 30 Hz to 140 Hz, and then the output performance gradually decreased with the acoustic frequency increase. When the frequency increased to 240 Hz, the peak open-circuit voltage dropped to about 24 V and then remained unchanged

with the increase of frequency, showing that the response frequency of the CHR-TENG is between 30 and 240 Hz. Throughout the 30 to 250 Hz sound frequency, the output voltage of the CHR-TENG is persistently above that of the dual-tube HR-TENG, indicating that the CHR-TENG has a better output performance and a wider response frequency.

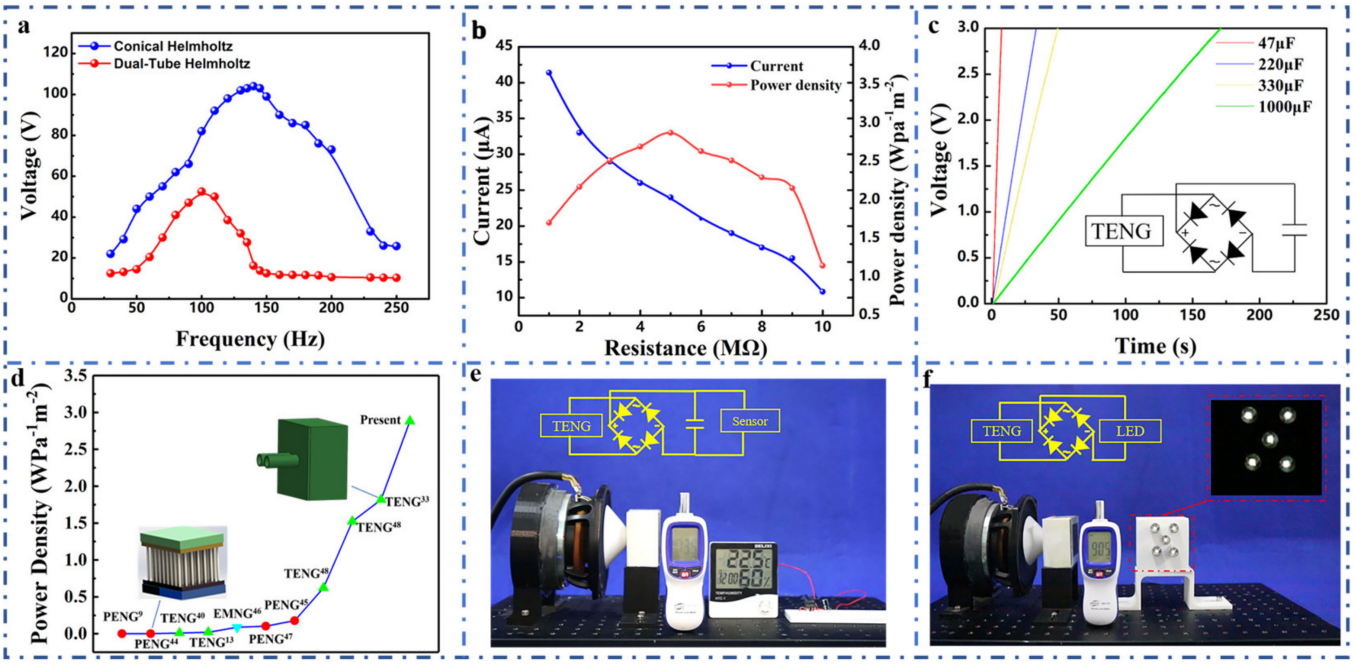

Figure 5. Demonstrations of the CHR-TENG for acoustic energy harvesting as a sustainable power source. (**a**) Comparison of the open-circuit voltage of the CHR-TENG and the dual-tube HR-TENG under excitation of the same acoustic conditions. (**b**) External resistance effect on the output performance of the CHR-TENG. (**c**) Charging of different capacitors by the CHR-TENG electrical output. (**d**) Power density comparison with previously acoustic energy harvesters. (**e**) Demonstration of the CHR-TENG for powering the sensor. (**f**) Demonstration of the CHR-TENG for powering LEDs.

To investigate the maximum output power of the CHR-TENG, the study was carried out by matching an external load to the acoustic energy harvesting device. Figure 5b depicts the effect of external resistance on the CHR-TENG output performance for the acoustic conditions of 140 Hz and 90 dB. As the external load resistance increases from 1MΩ to 10MΩ, the peak open-circuit current of the CHR-TENG gradually decreases, and the output power of the CHR-TENG for the same acoustic conditions first increases and then decreases (shown in Figure S7 in Supplementary Materials), showing a maximum power output when the load resistance is 5 MΩ. To make an equivalent comparison of output performance of various kinds of acoustic energy harvesters, the power density per unit of sound pressure is calculated. Particularly, the maximum power density of the CHR-TENG is 2.88 W/Pa·m^2. Experimental results show that the output performance of the CHR-TENG improved considerably (a 58.2% higher power density) compared to the previously published work by utilizing the coniform Helmholtz resonator to enhance the acoustic energy harvesting. A more detailed comparison of power density with previous acoustic energy harvesters is shown in Table S2 in the Supplementary Materials. The coniform Helmholtz resonator can enhance the acoustic energy harvesting, and, thus, more acoustic energy is transformed to electricity through TENG. Both the resonator cavity volume and the coniform angles would affect the output performance under different acoustic conditions. Therefore, a high-performance CHR-TENG could be designed and selected through structure optimization and applied in a specific acoustic scenario.

Figure 5c presents a demonstration experiment of the CHR-TENG charging capacitors with various capacities. Alternating current output of the CHR-TENG is supplied

to the capacitor ends through the rectifier bridge, and the electricity is then stored into the capacitor. Under the supply of the CHR-TENG, it took only about 6 s to charge a 47 μF capacitor to 3 V and about 165 s to charge a 1000 μF capacitor to 3 V, showing that the CHR-TENG has favorable charging performance for the capacitor. The power density of the CHR-TENG was calculated and compared with previously reported acoustic energy harvesters [9,13,32,33,44–48], as depicted in Figure 5d. Comparison of power density with previously acoustic energy harvesters is shown in Table S2 in Supplemental Materials. It can be seen from the figure that the optimal result in the literature has the power density per unit sound pressure 1.82 $W/Pa \cdot m^2$, while ours has that of 2.88 $W/Pa \cdot m^2$, showing a large improvement compared to the previous studies. In addition, as plotted in Figure 5e, the temperature and humidity sensor can be successfully switched on after charging the 1000 μF capacitor to 1.5 V. The sensor can function continuously while being powered by the CHR-TENG. Figure 5f shows the CHR-TENG can successfully light up as many as five 0.5 W commercial LED bulbs for acoustic energy harvesting by transforming acoustic energy to electricity. To examine the output performance of the acoustic energy harvester in real scenarios, the experimental results of the CHR-TENG testing in a ship's engine room and the stability of the device was performed. The power output performance of the CHR-TENG in a ship's engine room and stability test are shown in detail in Figures S6 and S8. Results show that the output capability of the harvester becomes weak due to the energy spreading in a wide space. In our future work, we will carry out further research by setting arrayed CHR-TENGs to eliminate the noise interference and adapting to the wideband acoustic frequency in a real application scenario. As for the stability test, experimental results indicate that there is hardly any change in the output performance after three days of tests, showing a good output stability characteristic.

3. Experimental Section

3.1. Fabrication of the CHR-TENG

The CHR-TENG consists of a coniform Helmholtz resonant cavity, an aluminum electrode with uniformly distributed acoustic holes and an FEP membrane with an ink-printed electrode. The front sound converging structure (or reflector) is fixed on the resonant cavity, and a coniform structure is designed to enhance the acoustic energy inside the resonator. Detailed dimensions of the CHR-TENG's resonant cavity are D_r 60 mm, D_n 15 mm, H_n 10 mm, H_c 20 mm and D_c 45 mm, respectively. An aluminum electrode with uniformly distributed sound holes (diameter 0.2 mm) is utilized as an electropositive friction layer, whose radius and thickness are 22.5 mm and 0.1 mm, respectively. The flexible FEP film is used as the electronegative frictional electric material with the thickness of 30 μm, and the radius of the working area is 22.5 mm. As the FEP film is insulative, this work is designed to transfer electrons by attaching conductive ink electrodes with micron thickness on the backside of the FEP film. Resonator housings of various shapes and sizes are produced by a 3D printer utilizing PLA materials with high levels of device precision. The high filling density housing has flat surface and excellent airtightness, which benefits sound waves reflection and the formation of the resonance effect.

3.2. Characterization and Electrical Output Measurement of the CHR-TENG

When measuring the power output performance, the CHR-TENG is mounted on an optical board with a loudspeaker (JBL) producing sound, which is driven and adjusted by a function generator (YE1311) with sine waves. The sound is transmitted through a power amplifier (SA-5016) with an accuracy and resolution of 1.5 db and 0.1 db respectively. The output signals include open-circuit voltage, short-circuit current and transferred charge, which can be measured with a Keithley 6514 electrostatic meter.

3.3. Numerical Simulation

COMSOL Multiphysics was used for simulating the sound pressure distribution of the coniform Helmholtz resonator cavity. A classic acoustics model of a resonating circuit with a known theoretical solution is applied. The membrane is simplified to be a rigid one. The environment outside the cavity is regarded as the standard atmospheric pressure. The inlet sound pressure is set to be the value of pressure measured in front of the cavity. Based on the above assumptions, a pressure acoustics–frequency domain physics is set up in a two-dimensional axisymmetric model with the parameters and geometry of the CHR-TENG. After the integration is set, the models are solved by the Asymptotic Waveform Evaluation solver and the frequency domain–modal solver.

4. Conclusions

In summary, we proposed a low-cost, easily fabricated and high-performance coniform Helmholtz resonator-based TENG for efficient acoustic energy harvesting. In the CHR-TENG, the coniform Helmholtz resonator plays a role in enhancing the collection of acoustic energy. Driven by the harvested acoustic energy, the FEP membrane in the CHR-TENG alternately contacts and separates from the aluminum electrode, thus generating continuous electricity output. The novel design in the CHR-TENG could improve its output performance and broaden its response band over harvesting acoustic energy. Compared with the conventional acoustic energy harvesting TENG devices, the CHR-TENG has improved output performance. Output performances of the CHR-TENG with varied geometrical sizes were systematically investigated under different sound energy conditions, and results showed that, with the optimized design, the maximum acoustic sensitivity per unit area of the CHR-TENG could reach 1.68 $V/Pa \cdot m^2$, while the power density per unit of sound pressure was 2.88 $W/Pa \cdot m^2$. In addition, the CHR-TENG was demonstrated to charge a 1000 μF capacitor up to 3 V in 165 s, power a sensor for continuous temperature and humidity monitoring and light up as many as 464 commercial LED bulbs for acoustic energy harvesting. The newly designed CHR-TENG not only provides an effective guide for efficient conversion of acoustic energy into electrical energy but also demonstrates the potential application of the CHR-TENG in powering electronic devices.

Supplementary Materials: The following are available online at https://www.mdpi.com/article/10.3390/nano11123431/s1, Figure S1: Surface topography image of (a) the normal FEP film and (b) the polished FEP film, Figure S2: Output performances of the CHR-TENGs. (a) The short-circuit current and (b) transfer charge of the CHR-TENGs with different reflector sizes under the same acoustic wave condition with the acoustic frequency ranging from 40 to 200 Hz, Figure S3: Output performances of the CHR-TENGs. (a) The short-circuit current and (b) transfer charge of the CHR-TENGs with different resonator thicknesses under the same acoustic wave condition with the acoustic frequency ranging from 40 to 250 Hz, Figure S4: Output per-formances of the CHR-TENGs. (a) The short-circuit current and (b) transfer charge of the CHR-TENGs with different coniform angles under the same acoustic wave conditions, with the acoustic frequency ranging from 20 to 200 Hz, Figure S5: Output performances of the CHR-TENGs. (a) The short-circuit current and (b) transfer charge of the CHR-TENGs with varied FEP film sizes under the same acoustic wave conditions, with the acoustic frequency ranging from 20 to 400 Hz. Figure S6. Schematic diagram of the CHR-TENG harvesting ship acoustic energy in a ship engine room. (a) open-circuit voltage and (b) short-circuit current. Figure S7. Power output performance of the CHR-TENG under the acoustic pressure level of 90 dB and acoustic frequency of 140Hz. Figure S8. Test of the stability output performance of the CHR-TENG under acoustic condition of sound pressure level 90dB and frequency 140Hz. (a) single test result and (b) comparison of the three day's output performance test. Video S1: Demonstration of the CHR-TENG powering a thermometer. Video S2: Demonstration of the CHR-TENG powering 0.5W LEDs. Video S3: Demonstration of CHR-TENG powering 464 LEDs. Table S1: Acoustic levels in various transportation scenarios. Table S2: Power density comparison with previously acoustic energy harvesters.

Author Contributions: Conceptualization, M.X.; investigation, H.Y. (Haichao Yuan), H.Y. (Hongyong Yu) and H.Z.; validation, H.Y. (Haichao Yuan), H.Y. (Hongyong Yu) and Q.Z.; data curation, H.Y.

(Hongyong Yu), X.L., L.L., Y.Z. and Z.X.; writing—original draft preparation, H.Y. (Haichao Yuan); writing—review and editing, H.Y. (Haichao Yuan) and M.X.; supervision, Y.L., X.P. and M.X.; project administration, M.X.; funding acquisition, M.X. All authors have read and agreed to the published version of the manuscript.

Funding: The work was supported by the National Natural Science Foundation of China (Grant Nos. 51879022, 51979045), the Fundamental Research Funds for the Central Universities, China (Grant Nos. 3132019330, 3132021340), Dalian Outstanding Young Scientific and Technological Talents Project (2021RJ11) and Innovation Group Project of Southern Marine Science and Engineering Guangdong Laboratory (Zhuhai) (No.311021013).

Institutional Review Board Statement: Not applicable.

Informed Consent Statement: Not applicable.

Data Availability Statement: The data used to support the findings of this study are available from the corresponding author upon request.

Conflicts of Interest: The authors declare no conflict of interest.

References

1. Ahmed, A.; Hassan, I.; El-Kady, M.F.; Radhi, A.; Jeong, C.K.; Selvaganapathy, P.R.; Zu, J.; Ren, S.; Wang, Q.; Kaner, R.B. Integrated Triboelectric Nanogenerators in the Era of the Internet of Things. *Adv. Sci.* **2019**, *6*, 1802230. [CrossRef] [PubMed]
2. Shi, Q.; Dong, B.; He, T.; Sun, Z.; Zhu, J.; Zhang, Z.; Lee, C. Progress in Wearable Electronics/Photonics—Moving toward the Era of Artificial Intelligence and Internet of Things. *InfoMat* **2020**, *2*, 1131–1162. [CrossRef]
3. Sripadmanabhan Indira, S.; Aravind Vaithilingam, C.; Oruganti, K.S.P.; Mohd, F.; Rahman, S. Nanogenerators as a Sustainable Power Source: State of Art, Applications, and Challenges. *Nanomaterials* **2019**, *9*, 773. [CrossRef] [PubMed]
4. Xue, C.; Li, J.; Zhang, Q.; Zhang, Z.; Hai, Z.; Gao, L.; Feng, R.; Tang, J.; Liu, J.; Zhang, W.; et al. A Novel Arch-Shape Nanogenerator Based on Piezoelectric and Triboelectric Mechanism for Mechanical Energy Harvesting. *Nanomaterials* **2014**, *5*, 36–46. [CrossRef] [PubMed]
5. Chao, P.C.-P. Energy Harvesting Electronics for Vibratory Devices in Self-Powered Sensors. *IEEE Sens. J.* **2011**, *11*, 3106–3121. [CrossRef]
6. Tang, X.; Wang, X.; Cattley, R.; Gu, F.; Ball, A.D. Energy Harvesting Technologies for Achieving Self-Powered Wireless Sensor Networks in Machine Condition Monitoring: A Review. *Sensors* **2018**, *18*, 4113. [CrossRef] [PubMed]
7. Lehtola, T.; Zahedi, A. Solar Energy and Wind Power Supply Supported by Storage Technology: A Review. *Sustain. Energy Technol. Assess.* **2019**, *35*, 25–31. [CrossRef]
8. Choi, J.; Jung, I.; Kang, C.-Y. A Brief Review of Sound Energy Harvesting. *Nano Energy* **2019**, *56*, 169–183. [CrossRef]
9. Qi, S.; Oudich, M.; Li, Y.; Assouar, B. Acoustic Energy Harvesting Based on a Planar Acoustic Metamaterial. *Appl. Phys. Lett.* **2016**, *108*, 263501. [CrossRef]
10. Hassan, H.F.; Hassan, S.I.S.; Rahim, R.A. Acoustic Energy Harvesting Using Piezoelectric Generator for Low Frequency Sound Waves Energy Conversion. *Int. J. Eng. Technol. (IJET)* **2014**, *5*, 4702–4707.
11. Sun, K.H.; Kim, J.E.; Kim, J.; Song, K. Sound Energy Harvesting Using a Doubly Coiled-up Acoustic Metamaterial Cavity. *Smart Mater. Struct.* **2017**, *26*, 075011. [CrossRef]
12. Yuan, M.; Cao, Z.; Luo, J.; Chou, X. Recent Developments of Acoustic Energy Harvesting: A Review. *Micromachines* **2019**, *10*, 48. [CrossRef]
13. Yang, A.; Li, P.; Wen, Y.; Lu, C.; Peng, X.; Zhang, J.; He, W. Enhanced Acoustic Energy Harvesting Using Coupled Resonance Structure of Sonic Crystal and Helmholtz Resonator. *Appl. Phys. Express* **2013**, *6*, 127101. [CrossRef]
14. Mann, B.P.; Sims, N.D. On the Performance and Resonant Frequency of Electromagnetic Induction Energy Harvesters. *J. Sound Vib.* **2010**, *329*, 1348–1361. [CrossRef]
15. Khan, M.B.; Kim, D.H.; Han, J.H.; Saif, H.; Lee, H.; Lee, Y.; Kim, M.; Jang, E.; Hong, S.K.; Joe, D.J.; et al. Performance Improvement of Flexible Piezoelectric Energy Harvester for Irregular Human Motion with Energy Extraction Enhancement Circuit. *Nano Energy* **2019**, *58*, 211–219. [CrossRef]
16. Khan, F. Izhar Piezoelectric Type Acoustic Energy Harvester with a Tapered Helmholtz Cavity for Improved Performance. *J. Renew. Sustain. Energy* **2016**, *8*, 054701. [CrossRef]
17. Li, L.; Wang, X.; Zhu, P.; Li, H.; Wang, F.; Wu, J. The Electron Transfer Mechanism between Metal and Amorphous Polymers in Humidity Environment for Triboelectric Nanogenerator. *Nano Energy* **2020**, *70*, 104476. [CrossRef]
18. Fan, F.-R.; Tian, Z.-Q.; Wang, Z.-L. Flexible Triboelectric Generator. *Nano Energy* **2012**, *1*, 328–334. [CrossRef]
19. Du, T.; Zuo, X.; Dong, F.; Li, S.; Mtui, A.E.; Zou, Y.; Zhang, P.; Zhao, J.; Zhang, Y.; Sun, P.; et al. A Self-Powered and Highly Accurate Vibration Sensor Based on Bouncing-Ball Triboelectric Nanogenerator for Intelligent Ship Machinery Monitoring. *Micromachines* **2021**, *12*, 218. [CrossRef] [PubMed]

20. Xu, M.; Wang, P.; Wang, Y.-C.; Zhang, S.L.; Wang, A.C.; Zhang, C.; Wang, Z.; Pan, X.; Wang, Z.L. A Soft and Robust Spring Based Triboelectric Nanogenerator for Harvesting Arbitrary Directional Vibration Energy and Self-Powered Vibration Sensing. *Adv. Energy Mater.* **2018**, *8*, 1702432. [CrossRef]
21. Xiao, X.; Zhang, X.; Wang, S.; Ouyang, H.; Chen, P.; Song, L.; Yuan, H.; Ji, Y.; Wang, P.; Li, Z.; et al. Honeycomb Structure Inspired Triboelectric Nanogenerator for Highly Effective Vibration Energy Harvesting and Self-Powered Engine Condition Monitoring. *Adv. Energy Mater.* **2019**, *9*, 1902460. [CrossRef]
22. Quan, T.; Wu, Y.; Yang, Y. Hybrid Electromagnetic–Triboelectric Nanogenerator for Harvesting Vibration Energy. *Nano Res.* **2015**, *8*, 3272–3280. [CrossRef]
23. Wang, Y.; Yang, E.; Chen, T.; Wang, J.; Hu, Z.; Mi, J.; Pan, X.; Xu, M. A Novel Humidity Resisting and Wind Direction Adapting Flag-Type Triboelectric Nanogenerator for Wind Energy Harvesting and Speed Sensing. *Nano Energy* **2020**, *78*, 105279. [CrossRef]
24. Xu, M.; Wang, Y.-C.; Zhang, S.L.; Ding, W.; Cheng, J.; He, X.; Zhang, P.; Wang, Z.; Pan, X.; Wang, Z.L. An Aeroelastic Flutter Based Triboelectric Nanogenerator as a Self-Powered Active Wind Speed Sensor in Harsh Environment. *Extrem. Mech. Lett.* **2017**, *15*, 122–129. [CrossRef]
25. Wang, Y.; Wang, J.; Xiao, X.; Wang, S.; Kien, P.T.; Dong, J.; Mi, J.; Pan, X.; Wang, H.; Xu, M. Multi-Functional Wind Barrier Based on Triboelectric Nanogenerator for Power Generation, Self-Powered Wind Speed Sensing and Highly Efficient Windshield. *Nano Energy* **2020**, *73*, 104736. [CrossRef]
26. Chen, P.; An, J.; Shu, S.; Cheng, R.; Nie, J.; Jiang, T.; Wang, Z.L. Super-Durable, Low-Wear, and High-Performance Fur-Brush Triboelectric Nanogenerator for Wind and Water Energy Harvesting for Smart Agriculture. *Adv. Energy Mater.* **2021**, *11*, 2003066. [CrossRef]
27. Xu, M.; Zhao, T.; Wang, C.; Zhang, S.L.; Li, Z.; Pan, X.; Wang, Z.L. High Power Density Tower-like Triboelectric Nanogenerator for Harvesting Arbitrary Directional Water Wave Energy. *ACS Nano* **2019**. [CrossRef] [PubMed]
28. Zhao, T.; Xu, M.; Xiao, X.; Ma, Y.; Li, Z.; Wang, Z.L. Recent Progress in Blue Energy Harvesting for Powering Distributed Sensors in Ocean. *Nano Energy* **2021**, *88*, 106199. [CrossRef]
29. Wang, Y.; Liu, X.; Wang, Y.; Wang, H.; Wang, H.; Zhang, S.L.; Zhao, T.; Xu, M.; Wang, Z.L. Flexible Seaweed-Like Triboelectric Nanogenerator as a Wave Energy Harvester Powering Marine Internet of Things. *ACS Nano* **2021**, *15*, 15700–15709. [CrossRef] [PubMed]
30. Wang, Y.; Liu, X.; Chen, T.; Wang, H.; Zhu, C.; Yu, H.; Song, L.; Pan, X.; Mi, J.; Lee, C.; et al. An Underwater Flag-like Triboelectric Nanogenerator for Harvesting Ocean Current Energy under Extremely Low Velocity Condition. *Nano Energy* **2021**, *90*, 106503. [CrossRef]
31. Yuan, M.; Li, C.; Liu, H.; Xu, Q.; Xie, Y. A 3D-Printed Acoustic Triboelectric Nanogenerator for Quarter-Wavelength Acoustic Energy Harvesting and Self-Powered Edge Sensing. *Nano Energy* **2021**, *85*, 105962. [CrossRef]
32. Chen, F.; Wu, Y.; Ding, Z.; Xia, X.; Li, S.; Zheng, H.; Diao, C.; Yue, G.; Zi, Y. A Novel Triboelectric Nanogenerator Based on Electrospun Polyvinylidene Fluoride Nanofibers for Effective Acoustic Energy Harvesting and Self-Powered Multifunctional Sensing. *Nano Energy* **2019**, *56*, 241–251. [CrossRef]
33. Zhao, H.; Xiao, X.; Xu, P.; Zhao, T.; Song, L.; Pan, X.; Mi, J.; Xu, M.; Wang, Z.L. Dual-Tube Helmholtz Resonator-Based Triboelectric Nanogenerator for Highly Efficient Harvesting of Acoustic Energy. *Adv. Energy Mater.* **2019**, *9*, 1902824. [CrossRef]
34. Fan, X.; Chen, J.; Yang, J.; Bai, P.; Li, Z.; Wang, Z.L. Ultrathin, Rollable, Paper-Based Triboelectric Nanogenerator for Acoustic Energy Harvesting and Self-Powered Sound Recording. *ACS Nano* **2015**, *9*, 4236–4243. [CrossRef]
35. Wang, Z.L. Triboelectric Nanogenerator (TENG)—Sparking an Energy and Sensor Revolution. *Adv. Energy Mater.* **2020**, *10*, 2000137. [CrossRef]
36. Zhou, Y.; Shen, M.; Cui, X.; Shao, Y.; Li, L.; Zhang, Y. Triboelectric Nanogenerator Based Self-Powered Sensor for Artificial Intelligence. *Nano Energy* **2021**, *84*, 105887. [CrossRef]
37. Chen, J.; Wang, Z.L. Reviving Vibration Energy Harvesting and Self-Powered Sensing by a Triboelectric Nanogenerator. *Joule* **2017**, *1*, 480–521. [CrossRef]
38. Wang, S.; Wang, Y.; Liu, D.; Zhang, Z.; Li, W.; Liu, C.; Du, T.; Xiao, X.; Song, L.; Pang, H.; et al. A Robust and Self-Powered Tilt Sensor Based on Annular Liquid-Solid Interfacing Triboelectric Nanogenerator for Ship Attitude Sensing. *Sens. Actuators A Phys.* **2021**, *317*, 112459. [CrossRef]
39. Yang, J.; Chen, J.; Liu, Y.; Yang, W.; Su, Y.; Wang, Z.L. Triboelectrification-Based Organic Film Nanogenerator for Acoustic Energy Harvesting and Self-Powered Active Acoustic Sensing. *ACS Nano* **2014**, *8*, 2649–2657. [CrossRef] [PubMed]
40. Cui, N.; Gu, L.; Liu, J.; Bai, S.; Qiu, J.; Fu, J.; Kou, X.; Liu, H.; Qin, Y.; Wang, Z.L. High Performance Sound Driven Triboelectric Nanogenerator for Harvesting Noise Energy. *Nano Energy* **2015**, *15*, 321–328. [CrossRef]
41. Wang, Z.; Wu, Y.; Jiang, W.; Liu, Q.; Wang, X.; Zhang, J.; Zhou, Z.; Zheng, H.; Wang, Z.; Wang, Z.L. A Universal Power Management Strategy Based on Novel Sound-Driven Triboelectric Nanogenerator and Its Fully Self-Powered Wireless System Applications. *Adv. Funct. Mater.* **2021**, *31*, 2103081. [CrossRef]
42. Wu, J.; Wang, X.; Li, H.; Wang, F.; Yang, W.; Hu, Y. Insights into the Mechanism of Metal-Polymer Contact Electrification for Triboelectric Nanogenerator via First-Principles Investigations. *Nano Energy* **2018**, *48*, 607–616. [CrossRef]
43. Pillai, M.A.; Deenadayalan, E. A Review of Acoustic Energy Harvesting. *Int. J. Precis. Eng. Manuf.* **2014**, *15*, 949–965. [CrossRef]
44. Cha, S.N.; Seo, J.-S.; Kim, S.M.; Kim, H.J.; Park, Y.J.; Kim, S.-W.; Kim, J.M. Sound-Driven Piezoelectric Nanowire-Based Nanogenerators. *Adv. Mater.* **2010**, *22*, 4726–4730. [CrossRef] [PubMed]

45. Yang, J.; Chen, J.; Yang, Y.; Zhang, H.; Yang, W.; Bai, P.; Su, Y.; Wang, Z.L. Broadband Vibrational Energy Harvesting Based on a Triboelectric Nanogenerator. *Adv. Energy Mater.* **2014**, *4*, 1301322. [CrossRef]
46. Khan, F.U.; Izhar, I. Acoustic-Based Electrodynamic Energy Harvester for Wireless Sensor Nodes Application. *Int. J. Mater. Sci. Eng.* **2013**, *1*, 72–78. [CrossRef]
47. Li, B.; You, J.H.; Kim, Y.-J. Low Frequency Acoustic Energy Harvesting Using PZT Piezoelectric Plates in a Straight Tube Resonator. *Smart Mater. Struct.* **2013**, *22*, 055013. [CrossRef]
48. Liu, J.; Cui, N.; Gu, L.; Chen, X.; Bai, S.; Zheng, Y.; Hu, C.; Qin, Y. A Three-Dimensional Integrated Nanogenerator for Effectively Harvesting Sound Energy from the Environment. *Nanoscale* **2016**, *8*, 4938–4944. [CrossRef] [PubMed]

nanomaterials

MDPI

Article

The Regulation of O_2 Spin State and Direct Oxidation of CO at Room Temperature Using Triboelectric Plasma by Harvesting Mechanical Energy

Xue Shi [1,†], Sumin Li [1,†], Bao Zhang [1,†], Jiao Wang [1], Xiaochen Xiang [1], Yifei Zhu [2], Ke Zhao [1], Wanyu Shang [1], Guangqin Gu [1], Junmeng Guo [1], Peng Cui [1], Gang Cheng [1,*] and Zuliang Du [1]

[1] Key Lab for Special Functional Materials, Ministry of Education, National & Local Joint Engineering Research Center for High-Efficiency Display and Lighting Technology, School of Materials Science and Engineering, Collaborative Innovation Center of Nano Functional Materials and Applications, Henan University, Kaifeng 475004, China; shixuehenandaxue@126.com (X.S.); amernsuli1981@163.com (S.L.); zhangbao@henu.edu.cn (B.Z.); 13203449093@163.com (J.W.); xiang17737488621@163.com (X.X.); kezhao_5@163.com (K.Z.); shangwanyu0525@163.com (W.S.); guguangqin@vip.henu.edu.cn (G.G.); junmengguo@163.com (J.G.); cuipeng@henu.edu.cn (P.C.); zld@henu.edu.cn (Z.D.)

[2] Institute of Aero-Engine, School of Mechanical Engineering, Xi'an Jiaotong University, Xi'an 710049, China; yifei.zhu.plasma@gmail.com

* Correspondence: chenggang@henu.edu.cn

† These authors contributed equally to this work.

Citation: Shi, X.; Li, S.; Zhang, B.; Wang, J.; Xiang, X.; Zhu, Y.; Zhao, K.; Shang, W.; Gu, G.; Guo, J.; et al. The Regulation of O_2 Spin State and Direct Oxidation of CO at Room Temperature Using Triboelectric Plasma by Harvesting Mechanical Energy. *Nanomaterials* **2021**, *11*, 3408. https://doi.org/10.3390/nano11123408

Academic Editors: Zhen Wen, Hengyu Guo, Longfei Wang and Detlef W. Bahnemann

Received: 16 November 2021
Accepted: 13 December 2021
Published: 16 December 2021

Abstract: Oxidation reactions play a critical role in processes involving energy utilization, chemical conversion, and pollutant elimination. However, due to its spin-forbidden nature, the reaction of molecular dioxygen (O_2) with a substrate is difficult under mild conditions. Herein, we describe a system that activates O_2 via the direct modulation of its spin state by mechanical energy-induced triboelectric corona plasma, enabling the CO oxidation reaction under normal temperature and pressure. Under optimized reaction conditions, the activity was 7.2 μmol h^{-1}, and the energy consumption per mole CO was 4.2 MJ. The results of kinetic isotope effect, colorimetry, and density functional theory calculation studies demonstrated that electrons generated in the triboelectric plasma were directly injected into the antibonding orbital of O_2 to form highly reactive negative ions O_2^-, which effectively promoted the rate-limiting step of O_2 dissociation. The barrier of the reaction of O_2^- ions and CO molecular was 3.4 eV lower than that of O_2 and CO molecular. This work provides an effective strategy for using renewable and green mechanical energy to realize spin-forbidden reactions of small molecules.

Keywords: triboelectric nanogenerator; mechanical energy; dioxygen activation; triboelectric corona plasma; O_2^- reactive species; spin conversion

1. Introduction

Molecular dioxygen ($^3O_2$) is the most green, pollution-free, and cheap terminal oxidant [1–8]. Unfortunately, ground state $^3O_2$ is usually chemically inert under normal temperature and pressure conditions, and the oxidation of compounds by $^3O_2$ is hindered by its spin-forbidden nature [1]. To enable the activation of $^3O_2$ at room temperature, considerable research efforts have been directed toward the regulation of its spin state. As a result, a number of approaches have been developed, such as the conversion of the triplet state of dioxygen ($^3O_2$) into singlet dioxygen ($^1O_2$) via external stimulation, e.g., by light irradiation [2,3,9,10]. This can be achieved under the assistance of a photosensitizer, as shown in Figure 1a. Under light illumination, the photosensitizer absorbs energy and is excited to an excited single state, which then undergoes intersystem crossing to produce an excited triplet state. The latter transfers its energy to $^3O_2$, which is converted to $^1O_2$, while the excited photosensitizer returns to its ground state. The two spin-paired valence

electrons of $^1O_2$ are in one π orbital, while the second π* orbital is empty, thereby lifting the spin blockade of $^3O_2$. Another method for the activation of $^3O_2$ consists of its one-electron reduction to superoxide $^2O_2^-$ (Figure 1b) [2,4–8], in which the electron is transferred to the $^3O_2$ molecule via metal/metal oxide catalysis or photocatalysis. The lowest unoccupied molecular orbital (LUMO) π* of $^2O_2^-$ has a single electron, which endows the molecule with free radical reactivity, easily reacting with a substrate. Nevertheless, both $^3O_2$ activation systems require the use of metals or metal oxides as catalysts or additives [1–5,11–15], with the concomitant heavy metal pollution and economic infeasibility of large-scale production. Thus, the development of an efficient system for the activation of $^3O_2$ for aerobic oxidation via the direct regulation of its spin state is still a huge challenge.

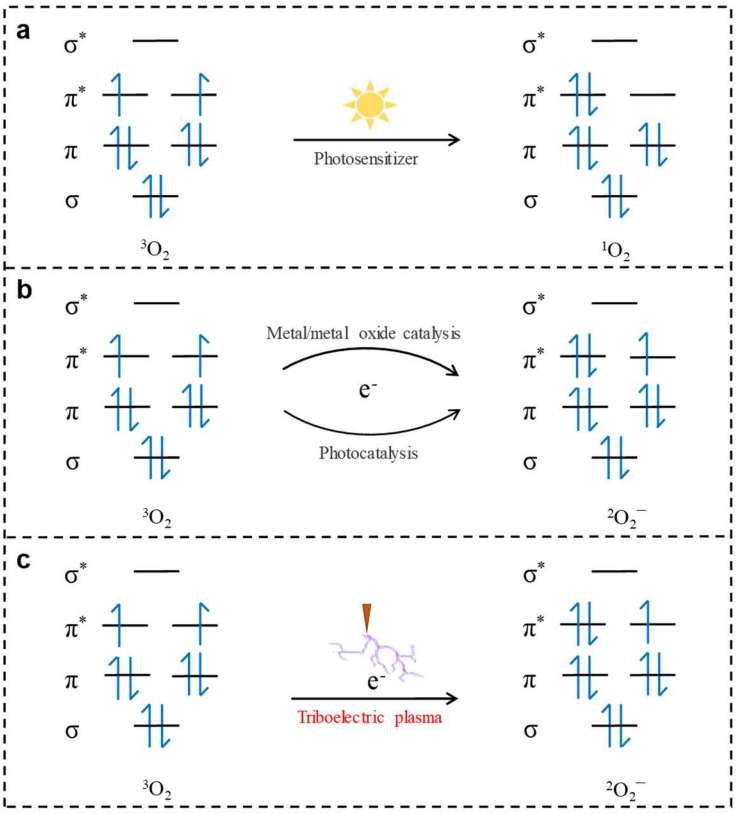

Figure 1. Spins conversion of molecular dioxygen using different methods. (**a**) Transformation of $^3O_2$ to $^1O_2$ under light irradiation with a photosensitizer. (**b**) Transformation of $^3O_2$ to $^2O_2^-$ under metal/metal oxide catalysis and photocatalysis. (**c**) Transformation of $^3O_2$ to $^2O_2^-$ using triboelectric plasma.

In this context, mechanical energy can be envisaged as an attractive source of activation energy because it is a ubiquitous, earth-abundant, and renewable energy that exists in various forms including wind energy, raindrop energy, tidal energy, and hydropower [16–23]. Compared with other renewable energy sources such as solar energy, mechanical energy offers the advantage of abundant reserves that are not affected by geographical location and weather [24,25]. In recent years, triboelectric nanogenerators (TENGs) have emerged as novel mechanical energy collection devices with broad application prospects in energy collection [26], gas sensing [27], and other fields [25,28,29]. A TENG is characterized by an advantageous high output voltage, which can directly generate a gas discharge forming triboelectric plasma [30,31]. During such a process, a large number of electrons generated through the avalanche effect can be captured by electronegative $^3O_2$ molecules; hence, electrons are injected into the LUMO energy level of $^3O_2$, enabling its conversion into $^2O_2^-$. Therefore, numerous electrons generated in the mechanical energy-induced triboelectric

plasma are directly transferred into the LUMO energy level of $^3O_2$, which is expected to overcome the spin-forbidden nature of its activation at room temperature (Figure 1c).

Herein, we report the use of triboelectric corona plasma for the direct modulation of the spin state of $^3O_2$, which enabled its activation for the direct carbon monoxide (CO) oxidation at room temperature and pressure. We selected the CO oxidation reaction as a model reaction to study the effect of $^3O_2$ spin change on its reactivity because it is a common model reaction of great significance in the fields of automobile exhaust treatment, fuel cells, and environmental protection. We used the high output voltage of a TENG to trigger the generation of triboelectric plasma from a gas and investigated the influence of the rotational speed of the TENG, the needle-plate distance, and the corona polarity on the triboelectric plasma. The optimal activity was 7.2 μmol h^{-1}, and the minimum energy required to convert 1 mol CO was 4.2 MJ. The results of colorimetry, kinetic isotope effect (KIE), and density functional theory (DFT) studies showed that high-energy electrons generated in the triboelectric plasma were directly injected into the π* antibonding orbital of $^3O_2$ to realize the activation of the O–O bonds at low temperature. This work provides a novel pathway for using mechanical energy to overcome the spin-forbidden transition of small molecules.

2. Materials and Methods

2.1. Carbon Monoxide (CO) Oxidation Triggered by Mechanical Energy-Induced Triboelectric Plasma

The system for the triboelectric plasma-triggered CO oxidation consisted of three parts: a TENG, a plasma oxidation reaction device, and an electrical test system. The freestanding rotating TENG with a diameter of 25 cm was composed of 10 μm of polytetrafluoroethylene (PTFE) film and a 30 μm Cu film as triboelectric layers and an electrode. The Cu and PTFE layers were adhered to polymethylmethacrylate. Two Cu films were connected to form the TENG electrodes through a rectifier bridge of the external circuit using Cu wires. When the triboelectric layers of the TENG were in contact with each other, opposite triboelectric charges were generated. When the PTFE triboelectric layer was moving, the two Cu electrodes generated a potential difference. The electrode of the triboelectric plasma was composed of a W needle and a Pt electrode plate. The radius of curvature of the W needle was 5 μm. The two discharge electrodes were located in a 500 mL reaction bottle, and the distance between the W needle and the Pt electrode plate was precisely adjusted using a three-dimensional moving platform.

The triboelectric plasma-triggered CO oxidation reaction was conducted in a self-made glass reactor (500 mL) under normal temperature and pressure. Using the TENG as the driving force, the output signal was recorded in an ammeter (Keithley 6514) and a voltmeter (Tektronix). The W needle and the Pt electrode plate (Tianjin Aida Hengsheng Technology Development Co., Ltd.,Tianjin, China, purity 99.99%) were fixed in the glass reactor, which then was purged with a mixed gas of $CO/O_2/He$ (1:20:79) (Henan Yuan Zheng Technology Development Co., Ltd., Kaifeng, China) for 10 min, and the air was replaced with the mixed gas three times. During the reaction, a carbon dioxide (CO_2) detector was used to determine the CO_2 concentration generated (Haipa air detector, accuracy 1 ppm), the reaction time was set to 1 h, the needle–plate distance was 3 mm, and the rotational speed of the TENG was 400 rpm. The effects of rotational speed of the TENG, needle-plate distance, the corona polarities, and working electrodes on the CO oxidation reaction activity were investigated.

2.2. Detection of $^2O_2^-$ Radicals

Nitro blue tetrazolium (NBT; Shandong West Asia Chemical Co., Ltd., Dongying, China) was reduced by O_2^- radicals to produce a blue product, which was insoluble in water [32]. The change in the absorbance of the solution was measured using ultraviolet-visible spectroscopy to detect the existence of reactive O_2^- radicals. The NBT aqueous solution had a maximum absorption peak at a wavelength of 260 nm. In a 3 mL glass reaction device, 2 mL of a 0.05 mmol L^{-1} NBT solution (V_{water}:$V_{propanol}$ = 98:2) was added.

A Cu mesh electrode was placed above the solution surface to avoid the quenching of highly energetic radicals, purged with $CO/O_2/He$ mixed gas, and then discharged for 30 min.

2.3. Isotope Labeling Experiment

The triboelectric plasma-triggered CO oxidation reaction was performed using $^{13}CO/^{18}O_2/Ar$ and $^{12}CO/^{16}O_2/Ar$ for 10 h. The composition and concentration of the isotopic products were determined by Wuhan Newrad Special Gas Co., Ltd., Wuhan, China.

2.4. Isotope Kinetics Effect (KIE) Experiment

The KIE experiments were conducted using $CO/^{16}O_2/He$ and $CO/^{18}O_2/He$ as the substrates under the conditions of the triboelectric plasma-triggered CO oxidation reaction for 1 h at room temperature and pressure. The KIE was calculated on the basis of the reaction rates obtained using $^{16}O_2$ and $^{18}O_2$ as reactants.

2.5. Density Functional Theory (DFT) Calculations

DFT calculations were performed using the Vienna Ab-initio Simulation Package (VASP) [33,34], taking advantage of the Projected Augmented Wave (PAW) [35] method. The Perdew–Burke–Ernzerhof functional was used to describe the exchange and correlation effects [36]. For all the geometry optimizations, the cutoff energy was set to 450 eV. Spin-polarization calculations were included in all cases. Singlet and triplet oxygen were modeled by controlling the numerical difference between spin-up electrons and spin-down electrons. The simulation box was constructed as a 21 Å × 22 Å × 20 Å box. The DFT calculation process was provided by the Cailiaoren APP.

2.6. Triboelectric Plasma Simulation

Triboelectric plasma simulation was performed using 2D PASSKEy code (PArallel Streamer Solver with KinEtics), which was used in modelling nanosecond surface discharges and proved by discharge morphology, propagation velocity, voltage–current curves of triboelectric plasma, and a point-to-plane configuration generated from the experiments [37–40]. Moreover, 0D model global plasma chemistry code ZDPlasKin was also utilized in a house parameter reconstruction module [41].

3. Results and Discussion

3.1. CO Oxidation System Driven by Mechanical Energy-Induced Triboelectric Plasma

As shown in Figure 2a and Figure S1, the designed system for CO oxidation driven by mechanical energy-induced triboelectric plasma consisted of three parts: a TENG, a plasma oxidation reaction device, and an electrical test system. The TENG, which was composed of a Cu film and a polytetrafluoroethylene (PTFE) film friction layer, was used as the driving force of the reaction. The plasma oxidation reaction device comprised a needle-plate electrode and a CO mixture gas ($CO/O_2/He$ = 1:20:79). The electrical test system consisted of a voltmeter and an ammeter. When the PTFE film was placed in contact with the Cu film, the surfaces of the two materials generated an equal amount of negative and positive triboelectric charge. By periodically rotating the PTFE film, a periodic potential difference was generated between the two Cu electrodes of the TENG, and such a potential difference was transformed into a direct current output signal by passing through a rectifier bridge. An external ammeter and voltmeter measured the electrical characteristics of the triboelectric plasma. The output voltage of the TENG (about 7.1 kV; Figure S2) was much greater than the threshold voltage of the CO mixture gas, which facilitated the discharge of the latter. For needle–plate distances (***d***) of 3–11 mm, the TENG triggered the CO mixture gas discharge and generated the triboelectric corona plasma. When the ***d*** value was less than 3 mm, the corona discharge signal was transformed into multiple pulse discharge signals. The $^3O_2$ spin conversion during the triboelectric plasma process is depicted in Figure 2b. Free electrons near the tip of the W needle were accelerated in the electric field to

form high-energy electrons [42–45], which then collided with the gas in the gap, generating the triboelectric plasma composed of a large number of electrons and positive ions via the avalanche effect. In the plasma region, some high-energy electrons were captured by the electronegative $^3O_2$ gas, and the $^3O_2$ molecules were transformed into reactive superoxide ions $^2O_2^-$, which could overcome the spin prohibition to realize the CO oxidation reaction at room temperature.

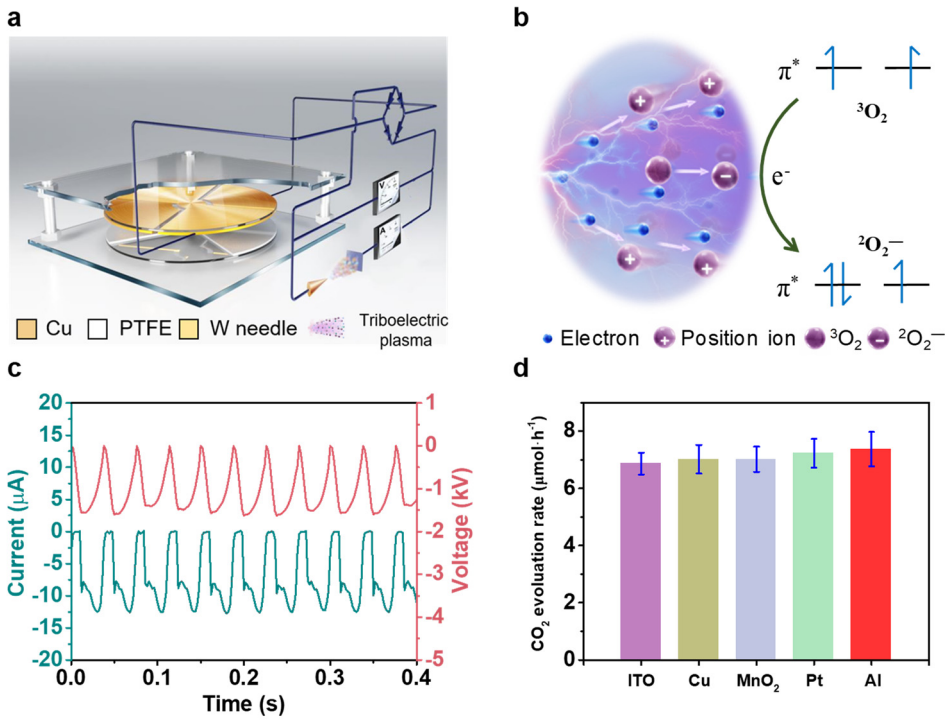

Figure 2. Schematic diagrams of the triboelectric plasma system. (**a**) Scheme of the triboelectric plasma oxidation system directly driven by a triboelectric nanogenerator (TENG). (**b**) $^3O_2$ spin conversion during the triboelectric plasma-induced process. (**c**) Electrical curves of the CO oxidation triggered by triboelectric plasma with a needle–plate distance of 3 mm using Pt as the electrode plate. (**d**) Activity for the triboelectric plasma-triggered CO oxidation with different electrode plate materials. Reaction conditions: negative corona, 3 mm needle–plate distance, 400 rpm rotation speed, $CO/O_2/He$ (1:20:79), 1 h discharge time, room temperature, and atmospheric pressure.

Figure 2c displays the electrical curve obtained for the CO oxidation system using triboelectric plasma generated by a TENG having a ***d*** of 3 mm. A pulse voltage peak of about 1.6 kV accompanied by a discharge current peak of 12.5 μA was generated in half a cycle. The time of the current pulse peak was 28 ms, which corresponds to the generation of triboelectric corona plasma. Figure 2d summarizes the CO oxidation activity of different electrode materials using the triboelectric plasma described in Figure 2c under normal temperature and pressure conditions. Almost all of the electrode materials showed a high CO oxidation activity of 6.9–7.4 μmol h^{-1}. An ^{18}O isotope labeling experiment confirmed that $^3O_2$ participated in the CO oxidation reaction (Figure S3). These results indicate that the CO oxidation was mainly controlled by the triboelectric plasma, whereas the electrode materials had a minor effect on the CO oxidation activity. Thus, we selected Pt as the electrode for the following experiments due to its stable performance.

3.2. Influence of Different Parameters on the CO Oxidation Activity

The rotational speed of the TENG, the needle–plate distance, and the corona polarity affect the state of the triboelectric corona plasma and hence the activity of the oxidation reaction between $^2O_2^-$ and CO. Taking negative corona as an example, we first investigated the effect of the rotational speed of the TENG on the CO oxidation activity, as shown

in Figure S4. Upon increasing the rotational speed, the discharge voltage was almost maintained at −1.6 kV, whereas the absolute value of the discharge current, the average power, and the CO oxidation activity increased from 2.9 μA, 1.0 mW, and 1.4 μmol h^{-1} to 14.7 μA, 9.2 mW, and 8.9 μmol h^{-1}, respectively. The energy consumption (EC) of the conversion of 1 mol CO remained virtually unchanged at 4.2 MJ mol^{-1}, indicating that the rotational speed has a weak effect on the EC of the CO oxidation reaction. Therefore, we selected 400 rpm as the rotational speed of the TENG for the subsequent experiments.

Figure S5 shows the relationship between ***d*** and the CO oxidation activity. As the ***d*** value increased from 3 to 11 mm, the absolute value of the discharge voltage increased from 1.6 to 3.9 kV, and the absolute value of the discharge current decreased from 12.5 to 5.7 μA. The average power decreased from 8.9 to 2.5 mW, the activity dropped from 7.2 to 0.2 μmol h^{-1}, and the corresponding EC increased significantly from 4.2 to 45.4 MJ mol^{-1}. According to these results, the optimal activity and minimum EC were achieved with a ***d*** of 3 mm, which we selected as the optimal needle–plate distance for the following experiments.

Then, we investigated the effect of the corona polarity on the CO oxidation activity, as shown in Figure 3. When ***d*** was 3 mm, the absolute value of the discharge voltage of the negative corona (1.6 kV) was lower than that of the positive corona (3.2 kV), and the absolute value of the discharge current of the negative corona (12.5 μA) was greater than that of the positive corona (12.3 μA). The average power of the negative corona (10.8 mW) was lower than that of the positive corona (8.9 mW). The CO oxidation activity of the negative corona (7.2 μmol h^{-1}) was 2.7 times that of the positive corona (2.8 μmol h^{-1}). Therefore, the calculated EC of the negative corona (4.2 MJ mol^{-1}) was much lower than that of the positive corona (14.6 MJ mol^{-1}). When ***d*** was 5 or 7 mm, the absolute value of discharge voltage and current and the activity trend were similar to those obtained with a ***d*** of 3 mm. The calculated average power of the negative corona was approximately equal for a ***d*** of 3–7 mm, whereas that under the condition of positive corona decreased significantly with increasing the distance. Meanwhile, the trend of the EC at different polarities proved to be irrespective of the ***d*** value. The above results imply that the negative corona afforded better activity and lower EC than the positive corona. Furthermore, we conducted cyclic experiments to evaluate the stability of the triboelectric plasma-triggered oxidation of CO, finding that the system maintained its activity for five runs (Figure S6).

3.3. Investigation of Dioxygen Activation by Triboelectric Plasma and Theoretical Calculations

Subsequently, to gain insight into the reason for the EC difference for the CO oxidation reaction between the positive and negative corona, we performed a nitro blue tetrazolium (NBT) assay to detect the reactive species derived from $^3O_2$ in the triboelectric plasma by colorimetry [32], as shown in Figure 4a. Upon the reaction of NBT with $^2O_2^-$, insoluble blue organic compounds were generated in the reaction solution, which caused a decrease in the absorbance of the solution at 260 nm. In the absence of triboelectric plasma, the absorbance of the NBT solution decreased under $CO/O_2/He$ atmosphere, suggesting the existence of $^2O_2^-$ radicals in the triboelectric plasma. Moreover, the absorption peak under the negative corona was lower than that under the positive corona, demonstrating that the former produced more $^2O_2^-$ radicals than the latter.

Next, we conducted kinetic isotope experiments under the same conditions using isotope-labeled and unlabeled $^3O_2$ to study the kinetics of the $^3O_2$ activation. Electron-driven reactions have been reported to show higher KIEs than thermally driven and light-driven reactions [46–48]. As shown in Figure 4b, we used the same ratio of CO mixed standard gas ($CO/^{16}O_2/He$, $CO/^{18}O_2/He$) to evaluate the rate of CO oxidation reaction under the negative corona. The reaction rate was found to be 7.2 μmol h^{-1} under $CO/^{16}O_2/He$ atmosphere and 6.5 μmol h^{-1} under $CO/^{18}O_2/He$ atmosphere. The KIE ($^{16}O_2$ rate/$^{18}O_2$ rate) of the negative corona was 1.11 ± 0.01, which is larger than that reported for traditional thermal catalytic CO oxidation reactions (KIE = 1.06) [46–48]. The larger KIE for the triboelectric plasma process is a typical feature of an electron-driven process and confirms that $^3O_2$ activation controls the entire reaction.

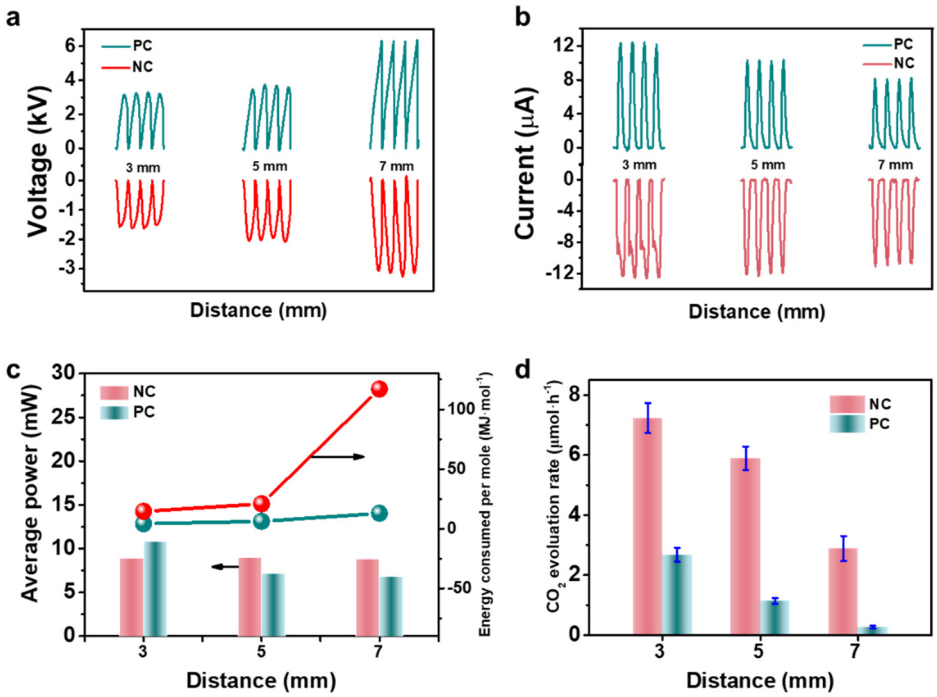

Figure 3. Activity dependence on the discharge polarities. (**a**) Voltage curves of different corona polarities; NC = negative corona. PC = positive corona. (**b**) Current curves of CO oxidation at different corona polarities. (**c**) Average power and energy consumption per mol CO at different corona polarities. (**d**) Activity of CO oxidation at different corona polarities. Reaction conditions: Pt as the electrode plate, $CO/O_2/He$ (1:20:79), 1 h discharge time, room temperature, and atmospheric pressure.

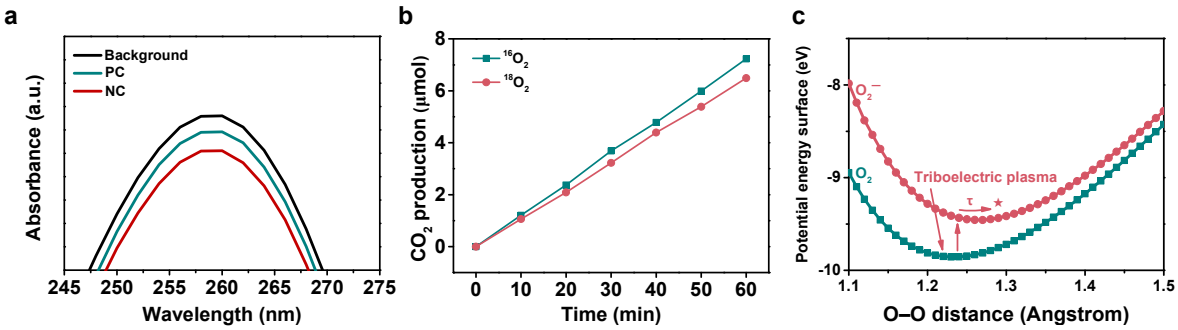

Figure 4. Activation of $^3O_2$. (**a**) Reactive oxygen generated from $^3O_2$ measured by colorimetry using a nitro blue tetrazolium solution; a.u. = arbitrary units. (**b**) Reaction rate for the triboelectric plasma-triggered CO oxidation measured at room temperature for $^{16}O_2$ and $^{18}O_2$ reactants. Reaction conditions: negative corona, 3 mm needle−plate distance, 400 rpm rotation speed, Pt as the electrode plate, $CO/O_2/He$ (1:20:79), 1 h discharge time, room temperature, and atmospheric pressure. (**c**) Density functional theory-calculated $^3O_2$ and $^2O_2^-$ potential energy surface. Excitation of triboelectric plasma allows the high-energetic electrons to be transferred to $^3O_2$, generating $^2O_2^-$. The $^3O_2$ molecule is negatively charged, and the O–O nuclear motion relaxes to an equilibrium state along the $^2O_2^-$ potential energy surface. ★ = equilibrium state. τ denotes the progression of $^2O_2^-$ along the $^2O_2^-$ potential energy surface as a function of time.

The larger KIE indicates that high-energy electrons promote the overall reaction via an electron-induced activation of $^3O_2$. Combined with the presence of $^3O_2$-derived reactive species as revealed by the colorimetry analysis, in the context of the reactions herein reported, we speculated that an energetic electron was directly transferred to the π^* antibonding orbital (i.e., LUMO energy level) of molecular $^3O_2$, resulting in the production of $^2O_2^-$, which effectively promoted the spin change and activation of $^3O_2$. To further study the electron transfer process from the triboelectric plasma to $^3O_2$ molecules, we determined

the potential energy surfaces of $^3O_2$ and $^2O_2{}^-$ (Figure 4c) by performing DFT and a linear expansion delta self-consistent field extension of DFT (ΔSCF-DFT), respectively. Figure 4c shows that the minimum energy required for populating the antibonding orbital of the $^3O_2$ molecule was 0.5 eV, which corresponds to the vertical transition energy between the potential energy surface of $^2O_2{}^-$ and the ground state $^3O_2$. Upon transferring an electron to the antibonding orbital of the $^2O_2$ molecule, the O–O bond (the O–O bond length in O_2 is 1.23 Å) underwent a stretching process: namely, the lowest potential energy configuration for the negatively charged $^2O_2{}^-$ ions exhibited a longer O–O bond of 1.32 Å [49].

3.4. Theoretical Simulation of Triboelectric Plasma

Figure 5a,b show the simulated time evolution of the electron density and the electron average energy under the negative corona with a ***d*** of 3 mm. As the time increased from 0.5 to 4.5 ns, electrons migrated from the tip of the W needle to the plate electrode, generating a plasma channel of a cylinder with a radius of 1.5 mm. The electron density was evenly distributed in the whole plasma channel, and the electron densities near the tip (point i), the middle (point ii), and the plate electrode (point iii) were 1.4×10^{19}, 1.97×10^{19}, and 4.9×10^{19} m^{-3}, respectively. The average energy of electrons was evenly distributed in the whole plasma. The average energy of electrons near the tip (point i), the middle (point ii), and the plate electrode (point iii) were 3.6, 5.4, and 4.4 eV, respectively. The lower energy of electrons near the tip was mainly caused by the electric field shielding effect of the plasma.

Figure 5c,d show the simulated time evolution of the electron density and the electron average energy for the positive corona. Upon increasing the time, electrons migrated from the tip of the W needle to the plate electrode, forming a core with a radius of 1.0 mm. The electron density near the needle tip (point i) and near the plate electrode (point iii) was 1.2×10^{18} and 2.4×10^{15} m^{-3}, respectively. The average energy of electrons was relatively high (about 9.5 eV) at the plasma head (point ii) and relatively low (about 0.75 eV) at the tail (point i), which was caused by the electric field shielding effect generated by the plasma.

The normalized electron energy distribution function of the three representative points (i, ii, and iii) is shown in Figure 5e. The distance between the needle tip and the three representative points was 0.6, 1.8, and 2.6 mm, respectively. The average energy of electrons at point i was lower than that at points ii and iii. For example, in point i, the energy of 100% electrons at the positive corona and 86% electrons at the negative corona was less than 5 eV. At points ii and iii, the energy of 61% electrons at the positive corona and 74% electrons at the negative corona was less than 5 eV, respectively. The energy of 73% electrons at the positive corona and 77% electrons at the negative corona was less than 5 eV. At point iii, the electron density of the positive corona was about four orders of magnitude smaller than that of the negative corona.

3.5. Mechanism of the Triboelectric Plasma-Triggered CO Oxidation

Figure 6 depicts two plausible mechanisms for the CO oxidation triggered by triboelectric plasma: pathways a and b. In pathway a, the formation of $^2O_2{}^-$ ions by changing the spin state of $^3O_2$ allows overcoming the spin-forbidden nature of the reaction between $^3O_2$ and CO, resulting in a low-energy barrier. This pathway includes three steps: (1) $^3O_2$ captures low-energy electrons to form $^2O_2{}^-$ ions with a potential barrier of 0.5 eV; (2) $^2O_2{}^-$ ions react with CO to form CO and O^- ion, and the energy barrier is 1.35 eV [50]; (3) O^- reacts with CO to produce CO_2 and e^- with an energy barrier of −4 eV. Pathway b comprises the direct reaction between $^3O_2$ and CO under the action of high-energy electrons, which proceeds through a high-energy triplet transition state. This process does not overcome the spin prohibition of the reaction between $^3O_2$ and CO; therefore, the energy barrier is high. This pathway includes two reaction processes: (1) under the action of high-energy electrons, $^3O_2$ reacts directly with CO to produce CO_2 and O atom, and the energy barrier is 5.2 eV; (2) The dioxygen atom reacts with CO to produce CO_2 with an energy barrier of −5.5 eV. The total energy barrier calculated for pathway a and pathway b was 1.85

and 5.2 eV, respectively. Therefore, pathway a is thermodynamically more favored than pathway b.

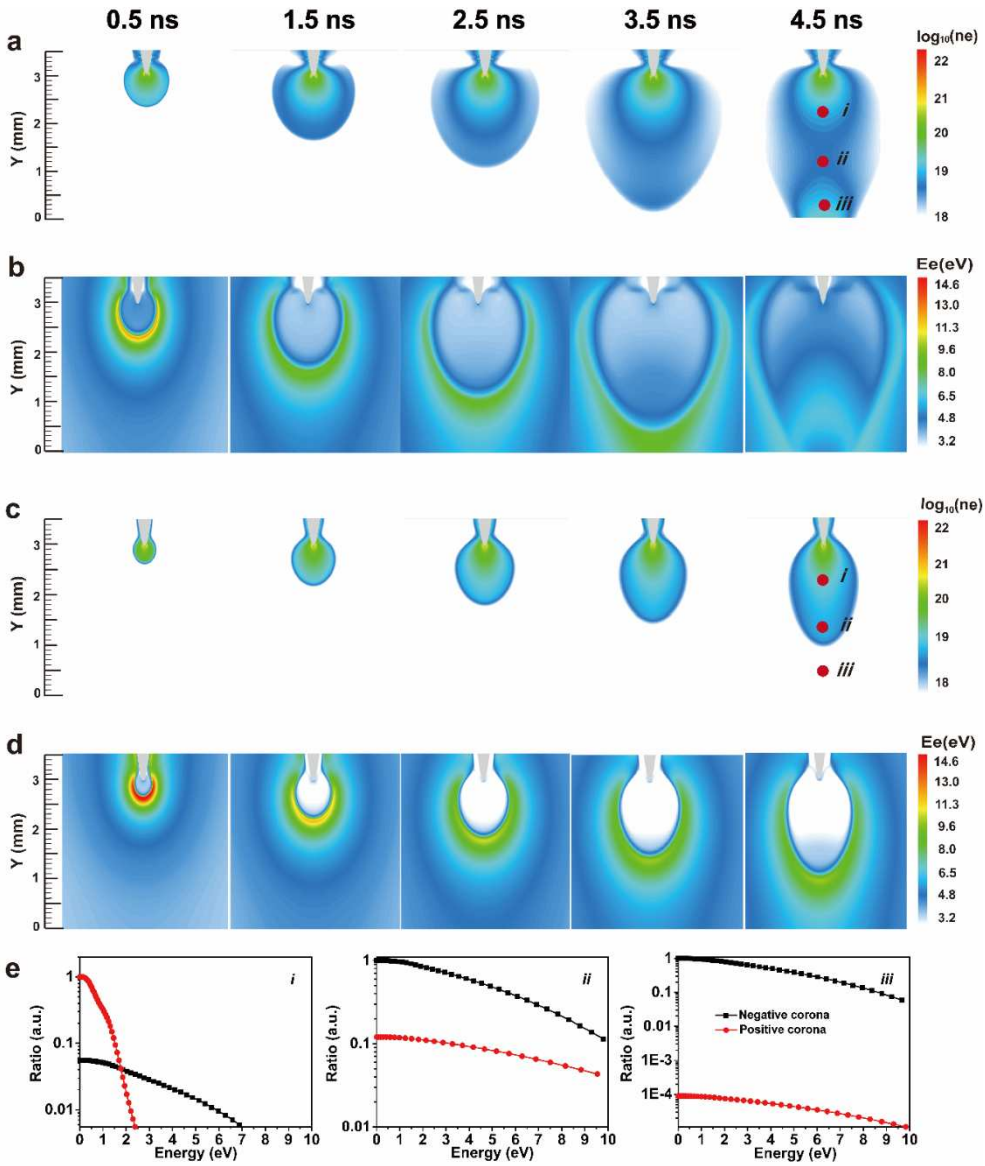

Figure 5. Triboelectric plasma simulation. (**a**) Time evolution of the electron density distribution in the negative corona. (**b**) Time evolution of the electron energy distribution in the negative corona. (**c**) Time evolution of the electron density distribution in the positive corona. (**d**) Time evolution of the electron energy distribution in the positive corona. (**e**) Electron energy distribution function of three representative points (i, ii, iii) both in the negative and the positive corona.

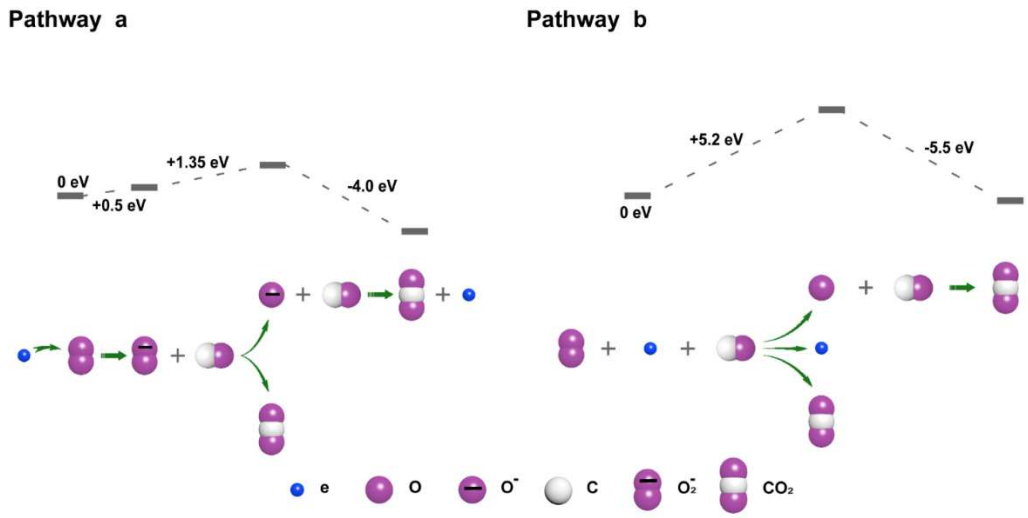

Figure 6. Reaction pathways for triboelectric plasma-triggered CO oxidation.

In the process of the negative corona, the average energy and average density of electrons were evenly distributed in the whole plasma channel. Except for the plasma head (near the plate electrode), the average energy of other electrons was less than 5 eV, and the energy was not sufficient for the process to proceed through pathway b, as shown in Figure 7. Therefore, in the whole plasma at the negative corona, pathway a occurs in almost all regions, whereas the process only proceeds through pathway b in the plasma head (plate electrode position). In the positive corona process, two obvious regions were formed in the plasma channel: a low-energy electron region near the needle tip and a high-energy electron region at the front edge of the plasma. The energy of electrons near the needle tip was very low; although it could produce highly active $^2O_2^-$ ions, it was not sufficient to promote $^2O_2^-$ decomposition. In the front of the plasma, 49% of the electrons have an energy greater than 5 eV, which is sufficient to overcome the energy barrier of pathway b. Therefore, in the positive corona, the oxidation of CO mainly occurred through pathways a and b. Finally, the proportion of pathway a in the negative corona was greater than that in the positive corona; therefore, the energy efficiency and activity of the negative corona were higher than those of the positive corona.

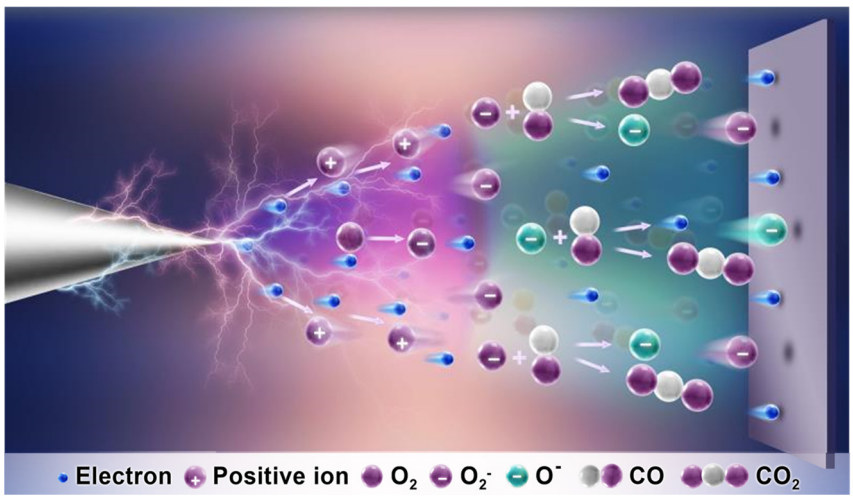

Figure 7. Schematic diagram of triboelectric plasma-triggered CO oxidation reaction at negative corona.

In the CO oxidation reaction, the activation of $^3O_2$ has always been considered as the key step [51]. At room temperature, since the $^3O_2$ molecule is in the triplet state, the oxidation needs to proceed through a high-energy triplet transition state to satisfy the spin

selection rules. Therefore, although the $^3O_2$ molecule has a strong oxidizing ability, the direct oxidation of CO is unfavorable in terms of reaction kinetics. This is the so-called spin conservation process. In thermally induced catalytic systems, the electrons of the *d* orbital of a transition metal are transferred to the antibonding orbital of $^3O_2$ (Table S1). Meanwhile, in photocatalytic systems, after the photogenerated carriers are separated on the photocatalyst, the electrons trapped on the reduction cocatalyst migrate to the antibonding orbital of the $^3O_2$ molecule. The $^3O_2$ single electron transfer to form $^2O_2{}^-$ at room temperature has been reported to require metal or metal oxide catalysts. In our system, the triboelectric corona plasma contains a large number of high-energy electrons that can be directly injected into the antibonding orbital of $^3O_2$ to produce highly active $^2O_2{}^-$, enabling the CO oxidation reaction. This system can directly realize the single electron transfer to form a $^2O_2{}^-$ free radical in the absence of a metal catalyst, which offers the advantages of low cost and no noble metal pollution [52]. The reaction device is simple and easy to operate, and the driving force of the reaction mainly comes from renewable and green mechanical energy.

4. Conclusions

We have developed a method that used the triboelectric corona plasma generated by a TENG under mechanical stimuli to change the spin state of O_2 molecules and trigger the CO oxidation reaction at room temperature. The rotation speed of the TENG, the needle–plate distance, and the corona polarity have an important influence on the CO oxidation reaction. Under a rotation speed of 400 rpm, a needle–plate distance of 3 mm, and negative corona, the optimal activity was 7.2 μmol h^{-1} and the lowest energy consumption per mole CO was 4.2 MJ. The high-energy electrons in the triboelectric corona plasma were directly injected into the antibonding orbitals of O_2 to form highly reactive $O_2{}^-$ radicals. The energy barrier of the reaction of the excited $O_2{}^-$ ions with CO is 3.4 eV lower than that of the O_2 reaction, effectively promoting the rate-limiting step of O–O bond dissociation in the CO oxidation reaction. This work provides a novel strategy that circumvents the spin-forbidden nature of the activation of small molecules through mechanical energy.

Supplementary Materials: The following are available online at https://www.mdpi.com/article/10.3390/nano11123408/s1, Figure S1: Diagram of triboelectric plasma oxidation of CO, Figure S2: Electric curves, Figure S3: Isotope experiment, Figure S4: The effect of different rotational speeds of TENG, Figure S5: The effect of different needle–plate distances, Figure S6: Cycle experiment, Table S1: Comparison of different methods of oxidation of CO.

Author Contributions: Conceptualization, X.S., B.Z. and S.L.; methodology, B.Z., X.X., Y.Z. and G.C.; formal analysis, X.S., S.L., X.X., Y.Z. and K.Z.; validation, J.W., K.Z., W.S. and G.G.; investigation, J.G. and P.C.; funding acquisition, B.Z., G.G., P.C., G.C. and Z.D.; supervision, G.C. and Z.D.; writing—original draft, B.Z.; writing—review and editing, G.C. and Z.D. All authors have read and agreed to the published version of the manuscript.

Funding: This research was funded by the National Natural Science Foundation of China, grant number 21902043, 61974040, 22005086, and 62104064; Chinese Postdoctoral Science Foundation, grant number 2020M672197; Postdoctoral Foundation of Henan Province, China, grant number 248472; Key Research & Development and Promotion Project of Henan Province, China, grant number 212102311004.

Institutional Review Board Statement: Not applicable.

Informed Consent Statement: Not applicable.

Data Availability Statement: The data are available upon reasonable request from the corresponding author.

Conflicts of Interest: The authors declare no conflict of interest.

References

1. Behler, J.; Delley, B.; Lorenz, S.; Reuter, K.; Scheffler, M. Dissociation of O_2 at Al(111): The role of spin selection rules. *Phys. Rev. Lett.* **2005**, *94*, 036104. [CrossRef] [PubMed]
2. Shen, X.M.; Liu, W.Q.; Gao, X.J.; Lu, Z.H.; Wu, X.C.; Gao, X.F. Mechanisms of oxidase and superoxide dismutation-like activities of gold, silver, platinum, and palladium, and their alloys: A general way to the activation of molecular oxygen. *J. Am. Chem. Soc.* **2015**, *137*, 15882–15891. [CrossRef] [PubMed]
3. Chen, Y.-Z.; Wang, Z.Y.U.; Wang, H.W.; Lu, J.L.; Yu, S.-H.; Jiang, H.-L. Singlet oxygen-engaged selective photo-oxidation over Pt nanocrystals/porphyrinic MOF: The roles of photothermal effect and Pt electronic state. *J. Am. Chem. Soc.* **2017**, *139*, 2035–2044. [CrossRef] [PubMed]
4. Sun, X.S.; Luo, X.; Zhang, X.D.; Xie, J.F.; Jin, S.; Wang, H.; Zheng, X.S.; Wu, X.J.; Xie, Y. Enhanced superoxide generation on defective surfaces for selective photooxidation. *J. Am. Chem. Soc.* **2019**, *141*, 3797–3801. [CrossRef]
5. Zhang, N.; Li, X.Y.; Ye, H.C.; Chen, S.M.; Ju, H.X.; Liu, D.B.; Lin, Y.; Ye, W.; Wang, C.M.; Xu, Q.; et al. Oxide defect engineering enables to couple solar energy into oxygen activation. *J. Am. Chem. Soc.* **2016**, *138*, 8928–8935. [CrossRef]
6. Zhang, B.; Yang, X.J.; Li, J.; Cheng, G. Selective aerobic oxidation of alkyl aromatics on Bi_2MoO_6 nanoplates decorated with Pt nanoparticles under visible light irradiation. *Chem. Commun.* **2018**, *54*, 12194–12197. [CrossRef]
7. Zhang, B.; Li, J.; Gao, Y.Y.; Chong, R.F.; Wang, Z.L.; Guo, L.; Zhang, X.W.; Li, C. To boost photocatalytic activity in selective oxidation of alcohols on ultrathin Bi_2MoO_6 nanoplates with Pt nanoparticles as cocatalyst. *J. Catal.* **2017**, *345*, 96–103. [CrossRef]
8. Zhang, B.; Li, J.; Zhang, B.Q.; Chong, R.F.; Li, R.G.; Yuan, B.; Lu, S.-M.; Li, C. Selective oxidation of sulfides on Pt/$BiVO_4$ photocatalyst under visible light irradiation using water as the oxygen source and dioxygen as the electron acceptor. *J. Catal.* **2015**, *332*, 95–100. [CrossRef]
9. Long, R.; Mao, K.K.; Gong, M.; Zhou, S.; Hu, J.H.; Zhi, M.; You, Y.; Bai, S.; Jiang, J.; Zhang, Q.; et al. Tunable oxygen activation for catalytic organic oxidation: Schottky junction versus plasmonic effects. *Angew. Chem. Int. Ed.* **2014**, *53*, 3205–3209. [CrossRef]
10. Zhang, B.; Li, J.; Guo, L.; Chen, Z.P.; Li, C. Photothermally promoted cleavage of beta-1,4-glycosidic bonds of cellulosic biomass on Ir/HY catalyst under mild conditions. *Appl. Catal. B* **2018**, *237*, 660–664. [CrossRef]
11. Hori, H.; Takashima, M.; Takase, M.; Ohtani, B. Kinetic analysis supporting multielectron reduction of oxygen in bismuth tungstate-photocatalyzed oxidation of organic compounds. *Catal. Today* **2018**, *313*, 218–223. [CrossRef]
12. Setvín, M.; Aschauer, U.; Scheiber, P.; Li, Y.-F.; Hou, W.Y.; Schmid, M.; Selloni, A.; Diebold, U. Reaction of O_2 with subsurface oxygen vacancies on TiO_2 anatase (101). *Science* **2013**, *341*, 988–991. [CrossRef]
13. Su, H.; Zhang, K.-X.; Zhang, B.; Wang, H.-H.; Yu, Q.Y.; Li, X.-H.; Antonietti, M.; Chen, J.S. Activating cobalt nanoparticles via the Mott-Schottky effect in nitrogen-rich carbon shells for base-free aerobic oxidation of alcohols to esters. *J. Am. Chem. Soc.* **2017**, *139*, 811–818. [CrossRef]
14. Jagadeesh, R.V.; Junge, H.; Pohl, M.M.; Radnik, J.; Bruckner, A.; Beller, M. Selective oxidation of alcohols to esters using heterogeneous Co_3O_4-N@C catalysts under mild conditions. *J. Am. Chem. Soc.* **2013**, *135*, 10776–10782. [CrossRef]
15. Wu, W.T.; Zhang, Q.G.; Wang, X.K.; Han, C.C.; Shao, X.D.; Wang, Y.X.; Liu, J.L.; Li, Z.T.; Lu, X.Q.; Wu, M.B. Enhancing selective photooxidation through Co-Nx-doped carbon materials as singlet oxygen photosensitizers. *ACS Catal.* **2017**, *7*, 7267–7273. [CrossRef]
16. Leung, S.-F.; Fu, H.-C.; Zhang, M.L.; Hassan, A.H.; Jiang, T.; Salama, K.N.; Wang, Z.L.; He, J.-H. Blue energy fuels: Converting ocean wave energy to carbon-based liquid fuels via CO_2 reduction. *Energy Environ. Sci.* **2020**, *13*, 1300–1308. [CrossRef]
17. You, H.L.; Wu, Z.; Zhang, L.H.; Ying, Y.R.; Liu, Y.; Fei, L.F.; Chen, X.X.; Jia, Y.M.; Wang, Y.J.; Wang, F.F.; et al. Harvesting the vibration energy of $BiFeO_3$ nanosheets for hydrogen evolution. *Angew. Chem. Int. Ed.* **2019**, *58*, 11779–11784. [CrossRef]
18. Gao, S.Y.; Zhu, Y.Z.; Chen, Y.; Tian, M.; Yang, Y.J.; Jiang, T.; Wang, Z.L. Self-power electroreduction of N_2 into NH_3 by 3D printed triboelectric nanogenerators. *Mater. Today* **2019**, *28*, 17–24. [CrossRef]
19. Fan, F.R.; Tian, Z.Q.; Wang, Z.L. Flexible triboelectric generator! *Nano Energy* **2012**, *1*, 328–334. [CrossRef]
20. Sahu, M.Š.; Silvija, H.S.; Padhan, A.M.; Živković, P.; Jokić, S.; Kim, H.J. Development of triboelectric nanogenerator and mechanical energy harvesting using argon ion-implanted kapton, zinc oxide and kapton. *Mater. Lett.* **2021**, *301*, 130290. [CrossRef]
21. Seo, J.H.; Sugato, S.; Manisha, K.; Hoe, J. Effect of cilia microstructure and ion injection upon single-electrode triboelectric nanogenerator for effective energy harvesting. *Mater. Lett.* **2021**, *304*, 130674. [CrossRef]
22. Venugopal, K.; Panchatcharam, P.; Chandrasekhar, A.; Shanmugasundaram, V. Comprehensive review on triboelectric nanogenerator based wrist pulse measurement: Sensor fabrication and diagnosis of arterial pressure. *ACS Sens.* **2021**, *6*, 1681–1694. [CrossRef]
23. Chandrasekhar, A.; Vivekananthan, V.; Khandelwal, G.; Kim, W.J.; Kim, S.J. Green energy from working surfaces: A contact electrification–enabled data theft protection and monitoring smart table. *Mater. Today Energy* **2020**, *18*, 100544. [CrossRef]
24. Feng, Y.W.; Ling, L.L.; Nie, J.; Han, K.; Chen, X.Y.; Bian, Z.F.; Li, H.X.; Wang, Z.L. Self-powered electrostatic filter with enhanced photocatalytic degradation of formaldehyde based on built-in triboelectric nanogenerators. *ACS Nano* **2017**, *11*, 12411–12418. [CrossRef]
25. Gao, S.Y.; Su, J.Z.; Wei, X.J.; Wang, M.; Tian, M.; Jiang, T.; Wang, Z.L. Self-powered electrochemical oxidation of 4-aminoazobenzene driven by a triboelectric nanogenerator. *ACS Nano* **2017**, *11*, 770–778. [CrossRef]

26. Cheng, G.; Zheng, H.W.; Yang, F.; Zhao, L.; Zheng, M.L.; Yang, J.J.; Qin, H.F.; Du, Z.L.; Wang, Z.L. Managing and maximizing the output power of a triboelectric nanogenerator by controlled tip-electrode air-discharging and application for UV sensing. *Nano Energy* **2018**, *44*, 208–216. [CrossRef]
27. Zhao, K.; Gu, G.Q.; Zhang, Y.N.; Zhang, B.; Yang, F.; Zhao, L.; Zheng, M.L.; Cheng, G.; Du, Z.L. The self-powered CO_2 gas sensor based on gas discharge induced by triboelectric nanogenerator. *Nano Energy* **2018**, *53*, 898–905. [CrossRef]
28. Li, A.Y.; Zi, Y.L.; Guo, H.Y.; Wang, Z.L.; Fernandez, F.M. Triboelectric nanogenerators for sensitive nano-coulomb molecular mass spectrometry. *Nat. Nanotechnol.* **2017**, *12*, 481–487. [CrossRef]
29. Han, K.; Luo, J.J.; Feng, Y.W.; Lai, Q.S.; Bai, Y.; Tang, W.; Wang, Z.L. Wind-driven radial-engine-shaped triboelectric nanogenerators for self-powered absorption and degradation of NO_X. *ACS Nano* **2020**, *14*, 2751–2759. [CrossRef]
30. Cheng, J.; Ding, W.B.; Zi, Y.L.; Lu, Y.J.; Ji, L.J.; Liu, F.; Wu, C.S.; Wang, Z.L. Triboelectric microplasma powered by mechanical stimuli. *Nat. Commun.* **2018**, *9*, 3733. [CrossRef]
31. Wong, M.-C.; Xu, W.; Hao, J.H. Microplasma-discharge-based nitrogen fixation driven by triboelectric nanogenerator toward self-powered mechano-nitrogenous fertilizer supplier. *Adv. Funct. Mater.* **2019**, *29*, 1904090. [CrossRef]
32. Goto, H.; Hanada, Y.; Ohno, T.; Matsumura, M. Quantitative analysis of superoxide ion and hydrogen peroxide produced from molecular oxygen on photoirradiated TiO_2 particles. *J. Catal.* **2004**, *225*, 223–229. [CrossRef]
33. Kresse, G.; Furthmüller, J. Efficient iterative schemes for ab initio total-energy calculations using a plane-wave basis set. *Phys. Rev. B* **1996**, *54*, 11169–11186. [CrossRef] [PubMed]
34. Kresse, G.; Hafner, J. Ab initio molecular-dynamics simulation of the liquid-metal-amorphous-semiconductor transition in germanium. *Phys. Rev. B* **1994**, *49*, 14251–14269. [CrossRef]
35. Blochl, P.E. Projector augmented-wave method. *Phys. Rev. B* **1994**, *50*, 17953–17979. [CrossRef]
36. Perdew, J.P.; Burke, K.; Ernzerhof, M. Generalized gradient approximation made simple. *Phys. Rev. Lett.* **1996**, *77*, 3865–3868. [CrossRef]
37. Zhu, Y.F.; Shcherbanev, S.; Baron, B.; Starikovskaia, S. Nanosecond surface dielectric barrier discharge in atmospheric pressure air: I. measurements and 2D modeling of morphology, propagation and hydrodynamic perturbations. *Plasma Sources Sci. Technol.* **2017**, *26*, 125004. [CrossRef]
38. Zhu, Y.F.; Starikovskaia, S. Fast gas heating of nanosecond pulsed surface dielectric barrier discharge: Spatial distribution and fractional contribution from kinetics. *Plasma Sources Sci. Technol.* **2018**, *27*, 124007. [CrossRef]
39. Zhu, Y.F.; Wu, Y.; Wei, B.; Xu, H.J.; Liang, H.; Jia, M.; Song, H.M.; Li, Y.H. Nanosecond-pulsed dielectric barrier discharge-based plasma-assisted anti-icing: Modeling and mechanism analysis. *J. Phys. D Appl. Phys.* **2019**, *53*, 145205. [CrossRef]
40. Kulikovsky, A.A. Positive streamer in a weak field in air: A moving avalanche-to-streamer transition. *Phys. Rev. E* **1997**, *57*, 7066–7074. [CrossRef]
41. Flitti, A.; Pancheshnyi, S. Gas heating in fast pulsed discharges in N_2–O_2 mixtures. *Phys. J. Appl. Phys.* **2009**, *45*, 21001. [CrossRef]
42. Bogaerts, A.; Neyts, E.C. Plasma technology: An emerging technology for energy storage. *ACS Energy Lett.* **2018**, *3*, 1013–1027. [CrossRef]
43. Mehta, P.; Barboun, P.; Go, D.B.; Hicks, J.C.; Schneider, W.F. Catalysis enabled by plasma activation of strong chemical bonds: A review. *ACS Energy Lett.* **2019**, *4*, 1115–1133. [CrossRef]
44. Mehta, P.; Barboun, P.; Herrera, F.A.; Kim, J.; Rumbach, P.; Go, D.B.; Hicks, J.C.; Schneider, W.F. Overcoming ammonia synthesis scaling relations with plasma-enabled catalysis. *Nat. Catal.* **2018**, *1*, 269–275. [CrossRef]
45. Chen, J.H.; Davidson, J.H. Model of the negative DC corona plasma comparison to the positive DC corona plasma. *Plasma Chem. Plasma Process.* **2003**, *23*, 83–102. [CrossRef]
46. Denzler, D.N.; Frischkorn, C.; Hess, C.; Wolf, M.; Ertl, G. Electronic excitation and dynamic promotion of a surface reaction. *Phys. Rev. Lett.* **2003**, *91*, 226102. [CrossRef]
47. Funk, S.; Bonn, M.; Denzler, D.N.; Hess, C.; Wolf, M.; Ertl, G. Desorption of CO from Ru(001) induced by near-infrared femtosecond laser pulses. *J. Chem. Phys.* **2000**, *112*, 9888–9897. [CrossRef]
48. Bonn, M.; Funk, S.; Hess, C.; Denzler, D.N.; Stampfl, C.; Scheffler, M.; Wolf, M.; Ertl, C. Phonon-versus electron-mediated desorption and oxidation of CO on Ru(0001). *Science* **1999**, *285*, 1042–1045. [CrossRef]
49. Das, A. A review of time economic innovative mnemonics in chemical education. *Int. J. Phys. Chem. Educ.* **2018**, *10*, 27–40. [CrossRef]
50. Paulson, J.F. Some negative-ion reactions with CO_2. *J. Chem. Phys.* **1970**, *52*, 963–964. [CrossRef]
51. Christopher, P.; Xin, H.; Linic, S. Visible-light-enhanced catalytic oxidation reactions on plasmonic silver nanostructures. *Nat. Chem.* **2011**, *3*, 467–472. [CrossRef]
52. Li, S.M.; Zhang, B.; Gu, G.Q.; Xiang, X.C.; Zhang, W.H.; Shi, X.; Zhao, K.; Zhu, Y.F.; Guo, J.M.; Cui, P.; et al. Triboelectric plasma decomposition of CO_2 at room temperature driven by mechanical energy. *Nano Energy* **2021**, *88*, 106287. [CrossRef]

nanomaterials

MDPI

Article

Magnetorheological Elastomer-Based Self-Powered Triboelectric Nanosensor for Monitoring Magnetic Field

Dong Wan [1,†], Ningchen Ma [2,†], Taochuang Zhao [1,†], Xiaojing Cui [1], Zhaosu Wang [1], Hulin Zhang [1] and Kai Zhuo [1,*]

[1] College of Information and Computer, Taiyuan University of Technology, Taiyuan 030024, China; 18771046115@163.com (D.W.); ztttry@163.com (T.Z.); cui85851328@163.com (X.C.); 15841531501@163.com (Z.W.); zhanghulin@tyut.edu.cn (H.Z.)

[2] AIEN Institute, Shanghai Ocean University, Shanghai 201306, China; mnc425@126.com

* Correspondence: zhuokai@tyut.edu.cn

† Dong Wan, Ningchen Ma and Taochuang Zhao contributed equally to the work.

Abstract: The adaptable monitoring of the ubiquitous magnetic field is of great importance not only for scientific research but also for industrial production. However, the current detecting techniques are unwieldly and lack essential mobility owing to the complex configuration and indispensability of the power source. Here, we have constructed a self-powered magnetic sensor based on a subtle triboelectric nanogenerator (TENG) that consists of a magnetorheological elastomer (MRE). This magnetic sensor relies on triboelectrification and electrostatic induction to produce electrical signals in response to the MRE's deformation induced by the variational magnetic field without using any external power sources. The fabricated magnetic sensor shows a fast response of 80ms and a desirable sensitivity of 31.6 mV/mT in a magnetic field range of 35–60 mT as well as preliminary vectorability enabled by the multichannel layout. Our work provides a new route for monitoring dynamic magnetic fields and paves a way for self-powered electric-magnetic coupled applications.

Keywords: self-powered; triboelectric; magnetorheological elastomer; magnetic

Citation: Wan, D.; Ma, N.; Zhao, T.; Cui, X.; Wang, Z.; Zhang, H.; Zhuo, K. Magnetorheological Elastomer-Based Self-Powered Triboelectric Nanosensor for Monitoring Magnetic Field. *Nanomaterials* **2021**, *11*, 2815. https://doi.org/10.3390/nano11112815

Academic Editors: Julian Maria Gonzalez Estevez and Régine Perzynski

Received: 22 September 2021
Accepted: 21 October 2021
Published: 23 October 2021

1. Introduction

The magnetic field is a vector quantity, which means that it has both magnitude and direction. For many years, researchers have been studying the application of magnetic fields [1–9], and have found that they play a significant role in geophysics, space technology, medical applications, and other areas [10–13]. Currently, there are many methods used to measure magnetic fields, such as magnetic force, hall effect, fluxgate, magnetic resonance, and superconductivity effects. Based on these methods, different principles of using magnetic field measurement instruments have been implemented, and all of these techniques for measuring magnetic fields have their benefits (Table S1) [14]. However, all of the above-mentioned measuring instruments require an external power supply, so it is urgent to develop a self-powered magnetic field monitoring instrument.

MRE is a magnetically sensitive smart composite material prepared from ferromagnetic particles and a polymer-like matrix, whose material properties can be quickly and reversibly controlled by an external magnetic field [15–21]. Because the matrix of MRE is a solid polymer material, the performance of MRE is simultaneously stable and reproducible. In recent years, a large number of researchers have started to focus on self-powered technologies [22–26]. Among them is TENG: an emerging technology that can directly convert mechanical energy into electrical energy [24,27–32]. Since TENG has a high sensitivity to mechanical triggering, many self-powered sensors based on TENG have been designed [16,24,33–38]. Here, we designed a self-powered magnetic field monitoring sensor.

In this work, we used styrene ethylene butylene styrene (SEBS) as a substrate and added magnetic fluid to prepare MRE films [39]. In order to measure the strength and direction of the magnetic field, a self-powered sensor based on the MRE of TENG is reported in this paper. The structure and mechanism of the MRE-based TENG are described here in detail, and the material properties of the MRE and the output signals of the sensor are systematically investigated. With the assistance of a programmable platform, the newly designed pointer-based TENG structure enables excellent real-time magnetic field monitoring and unique self-powered capabilities. This work promotes the use of TENG-based sensing applications for magnetic field measurement, which has important implications for IoT, robotics, and AI.

2. Discussion and Results

The structural design of the MRE-based TENG device is illustrated in Figure 1a. When a magnetic field perpendicular to the TENG is applied, the MRE film deforms and drives the PTFE close to the Al under the action of the magnetic field. At the right bottom, a photograph of the fabricated TENG is presented, which shows how the PTFE is conformally pasted on the MRE film. As illustrated in Figure 1b, the scanning electron microscopy (SEM) image of the MRE film shows that the ferruginous particles were uniformly distributed in the SEBS elastomer; this is verified via an EDS test plotted in Figure 1c. The emerging Fe originated from the mixed ferruginous powder, with the observed C and O elements resulting from the SEBS polymer. This is the same as the expected XRD result, indicating that the prepared film consists of Fe_3O_4 nanoparticles. As shown in Figure 1d, the diffraction peaks were concentrated at 30.6°, 35.8°, 45.2°, 63.01°, and 70.2°, and are consistent with the face-centered cubic Fe_3O_4 (JCPDS No. 19-0629). Figure 1e shows the hysteresis loop of the SEBS and MRE in the range of −10 k to 10 kG, which indicates that the MRE has superparamagnetism and zero coercivity at room temperature; this means that magnetism is completely attributed to the external magnetic field. Moreover, as we expected, SEBS did not change in the presence of the magnetic field. To test the mechanical property, the uni-axial tensile experiments were performed on the prepared MRE films with different component ratios of SEBS powder to liquid paraffin to magnetic fluid as shown in Figure 1f. As the applied strain increases, the stress rises accordingly in a proportional relationship. The stress gradually decreases as the liquid paraffin increases under the same strain condition. The best toughness was achieved at SEBS: liquid paraffin: magnetic fluid = 1:3:1, which could reach 400% strain, and the corresponding stress was 100 KPa. The actual stretching is shown in the illustration of Figure 1f, which indicates that MRE film has excellent tensile properties. In order to deliver a larger stretching range and better toughness, a 1:3:1 blending ratio of SEBS powder, to liquid paraffin to magnetic fluid was chosen for this experiment to make MRE films.

Figure 2a shows the electron cloud and potential energy profile diagram [40]. PTFE is used as a negative triboelectric electric material to build a triboelectric pair with Al, which also works as a single electrode. Until the atoms of PTFE and Al materials come into contact, their electron clouds remain separate (Figure 2a(i)). When PTFE and Al are close together within a magnetic field, the electron clouds of the atoms of the two materials overlap, forming ionic or covalent bonds. Then, electrons can be transferred from one atom to another (Figure 2a(ii)). When PTFE is separated from Al, the transferred electrons are still present on the material surface as electrostatic charges (Figure 2a(iii)). Figure 2b shows the working mechanism of the device. When the magnet is away from the TENG device, the MRE film is not deformed and the gap between the PTFE and Al films is stable. The charges on the surfaces of the PTFE and Al films are balanced, which does not cause a change in the open-circuit voltage (Figure 2b(i)). When the magnet slowly approaches the TENG device, the deformation of the MRE brings the PTFE film closer to the Al film (Figure 2b(ii,iii)). The deformation of the MRE film causes an electrical signal to be outputed by the TENG. The surface charge density between PTFE and Al is set to 1×10^{-5} C·m^{-2} by COMSOL software simulation. As illustrated in Figure 2c, when

MRE film transitions from the unbending state (i) to the intermediate state (ii) and then to the state with the maximum bending (iii), the potential difference between PTFE and Al interface becomes larger and larger as the separation distance increases, which drives the electrons to flow to the ground. Furthermore, when a gradually increasing magnetic field is applied to the TENG, the maximum force achieved by the mechanical simulation of the MRE is 70 kN/m^2, as shown in Figure S1.

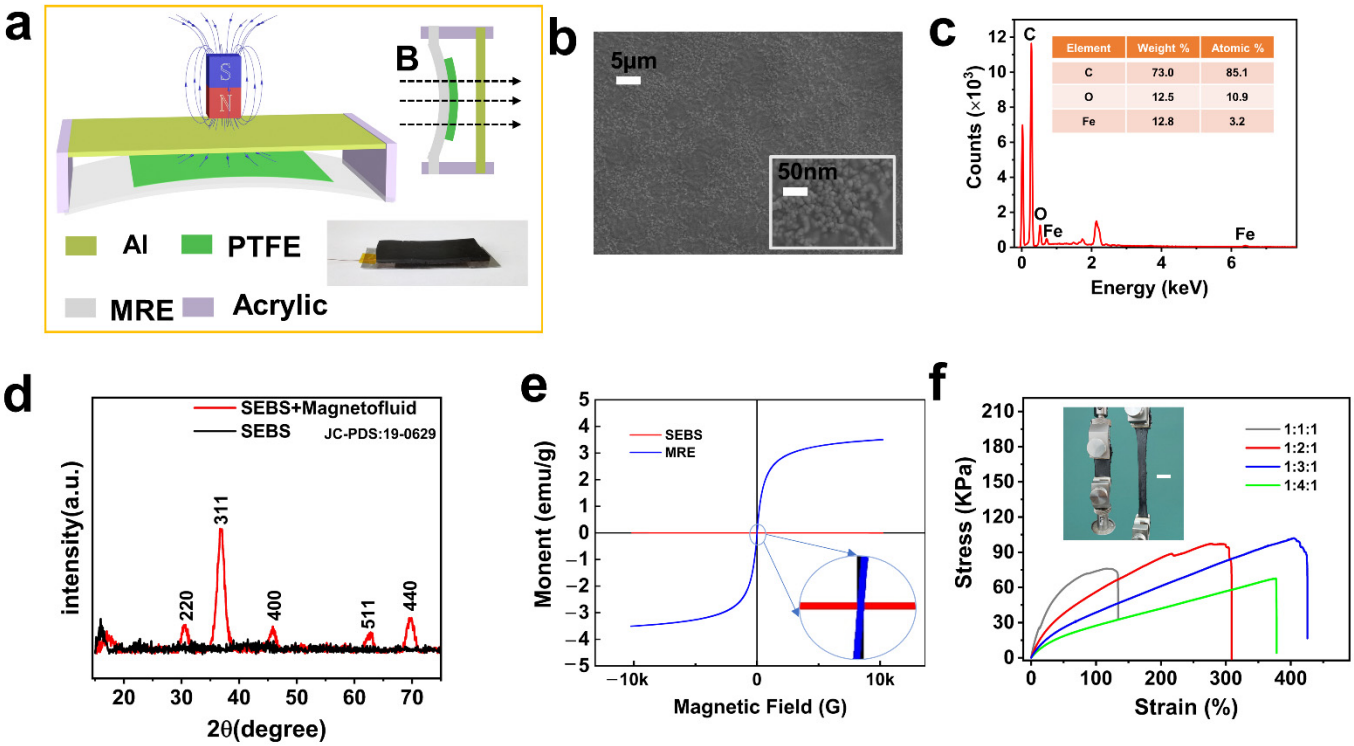

Figure 1. Device models and performance characterization. (**a**) Diagram of device and working model; (**b**) SEM images, (**c**) EDS and (**d**) XRD of the MRE film; (**e**) The hysteresis loop of the SEBS and MRE; (**f**) Stress and strain analysis of the MRE film in different proportions, and photographs of the actual stretching (scale bar is 2 cm).

In order to accurately test the electrical properties of the MRE-based TENG, a programmable linear motor was used. As shown in Figure 3a,b, the open-circuit voltage and short-circuit current are 30 V and 0.18 μA, respectively. In addition, the increase in the load resistance causes the voltage to increase, and the power tends to increase and then decrease, reaching a maximum of 1.3 μW at 80 MΩ, as depicted in Figure 3c. It means that the internal resistance of the TENG is about 80 MΩ, which provides the maximum output power in the external circuit when the load resistance is approximately equal to the internal resistance. Here, we changed the magnetic field strength and the frequency of the magnetic field applied to the TENG to observe the voltage output. As shown in Figure 3d and Figure S2, the higher the magnetic field strength, the higher the voltage output for the same frequency. With the rising frequency, the voltage also increases for the same magnetic field strength.

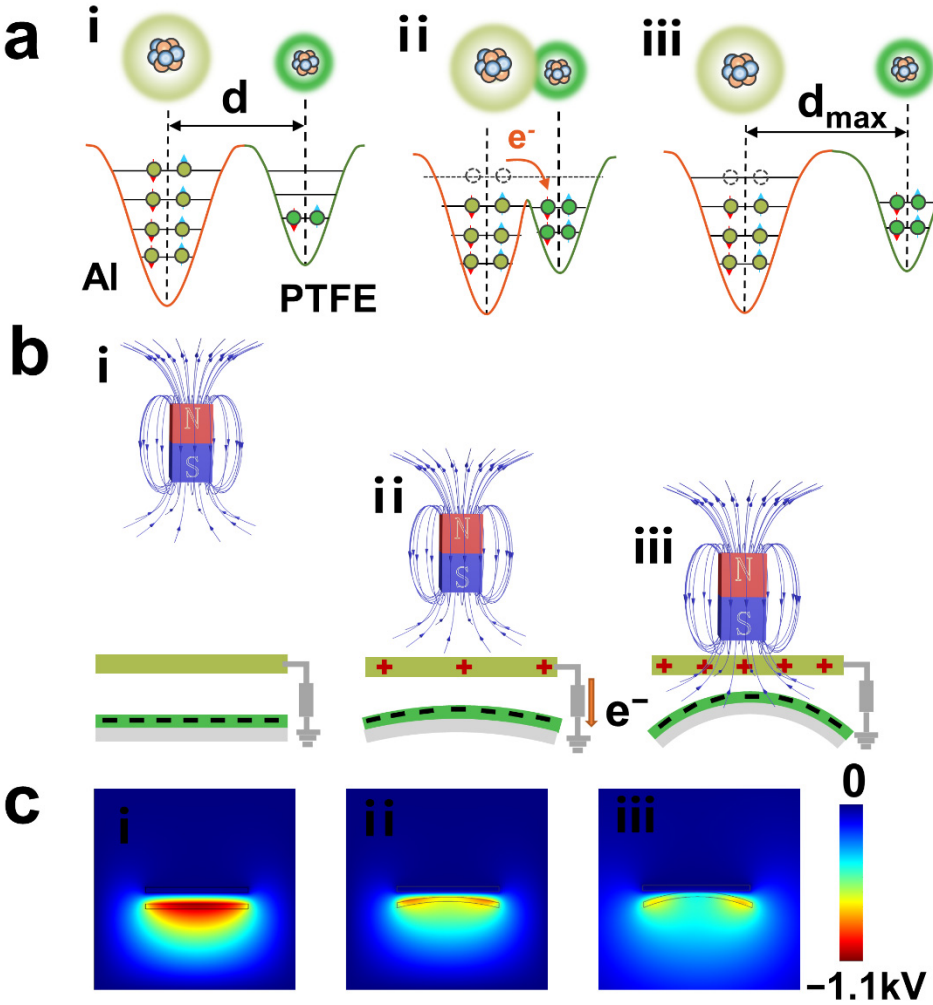

Figure 2. The working mechanism of the triboelectric nanogenerator. (**a**) Schematic of the electron cloud and potential energy profile of two atoms belonging to PTFE and Al, respectively; (**b**) A diagram of the working schematic; (**c**) Simulating the electric potential distribution diagram with COMSOL.

After previous tests, we have learned about the output signal characteristics of the MRE-based TENG affected by magnetic fields. Based on the LabVIEW program, a pointer-type magnetic field sensor was designed based on the TENG. The schematic diagram and physical picture are shown in the inset of Figure 4a, which uses an acrylic plate as the base of the cylinder, with Al electrodes symmetrically pasted on all four sides to form 4 channels and numbered. A long cylindrical MRE with multiple PTFE films is fixed in the middle of the cylinder as a pointer. Figure 4a,b plots the voltage output when the magnet is close to channel 1 in 3D and 2D, both of which clearly show a significant rise in voltage peaks and have a fast response of 80 ms. To judge the magnetic field strength by the magnitude of the electrical peak, the output voltage of the device under different magnetic field strengths is illustrated in Figure 4c. The output voltage grows slowly and shows a desirable sensitivity of 31.6 mV/mT when the magnetic field strength is less than 60 mT, while the output voltage increases significantly with a magnetic field strength greater than 60 mT. Durability is another critical factor for the sensor. During 2000 cycles of contact-separation cycles, the voltage reveals a negligible change, as depicted in Figure S3. All of these results suggest that the magnetic sensor is robust enough to work normally under various environmental conditions. To better demonstrate the monitoring capability of the sensor, we performed the test shown in Figure 4d and Figure S4. When a magnetic field is applied in one direction, the corresponding direction channel light turns red, while the other channel's lights remain

green, and the voltage value for each channel is shown in the interface. This result shows that the sensor we designed exhibits excellent real-time magnetic field monitoring and a unique self-powered capability. It also shows that the MRE-based TENG has great potential for magnetic field detection and other smart applications.

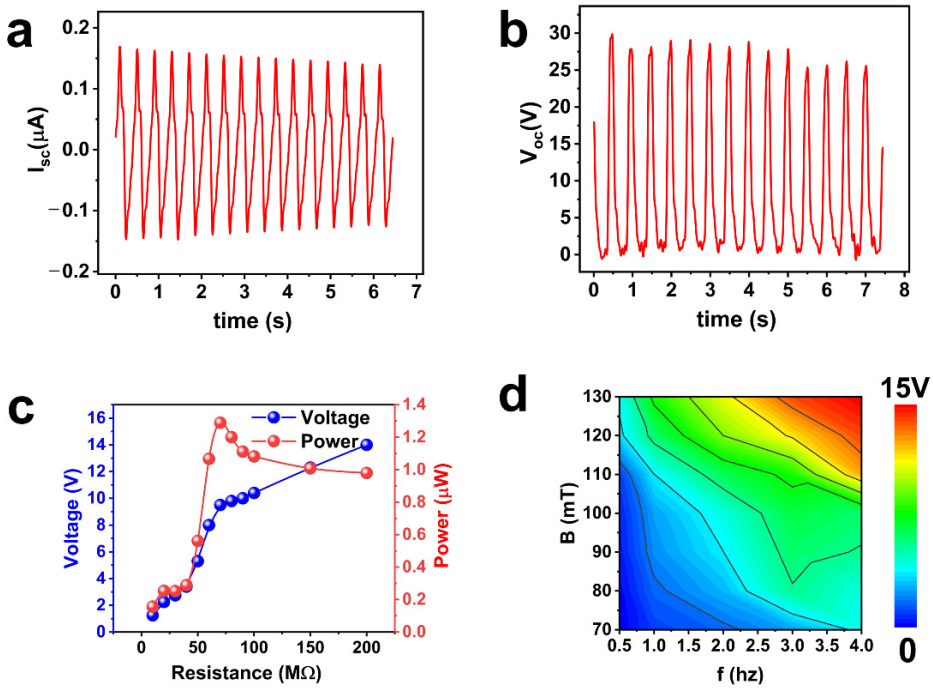

Figure 3. The output performance of TENG. (**a**,**b**) Open-circuit voltage and short-circuit current at the sliding velocity of 16 cm·s^{-1}; (**c**) Voltage and power under the different external load resistances; (**d**) The output performance of the TENG under different sliding frequencies and magnetic field strengths.

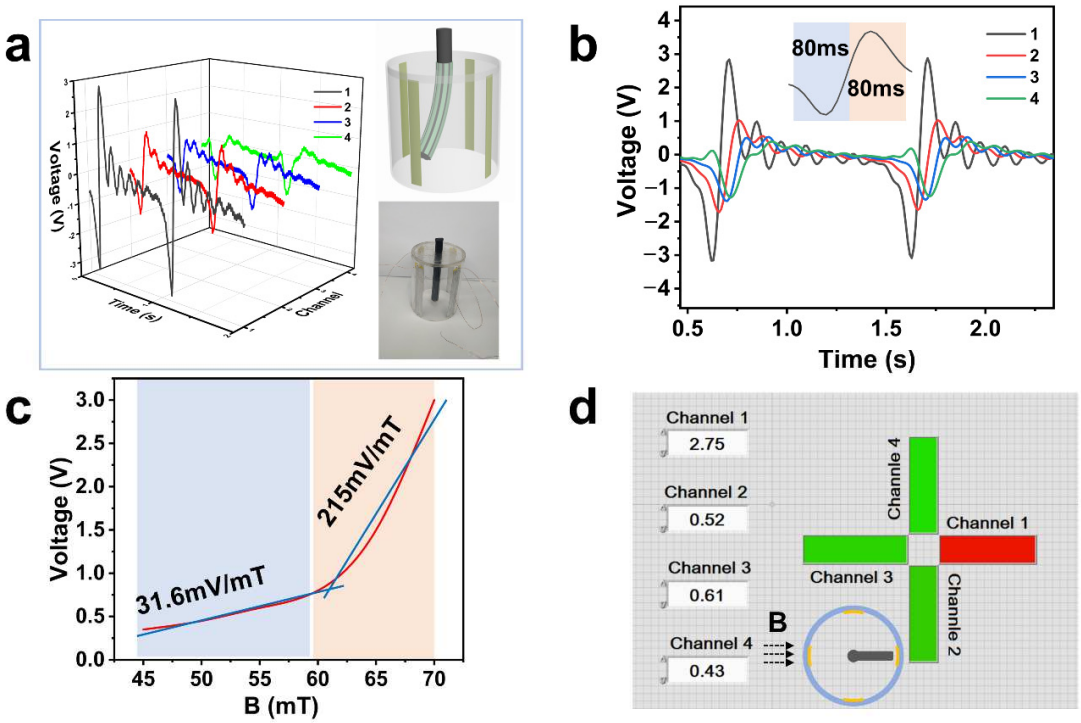

Figure 4. Magnetic field monitoring applications. Measured voltage signals of the sensor when the magnet is close to 1 in 3D (**a**) and 2D (**b**),inset is Sensormodel; (**c**) The output performance of a single channel of the sensor under different magnetic field strengths; (**d**) Mapping image when the magnet is close to channel 1.

3. Conclusions

In summary, we invented a self-powered magnetic field monitoring sensor consisting of the MRE-based TENG. MRE film is made by mixing SEBS powder with liquid paraffin and magnetic fluid in a certain mass ratio and then heating at high temperature to make an MRE film. Simulating the magnetic field environment, the MRE-based TENG exhibits good output performance with an open-circuit voltage and short-circuit current of 16 V and 0.18 μA, respectively, and a maximum output power of 1.3 μW at 80 MΩ. Finally, with the assistance of a programmable platform, the pointer-based TENG structure was designed to achieve excellent real-time magnetic field monitoring and a unique self-powered capability. The fabricated magnetic sensor shows a fast response of 80 ms and a desirable sensitivity of 31.6 mV/mT in a magnetic field range of 35–60 mT as well as the preliminary vectorability enabled by the multichannel layout. Our work provides a new route of magnetic field measurements and further pushes the application of triboelectric technology in future sensing.

4. Experimental Section

Preparation of MRE film: Firstly, SEBS powder (TSRC Nantong Industrial Co., Ltd., Nantong, China) was mixed with liquid paraffin (Shangqiu Liangfeng Health Care Co., Ltd., Shangqiu, China) and magnetic fluid (Ink king magnetic nanofluid company, Jiaxing, China) in a certain mass ratio and mixed in a beaker to obtain a homogeneous mixture. A certain amount of the mixture was put into a porcelain square with a length, width, and height of 60 mm, 30 mm, and 20 mm, respectively. Then, the porcelain ark was placed in a high-temperature resistance furnace (Shanghai Boxun Industrial Co., Ltd., Shanghai, China) and heated to 225 °C or 30 min. Finally, the porcelain ark was left at room temperature until the molten was cooled, solidified, and peeled from the porcelain ark carrier to obtain the MRE film.

Production of sensor: we used an acrylic cylinder with a diameter of 45 mm and a height of 60 mm as the housing for the magnetic field monitoring sensor. A cylinder MRE with a diameter of 7 mm and a height of 55 mm was fixed in the middle of the cylinder on top of the housing. Four 55 × 10 mm Al sheets, which serve as positive friction material and electrodes, were evenly attached to the inner wall of the housing as four channels. Multiple pieces of 1 mm × 55 mm PTFE films were attached around the cylindrical MRE as the negative friction material.

Output performance measurements: The MRE morphology was characterized by the SEM technique (Hitachi SU8020, Tokyo, Japan). Mechanical analysis was performed using a dynamic mechanical analyzer (Mark-10 Corporation, Copiague, NY, USA) based on an M5-20 dynamometer. In addition, all electrical measurements were performed through a programmable Labview platform consisting of a Keithley 6514, Stanford SR570, and a data acquisition module.

Supplementary Materials: The following are available online at https://www.mdpi.com/article/10.3390/nano11112815/s1, Figure S1: Simulation drawing of stress and strain experiment, Figure S2: The output performance of the TENG under different sliding frequencies and magnetic field strengths in 2D, Figure S3: The cycle tests of the TENG devices, Figure S4: Mapping image when the magnet is close to channels 2, 3 and 4, Table S1: Comparison of the achievement of our sensor with other competing sensing technologies.

Author Contributions: Conceptualization, H.Z. and K.Z.; methodology, H.Z.; software, N.M. and Z.W.; validation, H.Z. and K.Z.; formal analysis, Z.W. and X.C.; investigation, D.W.; resources, H.Z.; data curation, T.Z. and X.C.; writing—original draft preparation, D.W., N.M. and T.Z.; writing—review and editing, H.Z. and K.Z.; visualization, K.Z.; supervision, H.Z. and K.Z.; project administration, K.Z.; funding acquisition, H.Z. All authors have read and agreed to the published version of the manuscript.

Funding: This research was funded by Shanxi Scholarship Council of China, grant number HGKY2019022 and Youth Top Talent Program of Shanxi Province (2018).

Conflicts of Interest: The authors declare no conflict of interest.

References

1. Mishra, S.R.; Dickey, M.D.; Velev, O.D.; Tracy, J.B. Selective and directional actuation of elastomer films using chained magnetic nanoparticles. *Nanoscale* **2016**, *8*, 1309–1313. [CrossRef]
2. Su, Y.; Qiu, T.; Song, W.; Han, X.; Sun, M.; Wang, Z.; Xie, H.; Dong, M.; Chen, M. Melt Electrospinning Writing of Magnetic Microrobots. *Adv. Sci.* **2021**, *8*, 2003177. [CrossRef]
3. Schmauch, M.M.; Mishra, S.R.; Evans, B.A.; Velev, O.D.; Tracy, J.B. Chained Iron Microparticles for Directionally Controlled Actuation of Soft Robots. *ACS Appl. Mater. Interfaces* **2017**, *9*, 11895–11901. [CrossRef] [PubMed]
4. Hu, X.; Nian, G.; Liang, X.; Wu, L.; Yin, T.; Lu, H.; Qu, S.; Yang, W. Adhesive Tough Magnetic Hydrogels with High Fe_3O_4 Content. *ACS Appl. Mater. Interfaces* **2019**, *11*, 10292–10300. [CrossRef] [PubMed]
5. Feng, J.; Xuan, S.; Ding, L.; Gong, X. Magnetoactive elastomer/PVDF composite film based magnetically controllable actuator with real-time deformation feedback property. *Compos. Part A Appl. Sci. Manuf.* **2017**, *103*, 25–34. [CrossRef]
6. Gao, W.; Wang, L.; Wang, X.; Liu, H. Magnetic Driving Flowerlike Soft Platform: Biomimetic Fabrication and External Regulation. *ACS Appl. Mater. Interfaces* **2016**, *8*, 14182–14189. [CrossRef]
7. Li, C.; Lau, G.C.; Yuan, H.; Aggarwal, A.; Dominguez, V.L.; Liu, S.; Sai, H.; Palmer, L.C.; Sather, N.A.; Pearson, T.J.; et al. Fast and programmable locomotion of hydrogel-metal hybrids under light and magnetic fields. *Sci. Robot.* **2020**, *5*, eabb9822. [CrossRef]
8. Stanier, D.C.; Ciambella, J.; Rahatekar, S.S. Fabrication and characterisation of short fibre reinforced elastomer composites for bending and twisting magnetic actuation. *Compos. Part A Appl. Sci. Manuf.* **2016**, *91*, 168–176. [CrossRef]
9. Hajra, S.; Vivekananthan, V.; Sahu, M.; Khandelwal, G.; Joseph Raj, N.P.M.; Kim, S.J. Triboelectric nanogenerator using multiferroic materials: An approach for energy harvesting and self-powered magnetic field detection. *Nano Energy* **2021**, *85*, 105964. [CrossRef]
10. Fan, D.; Wang, Q.; Zhu, T.; Wang, H.; Liu, B.; Wang, Y.; Liu, Z.; Liu, X.; Fan, D.; Wang, X. Recent Advances of Magnetic Nanomaterials in Bone Tissue Repair. *Front. Chem.* **2020**, *8*, 745. [CrossRef]
11. Stepanov, R.A.; Sokoloff, D.D. Magnetic helicity and prospects for its observation in the interstellar medium. *Physics-Uspekhi* **2019**, *62*, 1208. [CrossRef]
12. Silveyra, J.M.; Ferrara, E.; Huber, D.L.; Monson, T.C. Soft magnetic materials for a sustainable and electrified world. *Science* **2018**, *362*. [CrossRef] [PubMed]
13. Su, S.; Li, H.; Huang, J.; Zhang, Z.; Liang, C.; Jiang, W.; Deng, A.; Liu, K.; Shi, Z.; Qian, D.; et al. Patterning Graphene Films by H2O-Based Magnetic-Assisted UV Photolysis. *ACS Appl. Mater. Interfaces* **2020**, *12*, 55382–55389. [CrossRef] [PubMed]
14. Shalaby, M.; Shokair, M.; Messiha, N.W. Electromagnetic Field Measurement Instruments: Survey. *Iran. J. Sci. Technol. Trans. Electr. Eng.* **2018**, *43*, 1–14. [CrossRef]
15. Ni, J.L.; Hu, F.; Feng, S.J.; Kan, X.C.; Han, Y.Y.; Liu, X.S. Soft magnetic properties of FeSiAl/carbonyl iron composites with high magnetic permeability and low magnetic loss. *J. Alloys Compd.* **2021**, *887*, 161337. [CrossRef]
16. Wang, S.; Yuan, F.; Liu, S.; Zhou, J.; Xuan, S.; Wang, Y.; Gong, X. A smart triboelectric nanogenerator with tunable rheological and electrical performance for self-powered multi-sensors. *J. Mater. Chem. C* **2020**, *8*, 3715–3723. [CrossRef]
17. Deng, H.; Sattari, K.; Xie, Y.; Liao, P.; Yan, Z.; Lin, J. Laser reprogramming magnetic anisotropy in soft composites for reconfigurable 3D shaping. *Nat. Commun.* **2020**, *11*, 6325. [CrossRef]
18. Zhu, M.; Qi, S.; Xie, Y.; Fu, J.; Yu, M. Transient responses of magnetorheological elastomer and isolator under shear mode. *Smart Mater. Struct.* **2019**, *28*, 044002. [CrossRef]
19. Davis, L.C. Model of magnetorheological elastomers. *J. Appl. Phys.* **1999**, *85*, 3348. [CrossRef]
20. Gong, X.L.; Zhang, X.Z.; Zhang, P.Q. Fabrication and characterization of isotropic magnetorheological elastomers. *Polym. Test.* **2005**, *24*, 669–676. [CrossRef]
21. Li, W.H.; Zhang, X.Z. A study of the magnetorheological effect of bimodal particle based magnetorheologicalelastomers. *Smart Mater. Struct.* **2010**, *19*, 035002. [CrossRef]
22. Wang, S.; He, M.; Weng, B.; Gan, L.; Zhao, Y.; Li, N.; Xie, Y. Stretchable and Wearable Triboelectric Nanogenerator Based on Kinesio Tape for Self-Powered Human Motion Sensing. *Nanomaterials* **2018**, *8*, 657. [CrossRef] [PubMed]
23. Zhang, H.; Yang, Y.; Hou, T.-C.; Su, Y.; Hu, C.; Wang, Z.L. Triboelectric nanogenerator built inside clothes for self-powered glucose biosensors. *Nano Energy* **2013**, *2*, 1019–1024. [CrossRef]
24. Guo, H.; Pu, X.; Chen, J.; Meng, Y.; Yeh, M.H.; Liu, G.; Tang, Q.; Chen, B.; Liu, D.; Qi, S.; et al. A highly sensitive, self-powered triboelectric auditory sensor for social robotics and hearing AIDS. *Sci. Robot.* **2018**, *3*, eaat2516. [CrossRef]
25. Cui, X.; Zhao, T.; Yang, S.; Xie, G.; Zhang, Z.; Zhang, Y.; Sang, S.; Lin, Z.-H.; Zhang, W.; Zhang, H. A spongy electrode-brush-structured dual-mode triboelectric nanogenerator for harvesting mechanical energy and self-powered trajectory tracking. *Nano Energy* **2020**, *78*, 105381. [CrossRef]
26. Ren, X.; Fan, H.; Zhao, Y.; Liu, Z. Flexible Lead-Free BiFeO3/PDMS-Based Nanogenerator as Piezoelectric Energy Harvester. *ACS Appl. Mater. Interfaces* **2016**, *8*, 26190–26197. [CrossRef]
27. Chen, C.; Guo, H.; Chen, L.; Wang, Y.C.; Pu, X.; Yu, W.; Wang, F.; Du, Z.; Wang, Z.L. Direct Current Fabric Triboelectric Nanogenerator for Biomotion Energy Harvesting. *ACS Nano* **2020**, *14*, 4585–4594. [CrossRef] [PubMed]
28. Chen, J.; Wang, Z.L. Reviving Vibration Energy Harvesting and Self-Powered Sensing by a Triboelectric Nanogenerator. *Joule* **2017**, *1*, 480–521. [CrossRef]

29. Wan, D.; Yang, J.; Cui, X.; Ma, N.; Wang, Z.; Li, Y.; Li, P.; Zhang, Y.; Lin, Z.; Sang, S.; et al. Human body-based self-powered wearable electronics for promoting wound healing driven by biomechanical motions. *Nano Energy* **2021**, *89*, 106465. [CrossRef]
30. Maharjan, P.; Bhatta, T.; Cho, H.; Hui, X.; Park, C.; Yoon, S.; Salauddin, M.; Rahman, M.T.; Rana, S.S.; Park, J.Y. A Fully Functional Universal Self-Chargeable Power Module for Portable/Wearable Electronics and Self-Powered IoT Applications. *Adv. Energy Mater.* **2020**, *10*, 2002782. [CrossRef]
31. Yang, X.; Chan, S.; Wang, L.; Daoud, W.A. Water tank triboelectric nanogenerator for efficient harvesting of water wave energy over a broad frequency range. *Nano Energy* **2018**, *44*, 388–398. [CrossRef]
32. Hajra, S.; Padhan, A.M.; Sahu, M.; Alagarsamy, P.; Lee, K.; Kim, H.J. Lead-free flexible Bismuth Titanate-PDMS composites: A multifunctional colossal dielectric material for hybrid piezo-triboelectric nanogenerator to sustainably power portable electronics. *Nano Energy* **2021**, *89*, 106316. [CrossRef]
33. Yang, Y.; Lin, L.; Zhang, Y.; Jing, Q.; Hou, T.-C.; Wang, Z.L. Self-Powered Magnetic Sensor Based on a Triboelectric Nanogenerator. *ACS Nano* **2012**, *6*, 10378–10383. [CrossRef]
34. Qi, S.; Guo, H.; Chen, J.; Fu, J.; Hu, C.; Yu, M.; Wang, Z.L. Magnetorheological elastomers enabled high-sensitive self-powered tribo-sensor for magnetic field detection. *Nanoscale* **2018**, *10*, 4745–4752. [CrossRef]
35. Cai, Y.W.; Zhang, X.N.; Wang, G.G.; Li, G.Z.; Zhao, D.Q.; Sun, N.; Li, F.; Zhang, H.Y.; Han, J.C.; Yang, Y. A flexible ultra-sensitive triboelectric tactile sensor of wrinkled PDMS/MXene composite films for E-skin. *Nano Energy* **2021**, *81*, 105663. [CrossRef]
36. Graham, S.A.; Chandrarathna, S.C.; Patnam, H.; Manchi, P.; Lee, J.W.; Yu, J.S. Harsh environment–tolerant and robust triboelectric nanogenerators for mechanical-energy harvesting, sensing, and energy storage in a smart home. *Nano Energy* **2021**, *80*, 105547. [CrossRef]
37. Zhang, T.; Wen, Z.; Liu, Y.; Zhang, Z.; Xie, Y.; Sun, X. Hybridized Nanogenerators for Multifunctional Self-Powered Sensing: Principles, Prototypes, and Perspectives. *iScience* **2020**, *23*, 101813. [CrossRef] [PubMed]
38. Lama, J.; Yau, A.; Chen, G.; Sivakumar, A.; Zhao, X.; Chen, J. Textile triboelectric nanogenerators for self-powered biomonitoring. *J. Mater. Chem. A* **2021**, *9*, 19149–19178. [CrossRef]
39. Song, X.; Wang, W.; Yang, F.; Wang, G.; Rui, X. The study of enhancement of magnetorheological effect based on natural rubber/thermoplastic elastomer SEBS hybrid matrix. *J. Intell. Mater. Syst. Struct.* **2020**, *31*, 339–348. [CrossRef]
40. Wang, Z.L.; Wang, A.C. On the origin of contact-electrification. *Mater. Today* **2019**, *30*, 34–51. [CrossRef]

nanomaterials

MDPI

Article

All-in-One Self-Powered Human–Machine Interaction System for Wireless Remote Telemetry and Control of Intelligent Cars

Tingting Zhang [1,2], Lingjie Xie [3], Junyan Li [3], Zheguan Huang [1,2], Hao Lei [4], Yina Liu [3], Zhen Wen [4,*], Yonglin Xie [2,*] and Xuhui Sun [4,*]

1 School of Nano Technology and Nano Bionics, University of Science and Technology of China, Hefei 230026, China; ttzhang2017@sinano.ac.cn (T.Z.); zghuang2017@sinano.ac.cn (Z.H.)
2 Inkjet Printing Technology Research Center, Printable Electronics Research Center, Suzhou Institute of Nano-Tech and Nano-Bionics, Chinese Academy of Sciences, Suzhou 215123, China
3 School of Science, Xi'an Jiaotong-Liverpool University, Suzhou 215123, China; 20174214077@stu.suda.edu.cn (L.X.); 20124def10@gmail.com (J.L.); Yina.Liu@xjtlu.edu.cn (Y.L.)
4 Jiangsu Key Laboratory for Carbon-Based Functional Materials and Devices, Institute of Functional Nano and Soft Materials (FUNSOM), Soochow University, Suzhou 215123, China; jacklei_zjou@163.com
* Correspondence: wenzhen2011@suda.edu.cn (Z.W.); ylxie2013@sinano.ac.cn (Y.X.); xhsun@suda.edu.cn (X.S.)

Abstract: The components in traditional human–machine interaction (HMI) systems are relatively independent, distributed and low-integrated, and the wearing experience is poor when the system adopts wearable electronics for intelligent control. The continuous and stable operation of every part always poses challenges for energy supply. In this work, a triboelectric technology-based all-in-one self-powered HMI system for wireless remote telemetry and the control of intelligent cars is proposed. The dual-network crosslinking hydrogel was synthesized and wrapped with functional layers to fabricate a stretchable fibrous triboelectric nanogenerator (SF-TENG) and a supercapacitor (SF-SC), respectively. A self-charging power unit containing woven SF-TENGs, SF-SCs, and a power management circuit was exploited to harvest mechanical energy from the human body and provided power for the whole system. A smart glove designed with five SF-TENGs on the dorsum of five fingers acts as a gesture sensor to generate signal permutations. The signals were processed by the microcontroller and then wirelessly transmitted to the intelligent car for remote telemetry and control. This work is of paramount potential for the application of various terminal devices in self-powered HMI systems with high integration for wearable electronics.

Keywords: human–machine interaction; triboelectric nanogenerator; self-powered sensing; self-charging power unit; remote telemetry and control

Citation: Zhang, T.; Xie, L.; Li, J.; Huang, Z.; Lei, H.; Liu, Y.; Wen, Z.; Xie, Y.; Sun, X. All-in-One Self-Powered Human–Machine Interaction System for Wireless Remote Telemetry and Control of Intelligent Cars. *Nanomaterials* **2021**, *11*, 2711. https://doi.org/10.3390/nano11102711

Academic Editor: Dong-Joo Kim

Received: 21 September 2021
Accepted: 11 October 2021
Published: 14 October 2021

1. Introduction

Human–machine interaction (HMI) systems have attracted tremendous attention with the rapid development of information technology and the urgent demands of the internet of things (IoTs) [1,2]. To effectively realize the function of HMI systems, they should traditionally consist of three components: multiblock sensors for detecting or monitoring objects' signals, microcontroller (MCU) modules for signal reception, identification, and processing, and terminal devices to receive the processed signals and respond accordingly [3–5]. Moreover, the energy supply is inevitable to power the system for continuous operation. Current commercialized HMI systems exist in every field that participates in human–machine information exchange, especially as wearable electronics for intelligent control [6,7].

Although there has been a significant advancement in terms of traditional HMI systems, two bottlenecks still need to be broken through to obtain a better wearing experience when the system adopts wearable electronics. First, the three typical components in addition to the energy supply part of HMI systems are independent and dispersed, which

presents low integration and difficulty obtaining a comfortable wearing experience [8–10]. In addition, continuous energy supply is necessary for powering the sensors and MCU circuits considering the front-to-back structure design of current systems [11–14]. Fiber energy devices are currently developed for powering wearable systems. Batteries with high densities are commonly used, but are too difficult to make, especially stretchable or fibrous batteries [15,16]. Therefore, the development of HMI systems with high integration and self-powered characteristics is still an intriguing challenge and remains an open area for investigations.

Triboelectric technology has been positively exploited in many fields since Wang's group first invented triboelectric nanogenerators (TENG), such as self-powered sensors, mechanical energy or blue energy harvesting, and high-voltage occasions [17–23]. Apparently, the employment of self-powered sensors in HMI systems can effectively reduce energy requirements since they generate electrical signals directly compared to previous resistive or capacitive sensors [24–27]. Simultaneously, the energy collected by TENG can be temporarily stored in energy storage devices, such as supercapacitors, which has been achieved through self-charging power units (SCPU) [28–31]. Based on these two functions, triboelectric technology provides a preeminent idea for solving the energy supply and integration problems of traditional HMI systems, which favorably promotes its creation and implementation [32,33].

In this work, we propose a prototype of an all-in-one self-powered HMI system relying on triboelectric technology. The detailed working flow chart of the system is shown in Supplementary Figure S1. First, SF-TENG was fabricated by employing a dual-network crosslinked hydrogel as the electrode and silicone rubber as a coating layer that served as a self-powered sensor. A smart glove was then designed by attaching five SF-TENG sensors on the dorsum of five fingers, which generated signals under different gestures. Then, the smart gloves were connected to the MCU part ulteriorly to detect and distinguish these signals. Supercapacitors with sandwiched structures were designed by attaching the CNT electrode film to the pre-stretched dual-network crosslinked hydrogel electrolytes. SCPU integrated with woven SF-TENGs, series supercapacitors, and a power management circuit were exploited to harvest mechanical energy from the human body and power the systems. Ultimately, the proposed integrated system was successfully applied in wireless remote telemetry and control for intelligent cars, which is of paramount potential for self-powered HMI systems with high integration for wearable electronics.

2. Experimental Section

2.1. Materials

Sodium alginate (SA), acrylamide (AAm), sodium chloride (NaCl), and calcium sulfate dihydrate ($CaSO_4 \cdot 2H_2O$) were obtained from Sinopharm Chemical Reagent Co., Ltd. (Shanghai, China). Ammonium persulfate (APS), N, N, N, N′-tetramethylenediamine (TMEDA), and N, N-methylenebisacrylamide (MBAA) were all derived from Sigma-Aldrich (Shanghai) Trading Co., Ltd. (Shanghai, China). Silicone rubber (Ecoflex 00-10) was manufactured by Smooth-On, Inc. (Marco Key, PA, USA). All materials or chemicals above were directly used as received without any further purification. All aqueous solutions were prepared using ultrapure water with resistivity $\geq$ 18.2 MΩ·cm.

2.2. Synthesis of the Hydrogels

AAm powders of 14 g were first dissolved in 60 mL ultrapure water. After 5 min of stirring, 2.8 g SA was slowly added into the solution and stirred for 8 h until completely dissolved. Then, we added different contents of NaCl as the electrolyte. We kept stirring for 30 min and then added MBAA (0.06% the weight of AAm) as the crosslinker and TEMED (0.25% the weight of AAm) as the crosslinking accelerator for polyacrylamide (PAAm), respectively. Then, APS (0.5% the weight of AAm), which was completely dissolved in 20 mL ultrapure water, was added as the initiator of PAAm. $CaSO_4 \cdot 2H_2O$ (13% the weight of SA) as the ionic crosslinker for SA was dissolved in 20 mL ultrapure water and added

dropwise to the pre-mixed solution. We then poured the gel solution into a PTFE mold with a size of 20 × 20 × 1 mm^3 and put it into a 50 °C oven for about three hours until the hydrogel was cured.

2.3. Fabrication of Fibrous and Woven TENG

The silicone rubber was used by mixing components A and B in a 1:1 weight ratio. The fibrous TENG was fabricated by coating the silicone rubber on the stretchable hydrogel electrode. As the shape of the hydrogel electrode was strip-shaped, after the silicone rubber was cured, the fibrous TENG was close to a cylindrical shape. The TENG fabric was obtained by manual weaving.

2.4. Fabrication of Supercapacitor

The hydrogel was first stretched to a strain of 400% and fixed with two clips; then, we carefully attached the CNT film on both sides to ensure that the electrodes did not touch each other and cause a short circuit. When multiple supercapacitors are connected in series, the upper and lower electrodes alternately replace external wires to form the integrated supercapacitor. After releasing the stain, we coated the silicone rubber on the outside as the encapsulation layer. Finally, we connected the CNT electrodes of the supercapacitors to the output port of the power management circuit by conductive tape for storing the energy from the TENG.

2.5. Characterization and Measurement

A scanning electron microscope (QUANTA FEG 250) (FEI Company, Hillsboro, OR, USA) was employed to characterize the surface morphology of the hydrogel. The Instron 3366 electronic universal testing machine (Instron Corporation, Canton, MA, USA) was employed to test the mechanical tensile strength of the hydrogel. The electrical output performance of the TENG, including short-circuit current, open-circuit voltage, and transfer charge, was tested by a programmable electrometer Keithley model 6514 (Tektronix, Beaverton, OR, USA), and real-time data acquisition was realized by a software platform, which was constructed based on the LabView (LabView 2015, National Instruments, Austin, TX, USA). For the supercapacitor electrochemical performance, such as cyclic voltammetry (CV) and galvanostatic charge–discharge (GCD) measurement, the electrochemical workstation (CHI 760E, Shanghai Shinstruments Co., Ltd., Shanghai, China) was utilized. The electrochemical impedance spectroscopy (EIS) was also tested by the electrochemical workstation. A piece of hydrogel with a size of 1 × 1 cm^2 was sandwiched between two sheets of stainless steel. The ionic conductivity was calculated by $\sigma = d/(R \times A)$, where d and A denote the thickness and area of the sample, respectively, and R is determined by the intercept of the EIS real axis.

3. Results and Discussion

3.1. Synthesis and Characterizations of Materials

The desired stretchable hydrogels were facilely synthesized by blending two monomers, namely, a covalently crosslinked polymer, polyacrylamide, and an ionically crosslinked polymer, alginate, followed by adding the initiator APS and $CaSO_4 \cdot 2H_2O$, respectively [34]. By dual-network crosslinking, the hydrogels obtained both elasticity and toughness, as shown in Figure 1a. The obtained hydrogel had three-dimensional hollow network structures from the scanning electron microscopy (SEM) image (Figure 1b). FTIR spectroscopy was also measured to further confirm the composition of the hydrogel (Supplementary Figure S2). Besides the high transparency and high stretchability (Supplementary Figure S3), the hydrogel also endured multiple deformation forms, including rolling, folding, twisting, and crumpling (Figure 1c). To enhance the ionic conductivity, different weight contents of NaCl between 0 and 2.5 g (about 17.8% the weight of AAm) were added into the hydrogel solution, and the electrochemical impedance spectroscopy (EIS) (Figure 1d) was measured. As shown in Supplementary Figure S4, the maximal ionic conductivity calcu-

lated from the EIS was 19.86 mS/cm when the NaCl content was 1.5 g, which was 14 times higher than the hydrogel without NaCl. This enhancement is mainly due to the increased abundance of free ions. As seen in Figure 1e, the addition of NaCl not only improved the ionic conductivity but also enhanced the mechanical property of the hydrogel. The stress reached more than 1300% when the NaCl content was 1.5 g. This is mainly attributed to the salting-out effect of NaCl, which induced the PAAm chain entanglements or formed micro-crystalline zones, further strengthening the hydrogel's mechanical performance. Moreover, the ionic conductivity almost stayed the same when stretching the hydrogel (Figure 1f), which ensured the stability to fabricate functional devices. Given these two key focuses of mechanical properties and ionic conductivity, the hydrogel synthesized by adding 1.5 g NaCl was employed for device fabrication in the next experiment.

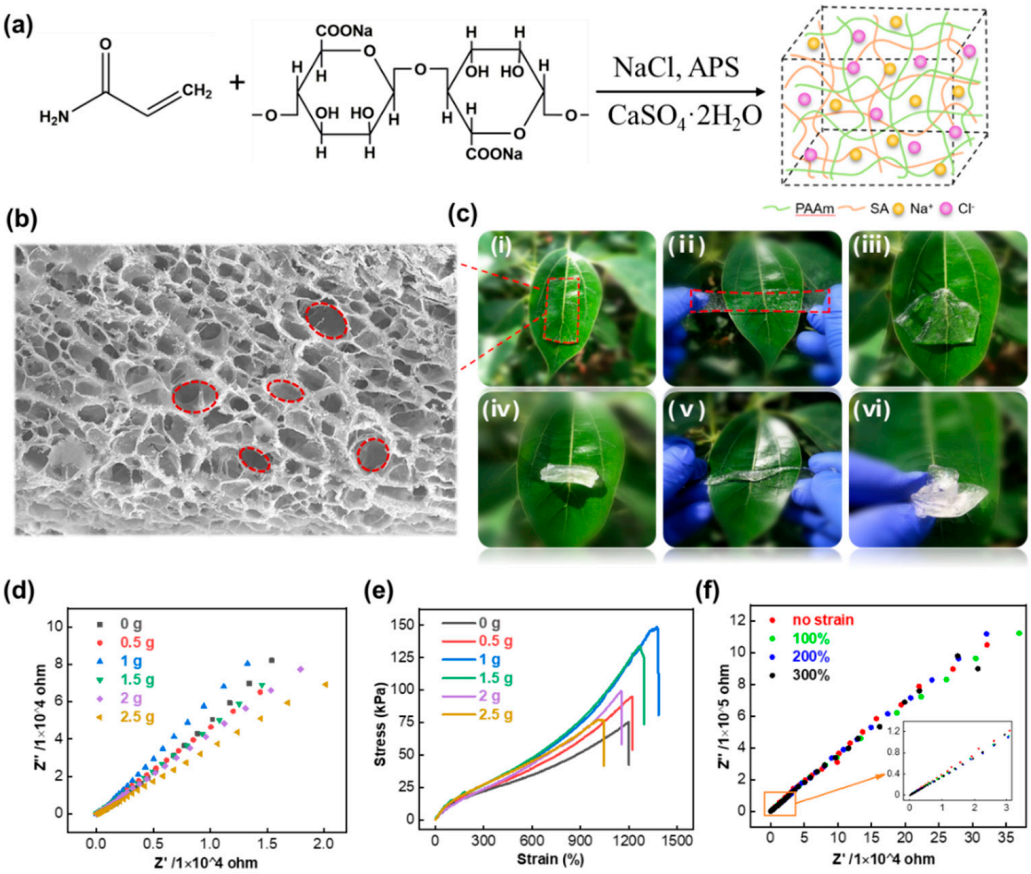

Figure 1. Synthesis and characterizations of dual-network crosslinked hydrogels. (**a**) Synthetic route of hybrid hydrogels containing sodium alginate and polyacrylamide with $CaSO_4 \cdot 2H_2O$ and APS served as initiators. (**b**) SEM image of freeze-dried composite hydrogels (scale bar: 50 µm). (**c**) Photographs of the hydrogel at different deformed states, namely, (i) original, (ii) stretching, (iii) rolling, (iv) folding, (v) twisting, and (vi) crumpling, respectively. (**d**) Electrochemical impedance spectroscopies (EIS) and (**e**) typical tensile stress–strain curves of hydrogel with different NaCl contents. (**f**) EIS of hydrogels with different strains when the content of NaCl was fixed at 1.5 g.

3.2. Electrical Performance of the SF-TENG

A fibrous stretchable TENG (FS-TENG) at the single-electrode mode was fabricated by coating the silicone rubber outside of the hydrogel ionic conductor, as shown in Figure 2a. The reason why silicone rubber was chosen as the encapsulation layer is due to its good stretchability, strong electron affinity and ability to prevent the hydrogel from losing water. Figure 2b schematically illustrates the working mechanism of SF-TENG for generating electricity under short-circuit conditions. The left part is from the front view, and the right part is a corresponding side view with a half-cut. When skin contacted the SF-

TENG, positive and negative charges were generated on the surface of the human skin and silicone rubber, respectively, due to their different electron affinities. Once the skin was separated from it, the interaction between the two opposite polarity charges decreased, leading to positive charges induced on the ionic conductor and electrons transferred to the outside from connected wires. When skin contacted the SF-TENG again, the triboelectric charges also returned to their original distribution state. The diameter of the SF-TENG is about 2 mm (Figure 2c), which is suitable for wearable devices. Simultaneously, it has excellent stretchability, which reaches 300% without fracture or breakage, as illustrated in Supplementary Figure S5. To evaluate the electrical output performance of the SF-TENG, the open-circuit voltage (V_{oc}), short-circuit current (I_{sc}), and transferred charges (Q_{tr}) were measured periodically by the linear motor. The testing schematic diagram of TENG at original and stretching states is provided in Supplementary Figure S6. The human skin was replaced by hog skin for long-term testing, and the area of hog skin was much larger than the TENG surface to ensure full contact between them. The electrical output of 10 cm TENG with the frequency varying from 0.5 to 2.5 Hz is shown in Figure 2d. It is noted that the V_{oc} and Q_{tr} almost stayed the same with values of 89.7 V and 26.3 nC, respectively. The I_{sc} increased from 0.53 to 1.58 μA with the increasing frequency. Moreover, the optimal resistance load decreased gradually with an increase in frequency, which is demonstrated in Figure 2e. This is mainly attributed to the decrease in intrinsic resistance of TENG with a higher movement speed [35]. Furthermore, the power reached the maximum value (~86.1 μW) at 20 MΩ when the frequency was 2.5 Hz. The transferred charges under different strains (0–250%) are shown in Figure 2f. It can be observed that as the strain increased, the Q_{tr} increased gradually until the strain reached 150% and then decreased. As displayed in Supplementary Figure S7, two factors caused this tendency: one was the surface charge enhancement due to the thinner thickness of silicone rubber, which had a positive effect on the output, and the other was the resistance enhancement of hydrogel electrode, which has the reverse effect. The former was dominant in small strains (<150%), while the latter had a greater impact when the strain was larger.

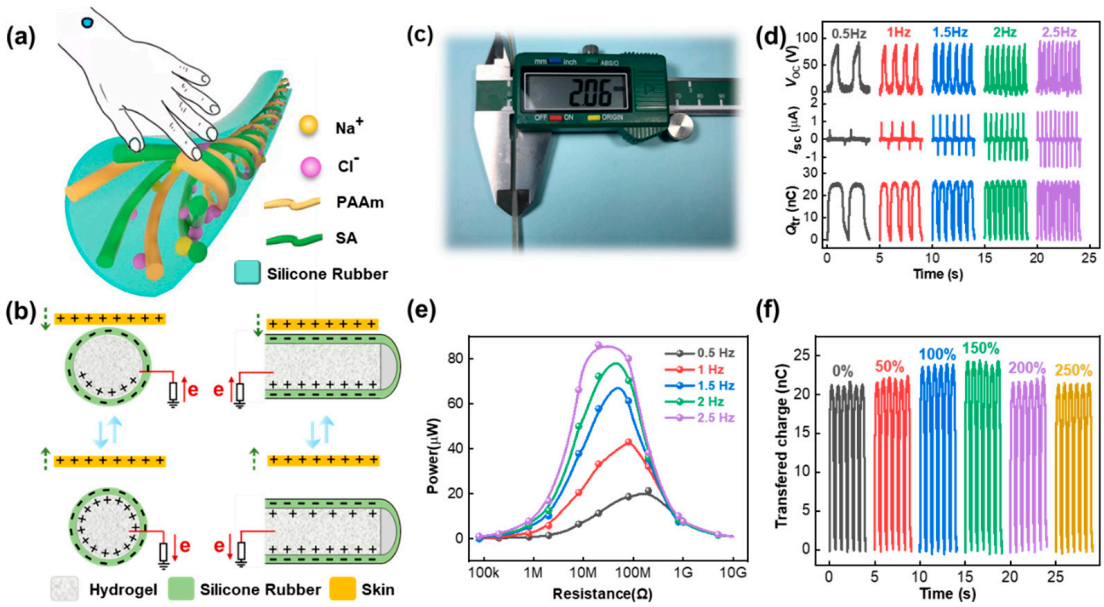

Figure 2. Working mechanism and electrical performance of the stretchable fibrous triboelectric nanogenerator (SF-TENG) at singleelectrode mode. (**a**) Schematic illustration of the SF-TENG when in contact with skin. (**b**) The working mechanism of the SFTENG for generating electricity under shortcircuit conditions. (**c**) Photograph of diameter measurement of TENG. (**d**) The electrical output performance of the single fiberbased TENG with different contact frequencies ranging from 0.5 to 2.5 Hz, including V_{oc}, I_{sc}, and Q_{tr}. (**e**) Dependence of the output power under external resistance load with different frequencies from 0.5 to 2.5 Hz. (**f**) Transferred charges under various strains (0~250%).

3.3. Fabrication Process and Electrochemical Performance of SF-SC

The hydrogel was also exploited as the electrolyte of the stretchable fibrous supercapacitor (SF-SC) as a common ionic conductor. To endow the supercapacitor with stretchability, CNT film was attached on both sides of the pre-stretched hydrogel, as illustrated in Figure 3a. The performance of SF-SC was characterized by the CV and GCD techniques provided by the electrochemical workstation. As shown in Figure 3b, the CV curves of a single unit SC were close to the rectangular shape at different scan rates ranging from 5 to 100 mV/s with the selected voltage window (0 to 0.8 V), thus indicating the quick electrochemical switching ability and good reaction reversibility of the device. The GCD curves with a typical symmetric triangular shape under the current load of 5 to 25 μA are shown in Figure 3c, which further validates the excellent capacitive behavior of the SC. The capacitance calculated from the GCD curves by the equation $C = (i \times \Delta t)/\Delta V$ was about 156.3 μF when the current load was 5 μA [36]. Figure 3d shows the CV curves of SF-SC at different strains, and there was little capacitance drop observed under each tensile state condition. For the sake of practical applications of the SF-SC as an energy supply, several single unit SCs were connected in series. Unlike the traditional wire connection methods, which are fragile and unable to endure large stains, the series SF-SCs were connected by the CNT film itself inside and silicone rubber outside to form an all-in-one device (Figure 3e). The CV and GCD curves of 1 to 4 units connected in series are displayed in Figure 3d,f, respectively. It can be observed that the voltage increased linearly according to the number of series-connected SC. Thus, the results demonstrate the fabricated SF-SCs have good adjustability and adaptability to various electronic applications.

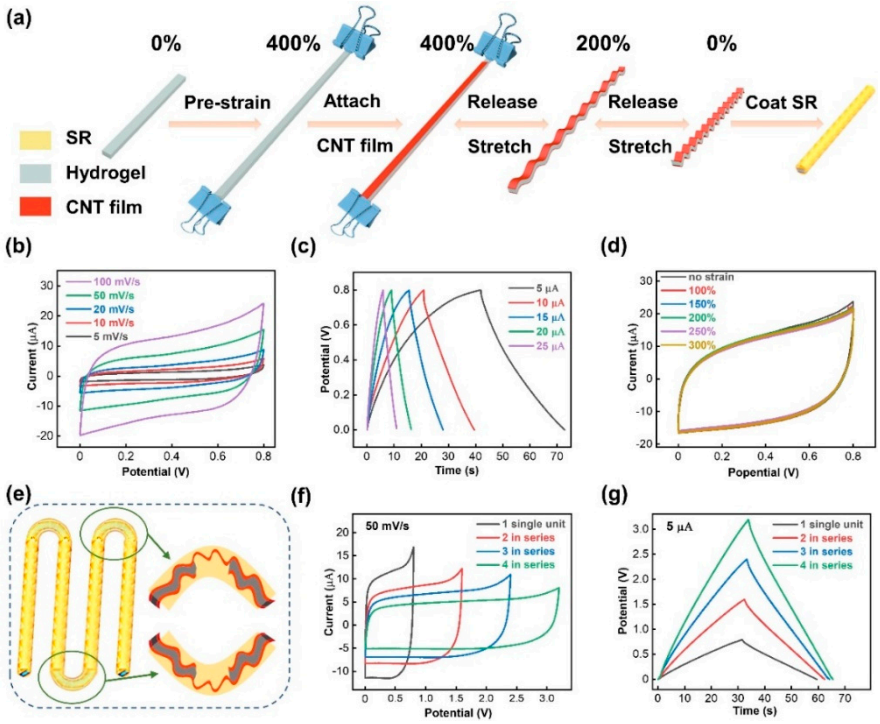

Figure 3. Schematic illustration and electrochemical performance of the stretchable fibrous supercapacitor (SF-SC). (**a**) Schematic illustration of the fabrication process. (**b**) CV curves of the SF-SC at different scanning rates (5–100 mV/s). (**c**) GCD curves at different current loadings (5–25 μA). (**d**) CV curves of the SF-SC under different strains (0–300%). (**e**) Schematic illustration of the series-connected SF-SCs. (**f**) CV and (**g**) GCD curves of various numbered series-connected SF-SCs (1 to 4).

3.4. Demonstration of the Self-Charging Power Unit

Figure 4 demonstrates the SCPU performance, which consisted of woven SF-TENGs, series-connected SF-SCs, and a power management circuit for high charging efficiency. In light of the pulse and low current output of a single unit SF-TENG, several devices

were woven together for the practical application, as shown in Figure 4a. The short-circuit current output of woven SF-TENGs was largely enhanced compared with the single unit; for example, the I_{sc} reached 15.8 μA at a contact frequency of 2.5 Hz (Figure 4b). As we know, a typical feature of TENG's electrical output is high voltage but low current, due to the pulsed output voltage with a short duration and limited frequency, making TENG unsuitable for direct use as a power source. Thus, a power management circuit was designed to convert the pulsed voltage into a steady continuous output (Figure 4c). The power management system mainly contained a rectifier to convert the AC to DC, a fixed value capacitor based on the TENG's inherent capacitance to extract maximal energy from the power source, a switch containing the silicon-controlled rectifier (SCR) and Zener diode to control the power flow paths, and a buck converter circuit. Figure 4d is the photograph of the power management circuit of which the diameter is about 2.4 cm, which is small enough to treat as a button or decoration in wearable electronics. Figure 4e shows the charging and working curve of four series-connected SF-SCs by manually patting the woven SF-TENGs cloth. It is worth noting that the charging voltage had a step-up characteristic attributed to the switching mode of the power management circuit. The switch did not turn on until the fixed value capacitor was charged to a specified voltage, which was set by the Zener diode. Once the switch turned on, the fixed value capacitor discharged to transfer the energy into the load through the buck converter circuit. After the discharge process was over, the switch turned off again and isolated the fixed value capacitor from the load. Considering that the sensor in the system was not continuously working, but was in a long-term dormant state, the SCPU, which always generated electricity, could trigger the MCU if the sleeping mechanism was included in the program. As shown in Figure 4f and Movie S1, when the series-connected SF-SCs were charged to 3 V in about 18 s, an Arduino Leonardo was successfully powered to work as the power-up indicator LED turned red, which would then be used for signal processing in the all-in-one self-powered HMI system.

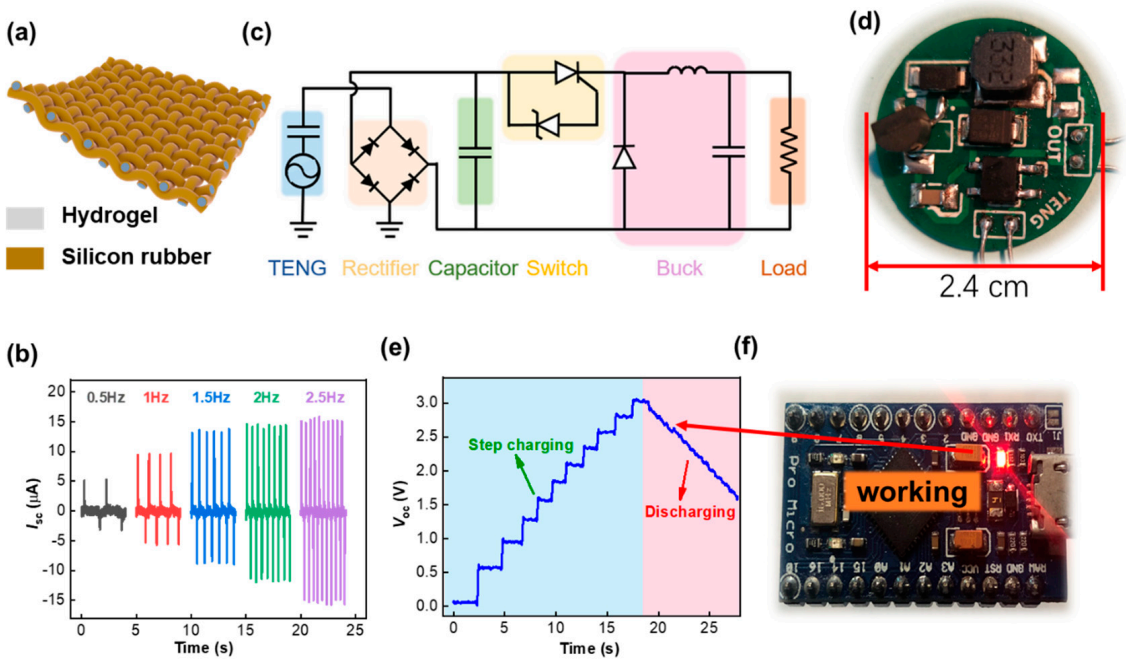

Figure 4. Demonstration of the self-charging power unit. (**a**) Schematic illustration of woven SF-TENGs into cloth. (**b**) Short-circuit current output with different contact frequencies ranging from 0.5 to 2.5 Hz. (**c**) Circuit diagram of the self-charging power unit containing woven SF-TENGs, power management system, and load. (**d**) Photograph of the power management system. (**e**) Charging and working curve of four series-connected SF-SCs by manually patting the woven SF-TENGs cloth and (**f**) powering the microcontroller.

3.5. Application of All-in-One Self-Powered HMI System

A smart glove was developed by attaching five SF-TENG sensors on the dorsum of five fingers (thumb/index/middle/ring/little finger) acting as the self-powered gesture sensors. As each sensor on different fingers may have undergone different squeeze deformations upon various gestures, their corresponding voltage output also differed and, therefore, real-time signal permutations could be achieved. For example, when all five fingers remained straight, the voltage outputs affiliated with them were kept approximately at zero. When one finger repeated the movement of bending and releasing, the sensor on this finger would generate a relatively high pulse voltage compared to the other four motionless fingers. Based on such results, ten different sign language permutations named from A to J are displayed in Figure 5a. The real-time monitored relative voltage changes corresponding to these sign language permutations are shown in Figure 5b. It is noted that different sign language gestures brought about completely different voltage combinations, thus indicating there will be dozens of signals, in theory, by one hand gesture. To detect and distinguish these signals, the smart glove was connected to a control board that contained an amplifier array, a microcontroller, and a 2.4 GHz remote controller. Simultaneously, the series-connected SF-SCs, which were charged to the working voltage by the woven SF-TENGs, provided energy to this control board. The block diagram of the entire system based on triboelectric technology is shown in Figure 5c. The signal was processed and decoded to a specific RC command via a programmable mapping logic system. Supplementary Figure S8 displays the state of the command code. The decoded command would then be wirelessly transmitted to the terminal product. The circuit model for connecting the smart gloves and terminal devices is schematically illustrated in Supplementary Figure S9. Specifically, as shown in Figure 5d and Movie S2, when the gestures with forward and turn left command were executed, the intelligent car received the signals wirelessly sent from the MCU and made a corresponding displacement movement. This demonstration shows the feasibility of adopting all-in-one self-powered HMI systems to achieve highly accurate gesture control for intelligent equipment.

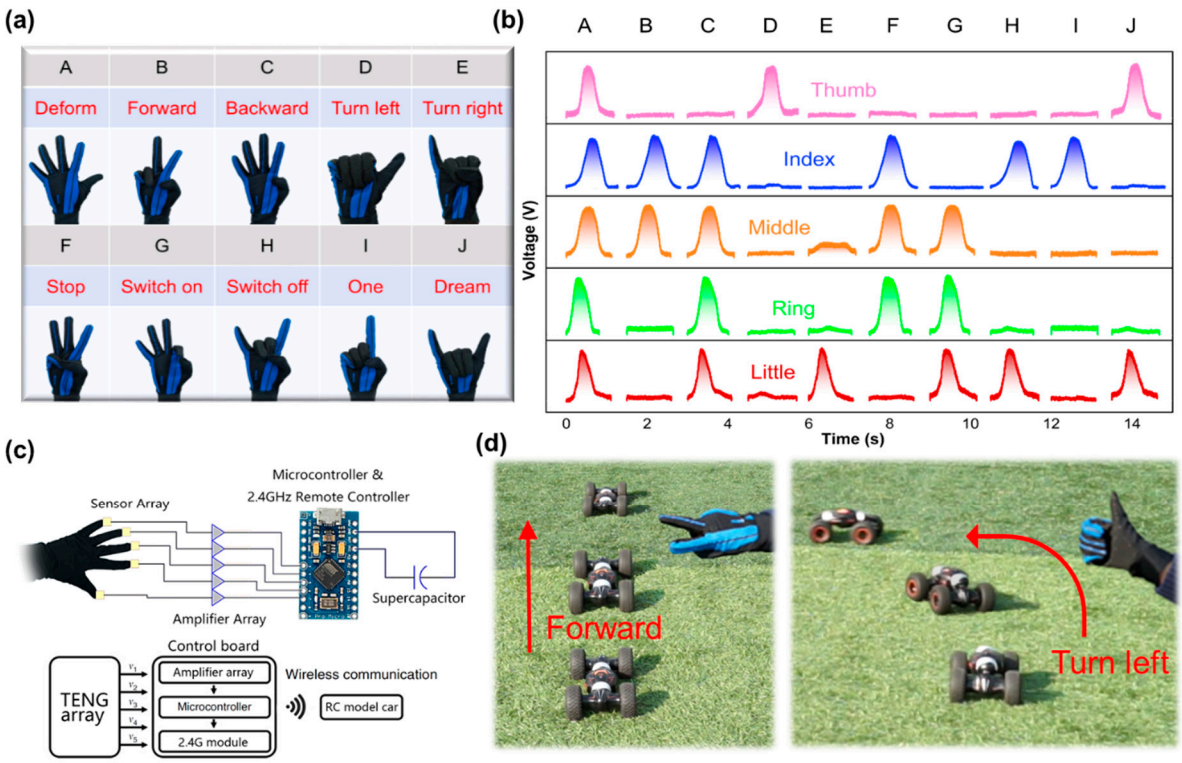

Figure 5. Application of all-in-one self-powered HMI system. (**a**) Photograph of a smart glove with five SF-TENG sensors attached on the dorsum of fingers, and images of ten different sign language gestures. (**b**) Real-time monitored relative

voltage changes under various sign language gestures as shown in (**a**). (**c**) Block diagram of the communicator based on SF-TENG sensors. SF-TENG sensors were connected to a control board that contains an amplifier array, a microcontroller, and a 2.4 GHz remote controller. (**d**) Photographs of 2 gestures (top inset), command codes (bottom inset), and corresponding motions of the intelligent car.

4. Conclusions

In conclusion, an all-in-one self-powered human–machine interaction system based on triboelectric technology was successfully fabricated by the combination of a self-powered triboelectric sensor, microcontroller, intelligent car, and self-powered charging unit. Dual-network crosslinking hydrogel with a high stress of 1300% and ion conductivity of 19.86 mS/cm wrapping with the silicone rubber dielectric layer fabricated the SF-TENG. A smart glove with five SF-TENG on the dorsum of five fingers served as self-powered sensors and generated signal permutations with different gestures. The signals were processed by the microcontroller and then wirelessly transmitted to the intelligent car for remote telemetry and control. During the working process, the SCPU integrated by woven TENG, a supercapacitor of 156.3 μF, and a power management circuit was exploited to harvest mechanical energy from the human body and successfully power the systems in about 18 s. Since the sensing and energy harvesting functions are both achieved by TENG, this all-in-one system is compactly integrated. In addition, due to the universality of various terminal devices, the system has great potential application value in self-powered HMI systems with wearable electronics.

Supplementary Materials: The supplementary materials are provided by the supporting information file. https://www.mdpi.com/article/10.3390/nano11102711/s1. Figure S1: The working flow chart of an all-in-one self-powered human-machine interaction system, Figure S2: FTIR spectra of the freeze-dried composite hydrogel, Figure S3: Optical images of hydrogel with different strains. The content of NaCl was fixed as 1.5 g, Figure S4: The calculated ionic conductivity(σ) of hydrogel with different NaCl contents, Figure S5: (a) Photos of SF-TENG at the original state and stretched state of 300% strain, (b) Diameter change at different stretch rates (0–300%), Figure S6: The testing schematic diagram of TENG at (a) original and (b) stretching state, Figure S7: The surface of silicone rubber becomes thinner (a) and the resistance of hydrogel increase (b) during stretching, Figure S8: The processed and decoded RC command via a programmable mapping logic system, Figure S9: The circuit model for connecting the smart gloves and terminal devices. Video S1: An Arduino Leonardo is successfully powered to work by the SCPU. Video S2: Wireless remote telemetry and control of intelligent car by smart glove.

Author Contributions: Conceptualization, T.Z. and Z.W.; methodology, T.Z., L.X., J.L. and Z.H.; investigation, T.Z., H.L. and Y.L.; writing—original draft preparation, T.Z.; writing—review and editing, Z.W., Y.X. and X.S. All authors have read and agreed to the published version of the manuscript.

Funding: This work was supported by the National Science and Technology Major Project from Minister of Science and Technology of China (no. 2018AAA0103104), National Natural Science Foundation of China (no. 61804103) and the Suzhou Science and Technology Development Planning Project: Key Industrial Technology Innovation (no. SYG202009), Research and Development of Inkjet Technology and Nozzle Devices (no. Y8AAY11001), Key Laboratory of Nanodevices of Jiangsu Province (no. 21SZ03) and China Postdoctoral Science Foundation (no. 2021T140494). This work was also supported by Collaborative Innovation Center of Suzhou Nano Science & Technology, the 111 Project and Joint International Research Laboratory of Carbon-Based Functional Materials and Devices.

Institutional Review Board Statement: Not applicable.

Informed Consent Statement: Not applicable.

Data Availability Statement: The data presented in this study are available on request from the corresponding author.

Conflicts of Interest: The authors declare no conflict of interest.

References

1. Shi, X.; Zuo, Y.; Zhai, P.; Shen, J.; Yang, Y.; Gao, Z.; Liao, M.; Wu, J.; Wang, J.; Xu, X.; et al. Large-area display textiles integrated with functional systems. *Nature* **2021**, *591*, 240–245. [CrossRef] [PubMed]
2. Pyo, S.; Lee, J.; Bae, K.; Sim, S.; Kim, J. Recent Progress in Flexible Tactile Sensors for Human-Interactive Systems: From Sensors to Advanced Applications. *Adv. Mater.* **2021**, *33*, 2005902. [CrossRef] [PubMed]
3. Shi, Q.; Dong, B.; He, T.; Sun, Z.; Zhu, J.; Zhang, Z.; Lee, C. Progress in wearable electronics/photonics—Moving toward the era of artificial intelligence and internet of things. *InfoMat* **2020**, *2*, 1131–1162. [CrossRef]
4. Xu, K.; Lu, Y.; Takei, K. Multifunctional Skin-Inspired Flexible Sensor Systems for Wearable Electronics. *Adv. Mater. Technol.* **2019**, *2*, 1131–1162. [CrossRef]
5. He, X.; Zi, Y.; Yu, H.; Zhang, S.L.; Wang, J.; Ding, W.; Zou, H.; Zhang, W.; Lu, C.; Wang, Z.L. An ultrathin paper-based self-powered system for portable electronics and wireless human-machine interaction. *Nano Energy* **2017**, *39*, 328–336. [CrossRef]
6. Tan, Y.J.; Godaba, H.; Chen, G.; Tan, S.T.M.; Wan, G.; Li, G.; Lee, P.M.; Cai, Y.; Li, S.; Shepherd, R.F.; et al. A transparent, self-healing and high-kappa dielectric for low-field-emission stretchable optoelectronics. *Nat. Mater.* **2020**, *19*, 182–188. [CrossRef] [PubMed]
7. Cao, R.; Pu, X.; Du, X.; Yang, W.; Wang, J.; Guo, H.; Zhao, S.; Yuan, Z.; Zhang, C.; Li, C.; et al. Screen-Printed Washable Electronic Textiles as Self-Powered Touch/Gesture Tribo-Sensors for Intelligent Human–Machine Interaction. *ACS Nano* **2018**, *12*, 5190–5196. [CrossRef] [PubMed]
8. Shi, Q.; Zhang, Z.; Chen, T.; Lee, C. Minimalist and multi-functional human machine interface (HMI) using a flexible wearable triboelectric patch. *Nano Energy* **2019**, *62*, 355–366. [CrossRef]
9. Chen, S.; Pang, Y.; Cao, Y.; Tan, X.; Cao, C. Soft Robotic Manipulation System Capable of Stiffness Variation and Dexterous Operation for Safe Human–Machine Interactions. *Adv. Mater. Technol.* **2021**, *6*, 2100084. [CrossRef]
10. Hou, C.; Geng, J.; Yang, Z.; Tang, T.; Sun, Y.; Wang, F.; Liu, H.; Chen, T.; Sun, L. A Delta-Parallel-Inspired Human Machine Interface by Using Self-Powered Triboelectric Nanogenerator Toward 3D and VR/AR Manipulations. *Adv. Mater. Technol.* **2020**, *6*, 202000912.
11. Wen, F.; Sun, Z.; He, T.; Shi, Q.; Zhu, M.; Zhang, Z.; Li, L.; Zhang, T.; Lee, C. Machine Learning Glove Using Self-Powered Conductive Superhydrophobic Triboelectric Textile for Gesture Recognition in VR/AR Applications. *Adv. Sci.* **2020**, *7*, 2000261. [CrossRef]
12. Zhang, C.; Liu, S.; Huang, X.; Guo, W.; Li, Y.; Wu, H. A stretchable dual-mode sensor array for multifunctional robotic electronic skin. *Nano Energy* **2019**, *62*, 164–170. [CrossRef]
13. Tang, G.; Shi, Q.; Zhang, Z.; He, T.; Sun, Z.; Lee, C. Hybridized wearable patch as a multi-parameter and multi-functional human-machine interface. *Nano Energy* **2020**, *81*, 105582. [CrossRef]
14. Qin, K.; Chen, C.; Pu, X.; Tang, Q.; He, W.; Liu, Y.; Zeng, Q.; Liu, G.; Guo, H.; Hu, C. Magnetic Array Assisted Triboelectric Nanogenerator Sensor for Real-Time Gesture Interaction. *Nano-Micro Lett.* **2021**, *13*, 1–9. [CrossRef] [PubMed]
15. Liu, Y.; Bao, R.; Tao, J.; Li, J.; Dong, M.; Pan, C. Recent progress in tactile sensors and their applications in intelligent systems. *Sci. Bull.* **2019**, *65*, 70–88. [CrossRef]
16. Wu, Z.; Cheng, T.; Wang, Z.L. Self-Powered Sensors and Systems Based on Nanogenerators. *Sensors* **2020**, *20*, 2925. [CrossRef] [PubMed]
17. Zhang, T.; Wen, Z.; Liu, Y.; Zhang, Z.; Xie, Y.; Sun, X. Hybridized Nanogenerators for Multifunctional Self-Powered Sensing: Principles, Prototypes, and Perspectives. *iScience* **2020**, *23*, 101813. [CrossRef]
18. Zhang, Y.; Peng, M.; Liu, Y.; Zhang, T.; Zhu, Q.; Lei, H.; Liu, S.; Tao, Y.; Li, L.; Wen, Z.; et al. Flexible Self-Powered Real-Time Ultraviolet Photodetector by Coupling Triboelectric and Photoelectric Effects. *ACS Appl. Mater. Interfaces* **2020**, *12*, 19384–19392. [CrossRef] [PubMed]
19. Zhang, T.; Wen, Z.; Lei, H.; Gao, Z.; Chen, Y.; Zhang, Y.; Liu, J.; Xie, Y.; Sun, X. Surface-Microengineering for High-Performance Triboelectric Tactile Sensor via Dynamically Assembled Ferrofluid Template. *Nano Energy* **2021**, *87*, 106215. [CrossRef]
20. Xie, L.; Zhai, N.; Liu, Y.; Wen, Z.; Sun, X. Hybrid Triboelectric Nanogenerators: From Energy Complementation to Integration. *Research* **2021**, *2021*, 1–23. [CrossRef]
21. Wang, Z.; Shi, Y.; Liu, F.; Wang, H.; Liu, X.; Sun, R.; Lu, Y.; Ji, L.; Wang, Z.L.; Cheng, J. Distributed mobile ultraviolet light sources driven by ambient mechanical stimuli. *Nano Energy* **2020**, *74*, 104910. [CrossRef]
22. Wang, J.; Zi, Y.; Li, S.; Chen, X. High-voltage applications of the triboelectric nanogenerator—Opportunities brought by the unique energy technology. *MRS Energy Sustain.* **2010**, *6*, 17. [CrossRef]
23. Kim, J.; Cho, H.; Han, M.; Jung, Y.; Kwak, S.S.; Yoon, H.; Park, B.; Kim, H.; Kim, H.; Park, J.; et al. Ultrahigh Power Output from Triboelectric Nanogenerator Based on Serrated Electrode via Spark Discharge. *Adv. Energy Mater.* **2020**, *10*, 2002312. [CrossRef]
24. Shen, Q.; Xie, X.; Peng, M.; Sun, N.; Shao, H.; Zheng, H.; Wen, Z.; Sun, X. Self-Powered Vehicle Emission Testing System Based on Coupling of Triboelectric and Chemoresistive Effects. *Adv. Funct. Mater.* **2018**, *28*, 1703420. [CrossRef]
25. Chen, C.; Wen, Z.; Shi, J.; Jian, X.; Li, P.; Yeow, J.T.W.; Sun, X. Micro triboelectric ultrasonic device for acoustic energy transfer and signal communication. *Nat. Commun.* **2020**, *11*, 1–9. [CrossRef]
26. Huang, C.; Chen, G.; Nashalian, A.; Chen, J. Advances in self-powered chemical sensing via a triboelectric nanogenerator. *Nanoscale* **2020**, *13*, 2065–2081. [CrossRef] [PubMed]

27. Gao, Q.; Cheng, T.; Wang, Z.L. Triboelectric mechanical sensors-Progress and prospects. *Extreme Mech. Lett.* **2021**, *42*, 101100. [CrossRef]
28. Zhou, C.; Yang, Y.; Sun, N.; Wen, Z.; Cheng, P.; Xie, X.; Shao, H.; Shen, Q.; Chen, X.; Liu, Y.; et al. Flexible self-charging power units for portable electronics based on folded carbon paper. *Nano Res.* **2018**, *11*, 4313–4322. [CrossRef]
29. Sun, N.; Wen, Z.; Zhao, F.; Yang, Y.; Shao, H.; Zhou, C.; Shen, Q.; Feng, K.; Peng, M.; Li, Y.; et al. All flexible electrospun papers based self-charging power system. *Nano Energy* **2017**, *38*, 210–217. [CrossRef]
30. Li, X.; Jiang, C.; Zhao, F.; Shao, Y.; Ying, Y.; Ping, J. A self-charging device with bionic self-cleaning interface for energy harvesting. *Nano Energy* **2020**, *73*, 104738. [CrossRef]
31. He, W.; Fu, X.; Zhang, D.; Zhang, Q.; Zhuo, K.; Yuan, Z.; Ma, R. Recent progress of flexible/wearable self-charging power units based on triboelectric nanogenerators. *Nano Energy* **2021**, *84*, 105880. [CrossRef]
32. Ding, W.; Wang, A.; Wu, C.; Guo, H.; Wang, Z.L. Human-Machine Interfacing Enabled by Triboelectric Nanogenerators and Tribotronics. *Adv. Mater. Technol.* **2019**, *4*, 1800487. [CrossRef]
33. Luo, Y.; Wang, Z.; Wang, J.; Xiao, X.; Li, Q.; Ding, W.; Fu, H.Y. Triboelectric bending sensor based smart glove towards intuitive multi-dimensional human-machine interfaces. *Nano Energy* **2021**, *89*, 106330. [CrossRef]
34. Sun, J.-Y.; Zhao, X.; Illeperuma, W.R.K.; Chaudhuri, O.; Oh, K.H.; Mooney, D.; Vlassak, J.J.; Suo, Z. Highly stretchable and tough hydrogels. *Nature* **2012**, *489*, 133–136. [CrossRef] [PubMed]
35. Wen, Z.; Yang, Y.; Sun, N.; Li, G.; Liu, Y.; Chen, C.; Shi, J.; Xie, L.; Jiang, H.; Bao, D.; et al. A Wrinkled PEDOT:PSS Film Based Stretchable and Transparent Triboelectric Nanogenerator for Wearable Energy Harvesters and Active Motion Sensors. *Adv. Funct. Mater.* **2018**, *28*. [CrossRef]
36. Yang, Y.; Xie, L.; Wen, Z.; Chen, C.; Chen, X.; Wei, A.; Cheng, P.; Xie, X.; Sun, X. Coaxial Triboelectric Nanogenerator and Supercapacitor Fiber-Based Self-Charging Power Fabric. *ACS Appl. Mater. Interfaces* **2018**, *10*, 42356–42362. [CrossRef]

nanomaterials

MDPI

Article

A Triboelectric Nanogenerator Based on Sodium Chloride Powder for Self-Powered Humidity Sensor

Zhuyu Ding [1], Ming Zou [2], Peng Yao [2], Zhiyuan Zhu [2,3] and Li Fan [2,*]

[1] College of Engineering and Technology, Southwest University, Chongqing 400715, China; dingzy@swu.edu.cn
[2] School of Electronic and Information Engineering, Southwest University, Chongqing 400715, China; zouming6289@email.swu.edu.cn (M.Z.); qw578592005@email.swu.edu.cn (P.Y.); zyuanzhu@swu.edu.cn (Z.Z.)
[3] Ocean College, Faculty of Engineering, Zhejiang University, Hangzhou 316021, China
* Correspondence: fanli123@swu.edu.cn

Abstract: Recently, the research of distributed sensor networks based on triboelectric technology has attracted extensive attention. Here, we reported a new triboelectric nanogenerator based on sodium chloride powder (S-TENG) to obtain mechanical energy. The polytetrafluoroethylene (PTFE) film and sodium chloride powder layer serve as the triboelectric pair. After testing and calculation, the internal resistance of S-TENG is 30 MΩ, and the output power of S-TENG (size: 6 cm × 6 cm) can arrive at the maximum value (about 403.3 μW). Furthermore, the S-TENG can achieve the open circuit voltage (V_{oc}) of 198 V and short-circuit current (I_{sc}) of 6.66 μA, respectively. Moreover, owing to the moisture absorption of sodium chloride powder, the S-TENG device also has the function of the humidity sensor. This work proposed a functional TENG device, and it can promote the advancement of self-powered sensors based on the TENG devices.

Keywords: triboelectric nanogenerator (TENG); sodium chloride powder; self-powered sensor; low-cost

Citation: Ding, Z.; Zou, M.; Yao, P.; Zhu, Z.; Fan, L. A Triboelectric Nanogenerator Based on Sodium Chloride Powder for Self-Powered Humidity Sensor. *Nanomaterials* **2021**, *11*, 2657. https://doi.org/10.3390/nano11102657

Academic Editor: Giuseppe Cappelletti

Received: 16 September 2021
Accepted: 5 October 2021
Published: 9 October 2021

1. Introduction

Recently, owing to the progress needs of the Internet of things (IoT), various sensor technologies show numerous application prospects widely in the domain of the (IoT) [1–3]. As a significant part of the IoT, distributed sensor network has attracted the attention of academia and industry [4,5]. Often, distributed sensor networks consist of many sensors, but this poses new challenges to energy supply [6]. It is noteworthy that renewable energy generation is widely concerned, such as solar energy, ocean wave, temperature difference energy, wind and other green energy [7]. Compared with traditional fossil energy (oil, coal and natural gas), renewable energy has the characteristics of rich reserves, and is inexhaustible, and can reduce environmental pollution [8,9]. Therefore, harvesting technologies based on green renewable energy, such as electromagnetic power generation technology, piezoelectric power generation technology, photoelectric power generation technology and thermoelectric power generation technology, have exploded over the past few years. However, there are still many challenges in energy harvesting efficiency and use environment. In addition, the high preparation cost is also an important reason to hinder its application in distributed sensor networks [10]. In recent years, with the development of energy storage technology, distributed sensor network nodes usually provide power by electronics. However, the limited service life of the battery has brought a lot of replacement and maintenance work. Furthermore, this has an impact on the development of the Internet of things [11,12]. In addition, there will be environmental pollution problems. Therefore, the development of new power generation technology is necessary and meaningful.

In 2012, Professor Wang and his research group reported the triboelectric nanogenerator (TENG). The TENG device can convert low frequency and low amplitude mechanical

energy into electrical energy output [13–21]. Furthermore, TENG devices exhibit an extensive application prospect in the fields of self-powered sensors, ocean wave energy and high-voltage power sources [22–25]. In addition, it has a profound and significant influence on the sustainable development of energy and environmental protection. The triboelectrification phenomenon can occur between most materials, and friction movement is everywhere in life [26,27]. Thus, the TENG devices have a wide range of preparation materials, and this also promotes the rapid development of TENG devices based on different triboelectric material combinations [28–30]. Up to now, TENG can gain almost all mechanical energy and convert it into electrical energy, such as ocean wave, breeze energy, human motion and other mechanical vibration energy in the form of low frequency [31–35]. In addition, TENG devices can respond to changes in the environment through changes in electrical output signals. Therefore, it is meaningful to develop a TENG device with a sensing function.

Here, we propose a novel triboelectric nanogenerator based on sodium chloride powder (S-TENG) to obtain mechanical energy. Furthermore, the S-TENG serves as the self-powered humidity sensor. It is noteworthy that sodium chloride is a kind of food material, which is non-toxic, pollution-free and rich in reserves. In addition, sodium chloride is easily soluble in water, which also creates conditions for material recycling. The polytetrafluoroethylene (PTFE) film and sodium chloride powder layer form the triboelectric pair. The conductive aluminum tape serves as the conductive electrode, and the glue section is used to paste triboelectric materials. From the results, the output power of S-TENG (size: 6 cm $\times$ 6 cm) can arrive at the maximum value (about 403.3 μW), and the internal resistance of S-TENG is 30 MΩ. Furthermore, the S-TENG can achieve the V_{oc} of 198 V and I_{sc} of 6.66 μA, respectively. Moreover, the S-TENG device can monitor environmental humidity.

2. Materials and Methods

In this design, the PTFE film (thickness: 120 μm) and sodium chloride powder layer form the triboelectric pair, and the aluminum foil serves as the conductive electrode. Figure 1a illustrates the detailed preparation process of S-TENG. Firstly, cut the aluminum tape into two pieces to fabricate the electrodes. It is worth noting that the conductive aluminum tape consists of aluminum and glue, and the glue can act as the adhesive to paste PTFE film and sodium chloride powder. Then, coat one piece of aluminum foil with PTFE film to form the PTFE/aluminum layer. As for another piece of aluminum tape, the sodium chloride powder is pasted on the glue surface to constitute the aluminum/sodium chloride powder layer. Finally, two triboelectric sections form the S-TENG device. In this work, we used the electrometer (Keithley 6517) to measure the electronic output, such as open circuit voltage (V_{oc}), short-circuit current (I_{sc}) and transfer charge. Additionally, we used mechanical vibration to provide the external force. Furthermore, the scanning electron microscope (SEM) images of PTFE film and sodium chloride powder layer were provided in Figures S1 and S2 of the Supporting Information.

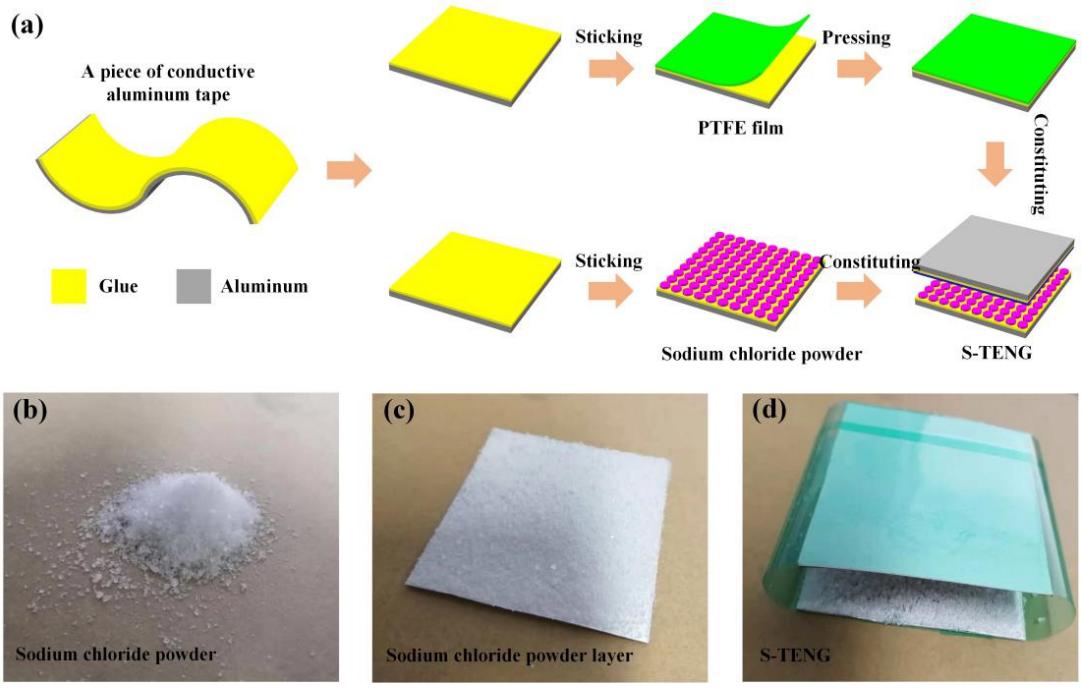

Figure 1. (**a**) The detailed preparation process of S-TENG using aluminum taper, PTFE film and sodium chloride powder. The photograph of (**b**) sodium chloride powder, (**c**) sodium chloride powder layer and (**d**) S-TENG.

3. Results and Discussion

The S-TENG can work under vertical motion conditions, and the operating mechanism of S-TENG is shown in Figure 2. Generally, the PTFE film can obtain electrons from other triboelectric materials during the triboelectric process. Thus, when PTFE film contact with the sodium chloride powder layer, the PTFE film surface will obtain electrons, and the sodium chloride powder layer will lose the same amount of electrons due to the contact electrification mechanism, as shown in Figure 2a. Then, when the surfaces of the PTFE film and sodium chloride powder layer separate (Figure 2b), the top electrode of the S-TENG device will generate a positive charge, and the electrode at the bottom of the S-TENG will produce the same amount of negative charge. In addition, this can lead to the generation of pulse current in the external circuit. When the maximum separation distance reaches a certain value, the charge transfer between the two electrodes reaches the saturation state. Furthermore, the circuit will not produce pulse current, as shown in Figure 2c. when the PTFE film surface is close to the sodium chloride powder layer surface, the negative charge at the top electrode will be transferred to the bottom electrode, and a reverse pulse current will be formed, as shown in Figure 2d.

Moreover, we connect loads with different resistance values to S-TENG and measure the output performance (output voltage and current) of S-TENG, as shown in Figure 3a. The mechanical vibrator can provide an external force to drive the S-TENG. In addition, the motion parameters (such as vibration frequency and maximum separation distance) are set as 6 Hz and 5 mm, respectively. The size of the S-TENG device is about 6 cm × 6 cm. As is shown in Figure 3b, when the resistance of the load grows from 1 MΩ to 1 GM, the V_{oc} of S-TENG will rise whereas the I_{sc} of S-TENG will drop, which also indicates that TENG devices usually have high V_{oc} and low I_{sc}. Furthermore, we calculated the output power (P) of S-TENG through the relationship $P = UI$. In addition, Figure 3c describes the calculation results and relations. From the results, the S-TENG device can realize the maximum output power of 403.3 μW. Meanwhile, the internal resistance of S-TENG is 30 MΩ. Furthermore, the S-TENG can achieve the V_{oc} of 198 V and I_{sc} of 6.66 μA, respectively, as shown in Figure 3d,e. Figure 3f illustrates that the charge transfer in the external circuit can reach 25.5 nC.

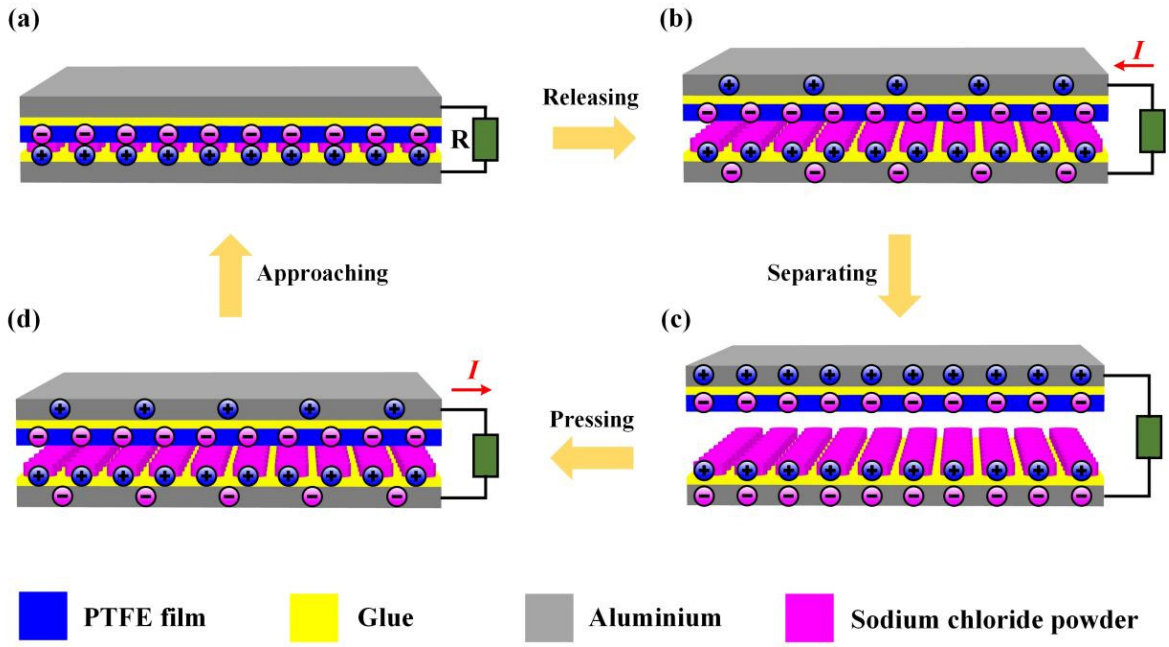

Figure 2. (**a**–**d**)The operating principle of S-TENG.

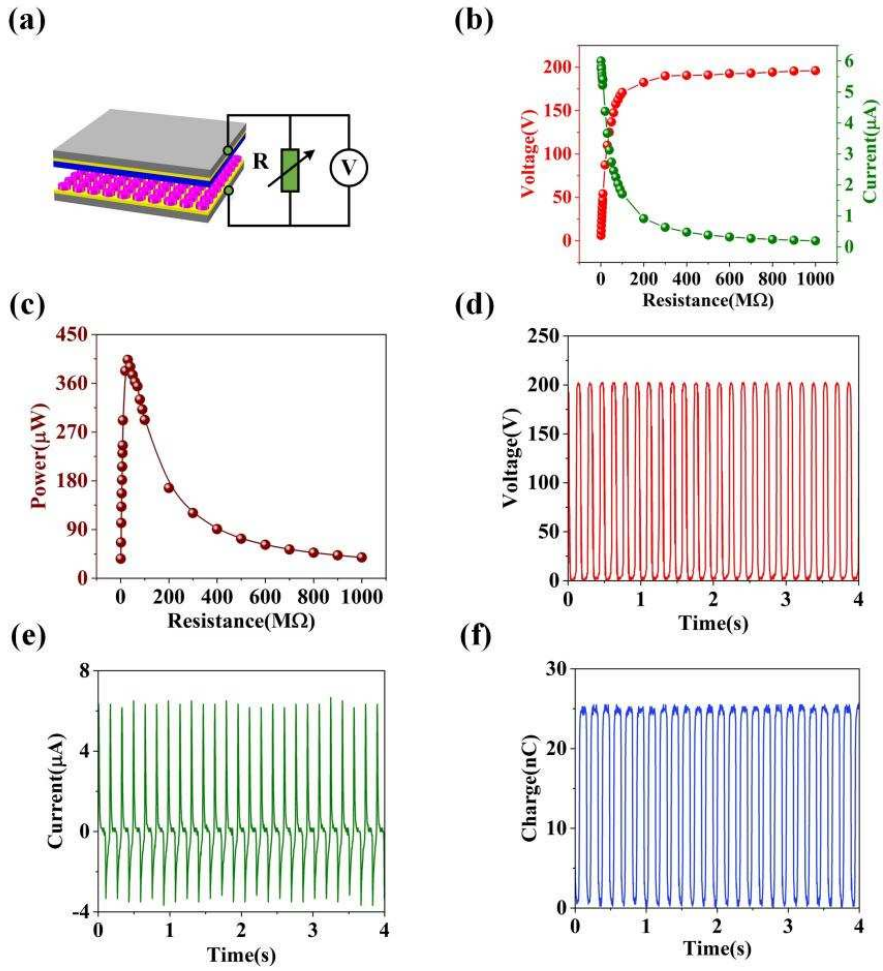

Figure 3. (**a**) The schematic diagram of electrical performance testing system about the S-TENG. (**b**,**c**) The relation between S-TENG output and resistance of loads. (**d**) I_{SC}, (**e**) V_{OC} and (**f**) charge transfer in the external circuit of S-TENG.

It is worthy to point out that the parameters of external excitation are the factors influencing the output characteristics of S-TENG. Therefore, we explored the influence of motion frequency and maximum separation distance on the electrical output of S-TENG. As shown in Figure 4a, when the working frequency rises from 2 Hz to 6 Hz, the I_{sc} of S-TENG will grow from 3.33 μA to 6.5 μA. The reason for the increase of S-TENG is that the higher motion frequency is conducive to the rapid transfer of charges. As illustrated in Figure 4b,c, when the working frequency rises from 2 Hz to 6 Hz, the V_{oc} of S-TENG will remain constant at about 198 V, and the transferred charge of S-TENG will also be unchanged at about 25.5 nC, which also indicates that the superiority of TENG devices in low-frequency motion energy harvesting. Moreover, the maximum separation distance between the PTFE film surface and sodium chloride powder layer surface can also influence the S-TENG electrical output. With the increase of the maximum separation distance (from 1 mm to 5 mm) shown in Figure 4c–e, the electrical output of S-TENG, such as I_{sc}, V_{oc} and transfer charge, will increase.

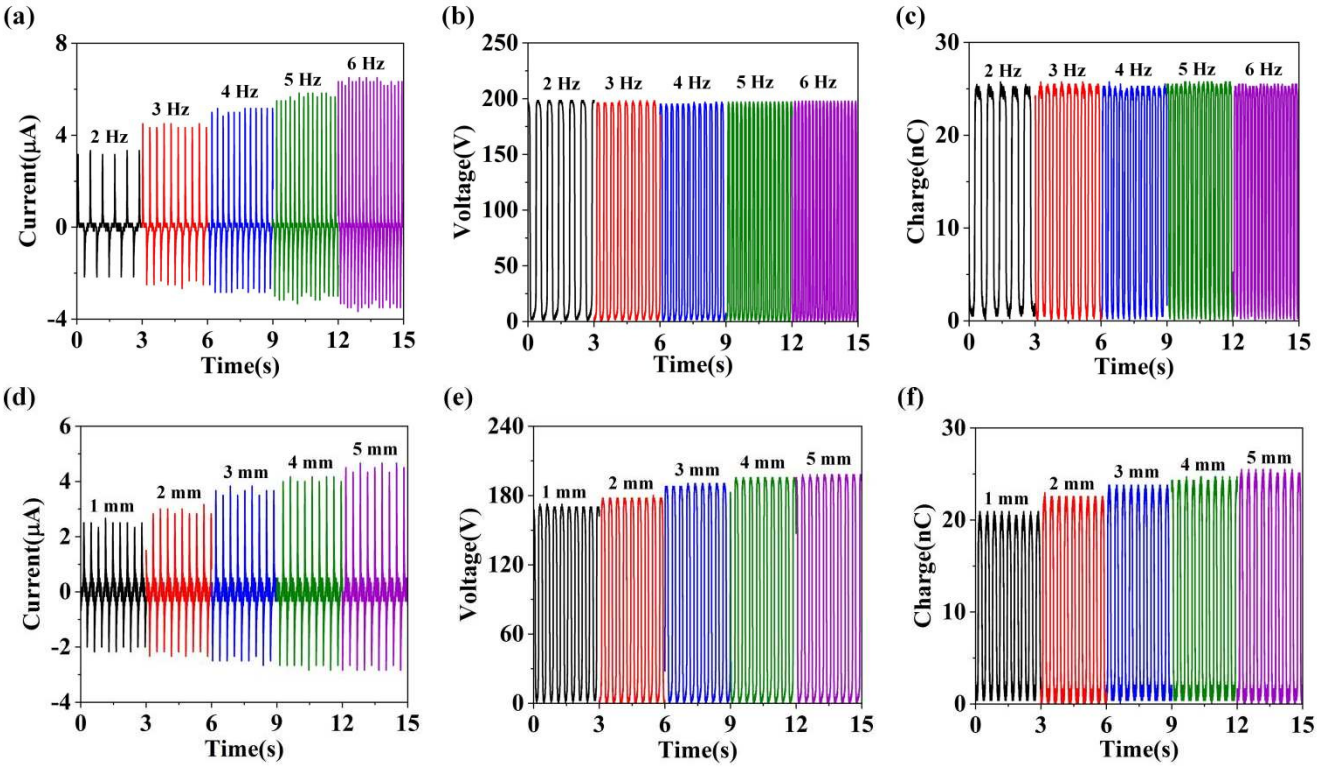

Figure 4. The (**a**) I_{sc}, (**b**) V_{oc} and (**c**) transfer charge of S-TENG under different operating frequencies. The (**d**) I_{sc}, (**e**) V_{oc} and (**f**) transfer charge of S-TENG under different maximum separation distance.

Moreover, considering the continuous work of S-TENG, we explored the electrical output of S-TENG under continuous operating conditions. Based on the results in Figure 5a, the S-TENG has good stability. Furthermore, we examine the charging effect of S-TENG with a power management circuit, as shown in Figure 5b. Here, we developed the relationship of S-TENG charging capacitors under different frequencies. Obviously, the higher the externally provided vibration frequency, the faster the rate of storing electric energy, as shown in Figure 5c. In addition, we also researched the influence of S-TENG charging different capacitors, as illustrated in Figure 5d. According to the experimental results, the larger the capacitor, the faster the charging speed.

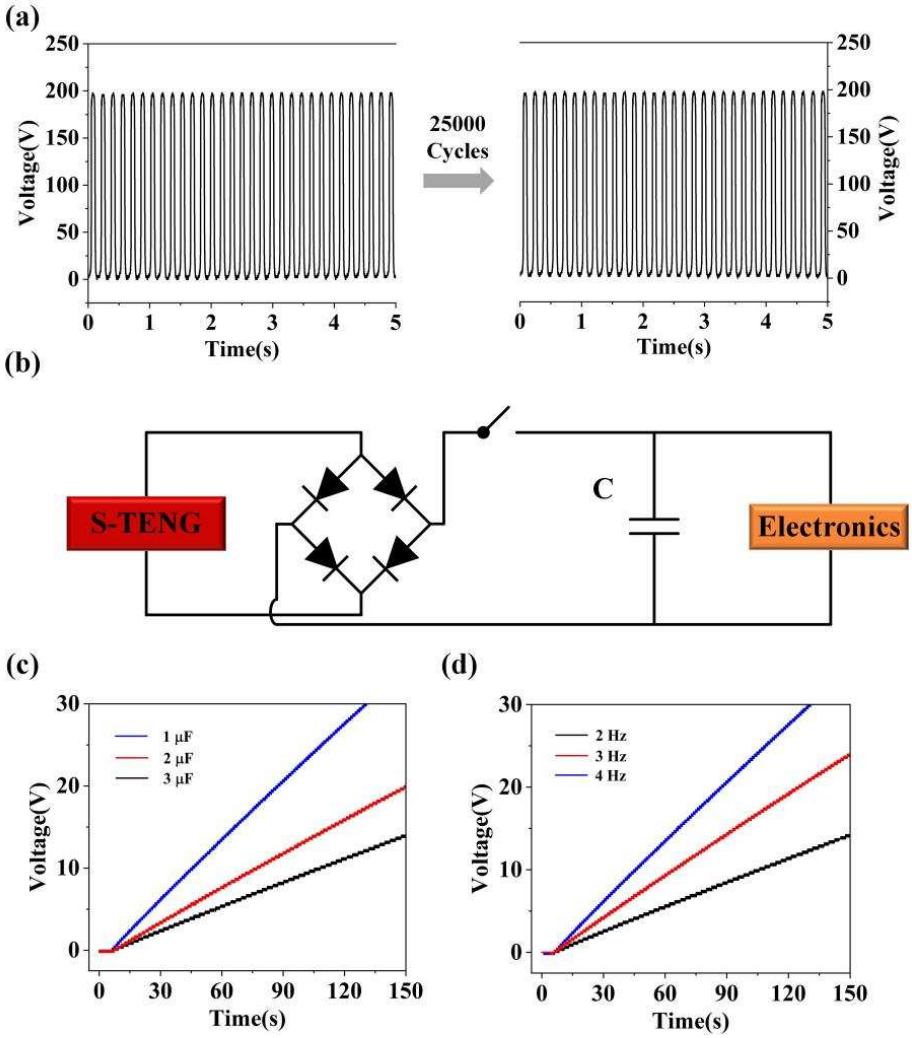

Figure 5. (**a**) The reliability test of S-TENG. (**b**) The schematic diagram of power management circuit based on the S-TENG. (**c**) The charging curve of S-TENG for different capacitors (from 1 μF to 3 μF) under the working frequency of 4 Hz. (**d**) The charging curve of S-TENG for 1 μF capacitor under different working frequencies (from 2 Hz to 4 Hz).

Often, TENG devices can convert moving mechanical energy into electrical energy during the contact and separation movement of triboelectric materials. In addition, the generated electrical signal is closely related to the influence of the working environment. Environmental factors will affect the electrical output signal produced by the TENG device, for example, relative humidity. It is noteworthy that sodium chloride powder has strong moisture absorption. Furthermore, this characteristic can make the S-TENG the self-powered humidity sensor by the electrical output signal change of the S-TENG device, as shown in Figure 6a,b. Specifically, the relative humidity will have a significant influence on the charge transfer of the TENG device. In this design, the sodium chloride powder plays the role of triboelectric material, and meanwhile, it is sensitive to relative humidity. Specifically, we measured the V_{oc}, I_{sc} and transferred charge of S-TENG under different relative humidity, as present in Figure 6c–e. According to the results, when the relative humidity rises, the electrical output (V_{oc}, I_{sc} and transferred charge) of S-TENG can grow, which indicates the S-TENG can monitor humidity changes.

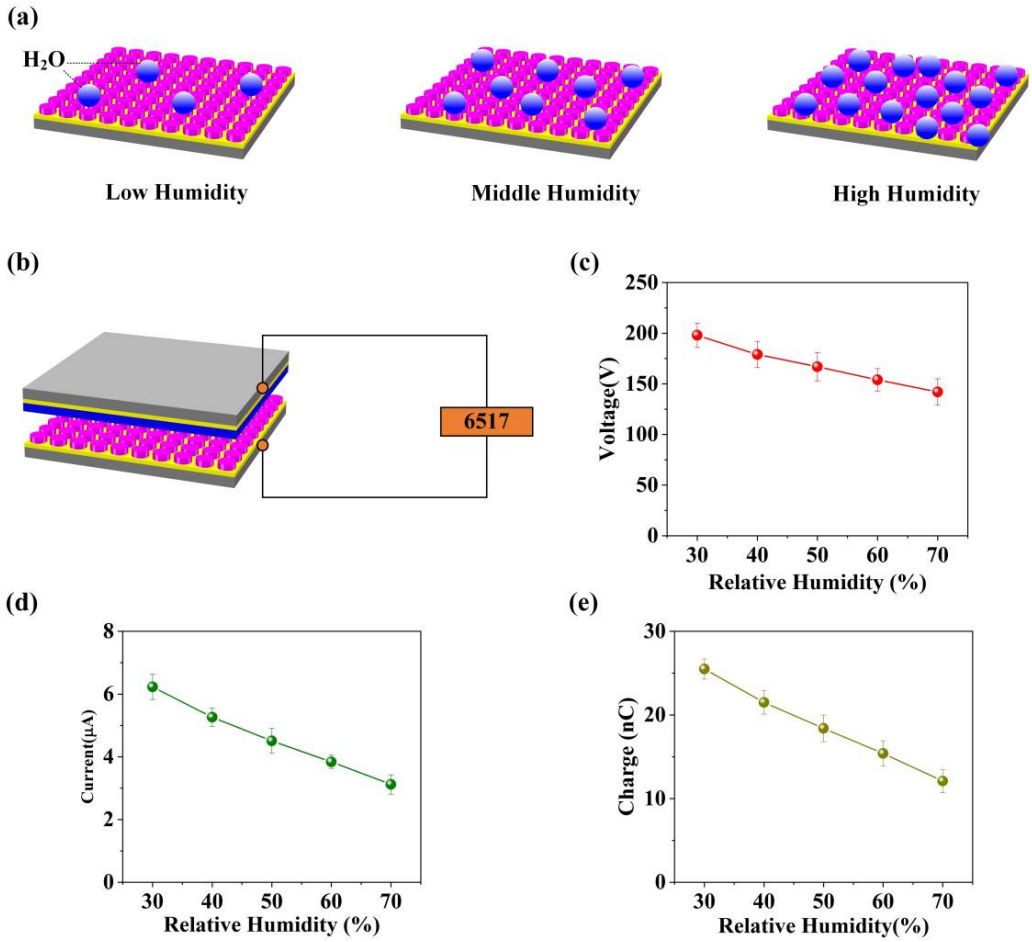

Figure 6. (**a**) The schematic illustration of the hygroscopicity for sodium chloride powder. (**b**) The relative humidity test system based on the S-TENG. (**c**–**e**) The electrical output of the S-TENG in different relative humidity conditions.

4. Conclusions

In conclusion, we propose a novel triboelectric nanogenerator based on sodium chloride powder (S-TENG) to obtain mechanical energy. In addition, the S-TENG serves as the self-powered humidity sensor. It is noteworthy that sodium chloride is a kind of food material, which is non-toxic, pollution-free and rich in reserves. The PTFE film and sodium chloride powder layer form the triboelectric pair. The conductive aluminum tape is used as the conductive electrode, and the glue section is used to paste triboelectric materials. From the results, the output power of S-TENG (size: 6 cm × 6 cm) can arrive at the maximum value (about 403.3 μW). Furthermore, the S-TENG can achieve the V_{oc} of 198 V and I_{sc} of 6.66 μA, respectively. Moreover, the S-TENG device can monitor environmental humidity.

Supplementary Materials: The following are available online at https://www.mdpi.com/article/10.3390/nano11102657/s1, Figure S1: The SEM images of PTFE before and after 24 k impact cycles. Figure S2: The SEM image of the NaCl powder layer surface.

Author Contributions: Writing—original draft preparation and editing, M.Z. and P.Y.; writing—review and project administration, Z.D., Z.Z. and L.F. All authors have read and agreed to the published version of the manuscript.

Funding: This work was supported by the Fundamental Research Funds for the Central Universities under Grants XDJK2019C028, SWU120017, 2020jd001. This work was supported by Zhejiang Provincial Natural Science Foundation of China (Grant No. LY20F040004) and National Natural Science Foundation of China (Grant No. 62074132).

Institutional Review Board Statement: This study does not involve human or animal experiments.

Informed Consent Statement: All the authors know and contribute to this article.

Data Availability Statement: Some or all data, models, or code generated or used during the study are proprietary or confidential in nature and may only be provided with restrictions.

Conflicts of Interest: The authors declare that they have no known competing financial interests or personal relationships that could have appeared to influence the work reported in this paper.

References

1. Zhao, X.J.; Zhu, G.; Fan, Y.J.; Li, H.Y.; Wang, Z.L. Triboelectric charging at the nanostructured solid/liquid interface for area-scalable wave energy conversion and its use in corrosion protection. *ACS Nano* **2015**, *9*, 7671–7677. [CrossRef]
2. Pu, X.; Liu, M.; Li, L.; Zhang, C.; Pang, Y.; Jiang, C.; Shao, L.; Hu, W.; Wang, Z.L. Efficient charging of Li-ion batteries with pulsed output current of triboelectric nanogenerators. *Adv. Sci.* **2016**, *3*, 1500255. [CrossRef]
3. Shi, B.; Zheng, Q.; Jiang, W.; Yan, L.; Wang, X.; Liu, H.; Yao, Y.; Li, Z.; Wang, Z.L. A packaged self-powered system with universal connectors based on hybridized nanogenerators. *Adv. Mater.* **2016**, *28*, 846–852. [CrossRef] [PubMed]
4. Han, X.; Du, W.; Yu, R.; Pan, C.; Wang, Z.L. Piezo-phototronic enhanced UV sensing based on a nanowire photodetector array. *Adv. Mater.* **2015**, *27*, 7963–7969. [CrossRef] [PubMed]
5. Wang, Z.L. Triboelectric nanogenerator (TENG)—Sparking an energy and sensor revolution. *Adv. Energy Mater.* **2020**, *10*, 2000137. [CrossRef]
6. Lei, R.; Shi, Y.; Ding, Y.; Nie, J.; Li, S.; Wang, F.; Zhai, H.; Chen, X.; Wang, Z.L. Sustainable high-voltage source based on triboelectric nanogenerator with a charge accumulation strategy. *Energy Environ. Sci.* **2020**, *13*, 2178–2190. [CrossRef]
7. Chen, C.; Guo, H.; Chen, L.; Wang, Y.-C.; Pu, X.; Yu, W.; Wang, F.; Du, Z.; Wang, Z.L. Direct current fabric triboelectric nanogenerator for biomotion energy harvesting. *ACS Nano* **2020**, *14*, 4585–4594. [CrossRef] [PubMed]
8. Luo, X.; Zhu, L.; Wang, Y.C.; Li, J.; Nie, J.; Wang, Z.L. A Flexible Multifunctional Triboelectric Nanogenerator Based on MXene/PVA Hydrogel. *Adv. Funct. Mater.* **2021**, *31*, 2104928. [CrossRef]
9. Zhang, P.; Guo, W.; Guo, Z.H.; Ma, Y.; Gao, L.; Cong, Z.; Zhao, X.J.; Qiao, L.; Pu, X.; Wang, Z.L. Dynamically Crosslinked Dry Ion-Conducting Elastomers for Soft Iontronics. *Adv. Mater.* **2021**, *33*, 2101396. [CrossRef]
10. Lin, S.; Chen, X.; Wang, Z.L. Contact Electrification at the Liquid–Solid Interface. *Chem. Rev.* **2021**. [CrossRef]
11. Aslam, A.; Mehmood, U.; Arshad, M.H.; Ishfaq, A.; Zaheer, J.; Khan, A.U.H.; Sufyan, M. Dye-sensitized solar cells (DSSCs) as a potential photovoltaic technology for the self-powered internet of things (IoTs) applications. *Sol. Energy* **2020**, *207*, 874–892. [CrossRef]
12. Su, Y.-S.; Ni, C.-F.; Li, W.-C.; Lee, I.-H.; Lin, C.-P. Applying deep learning algorithms to enhance simulations of large-scale groundwater flow in IoTs. *Appl. Soft Comput.* **2020**, *92*, 106298. [CrossRef]
13. Wang, S.; Lin, L.; Wang, Z.L. Nanoscale triboelectric-effect-enabled energy conversion for sustainably powering portable electronics. *Nano Lett.* **2012**, *12*, 6339–6346. [CrossRef] [PubMed]
14. Zhong, J.; Zhong, Q.; Fan, F.; Zhang, Y.; Wang, S.; Hu, B.; Wang, Z.L.; Zhou, J. Finger typing driven triboelectric nanogenerator and its use for instantaneously lighting up LEDs. *Nano Energy* **2013**, *2*, 491–497. [CrossRef]
15. Yang, X.; Zhu, G.; Wang, S.; Zhang, R.; Lin, L.; Wu, W.; Wang, Z.L. A self-powered electrochromic device driven by a nanogenerator. *Energy Environ. Sci.* **2012**, *5*, 9462–9466. [CrossRef]
16. Cheng, G.; Lin, Z.H.; Lin, L.; Du, Z.-L.; Wang, Z.L. Pulsed nanogenerator with huge instantaneous output power density. *ACS Nano* **2013**, *7*, 7383–7391. [CrossRef]
17. Yang, Y.; Zhang, H.; Chen, J.; Jing, Q.; Zhou, Y.S.; Wen, X.; Wang, Z.L. Single-electrode-based sliding triboelectric nanogenerator for self-powered displacement vector sensor system. *ACS Nano* **2013**, *7*, 7342–7351. [CrossRef] [PubMed]
18. Yang, Y.; Zhang, H.; Lin, Z.-H.; Zhou, Y.; Jing, Q.; Su, Y.; Yang, J.; Chen, J.; Hu, C.; Wang, Z.L. Human skin based triboelectric nanogenerators for harvesting biomechanical energy and as self-powered active tactile sensor system. *ACS Nano* **2013**, *7*, 9213–9222. [CrossRef]
19. Niu, S.; Liu, Y.; Wang, S.; Lin, L.; Zhou, Y.S.; Hu, Y.; Wang, Z.L. Theory of sliding-mode triboelectric nanogenerators. *Adv. Mater.* **2013**, *25*, 6184–6193. [CrossRef]
20. Zhang, B.; Wu, Z.; Lin, Z.; Guo, H.; Chun, F.; Yang, W.; Wang, Z.L. All-in-one 3D acceleration sensor based on coded liquid–metal triboelectric nanogenerator for vehicle restraint system. *Mater. Today* **2021**, *43*, 37–44. [CrossRef]
21. Zhao, Z.; Dai, Y.; Liu, D.; Zhou, L.; Li, S.; Wang, Z.L.; Wang, J. Rationally patterned electrode of direct-current triboelectric nanogenerators for ultrahigh effective surface charge density. *Nat. Commun.* **2020**, *11*, 6186. [CrossRef]
22. Gao, Q.; Cheng, T.; Wang, Z.L. Triboelectric mechanical sensors—Progress and prospects. *Extrem. Mech. Lett.* **2020**, *42*, 101100. [CrossRef]
23. Zhang, Y.; Huo, Z.; Wang, X.; Han, X.; Wu, W.; Wan, B.; Wang, H.; Zhai, J.; Tao, J.; Pan, C.; et al. High precision epidermal radio frequency antenna via nanofiber network for wireless stretchable multifunction electronics. *Nat. Commun.* **2020**, *11*, 5629. [CrossRef]

24. Xia, K.; Fu, J.; Xu, Z. Multiple-frequency high-output triboelectric nanogenerator based on a water balloon for all-weather water wave energy harvesting. *Adv. Energy Mater.* **2020**, *10*, 2000426. [CrossRef]
25. Xia, K.; Wu, D.; Fu, J.; Hoque, N.A.; Ye, Y.; Xu, Z. A high-output triboelectric nanogenerator based on nickel–copper bimetallic hydroxide nanowrinkles for self-powered wearable electronics. *J. Mater. Chem. A* **2020**, *8*, 25995–26003. [CrossRef]
26. Qu, X.; Ma, X.; Shi, B.; Li, H.; Zheng, L.; Wang, C.; Liu, Z.; Fan, Y.; Chen, X.; Li, Z.; et al. Refreshable braille display system based on triboelectric nanogenerator and dielectric elastomer. *Adv. Funct. Mater.* **2021**, *31*, 2006612. [CrossRef]
27. Guo, H.; Chen, J.; Wang, L.; Wang, A.C.; Li, Y.; An, C.; He, J.-H.; Hu, C.; Hsiao, V.K.S.; Wang, Z.L. A highly efficient triboelectric negative air ion generator. *Nat. Sustain.* **2021**, *4*, 147–153. [CrossRef]
28. Luo, J.; Wang, Z.L. Recent progress of triboelectric nanogenerators: From fundamental theory to practical applications. *EcoMat* **2020**, *2*, e12059. [CrossRef]
29. Ning, C.; Dong, K.; Cheng, R.; Yi, J.; Ye, C.; Peng, X.; Sheng, F.; Jiang, Y.; Wang, Z.L. Flexible and stretchable fiber-shaped triboelectric nanogenerators for biomechanical monitoring and human-interactive sensing. *Adv. Funct. Mater.* **2021**, *31*, 2006679. [CrossRef]
30. Jiang, Y.; Dong, K.; Li, X.; An, J.; Wu, D.; Peng, X.; Yi, J.; Ning, C.; Cheng, R.; Yu, P.; et al. Stretchable, Washable, and Ultrathin Triboelectric Nanogenerators as Skin-Like Highly Sensitive Self-Powered Haptic Sensors. *Adv. Funct. Mater.* **2021**, *31*, 2005584. [CrossRef]
31. Liang, X.; Jiang, T.; Feng, Y.; Lu, P.; An, J.; Wang, Z.L. Triboelectric nanogenerator network integrated with charge excitation circuit for effective water wave energy harvesting. *Adv. Energy Mater.* **2020**, *10*, 2002123. [CrossRef]
32. Xu, L.; Xu, L.; Luo, J.; Yan, Y.; Jia, B.-E.; Yang, X.; Gao, Y.; Wang, Z.L. Hybrid all-in-one power source based on high-performance spherical triboelectric nanogenerators for harvesting environmental energy. *Adv. Energy Mater.* **2020**, *10*, 2001669. [CrossRef]
33. Huang, J.; Yang, X.; Yu, J.; Han, J.; Jia, C.; Ding, M.; Sun, J.; Cao, X.; Sun, Q.; Wang, Z.L. A universal and arbitrary tactile interactive system based on self-powered optical communication. *Nano Energy* **2020**, *69*, 104419. [CrossRef]
34. Zhao, P.; Soin, N.; Prashanthi, K.; Chen, J.; Dong, S.; Zhou, E.; Zhu, Z.; Narasimulu, A.A.; Montemagno, C.D.; Yu, L.; et al. Emulsion electrospinning of polytetrafluoroethylene (PTFE) nanofibrous membranes for high-performance triboelectric nanogenerators. *ACS Appl. Mater. Interfaces* **2018**, *10*, 5880–5891. [CrossRef] [PubMed]
35. Taghavi, M.; Beccai, L. A contact-key triboelectric nanogenerator: Theoretical and experimental study on motion speed influence. *Nano Energy* **2015**, *18*, 283–292. [CrossRef]

nanomaterials

MDPI

Article

An Ionically Conductive, Self-Powered and Stable Organogel for Pressure Sensing

Li Wang [1,2,*], Zhengduo Wang [1], Yingtao Li [1], Yu Luo [1], Bingheng Lu [1,2], Yiyang Gao [3], Wei Yu [3], Guoxin Gao [3] and Shujiang Ding [3]

[1] Micro and Nano Technology Research Center, State Key Laboratory for Manufacturing Systems Engineering, Xi'an Jiaotong University, Xi'an 710049, China; wangzhengduo@stu.xjtu.edu.cn (Z.W.); liyingtao_lubu@163.com (Y.L.); yuluo825@mail.xjtu.edu.cn (Y.L.); bhlu@mail.xjtu.edu.cn (B.L.)
[2] National Innovation Institute of Additive Manufacturing, Xi'an 710000, China
[3] Xi'an Key Laboratory of Sustainable Energy Materials Chemistry, School of Chemistry, Xi'an Jiaotong University, Xi'an 710049, China; yilimengniu0616@stu.xjtu.edu.cn (Y.G.); yuwei2019@mail.xjtu.edu.cn (W.Y.); gaoguoxin@mail.xjtu.edu.cn (G.G.); dingsj@mail.xjtu.edu.cn (S.D.)
* Correspondence: wanglime@mail.xjtu.edu.cn; Tel.: +86-13991386876

Abstract: Gel-based ionic conductors are promising candidates for flexible electronics, serving as stretchable sensors or electrodes. However, most of them suffer from a short operating life, low conductivity and rely on an external power supply, limiting their practical application. Herein, we report a stable organogel ionic conductor with high conductivity and self-powering ability. Briefly, lithium trifluoromethanesulfonate, as a conductive salt, provides high conductivity and the poly(1,1-difluoroethylene) layers, as a self-powering system, supply stable energy output under the influence of pressure. Moreover, the proposed conductors withstand long-term and multi-cycle durability tests. The prepared auxiliary training device can withstand the impact of a basketball and detect the impact force, showing potential in passive sensing during practical applications.

Keywords: organogel; self-powered; stable; pressure sensing

Citation: Wang, L.; Wang, Z.; Li, Y.; Luo, Y.; Lu, B.; Gao, Y.; Yu, W.; Gao, G.; Ding, S. An Ionically Conductive, Self-Powered and Stable Organogel for Pressure Sensing. *Nanomaterials* **2022**, *12*, 714. https://doi.org/10.3390/nano12040714

Academic Editors: Zhen Wen and Miguel Gama

Received: 18 January 2022
Accepted: 18 February 2022
Published: 21 February 2022

1. Introduction

The properties of being able to closely fit the complex surface of an object, with strong anti-bending abilities and high electrical conductivity are important for flexible electronics [1–4], such as soft sensors [5–7], flexible displays [8,9], and wearable computing [10–12] and energy storage devices [13–15]. To achieve these characteristics, researchers have developed various materials and structures, such as nanocomposites [16,17], bionic structures [18–20], and sensor arrays [21,22]. However, the inherent high modulus and brittleness lead to an unacceptable mechanical mismatch [23,24] and the unsatisfying electrical conductivity [25,26] results in inevitable signal loss during transmission. Liu et al. have integrated perovskite solar cells (PSCs) into flexible strain sensors to realize continuous data recording without external power [27]. Although the high efficiency of PSC (8.41%) resulted in excellent stability and durability, the mismatch between tissues and PET substrate hinders the wearable applications of these sensors.

With Young's modulus values close to tissues, gels are the most promising candidates for flexible devices [2,28,29]. However, the conductivity of gels is not enough for their direct application in electronic devices [30]. Hence, the most effective method to enhance the conductivity is to add conductive fillers [31–34]. For instance, Yunsik Ohm et al. incorporated silver flakes (5 vol%) into the hydrogels and performed a partial dehydration process to remove a moderate amount of water and form the percolation channels [1]. Although silver-containing hydrogels possess high conductivity (350 $S \cdot cm^{-1}$), the silver flakes reduce stretchability, increase the Young's modulus and generate massive Joule heat under high currents, leading to catastrophic water loss and accelerating the gels' invalidation.

Researchers have explored numerous methods to overcome water loss, such as adding anti-freeze materials (e.g., polyelectrolytes, polyhydric alcohols) [35,36] or encapsulation [37,38]. Anti-freeze materials reduce the number of hydrogen bonds between water molecules and block the gel from freezing; however, water evaporation remains a challenge [39,40]. On the other hand, the packaging methods lock the water inside the container and reduce water evaporation; however, these methods are not suitable for freezing and boiling [6,41]. Therefore, organic ionic gels have been developed, which essentially circumvent the problems of hydrogels as organic solvents [42]. However, the high viscosity of organic gels hinders ionic movement and, in turn, reduces the conductivity [43]. Therefore, it is necessary to explore different approaches to enhance the conductivity of organic ionic gels.

Herein, we report high-conductivity organogel ionic conductors (OICs) and their piezoelectrically-enhanced analogs, using a one-step synthesis method, where propylene carbonate (PC), acryloyl morpholine (ACMO) and lithium trifluoromethanesulfonate (LiOTf) are employed as a solvent, monomer and ionically conductive salt, respectively. The as-prepared OICs exhibit high ionic conductivity (9.1×10^{-4} S·cm^{-1}) and a wide range of temperature tolerances (−70 to 100 °C). Moreover, OICs are further coated with poly(1,1-difluoroethylene) (PVDF) as the power supply. Owing to the penetration effect, the number of β-type crystals generated by PVDF on the OICs was found to be 70% higher than that on a glass substrate (40%). Furthermore, the self-powered OICs maintained high accuracy even after one month of storage, demonstrating broad application prospects as self-powered flexible conductors and sensors.

2. Materials and Methods

2.1. Materials

Propylene carbonate (PC), 4-acryloylmorpholine (ACMO, monomer), poly-ethylene-glycol diacrylate (PEGDA Mw~1000), 1-hydroxycyclohexyl phenyl ketone (184), lithium trifluoromethanesulfonate (LiOTf), N,N-dimethylformamide (DMF), Sudan III and poly(1,1-difluoroethylene) (PVDF) were purchased from Aladdin, Co. Ltd., Shanghai, China, and the silk fibroin (SF) was synthesized by our research team.

2.2. Preparation of OICs and Self-Powered OICs

The preparation process is summarized below [42]: PEGDA and 184 were employed as a cross-linker and photo-initiator, respectively. First, LiOTf, 184, ACMO (33 wt.%) and PEGDA were evenly dissolved in PC (64 wt.%) to create a transparent precursor of OICs under mechanical stirring for at least 15 min or 5 min of ultrasonication. The concentration of LiOTf was adjusted to 2.5 mol·L^{-1}, and PEGDA was fixed at 0.1 wt.%. Subsequently, the precursors were cured in a glass-wrapped polyethylene glycol terephthalate (PET) mold under irradiation of a 365 nm ultraviolet lamp for 5 min to obtain OICs. To obtain self-powered OICs, 1 g of PVDF was dissolved in 8 mL of DMF at 90 °C for 8 h to obtain a uniform solution. Subsequently, the as-prepared PVDF solution was scraped on OICs, followed by heating at 90 °C for 30 min.

2.3. Temperature Tolerance Characterization

OICs were prepared in a rectangular parallelepiped with the dimensions of 9 cm × 8 cm × 2 mm. Thermogravimetric analysis (TGA) was performed on TGA-DSC1 (METTLER TOLEDO Co., shanghai, China) in the temperature range of 25 to 150 °C. The heating rate was 10 °C·min^{-1} and the analysis was carried out under N_2 atmosphere. The dynamic thermomechanical analysis (DMA) was performed using Netzsch DMA242E (NETZSCH Co., Wittelsbacherstrasse, Germany) in the temperature range of −150 to −25 °C at a heating rate of 3 °C·min^{-1}.

2.4. Impedance Analysis

OICs were clamped between two copper sheets with the same diameter and thickness and connected to the system by a wire. A Princeton Applied Research Versa STAT3 (AMETEK Co. Ltd, Shanghai, China) was used to analyze the impedance in the frequency range of 1 Hz to 100 kHz, with a temperature range of 0 to 75 °C and a bias voltage of 5 mV.

2.5. Mechanical Characterization

OICs were prepared in the form of a rectangular parallelepiped with the dimensions of 9 cm × 8 cm × 2 mm. The mechanical testing was performed on Tytron 250 (MTS Co., Eden Prairie MN, USA) at a rate of 100 mm·min^{-1}. The initial distance was 20 mm.

2.6. Characterization of Self-Powered OICs

All OICs were stripped-off from the PET substrate before the verification test. Fourier transform infrared (FTIR) spectroscopy and X-ray diffraction (XRD) analysis were performed to evaluate the crystal structure of PVDF. The FTIR was performed using a Bruker VERTEX70 (city, the abbreviation of state, country Bruker Co., Billerica, MA, USA). The attenuated total reflection (ATR) mode was used, and the FTIR patterns were recorded in the wavelength range of 700 to 1500 cm^{-1}. The XRD analysis was performed using Bruker D8 ADVANCE (city, the abbreviation of state, country Bruker Co., Billerica, MA, USA), and the XRD patterns were recorded in the 2θ range of 10 to 30°, and the wavelength was 0.154 nm. The piezoelectric constant d_{33} was measured using a quasi-static method on a d_{33} measurement instrument (ZJ-3AN) (Institute of Acoustics, Chinese Academy of Sciences, Beijing, China).

3. Results

We designed the OICs according to the migration of ions in electrolytes, where the high migration speed and ionic concentration were expected to render high conductivity. As shown in Figure 1, the ions possess a small relative molecular mass (Mr) and high solubility in PC, which can flow inside the OICs due to the rapid migration of the center of gravity [44]. However, the ions in the figure on the left only move at a slow speed, or even get stuck in the network, unable to move and restricting the movement of other ions. In addition, unlike the electrolyte solution, the staggered polymeric network limits the ionic movement in the gel, implying that the network structure and ionic size influence the ionic movement [45]. The network of the gel on the left is more complex and denser, and, although it may have slightly better mechanical properties, it becomes an obstacle to ion motion because the complex network reduces the passability of the road and reduces the flux of ions. Hence, we aimed to simplify the network and use small-sized molecules to seamlessly pass through the messy network (Figure 1).

OICs demonstrate remarkable ionic conductivity and decent mechanical properties. As presented in Figure 2a, the electrical characterization revealed a significant ionic conductivity with 2.5 mol·L^{-1} of LiOTf. With the frequency growth, the impedance amplitude linearly decreased until 1 kHz, obtaining an impedance value of 19.6 Ω and reached the minimum at 100 kHz (15.56 Ω). Meanwhile, the negative phase angle also exhibited a similar downtrend in the frequency range of 100 Hz to 100 kHz and sharply attenuated from 72° to a near-zero degree at 100 kHz. At this time, the influence of the electrical double layer was weak enough, and the impedance amplitude became close to a real resistance value. The conductivity of OICs was calculated to be 9.1 × 10^{-4} S·cm^{-1}, exceeding the 7.9 × 10^{-4} S cm^{-1} of other similar types of organic ionic gels (Figure 2b). Surprisingly, the conductivity continuously climbed without any declining trend, contrary to that observed by other researchers, until the maximum solubility of LiOTf in PC, which indicates that the proposed composition significantly improved the saturation mobility of OICs. In addition, the stretch and recovery curves in Figure 2c show perfect overlap and minimal hysteresis until the strain reached 300%, indicating the superb tensile resilience of OICs. Consequently, unless otherwise specified, the LiOTf concentration in the OICs was fixed at 2.5 mol·L^{-1}.

Again, the salt with a relatively small size was shown to be more conducive to improving the conductivity of gels.

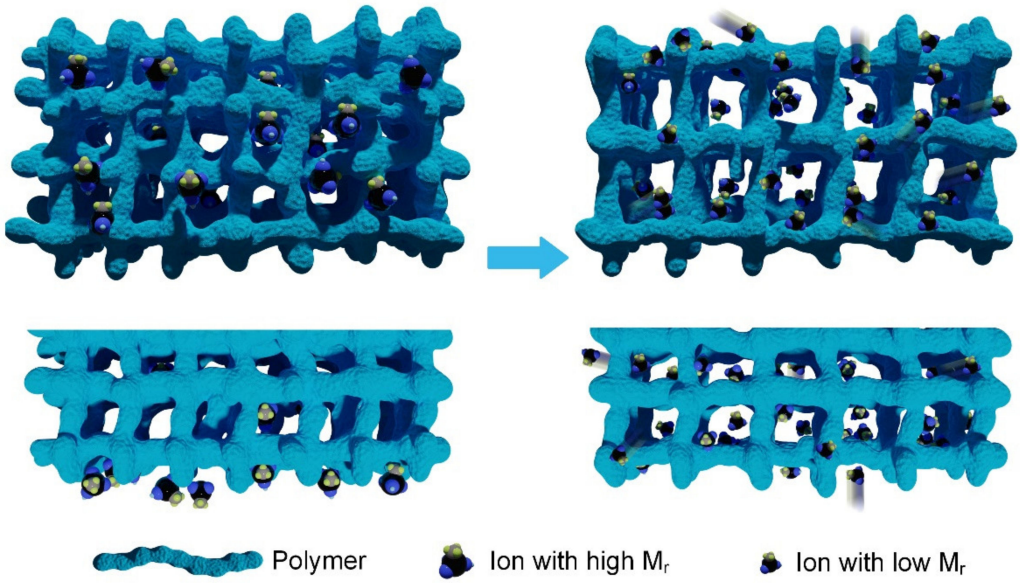

Figure 1. Schematic illustration of the proposed OICs.

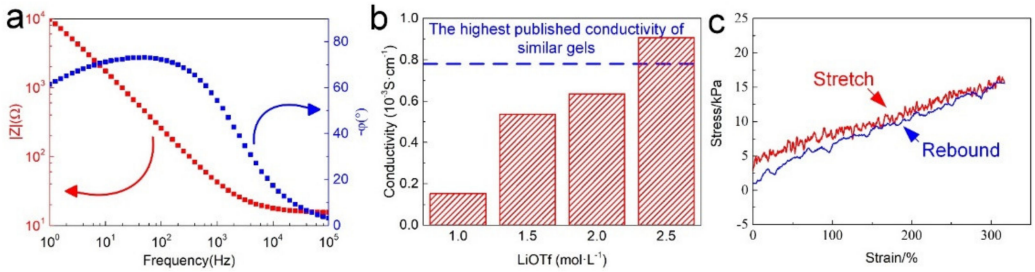

Figure 2. The electrical and mechanical properties of OICs: (**a**) frequency response of impedance magnitude (|Z|) and phase angle (φ), (**b**) conductivity of OICs at various LiOTf concentrations, (**c**) tensile and rebound curves of OICs.

OICs exhibited extraordinary temperature tolerances due to the presence of PC. The dynamic thermomechanical analysis (Figure 3a) revealed that the glass-transition temperature of the OICs was about −70 °C, which remained stable at low temperatures. Furthermore, the smooth storage modulus curve reflects the uniform structure of OICs. The thermogravimetric analysis (Figure 3b) demonstrates that OICs are strikingly stable at high temperatures compared with hydrogels. Hence, we did not observe any significant weight loss at 50 °C and only a slight reduction of 7.1 wt.% was observed at 100 °C. More surprisingly, the solvent in OICs was not completely volatilized even at >100 °C, endowing outstanding temperature tolerance and ensuring the normal operation of OICs at high temperatures. Then, we analyzed the conductivity of OICs at different temperatures (Figure 3c). As expected, the increase in temperature (0 to 75 °C) accelerated the migration of ions that directly promoted the conductivity from 0.4×10^{-3} to 1.4×10^{-3} S·cm^{-1}, respectively. Significantly, OICs presented an acceptable ionic conductivity over the entire temperature range, implying that OICs are suitable for most daily-life temperature conditions. Thus, the advantages of OICs in terms of temperature tolerance show that it is more competent for high- and low-temperature environments.

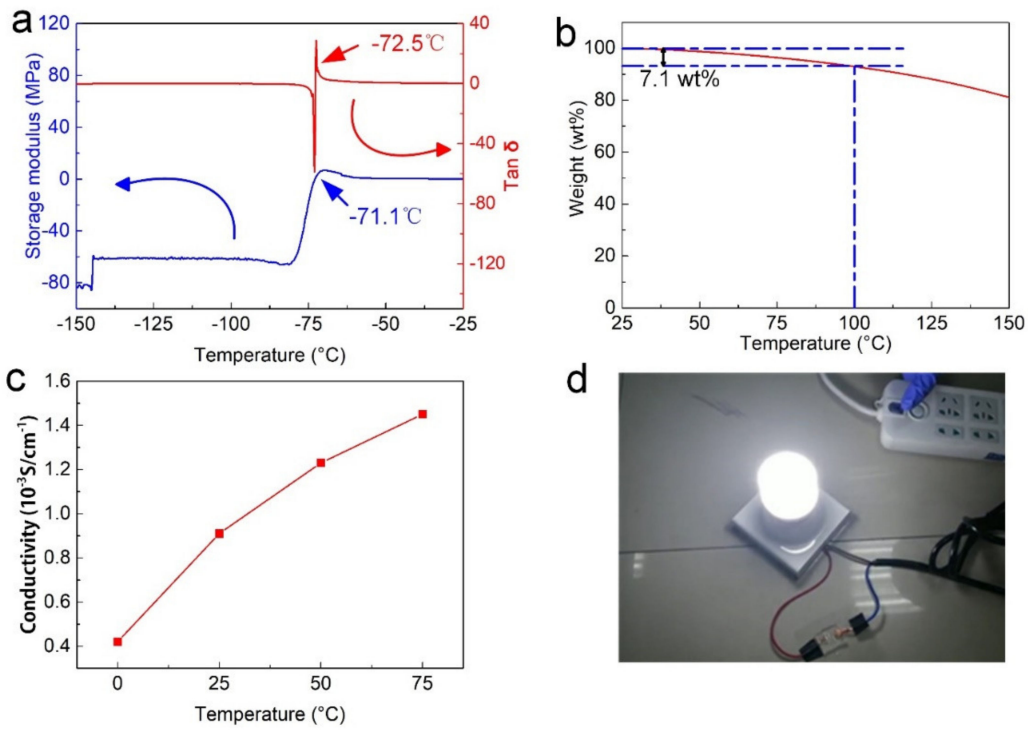

Figure 3. Thermal properties of OICs: (**a**) dynamic thermomechanical analysis and (**b**) thermogravimetric analysis. (**c**) Ionic conductivity of OICs in the temperature range of 0 to 75 °C, (**d**) lighting up a bulb using OICs instead of wires.

Finally, we further designed a circuit to visually display the ionic conductivity of OICs (Figure 3d). We replaced the wire with an OIC and successfully lit a household bulb (220 V). When the bulb was lit, no visible flicker was observed, and the brightness remained stable. Therefore, although the conductivity of OICs is not as outstanding as metallic conductors, OICs are still capable of replacing conventional wires.

Then, we covered OICs with PVDF to prepare a flexible conductor that could be self-powered. PVDF naturally crystallizes as a solvent, and this process is usually accompanied by heating. Suffering from easy evaporation of water, PVDF cannot be compounded with hydrogel, while OICs are different because of their extraordinary high-temperature resistance. Hence, self-powered OICs can be completed through a simple heating process (Figure 4a). Unlike dense and impervious substrates, such as glasses, the porous structure of OICs tends to absorb other solutions. In particular, DMF, as a selective organic solvent, can be used to dissolve PVDF and is perfectly miscible with the OIC precursors. As shown in Figure 4b, we added Sudan III for observation. DMF penetrates OIC to a depth of almost 1 mm after only 10 min of heating. Under the combined action of heat treatment, most of the DMF is lost, promoting the growth of PVDF crystals. At the same time, the liquid flows from PVDF solution to OIC reorient PVDF crystals to a certain extent, leading to a better polarization effect. Finally, a PVDF film about 40 μm thick was formed on the OIC (Figure 4c). As expected, PVDF cured on glass contained both α and β phases. Figure 4d presents the FTIR spectra of P-OICs, and we observed characteristic peaks for the α phase at 764 and 975 cm^{-1}, and β/γ characteristic peaks were observed at 510, 840 and 1401 cm^{-1}. When we heated PVDF on the OIC substrate at the same temperature, the intensity of each characteristic peak increased, indicating that the crystallinity of PVDF was significantly improved and therefore shows that better fluidity was beneficial to the formation of PVDF crystals. When we further increased the temperature to 90 °C, the α characteristic peaks at 764 and 975 cm^{-1} disappeared, which may have been due to the increased fluidity of DMF at higher temperatures, and the more intense directional flow of DMF promoting PVDF generation of the β-phase crystal form.

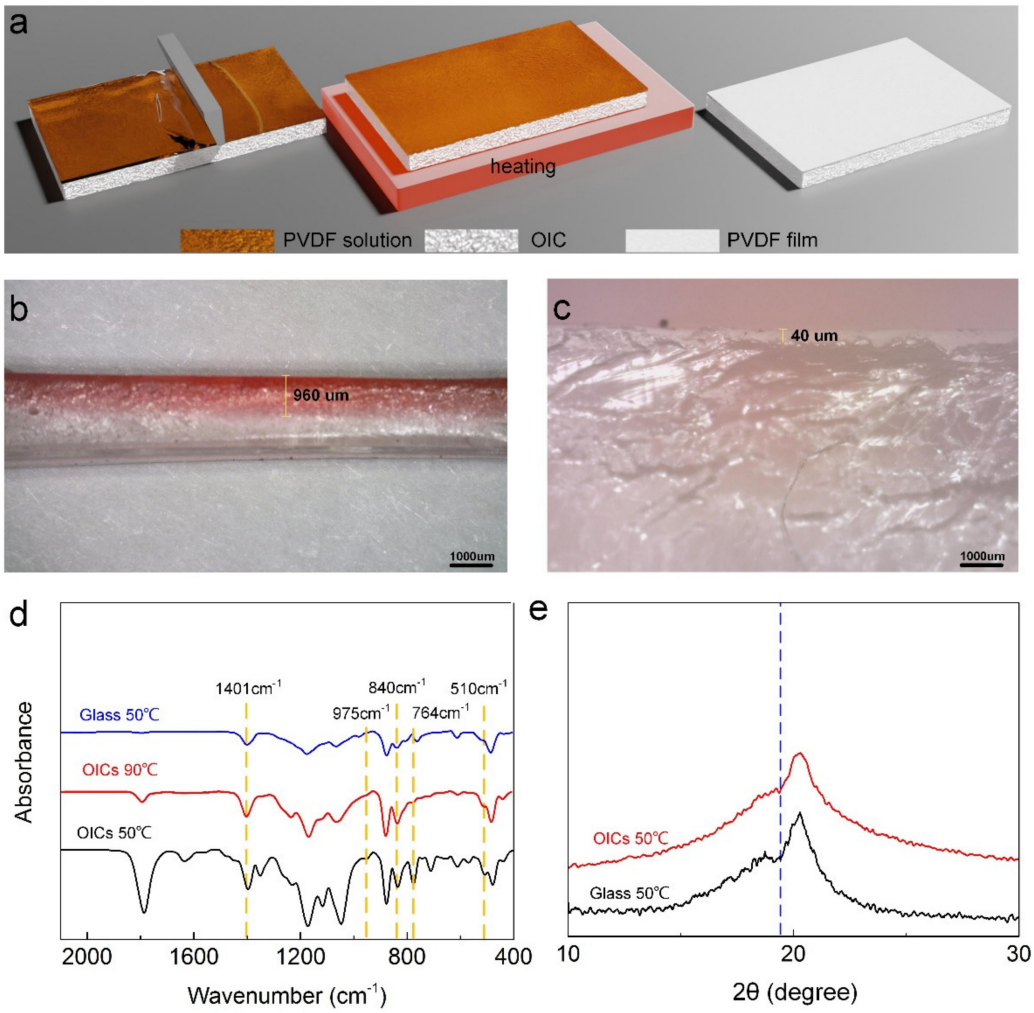

Figure 4. PVDF polarization detection. (**a**) Self-powered OIC preparation process, (**b**) penetration of DMF on OIC, and (**c**) the thickness of PVDF. (**d**) FTIR spectra of self-powered OICs on different substrates, and (**e**) XRD patterns of PVDF on glass and OICs after polarization.

The peak intensity from the PVDF film on the OIC substrate was stronger than that on the glass substrate, according to which β-shaped crystals on OICs and glass were calculated to be 70.2% and 42.8%, respectively, thereby showing better polarization of PVDF on OICs. The XRD patterns were consistent with FTIR data (Figure 4e): a shoulder peak from the OIC substrate at 2θ = 20.6° was smoother than the glass substrate, indicating a relatively higher content of β-shaped crystals in OICs. Hence, crystallization is more effective on OICs. One should note that the direct heating of the organic gel to form the PVDF piezoelectric layer provides a more efficient and simple self-powered strategy for various flexible materials.

We further investigated the influence of heating temperature and thickness of the PVDF layer on polarization. As shown in Figure 5a, the content of β-shaped crystals rose slightly with increasing temperature. The higher temperature not only accelerated the crystallization but also intensified the thermal movement of molecules, yielding a slow upward trend of β-shaped crystal quantity. With increase in PVDF layer thickness, the grain size gradually increased. At the thicknesses of 200, 400 and 800 μm, the average diameters of the grains were 5, 10 and 25 μm, respectively. Simultaneously, we also discovered that the content of β-shaped crystals was raised when we applied 400 μm PVDF (Figure 5b). However, a further increase in PVDF layer thickness exerted no visual effect on the number of β-shaped crystals. As seen in SEM images (Figure 5c), the nearby molecules reunited when the layer thickness was 200 μm, preventing PVDF from forming spherical crystals, but simply covering it. However, when the squeegee thickness was raised to 800 μm, the

spherical crystals continued to grow and even began to gradually merge, resulting in a low content of β-shaped crystals due to the overgrowth of grains. Hence, only a moderate thickness (400 μm) contributes to the desired crystalline state of PVDF.

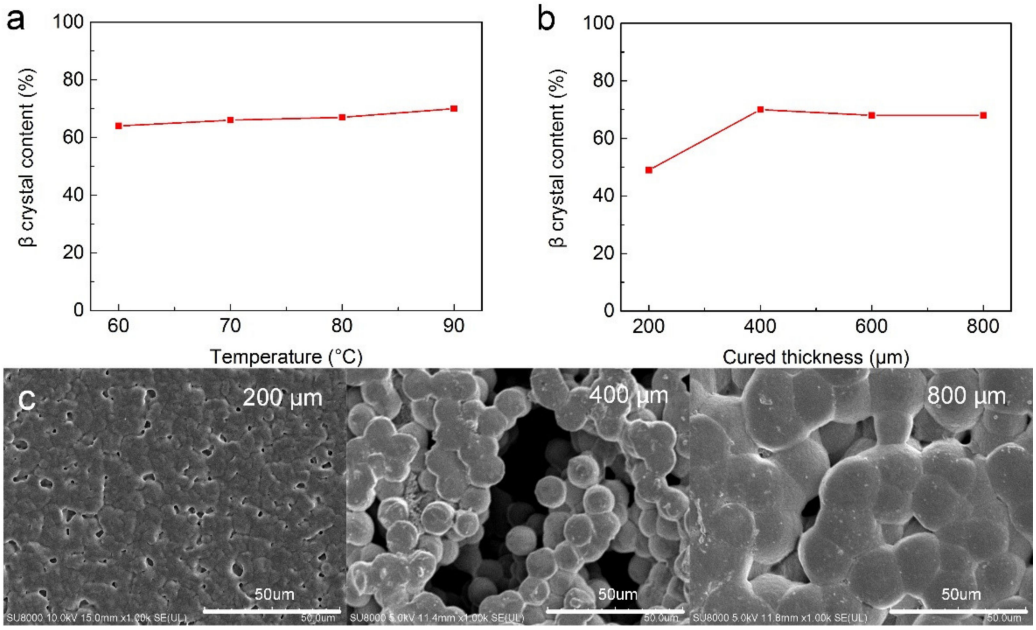

Figure 5. Polarization parameters of PVDF: β crystal content as a function of (**a**) temperature, (**b**) curing thickness, and (**c**) SEM images of PVDF layers with thicknesses of 200, 400 and 800 μm.

Meanwhile, the observed spherical crystals generally represented a high β-shaped crystal content [46]. Thus, the piezoelectric effect of self-powered OICs was assessed using a 400 μm thick PVDF layer polarized at 90 °C. The piezoelectric coefficient of the conductor was found to be 15 pC·N^{-1}, which is sufficient for OIC to work as a self-powered sensor.

The electromechanical response shows excellent operating life of self-powered OICs. We performed the electromechanical test on the excitation platform at a frequency of 3 Hz and an excitation force of 36 N (Figure 6a). The self-powered OIC responded sensitively to the excitation force input and produced a stable voltage of 3.52 V, indicating that it already had piezoelectric characteristics. Additionally, the working life needed to be tested to prove its potential as a sensor. Consequently, a strict durability test was performed (Figure 6b), where we measured the output consumption under the frequency of 5 Hz and excitation force of 24 N before and after 10,000 excitation cycles and 30 days of room-temperature storage. The self-powered OICs stabilized the output voltage for a long time, and the loss rate was less than 10%, showing a long working life.

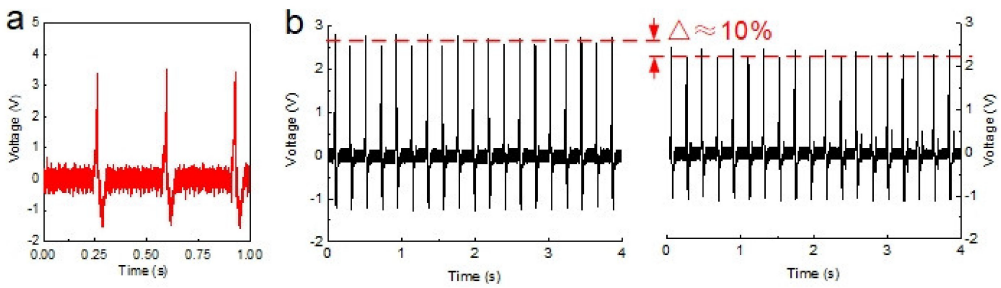

Figure 6. Piezoelectric characterization: (**a**) electromechanical response and (**b**) durability performance of self-powered OICs.

Finally, we simulated the application of self-powered OICs in basketball training (Figure 7). The basketball impact was simulated on a platform, where nine sensors were

arranged in a 3 × 3 matrix. According to the normal contact interval between two hits on the backboard, the excitation frequency was 1 Hz. When the impact occurred, the oscilloscope detected four signals indicating the hitting power and contact position, which can be used by coaches to train players.

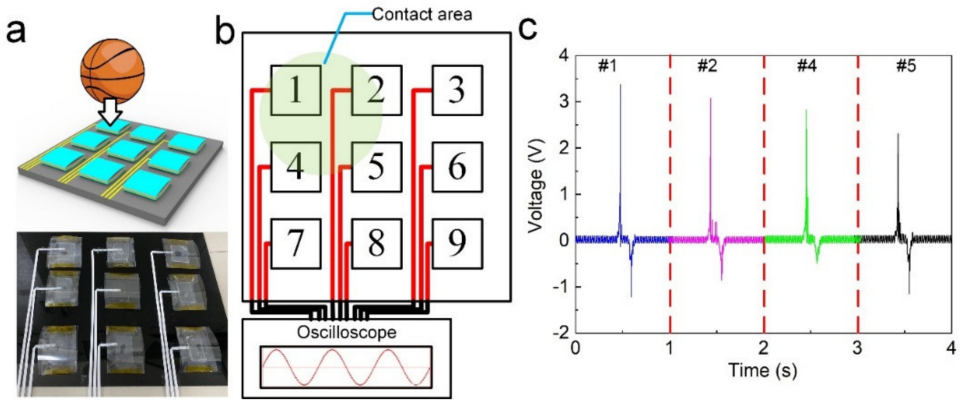

Figure 7. Application in basketball training: (**a**) the model and physical images of the basketball impact detection, (**b**) schematic diagram of the contact positions, and (**c**) the detected voltage.

4. Conclusions

In summary, we designed and manufactured highly conductive and self-powered OICs serving as self-powered sensors. The results revealed the ingenious choice of the small molecular weight lithium salt, which provided smooth ionic movement and enhanced the conductivity of OICs (9.1×10^{-4} S·cm^{-1}). Moreover, benefiting from the excellent temperature tolerance within a range of −70 to 100 °C, we have combined the OIC with a PVDF piezoelectric layer to prepare self-powered OICs, achieving a stable voltage output and long working life. The OICs showed excellent potential for a wide range of applications in daily life as passive pressure sensors.

Author Contributions: Conceptualization, W.Y. and G.G.; methodology, Y.L. (Yingtao Li) and Y.L. (Yu Luo); software, Y.L. (Yingtao Li) and Z.W.; validation, Y.L. (Yingtao Li) and Z.W.; formal analysis, L.W. and S.D.; investigation, Y.L. (Yu Luo); resources, Y.G.; data curation, Y.L. (Yingtao Li); writing—original draft preparation, Z.W.; writing—review and editing, Z.W.; visualization, Y.L. (Yingtao Li) and Z.W.; supervision, L.W.; project administration, B.L.; funding acquisition, L.W. All authors have read and agreed to the published version of the manuscript.

Funding: This research was supported by the Key-Area Research and Development Program of Guangdong, China [grant number 2020B090924003] and the Key R&D Program of Shaanxi Province [grant number 2021ZDLGY10-09].

Institutional Review Board Statement: Not applicable.

Informed Consent Statement: Not applicable.

Data Availability Statement: The data are available upon reasonable request from the corresponding author.

Conflicts of Interest: The authors declare no conflict of interest.

References

1. Ohm, Y.; Pan, C.; Ford, M.J.; Huang, X.; Liao, J.; Majidi, C. An electrically conductive silver–polyacrylamide–alginate hydrogel composite for soft electronics. *Nat. Electron.* **2021**, *4*, 185–192. [CrossRef]
2. Yuk, H.; Lu, B.; Zhao, X. Hydrogel bioelectronics. *Chem. Soc. Rev.* **2019**, *48*, 1642–1667. [CrossRef] [PubMed]
3. Zhang, Z.X.; Wang, L.; Yu, H.T.; Zhang, F.; Tang, L.; Feng, Y.Y.; Feng, W. Highly Transparent, Self-Healable, and Adhesive Organogels for Bio-Inspired Intelligent Ionic Skins. *ACS Appl. Mater. Interfaces* **2020**, *12*, 15657–15666. [CrossRef] [PubMed]

4. Zhu, J.; Li, F.X.; Wang, X.L.; Yu, J.Y.; Wu, D.Q. Hyaluronic Acid and Polyethylene Glycol Hybrid Hydrogel Encapsulating Nanogel with Hemostasis and Sustainable Antibacterial Property for Wound Healing. *ACS Appl. Mater. Interfaces* **2018**, *10*, 13304–13316. [CrossRef] [PubMed]
5. Oh, Y.S.; Kim, J.H.; Xie, Z.Q.; Cho, S.; Han, H.; Jeon, S.W.; Park, M.; Namkoong, M.; Avila, R.; Song, Z.; et al. Battery-free, wireless soft sensors for continuous multi-site measurements of pressure and temperature from patients at risk for pressure injuries. *Nat. Commun.* **2021**, *12*, 5008. [CrossRef]
6. Xu, W.; Huang, L.B.; Wong, M.C.; Chen, L.; Bai, G.X.; Hao, J.H. Environmentally Friendly Hydrogel-Based Triboelectric Nanogenerators for Versatile Energy Harvesting and Self-Powered Sensors. *Adv. Energy Mater.* **2017**, *7*, 1601529. [CrossRef]
7. Sahu, M.; Vivekananthan, V.; Hajra, S.; Khatua, D.K.; Kim, S.J. Porosity modulated piezo-triboelectric hybridized nanogenerator for sensing small energy impacts. *Appl. Mater. Today* **2021**, *22*, 100900. [CrossRef]
8. Gao, G.; Yang, F.; Zhou, F.; He, J.; Lu, W.; Xiao, P.; Yan, H.; Pan, C.; Chen, T.; Wang, Z.L. Bioinspired Self-Healing Human–Machine Interactive Touch Pad with Pressure-Sensitive Adhesiveness on Targeted Substrates. *Adv. Mater.* **2020**, *32*, 2004290. [CrossRef]
9. Wang, Z.; Cong, Y.; Fu, J. Stretchable and tough conductive hydrogels for flexible pressure and strain sensors. *J. Mater. Chem. B* **2020**, *8*, 3437–3459. [CrossRef]
10. Liu, X.; Liu, J.; Lin, S.; Zhao, X. Hydrogel machines. *Mater. Today* **2020**, *36*, 102–124. [CrossRef]
11. Yang, C.; Suo, Z. Hydrogel ionotronics. *Nat. Rev. Mater.* **2018**, *3*, 125–142. [CrossRef]
12. Wang, C.; Zhang, P.; Xiao, W.; Zhao, J.; Shi, M.; Wei, H.; Deng, Z.; Guo, B.; Zheng, Z.; Yu, Y. Visible-light-assisted multimechanism design for one-step engineering tough hydrogels in seconds. *Nat. Commun.* **2020**, *11*, 4694. [CrossRef]
13. Chun, S.; Choi, I.Y.; Son, W.; Jung, J.; Lee, S.; Kim, H.S.; Pang, C.; Park, W.; Kim, J.K. High-Output and Bending-Tolerant Triboelectric Nanogenerator Based on an Interlocked Array of Surface-Functionalized Indium Tin Oxide Nanohelixes. *ACS Energy Lett.* **2019**, *4*, 1748–1754. [CrossRef]
14. Qi, J.B.; Wang, A.C.; Yang, W.F.; Zhang, M.Y.; Hou, C.Y.; Zhang, Q.H.; Li, Y.G.; Wang, H.Z. Hydrogel-based hierarchically wrinkled stretchable nanofibrous membrane for high performance wearable triboelectric nanogenerator. *Nano Energy* **2020**, *67*, 104206. [CrossRef]
15. De Medeiros, M.S.; Chanci, D.; Martinez, R.V. Moisture-insensitive, self-powered paper-based flexible electronics. *Nano Energy* **2020**, *78*, 105301. [CrossRef]
16. Rahimi, A.; Herzog-Arbeitman, A.; García, J.M. Conductive Recyclable Organogel Composites. *Macromol. Mater. Eng.* **2019**, *304*, 1800583. [CrossRef]
17. Cai, J.; Zhang, X.; Liu, W.; Huang, J.; Qiu, X. Synthesis of highly conductive hydrogel with high strength and super toughness. *Polymer* **2020**, *202*, 122643. [CrossRef]
18. Chun, K.Y.; Seo, S.; Han, C.S. Self-Powered, Stretchable, and Wearable Ion Gel Mechanoreceptor Sensors. *ACS Sens.* **2021**, *6*, 1940–1948. [CrossRef]
19. Ji, Z.; Yan, C.; Yu, B.; Zhang, X.; Cai, M.; Jia, X.; Wang, X.; Zhou, F. 3D Printing of Hydrogel Architectures with Complex and Controllable Shape Deformation. *Adv. Mater. Technol.* **2019**, *4*, 1800713. [CrossRef]
20. Kazunari, Y.; Yuki, T.; Yuta, H.; Masaru, K.; Hidemitsu, F. 3D printing for gel robotics. In Proceedings of the SPIE Smart Structures and Materials + Nondestructive Evaluation and Health Monitoring, Denver, CO, USA, 4–8 March 2018.
21. Schroeder, T.B.H.; Guha, A.; Lamoureux, A.; VanRenterghem, G.; Sept, D.; Shtein, M.; Yang, J.; Mayer, M. An electric-eel-inspired soft power source from stacked hydrogels. *Nature* **2017**, *552*, 214–218. [CrossRef]
22. Hao, X.P.; Li, C.Y.; Zhang, C.W.; Du, M.; Ying, Z.M.; Zheng, Q.; Wu, Z.L. Self-Shaping Soft Electronics Based on Patterned Hydrogel with Stencil-Printed Liquid Metal. *Adv. Funct. Mater.* **2021**, *31*, 2105481. [CrossRef]
23. Li, G.X.; Li, L.W.; Zhang, P.P.; Chang, C.Y.; Xu, F.; Pu, X. Ultra-stretchable and healable hydrogel-based triboelectric nanogenerators for energy harvesting and self-powered sensing. *RSC Adv.* **2021**, *11*, 17437–17444. [CrossRef]
24. Wang, S.H.; Wang, Z.L.; Yang, Y. A One-Structure-Based Hybridized Nanogenerator for Scavenging Mechanical and Thermal Energies by Triboelectric-Piezoelectric-Pyroelectric Effects. *Adv. Mater.* **2016**, *28*, 2881–2887. [CrossRef] [PubMed]
25. Zhang, H.X.; Niu, W.B.; Zhang, S.F. Extremely Stretchable, Stable, and Durable Strain Sensors Based on Double-Network Organogels. *ACS Appl. Mater. Interfaces* **2018**, *10*, 32640–32648. [CrossRef]
26. Ahmed, K.; Naga, N.; Kawakami, M.; Furukawa, H. Extremely Soft, Conductive, and Transparent Ionic Gels by 3D Optical Printing. *Macromol. Chem. Phys.* **2018**, *219*, 1800216. [CrossRef]
27. Li, C.; Cong, S.; Tian, Z.N.; Song, Y.Z.; Yu, L.H.; Lu, C.; Shao, Y.L.; Li, J.; Zou, G.F.; Rummeli, M.H.; et al. Flexible perovskite solar cell-driven photo-rechargeable lithium-ion capacitor for self-powered wearable strain sensors. *Nano Energy* **2019**, *60*, 247–256. [CrossRef]
28. Li, Z.; Liu, Z.; Ng, T.Y.; Sharma, P. The effect of water content on the elastic modulus and fracture energy of hydrogel. *Extrem. Mech. Lett.* **2020**, *35*, 100617. [CrossRef]
29. Ming, Z.Z.; Pang, Y.; Liu, J.Y. Switching between Elasticity and Plasticity by Network Strength Competition. *Adv. Mater.* **2020**, *32*, 1906870. [CrossRef]
30. Rahman, M.S.; Shiblee, M.D.N.I.; Ahmed, K.; Khosla, A.; Ogawa, J.; Kawakami, M.; Furukawa, H. Flexible and Conductive 3D Printable Polyvinylidene Fluoride and Poly(N,N-dimethylacrylamide) Based Gel Polymer Electrolytes. *Macromol. Mater. Eng.* **2020**, *305*, 2000262. [CrossRef]

31. Alam, A.; Moussa, M. Preparation of graphene/poly(vinyl alcohol) composite hydrogel films with enhanced electrical and mechanical properties. *Polym. Compos.* **2020**, *41*, 809–816. [CrossRef]
32. Liu, X.; Miller, A.L.; Park, S.; Waletzki, B.E.; Zhou, Z.; Terzic, A.; Lu, L. Functionalized Carbon Nanotube and Graphene Oxide Embedded Electrically Conductive Hydrogel Synergistically Stimulates Nerve Cell Differentiation. *ACS Appl. Mater. Interfaces* **2017**, *9*, 14677–14690. [CrossRef] [PubMed]
33. Han, S.; Liu, C.; Lin, X.; Zheng, J.; Wu, J.; Liu, C. Dual Conductive Network Hydrogel for a Highly Conductive, Self-Healing, Anti-Freezing, and Non-Drying Strain Sensor. *ACS Appl. Polym. Mater.* **2020**, *2*, 996–1005. [CrossRef]
34. Wu, L.; Hu, Y.; Tang, P.; Wang, H.; Bin, Y. High stretchable, pH-sensitive and self-adhesive rGO/CMCNa/PAA composite conductive hydrogel with good strain-sensing performance. *Compos. Commun.* **2021**, *24*, 100669. [CrossRef]
35. Yang, Y.Y.; Yang, Y.T.; Cao, Y.X.; Wang, X.; Chen, Y.R.; Liu, H.Y.; Gao, Y.F.; Wang, J.F.; Liu, C.; Wang, W.J.; et al. Anti-freezing, resilient and tough hydrogels for sensitive and large-range strain and pressure sensors. *Chem. Eng. J.* **2021**, *403*, 126431. [CrossRef]
36. Chen, H.; Huang, J.; Liu, J.; Gu, J.; Zhu, J.; Huang, B.; Bai, J.; Guo, J.; Yang, X.; Guan, L. High toughness multifunctional organic hydrogels for flexible strain and temperature sensor. *J. Mater. Chem. A* **2021**, *9*, 23243–23255. [CrossRef]
37. Zhu, T.; Jiang, C.; Wang, M.L.; Zhu, C.Z.; Zhao, N.; Xu, J. Skin-Inspired Double-Hydrophobic-Coating Encapsulated Hydrogels with Enhanced Water Retention Capacity. *Adv. Funct. Mater.* **2021**, *31*, 2102433. [CrossRef]
38. Xu, R.D.; Qu, L.J.; Tian, M.W. Touch-sensing fabric encapsulated with hydrogel for human-computer interaction. *Soft Matter* **2021**, *17*, 9014–9018. [CrossRef]
39. Jian, Y.; Handschuh-Wang, S.; Zhang, J.; Lu, W.; Zhou, X.; Chen, T. Biomimetic anti-freezing polymeric hydrogels: Keeping soft-wet materials active in cold environments. *Mater. Horiz.* **2021**, *8*, 351–369. [CrossRef]
40. Sui, X.; Guo, H.; Chen, P.; Zhu, Y.; Wen, C.; Gao, Y.; Yang, J.; Zhang, X.; Zhang, L. Zwitterionic Osmolyte-Based Hydrogels with Antifreezing Property, High Conductivity, and Stable Flexibility at Subzero Temperature. *Adv. Funct. Mater.* **2020**, *30*, 1907986. [CrossRef]
41. Subraveti, S.N.; Raghavan, S.R. A Simple Way to Synthesize a Protective "Skin" around Any Hydrogel. *ACS Appl. Mater. Interfaces* **2021**, *13*, 37645–37654. [CrossRef]
42. Gao, Y.; Shi, L.; Lu, S.; Zhu, T.; Da, X.; Li, Y.; Bu, H.; Gao, G.; Ding, S. Highly Stretchable Organogel Ionic Conductors with Extreme-Temperature Tolerance. *Chem. Mater.* **2019**, *31*, 3257–3264. [CrossRef]
43. Sun, H.; Zhao, Y.; Jiao, S.; Wang, C.; Jia, Y.; Dai, K.; Zheng, G.; Liu, C.; Wan, P.; Shen, C. Environment Tolerant Conductive Nanocomposite Organohydrogels as Flexible Strain Sensors and Power Sources for Sustainable Electronics. *Adv. Funct. Mater.* **2021**, *31*, 2101696. [CrossRef]
44. Lee, Y.Y.; Kang, H.Y.; Gwon, S.H.; Choi, G.M.; Lim, S.M.; Sun, J.Y.; Joo, Y.C. A Strain-Insensitive Stretchable Electronic Conductor: PEDOT:PSS/Acrylamide Organogels. *Adv. Mater.* **2016**, *28*, 1636–1643. [CrossRef]
45. Ueda, C.; Park, J.; Hirose, K.; Konishi, S.; Ikemoto, Y.; Osaki, M.; Yamaguchi, H.; Harada, A.; Tanaka, M.; Watanabe, G.; et al. Behavior of supramolecular cross-links formed by host-guest interactions in hydrogels responding to water contents. *Supramol. Mater.* **2022**, *1*, 100001. [CrossRef]
46. Fu, W.L.; Du, P.Y.; Weng, W.J.; Han, G.Y. Preparation and structure of PVDF piezoelectric film. *Chin. J. Mater. Res.* **2005**, *3*, 21–26.

nanomaterials

MDPI

Article

Advanced Technology Evolution Pathways of Nanogenerators: A Novel Framework Based on Multi-Source Data and Knowledge Graph

Yufei Liu [1], Guan Wang [2], Yuan Zhou [3,*] and Yuhan Liu [2]

[1] Center for Strategic Studies, Chinese Academy of Engineering, Beijing 100088, China; liuyf@cae.cn
[2] National Numerical Control Systems Engineering Research Center, School of Mechanical Science and Engineering, Huazhong University of Science and Technology, Wuhan 430074, China; m202077010@hust.edu.cn (G.W.); liuyh_0116@hust.edu.cn (Y.L.)
[3] School of Public Policy and Management, Tsinghua University, Beijing 100084, China
* Correspondence: zhou_yuan@mail.tsinghua.edu.cn

Abstract: As an emerging nano energy technology, nanogenerators have been developed rapidly, which makes it crucial to analyze the evolutionary pathways of advanced technology in this field to help estimate the development trend and direction. However, some limitations existed in previous studies. On the one hand, previous studies generally made use of the explicit correlation of data such as citation and cooperation between patents and papers, which ignored the rich semantic information contained in them. On the other hand, the progressive evolutionary process from scientific grants to academic papers and then to patents was not considered. Therefore, this paper proposes a novel framework based on a separated three-layer knowledge graph with several time slices using grant data, paper data, and patent data. Firstly, by the representation learning method and clustering algorithm, several clusters representing specific technologies in different layers and different time slices can be obtained. Then, by calculating the similarity between clusters of different layers, the evolutionary pathways of advanced technology from grants to papers and then to patents is drawn. Finally, this paper monitors the pathways of some developed technologies, which evolve from grants to papers and then to patents, and finds some emerging technologies under research.

Keywords: nanogenerator; technology evolution pathway; knowledge graph; representation learning; multi-source data

Citation: Liu, Y.; Wang, G.; Zhou, Y.; Liu, Y. Advanced Technology Evolution Pathways of Nanogenerators: A Novel Framework Based on Multi-Source Data and Knowledge Graph. *Nanomaterials* **2022**, *12*, 838. https://doi.org/10.3390/nano12050838

Academic Editor: Federico Cesano

Received: 30 January 2022
Accepted: 25 February 2022
Published: 2 March 2022

1. Introduction

As a novel energy solution for micro and wearable wireless electronic devices, nanogenerators (NG) have been developed to harvest energy from the environment, including biomechanical energy, solar and wind energy, thermal energy, etc. [1]. Based on different physical effects, nanogenerators can be roughly divided into piezoelectric nanogenerators (PENGs), triboelectric nanogenerators (TENGs), and pyroelectric nanogenerators (PYENGs) [2]. Notably, nanogenerators present widespread applications other than energy harvesting, benefiting from related technologies such as 5G and Internet of Things (IoT) [3], nanomaterials [4], flexible sensors [5], and so on. To date, these applications can be divided into two domains. One is the innovative devices and techniques in the engineering domain (e.g., self-powered sensing systems, wearable devices [6]), the other is the biomedical domain (e.g., implantable devices, tissue regeneration [7]). Due to the rapid development and diversity of nanogenerator technology, identifying and understanding the evolutionary path of nanogenerator technology is crucial for decision-makers to capture the development trends and directions [8].

Some previous studies roughly described a sub-field development path of nanogenerator technology based on literature reviews. However, with the rapid development of

nanogenerators, the corresponding increase in literature makes it difficult to thoroughly analyze the evolutionary trends of the nanogenerator technologies based solely on literature reviews. Therefore, quantitative approaches such as bibliometrics, patent citation analysis, technology roadmap, and text mining are used to analyze the evolutionary trends [9,10]. However, citation networks only make use of the explicit correlation of data, which ignores the rich semantic information contained in them. To deal with this, the knowledge graph (KG), a constructed knowledge base with powerful semantic processing ability, is taken into consideration naturally [8]. Essentially, the knowledge graph is a semantic network with nodes and edges that reveals the entities and relationships and can formally describe things and relationships in the real world. In addition, at the level of research purpose, scholars only focused on the technology evolution pathways over time [11–19], which ignored the progressive evolutionary process from scientific grants to academic papers and then to patents, while technologies generally emerge with grants or papers and become sophisticated with patents.

In this paper, we propose a novel framework for monitoring the evolutionary paths of nanogenerator technology based on analyzing grants, papers, and patents data. The framework is shown in Figure 1. After multi-source data acquisition, the knowledge graph was constructed to capture semantic information between entities, as shown in the top right corner of Figure 1. Different colors of dots show the different types of entities (such as the author, paper, institution, and journal in paper knowledge graph), and the connections between dots show the relations between entities. Then, representation learning and clustering methods were used to cluster entities with similar topics, as shown in the bottom right corner in Figure 1, while the circles represent clusters and the black dots represent the grants, papers, and patents contained in clusters. Finally, we describe the evolutionary path from grants to papers and then to patents by connecting similar clusters.

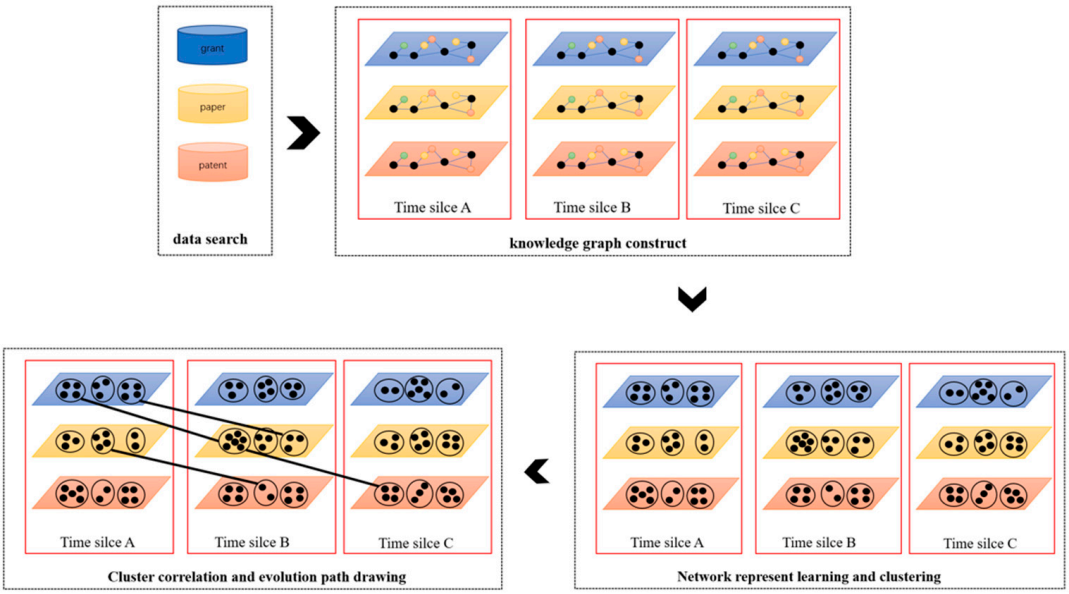

Figure 1. The framework to monitor the technology evolution pathways.

The key contributions of this paper can be summarized as follows:

1. The nanogenerator field is emergent and rapidly developed, making it hard to analyze the evolutionary pathways of advanced technologies. This paper proposed a novel framework to monitor the evolution pathways based on multi-source data and a knowledge graph.
2. When monitoring the evolution pathways, we applied the representation learning method and clustering method to connect similar entities, which enables the quantitative analysis of large-scale data, thus improving efficiency and accuracy.

3. This paper used multi-source data from three data sources and analyzed the evolutionary pathways between different data sources, which reflected the technology trends comprehensively and pluralistically.

2. Literature Review

2.1. Development of Nanogenerators

With the rise of the Internet of Things (IoT), advanced materials, and electronics, wearable and implantable devices have developed rapidly. Miniaturization and power continuity have become an important development direction of such devices, which puts high demands on power supply systems [20]. Traditional power methods such as lithium batteries and lead-acid batteries have the limitations of considerable size, short service life, poor flexibility, the possibility of environmental pollution, and the need for frequent replacement. Therefore, developing a new microelectronic power supply device with high flexibility and a sustainable power supply has become the focus of researchers.

Piezoelectric nanogenerators (PENG) using ZnO nanowires were first invented in 2006 by Wang Zhonglin based on the piezoelectric effect to harvest mechanical energy and convert it to electric power, which marked the beginning of self-power technology [21]. After that, other researchers made many attempts and improvements in piezoelectric materials. At present, the mainstream and mature piezoelectric materials include ZnO, $BaTiO_3$ [22], lead zirconate titanate (PZT) [23], and polyvinylidene fluoride (PVDF) [24]. While developing piezoelectric materials, triboelectric nanogenerators (TENG) came out in 2012, which is based on the conjunction of triboelectrification and electrostatic induction [25]. Compared with PENG, TENG has the advantages of having a high output, low cost, simple structure design, and excellent stability. Up to now, PENG and TENG have made significant progress in output performance, sensitivity, energy conversion rate, flexibility, and being environmentally friendly [26]. At the same time, some other types of nanogenerators have been developed, such as pyroelectricity nanogenerators (PYENG) and piezoelectric triboelectric hybrid nanogenerators (PTENG) [27].

2.2. Technology Evolution Pathways

As a law of nature, evolution occurs all the time. Additionally, there is also an evolution process in the field of technology [28]. At present, the definition of technology evolution is not unified. There are roughly two views among researchers: one holds that technology evolution is generated by the accumulation of continuous innovation behind technology, and the other holds that the development and change process of technology itself symbolizes technology evolution and the induction and display of various changes in the form of paths is the technology evolution pathway [29,30].

The early analysis methods of technology evolution were mainly qualitative methods, including morphologic analysis, Delphi survey [30], and technology roadmap [19], which is under the guidance of expert knowledge and experience and requires a lot of human participation. Therefore, qualitative methods have high research costs and subjectivity, making the research results inefficient and unstable. With the rapid growth of data mining technology, quantitative methods have been well applied in technology evolution analysis. The main quantitative analysis methods include patent citation analysis, patent classification analysis, text mining methods, etc.

Huenteler et al. analyzed the evolution process of technology based on the citation links of patents, while a citation network can reflect the flow process of knowledge [31]. Zhou et al. analyzed the technology layout and trends of solar cells based on patent classification by IPC code [32]. However, the citation network analysis and classification analysis do not take semantic information in the text corpus into consideration. Additionally, the IPC code does not change over time. Thus, it is unable to sensitively perceive the technology evolution for the rapidly developing or converging and emerging technology fields. To fully use the semantic information in patent text, text mining methods were taken into consideration to analyze technology evolution. Yoon et al. constructed a semantic network

using text mining methods to analyze the development trend of technology [33]. Miao et al. has studied more than 30,000 patents since the 1990s using text mining methods to obtain products and applications with application prospects and rule out traditional technologies with a declining trend [11]. However, text mining methods pay more attention to the semantic information carried by patent text while ignoring the relationship between patents. Naturally, researchers consider combining the patent citation network and text mining methods to research technology evolution trends. Li et al. monitored and forecast the development trend of nanogenerators by citation analysis and used a Hierarchical Dirichlet Process topic model to extract technological topics [8].

Moreover, most of the existing studies only focus on a single source of data such as patents and papers, ignoring the interaction between knowledge discovery represented by grants or papers and technologies applications represented by patents, as well as the correction and difference of the information.

2.3. Knowledge Graph and Representation Learning

With the advent of the information age, the explosive growth of multi-source heterogeneous data has brought significant challenges to the data organization and application in the big data environment. A knowledge graph (KG) is a structured knowledge base with strong semantic processing ability, which provides a new idea to solve these problems. KG comes from Google's next-generation intelligent semantic search engine technology. In essence, it is a semantic network that reveals the relationship between entities and can also formally describe things that existed in the real world and their relationships. Now KG has been used to refer to all kinds of large-scale knowledge bases. Within the KG, the storage structure of data and knowledge is a triple, such as $<s, p, o>$ or p (s, o), where s and o are nodes in the KG, representing subject entity knowledge and object entity knowledge, respectively, and p is the edge in the KG, meaning the relational knowledge from subject s to object o.

At present, general knowledge graph technology, such as Freebase, DBpedia, Wikidata, and so on, has played an essential role in the internet field, such as intelligent search, intelligent Q&A, and personalized recommendation. At the same time, it has been preliminarily applied in many areas such as finance, e-commerce, medical treatment, etc. Compared with the general knowledge graph, the domain knowledge graph has more knowledge sources, faster requirements for large-scale expansion, a more complex knowledge structure, higher requirements for knowledge quality, and broader application forms. In the field of nanogenerators, there is little literature on the application of knowledge to analyze the relationships between various entities.

A knowledge graph is a structured knowledge base that stores entities' features and relationships, which demands a data mining method to efficiently obtain specific knowledge from the vast knowledge base. In recent years, representation learning algorithms have developed rapidly. Their purpose is to learn the potential, informative, and low dimensional representation of entities, which can simplify the graph while retaining the graph structure, entities' features, labels, and other auxiliary information. Socher et al. defined the evaluation function for each triplet in the knowledge graph using a single-layer neural network. They solved the representation of each entity by maximizing the evaluation function [34]. Although the nonlinear model based on the single-layer neural network can capture the semantic relationship between entities well, the computational cost is considerable. Inspired by the phenomenon of translation invariance in word vector space, Bordes et al. proposed the TransE model to learn the representation of entities in the knowledge graph in vector space, and the relationship is regarded as the translation vector between related entity pairs to constrain the learning results [35]. The TransE model is simple to reduce the computational cost, and the performance is significantly improved compared with the previous models. Nevertheless, TransE still has many limitations, which has encouraged later researchers to put forward many improved models. Wang et al. thought that the same entity should have different vector representations under different relationships, so they

proposed the TransH model to improve the ability to deal with complex relationships [36]. Lin et al. further proposed the TransR model based on the belief that different relationships should correspond to different semantic spaces [37]. The TransR model represents entities in triples into the vector space corresponding to the relationships and then establishes the translation relationship between entity vectors proposed by the TransE model. On the basis of TransR, the TransD model further defines different projection matrices for head entity and tail entity and simplifies the number of parameters of matrix [38].

TransE and its improved model only use the relationship data between entities in the knowledge graph for representation and learning. However, a large amount of descriptive information about the entity itself has not been used. Occasionally, the graph neural network (GNN) has attracted the attention of relevant researchers. GNN is a deep learning model based on information propagation, which can use the structure information and node information of the graph for representation at the same time. However, most classical GNN models, such as GCN [39], GAT [40], GAE [41], etc., can only apply to the knowledge graph of a single type of entity and relationship. To deal with this, Cen et al. proposed the MEIRec model, which uses the meta-path sampling method to sample multiple subgraphs of unified formal structures to facilitate GNN representation learning [42]. Wang et al. proposed the HAN model, which calculates the adjacency matrix of different meta-paths and puts it into the GAT model to learn the graph representation [43].

3. Methods

3.1. Data

This study attempted to analyze the knowledge flow between different data sources. Firstly, using the term "nanogenerator* or nano-generator", we collected the papers of nanogenerators in the Thomson Reuters Web Of Science database (WOS) by the end of December 2021. Then, 3304 publications were retrieved from the whole database, including the publication's title, citation information, abstract, time, author, institution, DOI, and journal name. Likewise, using the term "nanogenerator* OR nanometer generator", we collected the patents and nanogenerators in the Derwent Innovation Index (DI) database by the end of December 2021. Then, 984 patents were retrieved from the database, including the patent's title, citation information, time, and institution. Finally, using the term "nanogenerator*", we collected the grants of nanogenerators in the grants database of the China Knowledge Centre for Engineering Science and Technology (CKCEST). A total of 169 grants were retrieved, including title, start date, keywords, abstract, and institution. The details of data acquisition are shown in Table 1.

Table 1. Description of data acquisition.

Data	Database	Time Range	Search Query	Amounts
Grants	China Knowledge Centre for Engineering Science and Technology (CKCEST)	2006–2021	nanogenerator*	169
Papers	Thomson Reuters Web Of science database (WOS)	2006–2021	TI = (nanogenerator* OR nano-generator*) AND PY = (2006–2021)	984
Patents	Derwent Innovation Index database (DI)	2006–2021	TI = (nanogenerator* OR nanometer generator) AND PY $\leq$ 2021	3304

3.2. Knowledge Graph of Different Time Slices

To make use of the semantic information in the multi-source data, we need to construct knowledge graphs to reflect the relationships between entities. Take paper data as an example. Based on the related entities of papers, such as author, institution, and journal, we can construct a mapping $r(s, o)$ to preserve the relationship of paper and other entities, while

s represents the source of the relationship and o represents the object of the relationship, and r represents the type of relationship. Then, we can obtain several relationships, such as papers published in a journal p (p, j), papers written by the author w (p, a), and papers owned by an institution o (p, i). In the meantime, by dealing with the citation information of papers, we can obtain the relationship of a paper cited by other papers c (p, p). For each type of relationship, we can construct a matrix M_{AB} to save the mapping, while A and B represent the type of entities.

Thus far, we have obtained the relationships between entities by the semantic information contained in papers. Next, we need to extract features that can reflect the similarity and differences of papers by the word vectorization method. Specifically, we can vectorize the title of papers by the doc2vec model (denoted by f_i). After vectorization, the paper with similar subject words in the title has higher vector similarity, which saves the feature information of papers. The process of knowledge graph construction of patents and grants is the same as that of papers.

After constructing the knowledge graph of different data sources, we cut it into three time-slices of 2006–2012, 2013–2017, and 2018–2021. The detail of the knowledge graph is shown in Table 2. While 2006–2012 represents the preliminary stage of nanogenerators because PENG was proposed in 2006 and TENG was proposed in 2012, 2013–2017 represents the development stage of nanogenerators, and 2018–2021 represents the present stage.

Table 2. Description of knowledge graph and meta-path selection.

Data Source	Time Slice	Number of Entities	Types of Relations	Meta-Paths
Grants	2006–2012	21	Contain (grant, keyword)	G-K-G
	2012–2017	76	Own (institution, grant)	G-I-G
	2017–2021	33		
Papers	2006–2012	134	Publish (journal, paper)	P-J-P
	2013–2017	825	Write (author, paper)	P-A-P
	2017–2021	2345	Cite (paper, paper)	P-I-P
			Own (institution, paper)	P-P
Patents	2006–2012	105	Cite (patent, patent)	P-P
	2013–2017	337	Own (institution, patent)	P-I-P
	2017–2021	542		

3.3. Heterogeneous Graph Attention Network for Representation Learning

In this paper, we use a Heterogeneous Graph Attention Network (HAN) to consider the graph topology and text information at the same time [43]. The HAN model is improved from the Graph Attention Network (GAT) model while reserving the attention mechanism of GAT and proposing a solution for heterogeneous graph representation learning [40]. The framework of HAN is shown in Figure 2.

First, the meta-path was defined as a path in the form of $E_1 \xrightarrow{R_1} E_2 \xrightarrow{R_2} \cdots \xrightarrow{R_n} E_{n+1}$ (abbreviated as $E_1E_2 \cdots E_{n+1}$), which describes the composite relation $R = R_1 \circ R_2 \circ \cdots \circ R_n$ between entities E_1 and E_{n+1}, where $\circ$ denotes the composition operator on relations.

Based on the definition of meta-path, we can extract relations between different papers, grants, or patents. For example, we can define the relation of journal co-occurrence of papers by the meta-path $P_1 \xrightarrow{published} J_1 \xrightarrow{publish} P_2$ (abbreviated as PJP). The complete meta-paths of different data sources are shown in Table 2. Specifically, based on the relationship we obtained in the process of knowledge graph construction, we can calculate the transformation matrix of different meta-paths by matrix multiplication ($M_{PP} = M_{PJ} \times M_{JP}$, M_{PP} can be denoted by $M_{\varphi i}$ while φi represent the type of entities).

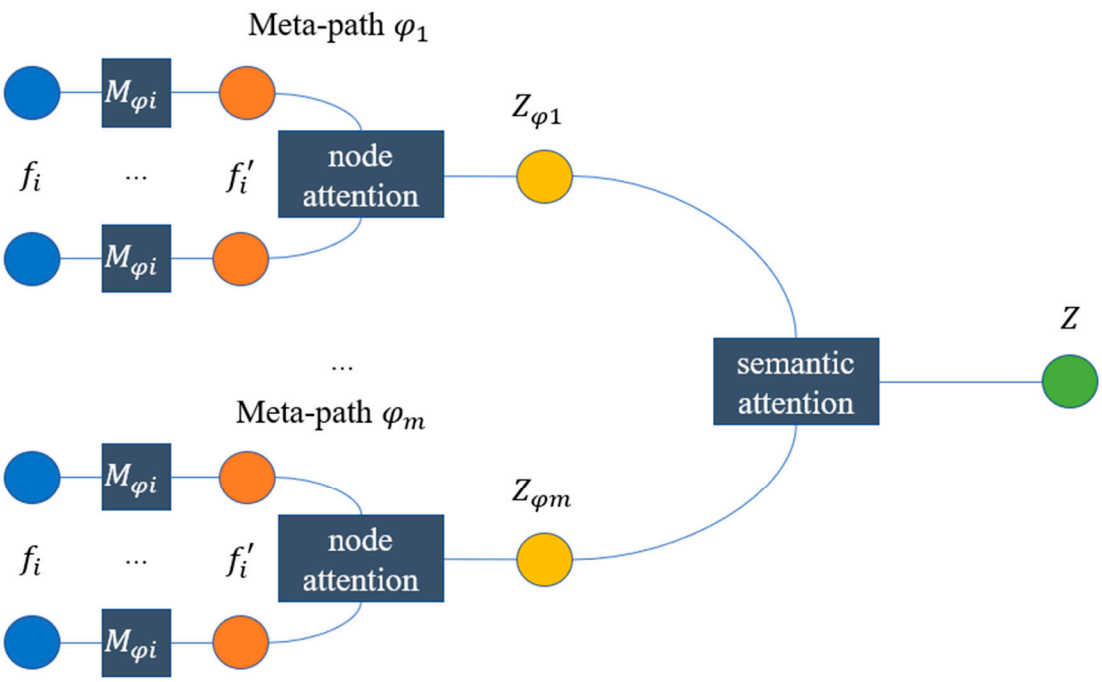

Figure 2. The framework of HAN.

Next, based on the transformation matrix of different meta-paths, for each type of entity (e.g., entities with type φi), we can conduct information propagation process as follows:

$$f_i' = M_{\varphi i} \cdot f_i \tag{1}$$

where f_i and f_i' are the original and processed features of node i, respectively.

After that, self-attention is leveraged to learn the weight among various kinds of entities. Given an entity pair (i, j) which are connected via meta-path φ, a node-level attention α_{ij}^{φ} can be learned to show how important entity j will be for entity i. The process can be formulated as follows:

$$\alpha_{ij}^{\varphi} = att_{node}\left(f_i',\ f_j',\ \varphi\right) \tag{2}$$

Then, the meta-path-based embedding of entity i can be aggregated by the neighbor's projected features with the corresponding coefficients as follows:

$$z_i^{\varphi} = \sigma\left(\sum_{j \epsilon \mathcal{N}_i^{\varphi}} \alpha_{ij}^{\varphi} \cdot f_j'\right) \tag{3}$$

where z_i^{φ} is the learned embedding of entity i for meta-path φ.

Given the meta-path set $\{\varphi_1, \varphi_2, \cdots \varphi_m\}$, after feeding features into entity-level attention, we can obtain m groups of semantic specific node embeddings, denoted as $\{Z_{\varphi 1}, Z_{\varphi 2}, \cdots Z_{\varphi m}\}$.

Generally, every node contains multiple types of semantic information, and semantic entity embedding can only reflect nodes from one aspect. To learn a more comprehensive node embedding, we need to fuse multiple semantics, which can be revealed by meta-paths. A novel semantic-level attention was proposed to automatically learn the importance of different meta-paths and fuse them. The learned weights of each meta-path can be shown as follows:

$$\left(\beta_{\varphi 1},\ \beta_{\varphi 2}, \cdots \beta_{\varphi m}\right) = att_{sem}\left(Z_{\varphi 1},\ Z_{\varphi 2}, \cdots, Z_{\varphi m}\right) \tag{4}$$

With the learned weights as coefficients, we can fuse these semantic-specific embeddings to obtain the final embedding Z as follows:

$$Z = \sum_{m=1}^{M} \beta_{\varphi m} \cdot Z_{\varphi m} \tag{5}$$

3.4. K-Means for Clustering and LDA for Topic Extracting

K-means is an unsupervised clustering algorithm, which identifies clusters $C = \{C_1, C_2, \cdots, C_k\}$ based on square error minimization for the given sample set $D = \{x_1, x_2, \cdots, x_n\}$. The process can be expressed as:

$$E = \sum_{i=1}^{k} \sum_{x \epsilon C_i} ||x - \mu_i||^2 \tag{6}$$

where $\mu_i = \frac{1}{|C_i|} \sum_{x \epsilon C_i} x$ is the mean vector for cluster C_i, and k is the number of clusters proposed to be classified.

In this paper, the final embedding of entities was used as the input of the K-means model for clustering. Then, we can obtain k clusters, which represent research sub-fields.

To clarify what each cluster means, we used the Latent Dirichlet Distribution (LDA) topic model to extract topic words for clusters. The LDA topic model is an unsupervised method for extracting hidden topics distribution of document and hidden word distribution of topics. It can represent each cluster by several important topics, and each topic contains several keywords.

3.5. Clusters Association for Evolutionary Path Identification

The mean value of entity embedding vectors was calculated to reflect the cluster vector. By calculating the similarity of different cluster vectors in different time slices or different data sources, we can connect clusters with the highest similarity to form technology evolution paths, in which the clusters' topics were used to reflect specific technologies. In this paper, the reciprocal of the Euclidean distance was used to measure the similarity of different clusters.

4. Results and Discussions

4.1. Representation Learning and Clustering

According to the proposed method in Section 3, the technology evolution pathway was identified and described. The multi-source data were utilized to construct the knowledge graphs of different data sources and different time slices. Based on these knowledge graphs, we can extract the transformation matrix $A \in \mathbb{R}^{n \times n}$ by different meta-paths, and the feature matrix $X \in \mathbb{R}^{n \times m}$ by doc2vec model, while n was the number of grant, paper, or patent entities in the knowledge graph, which can be found in Table 2 and m was the vector dimension of doc2vec output.

Then, the transformation matrix A and feature matrix X were input into the HAN model to learn the representation vector of entities. In this paper, we set the learning rate to 0.005, the dimension of the semantic-level attention vector to 128, the attention head K to 8, the dropout of attention to 0.6, and the training epochs to 200.

After using the trained model to get embedding vectors with 64 dimensions, we utilized K-means model to cluster these embedding vectors. In order to select the number of clusters accurately, we chose the number corresponding to the maximum silhouette coefficient while repeating clustering for cluster number change in ranges 2 to 10.

After clustering, we extracted keywords of clusters by LDA topic model using the text information in each cluster. We provide one topic and ten keywords for each cluster. The details can be found in Tables 3–5.

Table 3. Cluster information of grants.

Data Source	Time Slice	Cluster Number	Numbers of Entities	Keywords	Categories
Grants	2006–2012	0	19	nanometer, nanogenerator, structure, development, characteristic, application, utilize, piezoelectric, analysis, nanowire	PENG structure
Grants	2006–2012	1	2	nanometer, influence, wide band gap, energy, structure, research, characteristic, photoelectricity, stress, element	Undefined
Grants	2013–2017	0	55	nanogenerator, friction, drive, sensor, flexible, nanomaterial, structure, electric, piezoelectric, biology	PENG applications
Grants	2013–2017	1	12	piezoelectric, nanogenerator, ZnO, element, energy, structure, harvest, nanowire, power supply	PENG structure
Grants	2013–2017	2	9	nanometer, friction, structure, regulation, semiconductor, device, polymer, wearable, nanomaterial	Wearable devices
Grants	2018–2021	0	12	nanogenerator, structure, piezoelectric, wearable, biology, power supply, nanometer, element, application, detection	PENG applications
Grants	2018–2021	1	21	nanometer, friction, research, nanogenerator, harvest, performance, energy, mechanism, flexibility, application	TENG applications

Table 4. Cluster information of papers.

Data Source	Time Slice	Cluster Number	Numbers of Entities	Keywords	Categories
Paper	2006–2012	0	94	nanogenerator, piezoelectric, ZnO, flexible, transparent, sensor, nanowire, self-powered, array, substrate	PENG applications
Paper	2006–2012	1	28	nanogenerator, piezoelectric, nanostructure, ZnO, ultrasound, piezotronics, energy, nano-systems, oxide, self-powered	PENG structure
Paper	2006–2012	2	12	nanogenerator, self-powered, piezoelectric, graphene, alpha-particle, driven, actinium255, sensor, ZnO, energy	PENG materials
Paper	2013–2017	0	454	nanogenerator, triboelectric, energy, self-powered, harvesting, piezoelectric, sensor, flexible, wearable, system	Wearable devices

Table 4. *Cont.*

Data Source	Time Slice	Cluster Number	Numbers of Entities	Keywords	Categories
Paper	2013–2017	1	371	nanogenerator, triboelectric, piezoelectric, flexible, based, output, performance, effect, enhanced, application	Performance improvement
Paper	2018–2021	0	390	nanogenerator, piezoelectric, triboelectric, energy, harvesting, performance, composite, electrospun, nanofibers	Fiber structure
Paper	2018–2021	1	530	triboelectric, nanogenerator, performance, high, output, effect, charge, enhanced, effect, density	Performance improvement
Paper	2018–2021	2	918	triboelectric, nanogenerator, self-powered, sensor, wearable, flexible, system, monitoring, stretchable, motion	Wearable devices
Paper	2018–2021	3	507	triboelectric, nanogenerator, energy, harvesting, self-powered, mechanical, wave, water, wind, vibration	Energy source

Table 5. Cluster information of patents.

Data Source	Time Slice	Cluster Number	Numbers of Entities	Keywords	Categories
Patent	2006–2012	0	9	bubble, generator, treatment, water, method, involves, utilizing, based, micro-nano, controlled, nano	undefined
Patent	2006–2012	1	18	layer, zinc, substrate, piezoelectric, oxide, element, laminating, manufacturing, method, nanowire	Manufacturing method of PENG layers
Patent	2006–2012	2	35	piezoelectric, nanogenerator, structure, solar, power, electrical, conductive, energy, material, cell	PENG structure
Patent	2006–2012	3	43	electrode, layer, nanogenerator, substrate, piezoelectric, array, insulating, material, power, film	PENG materials
Patent	2013–2017	0	58	nanogenerator, energy, piezoelectric, element, storing, comprises, layer, substrate, electric, storage	PENGstructure
Patent	2013–2017	1	99	friction, layer, electrode, generator, nanogenerator, power, component, nano, surface, signal	TENG structure
Patent	2013–2017	2	56	friction, layer, triboelectric, nanogenerator, electrode, conductive, unit, power, generator, surface	TENG structure
Patent	2013–2017	3	60	layer, nanogenerator friction, electrode, film, polymer, piezoelectric, material, metal, flexible	TENG materials

Table 5. *Cont.*

Data Source	Time Slice	Cluster Number	Numbers of Entities	Keywords	Categories
Patent	2013–2017	4	64	generator, friction, device, energy, flexible, power, electric, nanogenerator, storage, nanometer	TENG application
Patent	2018–2021	0	128	friction, nanogenerator, connected, signal, electrode, system, layer, sensor, voltage, output	Performance improvement
Patent	2018–2021	1	106	triboelectric, nanogenerator, layer, film, piezoelectric, composite, material, electrode, flexible, generator	TENG materials
Patent	2018–2021	2	118	friction, nanogenerator, layer, energy, wearable, device, conductive, triboelectric, body, power	Wearable devices
Patent	2018–2021	3	87	layer, friction, electrode, nanogenerator, substrate, conductive, flexible, structure, material, comprises	TENG structure
Patent	2018–2021	4	103	friction, nanogenerator, generator, device, energy, water, plate, shaft, inner, connected, layer	TENG energy harvesting

All of the experimental procedures were based on Python 3 programming language and PyCharm platform.

From Tables 3–5, we can summarize the technology topic of different time slices. In 2006–2012, the main topic was the PENG structure and sensors based on PENG. In 2013–2017, the flexible sensors and wearable devices were the mainstream nanogenerator applications, while TENG began to appear and gradually replace PENG. In 2018–2021, wearable devices were still the research hotspots, while novel energy sources and the performance improvement of nanogenerators such as output voltage became the research questions.

4.2. Technology Evolution Pathways

Following the step of K-means, we calculate the vector distance of clusters in different time slices and connect the clusters with minimum distance while the minimum distance is smaller than the threshold (set to 2) to form the technology evolution pathways. The results are shown in Figure 3, in which the evolution pathways were automatically generated by calculating the similarity of the preceding clustering results using a written Python program. The dots in Figure 3 indicate the clusters which connect similar grants, papers, and patents. The line connections between dots indicate high similarity between different clusters, which can represent the knowledge flow and indicate the technology evolution pathways.

From Figure 3, we can analyze the knowledge flow pathways between data sources. First, we can find that the knowledge flows from grants to papers were faster than that from papers to patents, as the technologies proposed by grants can be found in papers in the same time slice but can be found in patents in the backward time slice. An explanation for this condition is that making a profound study is easier than applying theory to application.

Then, we can find several knowledge flows from research to application successfully. The most typical case is the wearable devices with nanogenerator sensors. Wearable devices were proposed by grants in cluster 2 in 2013–2017 based on the basic research of nanogenerator structures and materials, and then get a profound study by scholars in 2013–2017. Finally, after abundant research about the performance of flexible sensors and the development of remote monitoring and communication technology, wearable devices based on flexible and self-powered nanogenerators were applied in daily life. In addition, based on Figure 3, we can also monitor the evolutionary pathways of piezoelectric nanogenerators.

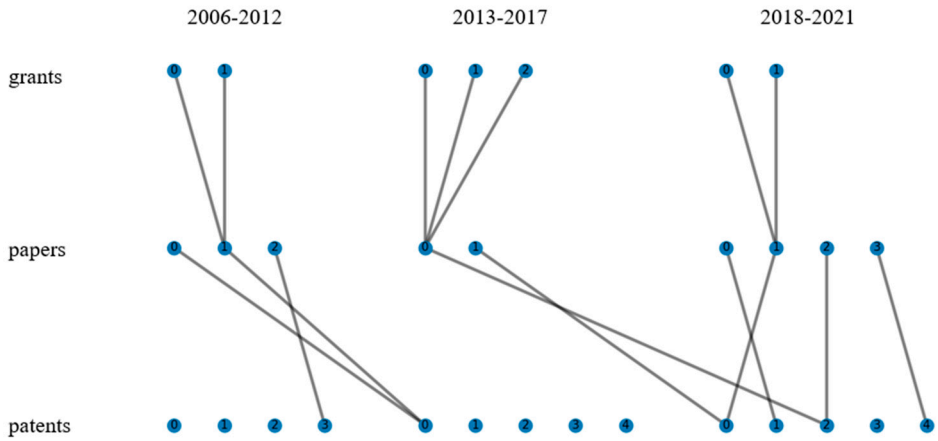

Figure 3. Evolution pathways between different data sources.

Except for these obvious evolution pathways, we can find several isolated short pathways in 2018–2021, which represent the technologies with strong innovativeness. Specifically, cluster 3 of papers in 2018–2021 contains the keywords "mechanical", "wave", "wind", "water", "vibration", "energy" and "harvesting", and cluster 4 of patents in 2018–2021 contains the keywords "water" and "energy". These keywords demonstrate that novel energy sources such as wind, water, and mechanical vibration became new research directions and hotspots. Cluster 0 of papers in 2018–2021 represents the fiber structure of nanogenerators, which indicates the innovation direction of nanogenerator structures.

5. Conclusions

This paper proposed a novel framework to monitor the evolutionary pathways of nanogenerator technology based on multi-source data and a knowledge graph. In the framework, the knowledge graph makes full use of text information, and the multi-source data fully considers the evolutionary pathways from different data perspectives. Additionally, we show that the novel framework is efficient and accurate.

We find some characteristics that the evolution process and knowledge flow from grants to patents is faster than that from papers to patents, which indicates that making a profound study is easier than applying theories to applications. We also monitor the complete evolution pathways of piezoelectric nanogenerators, wearable devices, and nanogenerator performance improvement technologies. While analyzing the evolution pathways, we also find several emerging research directions for nanogenerators, such as novel energy sources and fiber structure of nanogenerators.

However, due to the numbers of grants, papers, and patents in the nanogenerator field, we cannot unleash the full advantage of the knowledge graph and representation learning. In the meantime, the identification of cluster topics requires expert knowledge and human intervention. So, in future research, we will attempt to get more data and use the machine learning method to achieve the automatic classification of cluster topics.

Author Contributions: Conceptualization, Y.L. (Yufei Liu) and Y.Z.; methodology, Y.L. (Yufei Liu) and G.W.; software, validation, data curation, writing—original draft preparation, visualization, G.W.; resources, project administration, Y.L. (Yufei Liu); writing—review and editing, Y.L. (Yufei Liu) and Y.L. (Yuhan Liu); supervision, Y.Z.; funding acquisition, Y.Z. and Y.L. (Yufei Liu). All authors have read and agreed to the published version of the manuscript.

Funding: This research was funded by the National Natural Science Foundation of China [grant numbers 72104224, 71974107, L2124002, 91646102, L1924058]; the MOE (Ministry of Education in China) Project of Humanities and Social Sciences [grant number 16JDGC011]; the Construction Project of China Knowledge Center for Engineering Sciences and Technology [grant number CKCEST-2021-2-7]; the Tsinghua University Initiative Scientific Research Program [grant number 2019Z02CAU]; and

the Tsinghua University Project of Volvo-Supported Green Economy and Sustainable Development [grant number 20183910020].

Institutional Review Board Statement: Not applicable.

Informed Consent Statement: Not applicable.

Data Availability Statement: Not applicable.

Conflicts of Interest: The authors declare no conflict of interest.

References

1. Gabris, M.A.; Ping, J. Carbon nanomaterial-based nanogenerators for harvesting energy from environment. *Nano Energy* **2021**, *90*, 106494. [CrossRef]
2. Sun, M.; Li, Z.; Yang, C.; Lv, Y.; Yuan, L.; Shang, C.; Liang, S.; Guo, B.; Liu, Y.; Li, Z.; et al. Nanogenerator-based devices for biomedical applications. *Nano Energy* **2021**, *89*, 106461. [CrossRef]
3. Zhao, X.; Askari, H.; Chen, J. Nanogenerators for smart cities in the era of 5G and Internet of Things. *Joule* **2021**, *5*, 1391–1431. [CrossRef]
4. Mahapatra, B.; Patel, K.K.; Vidya; Patel, P.K. A review on recent advancement in materials for piezoelectric/triboelectric nanogenerators. *Mater. Today Proc.* **2021**, *46*, 5523–5529. [CrossRef]
5. Zhang, D.; Xu, Z.; Yang, Z.; Song, X. High-performance flexible self-powered tin disulfide nanoflowers/reduced graphene oxide nanohybrid-based humidity sensor driven by triboelectric nanogenerator. *Nano Energy* **2020**, *67*, 104251. [CrossRef]
6. Wang, S.; He, M.; Weng, B.; Gan, L.; Zhao, Y.; Li, N.; Xie, Y. Stretchable and Wearable Triboelectric Nanogenerator Based on Kinesio Tape for Self-Powered Human Motion Sensing. *Nanomaterials* **2018**, *8*, 657. [CrossRef]
7. Shin, D.M.; Hong, S.W.; Hwang, Y.H. Recent Advances in Organic Piezoelectric Biomaterials for Energy and Biomedical Applications. *Nanomaterials* **2020**, *10*, 123. [CrossRef]
8. Li, X.; Fan, M.; Zhou, Y.; Fu, J.; Yuan, F.; Huang, L. Monitoring and forecasting the development trends of nanogenerator technology using citation analysis and text mining. *Nano Energy* **2020**, *71*, 104636. [CrossRef]
9. Wang, B.; Liu, Y.; Zhou, Y.; Wen, Z. Emerging nanogenerator technology in China: A review and forecast using integrating bibliometrics, patent analysis and technology roadmapping methods. *Nano Energy* **2018**, *46*, 322–330. [CrossRef]
10. Li, M.; Zhou, Y. Visualizing the knowledge profile on self-powered technology. *Nano Energy* **2018**, *51*, 250–259. [CrossRef]
11. Miao, Z.; Du, J.; Dong, F.; Liu, Y.; Wang, X. Identifying technology evolution pathways using topic variation detection based on patent data: A case study of 3D printing. *Futures* **2020**, *118*, 102530. [CrossRef]
12. Liu, H.; Chen, Z.; Tang, J.; Zhou, Y.; Liu, S. Mapping the technology evolution path: A novel model for dynamic topic detection and tracking. *Scientometrics* **2020**, *125*, 2043–2090. [CrossRef]
13. Zhou, Y.; Dong, F.; Kong, D.; Liu, Y. Unfolding the convergence process of scientific knowledge for the early identification of emerging technologies. *Technol. Forecast. Soc. Change* **2019**, *144*, 205–220. [CrossRef]
14. Kong, D.; Yang, J.; Li, L. Early identification of technological convergence in numerical control machine tool: A deep learning approach. *Scientometrics* **2020**, *125*, 1983–2009. [CrossRef]
15. Zhou, Y.; Miao, Z.; Urban, F. China's leadership in the hydropower sector: Identifying green windows of opportunity for technological catch-up. *Ind. Corp. Change* **2020**, *29*, 1319–1343. [CrossRef]
16. Zhou, Y.; Dong, F.; Liu, Y.; Li, Z.; Du, J.; Zhang, L. Forecasting emerging technologies using data augmentation and deep learning. *Scientometrics* **2020**, *123*, 1–29. [CrossRef]
17. Zhou, Y.; Zang, J.; Miao, Z.; Minshall, T. Upgrading Pathways of Intelligent Manufacturing in China: Transitioning across Technological Paradigms. *Engineering* **2019**, *5*, 691–701. [CrossRef]
18. Zhou, Y.; Li, X.; Lema, R.; Urban, F. Comparing the knowledge bases of wind turbine firms in Asia and Europe: Patent trajectories, networks, and globalisation. *Sci. Public Policy* **2016**, *43*, 476–491. [CrossRef]
19. Liu, Y.; Zhou, Y.; Liu, X.; Dong, F.; Wang, C.; Wang, Z. Wasserstein GAN-Based Small-Sample Augmentation for New-Generation Artificial Intelligence: A Case Study of Cancer-Staging Data in Biology. *Engineering* **2019**, *5*, 156–163. [CrossRef]
20. Jin, L.; Zhang, B.; Zhang, L.; Yang, W. Nanogenerator as new energy technology for self-powered intelligent transportation system. *Nano Energy* **2019**, *66*, 104086. [CrossRef]
21. Wang, Z.L.; Song, J. Piezoelectric nanogenerators based on zinc oxide nanowire arrays. *Science* **2006**, *312*, 242–246. [CrossRef] [PubMed]
22. Shin, S.-H.; Kim, Y.-H.; Lee, M.H.; Jung, J.-Y.; Nah, J. Hemispherically aggregated $BaTiO_3$ nanoparticle composite thin film for high-performance flexible piezoelectric nanogenerator. *ACS Nano* **2014**, *8*, 2766–2773. [CrossRef] [PubMed]
23. Park, K.I.; Son, J.H.; Hwang, G.T.; Jeong, C.K.; Ryu, J.; Koo, M.; Choi, I.; Lee, S.H.; Byun, M.; Wang, Z.L.; et al. Highly-efficient, flexible piezoelectric PZT thin film nanogenerator on plastic substrates. *Adv. Mater.* **2014**, *26*, 2514–2520. [CrossRef] [PubMed]
24. Jin, L.; Ma, S.; Deng, W.; Yan, C.; Yang, T.; Chu, X.; Tian, G.; Xiong, D.; Lu, J.; Yang, W. Polarization-free high-crystallization β-PVDF piezoelectric nanogenerator toward self-powered 3D acceleration sensor. *Nano Energy* **2018**, *50*, 632–638. [CrossRef]
25. Fan, F.-R.; Tian, Z.-Q.; Lin Wang, Z. Flexible triboelectric generator. *Nano Energy* **2012**, *1*, 328–334. [CrossRef]

26. Khandelwal, G.; Minocha, T.; Yadav, S.K.; Chandrasekhar, A.; Maria Joseph Raj, N.P.; Gupta, S.C.; Kim, S.-J. All edible materials derived biocompatible and biodegradable triboelectric nanogenerator. *Nano Energy* **2019**, *65*, 104016. [CrossRef]
27. Singh, H.H.; Khare, N. Flexible ZnO-PVDF/PTFE based piezo-tribo hybrid nanogenerator. *Nano Energy* **2018**, *51*, 216–222. [CrossRef]
28. Erwin, D.H.; Krakauer, D.C. Insights into innovation. *Science* **2004**, *304*, 1117. [CrossRef]
29. Valverde, S.; Sole, R.V.; Bedau, M.A.; Packard, N. Topology and evolution of technology innovation networks. *Phys. Rev. E Stat. Nonlin. Soft Matter Phys.* **2007**, *76*, 056118. [CrossRef]
30. Boulkedid, R.; Abdoul, H.; Loustau, M.; Sibony, O.; Alberti, C. Using and reporting the Delphi method for selecting healthcare quality indicators: A systematic review. *PLoS ONE* **2011**, *6*, e20476. [CrossRef]
31. Huenteler, J.; Ossenbrink, J.; Schmidt, T.S.; Hoffmann, V.H. How a product's design hierarchy shapes the evolution of technological knowledge—Evidence from patent-citation networks in wind power. *Res. Pol.* **2016**, *45*, 1195–1217. [CrossRef]
32. Zhou, X.; Zhang, Y.; Porter, A.L.; Guo, Y.; Zhu, D. A patent analysis method to trace technology evolutionary pathways. *Scientometrics* **2014**, *100*, 705–721. [CrossRef]
33. Yoon, B.; Park, Y. A text-mining-based patent network: Analytical tool for high-technology trend. *J. High Technol. Manag. Res.* **2004**, *15*, 37–50. [CrossRef]
34. Socher, R.; Chen, D.; Manning, C.D.; Ng, A.Y. Reasoning With Neural Tensor Networks for Knowledge Base Completion. In Proceedings of the Annual Conference on Neural Information Processing Systems, Lake Tahoe, NV, USA, 5–10 December 2013; pp. 926–934.
35. Bordes, A.; Usunier, N.; Garcia-Duran, A. Translating Embeddings for Modeling Multi-relational Data. In Proceedings of the Annual Conference on Neural Information Processing Systems, Lake Tahoe, NV, USA, 5–10 December 2013; pp. 2787–2795.
36. Wang, Z.; Zhang, J.; Feng, J.; Chen, Z. Knowledge Graph Embedding by Translating on Hyperplanes. In Proceedings of the 28th AAAI Conference on Artificial Intelligence, Quebec City, QC, Canada, 27–31 July 2014; pp. 1112–1119.
37. Lin, Y.; Liu, Z.; Sun, M.; Liu, Y.; Zhu, X. Learning Entity and Relation Embeddings for Knowledge Graph Completion. In Proceedings of the 29th AAAI Conference on Artificial Intelligence, Austin, TX, USA, 25–30 January 2015; pp. 2181–2187.
38. Ji, G.; He, S.; Xu, L.; Liu, K.; Zhao, J. Knowledge Graph Embedding via Dynamic Mapping Matrix. In Proceedings of the 7th International Joint Conference on Natural Language Processing, Beijing, China, 26–31 July 2015; pp. 687–696.
39. Kipf, T.N.; Welling, M. Semi-Supervised Classification with Graph Convolutional Networks. In Proceedings of the 5th International Conference on Learning Representations, Toulon, France, 24–26 April 2017.
40. Velickovi, P.; Cucurull, G.; Casanova, A.; Romero, A.; Lio, P.; Bengio, Y. Graph Attention Networks. In Proceedings of the 6th International Conference on Learning Representations, Toulon, France, 30 April–3 May 2018.
41. Kipf, T.N.; Welling, M. Variational Graph Auto-Encoders. In Proceedings of the NIPS Workshop on Bayesian Deep Learning, Barcelona, Spain, 9–10 December 2016.
42. Fan, S.; Zhu, J.; Han, X.; Shi, C.; Hu, L.; Ma, B.; Li, Y. Metapath-guided Heterogeneous Graph Neural Network for Intent Recommendation. In Proceedings of the 25th ACM SIGKDD International Conference on Knowledge Discovery & Data Mining, Anchorage, AK, USA, 4–8 August 2019; pp. 2478–2486.
43. Wang, X.; Ji, H.; Shi, C.; Wang, B.; Cui, P.; Yu, P.; Ye, Y. Heterogeneous Graph Attention Network. In Proceedings of the 19th International Conference on World Wide Web, San Francisco, CA, USA, 13–17 May 2019.

nanomaterials

MDPI

Article

Unveiling Evolutionary Path of Nanogenerator Technology: A Novel Method Based on Sentence-BERT

Huailan Liu [1], Rui Zhang [1], Yufei Liu [2,*] and Cunxiang He [1]

[1] School of Mechanical Science and Engineering, Huazhong University of Science and Technology, Wuhan 430074, China; lhlan309@163.com (H.L.); zr2020@hust.edu.cn (R.Z.); hcx@hust.edu.cn (C.H.)
[2] Center for Strategic Studies, Chinese Academy of Engineering, Beijing 100088, China
* Correspondence: liuyf@cae.cn

Abstract: In recent years, nanogenerator technology has developed rapidly with the rise of cloud computing, artificial intelligence, and other fields. Therefore, the quick identification of the evolutionary path of nanogenerator technology from a large amount of data attracts much attention. It is of great significance in grasping technical trends and analyzing technical areas of interest. However, there are some limitations in previous studies. On the one hand, previous research on technological evolution has generally utilized bibliometrics, patent analysis, and citations between patents and papers, ignoring the rich semantic information contained therein; on the other hand, its evolution analysis perspective is single, and it is difficult to obtain accurate results. Therefore, this paper proposes a new framework based on the methods of Sentence-BERT and phrase mining, using multi-source data, such as papers and patents, to unveil the evolutionary path of nanogenerator technology. Firstly, using text vectorization, clustering algorithms, and the phrase mining method, current technical themes of significant interest to researchers can be obtained. Next, this paper correlates the multi-source fusion themes through semantic similarity calculation and demonstrates the multi-dimensional technology evolutionary path by using the "theme river map". Finally, this paper presents an evolution analysis from the perspective of frontier research and technology research, so as to discover the development focus of nanogenerators and predict the future application prospects of nanogenerator technology.

Keywords: technology evolutionary path; multi-source data; nanogenerator; text vectorization; theme mining; theme river map

Citation: Liu, H.; Zhang, R.; Liu, Y.; He, C. Unveiling Evolutionary Path of Nanogenerator Technology: A Novel Method Based on Sentence-BERT. *Nanomaterials* **2022**, *12*, 2018. https://doi.org/10.3390/nano12122018

Academic Editor: Fabrizio Pirri

Received: 10 May 2022
Accepted: 9 June 2022
Published: 11 June 2022

1. Introduction

Nanogenerators are an emerging technology that has attracted a great deal of attention. Nanogenerators are promising for applications in areas including, but not limited to, self-powered systems, mechanical or thermal energy harvesting, and smart wearable devices (SWD) [1–3]. At present, the innovation in and research on nanogenerators mainly faces two challenges. The first challenge is that since there are multiple evolutionary paths for nanogenerators, it is difficult to grasp their real development trend. The second challenge is that nanotechnology has many subfields, such as nanomaterials, nanoscale measurements, and nanoscale processing. Nanogenerator technology will cross-penetrate and converge with other nanotechnology sub-fields. The connection between these fields is constantly strengthening and changing. Therefore, it is of great practical significance to determine the development context of nanogenerators, unveil the evolutionary path, and judge the development trends and directions.

The evolutionary path of nanogenerator technology describes the emergence, transition, and demise of different technical themes, which can help researchers understand the history and status of the research field, so as to identify research areas of interest and gaps quickly. Some experts have studied the evolutionary path and trends of nanogenerator technology. These studies are based on expert knowledge and literature reviews, and the

research contents involve nanogenerators' research directions or a sub-field of nanogenerators [4–8]. With the rapid development of nanogenerators, some experts have used quantitative methods, such as bibliometrics, patent citation analysis, technology roadmap, and text mining, to analyze the evolution trend of nanogenerators [9,10]. However, the method of bibliometrics can only be used to conduct simple statistical analysis, and it is difficult to deeply examine technical texts to obtain specific technical descriptions. Patent citation analysis is limited by the type of citation data and ignores the technical knowledge contained in the literature. Furthermore, poor evolution information and biased results result from using single-dimensional data to contain the technology's evolutionary path. In order to solve the above problems, we consider the mining of the themes of technical texts in papers and patents through text-mining methods. The typical methods include statistics-based keyword extraction methods (such as TF-IDF and RAKE) and theme model methods (such as LDA, ATM), etc. Since the theme model method is not limited by the type of reference data, it can mine most of the data.

This paper proposes a multi-source data-association analysis framework based on the text vectorization method, which improves the traditional theme model method in two respects. On the one hand, this paper uses automatic phrase mining instead of keyword mining, which improves the mining depth of generator information and the interpretability of the results. On the other hand, this paper uses multi-source text information to identify the evolutionary path of nanogenerators. Next, this paper unveils the evolutionary path clearly through the method of theme river map, so as to discover the current development focus of nanogenerators and predict the future application prospects of nanogenerator technology.

2. Literature Review

2.1. Development of Nanogenerators

With the continuous development of emerging technologies in artificial intelligence, electronic information, and advanced materials, implantable and wearable electronic products have gained traction, such as devices implanted in vivo (pacemakers, neurostimulators), smart watches, glasses, and bracelets [11–19]. In practical medical applications, these electronic products can only be powered by an external power source, resulting in their bulky size and high energy consumption, and they need to be replaced regularly. Therefore, these electronic products require the characteristics of scalability and flexibility [20,21], and the development of sustainable forms of the power supply is the core source of competitiveness in the market. In 2006, Professor Zhong-Lin Wang invented the world's first piezoelectric nanogenerator (PENG) based on a ZnO nanowire array, which generates an electric field by piezoelectric polarization and drives the movement of electrons, converting mechanical energy into electricity [22]. The initial piezoelectric materials are generally ZnO [23–27], lead zirconate titanate (PZT) [28–34], $BaTiO_3$ (BT) [35–39], and polyvinylidene fluoride [40–43]. Triboelectric nanogenerators (TENG) were first produced in 2011 and were based on the combination of triboelectric electrification and electrostatic induction. Compared with PENGs, TENGs have the advantages of high yield, low cost, simple structural design, and good stability. Currently, TENGs are widely used in various fields due to their excellent performance [44–46], such as Shi et al.'s [47] self-powered flexible microfluidic sensor based on triboelectric charging at the liquid–solid interface, which is used for pressure-sensing and finger-movement-monitoring applications. Yi et al. [48] proposed a stretchable rubber-based TENG with a single-electrode mode as a self-powered body-motion sensor.

2.2. Technology Evolutionary Path

The technology evolutionary path originated in the 1940s, which can reveal technological evolution. As a powerful presentation of technological development, the technology evolutionary path can track historical development, explore knowledge diffusion, and predict future technological trends [49–52]. The technology evolutionary path describes the

emergence, transition, and demise of technologies, helping technical managers and related researchers to understand the process and the current state of technological development, in order to identify and locate major technologies and technical priorities quickly [53–62].

In the field of technological evolution research, the research methods mainly fall within the following categories: bibliometrics, social network analysis, and text mining. The common method of early technology evolutionary path research is bibliometrics, which analyzes technological evolution through simple index measurement, co-occurrence analysis, and co-citation analysis. The data sources for these analyses are mainly papers or patent data. Gao, L. et al. [63] proposed a technology life-cycle analysis combining a variety of patent metrics. Co-occurrence analysis is also an important analysis method in bibliometrics, including co-word analysis, proposed by Callon et al. [64], co-author analysis, proposed by Braun et al. [65], and co-citation analysis, proposed by Small [61], among others. The development of bibliometrics is relatively mature, and most of its methods are based on co-occurrence analysis and citation analysis. The principle of this method is relatively simple, and the results can be obtained quickly, but it is difficult to mine the technology evolutionary path directly in this way.

Social network analysis methods are used for the technical mining of the citation information contained in the scientific literature; specific examples of these methods include main path analysis and network topology clustering. Small [66] studied knowledge diffusion through main path analysis, and Kim and Shin [67] identified the main technical paths of HVDC technology through main path analysis. Network topology clustering enables the deeper mining of citation networks and identifies major research communities in the citation network. Chen et al. [68] used the Girvan–Newman clustering algorithm to identify clusters of patent citation networks and found several major technology clusters included in fuel-cell technology, thereby analyzing technological evolution. However, social network analysis ignores important semantic information in the literature data, and the depth of information mining is limited.

At present, the research on technological evolution is based on text mining for technology mining and quantitative analysis. For research data, such as patent papers, this method uses keyword extraction or the theme model to mine text information [69] (including titles, abstracts, claims, etc.) and analyzes the text information based on words or themes [70]. For example, Li et al. used citation analysis to monitor and predict the development trend of nanogenerators, and used the hierarchical Dirichlet Process theme model to extract technical themes [71].

2.3. Research on Multi-Source Data and Text Mining

Using papers or patents for technological evolution analysis alone can cause data defects, and the analysis results are often affected by the inherent characteristics of the data, which ultimately affect the accuracy of the analysis. Specifically, papers are focused on the advancement of scientific knowledge, so it is difficult to judge the application of the technology in industry [69]; patents are more inclined to describe the status of technological development but may ignore forward- scientific ideas [69]. In response to the problem of knowledge bias and lack of information caused by single data, some researchers have begun to consider multi-source data analysis to expand the data dimension and analysis perspective. They improve the comprehensiveness of technology evolution analysis by combining these mining data. In general, researchers collect different types of data (including papers, patents, product databases, trade data, news, policy reports, business data, etc.) and combine them with big data fusion and processing methods for technical mining.

In the current research on the technology evolutionary path, finding and presenting thematic information is the key issue, but the results obtained by the theme mining method are keywords, which are difficult to interpret manually. Keyword mining can be further optimized into phrase mining. Compared with technical keywords, technical phrases provide semantic metadata to summarize and describe documents. High-quality phrases

contain relatively complete technical information, which is easier for analysts to analyze and can greatly improve the efficiency of technical mining. In the field of phrase mining, TF-IDF is the earliest keyword or phrase extraction algorithm; it ranks phrases according to the frequency of words and inverse document frequency. It considers fewer information extraction factors, so the quality of phrases is usually uncontrollable. KEA is a classic supervised keyword extraction algorithm. It first finds candidate key phrases in the article according to the dictionary, then calculates the phrase feature values and predicts key phrases based on machine learning algorithms [72]. However, KEA is a supervised keyword extraction algorithm that relies on feature computation and has a low degree of automation.

The latest phrase mining research has made great breakthroughs, mainly including a series of phrase-mining algorithms proposed by Han Jiawei et al., such as TopMine, SegPhrase, and AutoPhrase. The previous unigram model (Uni-gram) regards words as the basic units and does not consider contextual meanings, while TopMine's theme mining of text corpus is carried out in two steps, avoiding the segmentation of words in a phrase. The first step carries out phrase mining for text segmentation, and the second step adds phrase constraints for LDA theme modeling [73]. TopMine is an unsupervised method based on frequency pattern mining and statistical analysis. The SegPhrase algorithm adds labeling work to TopMine, and the quality of the generated phrases is close to the phrase judgment ability of humans [74]. SegPhrase has good scalability and is suitable for large text corpora. In order to avoid manual labeling, Shang et al. [75] proposed the AutoPhrase algorithm. The aim of the AutoPhrase algorithm is to obtain many high-quality phrases from the public knowledge base, and to use these high-quality phrases to generate a large number of positive sample labels. AutoPhrase achieves better performance, further removing the need for additional manual labeling work [75].

3. Methods

This paper takes multi-source text information mining as the research starting point. First, we present the multi-source data we collected, such as papers and patents, in the field of nanogenerators. Next, we propose a new theme model method to support multi-source data fusion analysis. Finally, we analyze the field from the perspective of frontier science and technological application. We aim to identify the development priorities and future prospects of nanogenerators through the technology evolutionary path. This paper proposes a multi-source data theme modeling method, SKT (Sentence-BERT-KMeans++-TopMine), based on Sentence-BERT and phrase mining. The method flow is shown in Figure 1.

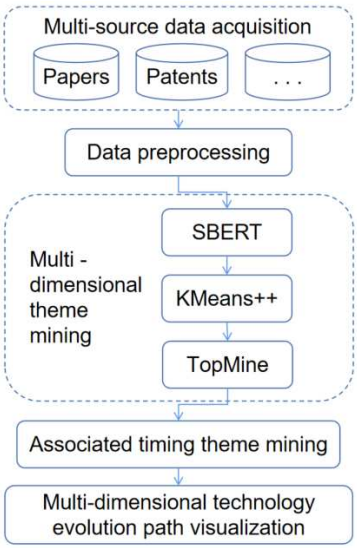

Figure 1. Method and process.

3.1. Data

First, we selected the Thomson Reuters database, Web of Science (WOS). By establishing a search strategy, we searched papers based on keywords in the field of nanogenerators. We collected paper data from 2006 to 2022, including the title of the article, citations, abstracts, and other information. Our patent data were then sourced from the Derwent Innovation Index (DII) and Derwent Innovation Platform (DI) databases. By combining the keywords in the field of nanogenerators and the relevant classification numbers to formulate a patent search formula, we collected patent data from 2006 to 2022, including patent names, citation information, times, and abstracts. Eventually, we retrieved 2373 papers and 984 patents.

3.2. Theme Modeling Based on Sentence-BERT

The theme modeling of multi-source text data in this paper includes three steps: multi-source text vectorization, document vector clustering to identify themes, and high-quality phrase mining to identify thematic content.

(1) Vectorization of multi-source text documents based on Sentence-BERT algorithm. Sentence-BERT is a Siamese network based on pre-trained BERT. It can obtain document vectors that are sufficiently semantically meaningful. The algorithm performs optimally on multiple semantic textual similarity (STS) benchmark tasks [76]. We used Sentence-BERT for vectorized representation of multi-source text data to achieve unified representation and fusion of multi-source text data in the same semantic vector space.

(2) Identify themes by clustering document vectors with the KMeans++ algorithm. KMeans++ algorithm is one of the commonly used unsupervised clustering algorithms, which can perform clustering tasks on unlabeled datasets. KMeans++ uses the vector distance as the standard for dividing categories. Its clustering process is fast and simple, so it is suitable for clustering of large vector data. In this paper, we use KMeans++ to perform clustering learning on document vector clusters and divide documents into subject categories. We regard one document cluster as one theme.

(3) Mining high-frequency phrases in document clusters as theme content based on TopMine. TopMine is an unsupervised, fully automatic phrase-extraction algorithm proposed by Han Jiawei et al. in 2014 [73]. Based on frequent pattern mining and statistical analysis, it can automatically extract high-quality phrases from a large number of emerging text corpora. This paper uses TopMine to extract key phrases from multi-source document sets, and the extracted phrases are used as the semantic content of theme document clusters, so as to complete the semantic representation of themes.

3.3. Unveiling Evolutionary Path Based on Associated Timing Theme

Before the time-series theme analysis, papers and patent data were segmented according to time, that is, divided into several document intervals. Next, we placed the text document into the corresponding time interval according to the year information. Subsequently, each document had three attributes: time segment number, multi-source data type (analysis dimension), and theme number, which were used for multi-dimensional time-series analysis.

Table 1 presents time slice processing of papers and patent data. This resulted in a total of seven time slices. Next, based on these seven time slices, the time-series theme evolution analysis of multi-source data was carried out.

Table 1. Time segment.

Time Segment Number	**1**	**2**	**3**	**4**	**5**	**6**	**7**
time segment	2006~2010	2010~2012	2012~2014	2014~2016	2016~2018	2018~2020	2020~2022

The multi-source time-series theme association has four association dimensions: (1) the association between sub-themes derived from the same type of data; (2) the association

between sub-themes derived from different types of data; (3) the association between the same multi-source fusion theme; (4) the association between different multi-source fusion themes. This paper focuses on the association between fusion themes. If the same sub-theme or fusion theme appeared continuously on the timeline, they were associated.

For the association of different fusion themes, we used cosine similarity between mean vectors of document clusters to judge, and the similarity between mean vectors was regarded as the semantic similarity of the fusion themes. The specific process was as follows: 1. Separate documents based on time segment and theme into clusters and obtain vectors of document clusters by index. 2. Calculate the mean vector of the batch of high-dimensional vectors; the mean vector is regarded as the theme semantic vector. 3. Calculate the cosine similarity between each pair of different themes in adjacent time segments, and plot the distribution of cosine similarities 4. Referring to the pre-similarity distribution diagram, set the similarity correlation threshold, and associate the corresponding theme pairs higher than this threshold.

The range of cosine similarity was (0~1). The closer the similarity is to 0, the more similar the themes. The key to the association of different themes is the selection of the similarity threshold. In order to obtain more effective information and less interfering information, the selection of threshold in this study tended to be conservative, so as to make fewer associations and introduce invalid interference information as little as possible, so as to make the final evolution diagram neat and easy to analyze.

3.4. Visualization of Multi-Dimensional Technology Evolutionary Path

The technology evolutionary path is suitable for presentation in the visual form of "theme river map". The primary use of river map is to present the theme evolution of text data. The implementation methods include ThemeRiver and TextFlow [77,78]. TextFlow is an extension of ThemeRiver. It expresses not only the changes in themes over time, but also the splitting and merging of various themes over time. For example, a theme is divided into two, or multiple themes are merged into one, at a certain time. This can help researchers to better intuitively analyze the evolution patterns between themes. In recent years, some researchers have used multi-source data for technical and industrial analysis [79]. This paper is mainly based on TextFlow's research work on river maps and uses the D3.js language for implementation [80]. Next, we present the design of a visualization scheme for multi-dimensional data fusion theme paths.

Figure 2 presents a thematic river map for unidimensional data. The "rivers" with varying thickness in the figure represent different themes, each of which is distinguished by a different color; each vertical line shows the time segment information, and the "red nodes" on the line represent different themes; the text above the red nodes is brief information about the theme, and the number in brackets is the node number.

As shown in Figure 3, the specific information presentation mainly includes the following improvements, which are not only conducive to the presentation of rich details but also to expert interactions or peer discussion: (1) Display of theme type, data source, and theme number. In "(43) 2S", on the left of Figure 3, 43 is the node number, 2 refers to the theme number, S represents that the theme dimension is in the scientific dimension, and the data source is the WOS paper data. (2) Presentation of the key information of the theme and help the content analysis of the theme. As shown in Figure 3, hovering the mouse near the red node causes the display of detailed information. The figure presents the detailed information of theme 11, including the list of high-frequency theme phrases TOP5 and five randomly selected pieces of document-title information. (3) Display of information on multi-source fusion themes and uses the abbreviation S/T, for Science and Technology, to indicate their attributes. For example, node 11, "theme (11) 5ST (9:1)", indicates that this is a fusion theme of Science and Technology, and the document ratio is 9:1. In the theme details list, the high-frequency-phrase list and phrase frequency are displayed, and the multi-source text titles of multi-source data sources are marked.

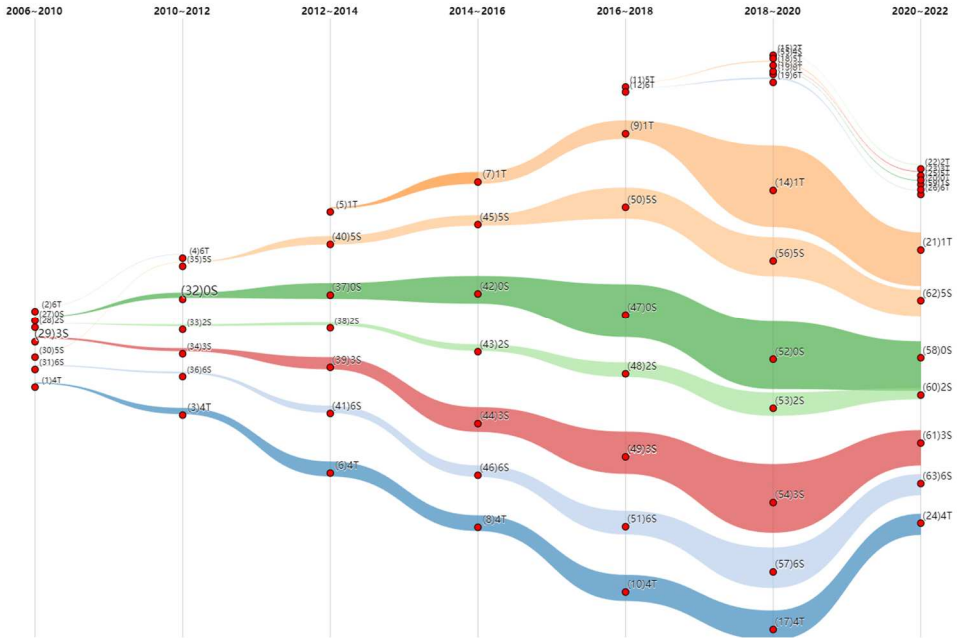

Figure 2. Multi-source theme river map.

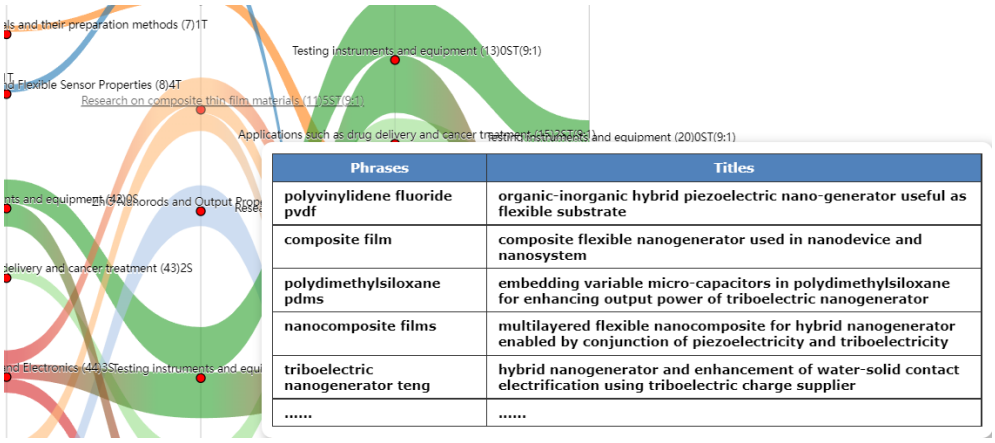

Phrases	Titles
polyvinylidene fluoride pvdf	organic-inorganic hybrid piezoelectric nano-generator useful as flexible substrate
composite film	composite flexible nanogenerator used in nanodevice and nanosystem
polydimethylsiloxane pdms	embedding variable micro-capacitors in polydimethylsiloxane for enhancing output power of triboelectric nanogenerator
nanocomposite films	multilayered flexible nanocomposite for hybrid nanogenerator enabled by conjunction of piezoelectricity and triboelectricity
triboelectric nanogenerator teng	hybrid nanogenerator and enhancement of water-solid contact electrification using triboelectric charge supplier
.....	.....

Figure 3. Information presentation of fusion themes.

4. Experimental Results and Discussion

4.1. Multi-Source Theme Identification and Association

According to the theme modeling method proposed in Section 3, we performed joint theme modeling on the papers and patent data corresponding to the scientific and technical layers. As shown in Table 2, according to the high-frequency phrases generated by the time-series theme mining, the seven themes were: testing instruments and equipment (theme 0), research on electrode materials and their preparation methods (theme 1), applications such as drug delivery and cancer treatment (theme 2), wearables and electronics (theme 3), piezoelectric materials and flexible sensor properties (theme 4), research on composite thin-film materials (theme 5), and ZnO nanorods and output properties (theme 6). Next, multi-source time-series theme mining and analysis were carried out to obtain the sub-theme information of each theme corresponding to the different data types and time segments. Finally, we carried out the association of the themes and then identified the theme evolutionary path.

Table 2. Theme modeling results of multi-source fusion texts.

Theme Number	Theme	High-Frequency Theme Phrases
0	Testing instruments and equipment	triboelectric-nanogenerator-based, 54; light-emitting-diodes (LEDs), 33; powered sensor, 32; surface charge density, 32; electronic devices, 30.
1	Research on electrode materials and their preparation methods	friction electric nano generator, 41; nano generator preparation, 30; friction electrode, 29; friction material, 23; electrode layers, 22.
2	Applications such as drug delivery and cancer treatment	triboelectric nanogenerator, 56; drug delivery, 17; cancer therapy, 13; electrical stimulation, 12; drug release, 11.
3	Wearables and electronics	triboelectric nanogenerator teng, 105; wearable electronics, 68; wearable devices, 45; electronic devices, 44; powered sensors, 36.
4	Piezoelectric materials and flexible sensor properties	piezoelectric nano generator, 29; flexible nano generator, 17; high molecular polymer insulating, 16; molecular polymer insulating layer, 16; piezoelectric layer, 16.
5	Research on composite thin-film materials	triboelectric nanogenerator teng, 47; polyvinylidene fluoride pvdf, 34; composite film, 24; polydimethylsiloxane pdms, 22; nanocomposite films, 20.
6	ZnO nanorods and output properties	triboelectric nanogenerator, 57; zno nanorods, 44; output performance, 29; piezoelectric output, 27; zinc oxide zno, 25; electrical output, 22;

We can also use the number of documents to measure the strength of the theme, as shown in Figure 4. This paper draws a schematic diagram of the evolution of multi-source themes with seven themes. The horizontal axis is the time segment from 2006 to 2022, and the vertical axis is the theme number. The themes are divided according to data types, including scientific sub-themes (WOS paper data), circled in blue, and technical sub-themes (DI patent data), circled in red. In the time-series theme-evolution diagram, most of the sub-themes are placed continuously along the timeline (as shown in the blue scientific theme on the timeline of theme 6, at the top of Figure 4), and some sub-themes merge (such as theme 6, where science and technology themes appeared simultaneously in multiple consecutive time segments after 2018).

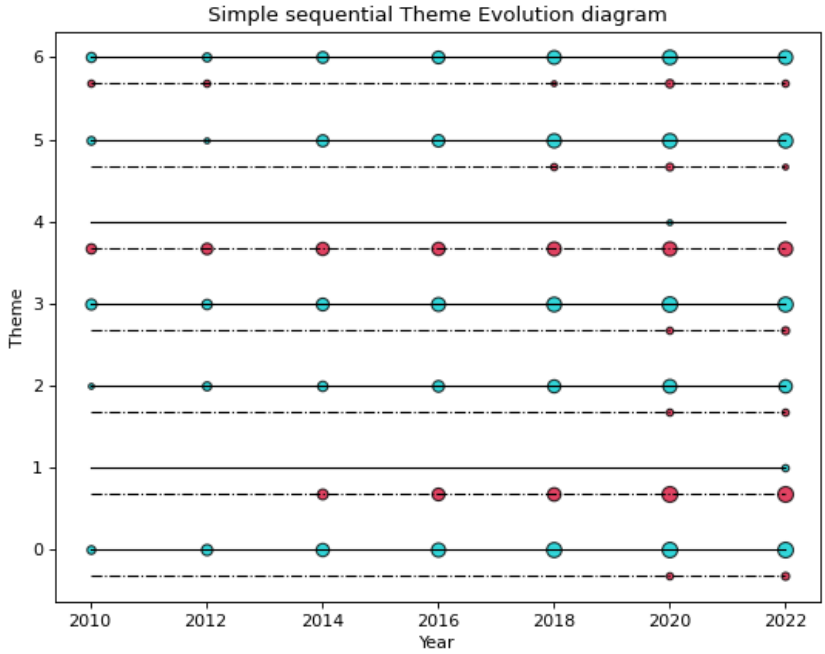

Figure 4. Multi-source data time-series theme-evolution diagram.

Next, we used the cosine similarities between the mean vectors to associate different themes, as shown in Figure 5. The cosine similarities were determined in pairs of non-identical themes in adjacent time segments; we then sorted the similarities from small to large and plotted the distribution of the theme cosine similarities. The actual distribution of the similarities was between 0 and 0.7, and the closer the similarity was to 0, the higher the value of the themes' association.

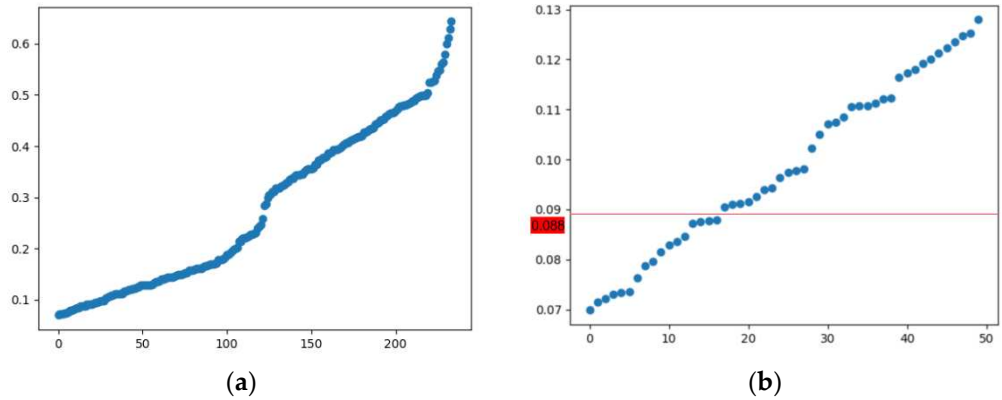

Figure 5. Cosine similarities distribution of adjacent themes: (**a**) Cosine similarities distribution among all adjacent themes; (**b**) distribution of cosine similarities for the top 50.

In order to increase the accuracy of the theme association, we screened out the top 50 cosine similarities. If we observe the similarities distribution in the lower-left corner of Figure 5a, as shown in Figure 5b, it can be seen that the distribution of similarities has a relatively obvious step-shaped change trend. This phenomenon is very helpful for the selection of similarities. Considering the number of associations and the size of the cosine similarities, we selected the second similarity with an obvious step-by-step position as the association threshold, that is, threshold(sim) = 0.088 was selected. This threshold is marked with a red horizontal line in Figure 5b.

After the above theme association experiments, we obtained 57 association relationships, including 17 non-identical pieces of theme association information and 40 of the same pieces of theme association information.

4.2. Visualization and Analysis of Multi-Dimensional Technology Evolutionary Path

After the above process, we finally obtained the multi-dimensional technology evolutionary path in the field of nanogenerators based on papers and patent data.

As can be seen from the river map, the intensity of all the themes was weak before 2014, and the research trend in this field was biased towards themes 0 and 3, namely "testing instruments and equipment" and "wearables and electronics". The use of wearable devices was proposed in 2013 on the basis of basic research on the structure and materials of nanogenerators, and it has also been studied in depth by scholars. The figure shows that composite film materials and zinc oxide nanorod materials have been vigorously developed since 2013. This has accelerated the application of nanotechnology in testing instruments, wearable devices, and electronic products [81]. The results in the figure are consistent with the actual development of nanogenerator technology. In addition, the overall intensity of the river map gradually became stronger after 2014, indicating that nanogenerator technology is developing rapidly.

As shown in Figure 6, a significant amount of technology integration and dispersion occurred around 2016–2018, during which opportunities and risks coexisted. We found some laws of development in this phenomenon. From Figure 6, it can be seen that there are three different types of technology evolution across different technologies: parallel development, collaborative development, and technology integration + collaborative development. Among them, theme 1, "research on electrode materials and their preparation methods", theme 2, "applications such as drug delivery and cancer treatment", and theme 4

"piezoelectric materials and flexible sensor properties" are under parallel development. These three rivers develop in parallel and rarely intersect. Since 2014, theme 0, "testing instruments and equipment", and theme 3, "wearables and electronics", have been developed in synergy, and these two rivers constantly infiltrate each other. Theme 6, "ZnO nanorods and output properties" has been continuously integrated into theme 5, "research on composite thin film materials", since 2018. There is both technical integration and synergistic development between the two themes.

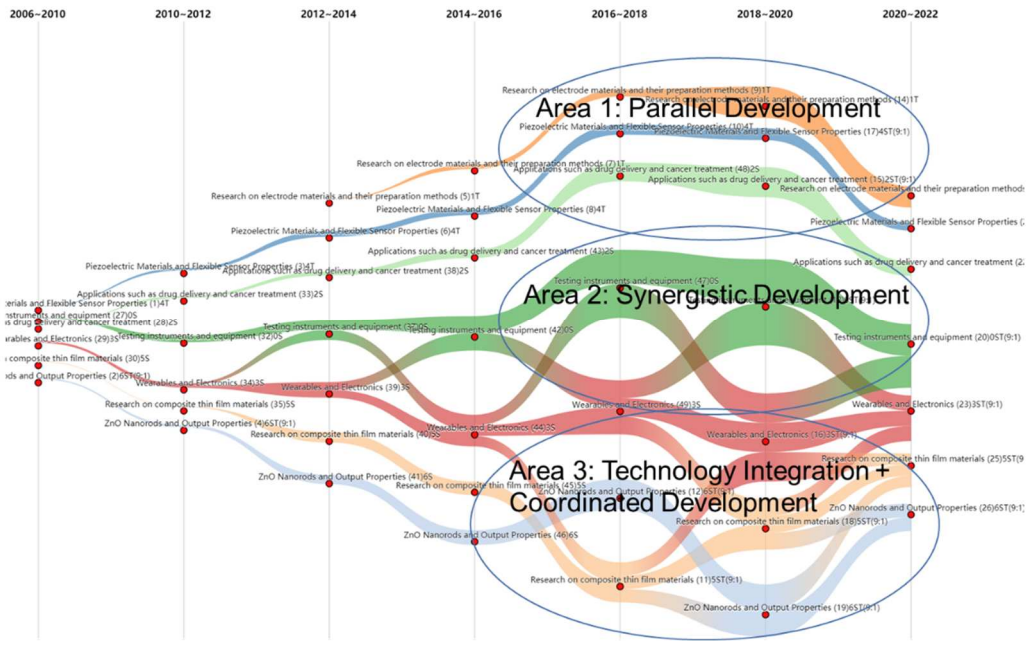

Figure 6. Evolutionary path of nanogenerator technology.

The technical evolution analysis of multi-source data in the field of nanogenerators reflects and proves the importance of multi-source data to technical analysis. From the river map, we obtained relatively rich technology evolutionary information and analyzed the development status of the nanogenerator field from the perspective of scientific research and technological applications. The improved river map visualization method in this paper is also conducive to the analysis of technological evolution and can improve the utilization of technology mining information.

5. Conclusions

This paper proposes a framework for monitoring the evolutionary path of nanogenerator technology based on the Sentence-BERT and phrase-mining methods. We represented technical themes with high-quality phrases through an improved theme evolution modeling approach (SKT) with multi-source text vectorization, which fuses paper and patent text data. The method combines both scientific and technological dimensions to analyze technological evolution in the field of nanogenerators. The experiments showed that our proposed framework is correct and effective.

The study found that TopMine constructs thematic content in the form of phrases, which can enrich thematic connotations and improve thematic interpretability compared with traditional keyword mining. For example, this paper identified themes such as composite thin-film materials, wearable devices, and electronics. The evolutionary path of nanogenerator technology visualized by the river map also revealed much important information. We found that the current development focus of nanogenerator technology is mainly concentrated in several directions, First, the research on electrode materials and their preparation methods and the research on piezoelectric materials and flexible sensor performance are in separate development stages, which indicates that these two research

directions are temporary. It is difficult to combine them with other research directions, and they are relatively isolated. Secondly, the research on zinc oxide nanorods and output properties and the research on composite thin film materials are in the stage of technological integration and coordinated development, which shows that these two research directions have undergone mature development. The current research in these two areas is fused and inter-penetrated. The future prospects of nanogenerator technology are mainly concentrated in several directions. For instance, applications such as drug delivery and cancer treatment are in separate development stages, which indicates that they may be in the early stage of application and less combined with other directions, such as detection instruments, equipment, and wearable devices. Furthermore, they are in the stage of coordinated development with electronic products, which shows that these two directions have passed the initial stage of development and are beginning to cooperate with and penetrate each other.

There are some limitations in this study. Specifically, follow-up research could further explore the following aspects: (1) The number of papers and patents in the field of nanogenerators is limited, and it is difficult to fully reflect the advantages of text vectorization and phrase mining. (2) Expert knowledge can be introduced at the multi-source theme identification stage to improve the effectiveness of the analysis of technological evolution.

Author Contributions: Conceptualization, H.L. and Y.L.; methodology, H.L. and R.Z.; software, validation, data curation, writing—original draft preparation, visualization, R.Z. and C.H.; resources, project administration, Y.L.; writing—review and editing, H.L. and Y.L.; supervision, Y.L.; funding acquisition, H.L. and Y.L. All authors have read and agreed to the published version of the manuscript.

Funding: This work was supported by the National Natural Science Foundation of China (grant numbers 72104224, 71974107, L2124002, 91646102, L1924058, and L1824043); the MOE (Ministry of Education in China) Project of Humanities and Social Sciences (grant number 16JDGC011); the Construction Project of China Knowledge Center for Engineering Sciences and Technology (grant number CKCEST-2022-1-30); the Tsinghua University Initiative Scientific Research Program (grant number 2019Z02CAU); and the Tsinghua University Project of Volvo-Supported Green Economy and Sustainable Development (grant number 20183910020).

Institutional Review Board Statement: Not applicable.

Informed Consent Statement: Not applicable.

Data Availability Statement: The data presented in this study are available on request from the corresponding author.

Conflicts of Interest: The authors declare no conflict of interest.

References

1. Cao, X.; Jie, Y.; Wang, N.; Wang, Z.L. Triboelectric Nanogenerators Driven Self-Powered Electrochemical Processes for Energy and Environmental Science. *Adv. Energy Mater.* **2016**, *6*, 1600665. [CrossRef]
2. Wen, Z.; Shen, Q.; Sun, X. Nanogenerators for Self-Powered Gas Sensing. *Nano-Micro Lett.* **2017**, *9*, 45. [CrossRef]
3. Fan, F.R.; Tang, W.; Wang, Z.L. Flexible Nanogenerators for Energy Harvesting and Self-Powered Electronics. *Adv. Mater.* **2016**, *28*, 4283–4305. [CrossRef]
4. Bai, Y.; Jantunen, H.; Juuti, J. Energy Harvesting Research: The Road from Single Source to Multisource. *Adv. Mater.* **2018**, *30*, 1707271. [CrossRef]
5. Chem, J.M.; Lee, J.; Kim, J.; Kim, Y.; Hossain, A.; Kim, S.; Ho, J. All-in-one energy harvesting and storage devices. *J. Mater. Chem. A* **2016**, *4*, 7983–7999.
6. Zhang, Y.; Xie, M.; Adamaki, V.; Khanbareh, H.; Bowen, C.R. Control of electro-chemical processes using energy harvesting materials and devices. *Chem. Soc. Rev.* **2017**, *46*, 7757–7786. [CrossRef]
7. Wu, C.; Wang, A.; Ding, W.; Guo, H.; Wang, Z.L. Triboelectric Nanogenerator: A Foundation of the Energy for the New Era. *Adv. Energy Mater.* **2018**, *9*, 1802906. [CrossRef]
8. Lin, Z. Nanogenerators, self-powered systems, blue energy, piezotronics and piezo-phototronics—A recall on the original thoughts for coining these fields. *Nano Energy* **2018**, *54*, 477–483.
9. Wang, B.; Liu, Y.; Zhou, Y.; Wen, Z. Emerging nanogenerator technology in China: A review and forecast using integrating bibliometrics, patent analysis and technology roadmapping methods. *Nano Energy* **2018**, *46*, 322–330. [CrossRef]
10. Li, M.; Zhou, Y. Visualizing the knowledge profile on self-powered technology. *Nano Energy* **2018**, *51*, 250–259. [CrossRef]

11. Azimi, S.; Golabchi, A.; Nekookar, A.; Rabbani, S.; Amiri, M.H.; Asadi, K.; Abolhasani, M.M. Self-powered cardiac pacemaker by piezoelectric polymer nanogenerator implant. *Nano Energy* **2021**, *83*, 105781. [CrossRef]
12. Lee, S.; Wang, H.; Wang, J.; Shi, Q.; Yen, S.-C.; Thakor, N.V.; Lee, C. Battery-free neuromodulator for peripheral nerve direct stimulation. *Nano Energy* **2018**, *50*, 148–158. [CrossRef]
13. Lee, S.; Wang, H.; Peh, W.Y.X.; He, T.; Yen, S.-C.; Thakor, N.V.; Lee, C. Mechano-neuromodulation of autonomic pelvic nerve for underactive bladder: A triboelectric neurostimulator integrated with flexible neural clip interface. *Nano Energy* **2019**, *60*, 449–456. [CrossRef]
14. Hassani, F.A.; Mogan, R.P.; Gammad, G.G.L.; Wang, H.; Yen, S.-C.; Thakor, N.V.; Lee, C. Toward self-control systems for neurogenic underactive bladder: A triboelectric nanogenerator sensor integrated with a bistable micro-actuator. *ACS Nano* **2018**, *12*, 3487–3501. [CrossRef] [PubMed]
15. Sultana, A.; Alam, M.; Garain, S.; Sinha, T.K.; Middya, T.R.; Mandal, D. An Effective Electrical Throughput from PANI Supplement ZnS Nanorods and PDMS-Based Flexible Piezoelectric Nanogenerator for Power up Portable Electronic Devices: An Alternative of MWCNT Filler. *ACS Appl. Mater. Interfaces* **2015**, *7*, 19091–19097. [CrossRef] [PubMed]
16. Pu, X.; Guo, H.; Chen, J.; Wang, X.; Xi, Y.; Hu, C.; Wang, Z.L. Eye motion triggered self-powered mechnosensational communication system using triboelectric nanogenerator. *Sci. Adv.* **2017**, *3*, e1700694. [CrossRef]
17. Ali, F.; Raza, W.; Li, X.; Gul, H.; Kim, K.-H. Piezoelectric energy harvesters for biomedical applications. *Nano Energy* **2019**, *57*, 879–902. [CrossRef]
18. Liu, Z.; Li, H.; Shi, B.; Fan, Y.; Wang, Z.L.; Li, Z. Wearable and Implantable Triboelectric Nanogenerators. *Adv. Funct. Mater.* **2019**, *29*, 1808820. [CrossRef]
19. Li, Z.; Zheng, Q.; Wang, Z.L.; Li, Z. Nanogenerator-based self-powered sensors for wearable and implantable electronics. *Research* **2020**, *2020*, 8710686. [CrossRef]
20. Chen, J.; Oh, S.K.; Zou, H.; Shervin, S.; Wang, W.; Pouladi, S.; Zi, Y.; Wang, Z.L.; Ryou, J.H. High-Output Lead-Free Flexible Piezoelectric Generator Using Single-Crystalline GaN Thin Film. *ACS Appl. Mater. Interfaces* **2018**, *10*, 12839–12846. [CrossRef]
21. He, X.; Zou, H.; Geng, Z.; Wang, X.; Ding, W.; Hu, F.; Zi, Y.; Xu, C.; Zhang, S.L.; Yu, H.; et al. A Hierarchically Nanostructured Cellulose Fiber-Based Triboelectric Nanogenerator for Self-Powered Healthcare Products. *Adv. Funct. Mater.* **2018**, *28*, 1805540.1–1805540.8. [CrossRef]
22. Wang, X.; Song, J.; Liu, J.; Wang, Z.L. Direct-Current Nanogenerator Driven by Ultrasonic Waves. *Science* **2007**, *316*, 102–105. [CrossRef]
23. Sahoo, R.; Mishra, S.; Unnikrishnan, L.; Mohanty, S.; Mahapatra, S.; Nayak, S.K.; Anwar, S.; Ramadoss, A. Enhanced dielectric and piezoelectric properties of Fe-doped ZnO/PVDF-TrFE composite films. *Mater. Sci. Semicond. Process.* **2020**, *117*, 105173. [CrossRef]
24. Zhang, L.; Bai, S.; Su, C.; Zheng, Y.B.; Qin, Y.; Xu, C.; Wang, Z.L. A high-reliability kevlar fiber-ZnO nanowires hybrid nanogenerator and its application on self-powered UV detection. *Adv. Funct. Mater.* **2015**, *25*, 5794–5798. [CrossRef]
25. Murillo, G.; Blanquer, A.; Vargas-Estevez, C.; Barrios, L.; Ibanez, E.; Nogues, C.; Esteve, J. Electromechanical nanogenerator-cell interaction modulates cell activity. *Adv. Mater.* **2017**, *29*, 1605048. [CrossRef] [PubMed]
26. Zhao, Y.; Deng, P.; Nie, Y.; Wang, P.; Zhang, Y.; Xing, L.; Xue, X. Biomolecule-adsorption-dependent piezoelectric output of ZnO nanowire nanogenerator and its application as self-powered active biosensor. *Biosens. Bioelectron.* **2014**, *57*, 269–275. [CrossRef] [PubMed]
27. Wang, Z.L. ZnO nanowire and nanobelt platform for nanotechnology. *Mater. Sci. Eng. R* **2009**, *64*, 33–71. [CrossRef]
28. Hinchet, R.; Yoon, H.-J.; Ryu, H.; Kim, M.-K.; Choi, E.-K.; Kim, D.-S.; Kim, S.-W. Transcutaneous ultrasound energy harvesting using capacitive triboelectric technology. *Science* **2019**, *365*, 491–494. [CrossRef] [PubMed]
29. Park, K.-I.; Son, J.H.; Hwang, G.-T.; Jeong, C.K.; Ryu, J.; Koo, M.; Choi, I.; Lee, S.H.; Byun, M.; Wang, Z.L.; et al. Highly-Efficient, Flexible Piezoelectric PZT Thin Film Nanogenerator on Plastic Substrates. *Adv. Mater.* **2014**, *26*, 2514–2520. [CrossRef]
30. Liu, S.; Zou, D.; Yu, X.; Wang, Z.; Yang, Z. Transfer-free PZT thin films for flexible nanogenerators derived from a single-step modified sol-gel process on 2D mica. *ACS Appl. Mater. Interfaces* **2020**, *12*, 54991–54999. [CrossRef] [PubMed]
31. Park, D.Y.; Joe, D.J.; Kim, D.H.; Park, H.; Han, J.H.; Jeong, C.K.; Park, H.; Park, J.G.; Joung, B.; Lee, K.J. Self-Powered Real-Time Arterial Pulse Monitoring Using Ultrathin Epidermal Piezoelectric Sensors. *Adv. Mater.* **2017**, *29*, 1702308. [CrossRef] [PubMed]
32. Zhu, C.; Guo, D.; Ye, D.; Jiang, S.; Huang, Y. Flexible PZT-integrated, bilateral sensors via transfer-free laser lift-off for multimodal measurements. *ACS Appl. Mater. Interfaces* **2020**, *12*, 37354–37362. [CrossRef] [PubMed]
33. Dagdeviren, C.; Javid, F.; Joe, P.; Von Erlach, T.; Bensel, T.; Wei, Z.; Saxton, S.; Cleveland, C.; Booth, L.; McDonnell, S.; et al. Flexible piezoelectric devices for gastrointestinal motility sensing. *Nat. Biomed. Eng.* **2017**, *1*, 807–817. [CrossRef] [PubMed]
34. Yang, Z.; Zhou, S.; Zu, J.; Inman, D. High-Performance Piezoelectric Energy Harvesters and Their Applications. *Joule* **2018**, *2*, 642–697. [CrossRef]
35. Selvarajan, S.; Kim, A.; Song, S.H. Biodegradable Piezoelectric Transducer for Powering Transient Implants. *IEEE Access* **2020**, *8*, 68219–68225. [CrossRef]
36. Su, H.X.; Wang, X.B.; Li, C.Y.; Wang, Z.F.; Wu, Y.H.; Zhang, J.W.; Zhang, Y.Z.; Zhao, C.L.; Wu, J.G.; Zheng, H.W. Enhanced energy harvesting ability of M. Sun et al. Nano Energy 89 (2021) 10646122 polydimethylsiloxane-BaTiO3-based flexible piezoelectric nanogenerator for tactile imitation application. *Nano Energy* **2021**, *83*, 105809. [CrossRef]
37. Qian, S.; Qin, L.; He, J.; Zhang, N.; Qian, J.; Mu, J.; Geng, W.; Hou, X.; Chou, X. A lead-free stretchable piezoelectric composite for human motion monitoring. *Mater. Lett.* **2020**, *261*, 127119. [CrossRef]

38. Jiang, L.; Yang, Y.; Chen, R.; Lu, G.; Li, R.; Xing, J.; Shung, K.K.; Humayun, M.S.; Zhu, J.; Chen, Y.; et al. Ultrasound-induced wireless energy harvesting for potential retinal electrical stimulation application. *Adv. Funct. Mater.* **2019**, *29*, 1902522. [CrossRef]
39. Jeong, C.K.; Han, J.H.; Palneedi, H.; Park, H.; Hwang, G.-T.; Joung, B.; Kim, S.-G.; Shin, H.J.; Kang, I.-S.; Ryu, J.; et al. Comprehensive biocompatibility of nontoxic and high-output flexible energy harvester using lead-free piezoceramic thin film. *APL Mater.* **2017**, *5*, 074102. [CrossRef]
40. Yu, X.; Liang, X.; Krishnamoorthy, R.; Jiang, W.; Zhang, L.; Ma, L.; Zhu, P.; Hu, Y.; Sun, R.; Wong, C.-P. Transparent and flexible hybrid nanogenerator with welded silver nanowire networks as the electrodes for mechanical energy harvesting and physiological signal monitoring. *Smart Mater. Struct.* **2020**, *29*, 045040. [CrossRef]
41. Gupta, S.; Bhunia, R.; Fatma, B.; Maurya, D.; Singh, D.; Prateek; Gupta, R.; Priya, S.; Gupta, R.K.; Garg, A. Multifunctional and flexible polymeric nanocomposite films with improved ferroelectric and piezoelectric properties for energy generation devices. *ACS Appl. Energy Mater.* **2019**, *2*, 6364–6374. [CrossRef]
42. Adadi, N.; Yadid, M.; Gal, I.; Asulin, M.; Feiner, R.; Edri, R.; Dvir, T. Electrospun fibrous PVDF-TrFe scaffolds for cardiac tissue engineering, differentiation, and maturation. *Adv. Mater. Technol.* **2020**, *5*, 1900820. [CrossRef]
43. Wang, A.; Liu, Z.; Hu, M.; Wang, C.; Zhang, X.; Shi, B.; Fan, Y.; Cui, Y.; Li, Z.; Ren, K. Piezoelectric nanofibrous scaffolds as in vivo energy harvesters for modifying fibroblast alignment and proliferation in wound healing. *Nano Energy* **2018**, *43*, 63–71. [CrossRef]
44. Zou, H.; Zhang, Y.; Guo, L.; Wang, P.; He, X.; Dai, G.; Zheng, H.; Chen, C.; Wang, A.; Xu, C.; et al. Quantifying the triboelectric series. *Nat. Commun.* **2019**, *10*, 1427. [CrossRef] [PubMed]
45. Zou, H.; Guo, L.; Xue, H.; Zhang, Y.; Shen, X.; Liu, X.; Wang, P.; He, X.; Dai, G.; Jiang, P.; et al. Quantifying and understanding the triboelectric series of inorganic non-metallic materials. *Nat. Commun.* **2020**, *11*, 2093. [CrossRef] [PubMed]
46. Cheng, X.; Zi, Y.; Wang, A.C. On the Electron-Transfer Mechanism in the Contact-Electrification Effect. *Adv. Mater.* **2018**, *30*, 1706790.
47. Shi, Q.; Wang, H.; Wang, T.; Lee, C. Self-powered liquid triboelectric microfluidic sensor for pressure sensing and finger motion monitoring applications. *Nano Energy* **2016**, *30*, 450–459. [CrossRef]
48. Yi, F.; Lin, L.; Niu, S.M.; Yang, P.K.; Wang, Z.N.; Chen, J.; Zhou, Y.S.; Zi, Y.L.; Wang, J.; Liao, Q.L.; et al. Stretchable-rubber-based triboelectric nanogenerator and its application as self-powered body motion sensors. *Adv. Funct. Mater.* **2015**, *25*, 3688–3696. [CrossRef]
49. Huang, Y.; Zhu, F.; Porter, A.L.; Zhang, Y.; Zhu, D.; Guo, Y. Exploring Technology Evolution Pathways to Facilitate Technology Management: From a Technology Life Cycle Perspective. *IEEE Trans. Eng. Manag.* **2020**, *68*, 1347–1359. [CrossRef]
50. Huang, Y.; Zhu, F.; Guo, Y.; Porter, A.L.; Zhang, Y.; Zhu, D. Exploring Technology evolution pathways to facilitate Technology management: A study of Dye-sensitized solar cells (DSSCs). In Proceedings of the 2016 Portland International Conference on Management of Engineering and Technology (PICMET), Honolulu, HI, USA, 4–8 November 2016; pp. 764–776.
51. Yu, J. From 3G to 4G: Technology evolution and path dynamics in China's mobile telecommunication sector. *Technol. Anal. Strat. Manag.* **2011**, *23*, 1079–1093. [CrossRef]
52. Adomavicius, G.; Bockstedt, J.C.; Gupta, A.; Kauffman, R.J. Technology roles and paths of influence in an ecosystem model of technology evolution. *Inf. Technol. Manag.* **2007**, *8*, 185–202. [CrossRef]
53. Zhou, Y.; Li, X.; Lema, R.; Urban, F. Comparing the knowledge bases of wind turbine firms in Asia and Europe: Patent trajectories, networks, and globalisation. *Sci. Public Policy* **2016**, *43*, 476–491. [CrossRef]
54. Zhou, Y.; Zang, J.; Miao, Z.; Minshall, T. Upgrading Pathways of Intelligent Manufacturing in China: Transitioning across Technological Paradigms—ScienceDirect. *Engineering* **2019**, *5*, 691–701. [CrossRef]
55. Zhou, Y.; Dong, F.; Liu, Y.; Ran, L. A deep learning framework to early identify emerging technologies in large-scale outlier patents: An empirical study of CNC machine tool. *Scientometrics* **2021**, *126*, 969–994. [CrossRef]
56. Zhou, Y.; Li, Z.; Liu, Y.; Deng, F. Network Proximity and Communities in Innovation Clusters across Knowledge, Business, and Geography: Evidence From China. *IEEE Trans. Eng. Manag.* **2020**, *68*, 1388–1397. [CrossRef]
57. Zhou, Y.; Zhou, R.; Chen, L.; Zhao, Y.; Zhang, Q. Environmental Policy Mixes and Green Industrial Development: An Empirical Study of the Chinese Textile Industry from 1998 to 2012. *IEEE Trans. Eng. Manag.* **2020**, *69*, 742–754. [CrossRef]
58. Xu, G.; Zhou, Y.; Ji, H. How Can Government Promote Technology Diffusion in Manufacturing Paradigm Shift? Evidence from China. *IEEE Trans. Eng. Manag.* **2020**, 1–13. [CrossRef]
59. Zhou, Y.; Lin, H.; Liu, Y.; Ding, W. A novel method to identify emerging technologies using a semi-supervised topic clustering model: A case of 3D printing industry. *Scientometrics* **2019**, *120*, 167–185. [CrossRef]
60. Zhou, Y.; Dong, F.; Kong, D.; Liu, Y. Unfolding the convergence process of scientific knowledge for the early identification of emerging technologies. *Technol. Forecast. Soc. Change.* **2019**, *144*, 205–220. [CrossRef]
61. Kong, D.; Zhou, Y.; Liu, Y.; Xue, L. Using the data mining method to assess the innovation gap: A case of industrial robotics in a catching-up country. *Technol. Forecast. Soc. Chang.* **2017**, *119*, 80–97. [CrossRef]
62. Xu, G.; Wu, Y.; Minshall, T.; Zhou, Y. Exploring innovation ecosystems across science, technology, and business: A case of 3D printing in China. *Technol. Forecast. Soc. Chang.* **2018**, *136*, 208–221. [CrossRef]
63. Gao, L.; Porter, A.L.; Wang, J.; Fang, X.; Zhang, X.; Ma, T.; Wang, W. Technology life cycle analysis method based on patent documents. *Technol. Forecast. Soc. Chang.* **2013**, *80*, 398–407. [CrossRef]
64. Callon, M.; Courtial, J.P.; Turner, W.A.; Bauin, S. From translations to problematic networks: An introduction to co-word analysis. *Soc. Sci. Inf.* **1983**, *22*, 191–235. [CrossRef]

65. Braun, T.; Glänzel, W.; Schubert, A. Publication and cooperation patterns of the authors of neuroscience journals. *Scientometrics* **2001**, *51*, 499–510. [CrossRef]
66. Small, H. Co-citation in the scientific literature: A new measure of the relationship between two documents. *J. Am. Soc. Inf. Sci.* **1973**, *24*, 265–269. [CrossRef]
67. Kim, J.; Shin, J. Mapping extended technological trajectories: Integration of main path, derivative paths, and technology junctures. *Scientometrics* **2018**, *116*, 1439–1459. [CrossRef]
68. Chen, S.-H.; Huang, M.-H.; Chen, D.-Z. Exploring technology evolution and transition characteristics of leading countries: A case of fuel cell field. *Adv. Eng. Inform.* **2013**, *27*, 366–377. [CrossRef]
69. Zhou, Y.; Dong, F.; Liu, Y.; Li, Z.; Du, J.; Zhang, L. Forecasting emerging technologies using data augmentation and deep learning. *Scientometrics* **2020**, *123*, 1–29. [CrossRef]
70. Liu, Y.; Zhou, Y.; Liu, X.; Dong, F.; Wang, C.; Wang, Z. Wasserstein GAN-Based Small-Sample Augmentation for New-Generation Artificial Intelligence: A Case Study of Cancer-Staging Data in Biology. *Engineering* **2019**, *5*, 156–163. [CrossRef]
71. Li, X.; Fan, M.; Zhou, Y.; Fu, J.; Yuan, F.; Huang, L. Monitoring and forecasting the development trends of nanogenerator technology using citation analysis and text mining. *Nano Energy* **2020**, *71*, 104636. [CrossRef]
72. Witten, I.H.; Paynter, G.W.; Frank, E.; Gutwin, C.; Nevill-Manning, C.G. KEA: Practical Automated Keyphrase Extraction. In *Design and Usability of Digital Libraries: Case Studies in the Asia Pacific*; Igi Global: Hershey, PA, USA, 2005; pp. 129–152.
73. El-Kishky, A.; Song, Y.; Wang, C.; Voss, C.R.; Han, J. Scalable topical phrase mining from text corpora. *Proc. VLDB Endow.* **2014**, *8*, 305–316. [CrossRef]
74. Liu, J.; Shang, J.; Wang, C.; Ren, X.; Han, J. Mining Quality Phrases from Massive Text Corpora. In Proceedings of the 2015 ACM SIGMOD International Conference on Management of Data, Melbourne, Victoria, Australia, 31 May–4 June 2015.
75. Shang, J.; Liu, J.; Jiang, M.; Ren, X.; Voss, C.R.; Han, J. Automated Phrase Mining from Massive Text Corpora. *IEEE Trans. Knowl. Data Eng.* **2018**, *30*, 1825–1837. [CrossRef] [PubMed]
76. Choi, H.; Kim, J.; Joe, S.; Gwon, Y. Evaluation of BERT and ALBERT Sentence Embedding Performance on Downstream NLP Tasks. In Proceedings of the 2020 25th International Conference on Pattern Recognition (ICPR), Milan, Italy, 10–15 January 2021; pp. 5482–5487.
77. Havre, S.; Hetzler, E.; Whitney, P.; Nowell, L. ThemeRiver: Visualizing thematic changes in large document collections. *IEEE Trans. Vis. Comput. Graph.* **2002**, *8*, 9–20. [CrossRef]
78. Cui, W.; Liu, S.; Tan, L.; Shi, C.; Song, Y.; Gao, Z.J.; Qu, H.; Tong, X. TextFlow: Towards Better Understanding of Evolving Topics in Text. *IEEE Trans. Vis. Comput. Graph.* **2011**, *17*, 2412–2421. [CrossRef]
79. Zhou, Y.; Miao, Z.; Urban, F. China's leadership in the hydropower sector: Identifying green windows of opportunity for technological catch-up. Industrial and Corporate Change. *Ind. Corp. Chang.* **2020**, *5*, 1319–1343.
80. Bostock, M.; Ogievetsky, V.; Heer, J. D^3 data-driven documents. *IEEE Trans. Vis. Comput. Graph.* **2011**, *17*, 2301–2309. [CrossRef]
81. Liu, Y.; Wang, G.; Zhou, Y.; Liu, Y. Advanced Technology Evolution Pathways of Nanogenerators: A Novel Framework Based on Multi-Source Data and Knowledge Graph. *Nanomaterials* **2022**, *12*, 838. [CrossRef]

nanomaterials

MDPI

Review

Review for Rare-Earth-Modified Perovskite Materials and Optoelectronic Applications

Bobo Li [1,†], Feng Tian [2,†], Xiangqian Cui [1], Boyuan Xiang [1], Hongbin Zhao [3], Haixi Zhang [4], Dengkui Wang [2], Jinhua Li [2], Xiaohua Wang [2], Xuan Fang [2,4,*], Mingxia Qiu [1,*] and Dongbo Wang [5]

1 College of New Materials and New Energies, Shenzhen Technology University, Shenzhen 518118, China; libobo@sztu.edu.cn (B.L.); 2070413004@stumail.sztu.edu.cn (X.C.); xiangboyuan@sztu.edu.cn (B.X.)
2 State Key Laboratory of High Power Semiconductor Lasers, School of Physics, Changchun University of Science and Technology, Changchun 130012, China; tianfengcust@163.com (F.T.); wccwss@foxmail.com (D.W.); lijh@cust.edu.cn (J.L.); biewang2001@126.com (X.W.)
3 State Key Laboratory of Advanced Materials for Smart Sensing, General Research Institute for Nonferrous Metals, Beijing 100088, China; zhaohongbin@grinm.com
4 School of Science and Engineering, The Chinese University of Hong Kong, Shenzhen 518172, China; zhanghaixi@cuhk.edu.cn
5 Department of Opto-Electronic Information Science, School of Materials Science and Engineering, Harbin Institute of Technology, Harbin 150001, China; wangdongbo@hit.edu.cn
* Correspondence: fangx@cust.edu.cn (X.F.); qiumingxia@sztu.edu.cn (M.Q.)
† The authors contribute equally to this work.

Abstract: In recent years, rare-earth metals with triply oxidized state, lanthanide ions (Ln^{3+}), have been demonstrated as dopants, which can efficiently improve the optical and electronic properties of metal halide perovskite materials. On the one hand, doping Ln^{3+} ions can convert near-infrared/ultraviolet light into visible light through the process of up-/down-conversion and then the absorption efficiency of solar spectrum by perovskite solar cells can be significantly increased, leading to high device power conversion efficiency. On the other hand, multi-color light emissions and white light emissions originated from perovskite nanocrystals can be realized via inserting Ln^{3+} ions into the perovskite crystal lattice, which functioned as quantum cutting. In addition, doping or co-doping Ln^{3+} ions in perovskite films or devices can effectively facilitate perovskite film growth, tailor the energy band alignment and passivate the defect states, resulting in improved charge carrier transport efficiency or reduced nonradiative recombination. Finally, Ln^{3+} ions have also been used in the fields of photodetectors and luminescent solar concentrators. These indicate the huge potential of rare-earth metals in improving the perovskite optoelectronic device performances.

Keywords: metal halide perovskite; rare-earth metal; solar cell; light-emitting diode; photodetector; luminescent solar concentrators

Citation: Li, B.; Tian, F.; Cui, X.; Xiang, B.; Zhao, H.; Zhang, H.; Wang, D.; Li, J.; Wang, X.; Fang, X.; et al. Review for Rare-Earth-Modified Perovskite Materials and Optoelectronic Applications. *Nanomaterials* **2022**, *12*, 1773. https://doi.org/10.3390/nano12101773

Academic Editor: Efrat Lifshitz

Received: 18 April 2022
Accepted: 16 May 2022
Published: 23 May 2022

1. Introduction

In the past 12 years, metal halide perovskite materials with the chemical formula of ABX_3, where A represents monovalent cation (such as CH_3NH^{3+}, $HNCHNH^{2+}$, Cs^+), B is divalent metal cation (such as Pb^{2+}, Sn^{2+}), and X represents halogen anion (such as I, Br and Cl), have triggered an enormous research wave [1–3]. Up to now, perovskite materials have been widely used in the field of photoelectronic devices, including solar cells, light-emitting diodes (LEDs), lasers, photodetectors, and so on, which is attributed to the excellent photo-electronic properties of broad absorption spectrum, tunable energy band gap, long charge carrier lifetime and length, low recombination loss and cost-effective preparation technology [4–7]. Both the power conversion efficiency (PCE) of perovskite solar cells (PSCs) and the external quantum efficiency of perovskite LEDs have exceeded 25% through the efforts of many researchers, which indicates the tremendous potential in the future commercial applications for the perovskite optoelectronic devices.

There have been many reports about improving the performance of perovskite devices. For example, in the field of perovskite solar cells, various methods have been demonstrated, including tuning the perovskite component proportion, controlling the film quality and crystalline size of perovskite active layer, optimizing the device structure, introducing plasmonic nano-converters, and so on [8–11]. Although these methods have boosted the PCE of PSCs, upper threshold value may be hampered for further development. The Shockley–Queisser limit is the theoretical limit of energy conversion for single-junction solar cells. As perovskite materials have an intrinsic band gap, there are also limits to the efficiency of perovskite solar cells. In order to break Shockley–Queisser limit, it is an effective method to utilize infrared light outside the intrinsic band gap of perovskite by introducing up-conversion or down-conversion materials into the solar cell. Rare-earth (RE) metals with triply oxidized state (lanthanide ions, Ln^{3+}) possess different kinds of energy transitions, which determined that they can emit fluorescence in a wide wavelength range covering from ultraviolet to intermediate infrared regions [12]. Herein, Ln^{3+} ions can be doped into semiconductor materials to act as light active centers, and then they can promote the light absorption and tailor the band gap of the host materials, thus playing the role of up-conversion or down-conversion. In addition, integrating Ln^{3+} into metal halide perovskite materials can be a feasible and effective approach because it minimizes the thermalization losses, through removing the load of mismatch between perovskite absorption spectra and the solar spectrum.

Due to these unique features, rare-earth doped into perovskite crystals and devices for optical and electrical control have been widely reported [13–21]. In this article, we review the applications of rare-earth metals in the perovskite photoelectric devices from the following parts: Firstly, Ln^{3+} ions can be doped as up-conversion of down-conversion materials, which can enhance the light absorption efficiency covering from ultraviolet (UV) to near-infrared (NIR) range in the perovskite solar cells. Secondly, Ln^{3+} ions can be used as quantum cutting or band gap tuning dopants to realize high photoluminescence quantum yield (PLQY) and tunable luminescence emission at different wavelength, and then can be efficiently used for white light emission. Thirdly, Ln^{3+} can be used for defect passivation or lead substitution in the perovskite devices. Additionally, Ln^{3+} can also be used in the field of photodetectors and luminescent solar concentrators. At the end of this paper, we give a future research outlook of this field via exploring the effective ideas and experiments which should be demonstrated.

2. Modified Strategy of Rare-Earth Metal in Perovskite Devices

There are three main ways of Ln^{3+} ion-modified perovskite photoelectric devices, as shown in Figure 1. Different methods have different hosts of rare earth ions and thus have different mechanisms of modified strategy. Figure 1a shows the introduction of a new conversion layer in the perovskite photoelectric device. By doping rare-earth ions into the host, this layer can play the role of up-conversion or down-conversion of light, thus improving the conversion efficiency of the device. The MFY_4 (M = Li, Na, K) family is a common host for this layer because of its excellent properties of low phonon energy and high transmittance. Figure 1b shows that rare-earth ions are doped into the electron transport layer or the hole transport layer. After doping, this layer can also play the role of conversion layer. Meanwhile, doping component modulates the transport layer, the flat band edge of the electron transport layer moves toward positive, and the electrons at the conduction band minimum are more easily transferred to the electron transport layer. Figure 1c shows that rare-earth ions are doped into the perovskite lattice. Ln^{3+} ion dopant introduces new energy levels, which not only affects the peak position and the intensity of the original perovskite band edge compound luminescence peak, but also produces a new Ln^{3+} ion luminescence peak in photoluminescence spectrum. Ln^{3+}-doped perovskite materials also have a good application prospect in various light-emitting devices due to the unique quantum-cutting mechanism. It should be noted that the luminescence of

individual perovskite materials can also be improved by rare-earth doping, not only doped into the active layer of perovskite multilayer devices.

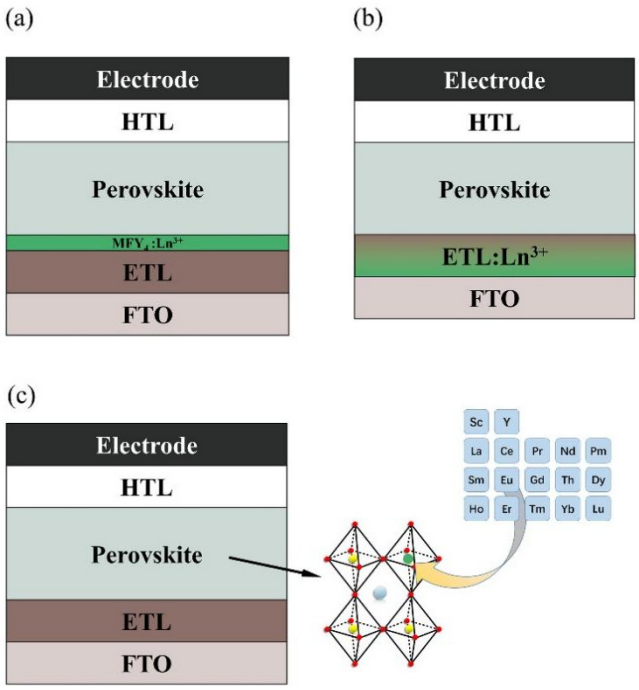

Figure 1. Three modified strategies of Ln^{3+} in perovskite device: (**a**) Inserting Ln^{3+}-based conversion layer in perovskite device; (**b**) Ln^{3+} ion mixed into carrier transport layer; (**c**) Ln^{3+} ion doped in perovskite active layer.

3. Applications of Ln^{3+} in Perovskite Solar Cells

As it is well-known, due to the intrinsic band gap of perovskite materials, perovskite-based solar cells are usually unable to utilize light beyond the visible region (the range of UV and NIR light), thus limiting further development of the device efficiency. Therefore, rare-earth metals with characteristics of up- or down-conversion fluorescence were introduced into perovskite to improve their availability of the solar spectrum.

3.1. Ln^{3+}-Based Up-Conversion Materials

Low-energy near-infrared light absorbed by Ln^{3+}-based up-conversion nanoparticles (UCNPs) can be converted to high-energy visible light which can be utilized in perovskite solar cells. For example, Yb^{3+}, Er^{3+}, Tm^{3+}, Ho^{3+}-doped or co-doped materials have been reported in up-conversion systems to achieve various up-converted fluorescence in the visible spectrum. The MYF_4 (M = Li, Na, K, Ru, and Cs) family has the characteristics of low phonon energy, high transmittance, and decrease in the influence of defect states, therefore, it has become an excellent host of Ln^{3+}. In 2016, the Yb^{3+} and Er^{3+} co-doped $LiYF_4$ transparent single crystal was synthesized and placed closed to the side of FTO in the PSCs by Song's team, which can induce efficient visible red and green emissions under two ranges of 900–1000 nm and 1500–1600 nm, as illustrated in Figure 2a. The up-conversion quantum efficiency of LiYF4:Yb^{3+}/Er^{3+} crystal was 5.72% under 980 nm light excitation (6.2 W cm^{-2}) and the PCE of LiYF4:Yb^{3+}/Er^{3+}/FTO/TiO_2/$MAPbI_3$/HTM/Au device was improved [22]. Having chosen the material, the next question was how to incorporate it into the structure of the device. Lin and co-workers fabricated the $CH_3NH_3PbI_3$-based PSCs by inserting monodisperse $NaYF_4$:Yb/Er up-conversion nanoparticles as the mesoporous electrode. A double hydrophilic PAA-b-PEO diblock copolymer was used as the nanoreactor for UCNPs. The incorporation of $NaYF_4$:Yb/Er UCNPs effectively reduced the non-absorption photon loss and harvested the NIR solar photons, followed by the absorption of emitted high-energy photons to generate extra photocurrents. The highest efficiency of $NaYF_4$:Yb/Er UCNPs-

based cell (FTO/compact-TiO_2/UCNP/$CH_3NH_3PbI_3$/Spiro-MeOTAD/Ag) was improved from 16.8% to 18.1% compared with the referenced TiO_2-based device (FTO/compact-TiO_2/mesoporous-TiO_2/$CH_3NH_3PbI_3$/Spiro-MeOTAD/Ag) [23]. Almost at the same time, Que's group introduced β-$NaYF_4$:Yb^{3+}/Tm^{3+}@$NaYF_4$ core-shell (NYF) nanoparticles into mesoscopic TiO2 scaffold layer which was used as an electron transport layer (ETL), thus, to enhance the NIR light harvest in perovskite solar cells (Figure 2b). As a result, under AM1.5G standard sunlight and 980 nm NIR laser irradiation, the best device based on NYF/TiO_2 ETL exhibited a PCE of 16.9% after the optimization of the film thickness and NYF/TiO_2 weight ratio, which was 20% higher than the pristine one [24].

In addition to the core-shell structure, the hexagonal nanoprism structure is also a feasible structure. Jang et al. used hexagonal β-$NaYF_4$:Yb^{3+}: Er^{3+} nanoprisms as up-converting medias to broaden the absorption spectrum range. The highest PCE of 15.98% was achieved via optimizing the amount of nanoprisms in the mesoporous TiO_2 layer [13]. Subsequently, up-conversion materials began to be introduced into perovskite layer. B-NaYF4:Yb/Er up-conversion nanocrystals were introduced into perovskite layer to fabricate planar ITO/ZnO/β-$NaYF_4$:Yb/Er-$CH_3NH_3PbI_3$/Spiro-OMeTAD/Ag PSCs, and the device structure diagram can be seen in Figure 2c. The up-conversion nanocrystals were beneficial for the perovskite film growth, resulting in uniform and pinhole-free surface morphology. In addition, the doped β-$NaYF_4$:Yb/Er also enabled NIR absorption. Therefore, the highest device PCE increased from 13.46% to 19.70% for the modified device [25]. In order to further enhance the NIR up-conversion efficiency, $Cu_{2-x}S$ was explored to serve as an antenna to sensitize Er_2O_3 up-conversion nanoparticles, which exhibited an intense localized surface plasmon resonance absorption band at near-infrared wavelengths. Based on this, m$Cu_{2-x}S$@SiO_2@Er_2O_3 nanocomposites were prepared and mixed into mesoporous TiO_2 ETL. The highest up-conversion luminescence was significantly boosted to 14.3% (inner quantum efficiency) and the excitation spectrum was expanded to the range of 800–1600 nm. Due to the electron transfer from oxygen defects to the conduction band of TiO_2, the photocurrent of the m$Cu_{2-x}S$@SiO_2@Er_2O_3-based device increased, resulting in a champion PCE of 17.8% [26]. In order to prevent the contact between the electron transport layer and the electrode, an insulation layer is often introduced to increase the photovoltage, and the up-conversion material can also be integrated to the insulation layer. Zhao et al. doped Ho^{3+} into $NaYbF_4$ to form high-fluorescent UCNPs and then mixed it into the ZrO_2 scaffold layer (Figure 2d). Under the synergistic effect of $NaYF_4$:Ho^{3+} and ZrO_2, additional photocurrent and photovoltage via up-conversion of NIR light to visible light, declined recombination rate and trap-state density, enhanced charge transfer and realized extraction efficiency, resulting in an overall PCE enhancement of 28.8% in the device of FTO/cp-TiO_2/mp-TiO_2/mp-ZrO_2-$NaYF_4$:Ho^{3+}/$FA_{0.4}MA_{0.6}PbI_3$/C anode [27]. Sebag and cooperators demonstrated the influence of inserting KY_7F_{22}:Yb^{3+},Er^{3+} UCNPs at the front- or rear-side of perovskite layer (FTO/KY_7F_{22}:Yb^{3+},Er^{3+}/$FA_{0.83}Cs_{0.17}Pb(I_{0.6}Br_{0.4})_3$/Spiro-MeOTAD/Au and FTO/$FA_{0.83}Cs_{0.17}Pb(I_{0.6}Br_{0.4})_3$/$KY_7F_{22}$:$Yb^{3+}$,$Er^{3+}$/Spiro-MeOTAD/Au) through the light-beam-induced current/fluorescence mapping technique, thus, to quantify the optical and electronic contribution of UCNPs. Figure 2e shows the device structure. The mapping results exhibited decreased green/red ration of up-conversion fluorescence spectra, which was attributed to the increased green fluorescence absorption of perovskite, indicating the optical contribution of UCNPs in the PSCs [28].

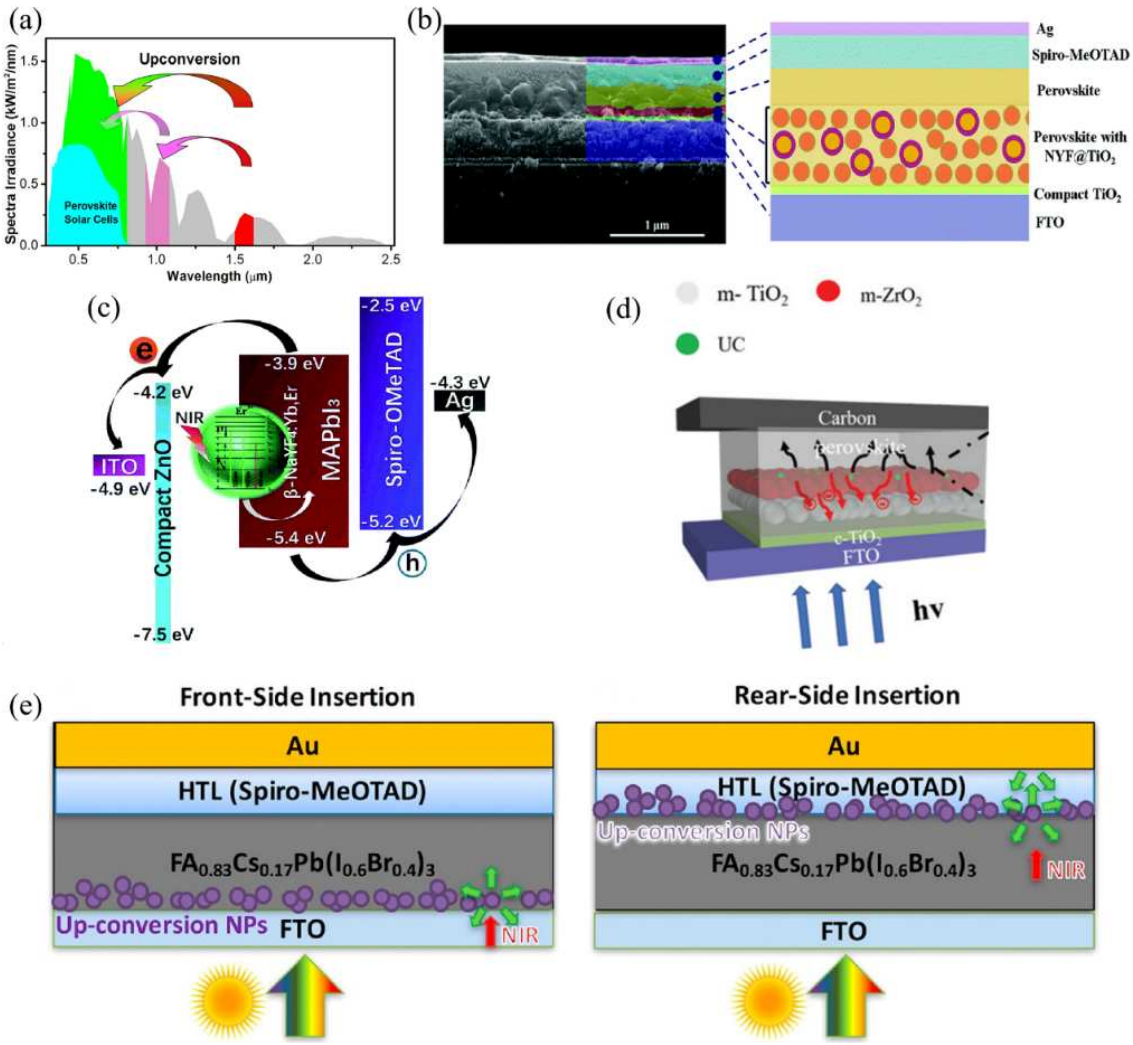

Figure 2. (**a**) The absorption regions of perovskite solar cells in the AM 1.5G solar spectrum via the up-conversion processes (Reprinted/adapted with permission from Ref. [22]. Copyright 2016 American Chemical Society); (**b**) Cross-sectional SEM image and schematic diagram of FTO/compact-TiO_2/$NaYF_4$:Yb/Er-$CH_3NH_3PbI_3$/Spiro-MeOTAD/Ag (Reprinted/adapted with permission from Ref. [24]. Copyright 2016 RSC Pub); (**c**) Energy transfer illustration in the device of ITO/ZnO/β-$NaYF_4$:Yb/Er-$CH_3NH_3PbI_3$/Spiro-OMeTAD/Ag (Reprinted/adapted with permission from Ref. [25]. Copyright 2017 RSC Pub); (**d**) Diagrams for device structure of FTO/cp-TiO_2/mp-TiO_2/mp-ZrO_2-$NaYF_4$:Ho^{3+}/$FA_{0.4}MA_{0.6}PbI_3$/C and mechanism of NIR light harvesting and up-conversion processes (Reprinted/adapted with permission from Ref. [24]. Copyright 2018 RSC Pub); (**e**) I Sketch maps for device structure of FTO/$FA_{0.83}Cs_{0.17}Pb(I_{0.6}Br_{0.4})_3$/Spiro-MeOTAD/Au with inserting KY_7F_{22}:Yb^{3+}, Er^{3+} UCNPs at the front- or rear-side of perovskite layer (Reprinted/adapted with permission from Ref. [28]. Copyright 2018 American Chemical Society).

Some research groups also integrated UCNPs into a hole transfer layer (HTL). For example, $NaLuF_4$:Yb,Er@$NaLuF_4$ core-shell nanoparticles were prepared by using a modified two-step co-precipitation process and then incorporated into PTAA layer in the device of FTO/TiO_2/γ-$CsPbI_3$/UCNPs-doped PTAA/Au, as seen in Figure 3a. Although the absorption spectrum was broadened to NIR range, the contribution of up-conversion effect to the PCE was almost negligible which was attributed to the ultralow luminescence efficiency of UCNPs. From the reflectance and absorption spectra, the researchers found that the light scattering effect played the predominant role, which prolonged the optical path length and enhanced the photoelectric current [29]. Huang's group introduced Li(Gd,Y)F4:Yb,Er up-conversion nanophosphors into Spiro-OMeTAD hole transport

layer. The highest PCE of the FTO/$cTiO_2$/$mTiO_2$/$CH_3NH_3PbI_3$/Li(Gd,Y)F_4:Yb,Er-doped Spiro-OMeTAD/Ag-Al was 18.34% with the optimized doping amount, while the bare device was only 14.69%, as seen in Figure 3b. Through the systematical measurement and analysis, the improvement of device performance was mainly attributed to the enhanced light harvesting in the range of 400–800 nm, accelerated carrier transport, and efficient charge separation/collection caused by Li(Gd,Y)F4:Yb,Er UCNPs [30]. Subsequently, Song et al. reported a complicated core-shell structure, which combined IR-783 dye molecules, $NaYF_4$:Yb^{3+},Er^{3+}@$NaYF_4$:Yb^{3+},Nd^{3+} UCNPs and Au nanorods (AuNRs). The energy- matched dye was used as an antenna to absorb NIR photons and the Au nanoparticle was used for local surface plasmonic resonance (Figure 3c). As a result, the up-conversion luminescent intensity was increased about 120 times. The PCE of the device (FTO/SnO_2/AuNRs-UCNPs-IR-783 dye/perovskite/Spiro-OMeTAD/Au) boosted to 20.5% under AM 1.5G simulated sunlight irradiation, created the highest record for the up-conversion perovskite solar cells based on rare-earth metal ions up to the report date [31].

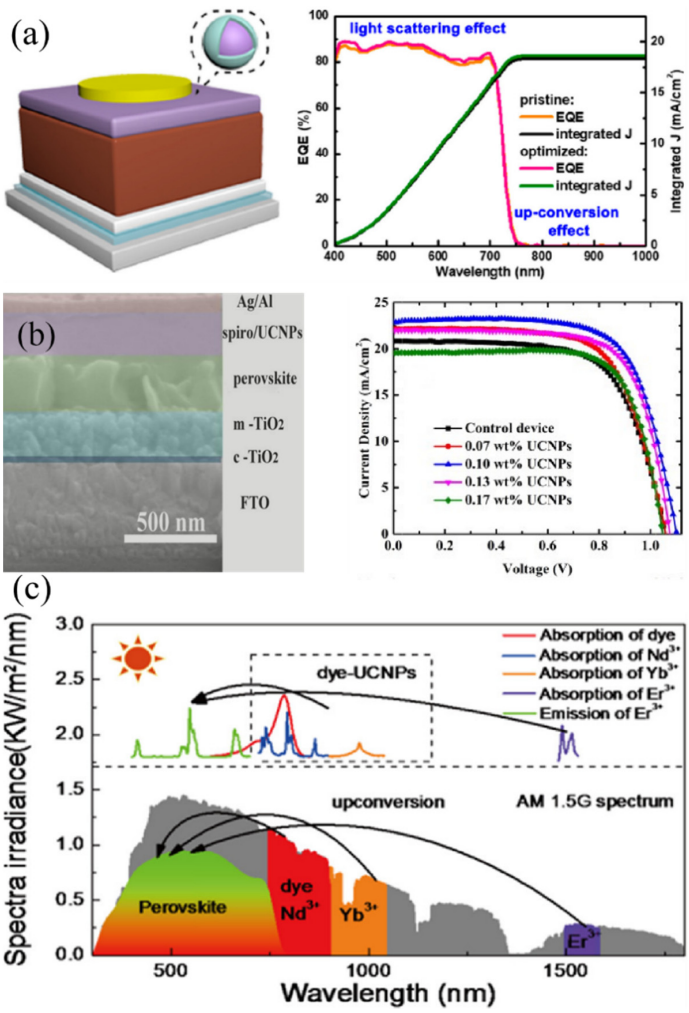

Figure 3. (**a**) Schematic device structure and external quantum efficiency curves of FTO/TiO_2/γ-$CsPbI_3$/$NaLuF_4$:Yb,Er@$NaLuF_4$ UCNPs-doped PTAA/Au (Reprinted/adapted with permission from Ref. [29]. Copyright 2019 American Chemical Society); (**b**) Cross-section SEM image for the device of FTO/$cTiO_2$/$mTiO_2$/$CH_3NH_3PbI_3$/Li(Gd,Y)F_4:Yb,Er-doped Spiro-OMeTAD/Ag-Al and *J-V* curves of devices with different amounts of UCNPs (Reprinted/adapted with permission from Ref. [30]. Copyright 2019 Elsevier); (**c**) The spectrum absorption range of PSCs and up-conversion spectral regions of dye-$NaYF_4$:Yb^{3+},Er^{3+}@$NaYF_4$:Yb^{3+},Nd^{3+} UCNPs (Reprinted/adapted with permission from Ref. [31]. Copyright 2020 American Chemical Society).

For rare-earth-based up-conversion materials used in perovskite solar cells, the hosts of Ln^{3+} ions, including single crystals of $NaYF_4$ and various core-shell structures, can be placed in various parts of the solar cell, including the electron/hole transporting layers, and the perovskite layer. Different combinations have their own advantages, but the most popular one is that the core-shell structure of $NaYF_4$ is integrated in the TiO_2 layer of the device. The unique advantage is that its energy level is well-matched to the electron transport layer very well, thus reducing the obstruction to the original electronic transport capability of the device.

As it can be seen, the MYF_4 family is a kind of well-host of Ln^{3+}-doping materials. In addition, the ETL can also be the host of Ln^{3+} dopant. Each host has its own merits and peculiarities. Most reports about Ln^{3+} doping have demonstrated the MYF_4 family as the host, which is due to that the MYF_4 family has excellent chemical and thermal stability, thus making Ln^{3+}-doped MYF_4 show good tolerance in various preparation processes in devices. Moreover, the high transmittance and low phonon energy ensure that the introduction of Ln^{3+}-doped MYF_4 layer will not have negative effects on other layers in the devices. In perovskite solar cells, the characteristics of the ETL have a great impact on the efficiency of the devices. The various doping and modified methods have been used to improve the carrier extract and transfer efficiency of ETL. Ln^{3+} ion-doping is a good way for ETL optimization, which endows the ETL with a new ability, that is, the IR light is converted to the visible light that the perovskite absorption layer can absorb. Specific device structure, doping hosts, and performance improvements are shown in Table 1.

Table 1. The PCE enhancement of up-conversion Ln^{3+}-doping solar cell device.

Device Structure	Doped Materials	PCE Enhancement	Ref.
UC crystals/FTO/TiO_2/$MAPbI_3$/HTM/Au	$LiYF_4$:Yb^{3+}, Er^{3+}	7.9% to 8.8%	[22]
FTO/compact-TiO_2/$NaYF_4$ core-shell nanoparticles-TiO_2/$MAPbI_3$/ Spiro-MeOTAD/Ag	NaYF4:Yb^{3+}, Tm^{3+}	14.1% to 16.9	[24]
FTO/compact-TiO_2/$NaYF_4$-TiO_2/$MAPbI_3$/Spiro-MeOTAD/Au	NaYF4:Yb^{3+}, Er^{3+}	13.7% to 16.0%	[17]
ITO/compact-TiO_2/ $NaYF_4$-$MAPbI_3$/ Spiro-MeOTAD/Ag	NaYF4:Yb^{3+}, Er^{3+}	13.46% to 19.70%	[25]
FTO/compact-TiO_2/TiO_2-$Cu_{2-x}S$@SiO_2@Er_2O_3 /$MAPbI_3$/Spiro-MeOTAD/Au	m$Cu_{2-x}S$@SiO_2@Er_2O_3	16.2% to 17.8%	[26]
FTO/compact-TiO_2/mp-TiO_2/mp-ZrO2- $NaYbF_4$ /$FA_{0.4}MA_{0.6}PbI_3$/C	$NaYF_4$:Ho^{3+}	10.9% to 14.3%	[27]
FTO/KY_7F_{22}-$Yb^{3+}Er^{3+}$/$FA_{0.83}Cs_{0.17}Pb(I_{0.6}Br_{0.4})_3$/Spiro/Au FTO/$FA_{0.83}Cs_{0.17}Pb(I_{0.6}Br_{0.4})_3$/$KY_7F_{22}$-$Yb^{3+}Er^{3+}$/Spiro/Au	KY_7F_{22}:Yb^{3+}, Er^{3+}	13.5% to 14.0%	[28]
FTO/TiO_2/$CsPbI_3$/UCNPs-PTAA/Au	$NaLuF_4$:Yb,Er@$NaLuF_4$	15.5% to 15.9%	[29]
FTO/c-TiO_2/m-TiO_2/$CH_3NH_3PbI_3$/Spiro-UCNP/Ag-Al	Li(Gd, Y)F_4:Yb^{3+}, Er^{3+}	14.7% to 18.3%	[30]
FTO/SnO_2/UCNPs-Dye-AuNRs/FAMACsPb(I, Br)$_3$	$NaYF_4$:Yb^{3+}, Er^{3+}@$NaYF_4$:Yb^{3+}, Nd^{3+} core-shell	19.4% to 20.5%	[31]
FTO/compact-TiO_2/$NaYF_4$/$MAPbI_3$/Spiro-MeOTAD/Ag	$NaYF_4$:Yb^{3+}, Er^{3+}	17.8% to 18.1%	[32]
FTO/compact-TiO_2/TiO_2 nanorods/$MAPbI_3$/Spiro-MeOTAD/Au	TiO_2:Yb^{3+}, Er^{3+}	10.6% to 12.9%	[33]
FTO/compact-TiO_2/TiO_2-ZrO_2-$NaYF_4$@SiO_2 /$MAPbI_3$/Carbon	$NaYF_4$:Yb^{3+}, Er^{3+}	8.2% to 9.9%	[34]
FTO/compact-TiO_2/$MAPbI_3$- TiO_2-$NaYF_4$@TiO_2 /Spiro-MeOTAD/Au	NaYF4:Yb^{3+}, Tm^{3+}	13.4% to 16.3%	[35]
ITO/SnO_2/$FAPbI_3$/UCNPs/Spiro-UCNPs/Au	$NaYF_4$:Yb^{3+}, Er^{3+}	16.0% to 18.0%	[36]

Table 1. *Cont.*

Device Structure	Doped Materials	PCE Enhancement	Ref.
FTO/TiO2/UCNPs/FACsPb(I,Br)$_3$/Spiro/Au	β-NaYF$_4$: Nd^{3+}, Yb^{3+}, Er^{3+}	18.0% to 19.2%	[37]
ITO/ZnO/IR806-UCNPs-MAPbI$_3$/Spiro/Ag	β-NaYF$_4$:Yb^{3+}, Er^{3+}	13.5% to 17.5%	[38]
FTO/TiO$_2$/UCNPs-(FA$_{0.83}$MA$_{0.17}$)$_{0.95}$Cs$_{0.05}$Pb(I$_{0.9}$Br$_{0.1}$)$_3$/Spiro/Au	NaYF$_4$:Yb^{3+}/Er^{3+}/Sc^{3+}@NaYF$_4$ core-shell	17.44% to 20.2%	[39]
FTO/Er-TiO$_2$/CH$_3$NH$_3$PbI$_{3-x}$Cl$_x$/Spiro/Ag	Er-doped TiO$_2$	9.1% to 10.6%	[40]
FTO/TiO$_2$ nanorod/UCNP/MAPbI$_3$/C	SiO$_2$/NaYF$_4$:Yb, Er@SiO$_2$	11.9% to 14%	[41]
FTO/UCNP-TiO$_2$/FAMACsPb(I, Br)$_3$/Spiro/Au	Er^{3+}-Yb^{3+}-Li$^+$ tri-doped TiO$_2$	14.0% to 16.5%	[42]

3.2. Ln^{3+}-Based Down-Conversion Materials

Rare-earth metals with 4f electronic structure can also be used as down-conversion materials which have the ability to absorb ultraviolet light and re-emit visible light. In 2014, Khan and coworkers prepared YVO$_4$:Eu^{3+} nano-phosphor layer on the bottom surface of perovskite solar cell (YVO$_4$:Eu^{3+}/Glass/FTO/cTiO$_2$/mTiO$_2$/CH$_3$NH$_3$PbI$_3$/HTM/Au, Figure 4a). On the one hand, the use of down-shifting material converted a part of UV spectrum to visible region, thus, to improve the short wavelength spectral response (300–400 nm). On the other hand, the capping layer could protect device from high energy UV radiation, thus, to reduce UV-induced device degradation [43]. Similar to up-conversion materials, down-conversion materials are integrated into the electron transporting layer. Kang et al. investigated the Au@Y$_2$O$_3$:Eu^{3+} dual-functional films combining the effects of wavelength down-conversion and localized surface plasmon resonance for the perovskite solar cells in 2017. The photocurrent density increased from 20.7 mA/cm^2 to 21.5 mA/cm^2 for the Au@Y$_2$O$_3$:Eu^{3+}-modified device (Figure 4b), which was also accompanied by improved stability [44]. Huang et al. used down conversion CeO$_2$:Eu^{3+} nanophosphor to improve the device performance, and the optimal CeO$_2$:Eu^{3+} was embedded into mesoporous TiO$_2$ layer. The device exhibited about 6.9% PCE enhancement and significantly slower decay toward UV light irradiation when compared with bare TiO$_2$-based device [45]. Another samarium (Sm)-based down-conversion material, Sr$_2$CeO$_4$:Sm^{3+}, was introduced in the PSCs to reduce photo-loss and photo-degradation, by Chi and cooperators. The Sr$_2$CeO$_4$:Sm^{3+} nanophosphors could convert UV-light in the range of 283~400 nm to visible light. The optimized device of FTO/cTiO$_2$/Sr$_2$CeO$_4$:Sm^{3+}/(CsFAMA)Pb(Br,I)$_3$/Spiro-OMeTAD/Au achieved the highest PCE of 17.9%, which was about 16.2% enhancement compared with the control device without optimization. Moreover, the device with Sr$_2$CeO$_4$:Sm^{3+} could maintain higher stability when exposed to UV-light irradiation (Figure 4c) or stored under ambient environment conditions for a much longer period [46]. Song's group explored CsPbCl$_{1.5}$Br$_{1.5}$:Yb^{3+},Ce^{3+} nanocrystals as a down-conversion material which can convert blue/UV photons into lower-energy photons with PLQYs exceeding 100% for commercial silicon solar cells. Then, the nanocrystals were self-assembled in front of the device through a liquid-phase depositing method, and Figure 4d exhibits the device structure. The co-doped nanocrystals exhibited a strong 988 nm near-infrared emission from the $^2F_{5/2}$–$^2F_{7/2}$ transition of Yb^{3+} ions, as well as the excitonic emission of CsPbCl$_{1.5}$Br$_{1.5}$ nanocrystals. The co-doping of Ce^{3+} can promote the process of quantum-cutting emission through energy transfer (electrons on the conduction relax to the 5d state of Ce^{3+} ions and then transfer to the Yb^{3+} ions). As a result, the highest PLQY of 146% can be achieved. The device PCE increased from 18.1% to 21.5% [47]. Later, the same group explored co-doping and tri-doping lanthanide ions in CsPbCl$_x$Br$_y$I$_{3-x-y}$ quantum dots to improve the quantum-cutting efficiency. It was found that the Yb^{3+}-Pr^{3+} and Yb^{3+}-Ce^{3+} pairs can effectively sensitize the emission of Yb^{3+}, which was due to the similar intermediate energy states of Pr^{3+} and Ce^{3+} with the exciton transition energy of perovskite QDs. As a result, Yb^{3+}-Pr^{3+}-Ce^{3+} tri-doped CsPbClBr$_2$ QDs exhibited the highest PLQY of 173%,

and 20% improvement in PCE can be achieved by introducing tri-doped QDs into a commercial CIGS solar cell. The PCE of devices based on different tri-doped perovskite QDs is summarized in Figure 4e [48]. Gamelin and co-workers utilized Yb^{3+}:$CsPb(Cl_{1-x}Br_x)_3$ as a quantum-cutting (QC) layer in single-junction PVs, and demonstrated the potential efficiency gains through detailed balance calculations. They found that the increased PCE was mainly attributed to the reduced reflection, thermalization, and nonradiative-recombination losses from UV and blue photons. Their calculations also revealed that Yb^{3+}:$CsPb(Cl_{1-x}Br_x)_3$ boosted performance in widely different geographic locations with substantially different spectral irradiances by combining PL saturation and real-world photon fluxes. The interplay between the QC PLQY, QC/PV optical coupling, and optimized QC and PV energy gaps is another key insight into the calculations, which can provide particle design rules for optimized QC/PV devices based on real-world materials and conditions [49]. Additionally, lanthanide ions were also reported to be used as interfacial modifiers in the PSCs. For example, $Eu(TTA)_2$(Phen)MAA was inserted at the interface of m-TiO_2/perovskite, and the device efficiency can be improved from 17% to 19.07% via effectively utilizing the incident UV light. The device structure and energy-level diagram are shown in Figure 4f. The inter-layer can also inhibit the device of UV-initiated degradation, thus, to effectively improve the device photostability [50].

The influence of down-conversion materials on perovskite solar cell is mainly reflected in the efficient conversion of ultraviolet light into visible light, improved light captures ability, and long-term stability. Moreover, the integration of down-conversion materials acts as light scatter during the propagation process inside the device, increasing the optical length and promoting the light absorption; these features improve the conversion efficiency of the device, as shown in Table 2.

Table 2. The PCE enhancement of down-conversion Ln^{3+}-doping solar cell device.

Device Structure	Doped Materials	PCE Enhancement	Ref.
DCNP/FTO/TiO_2/$CH_3NH_3PbI_3$/HTM/Au	YVO_4:Eu^{3+}	7.4% to 7.9%	[43]
FTO/cTiO_2/mTiO_2-CeO_2:Eu^{3+}/$MAPbI_3$/Spiro/Au	CeO_2:Eu^{3+}	10.1% to 10.8%	[45]
FTO/cTiO_2/DCNP/(CsFAMA)Pb(Br,I)$_3$/Spiro-OMeTAD/Au	Sr_2CeO_4:Sm^{3+}	15.4% to 17.9%	[46]
C-Si solar cell/Perovskite film as DCNP	Yb^{3+}, Ce^{3+} co-doped Cs $PbCl_{1.5}Br_{1.5}$	18.1% to 21.5%	[47]
Down-converter for $CuIn_{1-x}Ga_xSe_2$ (CIGS) and Si solar cell	Yb^{3+}, Ln^{3+}(Nd, Dy, Tb, Pr, Ce) doped-QDs	~20% enhancement	[48]
Down-conversion film for single-junction PV	Yb^{3+}:$CsPb(Cl_{1-x}Br_x)_3$	-	[49]
FTO/cTiO_2/mTiO_2-DCNP/$(FA_{0.83}MA_{0.17})_{0.95}Cs_{0.05}Pb(I_{0.83}Br_{0.17})_3$/Spiro/Au	$Eu(TTA)_2$(Phen)MAA	17.0% to 19.0%	[50]
$NaYF_4$:Eu^{3+}/FTO/TiO_2/$Cs_{0.05}(MA_{0.17}FA_{0.83})_{0.95}Pb(I_{0.83}Br_{0.17})_3$/Spiro/Au	$NaYF_4$:Eu^{3+}	17.6% to 20.1%	[51]

3.3. Optimization of Electron Transporting Layer or Perovskite Layer by Ln^{3+} Ions-Doping

Apart from the above summarized up- and down-conversion materials, Ln^{3+} ions can also be used as dopants in perovskite materials and devices to optimize the electronic properties. One common strategy is doping Ln^{3+} ions into the charge transport layer, thus, to tune the energy-level alignment or control the interfacial defects. In 2016, in the PSC, La^{3+} ions were used to tune the band alignment of TiO_2 layer through eliminating oxygen species and surface-inducing vacancies. The Fermi energy upward shifted from −4.55 eV to −4.43 eV for doped-La/TiO_2, as shown in Figure 5a, thus enhancing the open circuit voltage (V_{oc}) and fill factor (FF) [52]. Soon afterwards, a similar effect of tuning the Femi energy level can be realized by doping the Sm^{3+} rare-earth element into the TiO_2 electron transfer layer [53], and the results of the improved device performance can be seen in Figure 5b. Wu and co-workers improved the device efficiency to a champion value of 21.75% and good UV stability by using Sc^{3+}-tailored brookite TiO_2 mesoporous layer [54].

Other rare-earth elements, such as Er^{3+} ions, were also demonstrated to be doped into the TiO_2 layer in the $CH_3NH_3SnI_3$-based PSCs [55].

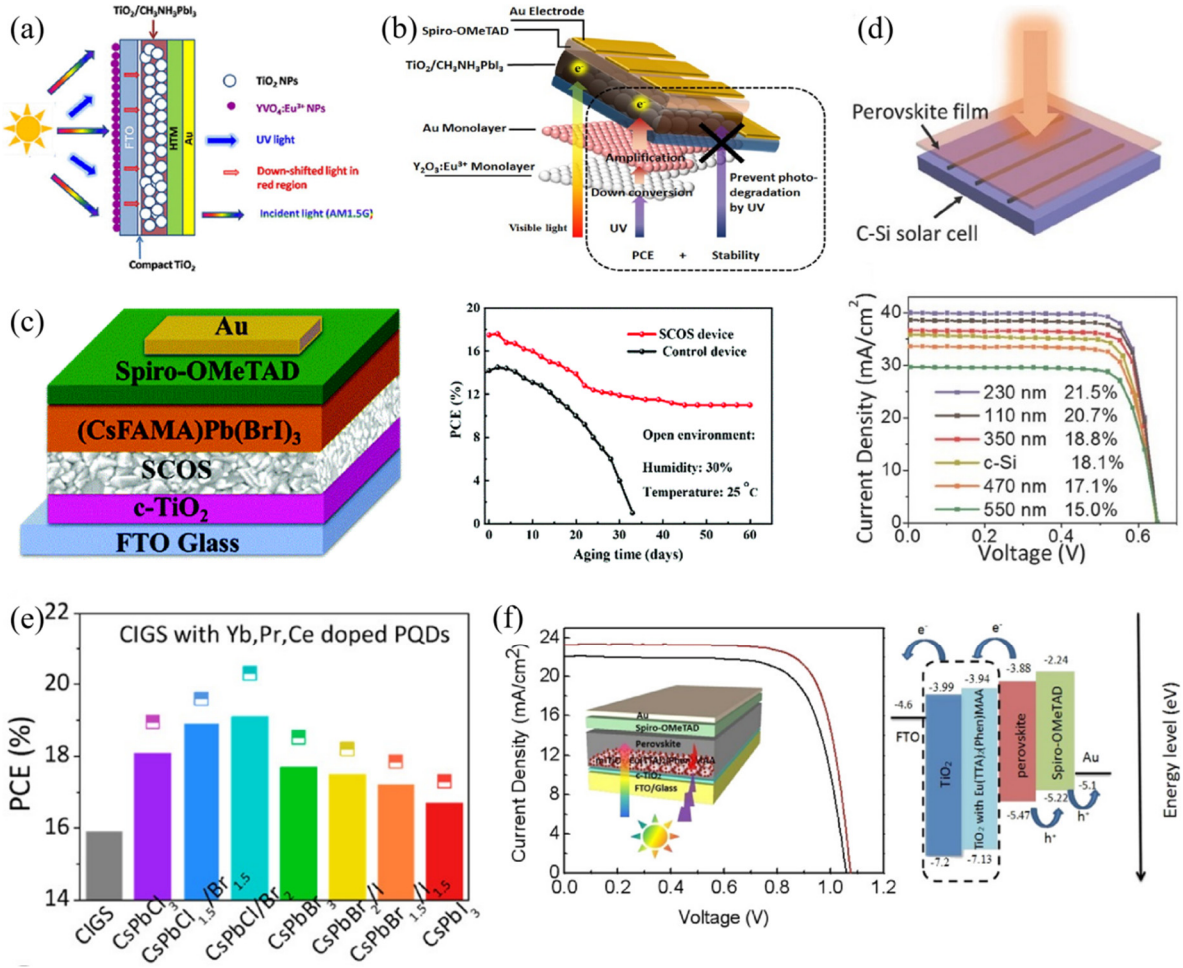

Figure 4. Schematic diagrams for (**a**) perovskite solar cell of YVO_4:Eu^{3+}/Glass/FTO/$cTiO_2$/$mTiO_2$/$CH_3NH_3PbI_3$/HTM/Au (Reprinted/adapted with permission from Ref. [43]. Copyright 2014 AIP Publishing) and (**b**) Au@Y_2O_3:Eu^{3+}-modified PSC with the functions of down-conversion and device stability enhancement (Reprinted/adapted with permission from Ref. [44]. Copyright 2017 Springer Nature); (**c**) Device structure of FTO/$cTiO_2$/Sr_2CeO_4:Sm^{3+}/(CsFAMA)Pb(Br,I)$_3$/Spiro-OMeTAD/Au and long-term stability measurements under open environment (Reprinted/adapted with permission from Ref. [46]. Copyright 2019 Royal Society of Chemistry); (**d**) Device structure and *J*-*V* curves for silicon solar cells by using $CsPbCl_{1.5}Br_{1.5}$:Yb^{3+},Ce^{3+} as down-conversion material (Reprinted/adapted with permission from Ref. [47]. Copyright 2017 John Wiley and Sons); (**e**) PCE comparisons for CIGS solar cells with Yb^{3+}-Pr^{3+}-Ce^{3+} tri-doped $CsPbCl_xBr_yCl_{3-x-y}$ ($x \geq 0$, $y \leq 3$, $x + y \leq 3$) quantum dots (Reprinted/adapted with permission from Ref. [48]. Copyright 2019 American Chemical Society); (**f**) Device structure and performance of Eu(TTA)$_2$(Phen)MAA-doped PSC and the corresponding energy-level alignment (Reprinted/adapted with permission from Ref. [50]. Copyright 2019 American Chemical Society).

Another important strategy is doping lanthanide ions in perovskite films or lattices. For example, Tang et al. introduced Sm^{3+} ions into $CsPbBr_3$ lattice and applied it into the device architecture of FTO/$cTiO_2$/$mTiO_2$/$CsPb_{0.97}Sm_{0.03}Br_3$/carbon. The strong interaction between Ln^{3+} and Br^- can change the surface energy during the crystal growth, thus facilitating to large formation of grains. Due to the increased grain size, prolonged carried lifetime and reduced charge carrier recombination, an ultrahigh V_{oc} of 1.594 V can be achieved and the highest PCE was improved from 6.99% to 10.14% [56]. A similar doping strategy

was realized by Patil and co-workers, who doped Sm^{3+} ion into $CsPbI_2Br$ perovskite to improve the film quality. The device of FTO/$cTiO_2$/$mTiO_2$/$CsPb_{0.97}Sm_{0.03}I_2Br$/P3HT/Au (Figure 5c) exhibited superior PCE and long-term stability [57]. Zhou and cooperators utilized Eu^{3+}-Eu^{2+} ion pair redox shuttle to decrease I^0 defects and oxide Pb^0 in a cyclic transition, following the reactions of ($2Eu^{3+}+Pb^0 \rightarrow 2Eu^{2+}+Pb^{2+}$) and ($Eu^{2+}+I^0 \rightarrow Eu^{2+}+I^0 \rightarrow Eu^{3+}+I^-$). As a result, the perovskite device can retain 93% efficiency under continuous 1 sun illumination or 91% PCE through thermal treating at 85 °C after 1000 h [58]. Later, Eu^{3+} ions were incorporated into inorganic $CsPbI_2Br$ perovskite, which can also reduce the charge recombination centers and prolong the crystal sizes as the above-mentioned Sm^{3+}. Eventually, the thermal stability under 85 °C and moisture stability under the humidity of 40% can be significantly improved [59].

Recently, Chen's group inserted an ultrathin Eu-MOF (metal-organic framework) layer as an interfacial modification layer in the device of ITO/SnO_2/Eu-MOF/FAMACsPb(I, Br)$_3$/Spiro-OMeTAD/Au. The Eu-MOF layer has multiple effects on the device properties, including improving the light absorption, changing the residual tensile strain into compressive strain and passivating the deep defect states. Through the synergistic impact induced by Eu-MOF, a highest PCE of 22.16% and long-term stability over 2000 h were achieved [60].

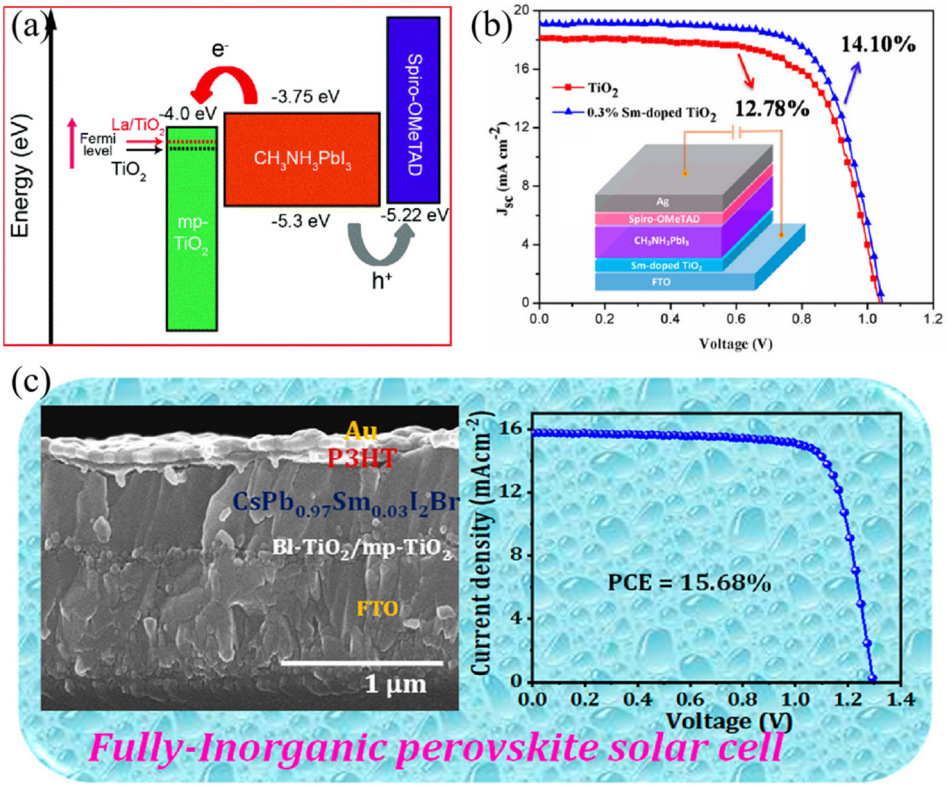

Figure 5. (**a**) Energy-level diagram for the device of FTO/La^{3+}-doped TiO_2/mp-TiO_2/$CH_3NH_3PbI_3$/Spiro-OMeTAD/Au (Reprinted/adapted with permission from Ref. [52]. Copyright 2016 American Chemical Society); (**b**) *J-V* curves of PSCs with and without doping Sm^{3+} ions (Reprinted/adapted with permission from Ref. [53]. Copyright 2017 American Chemical Society); (**c**) Cross-section of SEM image and *J-V* curve for the best perovskite device of FTO/$cTiO_2$/$mTiO_2$/$CsPb_{0.97}Sm_{0.03}I_2Br$/P3HT/Au (Reprinted/adapted with permission from Ref. [57]. Copyright 2020 American Chemical Society).

4. Application of Ln^{3+} in Perovskite Light-Emitting Diodes

Rare-earth doping changes the emission spectra of the perovskite materials, which can be divided into the blue shift, enhancement of the original perovskite luminescence and the new peak excited by the doped ions [61–66]. The temperature and doping concentration

will affect the luminescence characteristics [67,68]. Using Ln^{3+}-doping to modulate the luminescence characteristics of perovskite can expand the application of perovskite materials in light-emitting devices.

4.1. Adjusting the Luminescence Spectrum

It is well-known that the inferior performances of blue-violet and near-infrared emission based on perovskite materials will hinder their future commercial applications in multi-color displays. Therefore, it is important to improve the performances of the entire visible spectral region. There are many approaches to modulate the luminescence range of PVK, including doping of various ions or passivators, controlling the lattice size of PVK, or changing the composition proportion of perovskite, etc. This section focuses on the luminescence range of perovskite materials modulated by doping Ln^{3+} ions. The modulation of perovskite spectrum can be realized by doping rare-earth ions into the perovskite lattice. In order to investigate the effect of rare-earth ion-doping on the spectral position of emission and the corresponding changes in optical characteristics, Song et al. systematically demonstrated the doping of various Ln^{3+} ions (Ln^{3+} = Yb^{3+}, Er^{3+}, Dy^{3+}, Tb^{3+}, Eu^{3+}, Sm^{3+}, Ce^{3+}) in $CsPbCl_3$ nanocrystals in 2017. As it can be seen in Figure 6a, with the increase of the atomic number of the doped Ln^{3+} ions, from Ce to Yb, the primary excitation peak was gradually blue-shifted, which was due to the enlarged band gap of the perovskite host induced by the lattice contraction of doped NCs. The photoluminescence quantum yield for the Ln^{3+}-doped $CsPbCl_3$ NCs was enhanced, which was ascribed to the intrinsic emission of Ln^{3+} ions. In addition, Yb^{3+}-doped $CsPbCl_3$ NCs also exhibited strong NIR emission at around 1000 nm with high PLQY of 143% [69]. Then, they also doped different Ln elements (La, Y, Eu, Lu) into mixed $K_xCs_{1-x}PbCl_3$ quantum dots (QDs). As a result, the luminescence efficiency around 408 nm boosted to 31.2% for $K_xCs_{1-x}PbCl_3$: Eu^{3+} QDs from 10.3% for pristine $K_xCs_{1-x}PbCl_3$ QDs [61]. Soon afterwards, Gamelin et al. specially studied the quantum-cutting effect of Yb^{3+}-doped $CsPbCl_3$ NCs by using variable temperature photoluminescence (PL), transient absorption, and time-resolved photoluminescence (TRPL) measurements. The doped Yb^{3+} ions can induce a shallow defect level in the perovskite lattice, which is comparable with native defects for trapping photo-excited charge carriers. In the case of Yb^{3+}-doped NC (see Figure 6b), two neighboring excited Yb^{3+} ions were formed after energy transfer was captured by Yb^{3+}-induced defect from the C_SPbCl_3 excited states. Such nonradiative energy transfer process happened at a picosecond time scale [70]. They also found that efficient quantum cutting can be realized in the Yb^{3+}-doped $CsPb(Cl_{1-x}Br_x)_3$ thin films, and that the PLQY exceeded 190% for the NIR emission. This work also indicated that this quantum-cutting effect is only dependent on the Yb^{3+}-doped perovskite composition rather than the perovskite crystal morphologies [71]. In addition, for Pb-free metal halide double perovskite, the doping of Ln^{3+} ions also show well-modulated characteristics of emission wavelength. Yb^{3+} ions were to be incorporated into $Cs_2AgInCl_6$ double perovskite crystals (Figure 6c), resulting in 994 nm NIR emission [72]. Later, Ishii and Miyasaka used Yb^{3+}-doped $CsPbCl_3$ perovskite to obtain bright NIR light-emitting diode (LED, Figure 6d), and the maximum EQE around 1000 nm of the device is up to 5.9% [73]. Additionally, Yb^{3+} ions were also used to tune the fluorescent emission in lead-free double $Cs_2AgBiCl_6$ and $Cs_2AgBiBr_6$ perovskite NCs [67]. Recently, Miao and Han et al. doped Er^{3+} ions into the lead-free $Cs_2NaEr_{1-x}B_xCl_6$ (B is In, Sb or Bi) perovskite NCs, thus, to obtain effective NIR emission at a telecommunication wavelength of 1543 nm. Such NIR emission can be mainly attributed to the energy transition from $^4I_{13/2} \rightarrow {}^4I_{15/2}$ to Er^{3+} [74]. Recently, ultrasmall $CsPbX_3$ QDs formed on the surface of $NaYF_4$:Yb/Tm@$NaYF_4$:Yb core-shell UCNPs (see in Figure 6e) and could exhibit tunable down-conversion PL and up-conversion PL under UV and NIR excitation, respectively, which can be potentially applied in the field of fluorescent anticounterfeiting technology [75].

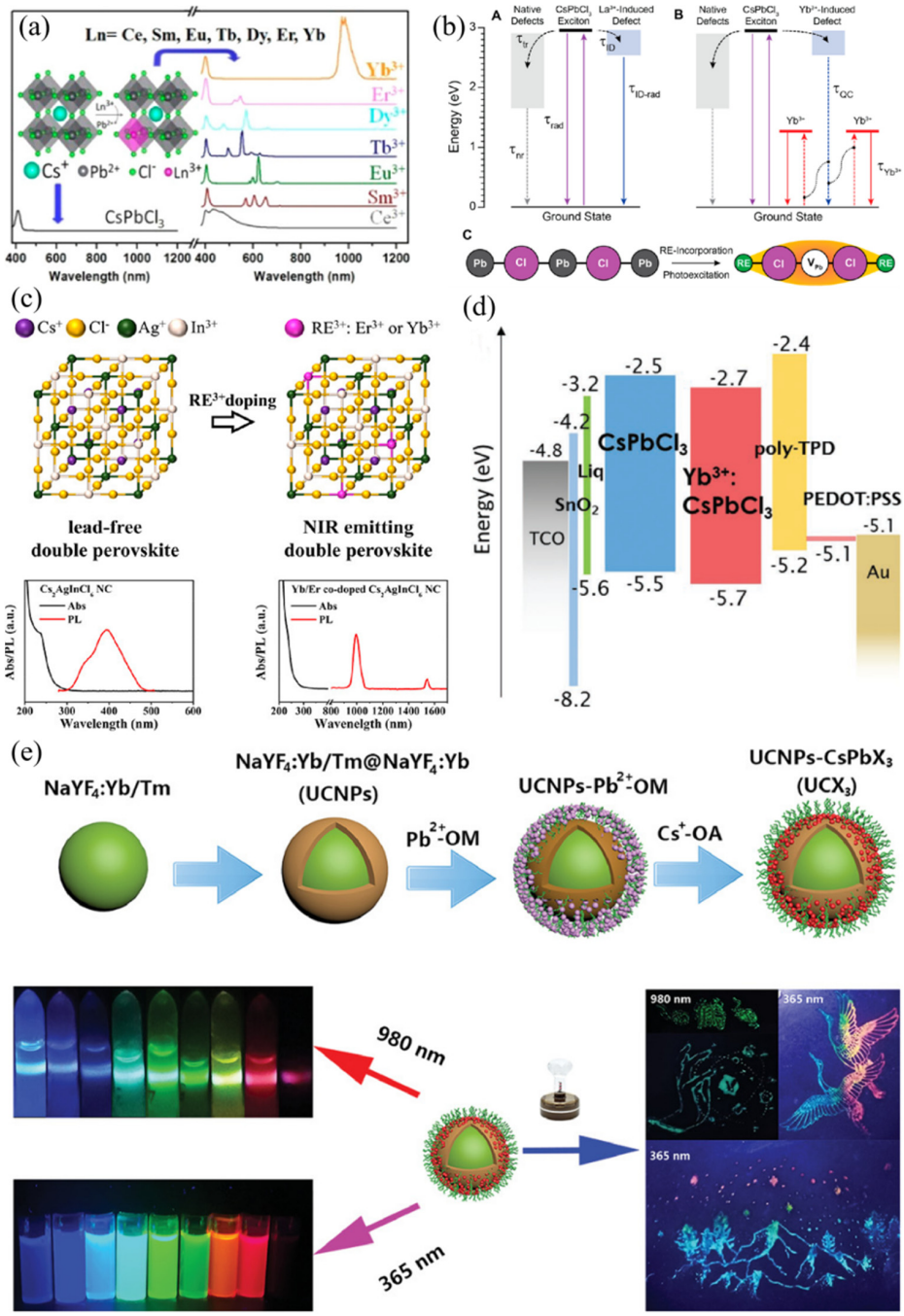

Figure 6. (**a**) Photoluminescence spectra of $CsPbCl_3$ nanocrystals with doping Yb^{3+}, Er^{3+}, Dy^{3+}, Tb^{3+}, Eu^{3+}, Sm^{3+}, Ce^{3+} ions, respectively (Reprinted/adapted with permission from Ref. [69]. Copyright 2017 American Chemical Society); (**b**) Schematic maps for La^{3+}- induced defect emission, Yb^{3+} sensitization mechanism, and charge-neutral vacancy-defect structure of Ln^{3+}-doped $CsPbCl_3$ nanocrystals (Reprinted/adapted with permission from Ref. [70]. Copyright 2018 American Chemical Society); (**c**) Crystal lattice structure of $Cs_2AgInCl_6$ perovskite with doping Ln^{3+} ions and the corresponding absorption/photoluminescence spectra (Reprinted/adapted with permission from Ref. [72]. Copyright 2019 American Chemical Society); (**d**) Energy-level diagram of perovskite LED with structure of TCO/SnO_2/Liq/Yb^{3+}:$CsPbCl_3$/poly-TPD/PEDOT:PSS/Au (Reprinted/adapted with permission from Ref. [73]. Copyright 2020 Wiley-VCH); (**e**) Fabrication process of $NaYF_4$:Yb/Tm@$NaYF_4$:Yb UCNPs-$CsPbX_3$ (X = Cl, Br, I or mixed halide elements) for full color anticounterfeiting (Reprinted/adapted with permission from Ref. [75]. Copyright 2021 John Wiley and Sons).

The influence of Ln^{3+} dopant on perovskite luminescence was mainly reflected in the change of the emission peak positions of pristine perovskite. For different kinds of rare-earth ions, the lengths of blue shift for emission peaks of pristine perovskite were various. With the increase of doping concentration, the emission peaks exhibited further blue shift. As the doped Ln^{3+} ions modified the internal defects of the original perovskite lattice, the overall performance of photoelectric and stability was enhanced.

4.2. White Light Emission

The Ln^{3+} ion co-doping can introduce new peaks in addition to the original perovskite excitation peak. Through the design of a particular structure, the purpose of white light emission can be achieved. White light emission and device based on rare metal ion pairs co-doped $CsPbCl_3$ NCs was reported, and the corresponding ion pairs were Ce^{3+}/Mn^{2+}, Ce^{3+}/Eu^{3+}, Ce^{3+}/Sm^{3+}, Bi^{3+}/Eu^{3+}, and Bi^{3+}/Sm^{3+}, as illustrated in Figure 7a. Here, Ce^{3+} ions not only act as the role of blue and green emitted components, but also sensitize the red emission of Mn^{2+}, Eu^{3+}, and Sm^{3+} ions. The optimal white light emission with the maximum PLQY value of 75% was achieved for the sample of Ce^{3+}/Mn^{2+} co-doped $CsPbCl_{1.8}Br_{1.2}$ NCs. Then the white light-emitting diode (WLED) combined co-doped perovskite NCs, GaN LED chip, and polystyrene was fabricated. The luminous efficiency and color rendering index (CRI) was 42 lm/W and over 90, respectively [76]. Considering that $CsPbX_3$ (X = Br, Cl, I) have a well luminescence in green and red parts, the white light emission can be realized by introducing the blue part through Ln^{3+}-doping. Monserrat and Zhang et al. prepared $CsPbBr_3$ nanocrystals by introducing Nd^{3+} ions as Pb-site dopants to achieve highly efficient blue emission. They explained the enhanced mechanism via theoretical calculation. The exciton binding energy changed after partial Pb-site replacement with Nb. On the one hand, the dopants can make the perovskite lattice constrictive and Pb-Br bond shortened, thus, to enhance exciton oscillator strength. On the other hand, the flattened valence and conduction bands increased the electron and hole effective masses. Both of these caused the enhancement of PLQY. Finally, an all-inorganic perovskite WLED based on Nd^{3+}-doped $CsPbBr_3$ NCs, $CsPbBr_3$ NCs, and $CsPbBr_{1.2}I_{1.8}$ NCs, which acted as blue-, green-, and red-emitted components, respectively, was prepared [77].

Recently, Giri and coworkers integrated Ce^{3+} and Tb^{3+} ions into 2D $CH_3NH_3PbBr_3$ nanosheets to obtain highly blue-emitted $MAPb_{1-x}Ce_xBr_3$ and $MAPb_{1-x}Tb_xCl_{3x}Br_{3x-3}$ perovskite nanomaterials. The down-converter white LED-based on UV LED chip (Figure 7b), $MAPb_{0.3}Ce_{0.7}Br_3$ and Rhodamine B exhibited CIE coordinates of (0.334, 0.326) [78]. In addition, Song's group reported the first electroluminescence (EL) white LED device based on Sm^{3+}-doped $CsPbCl_3$ NCs. The device structure was ITO/ZnO/PEI/Sm^{3+}-doped $CsPbCl_3$/TCTA/MoO_3/Au. The EL spectra were dependent on the doped Sm^{3+} ion concentration which nearly covered the entire visible spectrum region of 400~700 nm. The device structure and corresponding performances are exhibited in Figure 7c. When the Sm^{3+} ion concentration increased to 5.1 mmol%, the chromaticity coordinate (CIE) and CRI for the single-component WLED was (0.32, 0.31) and 0.93, respectively [79].

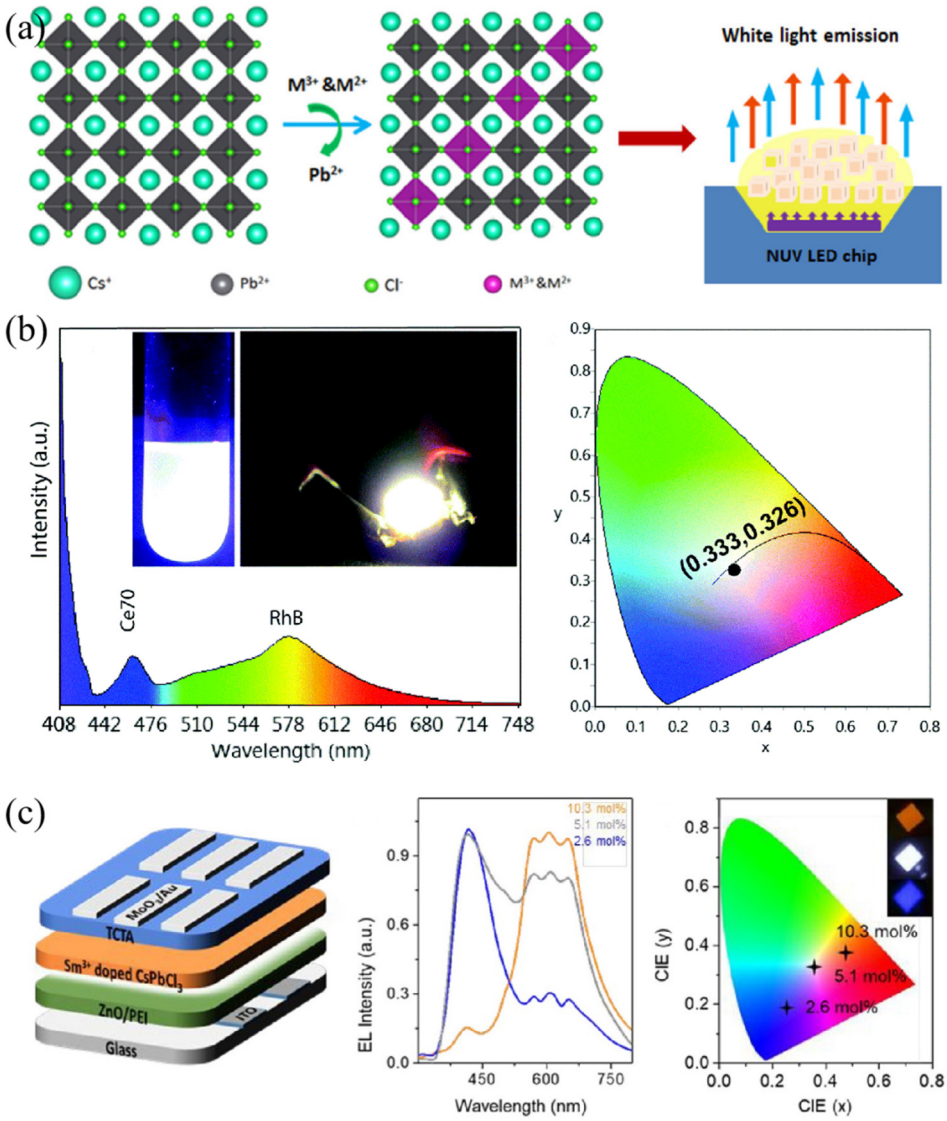

Figure 7. (**a**) Crystal structure of $CsPbCl_xBr_{3-x}$ with co-doping metal ion pairs (M^{3+}/M^{2+}) and the white LED combining $CsPbCl_{1.8}Br_{1.2}$:Ce^{3+}/Mn^{2+} and ultraviolet chip (Reprinted/adapted with permission from Ref. [76]. Copyright 2018 American Chemical Society); (**b**) EL spectrum, white light emission photograph and CIE chromaticity coordinates of WLED based on UV LED chip, Ce^{3+}:$CH_3NH_3PbBr_3$, and Rhodamine B (Reprinted/adapted with permission from Ref. [78]. Copyright 2021 Royal Society of Chemistry); (**c**) Device structure, EL spectra, and CIE coordinates for perovskite WLED based on Glass/PEI/Sm^{3+}:$CsPbCl_3$/TCTA/MoO_3/Au (Reprinted/adapted with permission from Ref. [79]. Copyright 2020 American Chemical Society).

4.3. Doping for Luminescence Enhancement

Apart from tuning the emitted spectrum, rare metals were also reported to modulate the PL/EL efficiency and kinetics via doping them into perovskite materials. For example, Yb^{3+} ions were introduced into $CsPb(Cl_{1-x}Br_x)_3$ perovskite nanocrystals. Meanwhile, the band gaps were tuned via changing the x value (x = 0~1). Through the quantum-cutting process induced by Yb^{3+} dopants, the maximum value of PLQY exceeded 200% [80]. As it can be seen in Figure 8a, the Ce^{3+} (103 pm) ion with similar ion radius to Pb^{2+} (119 pm) was introduced into the crystal structure of $CsPbBr_3$ without forming additional trap states, and the PLQY was significantly improved. Ultrafast transient absorption and TRPL were performed to reveal the mechanism. Near band-edge states can be formed and induced by doping ions, thus, to accelerate the process of hot-exciton relaxation and

exciton trapping to the band gap trap states. The average PL lifetimes were shortened after doping Ce^{3+}. The nonradiative trapping states were replaced by newly appeared band-edge PL emissions, which were beneficial for the PL enhancement. The LED with the structure of ITO/PEDOT:PSS/poly-TPD/Ce^{3+}-doped $CsPbBr_3$ NCs/TPBi/LiF/Al exhibited a highest EQE value of 4.4%, which was comparable with the pristine device (1.6%) [63]. Mohammed et al. introduced YCl_3 into $CsPbCl_3$ NCs for surface defect passivation through a post- synthetic dual-surface treatment. The Pb-Cl ion pair vacancies and uncoordinated Pb atoms on the perovskite NCs' surfaces could be counteracted by Y^{3+} and Cl^- ions, thus reducing the surface defects. As a result (Figure 8b), the PLQY of the post-treated NCs enhanced about 60 times compared with the pristine samples [81]. The surface passivation effect can also be realized in the case of $PrCl_3$-doped $CsPbBr_xCl_{3-x}$ QDs. The reduced nonradiative recombination centered on the NC surfaces mainly attributed to the enhancement of PLQY [82]. Song's group co-doped La^{3+} and F^- ions into $CsPbCl_3$ QDs to manipulate the optical performances through passivating the defects of Cl vacancies, resulting in improved PLQY of blue-violet emissions [68]. They also investigated the structural and optical variation tendency under high pressure with and without doping Eu^{3+} ions in the $CsPbCl_3$ QDs. The energy transfer efficiency from perovskite to Eu^{3+} ions was improved when treated under relatively high pressure, thus, this improved the PL intensity [66]. Li et al. reported B-site doping in $CH_3NH_3PbBr_3$ single crystal by using Er ion, and the photograph is shown in Figure 8c. A shallow defect level formed inside of the band gap of $CH_3NH_3PbBr_3$ boosted the PL emission intensity. Lower trap density and higher charge carrier mobility was also achieved [65]. In addition, rare-earth metal can be used as an interfacial layer in perovskite LED. For example, Yb with low work function (2.6 eV) was introduced in the device of ITO/TFB/Quasi-2D perovskite/TPBi/Yb/Ag (as seen in Figure 7d), which efficiently promoted the electron injection via lowering the energy-level barrier. The device performances of EQE and maximum luminance were considerably superior to the device with a traditional Mg or Liq cathode interfacial layer-based device [83].

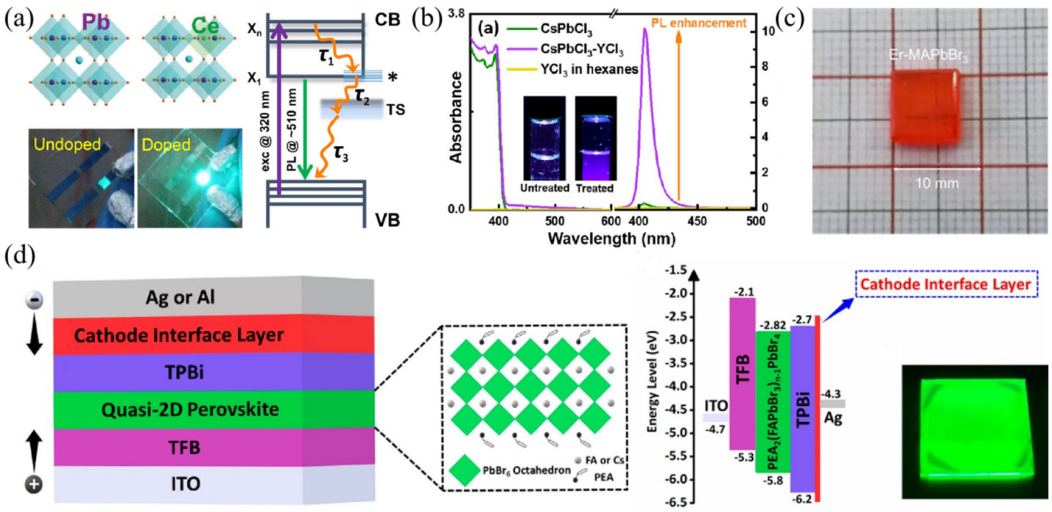

Figure 8. (**a**) Crystal lattice structure of Ce^{3+}-doped $CsPbBr_3$, LED photographs, and schematic diagram of photophysical mechanism (Reprinted/adapted with permission from Ref. [63]. Copyright 2018 American Chemical Society); (**b**) Absorption and PL spectra of Y^{3+}-doped $CsPbCl_3$ nanocrystals (Reprinted/adapted with permission from Ref. [81]. Copyright 2018 American Chemical Society); (**c**) Photograph of Er-doped $CH_3NH_3PbBr_3$ perovskite single crystal (Reprinted/adapted with permission from Ref. [65]. Copyright 2020 American Chemical Society); (**d**) Yb-modified device of ITO/TFB/Quasi-2D perovskite/TPBi/Yb/Ag: device schematic illustration, molecular structure of $PEA_2(FAPbBr_3)_{n-1}PbBr_4$, device energy band alignment, and fluorescence photograph of perovskite film (Reprinted/adapted with permission from Ref. [83]. Copyright 2020 American Chemical Society).

Recently, Cao and co-workers obtained functionalized $CsPbBr_3$ QDs with dual-stimuli-responsive optical encoding properties by using Eu complex for surface modification. According to the calculation, the absorption energy of the modified QDs increased, leading to good stability. Furthermore, the PL of Eu^{3+}: $CsPbBr_3$ QDs exhibited good temperature and PH response, which provided the possibility for their application in the field of securing encrypted information [84]. Han et al. fabricated a highly efficient and stable $Cs_2NaScCl_6$ perovskite single crystal. The Sc^{3+}-doped double perovskite showed a high PLQY of 29.05% for blue emission at the wavelength of 445 nm [85]. Detailed doping information and enhancement of luminescence efficiency are shown in Table 3.

Table 3. The PLQY enhancement of Ln^{3+}-doping PVK and the EQE enhancement of Ln^{3+}-doping perovskite LED.

Modified Materials	Main Emission Wavelength	PLQY/EQE	Ref
K^+ and lanthanide elements-doped $CsPbCl_3$ QDs	408 to 495 nm	90%	[61]
Eu^{3+} and Tb^{3+}-doping $CsPbBr_3$	592, 612/543, and 582 nm	-	[62]
Ce^{3+}-doped $CsPbBr_3$	516 to 510 nm	89%/4.4%	[63]
Er-doping $MAPbBr_3$ single crystals	546 nm	-	[65]
Eu^{3+}-doped $CsPbCl_3$	570 to 710 nm	-	[66]
Yb3+-doped Cs2AgBiX6	900–1200 nm	0.3 %/-	[67]
CsPbCl3QDs by co-doping La3+ and F- ions	410 nm	36.5%	[68]
Various lanthanide ions	270 to 420 and 1000 nm	143%/-	[69]
Yb^{3+} $CsPbCl_3$	990 nm	Over 100%	[70]
(Yb3+) $CsPb(Cl_{1-x}Br_x)_3$	990 nm	190%	[71]
Yb^{3+} and Yb^{3+}/Er^{3+} co-doped $CsPbCl_3$	986 nm	127.8%/-	[72]
Yb^{3+}-doped $CsPbCl_3$	1000 nm	Over 60%/5.9%	[73]
Cs2NaEr1-xBxCl6 (B: In, Sb, or Bi; x = 0, 0.13, and 0.5)	1543 nm	-	[74]
Yb^{3+}/Er^{3+} co-doped CsPbCl3 N	986 nm and 1533 nm	127.8%/-	[75]
Cr^{3+} Ce^{3+} Yb^{3+} tri-doped $CsPbCl_3$ QDs	405 to 394 and 980 nm	188%/-	[16]
$CsPbCl_3$: Mn^{2+}, Er^{3+}	580 to 600 nm	Enhanced by 100 times than origin/-	[18]
Ce^{3+} and Mn^{2+} co-doped $CsPbCl_{1.8}Br_{1.2}$	429, 460, and 592 nm	75%	[76]
Nd^{3+}-doped $CsPbBr_3$	459 nm	90%	[77]
Ce^{3+} and Tb^{3+}-doped $MAPbBr_3$	454 to 518 nm	100%/-	[78]
$MAPbBr_{3-x}I_x$-coated YAG:Ce^{3+} phosphors	490, 535, 550, 680, 715, 765 nm	-	[21]
Sm^{3+}-doped $CsPbCl_3$	565, 602, 645, and 710 nm	85%/1.2%	[79]
Yb^{3+}-doped $CsPb(Cl_{1-x}Br_x)_3$	979 nm	Approaching 200%/-	[80]
YCl_3-treated	394 and 404 nm	60%/-	[81]
Pre-optimize $CsPbCl_3$ using $PrCl_3$	407 and 404 nm	89%/-	[82]
Yb layer	536 nm	-/16.4%	[83]
Europium complex to CsPbBr3 QDs	500, 592, and 616 nm	-	[84]

Table 3. *Cont.*

Modified Materials	Main Emission Wavelength	PLQY/EQE	Ref
Sc-based double perovskite Cs2NaScCl6	459 and 635 nm	29.05%/-	[85]
Yb/Er-doped $Cs_2AgInCl_6$	395/996 and 1573 nm	3.6 ± 0.4%/-	[86]
Yb^{3+}-doped $CsPbCl_3$	980 nm	87.9%/-	[87]
Yb-doped $Cs_2AgInCl_6$	996 nm	3–4%/-	[88]
$CsPbX_3$ Zeolite-Y composite	400 to 600 nm	-	[89]

5. Application of Ln^{3+} in Solar Concentrators

The concept of luminescent solar concentrators (LSCs) is to concentrate direct and diffuse solar radiation. Luminophores for LSCs absorb large fractions of the solar spectrum, then emit photons into a light-capture medium with high PLQY, but do not absorb their own photoluminescence.

For example, Wu's group firstly proposed the concept quantum-cutting luminescent solar concentrator (QC-LSC) by using Yb^{3+}-doped perovskite NCs, as seen in Figure 9a. The internal optical efficiency (η_{int}) can be achieved to about 120% for Yb^{3+}: $CsPbCl_3$-based QC-LSC with a size of 25 cm^2, which is much higher than the previous records realized by using Mn^{2+}-doped QDs [19]. Similarly, Gamelin and coworkers demonstrated that Yb^{3+}-doped $CsPb(Cl_{1-x}Br_x)_3$ NC with large effective Stokes shift and high PLQY is one of the candidates for LSC luminophores (Figure 9b). In addition, the Yb^{3+}: $CsPb(Cl_{1-x}Br_x)_3$ NCs have an extremely low self-absorption rate [20].

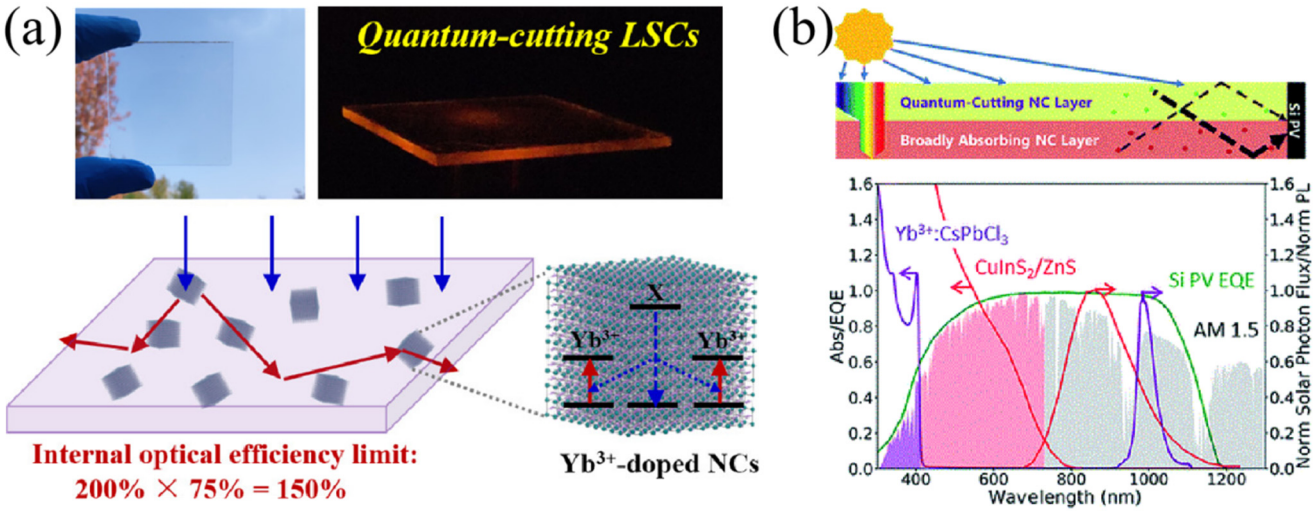

Figure 9. (**a**) The picture of Yb^{3+}-doped $CSPbCl_3$ LSC under sunlight and illustration of internal optical efficiency (Reprinted/adapted with permission from Ref. [19]. Copyright 2019 American Chemical Society); (**b**) Schematic maps of monolithic bilayer LSC and absorption/PL spectra of Yb^{3+}:$CsPbI_3$ nanocrystals (Reprinted/adapted with permission from Ref. [20]. Copyright 2018 Royal Society of Chemistry).

6. Application of Ln^{3+} in Photodetectors

In 2019, Lee and co-workers synthesized lead-free $CsYbI_3$ perovskite NCs with lower exciton binding energy than traditional Sn-based lead-free perovskite, which was beneficial for the application in the field of photodetectors. Due to the effective exciton dissociation and charge transport at the interface of $CsYbI_3$/Graphene, the highest photoresponsivity and external quantum efficiency (EQE) of the device (Si/SiO_2/(Au and Ti)/Graphene/$CsYbI_3$ NCs, seen in Figure 10a) were 2.4×10^3 A/W and 5.8×10^5%, respectively [90]. Du et al. reported Yb^{3+}, Er^{3+}, and Bi^{3+} tri-doped lead-free $Cs_2Ag_{0.6}Na_{0.4}InCl_6$

perovskite single crystals and applied for X-ray detection and an anti-counterfeiting technique. The doping elements improved the luminescence efficiency induced by the Jahn–Teller effect. The limit of X-ray detection reached 8.2 nGy s^{-1} [91]. Zn^{2+}, Yb^{3+}, and Tm^{3+} co-doped $CsPbF_3$ perovskite NCs were firstly fabricated for the application in the narrowband NIR photodetector. The device, based on Au nanorods array/Zn^{2+}, Yb^{3+}, Tm^{3+}: $CsPbF_3$ NCs, exhibited good performances (as seen in Figure 10b) with high responsivity of 106 A/W for the 980 nm spectral response [92]. In addition, Cr^{3+}, Yb^{3+}, e^{3+}: $CsPbCl_3$ perovskite QDs were coated onto a silicon photodetector for quantum cutting, thus, they realized a broad spectral response in the range of 200~1100 nm [16].

Bristowe and Cheetham et al. synthesized $(CH_3NH_3)KGdCl_6$ and $(CH_3NH_3)_2KYCl_6$ rare-earth-based hybrid double perovskite, and analyzed the crystal structure [93]. Recently, Zhang and Ruan synthesized hybrid hetero-structured NCs (as illustrated in Figure 10c) including two components of $CsPbBr_3$ QDs and $NaYF_4$:Yb, Tm UCNPs. The prepared NCs exhibited UV-excited green emission and NIR-excited UV-blue emission [94].

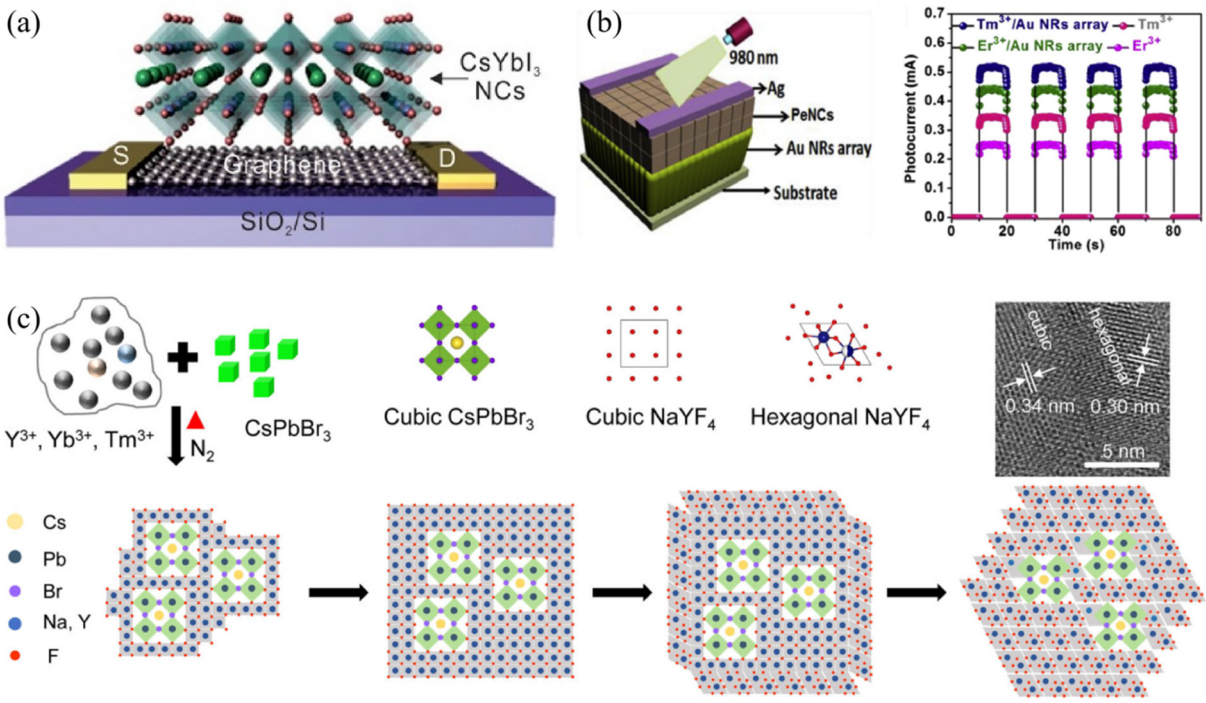

Figure 10. (**a**) Device structure of perovskite photodetector based on $CsYbI_3$/Graphene (Reprinted/adapted with permission from Ref. [90]. Copyright 2019 John Wiley and Sons); (**b**) Device configuration and photocurrent of the photodetectors based on $CsPbF_3$:Zn^{2+}-Yb^{3+}-Tm^{3+}(or Er^{3+})/Au nanorods (Reprinted/adapted with permission from Ref. [92]. Copyright 2020 Elsevier); (**c**) Schematic illustration for the formation of heterostructures $CsPbBr_3$-$NaYF_4$:Yb and Tm nanocrystals (Reprinted/adapted with permission from Ref. [94]. Copyright 2021 Springer Nature).

7. Conclusions and Outlook

In this study, we reviewed the recent development of rare-earth metal-modified metal halide perovskite materials and their corresponding optoelectronic devices. We discovered that different Ln^{3+} ions can absorb and emit light both in the UV and NIR regions, thus making up the deficiency of utilization for solar spectrum by perovskite materials. Therefore, Yb^{3+}, Er^{3+}, Tm^{3+}, Sc^{3+}, Nd^{3+}, and Ho^{3+} ions-based up-conversion nanoparticles were incorporated inside or proximal to the perovskite layer in the PSCs, resulting in higher device efficiency through broadening absorption spectral range to NIR region. Similarly, down-conversion nanocrystals-doping or co-doping with Eu^{3+}, Sm^{3+}, Yb^{3+}, Ce^{3+}, and Pr^{3+} ions can convert UV-light into visible light, which simultaneously improved PCE and prevented degradation triggered by UV-light in the perovskite solar

cells. Moreover, due to their unique electronic structure, Ln^{3+} ions (La^{3+}, Sc^{3+}, Sm^{3+}, Eu^{3+}, and so on) were also used as dopants to facilitate perovskite film growth, tailor the energy band alignment, and passivate the defect states, thus, to boost the device performances. In the field of perovskite light emission, Ln^{3+} ions including Yb^{3+}, Er^{3+}, Dy^{3+}, Tb^{3+}, Eu^{3+}, Sm^{3+}, Ce^{3+}, and Tm^{3+} ions were doped or co-doped into perovskite nanocrystals to realize multi-color emissions covering the entire visible spectral region. Based on this, Ln^{3+}-doped perovskite NCs were applicable for fabrication of white light-emitting diodes. Furthermore, Yb^{3+}, Ce^{3+}, Y^{3+}, Pr^{3+}, and Eu^{3+} ions were doped into perovskite lattice, which can form near band gap states, reduce Pb or halide vacancies or passivate surface defect, resulting in decreased nonradiative recombination centers and enhanced PLQY. Some Ln^{3+} ions, such as Y^{3+} ions, can also be used as an interfacial layer in the perovskite LED, which can promote the electron injection via lowering the energy-level barrier. Apart from the above two main application fields, Ln^{3+} ions have also been reported to be used in the fields of photodetectors and luminescent solar concentrators. These indicate the huge potential of rare-earth metals in improving the performances of the perovskite optoelectronic devices.

The host type of rare-earth ions determines the role of rare-earth ions in perovskite photoelectric devices. With MYF4 (M = Li, Na, K, Ru. and Cs) as host, Ln^{3+} ions-doping brings the ability of up-conversion, which enables solar cells to obtain a better life and efficiency. When the perovskite layer is used as the host, the introduction of Ln^{3+} ions reduce defects, increases efficiency, and introduces a new luminescence peak. Therefore, different hosts have completely different functions, and the future research on Ln^{3+} ions will also have new breakthroughs in the host types.

Based on these abundant research results, we suggest that additional investigations should be supplemented. (1) Although Ln^{3+} ions have been demonstrated to be effective in the perovskite light emissions, most work concentrated on the photoluminescence spectra and PLQY enhancement of perovskite materials. Extended work should focus on the device performances' enhancement of multi-color LED by doping Ln^{3+} ions, especially NIR and UV perovskite LEDs which needs to be implemented. (2) Luminescent solar concentrators based on perovskite materials and rare-earth metals need to be systematically studied, and their applications in photovoltaic field should be explored. (3) Perovskite photodetectors with high photocurrent and narrow spectrum responsivity should be further researched with the introduction of Ln^{3+} ions.

Author Contributions: Conceptualization, X.F. and M.Q.; methodology, X.F.; software, M.Q.; data curation, X.C., F.T. and B.X.; investigation, H.Z. (Hongbin Zhao) and M.Q.; resources, J.L.; writing—original draft preparation, B.L. and F.T.; writing—review and editing, F.T. and B.L.; supervision, X.W.; project administration, D.W. (Dengkui Wang) and D.W. (Dongbo Wang); funding acquisition, H.Z. (Haixi Zhang). All authors have read and agreed to the published version of the manuscript.

Funding: This research was funded by the National Natural Science Foundation of China (62074018, 62174015), the Developing Project of Science and Technology of Jilin Province (20200301052RQ, 20210509061RQ), the Natural Science Foundation of Jilin Province (20210101150JC, 20210101473JC, 20200201266JC), the Project of Education Department of Jilin Province (JJKH20210831KJ), the Natural Science Foundation of Guangdong Province (2020A1515010868), the Shenzhen Fundamental Research Fund (JCYJ20180307151538972), Shenzhen Post-doctoral Research Funding (20211063010010), the National Natural Science Foundation of China (2019A1515110230, 2021A1515012055), the Ministry of Education Industry-University Cooperation and Collaborative Education Project (202002105037), Shenzhen Technology Research Project (JSGG20201102162200002) and Shenzhen Technology University School-Enterprise Cooperation Project (20211064010033), the University Engineering Research Center of Crystal Growth and Applications of Guangdong Province (2020GCZX005), Special Innovative Projects of Guangdong Province (2020KTSCX125), and Shenzhen Stable Supporting Program (SZWD2021015), the major consulting research projects of the Chinese Academy of Engineering (No. 2021-HYZD-9), National Key R&D Program of China (No. 2021YFB320190X).

Institutional Review Board Statement: Not applicable.

Informed Consent Statement: Not applicable.

Conflicts of Interest: The authors declare no conflict of interest.

References

1. Protesescu, L.; Yakunin, S.; Bodnarchuk, M.I.; Krieg, F.; Caputo, R.; Hendon, C.H.; Yang, R.X.; Walsh, A.; Kovalenko, M.V. Nanocrystals of Cesium Lead Halide Perovskites (CsPbX3, X = Cl, Br, and I): Novel Optoelectronic Materials Showing Bright Emission with Wide Color Gamut. *Nano Lett.* **2015**, *15*, 3692–3696. [CrossRef] [PubMed]
2. Stranks, S.D.; Eperon, G.E.; Grancini, G.; Menelaou, C.; Alcocer, M.J.P.; Leijtens, T.; Herz, L.M.; Petrozza, A.; Snaith, H.J. Electron-Hole Diffusion Lengths Exceeding 1 Micrometer in an Organometal Trihalide Perovskite Absorber. *Science* **2013**, *342*, 341–344. [CrossRef] [PubMed]
3. Shi, D.; Adinolfi, V.; Comin, R.; Yuan, M.J.; Alarousu, E.; Buin, A.; Chen, Y.; Hoogland, S.; Rothenberger, A.; Katsiev, K.; et al. Low trap-state density and long carrier diffusion in organolead trihalide perovskite single crystals. *Science* **2015**, *347*, 519–522. [CrossRef] [PubMed]
4. Jiang, Y.; Leyden, M.R.; Qiu, L.; Wang, S.; Ono, L.K.; Wu, Z.; Juarez-Perez, E.J.; Qi, Y. Combination of Hybrid CVD and Cation Exchange for Upscaling Cs-Substituted Mixed Cation Perovskite Solar Cells with High Efficiency and Stability. *Adv. Funct. Mater.* **2018**, *28*, 1703835. [CrossRef]
5. Saliba, M.; Matsui, T.; Seo, J.Y.; Domanski, K.; Correa-Baena, J.P.; Nazeeruddin, M.K.; Zakeeruddin, S.M.; Tress, W.; Abate, A.; Hagfeldt, A.; et al. Cesium-containing triple cation perovskite solar cells: Improved stability, reproducibility and high efficiency. *Energy Environ. Sci.* **2016**, *9*, 1989–1997. [CrossRef]
6. Jeon, N.J.; Noh, J.H.; Yang, W.S.; Kim, Y.C.; Ryu, S.; Seo, J.; Seok, S.I. Compositional engineering of perovskite materials for high-performance solar cells. *Nature* **2015**, *517*, 476–480. [CrossRef]
7. Dou, L.T.; Yang, Y.; You, J.B.; Hong, Z.R.; Chang, W.H.; Li, G.; Yang, Y. Solution-processed hybrid perovskite photodetectors with high detectivity. *Nat. Commun.* **2014**, *5*, 5404. [CrossRef]
8. Akkerman, Q.A.; D'Innocenzo, V.; Accornero, S.; Scarpellini, A.; Petrozza, A.; Prato, M.; Manna, L. Tuning the Optical Properties of Cesium Lead Halide Perovskite Nanocrystals by Anion Exchange Reactions. *J. Am. Chem. Soc.* **2015**, *137*, 10276–10281. [CrossRef]
9. Laska, M.; Krzemińska, Z.; Kluczyk-Korch, K.; Schaadt, D.; Popko, E.; Jacak, W.A.; Jacak, J.E. Metallization of solar cells, exciton channel of plasmon photovoltaic effect in perovskite cells. *Nano Energy* **2020**, *75*, 104751. [CrossRef]
10. Ou, Z.; Yi, Y.; Hu, Z.; Zhu, J.; Wang, W.; Meng, H.; Zhang, X.; Jing, S.; Xu, S.; Hong, F.; et al. Improvement of CsPbBr3 photodetector performance by tuning the morphology with PMMA additive. *J. Alloys Compd.* **2020**, *821*. [CrossRef]
11. Im, J.H.; Lee, C.R.; Lee, J.W.; Park, S.W.; Park, N.G. 6.5% efficient perovskite quantum-dot-sensitized solar cell. *Nanoscale* **2011**, *3*, 4088–4093. [CrossRef] [PubMed]
12. Marin, R.; Jaque, D. Doping Lanthanide Ions in Colloidal Semiconductor Nanocrystals for Brighter Photoluminescence. *Chem. Rev.* **2021**, *121*, 1425–1462. [CrossRef] [PubMed]
13. Mir, W.J.; Sheikh, T.; Arfin, H.; Xia, Z.; Nag, A. Lanthanide doping in metal halide perovskite nanocrystals: Spectral shifting, quantum cutting and optoelectronic applications. *NPG Asia Mater.* **2020**, *12*, 9. [CrossRef]
14. Ferro, S.M.; Wobben, M.; Ehrler, B. Rare-earth quantum cutting in metal halide perovskites—A review. *Mater. Horiz.* **2021**, *8*, 1072–1083. [CrossRef] [PubMed]
15. Zhou, Y.; Chen, J.; Bakr, O.M.; Sun, H.-T. Metal-Doped Lead Halide Perovskites: Synthesis, Properties, and Optoelectronic Applications. *Chem. Mater.* **2018**, *30*, 6589–6613. [CrossRef]
16. Ding, N.; Xu, W.; Zhou, D.; Ji, Y.; Wang, Y.; Sun, R.; Bai, X.; Zhou, J.; Song, H. Extremely efficient quantum-cutting Cr3+, Ce3+, Yb3+ tridoped perovskite quantum dots for highly enhancing the ultraviolet response of Silicon photodetectors with external quantum efficiency exceeding 70%. *Nano Energy* **2020**, *78*, 105278. [CrossRef]
17. Roh, J.; Yu, H.; Jang, J. Hexagonal beta-NaYF4:Yb(3+), Er(3+) Nanoprism-Incorporated Upconverting Layer in Perovskite Solar Cells for Near-Infrared Sunlight Harvesting. *ACS Appl. Mater. Interfaces* **2016**, *8*, 19847–19852. [CrossRef]
18. Song, P.; Qiao, B.; Song, D.; Cao, J.; Shen, Z.; Xu, Z.; Zhao, S.; Wageh, S.; Al-Ghamdi, A. Modifying the Crystal Field of CsPbCl3:Mn(2+) Nanocrystals by Co-doping to Enhance Its Red Emission by a Hundredfold. *ACS Appl. Mater. Interfaces* **2020**, *12*, 30711–30719. [CrossRef]
19. Luo, X.; Ding, T.; Liu, X.; Liu, Y.; Wu, K. Quantum-Cutting Luminescent Solar Concentrators Using Ytterbium-Doped Perovskite Nanocrystals. *Nano Lett.* **2019**, *19*, 338–341. [CrossRef]
20. Cohen, T.A.; Milstein, T.J.; Kroupa, D.M.; MacKenzie, J.D.; Luscombe, C.K.; Gamelin, D.R. Quantum-cutting Yb3+-doped perovskite nanocrystals for monolithic bilayer luminescent solar concentrators. *J. Mater. Chem. A* **2019**, *7*, 9279–9288. [CrossRef]
21. Chen, L.-C.; Tseng, Z.-L.; Chang, W.-W.; Lin, Y.W. Warm white light-emitting diodes using organic–inorganic halide perovskite materials coated YAG:Ce3+ phosphors. *Ceram. Int.* **2018**, *44*, 3868–3872. [CrossRef]
22. Chen, X.; Xu, W.; Song, H.; Chen, C.; Xia, H.; Zhu, Y.; Zhou, D.; Cui, S.; Dai, Q.; Zhang, J. Highly Efficient LiYF4:Yb(3+), Er(3+) Upconversion Single Crystal under Solar Cell Spectrum Excitation and Photovoltaic Application. *ACS Appl. Mater. Interfaces* **2016**, *8*, 9071–9079. [CrossRef] [PubMed]
23. Meng, R.; He, Z.; Luo, X.; Zhang, C.; Chen, M.; Lu, H.; Yang, Y. Wide spectral response perovskite solar cells mixed with NaGdF4:Yb3+, Er3+@NaGdF4:Eu3+ core-shell rare earth nanoparticles. *Opt. Mater.* **2021**, 119. [CrossRef]

24. Que, M.; Que, W.; Yin, X.; Chen, P.; Yang, Y.; Hu, J.; Yu, B.; Du, Y. Enhanced conversion efficiency in perovskite solar cells by effectively utilizing near infrared light. *Nanoscale* **2016**, *8*, 14432–14437. [CrossRef]
25. Meng, F.L.; Wu, J.J.; Zhao, E.F.; Zheng, Y.Z.; Huang, M.L.; Dai, L.M.; Tao, X.; Chen, J.F. High-efficiency near-infrared enabled planar perovskite solar cells by embedding upconversion nanocrystals. *Nanoscale* **2017**, *9*, 18535–18545. [CrossRef]
26. Zhou, D.; Liu, D.; Jin, J.; Chen, X.; Xu, W.; Yin, Z.; Pan, G.; Li, D.; Song, H. Semiconductor plasmon-sensitized broadband upconversion and its enhancement effect on the power conversion efficiency of perovskite solar cells. *J. Mater. Chem. A* **2017**, *5*, 16559–16567. [CrossRef]
27. Li, Y.; Zhao, L.; Xiao, M.; Huang, Y.; Dong, B.; Xu, Z.; Wan, L.; Li, W.; Wang, S. Synergic effects of upconversion nanoparticles NaYbF4:Ho(3+) and ZrO2 enhanced the efficiency in hole-conductor-free perovskite solar cells. *Nanoscale* **2018**, *10*, 22003–22011. [CrossRef]
28. Sebag, M.S.; Hu, Z.; de Oliveira, K.L.; Xiang, H.; Gredin, P.; Mortier, M.; Billot, L.; Aigouy, L.; Chen, Z. Microscopic Evidence of Upconversion-Induced Near-Infrared Light Harvest in Hybrid Perovskite Solar Cells. *ACS Appl. Energ. Mater.* **2018**, *1*, 3537–3543. [CrossRef]
29. Liang, L.; Liu, M.; Jin, Z.; Wang, Q.; Wang, H.; Bian, H.; Shi, F.; Liu, S. Optical Management with Nanoparticles for a Light Conversion Efficiency Enhancement in Inorganic gamma-CsPbI3 Solar Cells. *Nano Lett.* **2019**, *19*, 1796–1804. [CrossRef]
30. Deng, X.; Zhang, C.; Zheng, J.; Zhou, X.; Yu, M.; Chen, X.; Huang, S. Highly bright Li(Gd,Y)F4:Yb,Er upconverting nanocrystals incorporated hole transport layer for efficient perovskite solar cells. *Appl. Surf. Sci.* **2019**, *485*, 332–341. [CrossRef]
31. Bi, W.; Wu, Y.; Chen, C.; Zhou, D.; Song, Z.; Li, D.; Chen, G.; Dai, Q.; Zhu, Y.; Song, H. Dye Sensitization and Local Surface Plasmon Resonance-Enhanced Upconversion Luminescence for Efficient Perovskite Solar Cells. *ACS Appl. Mater. Interfaces* **2020**, *12*, 24737–24746. [CrossRef]
32. He, M.; Pang, X.; Liu, X.; Jiang, B.; He, Y.; Snaith, H.; Lin, Z. Monodisperse Dual-Functional Upconversion Nanoparticles Enabled Near-Infrared Organolead Halide Perovskite Solar Cells. *Angew. Chem.* **2016**, *128*, 4352–4356. [CrossRef]
33. Wang, X.; Zhang, Z.; Qin, J.; Shi, W.; Liu, Y.; Gao, H.; Mao, Y. Enhanced Photovoltaic Performance of Perovskite Solar Cells Based on Er-Yb Co-doped TiO2 Nanorod Arrays. *Electrochim. Acta* **2017**, *245*, 839–845. [CrossRef]
34. Hu, J.; Qiao, Y.; Yang, Y.; Zhao, L.; Liu, W.; Li, S.; Liu, P.; Chen, M. Enhanced Performance of Hole-Conductor-Free Perovskite Solar Cells by Utilization of Core/Shell-Structured β-NaYF4:Yb3+,Er3+@SiO_2 Nanoparticles in Ambient Air. *IEEE J. Photovolt.* **2018**, *8*, 132–136. [CrossRef]
35. Liang, J.; Gao, H.; Yi, M.; Shi, W.; Liu, Y.; Zhang, Z.; Mao, Y. β-NaYF4:Yb3+, Tm_3+@TiO_2 core-shell nanoparticles incorporated into the mesoporous layer for high efficiency perovskite solar cells. *Electrochim. Acta* **2018**, *261*, 14–22. [CrossRef]
36. Xu, F.; Sun, Y.; Gao, H.; Jin, S.; Zhang, Z.; Zhang, H.; Pan, G.; Kang, M.; Ma, X.; Mao, Y. High-Performance Perovskite Solar Cells Based on NaCsWO3@ NaYF4@NaYF4:Yb,Er Upconversion Nanoparticles. *ACS Appl. Mater. Interfaces* **2021**, *13*, 2674–2684. [CrossRef]
37. Wang, M.; Wu, Y.; Juan, F.; Li, Y.; Shi, B.; Xu, F.; Jia, J.; Wei, H.; Cao, B. Enhanced photocurrent of perovskite solar cells by dual-sensitized β-NaYF4:Nd3+/Yb3+/Er3+ up-conversion nanoparticles. *Chem. Phys. Lett.* **2021**, *763*. [CrossRef]
38. Lai, X.; Li, X.; Lv, X.; Zheng, Y.-Z.; Meng, F.; Tao, X. Broadband dye-sensitized upconverting nanocrystals enabled near-infrared planar perovskite solar cells. *J. Power Sources* **2017**, *372*, 125–133. [CrossRef]
39. Guo, Q.; Wu, J.; Yang, Y.; Liu, X.; Jia, J.; Dong, J.; Lan, Z.; Lin, J.; Huang, M.; Wei, Y.; et al. High performance perovskite solar cells based on β-NaYF4:Yb3+/Er3+/Sc3+@NaYF4 core-shell upconversion nanoparticles. *J. Power Sources* **2019**, *426*, 178–187. [CrossRef]
40. Zhang, H.; Zhang, Q.; Lv, Y.; Yang, C.; Chen, H.; Zhou, X. Upconversion Er-doped TiO_2 nanorod arrays for perovskite solar cells and the performance improvement. *Mater. Res. Bull.* **2018**, *106*, 346–352. [CrossRef]
41. Qi, F.; Xiao, Y.; Yu, Z.; Liu, P.; Kong, S.; Li, F.; Zhang, H.; Wang, Y.; Zhao, X.-Z. Performance enhancement of hole-transport material free perovskite solar cells with TiO_2 nanorods modified with SiO_2/NaYF4:Yb,Er@SiO_2 for upconversion and charge recombination suppression. *Org. Electron.* **2019**, *73*, 152–158. [CrossRef]
42. Zhang, Z.; Qin, J.; Shi, W.; Liu, Y.; Zhang, Y.; Liu, Y.; Gao, H.; Mao, Y. Enhanced Power Conversion Efficiency of Perovskite Solar Cells with an Up-Conversion Material of Er(3+)-Yb(3+)-Li(+) Tri-doped TiO_2. *Nanoscale Res. Lett.* **2018**, *13*, 147. [CrossRef] [PubMed]
43. Chander, N.; Khan, A.F.; Chandrasekhar, P.S.; Thouti, E.; Swami, S.K.; Dutta, V.; Komarala, V.K. Reduced ultraviolet light induced degradation and enhanced light harvesting using YVO4:Eu3+ down-shifting nano-phosphor layer in organometal halide perovskite solar cells. *Appl. Phys. Lett.* **2014**, *105*, 033904. [CrossRef]
44. Kim, C.W.; Eom, T.Y.; Yang, I.S.; Kim, B.S.; Lee, W.I.; Kang, Y.S.; Kang, Y.S. Dual-Function Au@Y_2O_3:Eu(3+) Smart Film for Enhanced Power Conversion Efficiency and Long-Term Stability of Perovskite Solar Cells. *Sci. Rep* **2017**, *7*, 6849. [CrossRef]
45. Chen, W.; Luo, Q.; Zhang, C.; Shi, J.; Deng, X.; Yue, L.; Wang, Z.; Chen, X.; Huang, S. Effects of down-conversion CeO2:Eu3+ nanophosphors in perovskite solar cells. *J. Mater. Sci. Mater. Electron.* **2017**, *28*, 11346–11357. [CrossRef]
46. Rahman, N.U.; Khan, W.U.; Li, W.; Khan, S.; Khan, J.; Zheng, S.; Su, T.; Zhao, J.; Aldred, M.P.; Chi, Z. Simultaneous enhancement in performance and UV-light stability of organic–inorganic perovskite solar cells using a samarium-based down conversion material. *J. Mater. Chem. A* **2019**, *7*, 322–329. [CrossRef]
47. Zhou, D.; Liu, D.; Pan, G.; Chen, X.; Li, D.; Xu, W.; Bai, X.; Song, H. Cerium and Ytterbium Codoped Halide Perovskite Quantum Dots: A Novel and Efficient Downconverter for Improving the Performance of Silicon Solar Cells. *Adv. Mater.* **2017**, *29*. [CrossRef]

48. Zhou, D.; Sun, R.; Xu, W.; Ding, N.; Li, D.; Chen, X.; Pan, G.; Bai, X.; Song, H. Impact of Host Composition, Codoping, or Tridoping on Quantum-Cutting Emission of Ytterbium in Halide Perovskite Quantum Dots and Solar Cell Applications. *Nano Lett.* **2019**, *19*, 6904–6913. [CrossRef]
49. Crane, M.J.; Kroupa, D.M.; Gamelin, D.R. Detailed-balance analysis of Yb3+:CsPb(Cl1-xBrx)3 quantum-cutting layers for high-efficiency photovoltaics under real-world conditions. *Energy Environ. Sci.* **2019**, *12*, 2486–2495. [CrossRef]
50. Bi, W.; Wu, Y.; Zhang, B.; Jin, J.; Li, H.; Liu, L.; Xu, L.; Dai, Q.; Chen, C.; Song, H. Enhancing Photostability of Perovskite Solar Cells by Eu(TTA)2(Phen)MAA Interfacial Modification. *ACS Appl. Mater. Interfaces* **2019**, *11*, 11481–11487. [CrossRef]
51. Jia, J.; Dong, J.; Lin, J.; Lan, Z.; Fan, L.; Wu, J. Improved photovoltaic performance of perovskite solar cells by utilizing down-conversion NaYF4:Eu3+ nanophosphors. *J. Mater. Chem. C* **2019**, *7*, 937–942. [CrossRef]
52. Gao, X.X.; Ge, Q.Q.; Xue, D.J.; Ding, J.; Ma, J.Y.; Chen, Y.X.; Zhang, B.; Feng, Y.; Wan, L.J.; Hu, J.S. Tuning the Fermi-level of TiO2 mesoporous layer by lanthanum doping towards efficient perovskite solar cells. *Nanoscale* **2016**, *8*, 16881–16885. [CrossRef]
53. Xiang, Y.; Ma, Z.; Zhuang, J.; Lu, H.; Jia, C.; Luo, J.; Li, H.; Cheng, X. Enhanced Performance for Planar Perovskite Solar Cells with Samarium-Doped TiO2 Compact Electron Transport Layers. *J. Phys. Chem. C* **2017**, *121*, 20150–20157. [CrossRef]
54. Guo, Q.; Wu, J.; Yang, Y.; Liu, X.; Sun, W.; Wei, Y.; Lan, Z.; Lin, J.; Huang, M.; Chen, H.; et al. Low-temperature processed rare-earth doped brookite TiO_2 scaffold for UV stable, hysteresis-free and high-performance perovskite solar cells. *Nano Energy* **2020**, *77*, 105183. [CrossRef]
55. Venkatachalam, P.; Kalaivani, T.; Krishnakumar, N. Perovskite sensitized erbium doped TiO2 photoanode solar cells with enhanced photovoltaic performance. *Opt. Mater.* **2019**, *94*, 1–8. [CrossRef]
56. Duan, J.; Zhao, Y.; Yang, X.; Wang, Y.; He, B.; Tang, Q. Lanthanide Ions Doped CsPbBr3 Halides for HTM-Free 10.14%-Efficiency Inorganic Perovskite Solar Cell with an Ultrahigh Open-Circuit Voltage of 1.594 V. *Adv. Energy Mater.* **2018**, *8*. [CrossRef]
57. Patil, J.V.; Mali, S.S.; Hong, C.K. Boosting the Stability of Fully-Inorganic Perovskite Solar Cells through Samarium Doped CsPbI2Br Perovskite. *ACS Sustain. Chem. Eng.* **2020**, *8*, 16364–16371. [CrossRef]
58. Wang, L.; Zhou, H.; Hu, J.; Huang, B.; Sun, M.; Dong, B.; Zheng, G.; Huang, Y.; Chen, Y.; Li, L.; et al. AEu3+-Eu2+ ion redox shuttle imparts operational durability to Pb-I perovskite solar cells. *Science* **2019**, *363*, 265–270. [CrossRef]
59. Chen, L.; Wu, W.; Wang, J.; Qian, Z.; Liu, R.; Niu, Y.; Chen, Y.; Xie, X.; Zhang, H. Lanthanide Stabilized All-Inorganic CsPbI2Br Perovskite Solar Cells with Superior Thermal Resistance. *ACS Appl. Energy Mater.* **2021**, *4*, 3937–3944. [CrossRef]
60. Dou, J.; Zhu, C.; Wang, H.; Han, Y.; Ma, S.; Niu, X.; Li, N.; Shi, C.; Qiu, Z.; Zhou, H.; et al. Synergistic Effects of Eu-MOF on Perovskite Solar Cells with Improved Stability. *Adv. Mater.* **2021**, *33*, e2102947. [CrossRef]
61. Liu, Y.; Pan, G.; Wang, R.; Shao, H.; Wang, H.; Xu, W.; Cui, H.; Song, H. Considerably enhanced exciton emission of CsPbCl3 perovskite quantum dots by the introduction of potassium and lanthanide ions. *Nanoscale* **2018**, *10*, 14067–14072. [CrossRef] [PubMed]
62. Hu, Q.; Li, Z.; Tan, Z.; Song, H.; Ge, C.; Niu, G.; Han, J.; Tang, J. Rare Earth Ion-Doped CsPbBr3 Nanocrystals. *Adv. Opt. Mater.* **2018**, *6*, 1700864. [CrossRef]
63. Yao, J.S.; Ge, J.; Han, B.N.; Wang, K.H.; Yao, H.B.; Yu, H.L.; Li, J.H.; Zhu, B.S.; Song, J.Z.; Chen, C.; et al. Ce(3+)-Doping to Modulate Photoluminescence Kinetics for Efficient CsPbBr3 Nanocrystals Based Light-Emitting Diodes. *J. Am. Chem. Soc.* **2018**, *140*, 3626–3634. [CrossRef] [PubMed]
64. Mir, W.J.; Mahor, Y.; Lohar, A.; Jagadeeswararao, M.; Das, S.; Mahamuni, S.; Nag, A. Postsynthesis Doping of Mn and Yb into CsPbX3 (X = Cl, Br, or I) Perovskite Nanocrystals for Downconversion Emission. *Chem. Mater.* **2018**, *30*, 8170–8178. [CrossRef]
65. Rong, S.; Xiao, Y.; Jiang, J.; Zeng, Q.; Li, Y. Strongly Enhanced Photoluminescence and Photoconductivity in Erbium-Doped MAPbBr3 Single Crystals. *J. Phys. Chem. C* **2020**, *124*, 8992–8998. [CrossRef]
66. Jing, X.; Zhou, D.; Sun, R.; Zhang, Y.; Li, Y.; Li, X.; Li, Q.; Song, H.; Liu, B. Enhanced Photoluminescence and Photoresponsiveness of Eu3+ Ions-Doped CsPbCl3 Perovskite Quantum Dots under High Pressure. *Adv. Funct. Mater.* **2021**, *31*, 2100930. [CrossRef]
67. Chen, N.; Cai, T.; Li, W.; Hills-Kimball, K.; Yang, H.; Que, M.; Nagaoka, Y.; Liu, Z.; Yang, D.; Dong, A.; et al. Yb- and Mn-Doped Lead-Free Double Perovskite Cs2AgBiX6 (X = Cl(-), Br(-)) Nanocrystals. *ACS Appl. Mater. Interfaces* **2019**, *11*, 16855–16863. [CrossRef]
68. Zhai, Y.; Bai, X.; Pan, G.; Zhu, J.; Shao, H.; Dong, B.; Xu, L.; Song, H. Effective blue-violet photoluminescence through lanthanum and fluorine ions co-doping for CsPbCl3 perovskite quantum dots. *Nanoscale* **2019**, *11*, 2484–2491. [CrossRef]
69. Pan, G.; Bai, X.; Yang, D.; Chen, X.; Jing, P.; Qu, S.; Zhang, L.; Zhou, D.; Zhu, J.; Xu, W.; et al. Doping Lanthanide into Perovskite Nanocrystals: Highly Improved and Expanded Optical Properties. *Nano Lett.* **2017**, *17*, 8005–8011. [CrossRef]
70. Milstein, T.J.; Kroupa, D.M.; Gamelin, D.R. Picosecond Quantum Cutting Generates Photoluminescence Quantum Yields Over 100% in Ytterbium-Doped CsPbCl3 Nanocrystals. *Nano Lett.* **2018**, *18*, 3792–3799. [CrossRef]
71. Kroupa, D.M.; Roh, J.Y.; Milstein, T.J.; Creutz, S.E.; Gamelin, D.R. Quantum-Cutting Ytterbium-Doped CsPb(Cl1–xBrx)3 Perovskite Thin Films with Photoluminescence Quantum Yields over 190%. *ACS Energy Lett.* **2018**, *3*, 2390–2395. [CrossRef]
72. Zhang, X.; Zhang, Y.; Zhang, X.; Yin, W.; Wang, Y.; Wang, H.; Lu, M.; Li, Z.; Gu, Z.; Yu, W.W. Yb(3+) and Yb(3+)/Er(3+) Doping for Near-Infrared Emission and Improved Stability of CsPbCl3 Nanocrystals. *J. Mater. Chem. C* **2018**, *6*, 10101–10105. [CrossRef] [PubMed]
73. Ishii, A.; Miyasaka, T. Sensitized Yb(3+) Luminescence in CsPbCl3 Film for Highly Efficient Near-Infrared Light-Emitting Diodes. *Adv. Sci.* **2020**, *7*, 1903142. [CrossRef] [PubMed]

74. Wu, R.; Han, P.; Zheng, D.; Zhang, J.; Yang, S.; Zhao, Y.; Miao, X.; Han, K. All-Inorganic Rare-Earth-Based Double Perovskite Nanocrystals with Near-Infrared Emission. *Laser Photonics Rev.* **2021**, *15*, 2100218. [CrossRef]
75. Du, K.; Zhang, M.; Li, Y.; Li, H.; Liu, K.; Li, C.; Feng, J.; Zhang, H. Embellishment of Upconversion Nanoparticles with Ultrasmall Perovskite Quantum Dots for Full-Color Tunable, Dual-Modal Luminescence Anticounterfeiting. *Adv. Opt. Mater.* **2021**, *9*, 2100814. [CrossRef]
76. Pan, G.; Bai, X.; Xu, W.; Chen, X.; Zhou, D.; Zhu, J.; Shao, H.; Zhai, Y.; Dong, B.; Xu, L.; et al. Impurity Ions Codoped Cesium Lead Halide Perovskite Nanocrystals with Bright White Light Emission toward Ultraviolet-White Light-Emitting Diode. *ACS Appl. Mater. Interfaces* **2018**, *10*, 39040–39048. [CrossRef] [PubMed]
77. Xie, Y.; Peng, B.; Bravić, I.; Yu, Y.; Dong, Y.; Liang, R.; Ou, Q.; Monserrat, B.; Zhang, S. Highly Efficient Blue-Emitting CsPbBr3 Perovskite Nanocrystals through Neodymium Doping. *Adv. Sci.* **2020**, *7*, 2001698. [CrossRef]
78. Parveen, S.; Prasanna, P.K.; Chakraborty, S.; Giri, P.K. Stable deep blue emission with unity quantum yield in organic–inorganic halide perovskite 2D nanosheets doped with cerium and terbium at high concentrations. *J. Mater. Chem. C* **2021**, *9*, 2437–2454. [CrossRef]
79. Sun, R.; Lu, P.; Zhou, D.; Xu, W.; Ding, N.; Shao, H.; Zhang, Y.; Li, D.; Wang, N.; Zhuang, X.; et al. Samarium-Doped Metal Halide Perovskite Nanocrystals for Single-Component Electroluminescent White Light-Emitting Diodes. *ACS Energy Lett.* **2020**, *5*, 2131–2139. [CrossRef]
80. Milstein, T.J.; Kluherz, K.T.; Kroupa, D.M.; Erickson, C.S.; De Yoreo, J.J.; Gamelin, D.R. Anion Exchange and the Quantum-Cutting Energy Threshold in Ytterbium-Doped CsPb(Cl1- xBr x)3 Perovskite Nanocrystals. *Nano Lett.* **2019**, *19*, 1931–1937. [CrossRef]
81. Ahmed, G.H.; El-Demellawi, J.K.; Yin, J.; Pan, J.; Velusamy, D.B.; Hedhili, M.N.; Alarousu, E.; Bakr, O.M.; Alshareef, H.N.; Mohammed, O.F. Giant Photoluminescence Enhancement in CsPbCl3 Perovskite Nanocrystals by Simultaneous Dual-Surface Passivation. *ACS Energy Lett.* **2018**, *3*, 2301–2307. [CrossRef]
82. Luo, C.; Li, W.; Xiong, D.; Fu, J.; Yang, W. Surface pre-optimization of a mixed halide perovskite toward high photoluminescence quantum yield in the blue spectrum range. *Nanoscale* **2019**, *11*, 15206–15215. [CrossRef] [PubMed]
83. Ali, M.U.; Miao, J.; Cai, J.; Perepichka, D.F.; Yang, H.; Meng, H. Boosting Efficiency and Curtailing the Efficiency Roll-Off in Green Perovskite Light-Emitting Diodes via Incorporating Ytterbium as Cathode Interface Layer. *ACS Appl. Mater. Interfaces* **2020**, *12*, 18761–18768. [CrossRef] [PubMed]
84. Feng, P.; Yang, X.; Feng, X.; Zhao, G.; Li, X.; Cao, J.; Tang, Y.; Yan, C.H. Highly Stable Perovskite Quantum Dots Modified by Europium Complex for Dual-Responsive Optical Encoding. *ACS Nano* **2021**, *15*, 6266–6275. [CrossRef] [PubMed]
85. Zhang, R.; Wang, Z.; Xu, X.; Mao, X.; Xiong, J.; Yang, Y.; Han, K. All-Inorganic Rare-Earth Halide Double Perovskite Single Crystals with Highly Efficient Photoluminescence. *Adv. Opt. Mater.* **2021**, *9*, 2100689. [CrossRef]
86. Lee, W.; Hong, S.; Kim, S. Colloidal Synthesis of Lead-Free Silver–Indium Double-Perovskite Cs2AgInCl6 Nanocrystals and Their Doping with Lanthanide Ions. *J. Phys. Chem. C* **2019**, *123*, 2665–2672. [CrossRef]
87. Ma, J.-P.; Chen, Y.-M.; Zhang, L.-M.; Guo, S.-Q.; Liu, J.-D.; Li, H.; Ye, B.-J.; Li, Z.-Y.; Zhou, Y.; Zhang, B.-B.; et al. Insights into the local structure of dopants, doping efficiency, and luminescence properties of lanthanide-doped CsPbCl3 perovskite nanocrystals. *J. Mater. Chem. C* **2019**, *7*, 3037–3048. [CrossRef]
88. Mahor, Y.; Mir, W.J.; Nag, A. Synthesis and Near-Infrared Emission of Yb-Doped Cs2AgInCl6 Double Perovskite Microcrystals and Nanocrystals. *J. Phys. Chem. C* **2019**, *123*, 15787–15793. [CrossRef]
89. Sun, J.-Y.; Rabouw, F.T.; Yang, X.-F.; Huang, X.-Y.; Jing, X.-P.; Ye, S.; Zhang, Q.-Y. Facile Two-Step Synthesis of All-Inorganic Perovskite CsPbX3 (X = Cl, Br, and I) Zeolite-Y Composite Phosphors for Potential Backlight Display Application. *Adv. Funct. Mater.* **2017**, *27*, 1704371. [CrossRef]
90. Moon, B.J.; Kim, S.J.; Lee, S.; Lee, A.; Lee, H.; Lee, D.S.; Kim, T.W.; Lee, S.K.; Bae, S.; Lee, S.H. Rare-Earth-Element-Ytterbium-Substituted Lead-Free Inorganic Perovskite Nanocrystals for Optoelectronic Applications. *Adv. Mater.* **2019**, *31*, e1901716. [CrossRef]
91. Zeng, Z.; Huang, B.; Wang, X.; Lu, L.; Lu, Q.; Sun, M.; Wu, T.; Ma, T.; Xu, J.; Xu, Y.; et al. Multimodal Luminescent Yb(3+) /Er(3+) /Bi(3+) -Doped Perovskite Single Crystals for X-ray Detection and Anti-Counterfeiting. *Adv. Mater.* **2020**, *32*, e2004506. [CrossRef] [PubMed]
92. Ding, N.; Xu, W.; Zhou, D.; Pan, G.; Li, D.; Ji, Y.; Chen, X.; Yang, D.; Bai, X.; Ma, C.-G.; et al. Upconversion ladder enabled super-sensitive narrowband near-infrared photodetectors based on rare earth doped florine perovskite nanocrystals. *Nano Energy* **2020**, *76*, 105103. [CrossRef]
93. Deng, Z.; Wei, F.; Brivio, F.; Wu, Y.; Sun, S.; Bristowe, P.D.; Cheetham, A.K. Synthesis and Characterization of the Rare-Earth Hybrid Double Perovskites: (CH3NH3)2KGdCl6 and (CH3NH3)2KYCl6. *J. Phys. Chem. Lett.* **2017**, *8*, 5015–5020. [CrossRef] [PubMed]
94. Ruan, L.; Zhang, Y. NIR-excitable heterostructured upconversion perovskite nanodots with improved stability. *Nat. Commun.* **2021**, *12*, 219. [CrossRef] [PubMed]

nanomaterials

MDPI

Review

Application of Triboelectric Nanogenerator in Fluid Dynamics Sensing: Past and Future

Leo N. Y. Cao [1,2,†], Zijie Xu [1,2,†] and Zhong Lin Wang [1,2,3,*]

[1] CAS Center for Excellence in Nanoscience, Beijing Key Laboratory of Micro-Nano Energy and Sensor, Beijing Institute of Nanoenergy and Nanosystems, Chinese Academy of Sciences, Beijing 101400, China
[2] School of Nanoscience and Technology, University of Chinese Academy of Sciences, Beijing 100049, China
[3] School of Materials Science and Engineering, Georgia Institute of Technology, Atlanta, GA 30332-0245, USA
* Correspondence: zhong.wang@mse.gatech.edu
† These authors contributed equally to this work.

Abstract: The triboelectric nanogenerator (TENG) developed by Z. L. Wang's team to harvest random mechanical energy is a promising new energy source for distributed sensing systems in the new era of the internet of things (IoT) and artificial intelligence (AI) for a smart world. TENG has many advantages that make it suitable for a wide range of applications, including energy harvesting, environmental protection, wearable electronics, robotics, and self-powered sensors. Sensing as an important part of TENG applications is gradually expanding, with the in-depth study of TENG sensing in its working principle, material selection, processing technology, system integration, surface treatment, and back-end algorithms by researchers. In industry and academia, fluid dynamics sensing for liquid and air is urgently needed but lacking. In particular, local fluid sensing is difficult and limited to traditional sensors. Fortunately, with advantages for ordinary TENGs and TENGs as fluid dynamics sensors, fluid dynamics sensing can be better realized. Therefore, the paper summarizes the up-to-date work on TENGs as fluid dynamics sensors, discusses the advantages of TENGs as fluid dynamics sensors in-depth, and, most importantly, aims to explore possible new key areas to help guide the future direction of TENG in fluid dynamics sensing by addressing the key challenges.

Keywords: triboelectric nanogenerators; fluid dynamics sensing

Citation: Cao, L.N.Y.; Xu, Z.; Wang, Z.L. Application of Triboelectric Nanogenerator in Fluid Dynamics Sensing: Past and Future. *Nanomaterials* **2022**, *12*, 3261. https://doi.org/10.3390/nano12193261

Academic Editors: João Pedro Araujo, Zhen Wen, Hengyu Guo and Longfei Wang

Received: 5 August 2022
Accepted: 16 September 2022
Published: 20 September 2022

1. Introduction

With the rapid development of the Internet of Things (IoT) and artificial intelligence (AI) for a smart world, distributed sensing systems, which are the foundation of the fourth industrial revolution, are the most important developments in hardware in the era. The continuous development and prosperity of distributed sensing systems rely on distributed renewable sources of energy such as solar power, wind power, and mechanical vibration [1]. The triboelectric nanogenerator (TENG) developed by Z. L. Wang's team to harvest random mechanical energy is a promising new energy source in the new era because triboelectric electrification is ubiquitous with a wide selection of materials [2]. Compared to externally powered sensors, the development of self-powered active sensors powered by TENG is revolutionary. In addition, TENG has many other advantages such as an abundant choice of materials, low assembly requirement, and flexibility [3], making it suitable for many application areas, including energy harvesting, environmental protection, wearable electronics, robotics, and self-powered sensors [4].

An important part of TENG applications is sensing that focuses mainly on active mechanical and chemical sensors in the early stages. Additionally, early TENG can actively detect the static and dynamic processes from mechanical agitation with potential smart skin applications [5]. With the in-depth study of TENG sensing in its working principle, material selection, processing technology, system integration, surface treatment, and back-end algorithms by researchers, the application fields of TENG sensing are gradually expanding,

especially fluid dynamics sensing. Fluids, including gases and liquids, account for two of the three phases of matter and tend to flow, meeting the working principle of TENG: mechano-driven. Most importantly, fluid dynamics sensing is urgently needed in industry and academia. In particular, local fluid sensing is difficult and limited to traditional sensors.

Fortunately, with advantages for ordinary TENGs (discussed later in this section) and TENGs as fluid dynamics sensors (introduced in Section 4), fluid dynamics sensing can be better realized. For example, the self-powered characteristics of TENG can simplify the sensor structure, so that the disturbance of the sensor for the flow field is reduced. In addition, the diversity of material choices and the sensitivity to external stimuli give TENG an advantage over other existing sensing schemes in complex fluid environment sensing. Therefore, the objective of the paper is to summarize the recent work on TENG as fluid dynamics sensors, and, most importantly, explore possible new key areas to help guide the future direction of TENG in fluid dynamics sensing by addressing the key challenges (Figure 1).

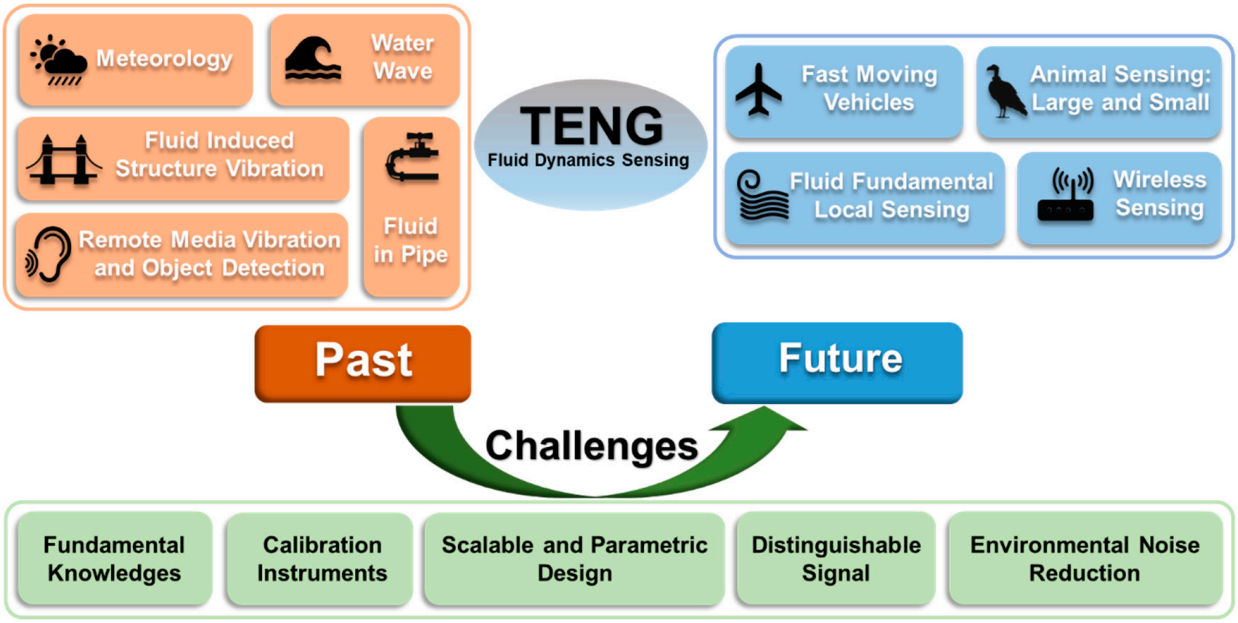

Figure 1. Opportunities and challenges of triboelectric nanogenerators for fluid dynamics sensing, from traditional fields to future technologies.

The review is structured as follows: in, the principles and advantages of TENG are first introduced (Section 2). We then summarize the up-to-date work on TENG primarily as fluid dynamics sensors for the local fluid phenomenon and environment (Section 3); in Section 4, we explore the possibility of TENG and offer guidance by addressing the needs of industry and academia by leveraging the advantages of the TENG as fluid dynamics sensors, focusing more on the local sensing of fluids. Finally, in Section 5, we discuss the challenges TENG faces to reach the milestone and become suitable, and practically applicable sensors with distinct uniqueness and advantages.

2. Introduction of TENG

Coupling the triboelectric effect and electrostatic induction, TENG was first invented by Wang's group in 2012 (Figure 2) to generate electricity through harvesting environmental mechanical energy that is ubiquitous but often wasted. More specifically, the electricity is converted by electrostatic induction through the electric field change, which is induced by mechanical separation after triboelectric or contact electrification transfers electrons from one surface of contacting materials to another according to the quantum mechanical transition model [6]. The model states that when two materials approach an atomically close

distance, electrons move toward the lowest available states due to strongly overlapping electron waves. The electron transfer model could be extended from solid–solid to liquid–solid, liquid–gas, and even liquid–liquid cases [7].

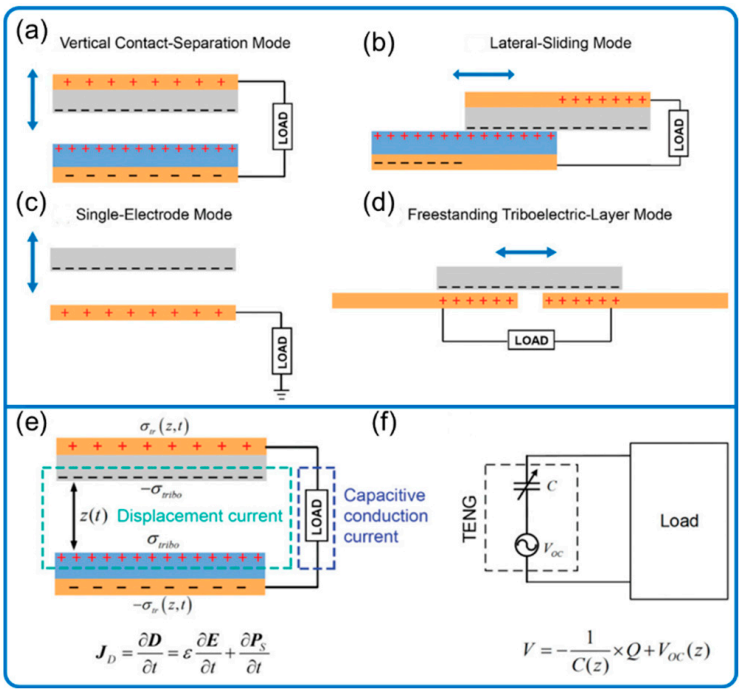

Figure 2. The four basic modes of TENG and its equivalent model. (**a**) Vertical contact separation mode, (**b**) lateral sliding mode, (**c**) single-electrode mode, and (**d**) freestanding triboelectric-layer mode. (**e**) The displacement current model of a contact-separation mode. (**f**) TENG's equivalent electrical circuit model. Reproduced with permission. Copyright 2018, Wiley Online Library [1].

2.1. Principle of TENG

The fundamental physics model of TENG was presented according to Maxwell's displacement current in 2017 [4,8–10]. The displacement current is from a transient electric field and media dielectric polarization and drives the conversion of mechanical energy into electricity. Mainly due to the independence of the surface charges on the electric field, a new term P_s, known as the Wang term, is added to Maxwell's equations to explain TENG's working mechanism [4]. The displacement current density (J_D) is then expanded as follows:

$$J_D = \varepsilon \frac{\partial E}{\partial t} + \frac{\partial P_S}{\partial t} = \varepsilon_0 \frac{\partial E}{\partial t} + \frac{\partial P}{\partial t} + \frac{\partial P_S}{\partial t}$$

where E, P, and P_s represent the electric field, medium polarization vector, and the added term from the presence of electrostatic surface charges, respectively; ε and ε_0 are the permittivity of the dielectrics and vacuum, respectively. The first term ($\varepsilon \partial E / \partial t$) represents the electromagnetic wave, which is predicted to emit from a high-frequency TENG [4] and later detected [11]. In addition, other wireless signals created by TENG were also detected and summarized in Wang et al. [12].

TENG can be categorized into four basic modes according to their electrodes and motion patterns: vertical contact separation, lateral sliding, single-electrode, and freestanding triboelectric-layer modes (Figure 2) [13]. In general, electrons are transferred back and forth from one electrode to another (generating electrical current) due to the change of electrical field caused by the mechano-driven location change of triboelectric materials. The electron transfer is slightly different for the single-electrode mode (Figure 2c) since it has only one electrode: the only electrode exchanges electrons with the ground. Each mode has its advantage in energy harvesting, manufacturing, and robustness [3,13]. In addition, the

various motion patterns give more flexibility to the sensors' working mechanism, design, and manufacturing. For example, the single-electrode mode for the TENG as a sensor may give the lowest energy output and thus signal-to-noise ratio (SNR) but can sense the object directly with the easiest setup since the triboelectric material, possibly the object being sensed (e.g., liquid), does not necessarily belong to the system. The displacement current model of contact separation mode and the equivalent electrical circuit model is described in Figure 2e,f, respectively.

2.2. Advantages of Ordinary TENG

In addition to multiple modes of operation, ordinary TENG has many other advantages, including wide material availability, lightweight, low cost, and high efficiency even at low operating frequencies. In addition, its sensitivity to external incentives and self-powered characteristics also broaden its scope of application. Advantages for TENGs as fluid dynamics sensors will be introduced in Section 4.

In principle, any material with different charge affinities can be used to construct TENG. Thus, due to the wide material selections, we can conveniently adjust the basic mechanical, physicochemical, and biological properties of the TENG to suit various application situations. Furthermore, TENGs are reported to generate power densities as high as several hundred Wm^{-2} which is sufficient to drive many small electronics, allowing self-powered sensing networks. In addition, thanks to the recent development, wireless data induced by TENG can be received in many ways (discussed in Section 4), providing an alternative framework for sensor network construction and data transmission [12].

3. TENG for Fluid Dynamics Sensing: Past

In physics and engineering, fluid dynamics is a branch of fluid mechanics that describes the flow of fluids, including aerodynamics (study of gases in motion) and hydrodynamics (study of liquids in motion). Here, we divide the fluid dynamics parameters that may be sensed by TENG sensors into two groups by scale: large- and local-scale properties. The large-scale properties include ambient fluid motions, such as wind, rain, and water wave, and their speed, direction, and pressure; the local-scale properties include the flow pattern and force under various situations on the local scale, such as laminar and turbulence flow and their development, boundary layer and its separation, flow pattern around immersed bodies, rotational fluid such as vortex, and streamlines in the local flow field (Figure 1).

This section summarizes the recent studies using TENG sensors to sense the above-mentioned fluid dynamics parameters. According to the application scenarios, we divided the fluid dynamics TENG sensors into five categories: 1 meteorology parameters, 2 fluids in pipes and tunnels, 3 remote media vibration and moving object, 4 sea wave motion, and 5 structure vibration due to moving fluid. As seen in the classification, a large part of the current work in fluid dynamics sensing involves large-scale properties. Note that this review only covers research where TENG is or could be used as a sensor or even battery-less sensor and excludes studies that merely use TENG as a power source to run commercial sensors. In addition, a few reviews summarized some overlapping or related contents to this article, but with different focuses: Gao et al. summarized sensors of wind and water in pipes in their review of triboelectric mechanical sensors [3]; Tang et al. discussed liquid and droplet content sensors using TENG [14]; Nguyen et al. summarized fluid-based TENG as power sources [15].

3.1. Meteorology-Related Sensing

Targeting on developing alternative smart tools for conventional weather reporting and monitoring (e.g., wind speed and direction, and rainfall amount), researchers have worked on meteorology-related TENG sensors (mostly battery-less sensors in the subsection) based on traditional measurement methods.

(a) Wind speed and direction: conventional wind cups and turbine.

One of the TENG sensor types for wind speed and direction measurement is similar to the wind vector sensor system (wind vane and cups or turbine) commonly used in traditional weather forecasting, where the rotation speed of the wind cups or turbine correlates well with wind speed (Figure 3). More specifically, they employed wind cups or wind turbines as the motion generator, rotational TENGs with graded electrodes for wind speed information, and an optional wind vane indicator providing possibly high-resolution wind direction.

Since the wind speed correlates well with the wind cup rotational speed (rpm), which corresponds to the TENG signal frequency, many of the rotational sensors use TENG signal frequency to correlate with and represent wind speed. Using signal frequency or peak counts to record data, similar to the encoding techniques in telecommunication, is also advantageous for noise reduction and data fidelity [16,17] compared to signal amplitude, which can be affected by environmental factors such as humidity and temperature.

To indicate constantly changed wind direction, they normally use wind vane, together with coded electrodes or other signal generators [18–20]. To differentiate multiple directions, graded signals with different levels are needed, requiring multiple signal channels in general. For example, eight independent signal channels were used to indicate eight wind directions in Wang et al. (Figure 3a) [18] and Han et al. (Figure 3d) [20]. Since the increasing number of signal acquisition channels will gradually increase system difficulty and complexity, signal encoding methods are often applied to address the problem [16,17]. For example, Zhang et al. achieved 8 wind direction detection within 2 s using only three electrical channels by encoding the electrodes with Gray code (Figure 3c), increasing the applicability and practicality drastically [19]. In addition to the wind vane method to indicate wind direction, the array of wind-direction-sensitive sensors is used and calibrated to indicate rough (low resolution) wind direction (Figure 3b) [21].

The detailed information of wind cup sensors is summarized in Table 1, including wind speed range, wind direction, and features. The general tested wind speed is from 2.0 to 15.0 m/s with some special cases, for example, Chen et al. (Figure 4a) developed a bladeless-turbine-based (tesla turbine) high-speed TENG sensor, up to 7500 rpm (11.0 to 28.0 L/min) [22]. Note that the upper limit of tested wind speed may be limited by the testing scenarios, methods, and apparatus; therefore, the stated wind speed may also be either inaccurate or biased if the testing apparatus and method are not well controlled. For example, only a few studies conducted standard measurements in well-controlled wind tunnels, so the wind speed value, especially the lowest starting wind speed is not claimed strictly, leaving an area to improve for sensor calibration.

Many wind speed sensors applied the freestanding mode for the TENG for better energy harvesting, while others used contact separation modes by converting rotational to linear motion [21,23], reducing device friction, wear, and minimum starting wind speed (Figure 4). Other attempts have been also tried to enhance device robustness and efficiency by applying, for example, soft contact (Figure 4b) [24], and automatic switch (Figure 4c,d) for contact and separation [25,26].

Most of the abovementioned devices can either work as a sensor themselves or harvest environmental energy to serve as small power sources for commercial sensors with low power consumption, often hybridized with electromagnetic generators (EMG) to increase power generation [18,19,25]. However, harvesting energy and sensing simultaneously in a single TENG device is difficult without any thoughtful treatment. To solve the problem, Lu et al. proposed a method of decoupling and extracting signals and energy so that the disk-type TENG can sense the wind speed, harvest wind energy, and process and send the signal to a wireless signal receiver simultaneously, achieving a truly closed-loop self-powered environmental sensing system [27].

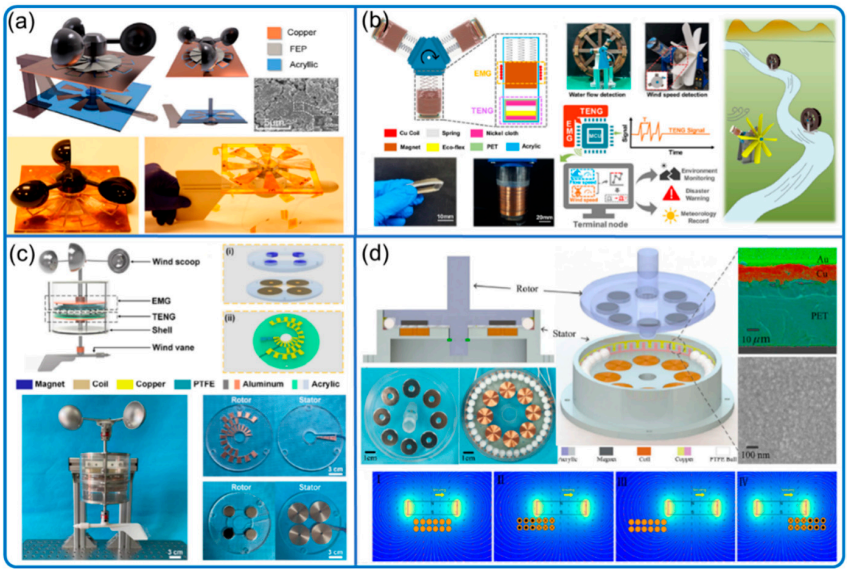

Figure 3. Sensing of wind speed with direction: conventional wind cups and turbine. (**a**) Soft friction system with wind vane. Reproduced with permission. Copyright 2018, American Chemical Society [18]. (**b**) Unmanned environment monitoring system. Reproduced with permission. Copyright 2021, Elsevier [21]. (**c**) Wind direction sensing with Gray code. Reproduced with permission. Copyright 2021, American Chemical Society [19]. (**d**) Rolling mode sensor with electromagnetic generator (EMG) direction indicator. Reproduced with permission. Copyright 2020, Elsevier [20].

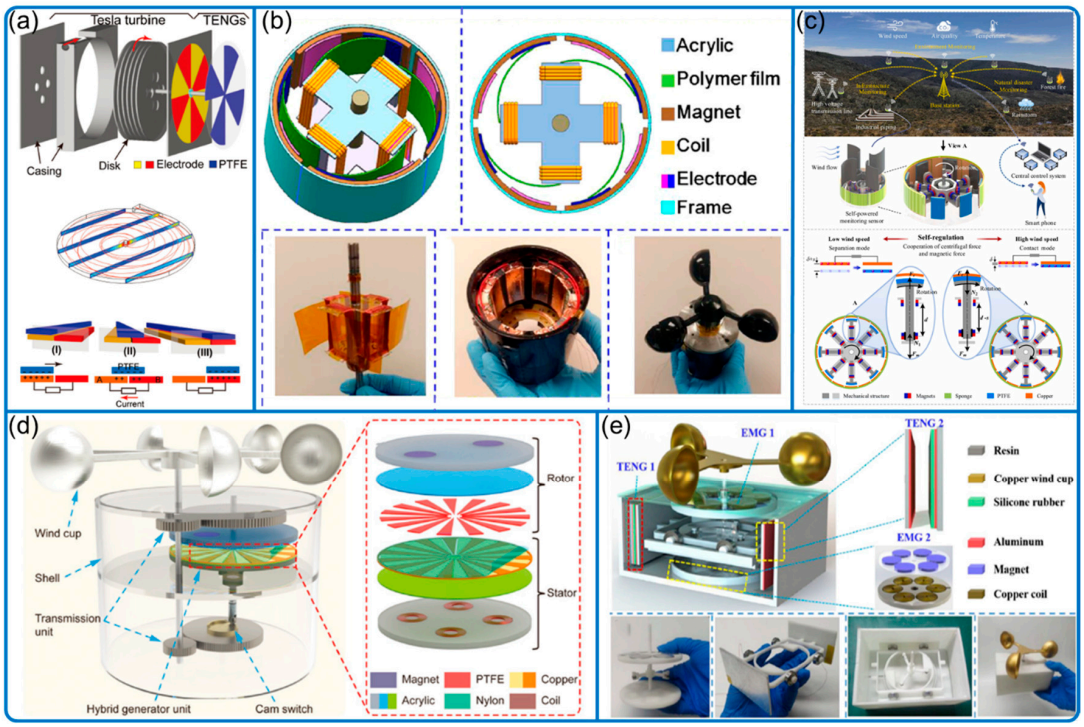

Figure 4. Conventional wind speed sensing with performance enhancement features. (**a**) Bladeless turbine structure. Reproduced with permission. Copyright 2018, Wiley Online Library [22]. (**b**) Ultra-low friction system. Reproduced with permission. Copyright 2018, American Chemical Society [24]. (**c**) Wind-speed-dependent self-regulation strategy. Reproduced with permission. Copyright 2022, Elsevier [26]. (**d**) Travel-controlled approach for high durability. Reproduced with permission. Copyright 2022, Wiley Online Library [25]. (**e**) Rotational to linear motion conversion. Reproduced with permission. Copyright 2020, Elsevier [23].

Table 1. Summary of traditional wind cup and vane style TENG sensors.

Reference	Wind Speed (m/s)	Wind Direction	Features
Wang et al. [24]	3.5 to 9.0	N/A	EMG hybrid device with ultra-low friction
Chen et al. [22]	N/A	N/A	A freestanding bladeless-turbine-based (tesla turbine)
Wang et al. [18]	2.7 to 8.0	Yes	Freestanding (soft contact) disk-like
Han et al. [20]	6.0 to 12.0	Yes, EMG indicator	Ball bearing-like with graded electrodes
Fan et al. [23]	4.0 to 15.0	N/A	A cam structure to convert rotational to linear motion
Lu et al. [27]	6.0 to 12.0	N/A	Freestanding mode disk-like
Zhang et al. [19]	3.0 to 15.0	Yes, with only 3 signal channels	Coded electrodes for wind direction within 2 s
Ye et al. [28]	1.55 to 15.0	N/A	Combined 3 TENGs (flag, disk-brush soft contact, and EMG)
Zhang et al. [21]	3.0 to 15.0	Yes, array of devices	Contact separation mode in rotational device
Ma et al. [29]	2.9 to 9.1	N/A	Wheat-straw based TENG
Zou et al. [26]	2.0 to 12.0	N/A	Self-regulated contact-separation mode; can start with low wind speed
He et al. [30]	3.77 to 11.91	N/A	Disk-brush-like freestanding mode
Luo et al. [25]	3.0 to 15.0	N/A	Travel-controlled approach with cam switch

(b) Wind speed and direction: flutter- and flag-type

This part includes flutter- and flag-type sensors that are susceptible to flow-induced vibration. The devices often consist of a rectangular cross-section tunnel, two electrically connected electrodes on both sides, and a long flexible membrane (in the middle of the flow along the flow direction) that can flutter along the flow so that wind energy can be harvested and the flow information can be also sensed by the periodic electrical signals from the current due to electrostatic induction between the film and electrodes (Figure 5) [31].

The experimental phenomenon and results are solid and obvious, but the theoretical fluttering explanation is often flawed. Many researchers investigated the problem from the perspective of aerodynamics [32–37]. However, even in pure aerodynamics, the answer is not clear. There are two main mechanisms to explain the flutter effect: (1) vortex-induced vibration by adding a bluff body before the membrane and governed by the Strouhal number and (2) without a bluff body, the membrane will also flutter due to the aerodynamic flutter effect. To thoroughly investigate the fluttering effect, Bae et al. divided the fluttering status into single, dual, and chaotic modes, which are indicated by two proposed dimensionless parameters: the nondimensional velocity and dimensionless mass of the flag. These dimensionless parameters are universal and extremely useful for future researchers. In addition, a mathematical relationship between the proposed parameters and fluttering degree, e.g., the fluttering frequency, can be further developed. Chen et al. (Figure 5e) developed a unified theoretical framework for the flutter phenomenon of both stiff and flexible piezoelectric materials, and validated by a micro wind belt system analyzer, in which the airflow rate is from 64 to around 260 m/s and the vibration frequency is up to several thousand Hz [34]. Olsen et al. explained the fluttering of a double-clamped membrane by Karman vortex shredding and gave an easy-to-use formula to calculate the vibration frequency based on the Strouhal number [36]. Numerical simulations were also conducted on membrane flutter and vibration with bending and torsion under various vibration frequencies [34,38,39]. All the above approaches are worth learning from.

However, few studies fully investigated the effect of the narrow tunnel on the airflow and the electrostatics on the membrane movement. On one hand, the confined airflow (disturbed by the fluttering membrane) is completely different from the flow in the open space due to the difference in boundary conditions. On the other hand, in the real situation with the narrow tunnel, two polarized electrodes on both sides of the fluttering membrane will attract the membrane since the membrane and its nearest electrode will always carry charges of opposite polarity. Thus, as it oscillates, the membrane does not tend to stay

in the middle but rather moves randomly to either electrode quickly. As the film reaches one electrode, the wind will blow away the membrane from the nearest electrode, creating rhythmic oscillation and smooth energy harvesting cycles. Therefore, the effect of confined flow and electrostatics should be considered in future theoretical and computational fluid dynamics studies on fluttering TENGs.

The detailed information of wind flutter-type sensors is summarized in Table 2, including wind speed range, wind direction, and features. The tested wind speed for the flutter-type sensors is from 0.5 to 32.0 m/s (a few studies without TENG tried much higher wind speed [32,34]). Similar to the conventional sensors with wind cups, the current trend is to correlate wind speed with electrical signal frequency, whose advantages were discussed in the previous subsection. However, the fluttering frequency has upper limits according to membrane material, structure, and natural frequency so the corresponding flow velocity that can be measured is limited. One way to increase the frequency is to change to the membrane with a higher upper limit for fluid speed, e.g., thin stainless steel foil; another way is to reduce the flow speed at the interested zones by expanding the tunnel cross-section along the flow direction [40,41] according to Bernoulli principle [42]. Thus, the measured frequency can represent higher wind speed, increasing the possible speed sensing range and expanding the application scenarios, e.g., airspeed monitoring for aircraft.

The flow direction can be measured by flutter- and flag-type sensors in two ways, similar to the traditional wind cup types. The first way is also using a wind vane to guide the device [43,44]. Another way is to use an array of direction-sensitive sensors [45] that have one (e.g., one end clamped types) or two (e.g., double-clamped types in Figure 5f [46]) favorable wind directions, a feature that is a drawback for energy harvesting, but a great benefit for sensing. Thus, by locating the sensors in the desired direction, the combined system can deliver the wind direction.

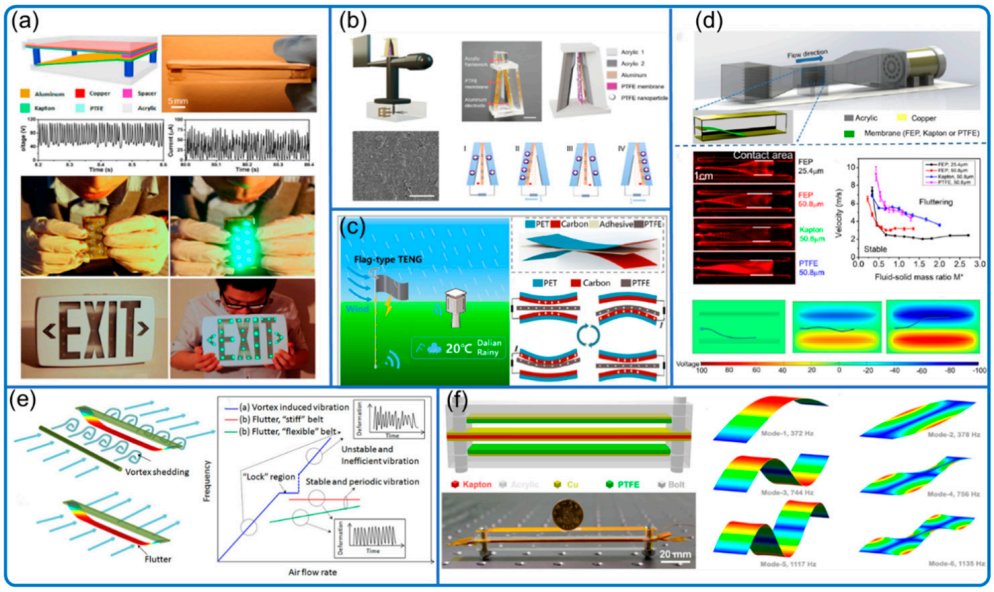

Figure 5. Typical flutter sensor and its mechanism discussion. (**a**) Flutter-type sensor system. Reproduced with permission. Copyright 2013, American Chemical Society [31]. (**b**) Wind vector detecting system. Reproduced with permission. Copyright 2021, Elsevier [43]. (**c**) Flag-type sensor. Reproduced with permission. Copyright 2020, Elsevier [44]. (**d**) Characterization of fluttering behavior and COMSOL simulation. Reproduced with permission. Copyright 2017, Elsevier [35]. (**e**) Theoretical model for flutter phenomenon. Reproduced with permission. Copyright 2016, AAAS [34]. (**f**) Double-clamped aero-elastic system. Reproduced with permission. Copyright 2015, American Chemical Society [39].

Compared to other types of sensors, flutter- and flag-type sensors have some unique advantages. First, their design is simpler and thus easier to manufacture. Second, they own minimum moving parts and don't contain gears, making them small in size in general with great scalability, which could be critical for expanding their application scenarios in the microscopic world. Finally, with minimum moving parts and mainly contact and separation motion, their robustness is much better than the rotational and frictional-based sensors.

Benefitting from the mentioned advantages, in addition to being the energy harvester and sensor, the flutter- and flag-type sensors have many other special functions and features as well (Figure 6). For example, Wang et al. (Figure 6c) constructed a flutter array system to work effectively as a wind barrier [46]. Roh et al. (Figure 6a) integrated the flutter sensor into a hybrid environmental energy harvesting and weather monitoring system [47]. Zhao et al. (Figure 6d) fabricated woven flag-type TENG in the size of 30 × 30 cm^2 with triboelectric and conductive belts [48]. Furthermore, Wang et al. (Figure 6b) achieved wireless sensing using mechanical−electrical−optical signal conversion, where the airflow speed is correlated with the light signal that is received remotely by the optical detection module [49].

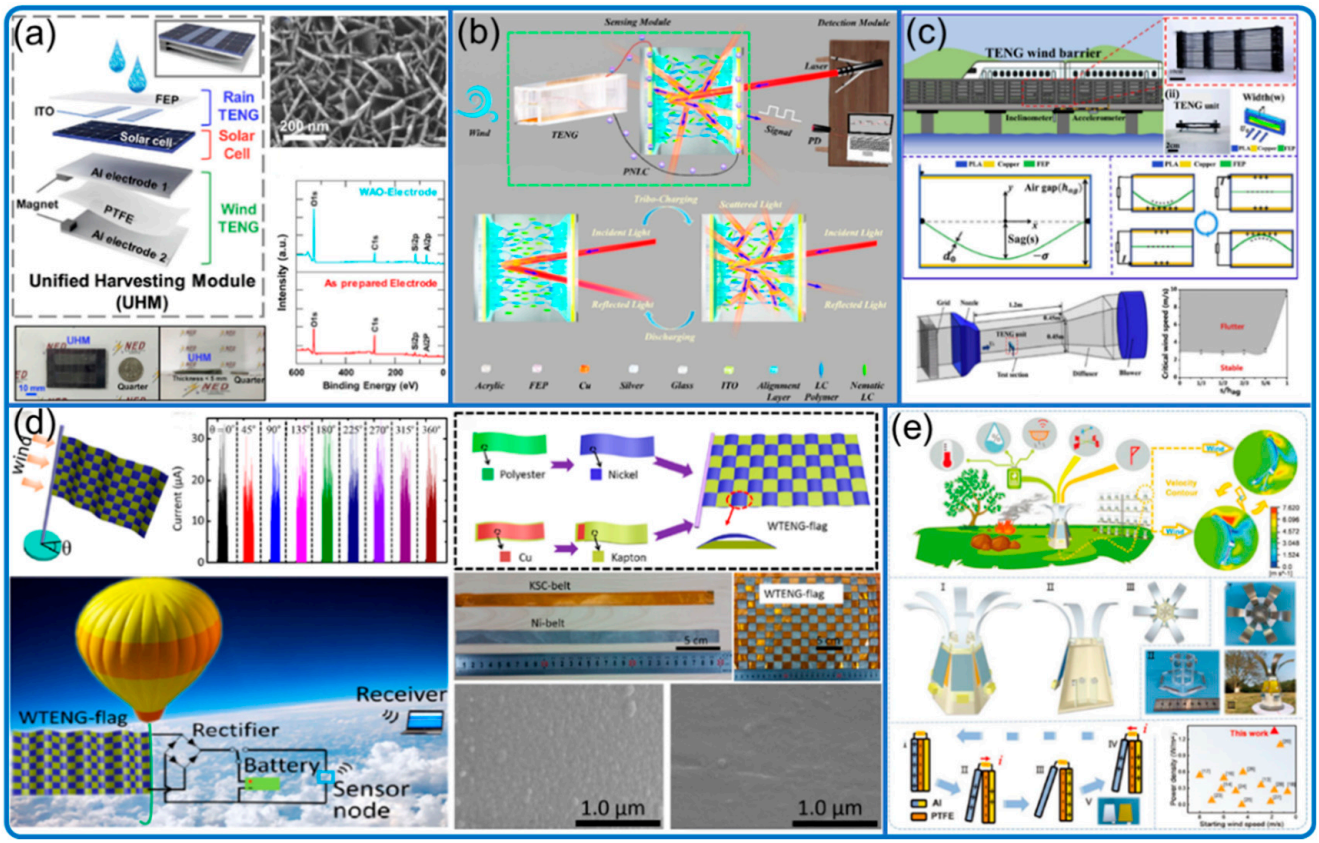

Figure 6. Flutter sensors' special functions and features. (**a**) Weather monitoring system. Reproduced with permission. Copyright 2020, Elsevier [47]. (**b**) Mechanical−electrical−optical signal conversion system. Reproduced with permission. Copyright 2021, American Chemical Society [49]. (**c**) Sensors as wind barrier. Reproduced with permission. Copyright 2020, Elsevier [46]. (**d**) Woven flag-type system. Reproduced with permission. Copyright 2016, American Chemical Society [48]. (**e**) Multidirectional fire detection system. Reproduced with permission. Copyright 2021, Wiley Online Library [45].

Table 2. Summary of flutter- and flag-type TENG sensors.

Reference	Wind Speed (m/s)	Wind Direction	Features
Yang et al. [31]	6.0 to 14.0	Yes, arrayed devices	The earliest flutter-type TENG
Zhao et al. [48]	3.0 to 32.0	N/A	Flag-type device with fabricated belts
Ravichandran et al. [40]	0.5 to 10	N/A	Venturi flutter-type; the interested zone wind speed is increased due to Bernoulli principle
Wang et al. [44]	2.0 to 7.5	Yes, circuit indicator with 4 directions	Flag-type with humidity resistance
Wang et al. [46]	4.0 to 11.0	N/A	Flutter-type TENGs as wind barrier
Zaw et al. [50]	1.5 to 2.7	Yes, wind direction sensitive	Flutter-type but ripped style TENG.
Roh et al. [47]	6.0 to 13.0	N/A	Weather monitoring system with rain and wind flutter TENG with solar panel
Li et al. [51]	1.6 to 14.0	N/A	Flutter-type TENG with carbon nano thorn arrays on the electrode
Liu et al. [41]	15.0 to 25.0	N/A	Flutter-type with expanded chamber
Xu et al. [43]	2.9 to 24.0	Yes	Flutter-type; photoelectric sensor for direction and wind blow toward the long side
Wang et al. [49]	2.5 to 10.0	N/A	Flutter-type; wireless sensing with mechanical−electrical−optical signal conversion
Zhang et al. [45]	1.8 to 4.3	Yes	Flow induced vibration; 6 wind directions by array; fire detection

(c) Rain monitoring:

Another meteorology sensing using TENG is rain monitoring. The traditional rain gauges mainly include siphoning, weighing, and tipping bucket types [52]. Similar to the traditional gauges, Hu et al. (Figure 7a) developed two rain bucket method mechanical TENGs with different resolutions to monitor the rain bucket motion change for real-time rainfall intensity monitoring from 0 to 288 mm/day with linear calibration curves [53].

In addition to the traditional rain gauge style sensor, the direct interaction between the raindrop and sensitive materials can be another possible way to sense the rain. In fact, the TENG field has extensive studies on solid–liquid interface contact electrification [54,55]. However, many of them focus on fundamental mechanisms and energy harvesting; few studies focus on rain monitoring. Until recently, Xu et al. (Figure 7c) designed autonomous rainfall monitoring and wireless transmission system completely driven by raindrop energy harvesting, paving the way for raindrop-powered wireless hygrometers [56]. The tested rain intensity is from 2.0 to 71.0 mm/min. When the rainfall is 71 mm/min, the rainfall data are automatically transmitted every 4 min within the range of 10 m. Another study (Figure 7b) takes advantage of the effect of hydrogen ion concentration on the material response and consequent TENG output to develop a pH sensor for acid rain [57].

3.2. Fluid Sensing in Pipes and Tunnels

Pipes and tunnels are other places where fluid dynamics sensing is important and suitable. A network of self-powered sensors will be important for cost reduction and risk alarming in the industry of pipeline transportation. Thus, researchers were exploring TENGs for fluid sensing in pipes and tunnels with three main types (Figure 8):

(a) Waterwheel-type

Wang et al. (Figure 8a) developed a waterwheel-type flow rate sensor in pipes from 80 to 400 mL/s (i.e., 4.8 to 24.0 L/min) with an anti-rust feature [58]. Similarly, He et al. (Figure 8b) developed a non-full pipe flow sensor (220 mm in diameter and 105 mm in width) monitoring the flow rate from 94 to 264 L/min, with an error rate under 1.95% [59].

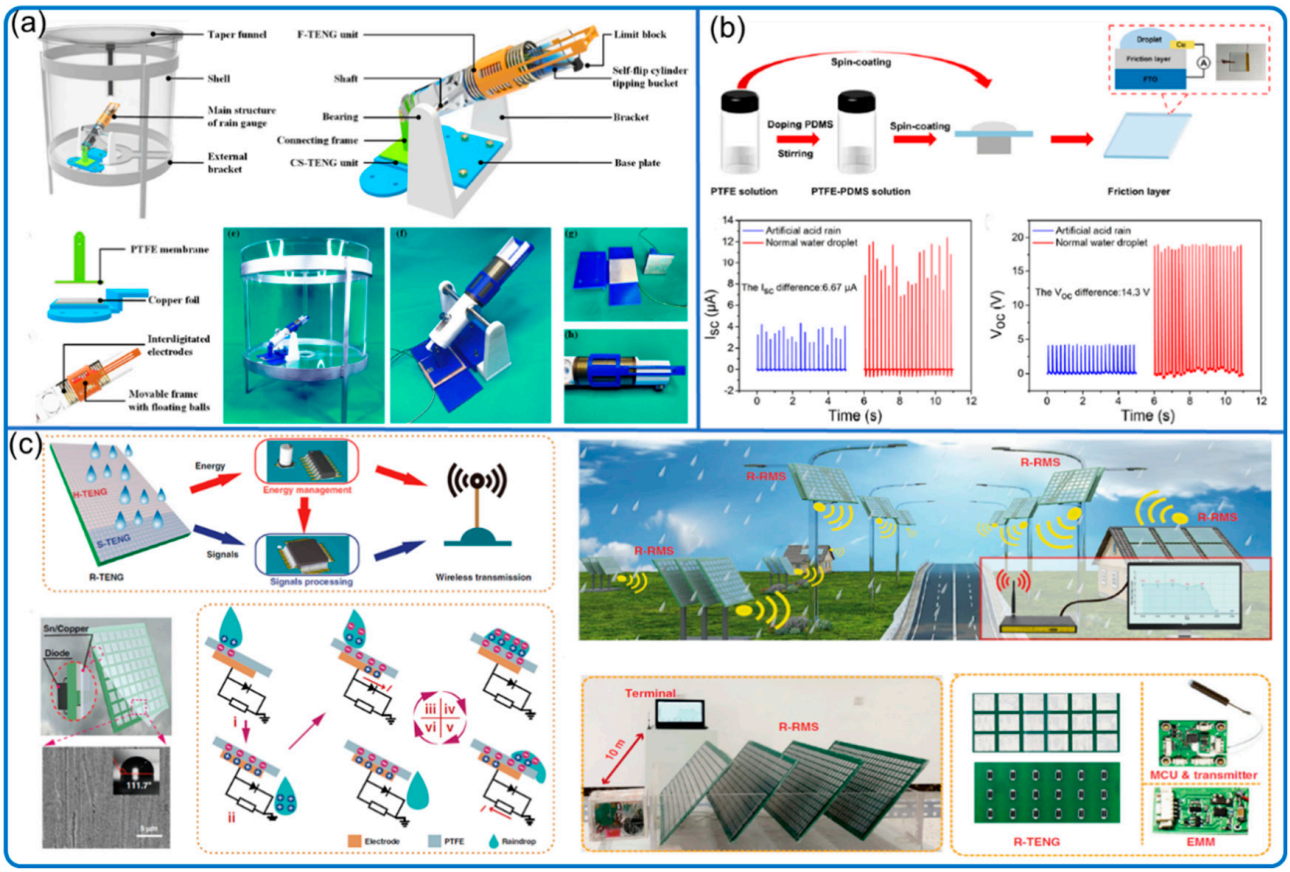

Figure 7. Rain monitoring TENG. (**a**) Tipping bucket rain gauge sensor. Reproduced with permission. Copyright 2022, Elsevier [53]. (**b**) Real-time acid rain sensor. Reproduced with permission. Copyright 2021, American Chemical Society [57]. (**c**) Raindrop-powered autonomous rainfall monitoring. Reproduced with permission. Copyright 2022, Springer [56].

(b) Solid–liquid interface contact electrification

Another sensor in He et al. [59] is a liquid-level sensor applying solid–liquid interface contact electrification. Using the same principle, Song et al. (Figure 8c) developed a sensor for microfluidic droplet sensing with good stability and responsiveness [60]. It also has good sensitivity to the droplet size with the droplet length from 3.0 to 13.5 mm. Zhang et al. developed liquid in a U-tube TENG for air pressure sensing (from about 0.1 to 0.54 kPa), where air humidity did not affect performance [61]. Cui et al. also developed a liquid in solid tube-based TENG sensor monitoring air pressure from −2.5 to −0.5 kPa and 0.5 to 2.5 kPa [62].

(c) Cylinder-type

Fu et al. (Figure 8d) applied a cylinder moved through varied area electrodes by air pressure to detect air pressure and flow rate in the tunnel with the pressure from 0.04 to 0.12 MPa at a step of 0.02 MPa and flowrate from 50 to 250 L/min at a step of 50 L/min [63]. The way the authors varied the area of detection, which is also used in other fields [64,65], to generate tunable signals is interesting and very useful in signal manipulation. Wang et al. (Figure 8e) later developed a rotameter style TENG sensor for liquid level and pneumatic flow from 10 to 200 L/min with a flow resolution of 2 L/min with real-time non-digital flow rate visualization [66].

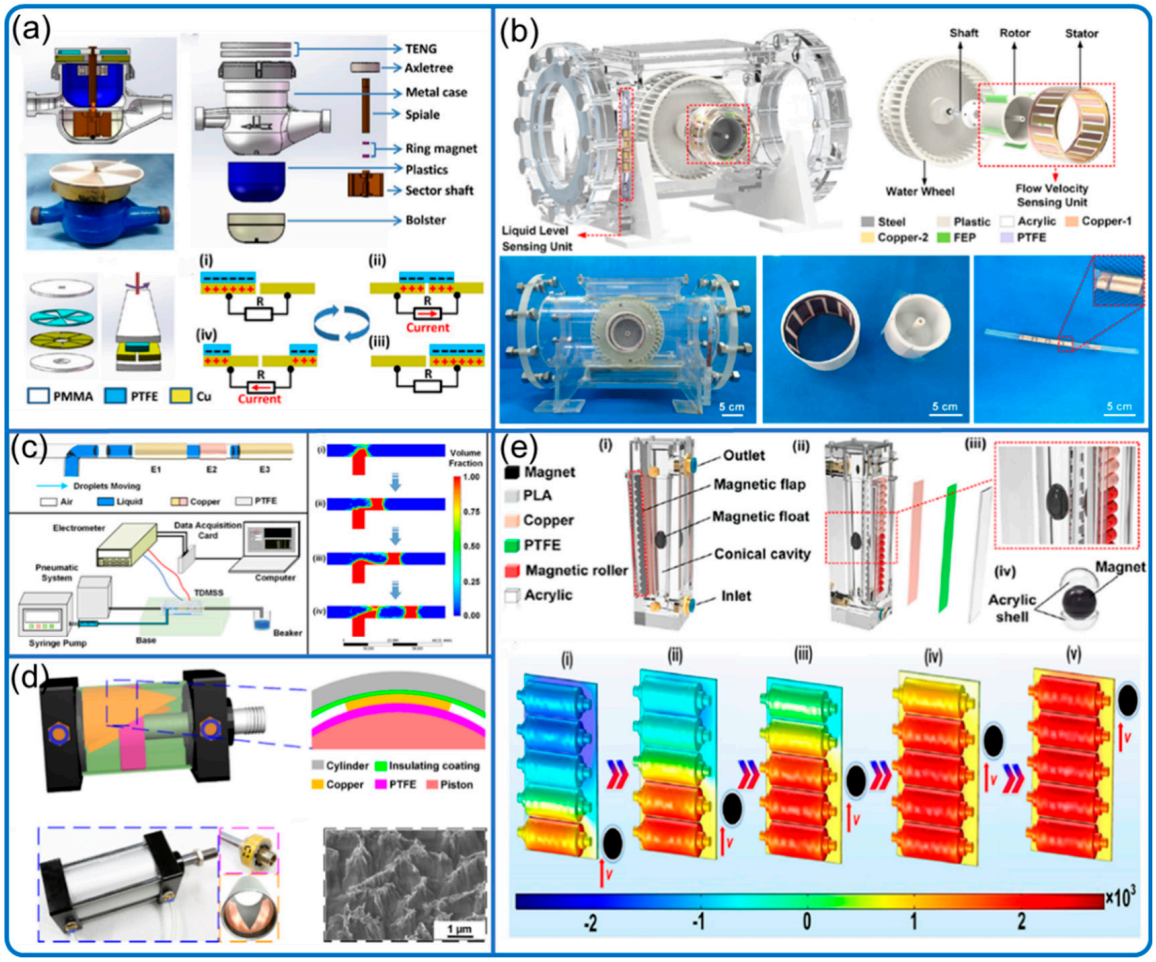

Figure 8. Fluid sensing in pipes and tunnels. (**a**) Anti-rust waterwheel-type system. Reproduced with permission. Copyright 2019, American Chemical Society [58]. (**b**) Non-full pipe fluidic flow and water level system. Reproduced with permission. Copyright 2022, American Chemical Society [59]. (**c**) Non-invasive droplet motion monitoring. Reproduced with permission. Copyright 2021, American Chemical Society [60]. (**d**) Pneumatic monitoring with varied-area electrodes. Reproduced with permission. Copyright 2017, American Chemical Society [63]. (**e**) Magnetic flap-type rotameter-like difunctional sensor. Reproduced with permission. Copyright 2020, American Chemical Society [66].

3.3. Remote Media Vibration and Object Sensing

Sound, a kind of acoustic wave, causes media vibration that can be detected by TENG sensors [67–69] (Figure 9). Arora et al. demonstrated an acoustic sensor (microphone) that is thin, flexible, and easily manufactured [68]. Its resonant frequency is approximately 275 Hz and the best acoustic sensitivity is −26.63 dB at 1000 Hz. Similarly, Guo et al. (Figure 9a) applied thin film TENG with holes and developed an auditory sensor for social robotics and hearing aids [67]. It has a broadband response from 100 to 5000 Hz and ultrahigh signal sensitivity (110 mV/dB). Chen et al. (Figure 9b) later claimed to have developed the smallest MEMS (micro-electro-mechanical systems) TENG device with micro-array in 50 μm-sized diaphragms, achieving underwater acoustic communication within 30 mm. Its signal-to-noise ratio (SNR) is 20.54 dB and its resonant frequency is as high as 1.17 MHz [69].

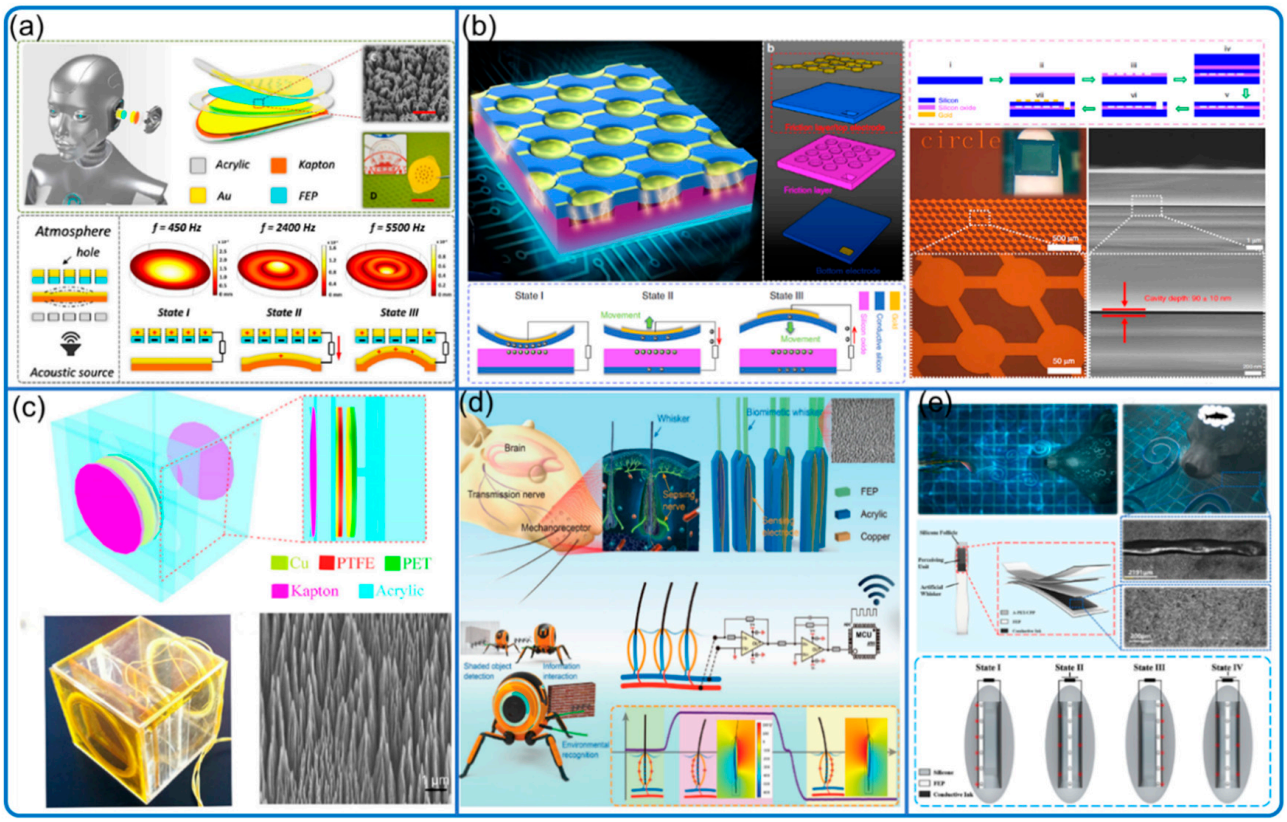

Figure 9. Remote media vibration sensor. (**a**) Auditory sensor. Reproduced with permission. Copyright 2018, AAAS [67]. (**b**) Micro triboelectric ultrasonic device. Reproduced with permission. Copyright 2020, American Chemical Society [69]. (**c**) Acoustic source locator in underwater environment. Reproduced with permission. Copyright 2015, Springer [70]. (**d**) Biomimetic hairy whiskers. Reproduced with permission. Copyright 2021, Wiley Online Library [71]. (**e**) Underwater bionic whisker sensor. Reproduced with permission. Copyright 2022, Elsevier [72].

The media vibration caused by objects, not only due to sound waves but also by surrounding water and air movement, can be also detected by TENG sensors, with appropriate algorithms [70–72]. Yu et al. (Figure 9c) developed an organic film TENG as an underwater acoustic source locator at low frequencies around 100 Hz [70]. It can detect up to 1.0 m with an error of about 0.2 m and the highest sensitivity –146 dB. Wang et al. (Figure 9e) developed a seal whisker-like, film-type sensor for underwater vortex perception and demonstrated its target tracking capabilities, with an SNR of about 19 dB without filtering [72]. As demonstrated, TENGs as vortex sensors should be further investigated and could be very useful for the fundamental study of fluid dynamics. In An et al. (Figure 9d), a bendable biomimetic whisker mechanoreceptor (film-type TENG) is designed for robotic tactile sensing [71]. The sensor has a very high SNR with a minimum exciting force of 1.129 μN thanks to the simple and functional design, making it also suitable to detect natural flow vibration and object-induced air movement. Furthermore, the sensor can be scaled down to a very small size and integrated within the airflow boundary layer, whose airflow situation can be sensed with minimal device impact.

3.4. Water Wave Motion

We roughly classify the TENG sea wave sensors into floating and fixed types (Figure 10). The floating types generally have more flexibility for setup and wider application scenarios than the fixed ones. The sensing mechanism is mainly solid–solid contact electrification, while a few studies applied liquid–solid contact electrification.

The wave parameters sensed here include wave height, magnitude, fluctuation, and other local parameters. For example, wave height can be sensed by the fixed liquid–solid plate TENG (Figure 10a) [73], the coral-like four-way TENG [74], and the buoy-driven TENG (Figure 10c) [75]; wave magnitude can be monitored in two grades by the TENG with cam gear (Figure 10d) [76]; wave surface fluctuation can be monitored by the floating jellyfish-like TENG with various working scenarios [77]. In addition to large-scale sensing, Bhatta et al. (Figure 10b) developed a powerful floating TENG-EMG hybrid wave motion sensor, offering various comprehensive wave-related local parameters, such as the wave speed, acceleration, frequency, direction, tilting angles, and wavelength with good accuracy [78].

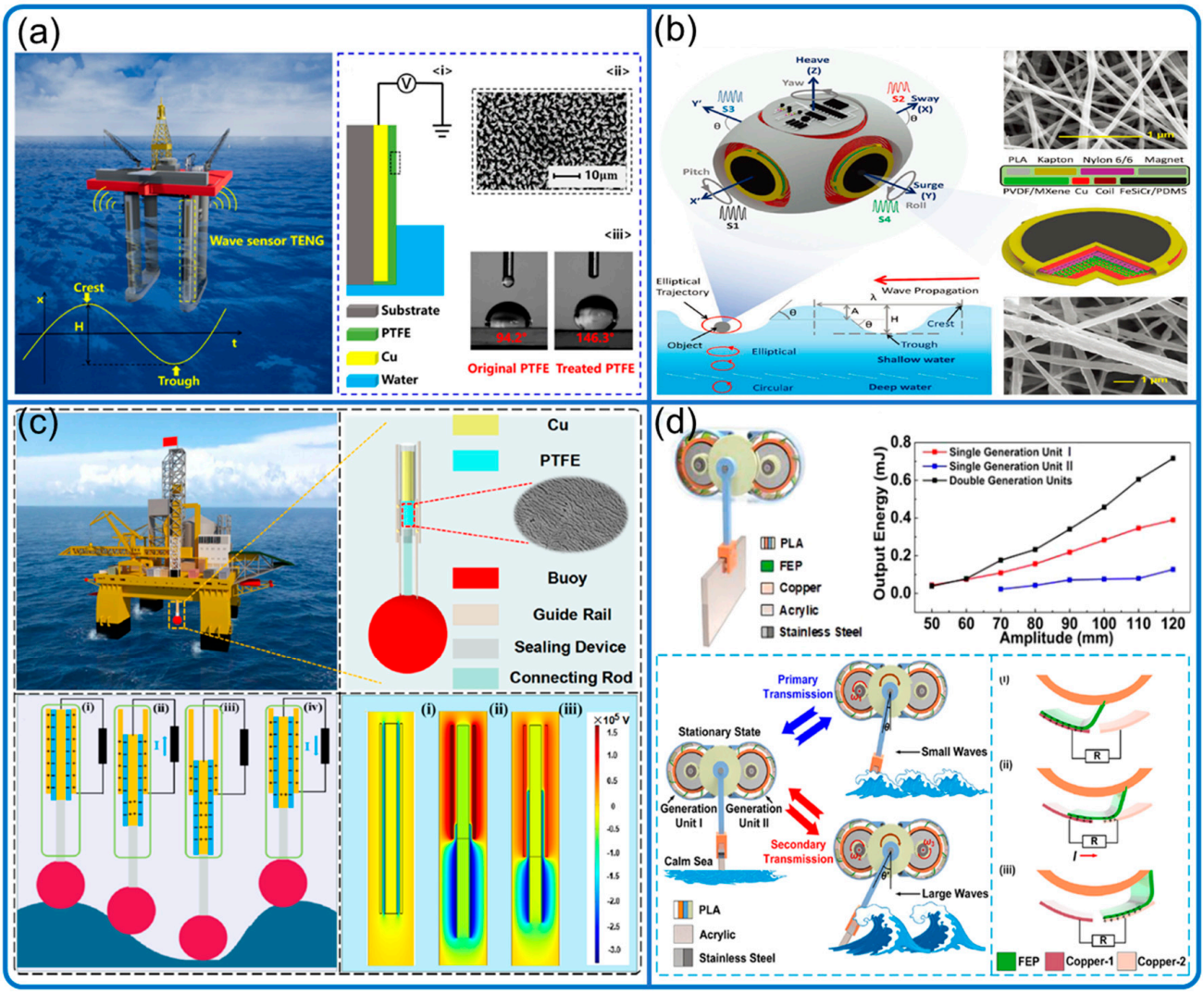

Figure 10. Sea wave motion sensing. (**a**) Highly sensitive wave sensor. Reproduced with permission. Copyright 2019, Elsevier [73]. (**b**) Self-powered arbitrary wave motion sensing system. Reproduced with permission. Copyright 2022, Wiley Online Library [78]. (**c**) Ocean surface water wave sensor. Reproduced with permission. Copyright 2020, American Chemical Society [75]. (**d**) Ocean wave sensor with graded energy harvesting. Reproduced with permission. Copyright 2021, American Chemical Society [76].

3.5. Structural Vibration Due to Moving Fluid

Flow-induced structural vibration is an area of interest and concern in both academia and industry. Especially in industry, it is a big problem for the safety of buildings, bridges,

grid lines, and fast-moving vehicles in the air and water, but also an opportunity for energy harvesting, for example, the bladeless vibration energy harvester [79,80].

Due to their cyclic nature, these vibrations, usually rhythmic, can be also monitored by TENG sensors (Figure 11). For example, power line galloping (self-excited vibration phenomenon with a low frequency) and aeolian (wind excitation phenomenon with high frequency) sensors have been developed by Gao et al. and Wu et al., respectively [81,82]. Gao et al. (Figure 11a) developed a TENG-EMG hybrid generator (pendulum-type) with grid line galloping energy harvesting and monitoring [81]. The horizontal, vertical, and elliptical galloping modes were physically simulated and tested by a scale reduction model, and the amplitude and frequency of the three modes were monitored over a range of 5.0 to 16.8 cm (with linear calibration curves) and 0.7 to 2.2 Hz, respectively. The broadband aeolian vibration sensing and its effective energy harvesting of transmission lines were achieved by a spring-mass type TENG (Figure 11b) in Wu et al. [82]. The sensed amplitude is from about 0.5 to 6.0 mm, with a broad frequency response region of 5–50 Hz. Unfortunately, the vibrations in both of the studies were not induced by airflow under a real aerodynamic situation, which is needed to further validate the senor performance in practical applications.

Bridge vibration can be also induced by moving fluid: either by (1) forced resonance caused by vortex shredding, or (2) aeroelastic self-excitation or "negative damping" flutter effect. For example, the dramatic collapse of the Tacoma Narrows Bridge was related to an aerodynamically induced vibration, a combination of forced and self-excited vibrations, where the critical cause is still under debate [83]. To monitor the bridge dynamic displacement (1.0 to 5.5 cm) and vibration acceleration (13.7 to 49.0 ms^{-2}), Yu et al. (Figure 11c) designed a dynamic displacement monitoring system (spring-mass in cylinder style) within a low-frequency working range (<5–10 Hz) [84].

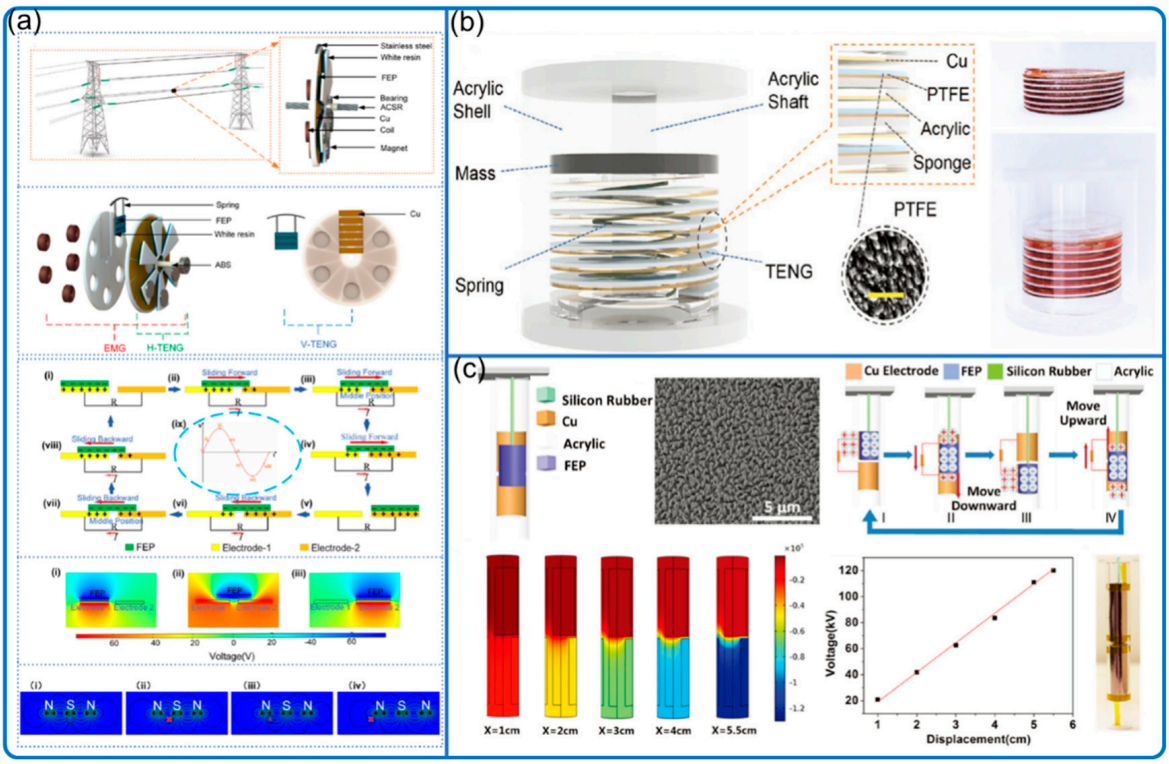

Figure 11. Structure vibration due to moving fluid. (**a**) Transmission lines galloping sensor. Reproduced with permission. Copyright 2022, Elsevier [81]. (**b**) Broadband aeolian vibration online monitoring of transmission lines. Reproduced with permission. Copyright 2022, Wiley Online Library [82]. (**c**) Bridge dynamic displacement monitoring system. Reproduced with permission. Copyright 2017, Wiley Online Library [84].

4. TENG for Fluid Dynamics Sensing: Future

The above section has summarized many applications of TENG in fluid dynamics sensing. However, to reveal the full potential of TENG for fluid dynamics sensing, we need to take advantage of TENG, and ultimately fill the gaps and meet the needs of industry and academia. In academia, alternative methods are needed to measure the in situ local fluid situations, e.g., vortex, boundary layer, and turbulence transition. The most reliable method to observe fluid dynamics is optical techniques, such as particle image velocimetry (PIV) and Schlieren imaging. However, these techniques require a sophisticated setup and critical experimental environment in the laboratory, making them not suitable for multi-scale field measurements, which play very important roles in the validation and application of fundamental theories.

In industry, especially aerospace, non-invasive sensors are in large demand, for flight safety, flight data acquisition, and aircraft design optimization by monitoring the local in situ fluid situation in real flight. The critical parameters include aircraft airspeed, friction drag force, vortex and boundary layer separation near the wing surface, and wing vibration. However, most of the traditional sensors need power with cables that will increase the weight. In addition, since most third-party sensors are not pre-designed in the body, the power supply and cables of the sensors will expose to the extreme atmosphere, creating a difficult scenario for high-speed aircraft because the fast-moving air may damage the cables, which also in turn disturb the airflow field and thus the flight condition and safety. As for light-weighted unmanned aerial vehicles (UAV), the increased weight from the whole sensor system could be another critical problem for efficient flight. Thus, the industry craves suitable sensors with the features of lightweight, plug-and-play, in situ, and battery-less, so that significant progress can be made in the aerodynamics theory development, aircraft design, and safety monitoring.

Fortunately, TENG sensors have the potential to fulfill some of the above needs in fluid dynamics sensing thanks to the following advantages: self-powered sensing, wireless signal transfer, scalability, material diversity, and flowability (Figure 12). As mentioned in Section 1, TENGs can actively generate electrical signals and have the potential to generate enough power to save and even transmit signals by the TENG alone, making the sensor setup and maintenance much easier than the conventional ones. Tao et al. designed a hierarchical honeycomb-structured structure for morphing airplane energy harvest, claimed as the first TENG used for aircraft, showing the feasibility of energy harvesting and self-powered sensing in the aerospace industry [85].

Furthermore, with the feasibility exploration and approach development of wireless transmission of TENG signal in air and water [11,12,86,87], even if the TENG is not powerful enough to run the whole system, the sensing signal can be also possibly received without any power supply and the need of signal pre-amplification. Wang et al. summarized TENG-based self-powered wireless communication into four major types of technological routes: tribo-induced electromagnetic wave generation, tribo-induced light propagation tuning, triboelectrification-induced electroluminescence, and tribo-assisted spectrometry, collectively known as tribophotonics [12].

In addition to signal generation and transferring, the adaptive design and easy manufacturing, thanks to its simple working mechanism and various working modes, endow TENGs with strong scalability, meaning that the complexity and difficulty of manufacturing are not heavily affected by the size of the devices. Many design techniques are highly scalable by avoiding the use of unscalable parts, such as traditional joints, screws, nuts, and gears. For example, compliant mechanism design can reduce parts, joints, and production processes, making it advantageous in the fabrication of micro-mechanisms [88]; origami and kirigami design [89] can easily transform a device into a 3D structure with the desired function from a 2D design, which is convenient for industrial-level and TENG friendly precision manufacturing techniques such as laser cutting, pre-stretching, printed circuit board (PCB), and microelectromechanical systems (MEMS).

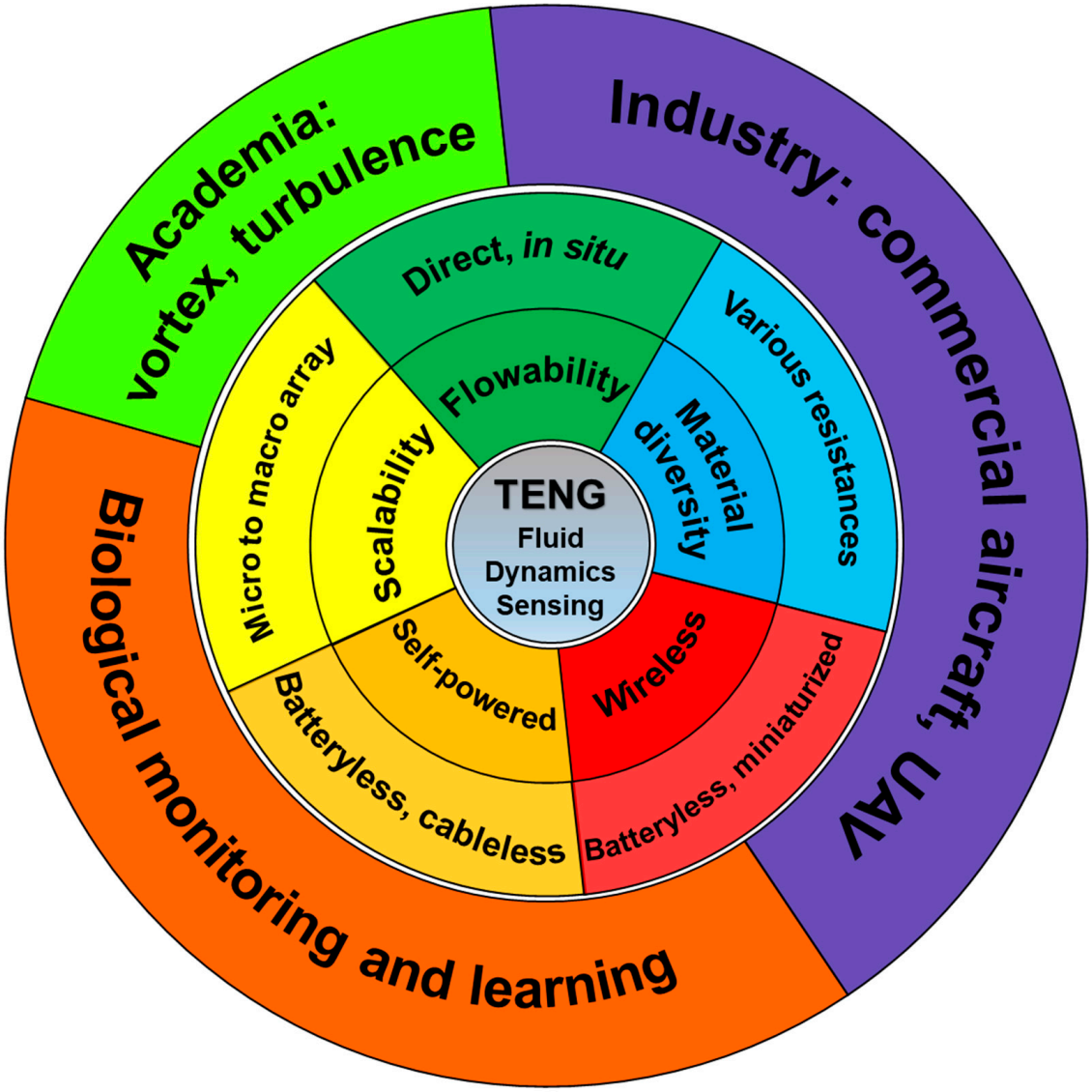

Figure 12. Schematics of advantages and future applications of TENGs for fluid dynamics sensing.

Consequently, the scalability gives TENG sensors better chances to form an array [69] and get applied to the microenvironment. For example, a rationally designed TENG can locate within the flow boundary layer and provide valuable local information for flow fundamental research. In addition, an array of such sensors can even deliver more comprehensive information in high spatial and temporal resolution [90]. In addition, TENG sensors with good scalability (better if with wireless communication) can be used for biological monitoring, data acquisition, and learning, where we can learn deeper and better from nature, especially its fluid-related phenomenon [91,92], e.g., flying of birds and swimming of fishes, allowing us to have innovations and breakthroughs in the engineering development for machines, vehicles, and robotics [93,94]. Of course, this influence has already penetrated deep into the TENG field [95–97]. For an instance, the study of seal whisker (vibrissa) suppressing vortex-induced vibrations provides us with a possible solution to increase the SNR (signal-to-noise ratio) for a TENG array system of object-induced vortex detection [98]. However, the investigation tools and approaches to study nature are limited. Tiny, lightweight, and scalable TENG sensor arrays will make a difference in the in situ fluid dynamics monitoring of living beings.

The material diversity that offers a wide selection of materials is another unique feature of TENG sensors, especially for fluid dynamics sensing. Fluids may contain a

variety of physical and chemical phenomena that make most sensors difficult to deploy and function. The situation is much better for TENG sensors, as almost any two materials can generate a high or low triboelectric signal so that we can choose the right ones from the large material library to suit specific, possibly extreme, and multi-physics environments (e.g., high temperature, pressure, electrical noise, bending, and friction environments) with better physicochemical performance such as high chemical resistance, hydrophobic/hydrophilic, temperature resistance (e.g., titanium–tantalum alloy), fatigue resistance, and shape memory (e.g., nitinol alloy), and light-weighted but high strength (e.g., carbon fiber). For example, similar to the flutter-type speed sensor, a thin metal foil, which can flow along with air, can be used as the fluttering material to sense high wind speed in high-temperature situations (e.g., airspeed sensing for aircraft) instead of polymer films, which are fragile with low-temperature resistance.

Another important property of TENGs for fluid dynamics sensing is flowability, which means that the TENG can conform to and move along with the moving fluid, making it very unique in the fluid sensing field. Most of the traditional sensors are fixed rigidly and cannot move with the fluid. A moving along sensor can give detailed and valuable in situ information on the fluid local status including vortex [99,100], boundary layer separation, and turbulence, which are some of the most difficult subjects for fundamental fluid research and critical for the field of fasting moving vehicles such as aircraft and submarine. As for those traditional fixed sensors for fluid dynamics, only the related but indirect parameters can be measured to calculate the interested parameters with many assumptions and simplifications. For example, the MEMS skin sensors for aircraft measure the fluid-related parameters, such as pressure and temperature, and indicate the flow turbulence and stall status indirectly through calculation with mathematical algorithms [101,102].

In this section, we have summarized the unique advantages of TENG in fluid dynamics sensing (including self-powered, wireless communication, flowability, a wide selection of material, and scalability) and their corresponding potential new applications that differ from the previous ones (Section 3). Hopefully, the new perspective can help TENG reach its full potential by providing brand-new and powerful tools and data for academia and industry in the new era of IoT and AI and offering more chances for TENG to constantly develop and show its ability.

5. Challenges and Possible Solutions

The three most important features and also the main challenges for qualified sensors, including TENG sensors, are sensitivity, selectivity, and stability. In this section, we discuss several challenges that TENGs are facing to consolidate their positions in the existing areas and reach their full potential and capabilities in the key new fields of fluid dynamics sensing and provide helpful tools and possible solutions (Figure 1).

Researchers need to master the fundamental knowledge and understanding of fluid dynamics, fluid mechanics, and aerodynamics for aircraft, so that (a) we know where to target and measure, and what to enhance and avoid; (b) we can choose the right TENG material and design with proper structure and casing to suit the fluid situation; (c) we can choose the right supporting calibration equipment to observe, calibrate, and validate the TENG sensors and eventually enhance their performance, according to the theories.

Here are some basic and, most importantly, easy-to-use principles and equations, especially with explicit solutions, to explain and analyze fluid dynamics:

(a) For inviscid flow, if we assume the fluid motion is governed by pressure and gravity forces only, Newton's second law applied to a fluid particle is in the form:

$$(\text{Net pressure force on partaicle}) + (\text{net gravity force on particle}) = (\text{partice mass}) \times (\text{particle accelaration})$$

As a result of the interplay among pressure, gravity, and acceleration, fluid mechanics has numerous useful applications. Furthermore, when applying Newton's second law on a fluid particle along the streamline, we obtained the celebrated Bernoulli equation.

(b) Bernoulli equation: a very powerful tool in fluid mechanics

$$p + \frac{1}{2}\rho V^2 + \rho g z = \text{constant along streamline}$$

where p is the fluid pressure, ρ is the fluid density, V is the flow velocity, g is the gravitational constant, and z is the elevation term. The equation basically means the sum of the pressure term, velocity term, and elevation term is constant along a streamline. Note that to use the equation correctly we must always remember the basic assumptions used to derive it: (1) negligible viscous effects, (2) steady flow, (3) incompressible flow, and (4) the equation is applicable along a streamline. This equation can be used conveniently together with the Coanda effect [103] which is the tendency of a fluid jet to stay attached to a curved surface, where the fluid will speed up and, according to the Bernoulli equation, has low pressure.

(c) Navier–Stokes equations: governing differential equations for incompressible Newtonian fluids

$$\rho\left(\frac{\partial V}{\partial t} + V \cdot \nabla V\right) = -\nabla P + \rho \mathrm{g} + \mu \nabla^2 V$$

Above is the form compactly expressed in vector notation. Detailed differential equations can be found in Munson et al. [42]. The Navier–Stokes equations are essential to all fluid mechanics. The equations' analytical solution has not been found yet; however, the numerical solution can be used in computational fluid dynamics (CFD), which is another powerful tool in understanding and explaining the fluid dynamics phenomena from a different perspective.

(d) Reynolds' number: generally, of importance in all types of fluid dynamics problems

$$R_e = \frac{\rho V l}{\mu}$$

where l is the characteristic length, μ is the fluid viscosity. This dimensionless number should match between simulations and experiments for comparable and accurate data. In addition, it could be used as a criterion to distinguish between laminar and turbulent flow. Note that the criteria are different according to the characteristic length and the scenarios, such as flow in the pipe and flow around the object.

(e) Strouhal number: a dimensionless number describing unsteady flow with a characteristic frequency of oscillation

$$S_t = \frac{\omega l}{V}$$

where ω is the frequency of vortex shedding, l is the characteristic length (for example, hydraulic diameter or the airfoil thickness), and V is the flow velocity. This number can be used to investigate the flow-induced vibration such as bridges and grid lines vibration in the wind, and vortex shredding in the water.

1. The testing, calibration, and validation instruments are needed for the proper design of TENG fluid dynamics sensors. This is also a challenge because the equipment is either expensive and difficult to handle or limited. To avoid discrepancy caused by the noise from the testing environment, we need well-controlled water and wind tunnels, (e.g., high speed or low turbulence wind tunnel) and optical observation systems, e.g., PIV (particle image velocimetry) flow velocity distribution measurement and Schlieren imaging systems. Inaccurate and loose testing apparatus may generate inaccurate calibration curves and deliver biased results during sensor design and testing phases. In addition, signal calibration and subsequent readjustment algorithms are also critical for pushing the instrument response to the desired parameters [64,65].

2. To take advantage of the scalability of TENG sensors, we must keep in mind scalable and parametric design, and the corresponding manufacturing techniques. For example, for the fluttering sensor, the system size is not as critical when used in an ordinary environment; however, when used for the flow boundary layer sensing, the system needs

to be as thin and small as possible to locate within the boundary layer and minimize the system disturbance to the flow. Thus, if scalability is kept in mind at the beginning of design, the sensor system can be easily transferred from a normal to a specific environment. Otherwise, any unscalable techniques (e.g., low-resolution techniques and parts) during the manufacturing process when changing scales will prevent the device from being scalable.

3. The core function of sensors, including TENG sensors, is signal selectivity, which is distinguishing different signals by responding selectively to the interested signals and filtering out noise signals. In other words, the system must be either very selective or the sensing process can be strictly controlled so that uninterested signals will not interfere with measurements. Therefore, sensor design for fluid dynamics must be very careful with assumptions and algorithms, since many indirect sensors rely on a stable environment and assume constant environmental parameters, such as fluid density, temperature, and pressure, which could be invalid during realistic measurements. This is also why in situ sensors with direct measurement (also the focus of TENG sensors) are always preferred when possible, with fewer assumptions to make and fewer variables to control. Furthermore, field measurements with realistic and multi-variables situations are required to ultimately validate the sensors [65].

4. Even if the sensors are well designed and calibrated, the multiphysics environment (water, high temperature, electrical field, and plasma shield) often found in fluids can still reduce the performance and lifespan of devices and disturb the signal generation and transmission. Thus, the solution is to find and apply the optimal design and materials, which are the unique advantages of TENGs, to cope with high bending, chemical, and humidity conditions, and to generate signals with a generally high SNR (signal-to-noise ratio).

Author Contributions: Conceptualization, L.N.Y.C. and Z.X.; writing—original draft preparation, L.N.Y.C.; writing—review and editing, L.N.Y.C., Z.X. and Z.L.W.; supervision, Z.L.W.; project administration, L.N.Y.C. and Z.X. All authors have read and agreed to the published version of the manuscript.

Funding: This research was funded by the National Key R & D Project from Minister of Science and Technology grant number 2021YFA1201601, National Natural Science Foundation of China grant numbers 52192610 and 52203324, and the Fundamental Research Funds for the Central Universities grant number E2E46804.

Acknowledgments: L.N.Y.C. thanks Erming Su for figure preparation and Yaxing Cao for literature searching.

Conflicts of Interest: The authors declare no conflict of interest.

References

1. Wu, C.; Wang, A.C.; Ding, W.; Guo, H.; Wang, Z.L. Triboelectric Nanogenerator: A Foundation of the Energy for the New Era. *Adv. Energy Mater.* **2019**, *9*, 1802906. [CrossRef]
2. Fan, F.R.; Tian, Z.Q.; Wang, Z.L. Flexible Triboelectric Generator. *Nano Energy* **2012**, *1*, 328–334. [CrossRef]
3. Gao, Q.; Cheng, T.; Wang, Z.L. Triboelectric Mechanical Sensors—Progress and Prospects. *Extrem. Mech. Lett.* **2021**, *42*, 101100. [CrossRef]
4. Wang, Z.L. On the First Principle Theory of Nanogenerators from Maxwell's Equations. *Nano Energy* **2020**, *68*, 104272. [CrossRef]
5. Wang, Z.L. Triboelectric Nanogenerators as New Energy Technology for Self-Powered Systems and as Active Mechanical and Chemical Sensors. *ACS Nano* **2013**, *7*, 9533–9557. [CrossRef]
6. Zou, H.; Guo, L.; Xue, H.; Zhang, Y.; Shen, X.; Liu, X.; Wang, P.; He, X.; Dai, G.; Jiang, P.; et al. Quantifying and Understanding the Triboelectric Series of Inorganic Non-Metallic Materials. *Nat. Commun.* **2020**, *11*, 2093. [CrossRef] [PubMed]
7. Wang, Z.L.; Wang, A.C. On the Origin of Contact-Electrification. *Mater. Today* **2019**, *30*, 34–51. [CrossRef]
8. Wang, Z.L. On Maxwell's Displacement Current for Energy and Sensors: The Origin of Nanogenerators. *Mater. Today* **2017**, *20*, 74–82. [CrossRef]
9. Wang, Z.L.; Jiang, T.; Xu, L. Toward the Blue Energy Dream by Triboelectric Nanogenerator Networks. *Nano Energy* **2017**, *39*, 9–23. [CrossRef]
10. Wang, Z.L. On the Expanded Maxwell's Equations for Moving Charged Media System—General Theory, Mathematical Solutions and Applications in TENG. *Mater. Today* **2022**, *52*, 348–363. [CrossRef]

11. Wang, H.; Wang, J.; Yao, K.; Fu, J.; Xia, X.; Zhang, R.; Li, J.; Xu, G.; Wang, L.; Yang, J.; et al. A Paradigm Shift Fully Self-Powered Long-Distance Wireless Sensing Solution Enabled by Discharge-Induced Displacement Current. *Sci. Adv.* **2021**, *7*, eabi6751. [CrossRef]
12. Wang, H.; Fu, J.; Wang, J.; Su, L.; Zi, Y. Tribophotonics: An Emerging Self-Powered Wireless Solution toward Smart City. *Nano Energy* **2022**, *97*, 107196. [CrossRef]
13. Wang, Z.L.; Lin, L.; Chen, J.; Niu, S.; Zi, Y. *Triboelectric Nanogenerators*; Green Energy and Technology; Springer International Publishing: Cham, Switzerland, 2016. [CrossRef]
14. Tang, W.; Chen, B.D.; Wang, Z.L. Recent Progress in Power Generation from Water/Liquid Droplet Interaction with Solid Surfaces. *Adv. Funct. Mater.* **2019**, *29*, 1901069. [CrossRef]
15. Nguyen, Q.T.; Ahn, K.K.K. Fluid-Based Triboelectric Nanogenerators: A Review of Current Status and Applications. *Int. J. Precis. Eng. Manuf.—Green Technol.* **2021**, *8*, 1043–1060. [CrossRef]
16. Wang, Z.; An, J.; Nie, J.; Luo, J.; Shao, J.; Jiang, T.; Chen, B.; Tang, W.; Wang, Z.L. A Self-Powered Angle Sensor at Nanoradian-Resolution for Robotic Arms and Personalized Medicare. *Adv. Mater.* **2020**, *32*, 2001466. [CrossRef]
17. Li, C.; Liu, D.; Xu, C.; Wang, Z.; Shu, S.; Sun, Z.; Tang, W.; Wang, Z.L. Sensing of Joint and Spinal Bending or Stretching via a Retractable and Wearable Badge Reel. *Nat. Commun.* **2021**, *12*, 2950. [CrossRef]
18. Wang, J.; Ding, W.; Pan, L.; Wu, C.; Yu, H.; Yang, L.; Liao, R.; Wang, Z.L. Self-Powered Wind Sensor System for Detecting Wind Speed and Direction Based on a Triboelectric Nanogenerator. *ACS Nano* **2018**, *12*, 3954–3963. [CrossRef]
19. Zhang, B.; Zhang, S.; Li, W.; Gao, Q.; Zhao, D.; Wang, Z.L.; Cheng, T. Self-Powered Sensing for Smart Agriculture by Electromagnetic-Triboelectric Hybrid Generator. *ACS Nano* **2021**, *15*, 20278–20286. [CrossRef]
20. Han, Q.; Ding, Z.; Sun, W.; Xu, X.; Chu, F. Hybrid Triboelectric-Electromagnetic Generator for Self-Powered Wind Speed and Direction Detection. *Sustain. Energy Technol. Assess.* **2020**, *39*, 100717. [CrossRef]
21. Zhang, Q.; Li, L.; Wang, T.; Jiang, Y.; Tian, Y.; Jin, T.; Yue, T.; Lee, C. Self-Sustainable Flow-Velocity Detection via Electromagnetic/Triboelectric Hybrid Generator Aiming at IoT-Based Environment Monitoring. *Nano Energy* **2021**, *90*, 106501. [CrossRef]
22. Chen, J.; Tang, W.; Han, K.; Xu, L.; Chen, B.; Jiang, T.; Wang, Z.L. Bladeless-Turbine-Based Triboelectric Nanogenerator for Fluid Energy Harvesting and Self-Powered Fluid Gauge. *Adv. Mater. Technol.* **2019**, *4*, 1800560. [CrossRef]
23. Fan, X.; He, J.; Mu, J.; Qian, J.; Zhang, N.; Yang, C.; Hou, X.; Geng, W.; Wang, X.; Chou, X. Triboelectric-Electromagnetic Hybrid Nanogenerator Driven by Wind for Self-Powered Wireless Transmission in Internet of Things and Self-Powered Wind Speed Sensor. *Nano Energy* **2020**, *68*, 104319. [CrossRef]
24. Wang, P.; Pan, L.; Wang, J.; Xu, M.; Dai, G.; Zou, H.; Dong, K.; Wang, Z.L. An Ultra-Low-Friction Triboelectric-Electromagnetic Hybrid Nanogenerator for Rotation Energy Harvesting and Self-Powered Wind Speed Sensor. *ACS Nano* **2018**, *12*, 9433–9440. [CrossRef]
25. Luo, Y.; Chen, P.; Cao, L.N.Y.; Xu, Z.; Wu, Y.; He, G.; Jiang, T.; Wang, Z.L. Durability Improvement of Breeze-Driven Triboelectric-Electromagnetic Hybrid Nanogenerator by a Travel-Controlled Approach. *Adv. Funct. Mater.* **2022**, 2205710. [CrossRef]
26. Zou, H.X.; Zhao, L.C.; Wang, Q.; Gao, Q.H.; Yan, G.; Wei, K.X.; Zhang, W.M. A Self-Regulation Strategy for Triboelectric Nanogenerator and Self-Powered Wind-Speed Sensor. *Nano Energy* **2022**, *95*, 106990. [CrossRef]
27. Lu, S.; Gao, L.; Chen, X.; Tong, D.; Lei, W.; Yuan, P.; Mu, X.; Yu, H. Simultaneous Energy Harvesting and Signal Sensing from a Single Triboelectric Nanogenerator for Intelligent Self-Powered Wireless Sensing Systems. *Nano Energy* **2020**, *75*, 104813. [CrossRef]
28. Ye, C.; Dong, K.; An, J.; Yi, J.; Peng, X.; Ning, C.; Wang, Z.L. A Triboelectric-Electromagnetic Hybrid Nanogenerator with Broadband Working Range for Wind Energy Harvesting and a Self-Powered Wind Speed Sensor. *ACS Energy Lett.* **2021**, *6*, 1443–1452. [CrossRef]
29. Ma, P.; Zhu, H.; Lu, H.; Zeng, Y.; Zheng, N.; Wang, Z.L.; Cao, X. Design of Biodegradable Wheat-Straw Based Triboelectric Nanogenerator as Self-Powered Sensor for Wind Detection. *Nano Energy* **2021**, *86*, 106032. [CrossRef]
30. He, L.; Zhang, C.; Zhang, B.; Yang, O.; Yuan, W.; Zhou, L.; Zhao, Z.; Wu, Z.; Wang, J.; Wang, Z.L. A Dual-Mode Triboelectric Nanogenerator for Wind Energy Harvesting and Self-Powered Wind Speed Monitoring. *ACS Nano* **2022**, *16*, 6244–6254. [CrossRef]
31. Yang, Y.; Zhu, G.; Zhang, H.; Chen, J.; Zhong, X.; Lin, Z.H.; Su, Y.; Bai, P.; Wen, X.; Wang, Z.L. Triboelectric Nanogenerator for Harvesting Wind Energy and as Self-Powered Wind Vector Sensor System. *ACS Nano* **2013**, *7*, 9461–9468. [CrossRef] [PubMed]
32. Perez, M.; Boisseau, S.; Gasnier, P.; Willemin, J.; Reboud, J.L. An Electret-Based Aeroelastic Flutter Energy Harvester. *Smart Mater. Struct.* **2015**, *24*, 035004. [CrossRef]
33. Zhang, J.; Childress, S.; Libchaber, A.; Shelley, M. Flexible Filaments in a Flowing Soap Film as a Model for One-Dimensional Flags in a Two-Dimensional Wind. *Nature* **2000**, *408*, 835–839. [CrossRef] [PubMed]
34. Chen, Y.; Mu, X.; Wang, T.; Ren, W.; Yang, Y.; Wang, Z.L.; Sun, C.; Gu, A.Y. Flutter Phenomenon in Flow Driven Energy Harvester-A Unified Theoretical Model for "Stiff" and "Flexible" Materials. *Sci. Rep.* **2016**, *6*, 35180. [CrossRef] [PubMed]
35. Xu, M.; Wang, Y.C.; Zhang, S.L.; Ding, W.; Cheng, J.; He, X.; Zhang, P.; Wang, Z.; Pan, X.; Wang, Z.L. An Aeroelastic Flutter Based Triboelectric Nanogenerator as a Self-Powered Active Wind Speed Sensor in Harsh Environment. *Extrem. Mech. Lett.* **2017**, *15*, 122–129. [CrossRef]
36. Olsen, M.; Zhang, R.; Örtegren, J.; Andersson, H.; Yang, Y.; Olin, H. Frequency and Voltage Response of a Wind-Driven Fluttering Triboelectric Nanogenerator. *Sci. Rep.* **2019**, *9*, 5543. [CrossRef]

37. Bae, J.; Lee, J.; Kim, S.; Ha, J.; Lee, B.-S.; Park, Y.; Choong, C.; Kim, J.-B.; Wang, Z.L.; Kim, H.-Y.; et al. Flutter-Driven Triboelectrification for Harvesting Wind Energy. *Nat. Commun.* **2014**, *5*, 4929. [CrossRef]
38. Wang, S.; Mu, X.; Yang, Y.; Sun, C.; Gu, A.Y.; Wang, Z.L. Flow-Driven Triboelectric Generator for Directly Powering a Wireless Sensor Node. *Adv. Mater.* **2015**, *27*, 240–248. [CrossRef]
39. Wang, S.; Mu, X.; Wang, X.; Gu, A.Y.; Wang, Z.L.; Yang, Y.; Al, W.E.T. Elasto-Aerodynamics-Driven Triboelectric Nanogenerator for Scavenging Air-Flow Energy. *ACS Nano* **2015**, *9*, 9554–9563. [CrossRef]
40. Ravichandran, A.N.; Calmes, C.; Serres, J.R.; Ramuz, M.; Blayac, S. Compact and High Performance Wind Actuated Venturi Triboelectric Energy Harvester. *Nano Energy* **2019**, *62*, 449–457. [CrossRef]
41. Liu, Y.; Liu, J.; Che, L. A High Sensitivity Self-Powered Wind Speed Sensor Based on Triboelectric Nanogenerators (Tengs). *Sensors* **2021**, *21*, 2951. [CrossRef]
42. Munson, B.R.; Okiishi, T.H.; Huebsch, W.W.; Rothmayer, A.P. *Fundamentals of Fluid Mechanics*, 7th ed.; John Wiley & Sons, Inc.: Hoboken, NJ, USA, 2013.
43. Xu, Q.; Lu, Y.; Zhao, S.; Hu, N.; Jiang, Y.; Li, H.; Wang, Y.; Gao, H.; Li, Y.; Yuan, M.; et al. A Wind Vector Detecting System Based on Triboelectric and Photoelectric Sensors for Simultaneously Monitoring Wind Speed and Direction. *Nano Energy* **2021**, *89*, 106382. [CrossRef]
44. Wang, Y.; Yang, E.; Chen, T.; Wang, J.; Hu, Z.; Mi, J.; Pan, X.; Xu, M. A Novel Humidity Resisting and Wind Direction Adapting Flag-Type Triboelectric Nanogenerator for Wind Energy Harvesting and Speed Sensing. *Nano Energy* **2020**, *78*, 105279. [CrossRef]
45. Zhang, X.; Hu, J.; Yang, Q.; Yang, H.; Yang, H.; Li, Q.; Li, X.; Hu, C.; Xi, Y.; Wang, Z.L. Harvesting Multidirectional Breeze Energy and Self-Powered Intelligent Fire Detection Systems Based on Triboelectric Nanogenerator and Fluid-Dynamic Modeling. *Adv. Funct. Mater.* **2021**, *31*, 2106527. [CrossRef]
46. Wang, Y.; Wang, J.; Xiao, X.; Wang, S.; Kien, P.T.; Dong, J.; Mi, J.; Pan, X.; Wang, H.; Xu, M. Multi-Functional Wind Barrier Based on Triboelectric Nanogenerator for Power Generation, Self-Powered Wind Speed Sensing and Highly Efficient Windshield. *Nano Energy* **2020**, *73*, 104736. [CrossRef]
47. Roh, H.; Kim, I.; Kim, D. Ultrathin Unified Harvesting Module Capable of Generating Electrical Energy during Rainy, Windy, and Sunny Conditions. *Nano Energy* **2020**, *70*, 104515. [CrossRef]
48. Zhao, Z.; Pu, X.; Du, C.; Li, L.; Jiang, C.; Hu, W.; Wang, Z.L. Freestanding Flag-Type Triboelectric Nanogenerator for Harvesting High-Altitude Wind Energy from Arbitrary Directions. *ACS Nano* **2016**, *10*, 1780–1787. [CrossRef]
49. Wang, J.; Liu, P.; Meng, C.; Kwok, H.S.; Zi, Y. Tribo-Induced Smart Reflector for Ultrasensitive Self-Powered Wireless Sensing of Air Flow. *ACS Appl. Mater. Interfaces* **2021**, *13*, 21450–21458. [CrossRef]
50. Zaw, N.Y.W.; Roh, H.; Kim, I.; Goh, T.S.; Kim, D. Omnidirectional Triboelectric Nanogenerator Operated by Weak Wind towards a Self-Powered Anemoscope. *Micromachines* **2020**, *11*, 414. [CrossRef]
51. Li, X.; Li, Y.; Zhang, M.; Yang, Z.; Wang, K.; Huang, C. Carbon Nano Thorn Arrays Based Water/Cold Resisted Nanogenerator for Wind Energy Harvesting and Speed Sensing. *Nano Energy* **2021**, *90*, 106571. [CrossRef]
52. Villarini, G.; Mandapaka, P.V.; Krajewski, W.F.; Moore, R.J. Rainfall and Sampling Uncertainties: A Rain Gauge Perspective. *J. Geophys. Res. Atmos.* **2008**, *113*, 1–12. [CrossRef]
53. Hu, Y.; Zhou, J.; Li, J.; Ma, J.; Hu, Y.; Lu, F.; He, X.; Wen, J.; Cheng, T. Tipping-Bucket Self-Powered Rain Gauge Based on Triboelectric Nanogenerators for Rainfall Measurement. *Nano Energy* **2022**, *98*, 107234. [CrossRef]
54. Zhan, F.; Wang, A.C.; Xu, L.; Lin, S.; Shao, J.; Chen, X.; Wang, Z.L. Electron Transfer as a Liquid Droplet Contacting a Polymer Surface. *ACS Nano* **2020**, *14*, 17565–17573. [CrossRef] [PubMed]
55. Lin, S.; Chen, X.; Wang, Z.L. Contact Electrification at the Liquid-Solid Interface. *Chem. Rev.* **2021**, *122*, 5209–5232. [CrossRef] [PubMed]
56. Xu, C.; Fu, X.; Li, C.; Liu, G.; Gao, Y.; Qi, Y.; Bu, T.; Chen, Y.; Wang, Z.L.; Zhang, C. Raindrop Energy-Powered Autonomous Wireless Hyetometer Based on Liquid–Solid Contact Electrification. *Microsyst. Nanoeng.* **2022**, *8*, 30. [CrossRef]
57. Liu, H.; Dong, J.; Zhou, H.; Yang, X.; Xu, C.; Yao, Y.; Zhou, G.; Zhang, S.; Song, Q. Real-Time Acid Rain Sensor Based on a Triboelectric Nanogenerator Made of a PTFE-PDMS Composite Film. *ACS Appl. Electron. Mater.* **2021**, *3*, 4162–4171. [CrossRef]
58. Wang, W.; Wu, Y.; Chang, Z.; Chen, F.; Wang, H.; Gu, G.; Zheng, H.; Cheng, G.; Wang, Z.L. Self-Powered Intelligent Water Meter for Electrostatic Scale Preventing, Rust Protection, and Flow Sensor in a Solar Heater System. *ACS Appl. Mater. Interfaces* **2019**, *11*, 6396–6403. [CrossRef]
59. He, S.; Wang, Z.; Zhang, X.; Yuan, Z.; Sun, Y.; Cheng, T.; Wang, Z.L. Self-Powered Sensing for Non-Full Pipe Fluidic Flow Based on Triboelectric Nanogenerators. *ACS Appl. Mater. Interfaces* **2022**, *14*, 2825–2832. [CrossRef]
60. Song, Z.; Zhang, X.; Wang, Z.; Ren, T.; Long, W.; Cheng, T.; Wang, Z.L. Nonintrusion Monitoring of Droplet Motion State via Liquid-Solid Contact Electrification. *ACS Nano* **2021**, *15*, 18557–18565. [CrossRef] [PubMed]
61. Zhang, X.; Zheng, Y.; Wang, D.; Zhou, F. Solid-Liquid Triboelectrification in Smart U-Tube for Multifunctional Sensors. *Nano Energy* **2017**, *40*, 95–106. [CrossRef]
62. Cui, X.; Zhang, H.; Cao, S.; Yuan, Z.; Ding, J.; Sang, S. Tube-Based Triboelectric Nanogenerator for Self-Powered Detecting Blockage and Monitoring Air Pressure. *Nano Energy* **2018**, *52*, 71–77. [CrossRef]
63. Fu, X.P.; Bu, T.Z.; Xi, F.B.; Cheng, T.H.; Zhang, C.; Wang, Z.L. Embedded Triboelectric Active Sensors for Real-Time Pneumatic Monitoring. *ACS Appl. Mater. Interfaces* **2017**, *9*, 32352–32358. [CrossRef] [PubMed]

64. Ranjan, M.; Dhaniyala, S. Theory and Design of a New Miniature Electrical-Mobility Aerosol Spectrometer. *J. Aerosol Sci.* **2007**, *38*, 950–963. [CrossRef]
65. Cao, L.N.Y.; Pui, D.Y.H. A Novel Weighted Sum Method to Measure Particle Geometric Surface Area in Real-Time. *J. Aerosol Sci.* **2018**, *117*, 11–23. [CrossRef]
66. Wang, Z.; Yu, Y.; Wang, Y.; Lu, X.; Cheng, T.; Bao, G.; Wang, Z.L. Magnetic Flap-Type Difunctional Sensor for Detecting Pneumatic Flow and Liquid Level Based on Triboelectric Nanogenerator. *ACS Nano* **2020**, *14*, 5981–5987. [CrossRef]
67. Guo, H.; Pu, X.; Chen, J.; Meng, Y.; Yeh, M.H.; Liu, G.; Tang, Q.; Chen, B.; Liu, D.; Qi, S.; et al. A Highly Sensitive, Self-Powered Triboelectric Auditory Sensor for Social Robotics and Hearing AIDS. *Sci. Robot.* **2018**, *3*, eaat2516. [CrossRef]
68. Arora, N.; Zhang, S.L.; Shahmiri, F.; Osorio, D.; Wang, Y.-C.; Gupta, M.; Wang, Z.; Starner, T.; Wang, Z.L.; Abowd, G.D. SATURN: A Thin and Flexible Self-Powered Microphone Leveraging Triboelectric Nanogenerator. *Proc. ACM Interact. Mob. Wearable Ubiquitous Technol.* **2018**, *2*, 1–28. [CrossRef]
69. Chen, C.; Wen, Z.; Shi, J.; Jian, X.; Li, P.; Yeow, J.T.W.; Sun, X. Micro Triboelectric Ultrasonic Device for Acoustic Energy Transfer and Signal Communication. *Nat. Commun.* **2020**, *11*, 4143. [CrossRef]
70. Yu, A.; Song, M.; Zhang, Y.; Zhang, Y.; Chen, L.; Zhai, J.; Wang, Z.L. Self-Powered Acoustic Source Locator in Underwater Environment Based on Organic Film Triboelectric Nanogenerator. *Nano Res.* **2015**, *8*, 765–773. [CrossRef]
71. An, J.; Chen, P.; Wang, Z.; Berbille, A.; Pang, H.; Jiang, Y.; Jiang, T.; Wang, Z.L. Biomimetic Hairy Whiskers for Robotic Skin Tactility. *Adv. Mater.* **2021**, *33*, 2101891. [CrossRef]
72. Wang, S.; Xu, P.; Wang, X.; Zheng, J.; Liu, X.; Liu, J.; Chen, T.; Wang, H.; Xie, G.; Tao, J.; et al. Underwater Bionic Whisker Sensor Based on Triboelectric Nanogenerator for Passive Vortex Perception. *Nano Energy* **2022**, *97*, 107210. [CrossRef]
73. Xu, M.; Wang, S.; Zhang, S.L.; Ding, W.; Kien, P.T.; Wang, C.; Li, Z.; Pan, X.; Wang, Z.L. A Highly-Sensitive Wave Sensor Based on Liquid-Solid Interfacing Triboelectric Nanogenerator for Smart Marine Equipment. *Nano Energy* **2019**, *57*, 574–580. [CrossRef]
74. Wang, X.; Xu, P.; Liu, J.; Wang, T.; Wang, S.; Guan, T.; Liu, X.; Chen, T.; Zheng, J.; Tao, J.; et al. Bio-Inspired Coral-like Sensor Aiming at Ocean Wave Monitoring. In Proceedings of the 2021 China Automation Congress (CAC), Beijing, China, 22–24 October 2021; pp. 908–912. [CrossRef]
75. Zhang, C.; Liu, L.; Zhou, L.; Yin, X.; Wei, X.; Hu, Y.; Liu, Y.; Chen, S.; Wang, J.; Wang, Z.L. Self-Powered Sensor for Quantifying Ocean Surface Water Waves Based on Triboelectric Nanogenerator. *ACS Nano* **2020**, *14*, 7092–7100. [CrossRef] [PubMed]
76. Xu, Y.; Yang, W.; Lu, X.; Yang, Y.; Li, J.; Wen, J.; Cheng, T.; Wang, Z.L. Triboelectric Nanogenerator for Ocean Wave Graded Energy Harvesting and Condition Monitoring. *ACS Nano* **2021**, *15*, 16368–16375. [CrossRef] [PubMed]
77. Chen, B.D.; Tang, W.; He, C.; Deng, C.R.; Yang, L.J.; Zhu, L.P.; Chen, J.; Shao, J.J.; Liu, L.; Wang, Z.L. Water Wave Energy Harvesting and Self-Powered Liquid-Surface Fluctuation Sensing Based on Bionic-Jellyfish Triboelectric Nanogenerator. *Mater. Today* **2018**, *21*, 88–97. [CrossRef]
78. Bhatta, T.; Maharjan, P.; Shrestha, K.; Lee, S.; Salauddin, M.; Rahman, M.T.; Rana, S.M.S.; Sharma, S.; Park, C.; Yoon, S.H.; et al. A Hybrid Self-Powered Arbitrary Wave Motion Sensing System for Real-Time Wireless Marine Environment Monitoring Application. *Adv. Energy Mater.* **2022**, *12*, 2102460. [CrossRef]
79. Tandel, R.; Shah, S.; Tripathi, S. A State-of-Art Review on Bladeless Wind Turbine. *J. Phys. Conf. Ser.* **2021**, *1950*, 012058. [CrossRef]
80. Wang, J.; Geng, L.; Ding, L.; Zhu, H.; Yurchenko, D. The State-of-the-Art Review on Energy Harvesting from Flow-Induced Vibrations. *Appl. Energy* **2020**, *267*, 114902. [CrossRef]
81. Gao, S.; Zeng, X.; Zhang, G.; Zhang, J.; Chen, Y.; Feng, S.; Lan, W.; Zhou, J.; Wang, Z.L. Triboelectric–Electromagnetic Hybridized Module for Energy Harvesting of Power Transmission Lines Galloping and Self-Powered Galloping State Monitoring. *Nano Energy* **2022**, *101*, 107530. [CrossRef]
82. Wu, H.; Wang, J.; Wu, Z.; Kang, S.; Wei, X.; Wang, H.; Luo, H.; Yang, L.; Liao, R.; Wang, Z.L. Multi-Parameter Optimized Triboelectric Nanogenerator Based Self-Powered Sensor Network for Broadband Aeolian Vibration Online-Monitoring of Transmission Lines. *Adv. Energy Mater.* **2022**, *12*, 2103654. [CrossRef]
83. Billah, K.Y.; Scanlan, R.H. Resonance, Tacoma Narrows Bridge Failure, and Undergraduate Physics Textbooks. *Am. J. Phys.* **1991**, *59*, 118–124. [CrossRef]
84. Yu, H.; He, X.; Ding, W.; Hu, Y.; Yang, D.; Lu, S.; Wu, C.; Zou, H.; Liu, R.; Lu, C.; et al. A Self-Powered Dynamic Displacement Monitoring System Based on Triboelectric Accelerometer. *Adv. Energy Mater.* **2017**, *7*, 1700565. [CrossRef]
85. Tao, K.; Chen, Z.; Yi, H.; Zhang, R.; Shen, Q.; Wu, J.; Tang, L.; Fan, K.; Fu, Y.; Miao, J.; et al. Hierarchical Honeycomb-Structured Electret/Triboelectric Nanogenerator for Biomechanical and Morphing Wing Energy Harvesting. *Nano-Micro Lett.* **2021**, *13*, 123. [CrossRef] [PubMed]
86. Zhao, H.; Xu, M.; Shu, M.; An, J.; Ding, W.; Liu, X.; Wang, S.; Zhao, C.; Yu, H.; Wang, H.; et al. Underwater Wireless Communication via TENG-Generated Maxwell's Displacement Current. *Nat. Commun.* **2022**, *13*, 3325. [CrossRef] [PubMed]
87. Zhang, C.; Chen, J.; Xuan, W.; Huang, S.; Shi, L.; Cao, Z.; Ye, Z.; Li, Y.; Wang, X.; Dong, S.; et al. Triboelectric Nanogenerator-Enabled Fully Self-Powered Instantaneous Wireless Sensor Systems. *Nano Energy* **2022**, *92*, 106770. [CrossRef]
88. Howell, L.L. Compliant Mechanisms. In *21st Century Kinematics*; McCarthy, J.M., Ed.; Springer: London, UK, 2013; pp. 189–216. [CrossRef]
89. Yang, P.K.; Lin, Z.H.; Pradel, K.C.; Lin, L.; Li, X.; Wen, X.; He, J.H.; Wang, Z.L. Paper-Based Origami Triboelectric Nanogenerators and Self-Powered Pressure Sensors. *ACS Nano* **2015**, *9*, 901–907. [CrossRef]

90. Deng, Z.; Xu, L.; Qin, H.; Li, X.; Duan, J.; Hou, B.; Wang, Z.L. Rationally Structured Triboelectric Nanogenerator Arrays for Harvesting Water Current Energy and Self-Powered Sensing. *Adv. Mater.* **2022**, 2205064. [CrossRef]
91. Vogel, S. *Life in Moving Fluids: The Physical Biology of Flow*; Princeton University Press: Princeton, NJ, USA, 1994. [CrossRef]
92. Vogel, S. *Life's Devices: The Physical World of Animals and Plants*; Princeton University Press: Princeton, NJ, USA, 1988. [CrossRef]
93. Hu, D.L.; Chan, B.; Bush, J.W.M. The Hydrodynamics of Water Strider Locomotion. *Nature* **2003**, *424*, 663–666. [CrossRef]
94. Kim, B.H.; Li, K.; Kim, J.T.; Park, Y.; Jang, H.; Wang, X.; Xie, Z.; Won, S.M.; Yoon, H.J.; Lee, G.; et al. Three-Dimensional Electronic Microfliers Inspired by Wind-Dispersed Seeds. *Nature* **2021**, *597*, 503–510. [CrossRef] [PubMed]
95. Zhang, S.; Chi, M.; Mo, J.; Liu, T.; Liu, Y.; Fu, Q.; Wang, J.; Luo, B.; Qin, Y.; Wang, S.; et al. Bioinspired Asymmetric Amphiphilic Surface for Triboelectric Enhanced Efficient Water Harvesting. *Nat. Commun.* **2022**, *13*, 4168. [CrossRef]
96. Wang, X.; Shi, Y.; Yang, P.; Tao, X.; Li, S.; Lei, R.; Liu, Z.; Wang, Z.L.; Chen, X. Fish-Wearable Data Snooping Platform for Underwater Energy Harvesting and Fish Behavior Monitoring. *Small* **2022**, *18*, 2107232. [CrossRef]
97. Li, W.; Pei, Y.; Zhang, C.; Kottapalli, A.G.P. Bioinspired Designs and Biomimetic Applications of Triboelectric Nanogenerators. *Nano Energy* **2021**, *84*, 105865. [CrossRef]
98. Hanke, W.; Witte, M.; Miersch, L.; Brede, M.; Oeffnet, J.; Michael, M.; Hanke, F.; Leder, A.; Dehnhardt, G. Harbor Seal Vibrissa Morphology Suppresses Vortex-Induced Vibrations. *J. Exp. Biol.* **2010**, *213*, 2665–2672. [CrossRef]
99. Zhang, R.; Lin, L.; Jing, Q.; Wu, W.; Zhang, Y.; Jiao, Z.; Yan, L.; Han, R.P.S.; Wang, Z.L. Nanogenerator as an Active Sensor for Vortex Capture and Ambient Wind-Velocity Detection. *Energy Environ. Sci.* **2012**, *5*, 8528–8533. [CrossRef]
100. Wang, Y.; Liu, X.; Chen, T.; Wang, H.; Zhu, C.; Yu, H.; Song, L.; Pan, X.; Mi, J.; Lee, C.; et al. An Underwater Flag-like Triboelectric Nanogenerator for Harvesting Ocean Current Energy under Extremely Low Velocity Condition. *Nano Energy* **2021**, *90*, 106503. [CrossRef]
101. Wang, Y.; Hu, S.; Xiong, T.; Huang, Y.; Qiu, L. Recent Progress in Aircraft Smart Skin for Structural Health Monitoring. *Struct. Health Monit.* **2021**, *21*, 2453–2480. [CrossRef]
102. Na, X.; Gong, Z.; Dong, Z.; Shen, D.; Zhang, D.; Jiang, Y. Flexible Skin for Flight Parameter Estimation Based on Pressure and Velocity Data Fusion. *Adv. Intell. Syst.* **2022**, *4*, 2100276. [CrossRef]
103. Wille, R.; Fernholz, H. Report on the First European Mechanics Colloquium, on the Coanda Effect. *J. Fluid Mech.* **1965**, *23*, 801–819. [CrossRef]

nanomaterials

MDPI

Review

Recent Progress Regarding Materials and Structures of Triboelectric Nanogenerators for AR and VR

Jinhao Si, Ruiguang Duan, Menglin Zhang and Xiaomin Liu *

School of Physics and Microelectronics, Zhengzhou University, Zhengzhou 450001, China; jinhao_si@163.com (J.S.); ruiguang163@163.com (R.D.); menlinza@126.com (M.Z.)
* Correspondence: liuxmamara@zzu.edu.cn

Abstract: With the continuous advancement in technology, electronic products used in augmented reality (AR) and virtual reality (VR) have gradually entered the public eye. As a result, the power supplies of these electronic devices have attracted more attention from scientists. Compared to traditional power sources, triboelectric nanogenerators (TENGs) are gradually being used for energy harvesting in self-powered sensing technology such as wearable flexible electronics, including AR and VR devices due to their small size, high conversion efficiency, and low energy consumption. As a result, TENGs are the most popular power supplies for AR and VR products. This article first summarizes the working mode and basic theory of TENGs, then reviews the TENG modules used in AR and VR devices, and finally summarizes the material selection and design methods used for TENG preparation. The friction layer of the TENG can be made of a variety of materials such as polymers, metals, and inorganic materials, and among these, polytetrafluoroethylene (PTFE) and polydimethylsiloxane (PDMS) are the most popular materials. To improve TENG performance, the friction layer material must be suitable. Therefore, for different application scenarios, the design methods of the TENG play an important role in its performance, and a reasonable selection of preparation materials and design methods can greatly improve the work efficiency of the TENG. Lastly, we summarize the current research status of nanogenerators, analyze and suggest future application fields, and summarize the main points of material selection.

Keywords: nanomaterials; triboelectric nanogenerator; AR and VR; self-powered sensing

Citation: Si, J.; Duan, R.; Zhang, M.; Liu, X. Recent Progress Regarding Materials and Structures of Triboelectric Nanogenerators for AR and VR. *Nanomaterials* **2022**, *12*, 1385. https://doi.org/10.3390/nano12081385

Academic Editors: Francisco Javier García Ruiz and Antonino Famular

Received: 5 January 2022
Accepted: 15 April 2022
Published: 18 April 2022

1. Introduction

The triboelectricity phenomenon has a history that dates back more than 2000 years. When two objects rub against each other, one object loses electrons, while the other object gains electrons [1]. The basic working principle of a triboelectric nanogenerator (TENG) is to generate charges on a material surface by bringing two different friction materials into contact with each other to generate relative motion. When two different material layers produce relative motion, the two materials have different electron binding abilities, where one material inevitably loses electrons and the other material gains electrons. Therefore, the same number of charges with opposite polarities can be generated on the two material surfaces. According to the different electron binding abilities of the different materials, these materials can be arranged in order from high to low, known as the series of triboelectric materials, which can be used as a reference for material selection [2,3]. Due to the wide variety of triboelectric materials, a suitable pair of triboelectric materials depends not only on their chemical composition but also on their physical properties, such as hardness, toughness, and shape [4]. Therefore, selecting an appropriate pair of triboelectric materials is difficult, and it was not until the advent of the first triboelectric nanogenerator in 2012 that this problem was effectively solved [5]. Currently, the most popular materials include polytetrafluoroethylene (PTFE), polydimethylsiloxane (PDMS), and fluorinated ethylene propylene (FEP). Researchers have conducted applicability studies on various materials

to explore their performance characteristics for different application scenarios, and their TENG applications include tidal energy harvesting [5–9], self-powered sensors [10–12], and wearable flexible electronic devices [13–18]. PTFE is often used to manufacture TENG modules in wearable flexible electronic devices, as PTFE film is non-toxic and has the characteristics of flexibility, transparency, and mechanical stability [19–21]. In addition, PTFE film corona offers a fast charging time with high efficiency, based on the PTFE film preparation of TENG. It also has a generally high energy conversion efficiency, high output voltage, and stable characteristics [22]. PDMS is often used in self-powered, sensing, and flexible electronic devices because of its inherent elasticity and excellent biocompatibility [23–26]. In addition, PDMS films can achieve full contact with skin as they can freely distort and deform, resulting in widespread interest in the material industry [27,28]. When PDMS is embedded with microstructures and various sensitive materials on the surface, the sensor exhibits high sensitivity, good linearity, and strong flexibility. More importantly, the microstructure of the PDMS film can effectively reduce adhesion between materials, thus promoting relative sliding between the friction layers. Therefore, there is an urgent need to use PDMS elastomers as the main body to improve the friction characteristics of the friction layer, and to create TENG with combined excellent flexibility and high output performance [29].

TENG uses the principle of triboelectricity, where the friction between two materials is used to convert mechanical energy into other forms. Compared to traditional power supplies, TENGs can convert scattered and difficult-to-use mechanical energy into electrical energy [30]. Furthermore, these materials have advantages such as low cost, a simple design, convenient carrying, a high conversion rate, and a variety of material choices [31,32]. Due to the rapid development of artificial intelligence, there is an increasing demand for green energy and wearable electronic products. Compared to other forms of green energy, mechanical energy is the most widely distributed energy in the natural environment and daily life, and it is not affected by the external environment [33]. Therefore, determining how to use TENGs to convert mechanical energy into electrical energy and maximize conversion efficiency has received considerable research attention. Moreover, as a result of the rapid development of the Internet of Things industry, human–computer interactions and intelligent perception have gradually entered our daily lives, and human–computer interactions are no longer limited to voice commands [34]. For example, gesture recognition can be used for target control, and gesture recognition has been used in VR and AR with good developmental prospects. Among them, TENG-based AR and VR technology is on the rise (Figure 1). Compared to traditional control methods, some AR and VR applications have allowed users to experience convenient and intelligent operations [35] such as VR glasses [36,37], VR gloves [15,38] and flexible patches. VR gloves can replace the traditional computer mouse and keyboard accessories to achieve a non-contact operating computer interface. Furthermore, through intelligent perception technology, game players can have a more immersive experience.

This article discussed the selection of TENG materials including PTFE, PDMS, and other materials, and analyzed the advantages and disadvantages of the different materials. Subsequently, TENG material structures and designs for AR and VR equipment were introduced, and the applications of AR and VR equipment based on TENG were summarized, including gloves and flexible patches. Furthermore, TENG was used as a self-powered sensor module to realize human–computer interactions between the human and the computer screen, realize the intelligent perception of virtual objects, and achieve control. Finally, this article summarized the developmental status of TENG worldwide and discussed the developmental prospects and challenges of further TENG applications for AR and VR in the future.

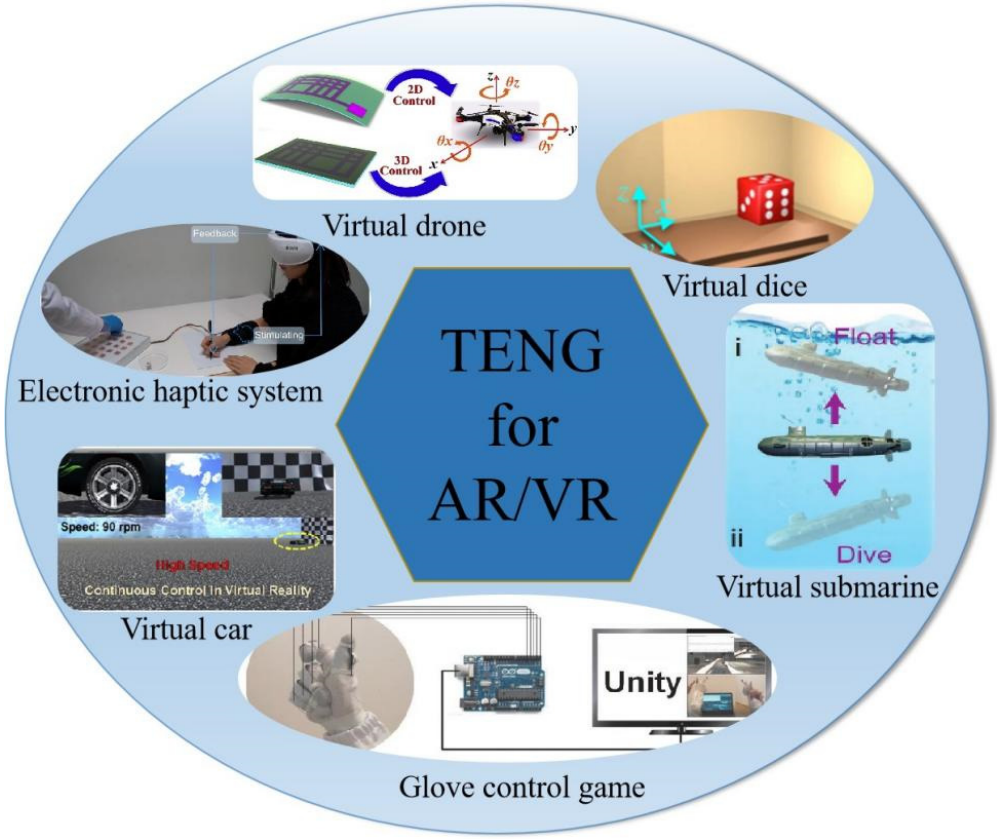

Figure 1. Application of TENG in AR and VR. Reprinted with permission from Ref. [39]. Copyright 2021 Science Advances; Reprinted with permission from Ref. [40]. Copyright 2019 Nano Energy; Reprinted with permission from Ref. [41]. Copyright 2018 Nano Energy; Reprinted with permission from Ref. [34]. Copyright 2021 Advanced Materials Technologies; Reprinted with permission from Ref. [42]. Copyright 2020 Advanced Science; Reprinted with permission from Ref. [43]. Copyright 2020 Nano Energy.

2. The Basic Theory for TENG

The working modes of TENG can be generally divided into three categories: contact-separation mode, sliding mode, and freestanding mode. Each mode can be further divided into single and double electrodes [44], as shown in Figure 2. The contact-separation mode is composed of two types of dielectrics that face each other, which can be divided into positive and negative electrodes. When the two electrodes are in contact, the dielectric surface generates a charge [45]. However, when the two electrodes are separated, a potential difference is generated on the surface of the two dielectrics, and the charge from the positive electrode is transferred to the negative electrode. When the two electrodes come into contact again, the electrons move in opposite directions, and an alternating current is generated through this alternating back-and-forth process [46]. The sliding mode consists of the relative motion of two dielectrics, where the surfaces of the two materials generate charges due to friction; thus, a potential difference forms between the positive and negative electrodes [47–49]. The change in the effective contact area of the two dielectrics during the relative motion causes a potential difference to occur, while periodic changes result in alternating current [50]. Freestanding is based on the natural friction between the friction material and the surrounding air. In this mode, the charge on the triboelectric layer can last a long time; thus, no external drive is required [51,52]. Moreover, the movement of the triboelectric layers is irregular and an asymmetric electric field is formed, generating triboelectric energy between the triboelectric layers. Compared to the first two modes, no direct contact occurs between the freestanding triboelectric layers; thus, wear between

materials is reduced. In the case of the single-electrode configuration, one output terminal is connected to the electrode, and the other output terminal is virtually grounded, and in the double-electrode configuration, both output terminals are connected to the electrode. Among these configurations, the advantages of dual electrodes include higher flexibility and a wider range of motion [53]. For example, when a car is running, the tire and the ground is triboelectrically charged. The tire can be used as an output electrode while the ground acts as another electrode. In this case, a single-electrode mode would be suitable. However, because of the lack of a real reference electrode, the resulting voltage and current may be unstable, while the double-electrode modes do not have such a problem [54,55]. Therefore, choosing the correct electrode configuration for each application is important.

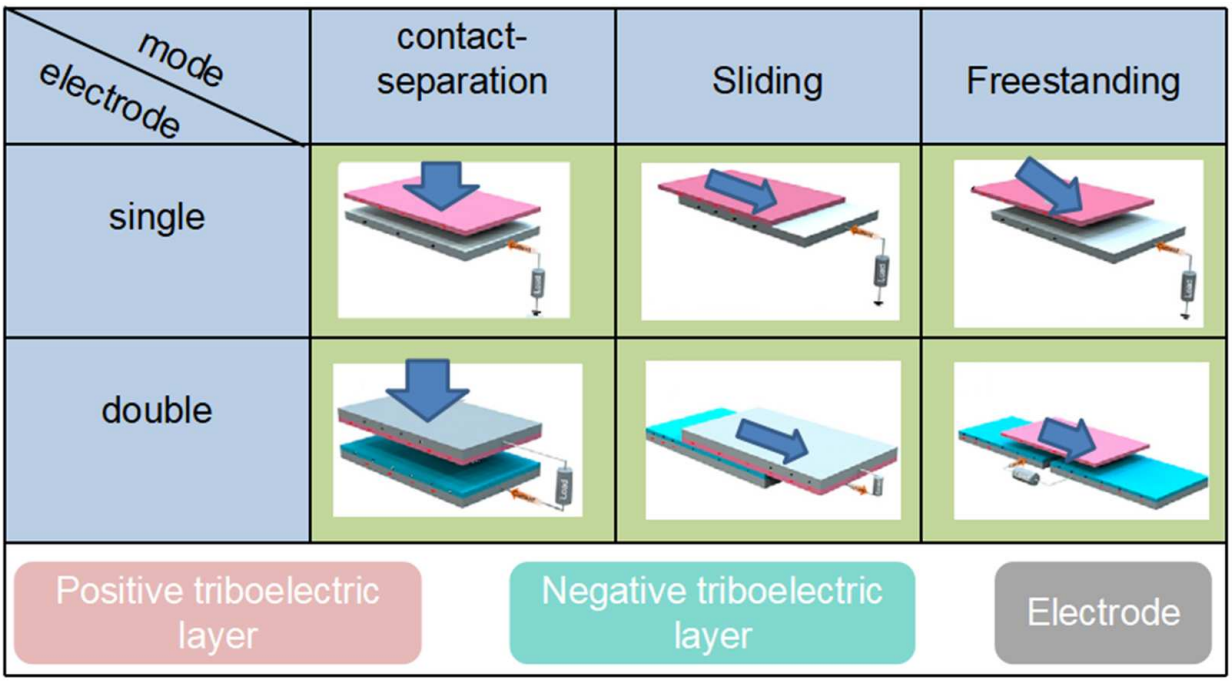

Figure 2. Working modes of TENG.

The charge transfer mechanism in triboelectric electrification has always been a vexing conundrum among scientists. In 2017, Zhonglin Wang et al. proposed a new method to investigate the charge transfer changes of TENGs with temperature [56], and determined why the charges generated in triboelectric electrification were easily retained in the material at room temperature. For the polymers and amorphous materials summarized in this paper, an electron cloud-potential well model proposed by Zhonglin Wang et al. was used to explain the charge transfer mechanism in most polymer materials [57]. As shown in Figure 3, electron clouds were formed by the electrons, which were localized within the atoms and occupied specific atomic orbitals. The atoms were represented by potential wells, whose outer layers were bound by the electrons that formed the atomic electron clouds [58]. As shown in Figure 3a,d the distance between the electron clouds, EA, and EB, consisted of the occupied energy levels of the electrons in the atoms of materials A and B, E1 and E2 were the potential energies required for the electrons to escape from the material surface, and EA and EB were smaller than E1 and E2, respectively. Before the two materials came into contact, electrons could not transfer due to the trapping effect of the potential wells. When material A made contact with material B, the single potential well became a double well potential, and the electrons could move from material A to material B [59], as shown in Figure 3b. When materials A and B were separated, most of the electrons that were transferred to material B were retained due to the potential energy E2 in material B [60], as shown in Figure 3c. Therefore, positively charged material A and the negatively

charged material B exhibited a contact electrification effect. As the temperature increased, the electrons contained more energy, which made it easier to jump out of the potential well and return to the original material, as shown in Figure 3d. This model elucidated why the charge generated by contact electrification remained constant due to the potential barrier of the material.

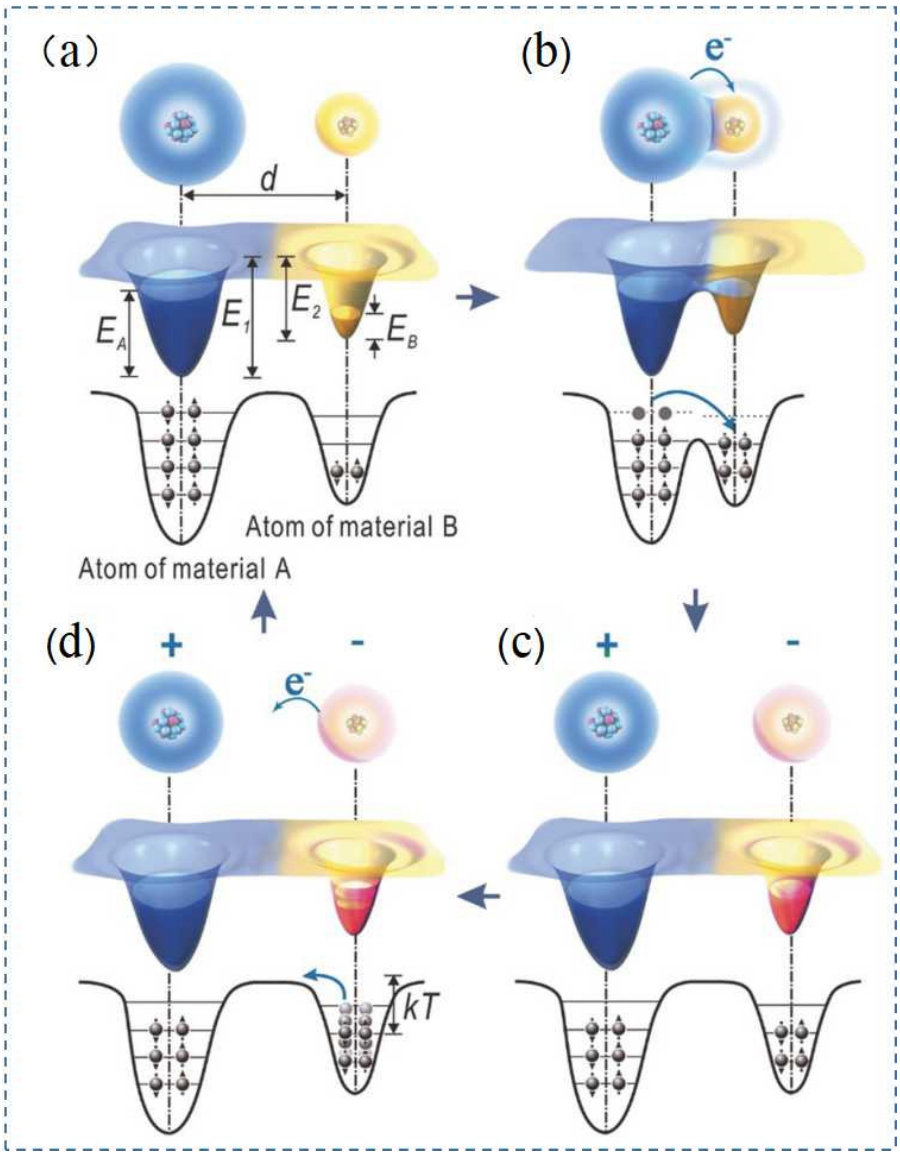

Figure 3. Electron transfer model of TENG. Reprinted with permission from ref. [56]. Copyright 2018 Advanced Materials. (**a**) Material A and material B before contact; (**b**) the two materials in contact; (**c**) the two materials separated; and (**d**) with increasing temperature, electric charges were released by the atoms.

What is worth mentioning is that Wang Zhonglin expanded the most famous Maxwell equations in electrodynamics in 2021 to develop the theoretical framework of nanogenerators [61]. The expanded Maxwell equations include not only all the connotations of the classical Maxwell equations but also the electromagnetic coupling effect resulting from the motion of the charged medium, and the theoretical architecture of the nanogenerator. So far, worldwide attention has been paid to the research of nanogenerators because of their important applications in micro-nano energy, self-driven sensing, blue energy, and artificial intelligence [62,63]. Nanogenerators convert mechanical energy into electrical signals with displacement current as a driving force. In 2017, Wang Zhonglin expanded the expression

of displacement current for the first time to derive the output power of nanogenerators [5]. In 2019, the analytically deduced transport equation of nanogenerators and the analytical solutions to the four modes of TENG given by Wang Zhonglin laid the overall theoretical framework of nanogenerators and formed the theoretical basis for the development of this discipline [61,64].

3. Material Selection for TENG

There are many types of factors that affect TENG performance, and among them, material selection plays a decisive role. This is because the physical and chemical properties of triboelectric materials can directly change TENG performance [1,4]. Several parameters such as power density stability, flexibility, and sustainability must be considered when designing TENG for specific applications [3]. In addition to high frictional electrical properties, there are different requirements for materials depending on the application. Some materials are suitable for energy collection, other materials are suitable for supercapacitors in self-powered sensing systems, while two-dimensional materials have bi-functional properties [1,44]. For example, Vimal Kumar Mariappana et al. discovered a paper-like carbyne material [65], and TENG prepared with this thin film exhibited good power density and energy density. In addition, due to its extensibility and stability, the two-dimensional material could be used to develop self-powered implantable nanodevices repairable by the human body [66]. Minsu Seol et al. studied the triboelectric charge behavior of various two-dimensional materials such as MoS2, WS2, and graphene oxide in the triboelectric series, and determined that the charge transfer efficiency between the tribomaterials had an obvious relationship with the effective work function [31]. In addition, the charge characteristics of the friction material could be modified by chemical doping. Hypothetically, to generate more charges or obtain higher output from TENG, two materials with significantly different charge affinities are preferred. Theoretically, the greater the difference in charge affinity of the two materials, the stronger the output voltage and current of the TENG prepared from the two materials. However, in practice, the two materials with the largest difference in charge affinity are not selected, as triboelectric electrification between the two materials depend not only on their chemical composition but also on other physical properties such as elasticity, friction, and surface topography [67]. The triboelectric effect of the materials is usually represented by the surface charge density of the material. Even for the same material, different triboelectric charging processes result in different surface charge densities. By analyzing the above nanomaterials, studies have shown that many have good triboelectric properties; moreover, the nanomaterials also exhibit good piezoelectric properties. One such example is polylactic acid (PLA). As a biomaterial, PLA has been widely used due to its unique advantages such as biocompatibility, biodegradability, and piezoelectricity [68,69]. The piezoelectric properties of PLA are related to its crystallinity, crystal phase, and temperature, and the piezoelectric constant of PLA is a function of its crystallinity [70–73]. Thus, by determining the piezoelectric constant of nanomaterials, one can compare the piezoelectric or triboelectric properties of materials [74–76].

After reviewing numerous TENG-related articles, we concluded that the following materials were most widely used: PTFE [19,22,77–81], PDMS [29,82–85], FEP [86–88], polyester polyethylene terephthalate (PET) [30,89], and graphene [61,85,86]. Figure 4 presents the preparation and characterization of triboelectric materials such as PTFE and PDMS. The nanostructure on the surface of the PDMS material is clearly visible in Figure 4a, and the TENG prepared from this thin film exhibited high transparency and stable voltage output characteristics, as shown in Figure 4b. Figure 4c,d shows the structure diagrams at different stages during PTFE preparation according to the biaxial stretching method, and finally, a porous PTFE film was prepared. Figure 4e–g shows characterization of the mixed PTFE and PDMS films [81]. The voltage and current variation characteristics of the PDMS films with different PTFE content were analyzed, indicating that the triboelectric properties of the PDMS films could be improved by adding a suitable amount of PTFE to the PDMS films. Figure 4h shows a comparison of the charge affinity among the triboelectric material

family, showing that MOS2 was between PTFE and PDMS. This order also indicated ordering of the triboelectric properties among the individual materials. These materials were also used in the AR and VR products reviewed in this paper. In addition to the above triboelectric materials, cellulosic materials [90] have attracted significant attention due to their high reproducibility and production efficiency [32], and the output power densities of cellulose-based TENG have greatly improved [91]. Currently, altering the chemical properties of engineered polymers is of interest, as the modification method can regulate the ability of the material surfaces to rub against each other and generate electric charges, thereby increasing the power output of the TENG [1]. For example, studies have shown that the hydrophobicity and electrical conductivity of the TENG materials could be changed by a coating process. Furthermore, inorganic triboelectric two-dimensional materials such as MoS2 [92] and WS [93,94] have received attention, and the charge mechanisms of these materials are well known. However, these materials are difficult to prepare due to their physical properties such as large-area single crystal films. Therefore, research on these materials is still limited.

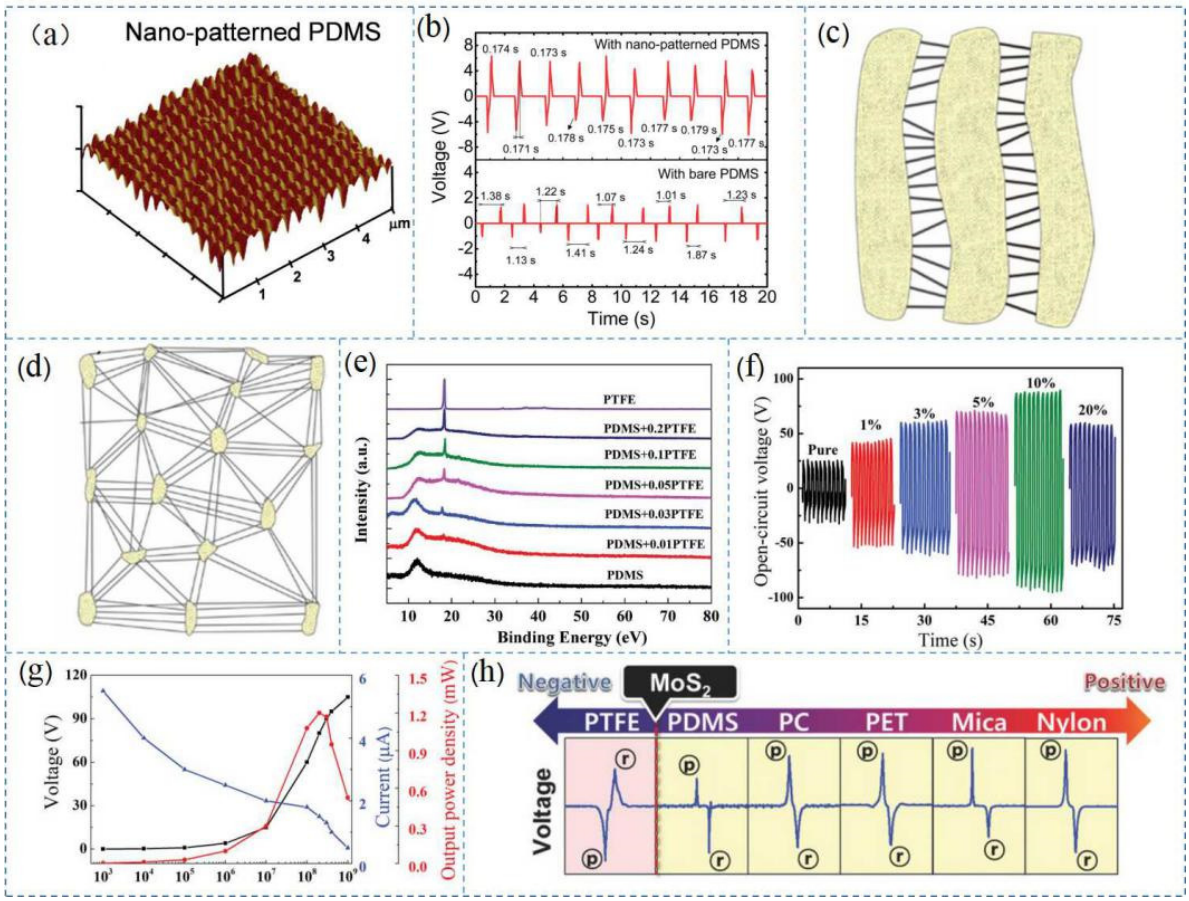

Figure 4. Preparation and characterization of the materials. (**a**) AFM images of PDMS; (**b**) output voltages of the triboelectric nanogenerators based on PDMS. Reprinted with permission from Ref. [95]. Copyright 2014 Royal Society of Chemistry; (**c**,**d**) PTFE structures during preparation. Reprinted with permission from Ref. [96]. Copyright 2018 Journal of Membrane Science; (**e**) XRD patterns of the PDMS-PTFE films; (**f**) output voltages of the PDMS-PTFE films; (**g**) relationship between output performance of the PDMS-PTFE films and the external load. Reprinted with permission from Ref. [81]. Copyright 2019, Advanced Electronic Materials; and (**h**) output voltage of the triboelectric series of materials. Reprinted with permission from Ref. [31]. Copyright 2018 Advanced Materials.

Currently, there are four basic types of triboelectric nanogenerators: single electrode [97], contact separation [98], lateral sliding [99], and independent triboelectric layer [60] modes. Triboelectric materials are placed in vertical contact in the single electrode and contact separation modes, and there are many materials to choose from. Unlike the first two modes, lateral sliding and independent triboelectric layer modes have specific requirements for materials, namely low friction coefficients. If the friction coefficient of the material is high, the relative sliding between the two materials wear away the material. Thus, PTFE and PDMS have been widely used in these two modes due to their low friction coefficients.

4. The Structures of TENG

Over the past two years, nanogenerators have been used more frequently in wearable devices, especially gloves. Figure 5a shows two TENG configurations proposed by Li et al. to meet the requirements for full human-machine interface (HMI) functionality and simplified signal processing capabilities. The TENG was composed of PEDOT (poly(3,4-ethylenedioxythiophene)), which consisted of a PSS (poly(styrene sulfonate)) coating with silicone [100]. PEDOT:PSS was chosen because the material offers many excellent properties such as its physical and chemical properties, which are stable at normal temperature and pressure, and the material exhibits good transparency, good electrical conductivity, easy preparation, strong film-forming abilities, and a low cost. As shown in Figure 5b, Feng et al. proposed a simple coating method for carbon nanotubes (CNTs) [101], achieving super-hydrophobic textiles with improved output performance [102]. The mechanism of the material exhibiting superhydrophobicity while also maintaining excellent triboelectric properties was due to two factors: First, water droplets had difficulty adhering to the surfaces of CNT and TPE materials due to the obstruction of the superhydrophobic interface, which improved its waterproof performance. Second, because the rough structure of the CNT and TPE composite surface increased the actual surface area, the friction force was enhanced and the triboelectric effect became more pronounced. In addition, superhydrophobic textiles can quickly resolve moisture and dry quickly in wet environments. Using this textile solved the problem of the output voltage being susceptible to humidity. As shown in Figure 5c, a flexible single-electrode two-dimensional control patch was produced, which could realize in-plane two-dimensional motion control. The control patch consisted of only three thin layers, namely a PET base layer, a grasping pattern Al electrode layer, and a PTFE friction layer [103]. The working principle of the two-dimensional control patch was based on contact electrification and electrostatic induction between the PTFE and the glove. Due to the different binding abilities to electrons of the two materials, a potential difference was generated between the PTFE friction surface and the glove. Thus, voltage output was generated on the peripheral circuit, which acted as a power source. Figure 5d shows the triboelectric interaction patch with four sensing electrodes, as proposed by Qiongfeng et al. As a flexible multifunctional human-machine interface, it was used to detect various human–machine interactions [66]. This patch was also composed of a PET substrate, an open-loop aluminum electrode (E1~E4), and a PTFE friction layer.

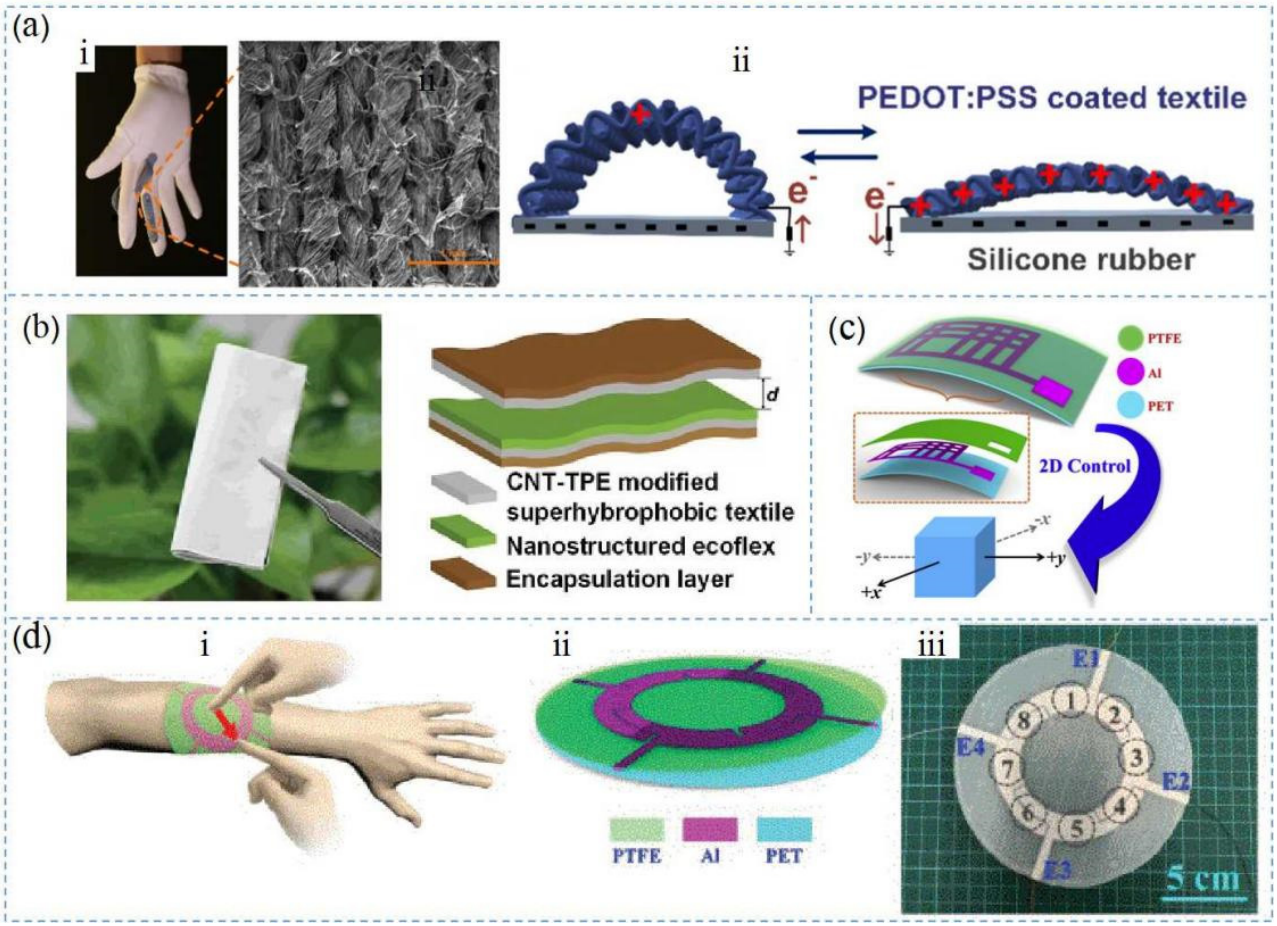

Figure 5. Materials of the wearable TENG: (**a**) material structures of the textiles. Reprinted with permission from ref. [38]. Copyright 2019 Nano Energy; (**b**) material structure of the superhydrophobic textile TENG. Reprinted with permission from ref. [42]. Copyright 2020 Advanced Science; (**c**) material structure of TENG to control a virtual UAV, Reprinted with permission from ref. [40]. Copyright 2019 Nano Energy; (**d**) material structure of triboelectric patch on a human arm. Reprinted with permission from ref. [104]. Copyright 2020 IEEE.

Figure 6a shows a self-powered delta-parallel human–machine interface (DT-HMI), which was proposed by Cheng et al. In the DT-HMI, the friction materials used by the TENG were copper sheets and FEP films. During the initial state, the surface charge of the copper sheet was balanced. When the gear rotated clockwise, the positive charges in the FEP film and copper sheet were offset, causing the negative charges on the copper sheet to repel the ground [105]. When the current flowed from the ground to the copper electrode, the copper electrode generated a negative pulse. However, detaching the copper sheet and the FEP membrane produced a positive current signal. Figure 6b shows a TENG-based three-dimensional control sensor proposed by Tao et al., which was used to detect and control the movement of objects in a three-dimensional (3D) virtual space. This device consisted of two identical non-planar TENG sensing modules [106], and the module was composed of two hemispheres and PTFE film. The PTFE structure was designed with a hemispherical bottom in order to increase the contact area of the friction material, thereby increasing the triboelectric charge density of the TENG. In addition, Zhu et al. developed a continuous DC nanogenerator using one-way charge transport and double-cross TENG, as shown in Figure 6c [107]. The rotating disc was composed of porous cloth and the intermediate material cloth was assembled with an acrylic ring [108,109], while a dielectric pair was connected to the top stator. The dielectric materials consisted of PMMA (poly(methyl methacrylate)) and PVC (polyvinyl chloride), respectively, where

the PMMA dielectric exhibited a positive surface charge upon contact with the cloth, and the PVC dielectric exhibited a negative surface charge on the cloth during operation [110]. Many materials can be used as intermediate materials when arranged in the order of the three frictional polar materials, such as natural rubber and paper. Considering PVC and PMMA, Zhu et al. found that a porous cloth with friction-induced polarity reversal was an ideal intermediate material due to its mechanical strength and flexibility as a friction layer [43]. The experimental results showed that the larger the contact area between the intermediate material and the medium, the better the triboelectric performance, the higher the voltage obtained, and the more charges that were transferred. Therefore, the contact area between the intermediate material and the dielectric material should be increased as much as possible. The PMMA film was located on the left side on one quarter of the disk, and PVC was located on the right side on the other quarter of the disk. Bottom electrodes A and B consisted of wire electrodes placed in the bottom stator, and the wire electrodes were made of cloth coated with nickel metal. This electrode was chosen due to its mechanical properties, as it was flexible and easily integrated into the equipment [111]. Figure 6d shows an electronic system (ET) based on a TENG for a virtual haptic experience, where the different polymer films were made of PTFE, Kapton, PET, and PEN [112]. Regarding the selection of materials for the ET interface, PTFE was selected as a negative triboelectric material because of its good charging performance and low cost after corona polarization. Ion bombardment technology has recently been used to modify capacitor energy storage materials, and experiments showed that this method significantly improved the triboelectric properties of Kapton film [39]. In this study, a similar ion bombardment technology was used to improve and enhance TENG in the ET system. In addition, as shown in our previous work, ion radiation could not be improved due to the weak thermal stability of the PET film [39]. Therefore, in this study, because polyethylene naphthalate (PEN) had high thermal stability, we selected it as an alternative material.

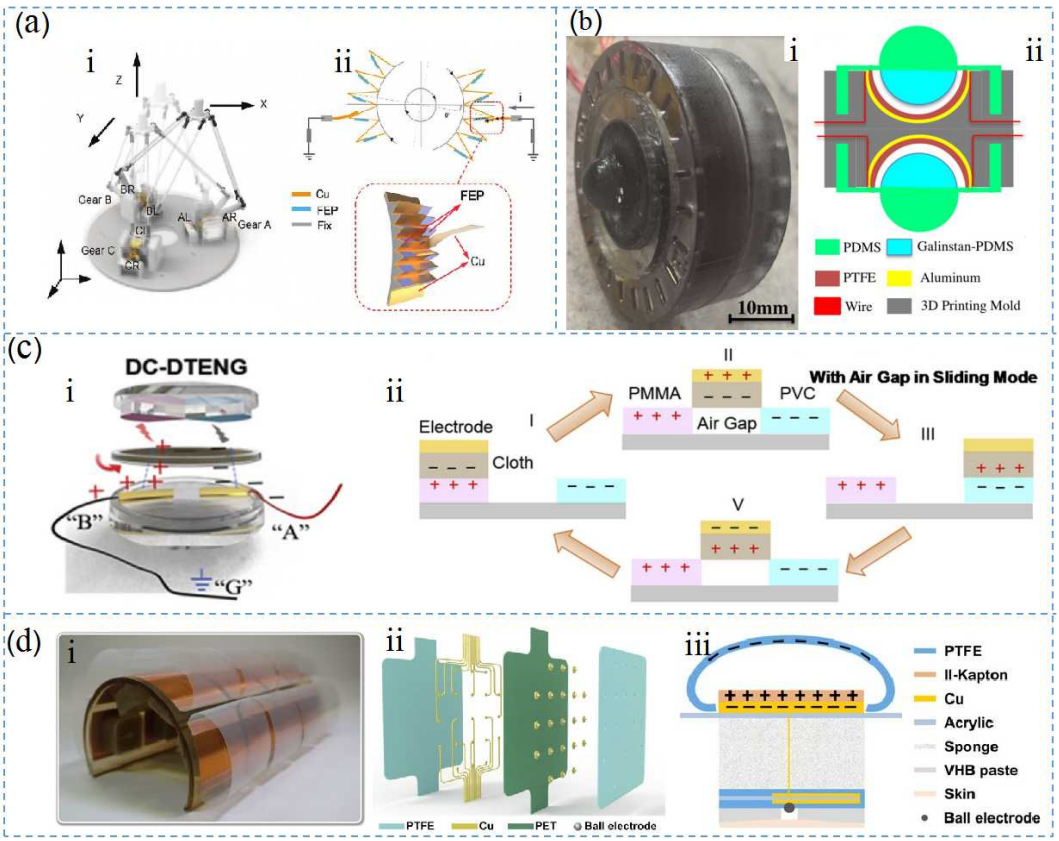

Figure 6. Structure of the VR products: (**a**) TENG fabricated from the FEP film used for mobile platform

control, Reprinted with permission from Ref. [34]. Copyright 2021 Advanced Materials Technologies; (**b**) material structures and physical photos of a self-powered sensor made with PDMS and PTFE, Reprinted with permission from Ref. [41]. Copyright 2018 Nano Energy; (**c**) internal structure diagram and material hierarchy diagram of DC-DTENG, Reprinted with permission from Ref. [43]. Copyright 2020 Nano Energy; (**d**) material structure of an electro-tactile system based on TENG and spherical electrode array formation, Reprinted with permission from Ref. [39]. Copyright 2021 Science Advances.

5. Applications of TENG in AR and VR

Qiongfeng et al. proposed a TENG based on two configurations to realize more HMI functions and make signal processing easier. Each sensor consisted of a PEDOT:PSS-coated textile tape and the gloves were coated with a layer of silicone film (Figure 7a) [113]. This type of HMI was used for unmanned driving technology, and the operation technology was simple and intuitive, as the four sensors were represented by different finger movements. Figure 7b shows the real-time outputs of the sensors when the fingers were bent downward at different angles at the same speed [114]. This HMI could control the car, drive it in different directions, and the running state of the car could be changed according to the finger bending angle and strength of the operator (Figure 7c,d).

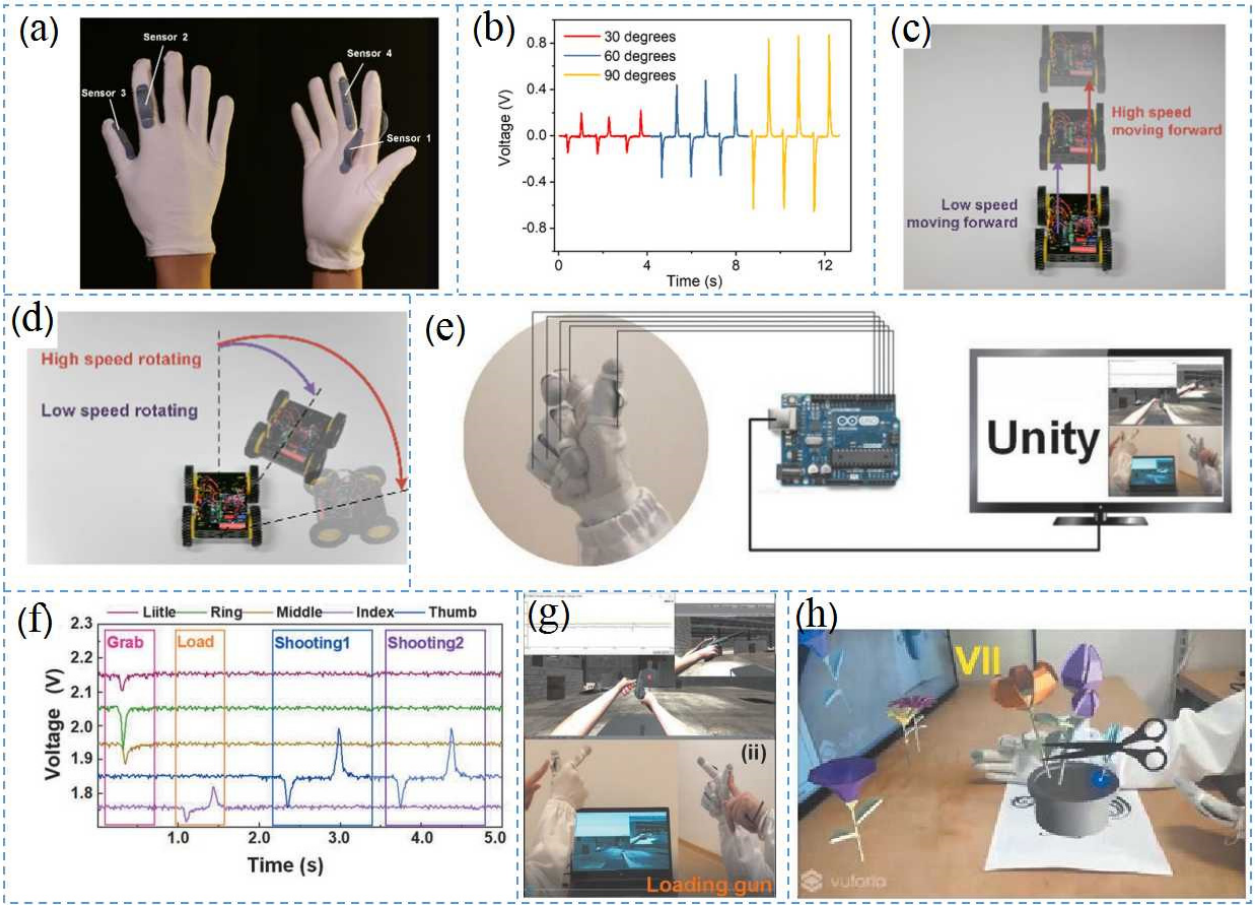

Figure 7. Applications of TENG-based VR gloves: (**a**) self-powered gloves using a PEDOT:PSS coating process; (**b**) voltage output of the sensor when the index finger was bent at different angles; (**c**,**d**) different driving states of wireless vehicles controlled by gloves. Reprinted with permission from Ref. [38]. Copyright 2019 Nano Energy; (**e**) schematic diagram of machine learning glove-controlled gunplay based on self-powered conductive superhydrophobic triboelectric textiles; (**f**) signal modes for fetching, loading, and firing; (**g**) screenshot of gun loading action in Unity VR space; and (**h**) virtual illustration of glove control. Reprinted with permission from Ref. [42]. Copyright 2020 Advanced Science.

To address the issue of human sweat on glove performance, a simple CNT and TPE coating method was proposed by Qiongfeng et al., which is shown in Figure 7e, to achieve superhydrophobic triboelectric textiles with improved performance [115,116]. The super-hydrophobic fabric recovered quickly from high humidity conditions seven times faster than the original fabric, and the triboelectric properties were three times better. Superhydrophobic triboelectric textiles collected biomechanical energy from human activities at four times the power density of the original textiles [117]. In a high humidity environment, superhydrophobic textiles with anti-perspiration properties can monitor human movements without obvious output voltage deterioration. Figure 7g,h shows the applications of superhydrophobic triboelectric gloves in an AR space. Figure 7g shows the control of firearms in a 3D shooting game, where each sensor on the glove was connected to a single-chip microcomputer and controlled through a serial port. Python was used for real-time processing and analysis, and the commands were sent to Unity. The shooter controls included "grab the gun", "reload", and "shoot", which were achieved through three different signal modes. First, the user bent their fingers so that the super-hydrophobic textile was in full contact with the ecoflex, and the characters in Unity responded to this command and grabbed the gun. In the second stage, the user pressed the sensor button to trigger the refill command, and the index finger was bent for the shooting command. The flower arrangements shown in Figure 7h were based on a variety of gestures such as "water", "spin", "light", "pick", "trim", and "stop". After training in deep learning model, the average accuracy for gesture recognition reached 96.75% [118].

Zixuan et al. proposed a triboelectric interaction patch with only four sensing electrodes for a flexible multifunctional human–machine interface to detect various action signals, allowing the user to set an operating area in advance to control the input and output relationship of the four electrodes to achieve position detection (Figure 8a) [119]. The triboelectric patch exhibited accurate sensing ability and could adapt to finger tapping, sliding, and other common finger movements. The TENG was operated by sliding fingers on the eight defined points shown in Figure 8b,c. Using the ratio of each voltage, the position perception performance of these eight points in the two scenarios could be identified. Thus, the triboelectric patch could be used for UAV control, and the output signal and corresponding UAV movements are shown in Figure 8d [120].

To further improve the practicality of the equipment and achieve a minimalist control interface, Qiongfeng et al. developed a control patch with a single electrode to control a UAV in a virtual space and demonstrated the 3D control capabilities of the equipment (Figure 8e). The control system consisted of a 3D control patch, which was used to generate the dual-channel control signals [121], a processing circuit, and an MCU used to calculate the number of dual-channel output peak values. After receiving the control commands, the computer generated the corresponding actions for the UAV. Figure 8e shows the two-channel signals and six degrees of freedom obtained after the 3D control patch was processed by the circuit.

Figure 9a shows a new self-powered DT-HMI which was combined with the output signal from a TENG sensor, achieving 2/3D control for VR and AR interactions, robotics, and other applications. The DT-HMI consisted of three parallel branches connected between the movable platform and the fixed base, where each branch consisted of a drive bar and a passive bar. At the end of the drive lever, there were three sensitive gears (A, B, and C), each with two TENGs for clockwise and counterclockwise angle identification. Since each gear had two TENGs, there was a total of six TENGs for three gears. The electrical signals of the six TENGs produced different peaks in different operating modes (Figure 9b). Figure 9c shows an application that controlled the movement of a virtual submarine through a mobile platform. By identifying the digital status signals from the six TENG outputs, different operation commands of the submarine in different states such as diving, floating, forward and backward movement, and movement relative to the moving platform were defined. For 3D operation of the submarine model floating and diving, the mobile platform would move upward or downward, triggering the entire left side TENG sensing of the gears or the entire

right side TENG sensing of the gears. Similarly, moving in different directions through gear commands with different control codes achieved different motion states of the submarines in the water. As shown in Figure 9d [122], DT-HMI was used for AR liver resection in virtual minimally invasive surgery, and the camera was used for a plane image recognition control script, which mainly consisted of a scalpel, pliers, liver resection, and instrument switching. The TENG sensor gear was mainly used for instrument operation, and the AR output signal represented the movement states. Although the procedure above demonstrated a simple operation, it still showed the value of the TENG for surgical applications.

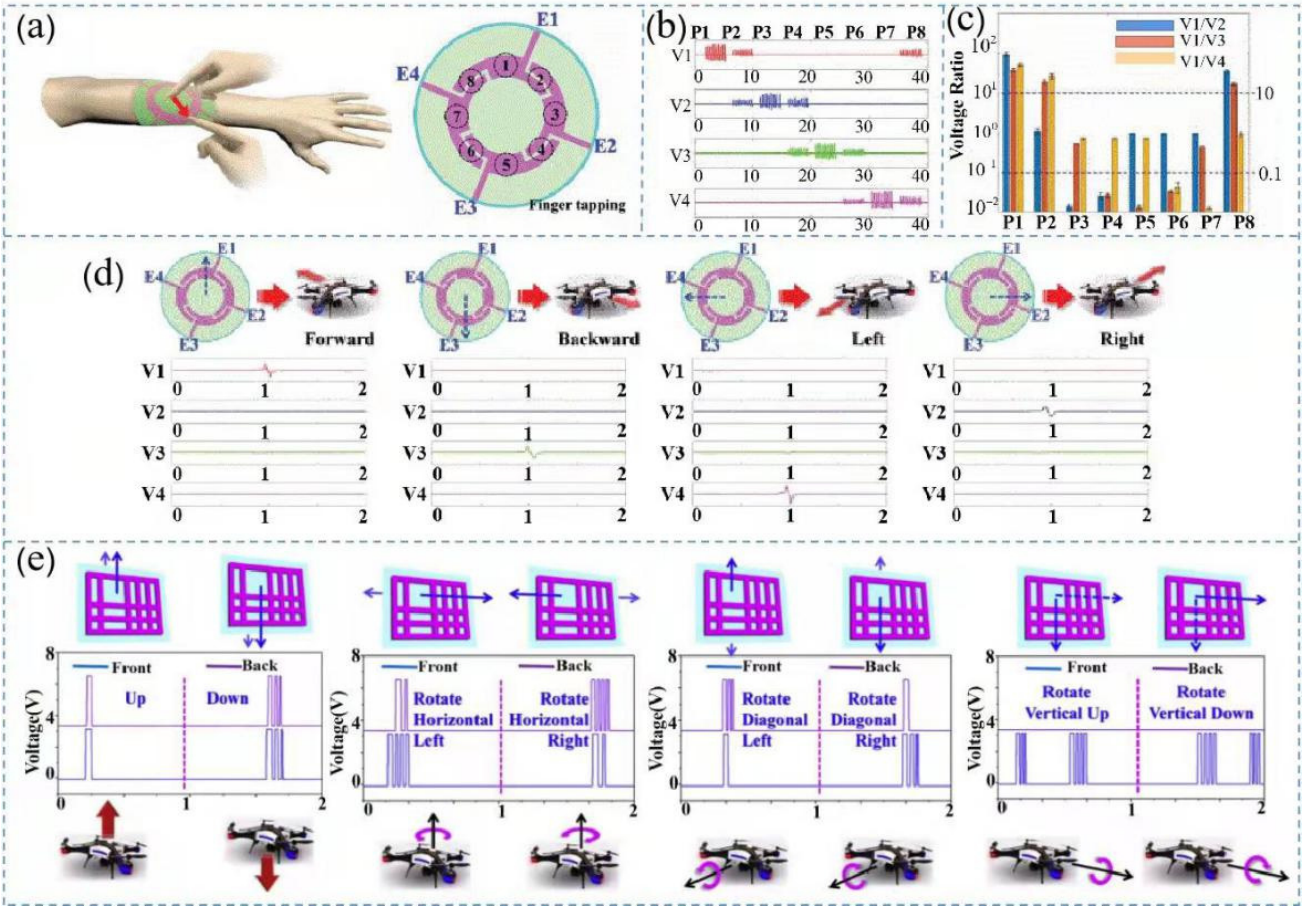

Figure 8. Virtual UAV control based on TENG: (**a**) triboelectric patch attached to the skin of a human arm; (**b**,**c**) output signals corresponding to finger tapping and sliding of the patch; (**d**) triboelectric patch controlling signal output corresponding to the horizontal movement of the UAV, Reprinted with permission from Ref. [104]. Copyright 2020 IEEE; and (**e**) corresponding signal output of the UAV when it moved through 3D space. Reprinted with permission from Ref. [40]. Copyright 2019 Nano Energy.

Due to the large size, poor portability, and difficult operation of the DT-HMI, a new TENG-based sensor was developed to control the movement of a virtual object. The structure of the sensor was three-dimensional, symmetrical, and composed of eight independent sensing electrodes and two touch balls, with human–computer interaction functions, to realize three-dimensional force information perception and VR control [123]. Thus, by analyzing the relevant properties of the force and the electrode, the triboelectric mechanism was used for the first time to detect a six-axis direction in 3D space. As a result, the researchers successfully realized the control function of the sensor in a VR interface. To avoid electromagnetic interference between the eight sensing signals, the following method was adopted [124]. First, the circuit in the A/D converter used differential input. Then, the

sensor was set with a high threshold trigger in the software to distinguish instructions from the interference. Figure 10a–h shows a schematic diagram of the controlling parts for virtual assembly and the corresponding axial voltage changes. By controlling the movements of each part and by selecting and releasing certain instructions, the three parts operated in turn to complete the assembly process [125]. Figure 10i,j shows a schematic depicting the controlled movements of virtual dice in a game.

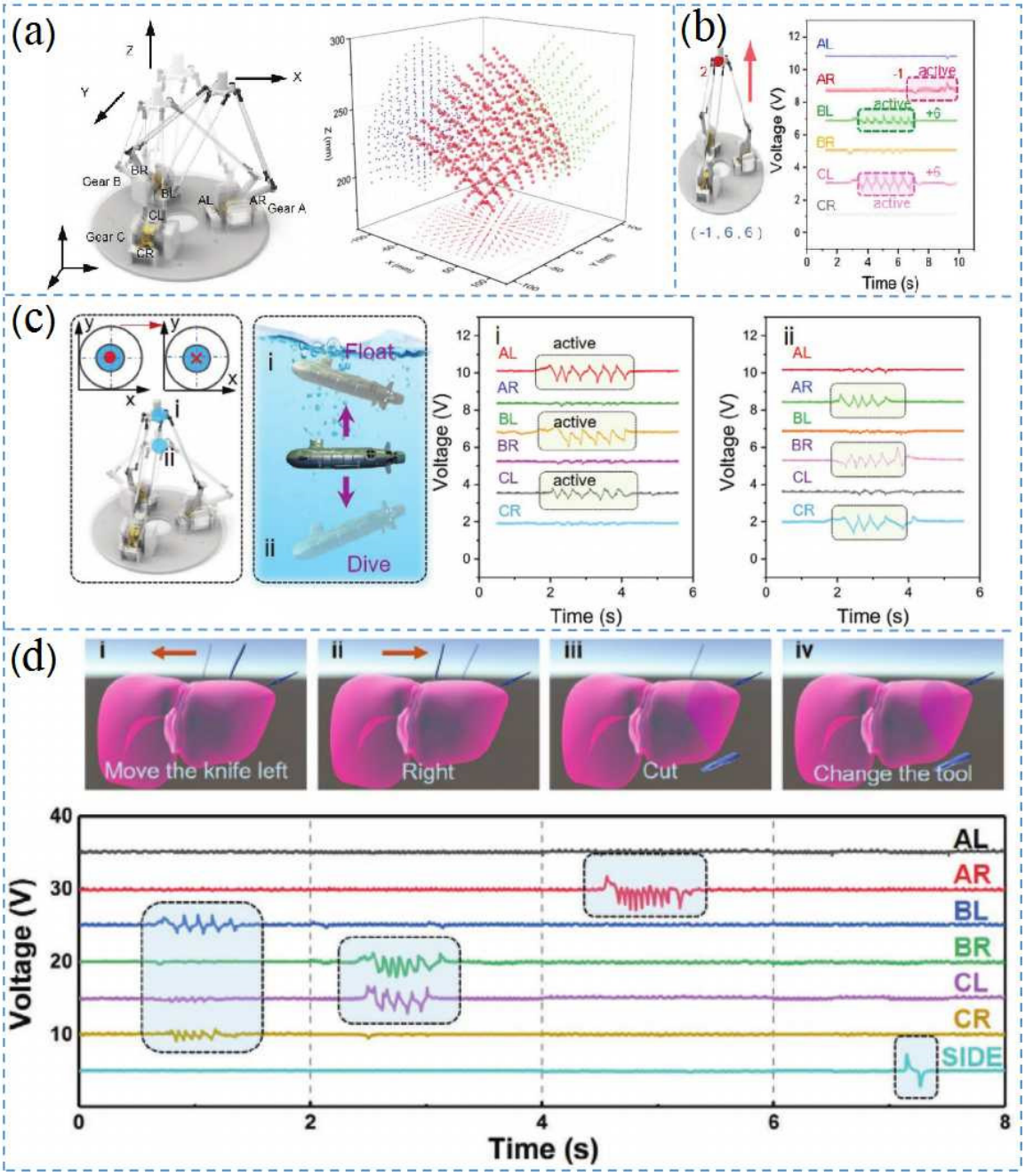

Figure 9. Application of delta-parallel-inspired human–machine interface (DT-HMI) on AR and VR, Reprinted with permission from ref. [34]. Copyright 2021 Advanced Materials Technologies. (**a**) delta manipulator movement controlling the platform based on self-powered triboelectric nanogenerator and its reachable spatial points; (**b**) output electrical signal of the platform when the manipulator moved; (**c**) platform controlling the submarine's movement during rising and diving and corresponding output voltage changes; and (**d**) augmented reality surgery training program for liver resection with DT-HMI.

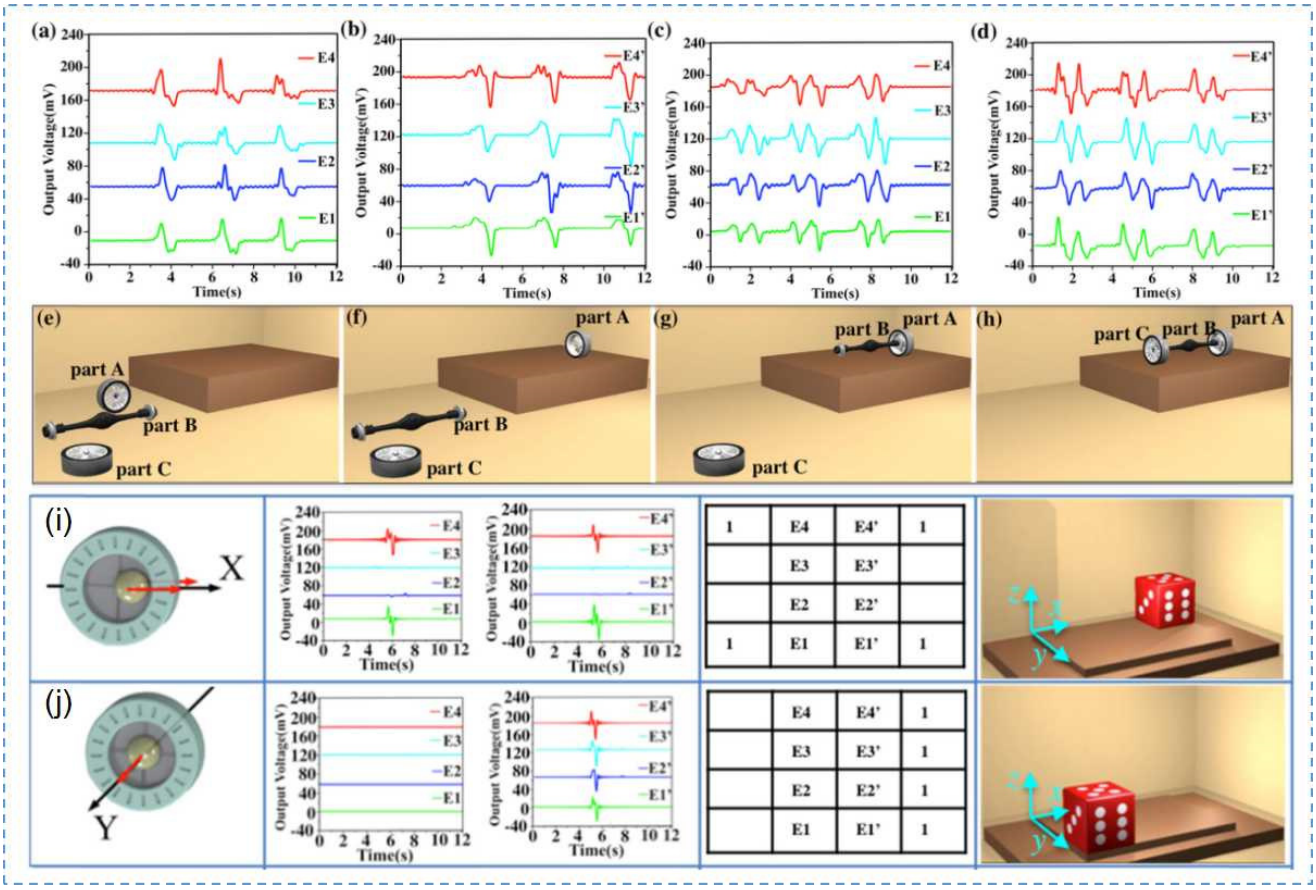

Figure 10. Using 3D self-powered sensor AR interface of virtual assembly, Reprinted with permission from Ref. [41]. Copyright 2018 Nano Energy. (**a**–**h**) part assembly process and corresponding voltage changes; and (**i**,**j**) relationship between six-axis operation strategy for 3D control sensor and voltage curve with AR interface control dice.

Tactile sensing plays an important role in VR and AR systems. Based on the ET interface formed by the TENG and spherical electrode array, Yuxiang et al. proposed a self-powered, painless, and highly sensitive ET system for a virtual tactile experience [126]. The structure of the ET unit is shown in Figure 11a [127]. This TENG-based ET system could be used in many fields, including for virtual haptic displays, Braille commands (Figure 11b) [128], intelligent protective clothing (Figure 11c), and even neural stimulation. The conversion of mechanical energy into direct current was also important for the next generation of self-contained Internet of Things and real-time virtual reality control. By using a porous material with frictional polarity reversal as the charge transport carrier, the charge was transferred unidirectionally between the hyper-negative and hyper-positive materials and the repulsive discharge through the wire electrode [129], forming a stable DC output (Figure 11d). Due to the charge transfer and repulsive discharges, obtaining a much higher DC output voltage was easier compared to the air breakdown mechanism [130]. Figure 11e shows a racing control game in a virtual space, based on continuous DC double-crossing TENGs (DC-DTENG). The continuous control of acceleration, constant speed, and further acceleration and deceleration was identified with real-time connection in real and virtual space [131]. Notably, the car in the virtual space was completely controlled by the corresponding continuous output signals of the real DC-DTENG with mechanical activity.

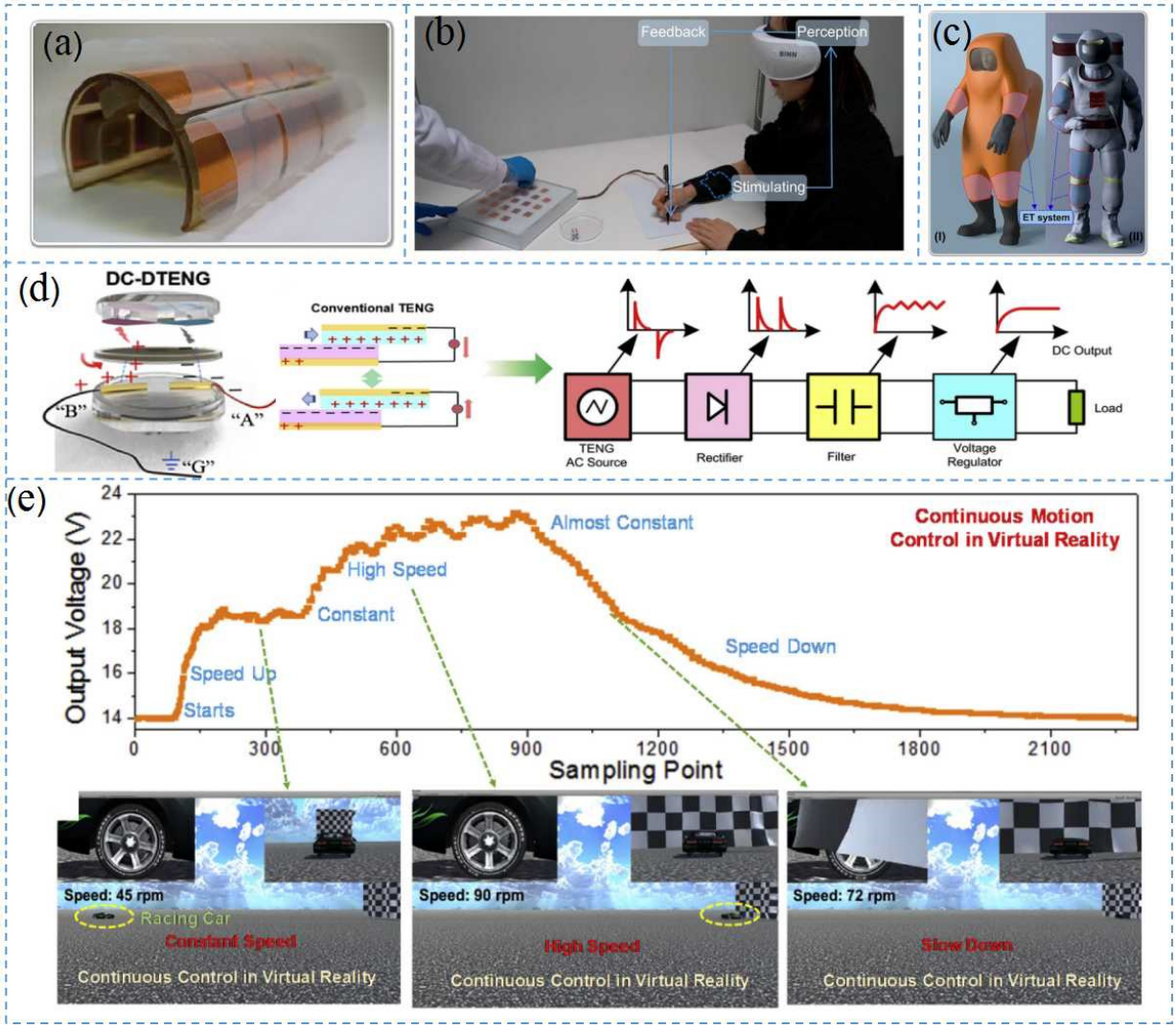

Figure 11. VR application of TENG: (**a**) unit structure of a self-powered, painless, and highly sensitive electro-tactile (ET) system based on TENG and spherical electrode arrays; (**b**) ET system applied to a dynamic braille display; (**c**) positive pressure suits and spacesuits equipped with ET systems, Reprinted with permission from ref. [39]. Copyright 2021 Science Advances; (**d**) DC-DTENG using an external electric device for DC output; and (**e**) DC-DTENG controlling the output voltage when the virtual vehicle performed at different speeds, Reprinted with permission from ref. [43]. Copyright 2020 Nano Energy.

In this paper, various TENG-based designs for AR and VR applications were summarized. Among them, flexible wearable devices made from two-dimensional materials were the most common, such as flexible electronic system designed by Yuxiang Shi et al., which could be worn on the arm for virtual environment control. Additionally, we highlighted waterproof textiles designed by Feng Wen et al., and the flexible control patch designed by Qiongfeng Shi et al., which could be worn on the human body to realize energy collection. The advantages of these designs included their small size, wearability, flexible operation, and low cost. These designs mainly differed in their wearable portions, as some were gloves and some were two-dimensional patches worn on the arm. In addition, the application scenarios were different, as some were used to control the computer screen, some were used for energy harvesting in real sports, and others were used in the field of biomedicine to realize simulated surgery.

6. Future Applications for TENG

TENG may likely be widely used in the medical field in the future. In recent years, the novel coronavirus epidemic has swept the world, which has significantly impacted human health. To monitor the health status of patients, TENG-based breathing sensors could be integrated with masks to monitor patients in real time. The respiratory status of a patient is shown in Figure 12a,b [132]. Integrating TENG with cancer treatment equipment could also be used to monitor their condition at home for an extended period without the need for an external power supply, as shown in Figure 12c [133]. A TENG-based biodegradable bandage sensor could be used to monitor the physiological state of the human body in real time, and the sensor could be reused, as shown in Figure 12d,e [134]. The TENG-based electroporation system has been shown to deliver drugs to mice, as presented in Figure 12f. If TENG could be combined with AR and VR in telemedicine and surgical treatment applications, it would benefit more patients. Therefore, TENG experiments in the medical field may likely be implemented into practical applications, offering significant contributions to the medical field and a benefit to human health.

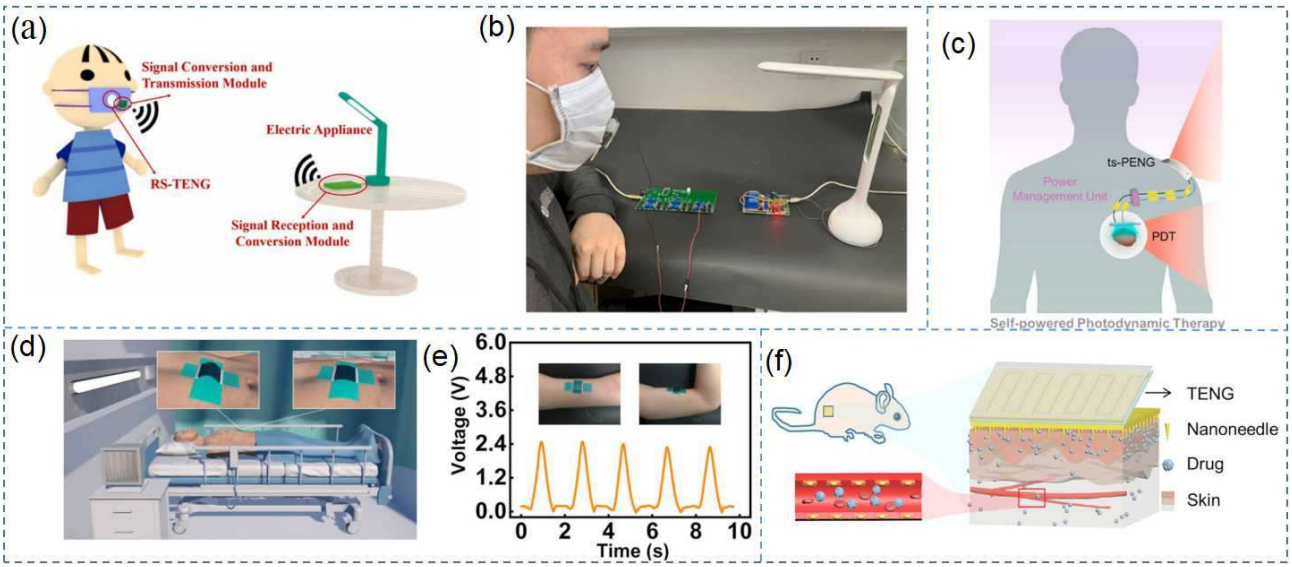

Figure 12. Use of TENG in future medical applications. (**a**,**b**) TENG-based respiratory monitoring face mask. Reprinted with permission from ref. [132]. Copyright 2022 Nano Energy; (**c**) TENG-based cancer treatment device. Reprinted with permission from ref. [133]. Copyright 2022 Nano Energy; (**d**) TENG-based bandage sensor; (**e**) bandage sensor attached to the arm to measure the voltage signal. Reprinted with permission from ref. [134]. Copyright 2022 Nano Energy; (**f**) schematic diagram of drug delivery based on TENG.

7. Summary and Outlook

This paper described in detail the types of materials that can be used for triboelectric nanogenerators, including PTFE and PDMS, which are the most commonly used triboelectric materials for the triboelectric layer in TENGs, especially for TENGs operating in transverse sliding and independent triboelectric layer modes. In addition to material selection, a better understanding of materials is needed to improve the triboelectrification effect, such as chemical etching and coating, as it can be used to fit the two friction materials more closely together to improve the TENG power output. This paper also described the applications of triboelectric nanogenerators in AR, VR, and other wearable electronic devices, and summarized the design methods of TENGs as self-powered sensor modules in these devices.

The current method of designing a self-powered sensor module is relatively complicated and difficult to integrate with electronic equipment; therefore, it is difficult to realize for large-scale industrial production. The design and integration of triboelectric

nanogenerators requires further research. Moreover, the stability and reliability of TENGs may seriously degrade due to the unavoidable mechanical and environmental effects that the devices are often subjected to during use. These factors can easily result in material and device failure, causing problems such as lower output voltage, shortened lifespan, and potential safety hazards. Therefore, TENG robustness and reliability are issues that must still be addressed. In the future, nanogenerators may require more in-depth research regarding applications in the field of wearable electronic equipment, especially in the field of medical detection devices. The pursuit of future medical detection devices is focused on lightweight and family-oriented applications, which is not sufficient for every patient. Users want to check their own health status; thus, if wearable nanogenerators are to have better medical field applications in the future, they must be inseparable from the choice of materials, such as those with good biocompatibility, good sweat resistance, flexibility, and mechanical stability. At the same time, the corrosion resistance and degradation of materials in physiological environments should be considered, and new device integration and packaging technologies should be developed to fully realize the wide use of TENGs.

Author Contributions: Conceptualization, J.S. and R.D.; methodology, J.S.; validation, J.S., R.D. and M.Z.; writing—original draft preparation, J.S.; writing—review and editing, J.S.; supervision, X.L.; project administration, X.L.; funding acquisition, X.L. All authors have read and agreed to the published version of the manuscript.

Funding: This research was funded by [Science and Technology Department of Henan Province] grant number [202102210392].

Institutional Review Board Statement: Not applicable.

Informed Consent Statement: Not applicable.

Data Availability Statement: No new data were created or analyzed in this study. Data sharing is not applicable to this article.

Conflicts of Interest: The authors declare no conflict of interest.

References

1. Rathore, S.; Sharma, S.; Swain, B.P.; Ghadai, R.K. A Critical Review on Triboelectric Nanogenerator. *IOP Conf. Ser. Mater. Sci. Eng.* **2018**, *377*, 012186. [CrossRef]
2. Zou, H.; Zhang, Y.; Guo, L.; Wang, P.; He, X.; Dai, G.; Zheng, H.; Chen, C.; Wang, A.C.; Xu, C.; et al. Quantifying the Triboelectric Series. *Nat. Commun.* **2019**, *10*, 1427. [CrossRef] [PubMed]
3. Khandelwal, G.; Maria Joseph Raj, N.P.; Kim, S.J. Materials Beyond Conventional Triboelectric Series for Fabrication and Applications of Triboelectric Nanogenerators. *Adv. Energy Mater.* **2021**, *11*, 2101170. [CrossRef]
4. Zhang, R.; Olin, H. Material Choices for Triboelectric Nanogenerators: A Critical Review. *EcoMat* **2020**, *2*, e12062. [CrossRef]
5. Wang, Z.L. On Maxwell's Displacement Current for Energy and Sensors: The Origin of Nanogenerators. *Mater. Today* **2017**, *20*, 74–82. [CrossRef]
6. Liu, G.; Xiao, L.; Chen, C.; Liu, W.; Pu, X.; Wu, Z.; Hu, C.; Wang, Z.L. Power Cables for Triboelectric Nanogenerator Networks for Large-Scale Blue Energy Harvesting. *Nano Energy* **2020**, *75*, 104975. [CrossRef]
7. Zi, Y.; Wang, J.; Wang, S.; Li, S.; Wen, Z.; Guo, H.; Wang, Z.L. Effective Energy Storage from a Triboelectric Nanogenerator. *Nat. Commun.* **2016**, *7*, 10987. [CrossRef]
8. Chen, J.; Yang, J.; Li, Z.; Fan, X.; Zi, Y.; Jing, Q.; Guo, H.; Wen, Z.; Pradel, K.C.; Niu, S.; et al. Networks of Triboelectric Nanogenerators for Harvesting Water Wave Energy: A Potential Approach toward Blue Energy. *ACS Nano* **2015**, *9*, 3324–3331. [CrossRef]
9. Zhai, N.; Wen, Z.; Chen, X.; Wei, A.; Sha, M.; Fu, J.; Liu, Y.; Zhong, J.; Sun, X. Blue Energy: Blue Energy Collection toward All-Hours Self-Powered Chemical Energy Conversion (Adv. Energy Mater. 33/2020). *Adv. Energy Mater.* **2020**, *10*, 2070139. [CrossRef]
10. Zhou, X.; Parida, K.; Halevi, O.; Liu, Y.; Xiong, J.; Magdassi, S.; Lee, P.S. All 3D-Printed Stretchable Piezoelectric Nanogenerator with Non-Protruding Kirigami Structure. *Nano Energy* **2020**, *72*, 104676. [CrossRef]
11. Bharti, D.K.; Gupta, M.K.; Kumar, R.; Sathish, N.; Srivastava, A.K. Non-Centrosymmetric Zinc Silicate-Graphene Based Transparent Flexible Piezoelectric Nanogenerator. *Nano Energy* **2020**, *73*, 104821. [CrossRef]
12. Mao, Y.; Zhang, N.; Tang, Y.; Wang, M.; Chao, M.; Liang, E. A Paper Triboelectric Nanogenerator for Self-Powered Electronic Systems. *Nanoscale* **2017**, *9*, 14499–14505. [CrossRef]

13. Qin, K.; Chen, C.; Pu, X.; Tang, Q.; He, W.; Liu, Y.; Zeng, Q.; Liu, G.; Guo, H.; Hu, C. Magnetic Array Assisted Triboelectric Nanogenerator Sensor for Real-Time Gesture Interaction. *Nano-Micro Lett.* **2021**, *13*, 51. [CrossRef]
14. Wan, J.; Wang, H.; Miao, L.; Chen, X.; Song, Y.; Guo, H.; Xu, C.; Ren, Z.; Zhang, H. A Flexible Hybridized Electromagnetic-Triboelectric Nanogenerator and Its Application for 3D Trajectory Sensing. *Nano Energy* **2020**, *74*, 104878. [CrossRef]
15. Chiu, C.M.; Chen, S.W.; Pao, Y.P.; Huang, M.Z.; Chan, S.W.; Lin, Z.H. A Smart Glove with Integrated Triboelectric Nanogenerator for Self-Powered Gesture Recognition and Language Expression. *Sci. Technol. Adv. Mater.* **2019**, *20*, 964–971. [CrossRef]
16. Guo, H.; Yeh, M.H.; Lai, Y.C.; Zi, Y.; Wu, C.; Wen, Z.; Hu, C.; Wang, Z.L. All-in-One Shape-Adaptive Self-Charging Power Package for Wearable Electronics. *ACS Nano* **2016**, *10*, 10580–10588. [CrossRef]
17. Wen, Z.; Yang, Y.; Sun, N.; Li, G.; Liu, Y.; Chen, C.; Shi, J.; Xie, L.; Jiang, H.; Bao, D.; et al. A Wrinkled PEDOT:PSS Film Based Stretchable and Transparent Triboelectric Nanogenerator for Wearable Energy Harvesters and Active Motion Sensors. *Adv. Funct. Mater.* **2018**, *28*, 1803684. [CrossRef]
18. Wang, S.; He, M.; Weng, B.; Gan, L.; Zhao, Y.; Li, N.; Xie, Y. Stretchable and Wearable Triboelectric Nanogenerator Based on Kinesio Tape for Self-Powered Human Motion Sensing. *Nanomaterials* **2018**, *8*, 657. [CrossRef]
19. Zhang, Z.; Cai, J. High Output Triboelectric Nanogenerator Based on PTFE and Cotton for Energy Harvester and Human Motion Sensor. *Curr. Appl. Phys.* **2021**, *22*, 1–5. [CrossRef]
20. Cheedarala, R.K.; Song, J. Il Harvesting of Flow Current through Implanted Hydrophobic PTFE Surface within Silicone-Pipe as Liquid Nanogenerator. *Sci. Rep.* **2022**, *12*, 1–14. [CrossRef]
21. Liu, H.; Dong, J.; Zhou, H.; Yang, X.; Xu, C.; Yao, Y.; Zhou, G.; Zhang, S.; Song, Q. Real-Time Acid Rain Sensor Based on a Triboelectric Nanogenerator Made of a PTFE-PDMS Composite Film. *ACS Appl. Electron. Mater.* **2021**, *3*, 4162–4171. [CrossRef]
22. Li, Z.B.; Li, H.Y.; Fan, Y.J.; Liu, L.; Chen, Y.H.; Zhang, C.; Zhu, G. Small-Sized, Lightweight, and Flexible Triboelectric Nanogenerator Enhanced by PTFE/PDMS Nanocomposite Electret. *ACS Appl. Mater. Interfaces* **2019**, *11*, 20370–20377. [CrossRef] [PubMed]
23. Liu, Y.; Li, E.; Yan, Y.; Lin, Z.; Chen, Q.; Wang, X.; Shan, L.; Chen, H.; Guo, T. A One-Structure-Layer PDMS/Mxenes Based Stretchable Triboelectric Nanogenerator for Simultaneously Harvesting Mechanical and Light Energy. *Nano Energy* **2021**, *86*, 106118. [CrossRef]
24. Hajra, S.; Padhan, A.M.; Sahu, M.; Alagarsamy, P.; Lee, K.; Kim, H.J. Lead-Free Flexible Bismuth Titanate-PDMS Composites: A Multifunctional Colossal Dielectric Material for Hybrid Piezo-Triboelectric Nanogenerator to Sustainably Power Portable Electronics. *Nano Energy* **2021**, *89*, 106316. [CrossRef]
25. Yang, C.R.; Ko, C.T.; Chang, S.F.; Huang, M.J. Study on Fabric-Based Triboelectric Nanogenerator Using Graphene Oxide/Porous PDMS as a Compound Friction Layer. *Nano Energy* **2022**, *92*, 106791. [CrossRef]
26. Lee, K.; Mhin, S.; Han, H.S.; Kwon, O.; Kim, W.B.; Song, T.; Kang, S.; Kim, K.M. A High-Performance PDMS-Based Triboelectric Nanogenerator Fabricated Using Surface-Modified Carbon Nanotubes. *J. Mater. Chem. A* **2022**, *10*, 1299–1308. [CrossRef]
27. Vijoy, K.V.; John, H.; Saji, K.J. Self-Powered Ultra-Sensitive Millijoule Impact Sensor Using Room Temperature Cured PDMS Based Triboelectric Nanogenerator. *Microelectron. Eng.* **2022**, *251*, 111664. [CrossRef]
28. Cai, Y.W.; Zhang, X.N.; Wang, G.G.; Li, G.Z.; Zhao, D.Q.; Sun, N.; Li, F.; Zhang, H.Y.; Han, J.C.; Yang, Y. A Flexible Ultra-Sensitive Triboelectric Tactile Sensor of Wrinkled PDMS/MXene Composite Films for E-Skin. *Nano Energy* **2021**, *81*, 105663. [CrossRef]
29. Wang, J.; Qian, S.; Yu, J.; Zhang, Q.; Yuan, Z.; Sang, S.; Zhou, X.; Sun, L. Flexible and Wearable PDMS-Based Triboelectric Nanogenerator for Self-Powered Tactile Sensing. *Nanomaterials* **2019**, *9*, 1304. [CrossRef]
30. Zhang, B.; Tang, Y.; Dai, R.; Wang, H.; Sun, X.; Qin, C.; Pan, Z.; Liang, E.; Mao, Y. Breath-Based Human–Machine Interaction System Using Triboelectric Nanogenerator. *Nano Energy* **2019**, *64*, 103953. [CrossRef]
31. Seol, M.; Kim, S.; Cho, Y.; Byun, K.E.; Kim, H.; Kim, J.; Kim, S.K.; Kim, S.W.; Shin, H.J.; Park, S. Triboelectric Series of 2D Layered Materials. *Adv. Mater.* **2018**, *30*. [CrossRef] [PubMed]
32. Chao, S.; Ouyang, H.; Jiang, D.; Fan, Y.; Li, Z. Triboelectric Nanogenerator Based on Degradable Materials. *EcoMat* **2021**, *3*, 1–19. [CrossRef]
33. Chen, T.; Shi, Q.; Yang, Z.; Liu, J.; Liu, H.; Sun, L.; Lee, C. A Self-Powered Six-Axis Tactile Sensor by Using Triboelectric Mechanism. *Nanomaterials* **2018**, *8*, 503. [CrossRef] [PubMed]
34. Hou, C.; Geng, J.; Yang, Z.; Tang, T.; Sun, Y.; Wang, F.; Liu, H.; Chen, T.; Sun, L. A Delta-Parallel-Inspired Human Machine Interface by Using Self-Powered Triboelectric Nanogenerator Toward 3D and VR/AR Manipulations. *Adv. Mater. Technol.* **2021**, *6*, 1–14. [CrossRef]
35. Liu, X.-M.; Niu, Z.-Y.; Zhang, B.-B.; Du, M.-Z.; Chen, P.-B. Zoom Unit in Augmented Reality: Liquid Lens. *Sci. Adv. Mater.* **2021**, *13*, 537–544. [CrossRef]
36. Pu, X.; Guo, H.; Chen, J.; Wang, X.; Xi, Y.; Hu, C.; Wang, Z.L. Eye Motion Triggered Self-Powered Mechnosensational Communication System Using Triboelectric Nanogenerator. *Sci. Adv.* **2017**, *3*, 1–8. [CrossRef]
37. Liu, X.M.; Zhang, B.B.; Niu, Z.Y.; Du, M.Z.; Li, S.X. Research Progress of Liquid Crystal Polymer Composites in Augmented and Virtual Reality. *Sci. Adv. Mater.* **2021**, *13*, 522–529. [CrossRef]
38. He, T.; Sun, Z.; Shi, Q.; Zhu, M.; Anaya, D.V.; Xu, M.; Chen, T.; Yuce, M.R.; Thean, A.V.Y.; Lee, C. Self-Powered Glove-Based Intuitive Interface for Diversified Control Applications in Real/Cyber Space. *Nano Energy* **2019**, *58*, 641–651. [CrossRef]
39. Shi, Y.; Wang, F.; Tian, J.; Li, S.; Fu, E.; Nie, J.; Lei, R.; Ding, Y.; Chen, X.; Wang, Z.L. Self-Powered Electro-Tactilesystem for Virtual Tactile Experiences. *Sci. Adv.* **2021**, *7*, 1–11. [CrossRef]

40. Shi, Q.; Qiu, C.; He, T.; Wu, F.; Zhu, M.; Dziuban, J.A.; Walczak, R.; Yuce, M.R.; Lee, C. Triboelectric Single-Electrode-Output Control Interface Using Patterned Grid Electrode. *Nano Energy* **2019**, *60*, 545–556. [CrossRef]
41. Chen, T.; Zhao, M.; Shi, Q.; Yang, Z.; Liu, H.; Sun, L.; Ouyang, J.; Lee, C. Novel Augmented Reality Interface Using a Self-Powered Triboelectric Based Virtual Reality 3D-Control Sensor. *Nano Energy* **2018**, *51*, 162–172. [CrossRef]
42. Wen, F.; Sun, Z.; He, T.; Shi, Q.; Zhu, M.; Zhang, Z.; Li, L.; Zhang, T.; Lee, C. Machine Learning Glove Using Self-Powered Conductive Superhydrophobic Triboelectric Textile for Gesture Recognition in VR/AR Applications. *Adv. Sci.* **2020**, *7*, 1–15. [CrossRef] [PubMed]
43. Zhu, J.; Wang, H.; Zhang, Z.; Ren, Z.; Shi, Q.; Liu, W.; Lee, C. Continuous Direct Current by Charge Transportation for Next-Generation IoT and Real-Time Virtual Reality Applications. *Nano Energy* **2020**, *73*, 104760. [CrossRef]
44. Kim, W.G.; Kim, D.W.; Tcho, I.W.; Kim, J.K.; Kim, M.S.; Choi, Y.K. Triboelectric Nanogenerator: Structure, Mechanism, and Applications. *ACS Nano* **2021**, *15*, 258–287. [CrossRef] [PubMed]
45. Cao, Z.; Chu, Y.; Wang, S.; Wu, Z.; Ding, R.; Ye, X. A Strategy to Reduce Air Breakdown Effect and Boost Output Energy for Contact-Separation Mode Triboelectric Nanogenerator. In Proceedings of the 2021 21st International Conference on Solid-State Sensors, Actuators and Microsystems (Transducers), Orlando, FL, USA, 20–24 June 2021; pp. 451–454. [CrossRef]
46. Liu, Y.; Liu, G.; Bu, T.; Zhang, C. Effects of Interfacial Acid–Base on the Performance of Contact–Separation Mode Triboelectric Nanogenerator. *Mater. Today Energy* **2021**, *20*, 100686. [CrossRef]
47. Song, W.Z.; Qiu, H.J.; Zhang, J.; Yu, M.; Ramakrishna, S.; Wang, Z.L.; Long, Y.Z. Sliding Mode Direct Current Triboelectric Nanogenerators. *Nano Energy* **2021**, *90*, 106531. [CrossRef]
48. Xia, Z.; Feng, P.Y.; Jing, X.; Li, H.; Mi, H.Y.; Liu, Y. Design and Optimization Principles of Cylindrical Sliding Triboelectric Nanogenerators. *Micromachines* **2021**, *12*, 567. [CrossRef]
49. Lee, Y.; Kang, S.G.; Jeong, J. Sliding Triboelectric Nanogenerator with Staggered Electrodes. *Nano Energy* **2021**, *86*, 106062. [CrossRef]
50. Zhou, L.; Liu, D.; Wang, J.; Wang, Z.L. Triboelectric Nanogenerators: Fundamental Physics and Potential Applications. *Friction* **2020**, *8*, 481–506. [CrossRef]
51. Sun, W.; Jiang, Z.; Xu, X.; Han, Q.; Chu, F. Harmonic Balance Analysis of Output Characteristics of Free-Standing Mode Triboelectric Nanogenerators. *Int. J. Mech. Sci.* **2021**, *207*, 106668. [CrossRef]
52. Zou, H.X.; Zhao, L.C.; Wang, Q.; Gao, Q.H.; Yan, G.; Wei, K.X.; Zhang, W.M. A Self-Regulation Strategy for Triboelectric Nanogenerator and Self-Powered Wind-Speed Sensor. *Nano Energy* **2022**, *95*, 106990. [CrossRef]
53. Chen, X.; Ren, Z.; Han, M.; Wan, J.; Zhang, H. Hybrid Energy Cells Based on Triboelectric Nanogenerator: From Principle to System. *Nano Energy* **2020**, *75*, 104980. [CrossRef]
54. Zhang, Z.; Bai, Y.; Xu, L.; Zhao, M.; Shi, M.; Wang, Z.L.; Lu, X. Triboelectric Nanogenerators with Simultaneous Outputs in Both Single-Electrode Mode and Freestanding-Triboelectric-Layer Mode. *Nano Energy* **2019**, *66*, 104169. [CrossRef]
55. Jo, S.; Kim, I.; Jayababu, N.; Kim, D. Performance-Enhanced Triboelectric Nanogenerator Based on the Double-Layered Electrode Effec. *Polymers* **2020**, *12*, 2854. [CrossRef]
56. Xu, C.; Zi, Y.; Wang, A.C.; Zou, H.; Dai, Y.; He, X.; Wang, P.; Wang, Y.C.; Feng, P.; Li, D.; et al. On the Electron-Transfer Mechanism in the Contact-Electrification Effect. *Adv. Mater.* **2018**, *30*, 1–9. [CrossRef]
57. Ahn, J.H.; Hwang, J.Y.; Kim, C.G.; Nam, G.H.; Ahn, K.K. Unsteady Streaming Flow Based TENG Using Hydrophobic Film Tube with Different Charge Affinity. *Nano Energy* **2020**, *67*, 104269. [CrossRef]
58. Liang, X.; Jiang, T.; Feng, Y.; Lu, P.; An, J.; Wang, Z.L. Triboelectric Nanogenerator Network Integrated with Charge Excitation Circuit for Effective Water Wave Energy Harvesting. *Adv. Energy Mater.* **2020**, *10*, 1–8. [CrossRef]
59. Wang, Z.L. Maxwell's Equations for a Mechano-Driven, Shape-Deformable, Charged-Media System, Slowly Moving at an Arbitrary Velocity Field v(r,T). *arXiv* **2022**, arXiv:2202.13768.
60. Niu, S.; Wang, Z.L. Theoretical Systems of Triboelectric Nanogenerators. *Nano Energy* **2014**, *14*, 161–192. [CrossRef]
61. Wang, Z.L. On the Expanded Maxwell's Equations for Moving Charged Media System—General Theory, Mathematical Solutions and Applications in TENG. *Mater. Today* **2021**, *52*, 348–363. [CrossRef]
62. Salauddin, M.; Rana, S.M.S.; Sharifuzzaman, M.; Rahman, M.T.; Park, C.; Cho, H.; Maharjan, P.; Bhatta, T.; Park, J.Y. A Novel MXene/Ecoflex Nanocomposite-Coated Fabric as a Highly Negative and Stable Friction Layer for High-Output Triboelectric Nanogenerators. *Adv. Energy Mater.* **2021**, *11*, 1–12. [CrossRef]
63. Rana, S.M.S.; Rahman, M.T.; Salauddin, M.; Sharma, S.; Maharjan, P.; Bhatta, T.; Cho, H.; Park, C.; Park, J.Y. Electrospun PVDF-TrFE/MXene Nanofiber Mat-Based Triboelectric Nanogenerator for Smart Home Appliances. *ACS Appl. Mater. Interfaces* **2021**, *13*, 4955–4967. [CrossRef] [PubMed]
64. Wang, Z.L. On the First Principle Theory of Nanogenerators from Maxwell's Equations. *Nano Energy* **2020**, *68*, 104272. [CrossRef]
65. Mariappan, V.K.; Krishnamoorthy, K.; Pazhamalai, P.; Kim, S.J. Exploring the Bifunctional Properties of Paper-like Carbyne-Enriched Carbon for Maintenance-Free Self-Powered Systems. *Mater. Adv.* **2020**, *1*, 1644–1652. [CrossRef]
66. Han, S.A.; Lee, J.H.; Seung, W.; Lee, J.; Kim, S.W.; Kim, J.H. Patchable and Implantable 2D Nanogenerator. *Small* **2021**, *17*, e1903519. [CrossRef] [PubMed]
67. Mariappan, V.K.; Krishnamoorthy, K.; Pazhamalai, P.; Natarajan, S.; Sahoo, S.; Nardekar, S.S.; Kim, S.J. Antimonene Dendritic Nanostructures: Dual-Functional Material for High-Performance Energy Storage and Harvesting Devices. *Nano Energy* **2020**, *77*, 105248. [CrossRef]

68. Farahani, A.; Zarei-Hanzaki, A.; Abedi, H.R.; Tayebi, L.; Mostafavi, E. Polylactic Acid Piezo-Biopolymers: Chemistry, Structural Evolution, Fabrication Methods, and Tissue Engineering Applications. *J. Funct. Biomater.* **2021**, *12*, 71. [CrossRef]
69. Kheradmandfard, M.; Penkov, O.V.; Kashani-Bozorg, S.F.; Lee, J.S.; Kim, C.-L.; Khadem, M.; Cho, S.-W.; Hanzaki, A.Z.; Kim, D.-E. Exceptional Improvement in the Wear Resistance of Biomedical β-Type Titanium Alloy with the Use of a Biocompatible Multilayer Si/DLC Nanocomposite Coating. *Ceram. Int.* **2022**. [CrossRef]
70. Le, T.H.; Mai, U.K.G.; Huynh, D.P.; Nguyen, H.T.; Luu, A.T.; Bui, V.T. Surfactant-Free GO-PLA Nanocomposite with Honeycomb Patterned Surface for High Power Antagonistic Bio-Triboelectric Nanogenerator. *J. Sci. Adv. Mater. Devices* **2022**, *7*, 100392. [CrossRef]
71. Chau, N.M.; Le, T.H.; Huynh, D.P.; Truong, T.H.; Nguyen Dinh, M.T.; La, T.T.H.; Bui, V.T. Surface Patterning of GO-S/PLA Nanocomposite with the Assistance of an Ionic Surfactant for High-Performance Triboelectric Nanogenerator. *Int. J. Energy Res.* **2021**, *45*, 20047–20056. [CrossRef]
72. Farahani, A.; Zarei-Hanzaki, A.; Abedi, H.R.; Haririan, I.; Akrami, M.; Aalipour, Z.; Tayebi, L. An Investigation into the Polylactic Acid Texturization through Thermomechanical Processing and the Improved D33 Piezoelectric Outcome of the Fabricated Scaffolds. *J. Mater. Res. Technol.* **2021**, *15*, 6356–6366. [CrossRef]
73. Aalipour, Z.; Zarei-Hanzaki, A.; Moshiri, A.; Abedi, H.R.; Waryoba, D.; Kisko, A.; Karjalainen, L.P. Strain Dependency of Dynamic Recrystallization during Thermomechanical Processing of Mg-Gd-Y-Zn-Zr Alloy. *J. Mater. Res. Technol.* **2022**, *18*, 591–598. [CrossRef]
74. Zheng, T.; Yue, Z.; Wallace, G.G.; Du, Y.; Higgins, M.J. Nanoscale Piezoelectric Effect of Biodegradable PLA-Based Composite Fibers by Piezoresponse Force Microscopy. *Nanotechnology* **2020**, *31*, 37. [CrossRef]
75. Chakhchaoui, N.; Frahan, R.; Eddiai, A.; Meddad, M.; Cherkaoui, O.; Boughaleb, Y.; Van Langenhove, L. Improved Piezoelectric Properties of PLA/PZT Hybrid Composite Films. *IOP Conf. Ser. Mater. Sci. Eng.* **2020**, *827*, 5–10. [CrossRef]
76. Paghandeh, M.; Zarei-Hanzaki, A.; Abedi, H.R.; Vahidshad, Y.; Minarik, P. The Correlation of C-to-a Axial Ratio and Slip Activity of Martensite Including Microstructures during Thermomechanical Processing of Ti-6Al-4V Alloy. *J. Mater. Res. Technol.* **2022**, *18*, 577–583. [CrossRef]
77. Dudem, B.; Kim, D.H.; Mule, A.R.; Yu, J.S. Enhanced Performance of Microarchitectured PTFE-Based Triboelectric Nanogenerator via Simple Thermal Imprinting Lithography for Self-Powered Electronics. *ACS Appl. Mater. Interfaces* **2018**, *10*, 24181–24192. [CrossRef] [PubMed]
78. Xia, K.; Zhu, Z.; Zhang, H.; Xu, Z. A Triboelectric Nanogenerator as Self-Powered Temperature Sensor Based on PVDF and PTFE. *Appl. Phys. A Mater. Sci. Process.* **2018**, *124*, 520. [CrossRef]
79. Zhao, P.; Soin, N.; Prashanthi, K.; Chen, J.; Dong, S.; Zhou, E.; Zhu, Z.; Narasimulu, A.A.; Montemagno, C.D.; Yu, L.; et al. Emulsion Electrospinning of Polytetrafluoroethylene (PTFE) Nanofibrous Membranes for High-Performance Triboelectric Nanogenerators. *ACS Appl. Mater. Interfaces* **2018**, *10*, 5880–5891. [CrossRef]
80. Wang, M.; Zhang, N.; Tang, Y.; Zhang, H.; Ning, C.; Tian, L.; Li, W.; Zhang, J.; Mao, Y.; Liang, E. Single-Electrode Triboelectric Nanogenerators Based on Sponge-like Porous PTFE Thin Films for Mechanical Energy Harvesting and Self-Powered Electronics. *J. Mater. Chem. A* **2017**, *5*, 12252–12257. [CrossRef]
81. Li, G.Z.; Wang, G.G.; Ye, D.M.; Zhang, X.W.; Lin, Z.Q.; Zhou, H.L.; Li, F.; Wang, B.L.; Han, J.C. High-Performance Transparent and Flexible Triboelectric Nanogenerators Based on PDMS-PTFE Composite Films. *Adv. Electron. Mater.* **2019**, *5*, 1–8. [CrossRef]
82. Su, H.; Wang, X.; Li, C.; Wang, Z.; Wu, Y.; Zhang, J.; Zhang, Y.; Zhao, C.; Wu, J.; Zheng, H. Enhanced Energy Harvesting Ability of Polydimethylsiloxane-BaTiO3-Based Flexible Piezoelectric Nanogenerator for Tactile Imitation Application. *Nano Energy* **2021**, *83*, 105809. [CrossRef]
83. He, X.; Mu, X.; Wen, Q.; Wen, Z.; Yang, J.; Hu, C.; Shi, H. Flexible and Transparent Triboelectric Nanogenerator Based on High Performance Well-Ordered Porous PDMS Dielectric Film. *Nano Res.* **2016**, *9*, 3714–3724. [CrossRef]
84. Ko, Y.H.; Nagaraju, G.; Lee, S.H.; Yu, J.S. PDMS-Based Triboelectric and Transparent Nanogenerators with ZnO Nanorod Arrays. *ACS Appl. Mater. Interfaces* **2014**, *6*, 6631–6637. [CrossRef] [PubMed]
85. Dudem, B.; Huynh, N.D.; Kim, W.; Kim, D.H.; Hwang, H.J.; Choi, D.; Yu, J.S. Nanopillar-Array Architectured PDMS-Based Triboelectric Nanogenerator Integrated with a Windmill Model for Effective Wind Energy Harvesting. *Nano Energy* **2017**, *42*, 269–281. [CrossRef]
86. Pan, L.; Wang, J.; Wang, P.; Gao, R.; Wang, Y.C.; Zhang, X.; Zou, J.J.; Wang, Z.L. Liquid-FEP-Based U-Tube Triboelectric Nanogenerator for Harvesting Water-Wave Energy. *Nano Res.* **2018**, *11*, 4062–4073. [CrossRef]
87. Wu, H.; Wang, Z.; Zi, Y. Multi-Mode Water-Tube-Based Triboelectric Nanogenerator Designed for Low-Frequency Energy Harvesting with Ultrahigh Volumetric Charge Density. *Adv. Energy Mater.* **2021**, *11*, 2100038. [CrossRef]
88. Lin, L.; Xie, Y.; Niu, S.; Wang, S.; Yang, P.K.; Wang, Z.L. Robust Triboelectric Nanogenerator Based on Rolling Electrification and Electrostatic Induction at an Instantaneous Energy Conversion Efficiency of ∼55%. *ACS Nano* **2015**, *9*, 922–930. [CrossRef]
89. Xiong, J.; Cui, P.; Chen, X.; Wang, J.; Parida, K.; Lin, M.F.; Lee, P.S. Skin-Touch-Actuated Textile-Based Triboelectric Nanogenerator with Black Phosphorus for Durable Biomechanical Energy Harvesting. *Nat. Commun.* **2018**, *9*, 1–9. [CrossRef]
90. Roy, S.; Ko, H.U.; Maji, P.K.; Van Hai, L.; Kim, J. Large Amplification of Triboelectric Property by Allicin to Develop High Performance Cellulosic Triboelectric Nanogenerator. *Chem. Eng. J.* **2020**, *385*, 123723. [CrossRef]
91. Yao, C.; Yin, X.; Yu, Y.; Cai, Z.; Wang, X. Chemically Functionalized Natural Cellulose Materials for Effective Triboelectric Nanogenerator Development. *Adv. Funct. Mater.* **2017**, *27*, 1–7. [CrossRef]

92. Kim, M.; Lee, C.J.; Kim, S.H.; Park, M.U.; Yang, J.; Yi, Y.; Yoo, K.H. Tribodiffusion-Driven Triboelectric Nanogenerators Based on MoS2. *J. Mater. Chem. A* **2021**, *9*, 10316–10325. [CrossRef]
93. Zhang, L.M.; Han, C.B.; Jiang, T.; Zhou, T.; Li, X.H.; Zhang, C.; Wang, Z.L. Multilayer Wavy-Structured Robust Triboelectric Nanogenerator for Harvesting Water Wave Energy. *Nano Energy* **2016**, *22*, 87–94. [CrossRef]
94. Xu, M.; Wang, S.; Zhang, S.L.; Ding, W.; Kien, P.T.; Wang, C.; Li, Z.; Pan, X.; Wang, Z.L. A Highly-Sensitive Wave Sensor Based on Liquid-Solid Interfacing Triboelectric Nanogenerator for Smart Marine Equipment. *Nano Energy* **2019**, *57*, 574–580. [CrossRef]
95. Ko, Y.H.; Lee, S.H.; Leem, J.W.; Yu, J.S. High Transparency and Triboelectric Charge Generation Properties of Nano-Patterned PDMS. *RSC Adv.* **2014**, *4*, 10216–10220. [CrossRef]
96. Feng, S.; Zhong, Z.; Wang, Y.; Xing, W.; Drioli, E. Progress and Perspectives in PTFE Membrane: Preparation, Modification, and Applications. *J. Memb. Sci.* **2018**, *549*, 332–349. [CrossRef]
97. Shao, J.; Willatzen, M.; Shi, Y.; Wang, Z.L. 3D Mathematical Model of Contact-Separation and Single-Electrode Mode Triboelectric Nanogenerators. *Nano Energy* **2019**, *60*, 630–640. [CrossRef]
98. Cao, Z.; Chu, Y.; Wang, S.; Ye, X. Theoretical Analysis of Sensor Properties of Contact-Separation Mode Nanogenerator-Based Sensors. *Nano Energy* **2021**, *79*, 105450. [CrossRef]
99. Wang, Z.L.; Lin, L.; Chen, J.; Niu, S.; Zi, Y. *Triboelectric Nanogenerator: Lateral Sliding Mode*; Springer: Cham, Switzerland, 2016; ISBN 9783319400396.
100. Zhu, M.; Sun, Z.; Zhang, Z.; Shi, Q.; He, T.; Liu, H.; Chen, T.; Lee, C. Haptic-Feedback Smart Glove as a Creative Human-Machine Interface (HMI) for Virtual/Augmented Reality Applications. *Sci. Adv.* **2020**, *6*, eaaz8693. [CrossRef]
101. Sun, H.; Tian, H.; Yang, Y.; Xie, D.; Zhang, Y.C.; Liu, X.; Ma, S.; Zhao, H.M.; Ren, T.L. A Novel Flexible Nanogenerator Made of ZnO Nanoparticles and Multiwall Carbon Nanotube. *Nanoscale* **2013**, *5*, 6117–6123. [CrossRef]
102. Kwon, D.H.; Kwon, J.H.; Jeong, J.; Lee, Y.; Biswas, S.; Lee, D.W.; Lee, S.; Bae, J.H.; Kim, H. Textile Triboelectric Nanogenerators with Diverse 3d-Spacer Fabrics for Improved Output Voltage. *Electronics* **2021**, *10*, 937. [CrossRef]
103. Chen, T.; Shi, Q.; Zhu, M.; He, T.; Sun, L.; Yang, L.; Lee, C. Triboelectric Self-Powered Wearable Flexible Patch as 3D Motion Control Interface for Robotic Manipulator. *ACS Nano* **2018**, *12*, 11561–11571. [CrossRef] [PubMed]
104. Shi, Q.; Zhang, Z.; Lee, C. Multi-Functional Human-Machine Interface (HMI) Using Flexible Wearable Triboelectric Nanogenerator for Diversified Interacting Applications. In Proceedings of the 2019 19th International Conference on Micro and Nanotechnology for Power Generation and Energy Conversion Applications (PowerMEMS), Krakow, Poland, 2–6 December 2019; pp. 1–4. [CrossRef]
105. Lin, H.; He, M.; Jing, Q.; Yang, W.; Wang, S.; Liu, Y.; Zhang, Y.; Li, J.; Li, N.; Ma, Y.; et al. Angle-Shaped Triboelectric Nanogenerator for Harvesting Environmental Wind Energy. *Nano Energy* **2019**, *56*, 269–276. [CrossRef]
106. Zhou, D.; Wang, N.; Yang, T.; Wang, L.; Cao, X.; Wang, Z.L. A Piezoelectric Nanogenerator Promotes Highly Stretchable and Self-Chargeable Supercapacitors. *Mater. Horizons* **2020**, *7*, 2158–2167. [CrossRef]
107. Tengs, T.N. A High Sensitivity Self-Powered Wind Speed Sensor Based on Triboelectric Nanogenerators (TENGs). *Sensors* **2021**, *21*, 2951. [CrossRef]
108. Zhang, N.; Qin, C.; Feng, T.; Li, J.; Yang, Z.; Sun, X.; Liang, E.; Mao, Y.; Wang, X. Non-Contact Cylindrical Rotating Triboelectric Nanogenerator for Harvesting Kinetic Energy from Hydraulics. *Nano Res.* **2020**, *13*, 1903–1907. [CrossRef]
109. Wang, M.; Zhang, J.; Tang, Y.; Li, J.; Zhang, B.; Liang, E.; Mao, Y.; Wang, X. Air-Flow-Driven Triboelectric Nanogenerators for Self-Powered Real-Time Respiratory Monitoring. *ACS Nano* **2018**, *12*, 6156–6162. [CrossRef]
110. Alghunaim, N.S. Spectroscopic Analysis of PMMA/PVC Blends Containing CoCl2. *Results Phys.* **2015**, *5*, 331–336. [CrossRef]
111. Jiang, J.; Guan, Q.; Liu, Y.; Sun, X.; Wen, Z. Abrasion and Fracture Self-Healable Triboelectric Nanogenerator with Ultrahigh Stretchability and Long-Term Durability. *Adv. Funct. Mater.* **2021**, *31*, 2105380. [CrossRef]
112. Wissler, M.; Mazza, E. Mechanical Behavior of an Acrylic Elastomer Used in Dielectric Elastomer Actuators. *Sensors Actuators A Phys.* **2007**, *134*, 494–504. [CrossRef]
113. Zhao, X.; Zhang, Z.; Xu, L.; Gao, F.; Zhao, B.; Ouyang, T.; Kang, Z.; Liao, Q.; Zhang, Y. Fingerprint-Inspired Electronic Skin Based on Triboelectric Nanogenerator for Fine Texture Recognition. *Nano Energy* **2021**, *85*, 106001. [CrossRef]
114. Kim, I.; Roh, H.; Yu, J.; Jayababu, N.; Kim, D. Boron Nitride Nanotube-Based Contact Electrification-Assisted Piezoelectric Nanogenerator as a Kinematic Sensor for Detecting the Flexion–Extension Motion of a Robot Finger. *ACS Energy Lett.* **2020**, *5*, 1577–1585. [CrossRef]
115. Tang, Y.; Zhou, H.; Sun, X.; Diao, N.; Wang, J.; Zhang, B.; Qin, C.; Liang, E.; Mao, Y. Triboelectric Touch-Free Screen Sensor for Noncontact Gesture Recognizing. *Adv. Funct. Mater.* **2020**, *30*, 1907893. [CrossRef]
116. Tang, Y.; Zhou, H.; Sun, X.; Feng, T.; Zhao, X.; Wang, Z.; Liang, E.; Mao, Y. Cotton-Based Naturally Wearable Power Source for Self-Powered Personal Electronics. *J. Mater. Sci.* **2020**, *55*, 2462–2470. [CrossRef]
117. Liao, W.; Liu, X.; Li, Y. Transparent, Stretchable, Temperature-Stable and Self-Healing Ionogel-Based Triboelectric Nanogenerator for Biomechanical Energy Collection. *Nano Res.* **2021**, *15*, 2060–2068. [CrossRef]
118. Rana, S.M.S.; Rahman, M.T.; Salauddin, M.; Maharjan, P.; Bhatta, T.; Cho, H.; Park, J.Y. A Human-Machine Interactive Hybridized Biomechanical Nanogenerator as a Self-Sustainable Power Source for Multifunctional Smart Electronics Applications. *Nano Energy* **2020**, *76*, 105025. [CrossRef]

119. Li, H.; Koh, C.S.L.; Lee, Y.H.; Zhang, Y.; Phan-Quang, G.C.; Zhu, C.; Liu, Z.; Chen, Z.; Sim, H.Y.F.; Lay, C.L.; et al. A Wearable Solar-Thermal-Pyroelectric Harvester: Achieving High Power Output Using Modified RGO-PEI and Polarized PVDF. *Nano Energy* **2020**, *73*, 104723. [CrossRef]
120. Chen, J.; Pu, X.; Guo, H.; Tang, Q.; Feng, L.; Wang, X.; Hu, C. A Self-Powered 2D Barcode Recognition System Based on Sliding Mode Triboelectric Nanogenerator for Personal Identification. *Nano Energy* **2018**, *43*, 253–258. [CrossRef]
121. Yuan, M.; Li, C.; Liu, H.; Xu, Q.; Xie, Y. A 3D-Printed Acoustic Triboelectric Nanogenerator for Quarter-Wavelength Acoustic Energy Harvesting and Self-Powered Edge Sensing. *Nano Energy* **2021**, *85*, 105962. [CrossRef]
122. Surmenev, R.A.; Chernozem, R.V.; Pariy, I.O.; Surmeneva, M.A. A Review on Piezo- and Pyroelectric Responses of Flexible Nano- and Micropatterned Polymer Surfaces for Biomedical Sensing and Energy Harvesting Applications. *Nano Energy* **2021**, *79*, 105442. [CrossRef]
123. Ji, X.; Zhao, T.; Zhao, X.; Lu, X.; Li, T. Triboelectric Nanogenerator Based Smart Electronics via Machine Learning. *Adv. Mater. Technol.* **2020**, *5*, 1900921. [CrossRef]
124. Xiang, S.; Liu, D.; Jiang, C.; Zhou, W.; Ling, D.; Zheng, W.; Sun, X.; Li, X.; Mao, Y.; Shan, C. Liquid-Metal-Based Dynamic Thermoregulating and Self-Powered Electronic Skin. *Adv. Funct. Mater.* **2021**, *31*, 2100940. [CrossRef]
125. Zhu, M.; Yi, Z.; Yang, B.; Lee, C. Making Use of Nanoenergy from Human–Nanogenerator and Self-Powered Sensor Enabled Sustainable Wireless IoT Sensory Systems. *Nano Today* **2021**, *36*, 101016. [CrossRef]
126. Hanani, Z.; Izanzar, I.; Amjoud, M.; Mezzane, D.; Lahcini, M.; Uršič, H.; Prah, U.; Saadoune, I.; El Marssi, M.; Luk'yanchuk, I.A.; et al. Lead-Free Nanocomposite Piezoelectric Nanogenerator Film for Biomechanical Energy Harvesting. *Nano Energy* **2021**, *81*, 105661. [CrossRef]
127. Zhang, W.; Deng, L.; Yang, L.; Yang, P.; Diao, D.; Wang, P.; Wang, Z.L. Multilanguage-Handwriting Self-Powered Recognition Based on Triboelectric Nanogenerator Enabled Machine Learning. *Nano Energy* **2020**, *77*, 105174. [CrossRef]
128. Tcho, I.W.; Kim, W.G.; Choi, Y.K. A Self-Powered Character Recognition Device Based on a Triboelectric Nanogenerator. *Nano Energy* **2020**, *70*, 104534. [CrossRef]
129. Cheng, P.; Guo, H.; Wen, Z.; Zhang, C.; Yin, X.; Li, X.; Liu, D.; Song, W.; Sun, X.; Wang, J.; et al. Largely Enhanced Triboelectric Nanogenerator for Efficient Harvesting of Water Wave Energy by Soft Contacted Structure. *Nano Energy* **2019**, *57*, 432–439. [CrossRef]
130. Jiang, J.; Zhang, Y.; Shen, Q.; Zhu, Q.; Ge, X.; Liu, Y.; Wen, Z.; Sun, X. A Self-Powered Hydrogen Leakage Sensor Based on Impedance Adjustable Windmill-like Triboelectric Nanogenerator. *Nano Energy* **2021**, *89*, 106453. [CrossRef]
131. Guo, R.; Zhang, H.; Pei, Z.; Yang, S.; Ge, C.; Sang, S.; Hao, R. A Voiceprint Recognition Sensor Based on a Fully 3D-Printed Triboelectric Nanogenerator via a One-Step Molding Route. *Adv. Eng. Mater.* **2020**, *22*, 1901560. [CrossRef]
132. Lu, Q.; Chen, H.; Zeng, Y.; Xue, J.; Cao, X.; Wang, N.; Wang, Z. Intelligent Facemask Based on Triboelectric Nanogenerator for Respiratory Monitoring. *Nano Energy* **2022**, *91*, 106612. [CrossRef]
133. Chen, M.; Zhou, Y.; Lang, J.; Li, L.; Zhang, Y. Triboelectric Nanogenerator and Artificial Intelligence to Promote Precision Medicine for Cancer. *Nano Energy* **2022**, *92*, 106783. [CrossRef]
134. Wang, T.; Li, S.; Tao, X.; Yan, Q.; Wang, X.; Chen, Y.; Huang, F.; Li, H.; Chen, X.; Bian, Z. Fully Biodegradable Water-Soluble Triboelectric Nanogenerator for Human Physiological Monitoring. *Nano Energy* **2022**, *93*, 106787. [CrossRef]

MDPI
St. Alban-Anlage 66
4052 Basel
Switzerland
Tel. +41 61 683 77 34
Fax +41 61 302 89 18
www.mdpi.com

Nanomaterials Editorial Office
E-mail: nanomaterials@mdpi.com
www.mdpi.com/journal/nanomaterials

MDPI
St. Alban-Anlage 66
4052 Basel
Switzerland

Tel: +41 61 683 77 34

www.mdpi.com

ISBN 978-3-0365-5901-8